NATIONAL AERONAUTICS AND SPACE ADMINISTRATION

Cards

Space Programs Summary No. 37-33, Volume IV

for the period April 1, 1965, to May 31, 1965

Supporting Research and Advanced Development

GPO PRICE $ _____

CSFTI PRICE(S) $ _____

Hard copy (HC) 7.00

Microfiche (MF) 1.75

ff 653 July 65

JET PROPULSION LABORATORY
CALIFORNIA INSTITUTE OF TECHNOLOGY
PASADENA, CALIFORNIA

June 30, 1965

NATIONAL AERONAUTICS AND SPACE ADMINISTRATION

Space Programs Summary No. 37-33, Volume IV

for the period April 1, 1965, to May 31, 1965

Supporting Research and Advanced Development

JET PROPULSION LABORATORY
CALIFORNIA INSTITUTE OF TECHNOLOGY
PASADENA, CALIFORNIA

June 30, 1965

Preface

The *Space Programs Summary* is a six-volume, bimonthly publication that documents the current project activities and supporting research and advanced development efforts conducted or managed by JPL for the NASA space exploration programs. The titles of all volumes of the *Space Programs Summary* are:

Vol. I. The Lunar Program (Confidential)

Vol. II. The Planetary–Interplanetary Program (Confidential)

Vol. III. The Deep Space Network (Unclassified)

Vol. IV. Supporting Research and Advanced Development (Unclassified)

Vol. V. Supporting Research and Advanced Development (Confidential)

Vol. VI. Space Exploration Programs and Space Sciences (Unclassified)

The *Space Programs Summary*, Vol. VI consists of an unclassified digest of appropriate material from Vols. I, II, and III; an original presentation of technical supporting activities, including engineering development of environmental-test facilities, and quality assurance and reliability, and a reprint of the space science instrumentation studies of Vols. I and II.

W. H. Pickering, *Director*
Jet Propulsion Laboratory

Space Programs Summary No. 37-33, Volume IV

Prepared under Contract No. NAS 7-100, National Aeronautics & Space Administration

Contents

SYSTEMS DIVISION

GUIDANCE AND CONTROL DIVISION

Contents (Cont'd)

Contents (Cont'd)

ENGINEERING FACILITIES DIVISION

PROPULSION DIVISION

Contents (Cont'd)

SPACE SCIENCES DIVISION

Contents (Cont'd)

Contents (Cont'd)

SYSTEMS DIVISION

I. Systems Analysis

A. Effect of Non-Gravitational Perturbations on Minimum Energy Interplanetary Transfer Orbits

G. A. Flandro

1. Introduction

The purpose of this article is to establish the relative importance of several non-aerodynamic, non-gravitational orbital perturbations. Numerical results are given for the following effects: (1) solar radiation pressure, (2) reaction forces due to leaks in pressurized systems, (3) perturbation due to unbalanced attitude control reaction devices, (4) reaction force due to directional antenna emission, and (5) reaction force due to unsymmetrical emission of thermal energy from the spacecraft surfaces. Comparisons of these effects are made in terms of change of magnitude of the miss vector at the target planet, $\Delta\mathbf{B}$, which would result if the orbit were not corrected for the perturbing effect. Hohmann minimum energy ellipses are used as basis orbits for computational simplicity. An asymptotic expansion technique due to Kevorkian and Cole (Refs. 1 and 2) was utilized for most of the perturbation calculations. Mathematical models for the perturbing effects evaluated here were discussed previously in *SPS 37-30*, Vol. IV, pp. 6–14. The notation used is defined in Table 1.

Table 1. Definition of symbols

a_0	semi-major axis of unperturbed orbit
A	projected area of spacecraft in radial direction
ΔB	change in impact parameter due to perturbation
C_i	parameter defining magnitude of ith perturbation
$(C_f)_K$	solar radiation pressure force coefficient ($K = r, \phi, n$)
$(C_m)_K$	solar radiation pressure moment coefficient ($K = r, \phi, n$)
e	effective spacecraft surface emissivity
$(F_l)_K$	force due to gas leakage ($K = r, \phi, n$)
l_a	antenna moment arm
l_j	attitude control jet moment arm
m	spacecraft mass
P	antenna radiation power
T	time of flight
T_t	total high-gain transmission time
ΔT	radial temperature differential
ξ	attitude control jet unbalance factor
θ	angle between antenna pointing direction and $-r$ axis
Subscripts	
r	radial direction
ϕ	transverse direction
n	normal direction

Table 2. Typical spacecraft characteristics

Target	Semi-major axis of minimum energy orbit, AU	Spacecraft mass m, kg	Radial projected area A, m²	High-gain transmission power P, w	C_1, m²/kg	C_2, m²/kg	C_{10}, w/kg
Mercury	0.693	273	3.5	10	2.1×10^{-3}	—	1.9×10^{-3}
Venus (*Mariner II*)	0.861	203	4.0	3	2.7×10^{-3}	1.7×10^{-3} *	1.4×10^{-3}
Mars (*Mariner IV*)	1.26	260	11.0	10	4.7×10^{-3}	—	2×10^{-3}
Asteroid (Ceres)	1.89	500	3.0	10	1.8×10^{-3}	—	2×10^{-3}
Jupiter	3.10	590	3.0	20	2.5×10^{-3}	—	4×10^{-3}

*From flight data

2. Spacecraft Characteristics

The spacecraft parameters which determine the magnitudes of the microaccelerations produced by the perturbing effects c[illegible] collected into several characteristic dimensional groups as defined in Table 2. These are based on simplified versions of the perturbation models given in *SPS 37-30*, Vol. IV, pp. 6–14. The following assumptions were made to facilitate the order-of-magnitude perturbation calculations: (1) spacecraft mass remains constant from injection to planetary encounter, (2) vehicle is attitude-stabilized and Sun-oriented, (3) the dominating attitude disturbing moment is generated by solar radiation pressure acting on an asymmetrically-mounted high-gain antenna, (4) perturbing forces due to gas leakage from pressurized systems remain constant in direction and magnitude, (5) radio transmission from the directional antenna is uniformly distributed in time, and (6) high-gain antenna pointing direction remains essentially fixed throughout flight.

Typical values for the perturbation coefficients are given in Table 3 for several representative space vehicles. Flights beyond the orbit of Mars are assumed to involve spacecraft which do not utilize solar power generation. The parameters used in the calculations for these vehicles are based on the conceptual designs presented in Ref. 3.

3. Effect of Perturbations on Hohmann Orbits

The order-of-magnitude perturbation calculations were based on the "two time-variable" asymptotic expansion technique (Ref. 1 and *SPS 37-30*, Vol. IV, pp. 6–14). Radial perturbations proportional to the inverse square of the radial distance r were estimated by adjusting the solar gravitational constant.[1] Circular orbits with zero inclination to the ecliptic were assumed for all planets, and minimum energy transfer ellipses were utilized as basis orbits. The change in the magnitude of target miss vector B was calculated for each component of each perturbation,[2] and the results are presented in graphical form in

[1] Melbourne, W. G., "Radiation Pressure Perturbations of Interplanetary Trajectories," Technical Memorandum No. 312-151, Jet Propulsion Laboratory, Pasadena, California, December 11, 1961.

[2] B is a vector with magnitude equal to the perpendicular distance between the center of the target planet and the incoming asymptote of the unperturbed trajectory.

Table 3. Perturbation coefficients

Perturbation	Coefficient		
	Radial	Transverse	Normal
Solar radiation pressure	$C_1 = \frac{(C_f)_r A}{m}$	$C_2 = \frac{(C_f)_\theta A}{m}$	$C_3 = \frac{(C_f)_n A}{m}$
Leaks in pressurized system	$C_4 = \frac{(F_l)_r}{m}$	$C_5 = \frac{(F_l)_\theta}{m}$	$C_6 = \frac{(F_l)_n}{m}$
Attitude control reaction device unbalance	$C_7 = \left(\frac{\xi l_u}{l_l}\right)_r \frac{(C_f)_r A}{m}$	$C_8 = \left(\frac{\xi l_u}{l_l}\right)_\theta \frac{(C_f)_\theta A}{m}$	$C_9 = \left(\frac{\xi l_u}{l_l}\right)_n \frac{(C_f)_n A}{m}$
High-gain antenna emission	$C_{10} = \frac{P}{m}\left(\frac{T_t}{T}\right)\cos\theta$	$C_{11} = \frac{P}{m}\left(\frac{T_t}{T}\right)\sin\theta$	
Unsymmetrical emission of thermal energy	$C_{12} = \frac{e(\Delta T)^4 A}{m}$		

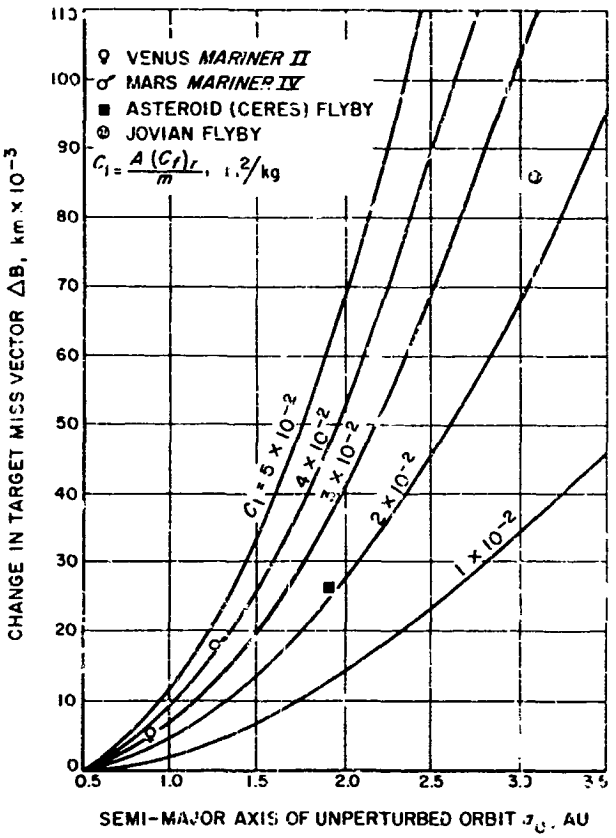

Fig. 1. Change in target miss vector due to solar radiation pressure (radial component)

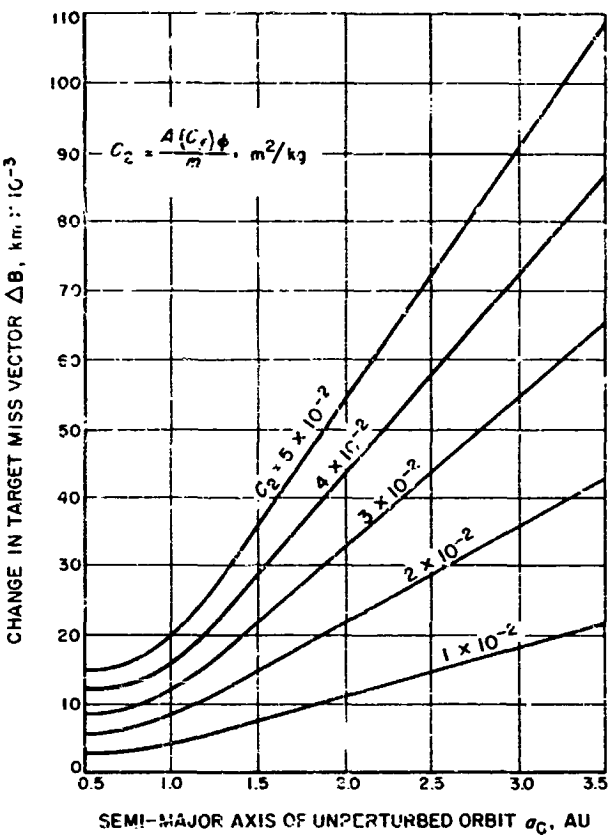

Fig. 2. Change in target miss vector due to solar radiation pressure (transverse component)

Figs. 1–12. The absolute value of the change in the miss vector, ΔB, in each case is plotted against the unperturbed semi-major axis of the transfer orbit. Plots are given for several values of the corresponding characteristic quantity C_i. These are intended to bracket the expected range of values for the spacecraft designs considered here. Plots are included for radial, transverse, and normal components of most perturbations, although transverse and normal components should be negligible for Sun-oriented, attitude-stabilized spacecraft in most cases. The plots indicate that the non-radial effects could become important for tumbling vehicles, for spacecraft with asymmetrical reflectivity patterns, and in the case of unbalanced attitude control devices with thrust components in the normal or tangential directions.

The effect of thermal energy emission was estimated by assuming a radiation pattern symmetrical about the radial direction with an average temperature differential ΔT between the illuminated and unilluminated surfaces. Non-radial effects may be of importance in the case of vehicle designs utilizing onboard energy generation systems with associated energy radiation devices. The plots of Fig. 12 are typical of solar-powered, Sun-oriented spacecraft. A value of $C_{12} = 10^4$ corresponds to a temperature differential of about 30°K.

No attempt has been made to include estimates for the perturbing effect of micrometeorite impacts, due to the present uncertainty in flux density. Some studies[3] indicate that perturbations from this source could exceed the solar radiation pressure effects. The results for the gas leak perturbation (Figs. 4, 5, 6) can be used for a rough estimate of the effect of micrometeorite flux (or other perturbation), if the acceleration is assumed constant in magnitude and direction throughout flight.

[3]Stephenson, R. R., "On the Possibility of Measurable Spacecraft Attitude and Trajectory Perturbations due to Micrometeoroid Pressure," IOM 312.5-66, Jet Propulsion Laboratory, Pasadena, California, January 7, 1965.

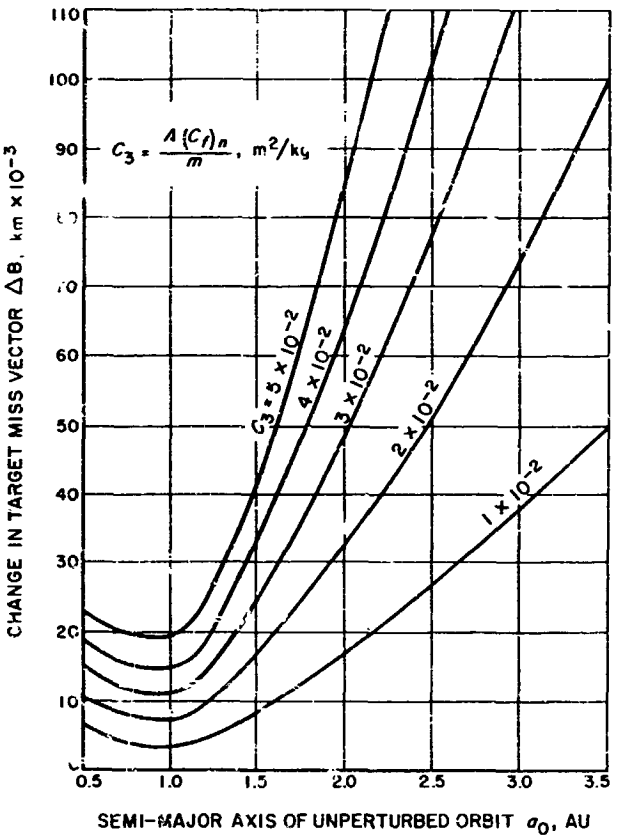

Fig. 3. Change in target miss vector due to solar radiation pressure (normal component)

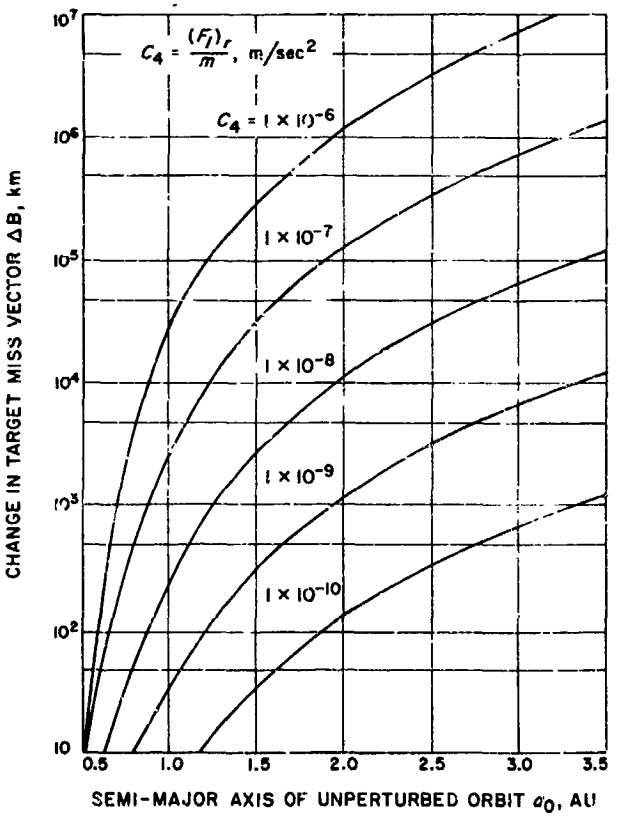

Fig. 4. Change in target miss vector due to pressurized system leaks (radial component)

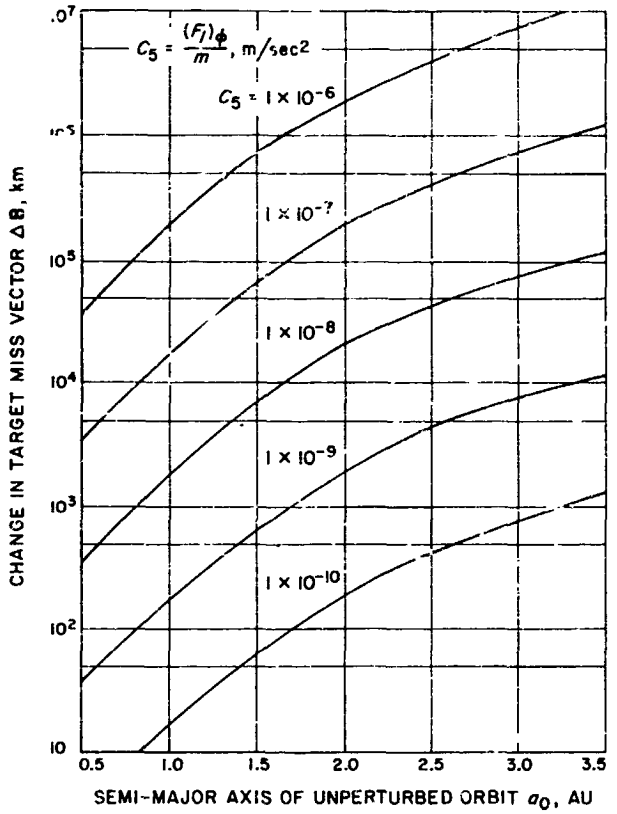

Fig. 5. Change in target miss vector due to pressurized system leaks (transverse component)

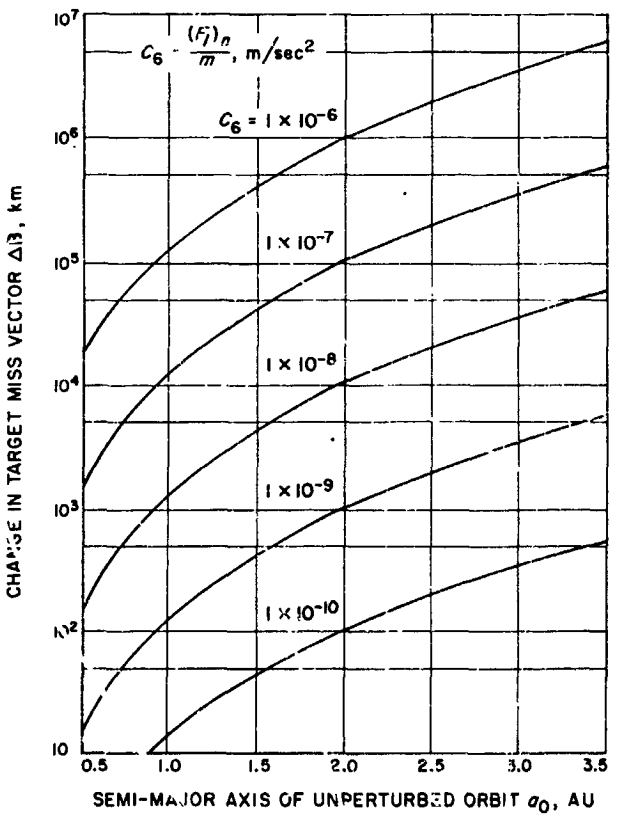

Fig. 6. Change in target miss vector due to pressurized system leaks (normal component)

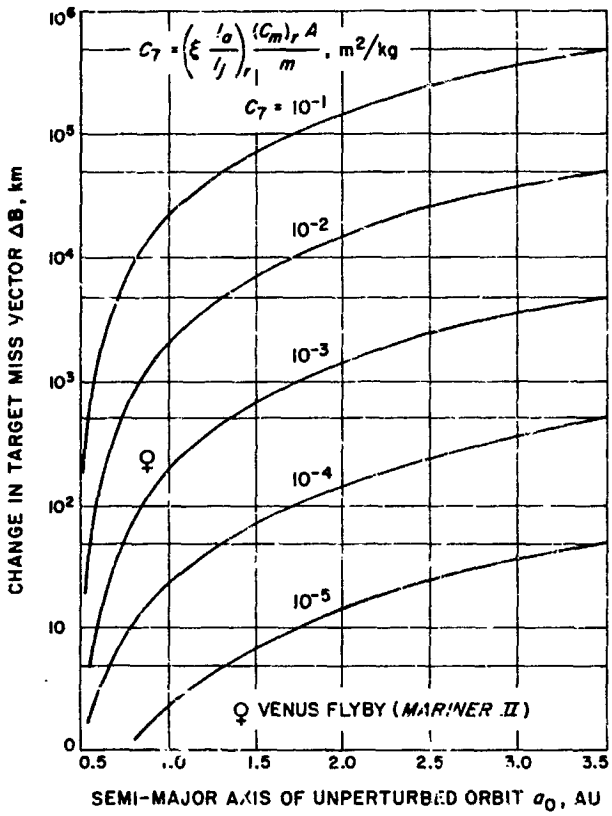

Fig. 7. Change in target miss vector due to unbalanced attitude control jets (radial component)

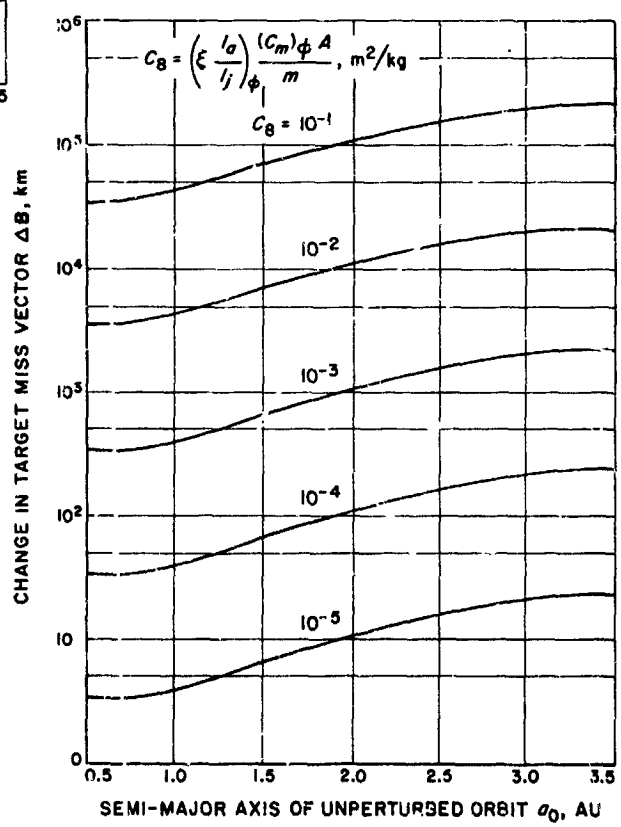

Fig. 8. Change in target miss vector due to unbalanced attitude control jets (transverse component)

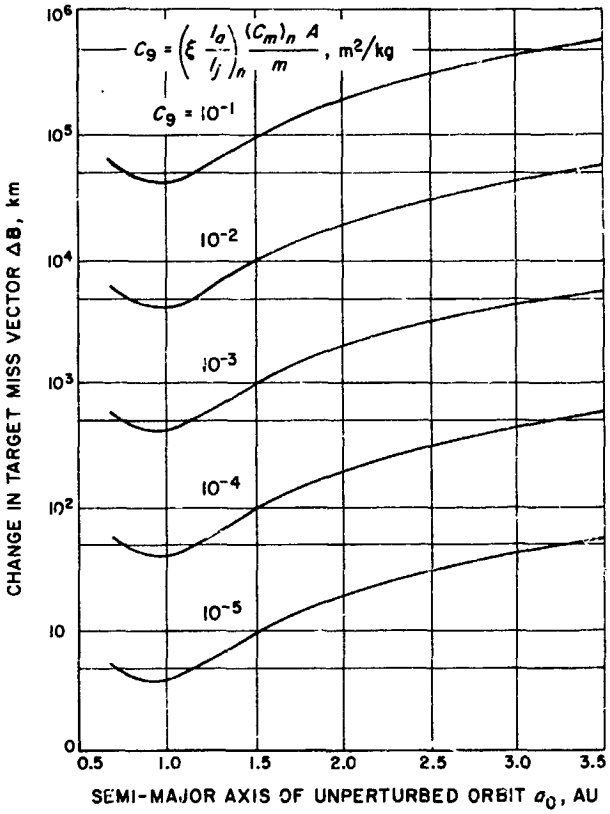

Fig. 9. Change in target miss vector due to unbalanced attitude control jets (normal component)

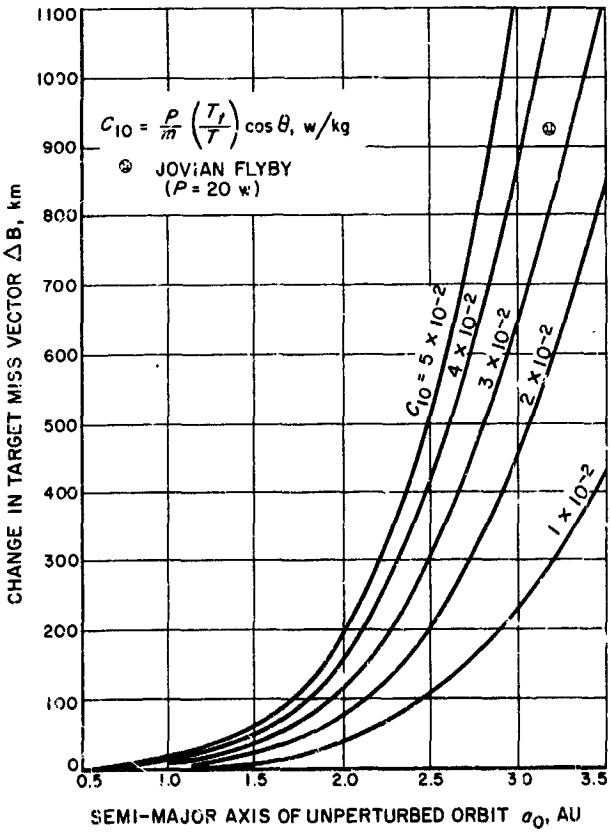

Fig. 10. Change in target miss vector due to high-gain antenna emission (radial component)

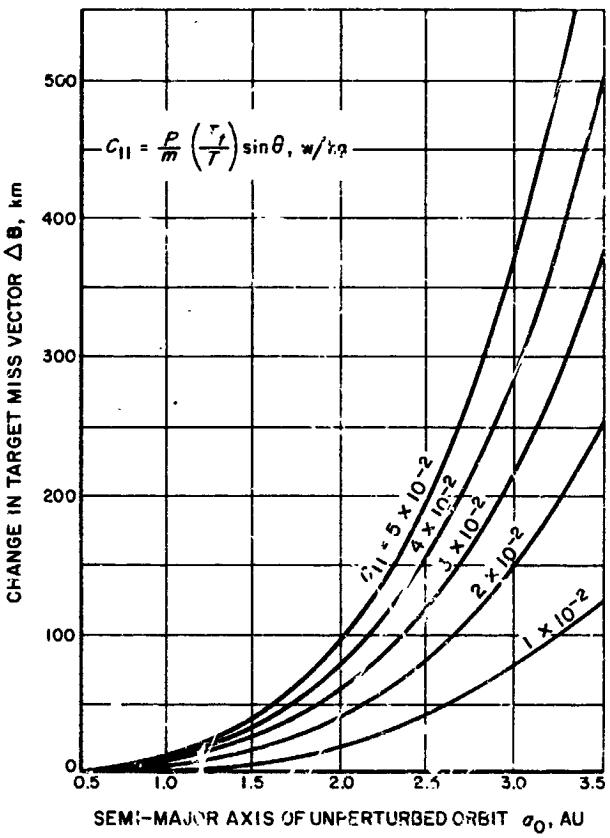

Fig. 11. Change in target miss vector due to high-gain antenna emission (transverse component)

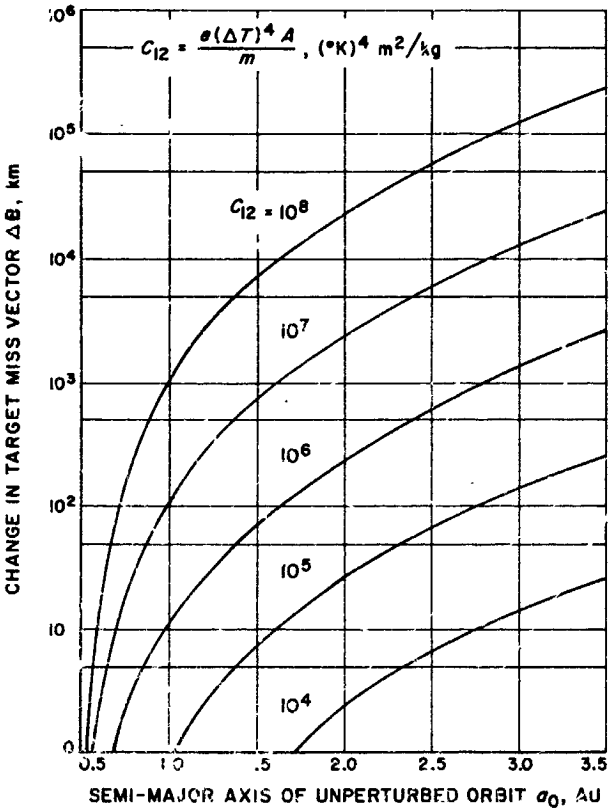

Fig. 12. Change in target miss vector due to thermal energy emission

B. An Investigation of the Orbit Redetermination Process Following the First Midcourse Maneuver

J. O. Light

1. Introduction to the Problem

The design and analysis of deep space missions requires a knowledge of our ability to determine the flight path of the spacecraft from Earth-based observations. In fulfillment of this requirement, pre-mission orbit determination techniques are utilized to predict the magnitude of the orbit determination uncertainties which will be encountered on various trajectories. These pre-mission studies are usually accomplished by the JPL Orbit Determination Program (ODP), a complex 7094 program which yields numerical characterizations of the covariance matrix of estimated quantities on a particular trajectory. The inherent complexity of this program, though necessary to derive accurate estimates for a specific trajectory, hinders its ability to explain the parametric dependence of the orbit determination knowledge upon certain geometric characteristics of trajectories. We thus need to develop analytical techniques and simple model simulations which can perform this task, and isolate those properties of the flight path which are truly crucial to adequate orbit determination. It is clear that such techniques will be essential to the eventual understanding of the complexities involved in the numerical solution of orbit determination problems. These types of analytic methods have been developed and used to investigate the characteristics of the orbit redetermination process following the first midcourse maneuver of an interplanetary mission.

2. Orbit Redetermination and the Simple-Model Simulation

On a typical interplanetary mission, the first midcourse correction to the trajectory is performed a few days past injection on the basis of the orbit determination knowledge accrued near the Earth. After this maneuver, an estimate of the new trajectory is obtained by using a priori estimates of the position and velocity of the probe, and new doppler data which is accumulated following the maneuver. A simple model has been employed to represent the trajectory of the spacecraft immediately following this first midcourse correction. The near-Earth portion of the trajectory is a hyperbola with one focus at the Earth. By the time of the midcourse maneuver, the probe is, for all practical purposes, on the asymptote of the escape hyperbola. To a first approximation, then, the probe is traveling away from the Earth on a straight line which is displaced from the Earth by some distance, conventionally referred to as $|\bar{b}|$, the magnitude of the miss vector. This geometry is shown in Fig. 13. For the purposes of this study, we shall assume that the motion of the probe consists of this nominal straight-line motion, with perturbations caused by effects such as the gravitational attraction of the Sun.

Also, for the purposes of this study, we shall assume that the pre-mission orbit determination process can be reduced to the following computations. If we derive a linear unbiased minimum variance estimate of n quantities q_j, using m doppler readings $\dot{\rho}_i$, and we assume that the noise on the doppler is stationary and uncorrelated, and we neglect a priori estimates, then the covariance matrix of the estimated quantities can be written:

$$\Lambda_q^* = \sigma_{\dot{\rho}}^2 \left[\sum_{i=1}^{m} B_i B_i^t \right]^{-1} \tag{1}$$

where

$$B_i^t \triangleq \left[\frac{\partial \dot{\rho}_i}{\partial q_1}, \frac{\partial \dot{\rho}_i}{\partial q_2}, \ldots, \frac{\partial \dot{\rho}_i}{\partial q_n} \right]$$

$\sigma_{\dot{\rho}}^2 \triangleq$ variance of doppler noise

$m \triangleq$ number of observations

The quality of the orbit determination knowledge obviously depends upon the partials $\partial \dot{\rho}_i / \partial q_n$. In particular, it can be easily demonstrated that the elements of the covariance matrix become unbounded if these partials are linearly dependent over the tracking interval; if these partials are almost linearly dependent, then the covariance matrix is large though finite, and poor orbit determination knowledge will be obtained. Our initial inquiry will then be directed toward the analytic form of these partials along the simple model of the probe's motion following the first midcourse maneuver.

In general, these partials can be derived as follows:

$$\dot{\rho}(t) = \frac{\overline{r(t)} \cdot \overline{v(t)}}{|\overline{r(t)}|} \tag{2}$$

where $\overline{r(t)}$ is the position vector of the spacecraft relative to the observing station, and $\overline{v(t)}$ is the velocity vector of the spacecraft relative to the observing station.

By differentiating, we obtain

$$\frac{\partial \dot{\rho}(t)}{\partial q_j} = \frac{1}{|\overline{r(t)}|} \left[\sum_{i=1}^{3} \left(r_i(t) \frac{\partial v_i(t)}{\partial q_j} + v_i(t) \frac{\partial r_i(t)}{\partial q_j} \right) \right]$$

$$- \frac{\overline{r(t)} \cdot \overline{v(t)}}{|\overline{r(t)}|^2} \frac{\partial}{\partial q_j} [|\overline{r(t)}|] \tag{3}$$

We shall assume that the quantities we want to estimate are the three components of the spacecraft's velocity immediately following the first midcourse maneuver. We shall further assume that the position of the spacecraft is known at the time of the midcourse maneuver, and that the maneuver contributes only velocity uncertainties, leaving the position known. The partial

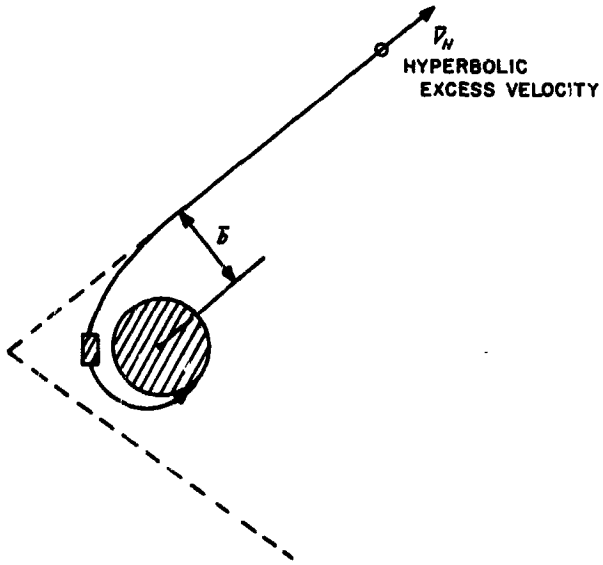

Fig. 13. Near-Earth geometry

derivatives that will result from this model are complex functions of the state vector in a general coordinate system. However, considerable simplification is possible with a proper choice of coordinate system, i.e., that coordinate system which takes advantage of the near straight-line motion of the spacecraft. When we begin tracking the spacecraft immediately following the first midcourse maneuver (hereafter referred to as time t_0), it is moving away from the Earth with a velocity $\bar{V}_H$. The plane determined by this velocity vector and the position vector from the barycenter of the Earth-Moon system to the probe is the plane of motion of the probe. As shown in Fig. 14, we will choose the 1 direction along the velocity vector of the probe at t_0, the 2 direction in the plane of motion perpendicular to 1, and the 3 direction out of the plane of motion, completing the orthogonal system.

Having assumed near straight-line motion of the spacecraft, and having specified the coordinate system and quantities to be estimated, it can be shown the general form of the partials in Eq. (3) reduces to

$$\frac{\partial \dot{\rho}(t)}{\partial v_{p1}(t_0)} = 1$$

$$\frac{\partial \dot{\rho}(t)}{\partial v_{p2}(t_0)} = \frac{r_2(t)}{\bar{V}_H}\left(\frac{t-t_0}{t}\right) + \frac{r_2(t)}{\bar{V}_H}\frac{t_0}{t^2}$$

$$\frac{\partial \dot{\rho}(t)}{\partial v_{p3}(t_0)} = \frac{r_3(t)}{\bar{V}_H}\left(\frac{t-t_0}{t}\right) + \frac{r_3(t)}{\bar{V}_H}\frac{t_0}{t^2} \qquad (4)$$

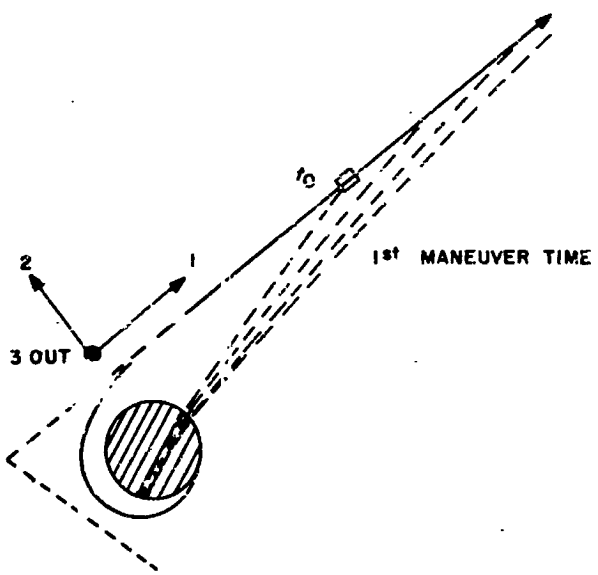

Fig. 14. Near-Earth orbit redetermination

where $v_{pi}(t_0) \triangleq$ velocity component of the probe relative to the barycenter, immediately following the midcourse correction; $v_j(t) \triangleq$ velocity component of the probe *relative to the observing station*, at some later time t; and $r_j(t) \triangleq$ position component of the probe *relative to the observing station*, at some later time t.

3. Possible Contributions to the Analytic Form of the Partials

The partials of the doppler data in the 2 and 3 directions will be dependent upon the terms $r_j(t)$ and $v_j(t)$, which are the components of position and velocity of the probe relative to the observing station. These terms consist of the nominal-straight-line motion of the probe relative to the barycenter, the deviations of the probe from straight-line motion, *and* the motion of the observing stations relative to the barycenter, which causes "apparent" deviations from straight-line motion. There are four possible contributions to these terms in the 2 and 3 directions: (1) the displacement of the $\bar{V}_H$ vector from the barycenter, i.e., the perpendicular distance to the line of motion of the probe, (2) the motion of the center of the Earth with respect to the barycenter, (3) the motion of the observing stations with respect to the center of the Earth, and (4) the bending of the trajectory of the spacecraft due to the gravitational field of the Sun. Each of these effects is described in detail in the following paragraphs.

a. Effect 1, the displacement of the line of motion. The perpendicular distance from the barycenter to the line of motion of the probe is closely related to the $\bar{b}$ vector of the original near-Earth hyperbola. It is typically 25,000 km on an interplanetary trajectory, though it varies with the $\bar{V}_H$ of that trajectory. From the definition of our coordinate system, $\bar{b}$ lies solely in the 2 direction. Thus $\partial\dot{\rho}(t)/\partial v_{p2}(t_0)$ will never be zero, but the partial derivative in the 3 direction is not affected.

b. Effect 2, the rotation of the Earth around the barycenter. The center of the Earth rotates about the barycenter with a period of 27.3 days, and an amplitude of about 5000 km. The plane of motion is inclined at a few degrees to the ecliptic, and components of this motion can appear in the 2 and 3 directions. Notice [Eq. (4)] that contributions to the analytic partials can occur from both non-zero *position* coordinates $r_j(t)$ and non-zero *velocities* $v_j(t)$ in either the 2 or 3 direction. The non-zero position coordinates correspond to the conventional parallax effect, which is well-known. A changing $r_j(t)$ effectively means we are observing the trajectory of the

probe from different "viewing angles," a condition long recognized to be an aid to good orbit determination knowledge. However, the contributions of the $v_j(t)$ terms, which we shall hereafter refer to as "velocity parallax," also affect the partials. The presence of these terms indicates that we obtain contributions to the orbit determination partials in a particular direction because of the *relative velocity* of the observing station and the probe in that direction, *regardless of the resulting position changes*. It is important to understand the distinction between the conventional position parallax and the velocity parallax described above, for in the case of straight-line motion the dominant effect will turn out to be the velocity parallax. A brief discussion of the basic doppler equations will be helpful in understanding the source of the parallax effects.

$$\dot{\rho}(t) = \frac{\overline{r(t)}}{|\overline{r(t)}|} \cdot \overline{v(t)} \qquad (5)$$

Both the position and velocity of the probe at time t are functions of the velocity at some earlier time t_0. In functional form

$$\dot{\rho}(t, \bar{v}_0) = \frac{\bar{r}}{|\bar{r}|}(t, \bar{v}_0) \cdot \bar{v}(t, \bar{v}_0) \qquad (6)$$

Now observe, for example, the contributions from the 3 direction. Because of the dot product, non-zero position coordinates in the 3 direction are necessary to observe the instantaneous velocity $v_3(t, \bar{v}_0)$; and non-zero velocities in the 3 direction are necessary to observe the instantaneous position $r_3(t, \bar{v}_0)$. But both the instantaneous v_3 and r_3 are functions of $\bar{v}_0$, as shown, so that both effects give us information about $\bar{v}_0$. The relative contributions of these two phenomena to the orbit determination knowledge will vary with the orbit determination problem; for some types of problems the position parallax may dominate, while for others (straight-line motion) the velocity parallax may dominate. In the general case though, both effects will be present and their relative importance must be a matter of concern for analytical orbit determination studies.

Referring back to the motion of the center of the Earth with respect to the barycenter, we shall obtain sinusoidal contributions to the partials in both the $r_j(t)$ and $v_j(t)$ terms. The size of these sinusoidal terms will be determined by the amplitude and period of rotation, and by the orientation of the motion with respect to the 2 and 3 directions. In the general case, we will have sine and cosine terms in both the 2 and 3 directions.

c. Effect 3, the rotation of the observing stations. The observing stations rotate in a plane displaced from and parallel to the equatorial plane of the Earth with a period of 1 day and an amplitude of about 5500 km. The discussion of barycenter rotation applies equally well to this rotation, with the addition of the constant terms describing the displacement of the planes of rotation from the center of the Earth. In the general case, then, we will get sine, cosine, and constant terms in the 2 and 3 directions, including both position and velocity parallax, and the magnitude of these terms will again be determined by the amplitude and period of rotation, the size of displacement, and the orientation of these motions with respect to the 2 and 3 directions.

d. Effect 4, the gravity bending effect. As the spacecraft moves away from the Earth, its position in the gravitational field of the Sun changes. With this change in position, the spacecraft and Earth experience different gravitational attractions toward the Sun, resulting in a curvature of the spacecraft's trajectory as viewed from the Earth. In general this curvature can occur both in the plane of motion of the probe, and normal to that plane, resulting in a changing instantaneous plane of motion relative to the Earth. In the general case, the perturbations to the straight-line motion will result in non-zero position and velocity components in all directions, which can be shown to approximately obey

$$\{\Delta V(t)\} = h_0 \begin{Bmatrix} l \\ m \\ n \end{Bmatrix} \frac{(t^2 - t_c^2)}{2} \qquad (7)$$

$$\{\Delta r(t)\} = h_0 \begin{Bmatrix} l \\ m \\ n \end{Bmatrix} \frac{(t - t_0)^2 (t + 2t_0)}{6} \qquad (8)$$

where

$$h_0 \text{ and } \begin{Bmatrix} l \\ m \\ n \end{Bmatrix}$$

are a constant and a constant vector, respectively. These perturbations to the straight-line motion can be evaluated only after computing

$$h_0 \text{ and } \begin{Bmatrix} l \\ m \\ n \end{Bmatrix}$$

but they are presented in this form to display their time-dependence. While the previous effects (Earth's rotation etc) introduced $r_j(t)$ and $v_j(t)$, which were constants or

sinusoidal oscillations with constant amplitudes, the perturbations from this last effect are polynomials, which become very large for large values of t. This implies that: (1) for large values of t, the gravity bending effects will probably dominate, unless elements of

$$\begin{Bmatrix} l \\ m \\ n \end{Bmatrix}$$

are zero, and (2) as t gets very large, the position deviations due to gravity bending get so large that the straight-line approximations break down. This is of course exactly what happens as the spacecraft progresses on its heliocentric trajectory.

A careful geometric analysis of this gravity bending effect yields the following interesting result. If the normal to the spacecraft's geocentric plane of motion has no component along the Earth–Sun line, the gravity bending effect cannot give orbit determination knowledge of the out-of-plane velocity component. This condition describes an important class of near-Earth trajectories which includes those trajectories whose near-Earth phase of motion coincides with the ecliptic plane. Furthermore, it can be shown that for every $\overline{V}_H$ (that is for every heliocentric trajectory) a near-Earth trajectory can be found which results in this condition.

4. The Relative Importance of the Contributions to the Orbit Redetermination Process

To ascertain which of the four effects described above yield adequate orbit determination knowledge we must determine which of these contributions to the partials yield linearly independent partials. First of all, the partials will be linearly dependent if one of them is always zero, and they will be almost linearly dependent if one of them is always very small. Large contributions to the partials are therefore a necessary but not sufficient condition to avoid "proximity to linear dependence" of the tracking partials.

As we have explained previously, the following functional forms will be exhibited by the four phenomena:

(1) *Displacement of the straight-line motion*—a constant position term which lies, by definition, solely in the 2 direction.

(2) *Rotation about the barycenter*—sinusoidal position *and* velocity terms projected in both the 2 and 3 directions, with a period of 27.3 days.

(3) *Observing station rotation*—sinusoidal position *and* velocity terms projected in both the 2 and 3 directions, with a period of 1 day.

(4) *Gravity bending effect*—position *and* velocity terms projected in both the 2 and 3 directions which display a polynominal dependence on time.

Typical values for these contributions can be obtained by averaging their magnitudes over all possible orientations of the spacecraft trajectory. These typical values are plotted as a function of time in Fig. 15, assuming the tracking began at $t_0 = 5$ days. More specifically, the magnitudes of $\partial \dot{\rho}(t)/\partial v_{pj}(t_0)$ are plotted with appropriately averaged $r_j(t)$ and $v_j(t)$ terms inserted for each of the four effects. Curves 2 and 3 in this figure should actually be sinusoidal oscillations within the "envelopes" that are plotted, but for the sake of clarity the oscillations have been omitted and only the amplitudes or "envelopes" remain. Clearly the rotation of the observing stations (Curve 3) gives the largest contribution to the partials over our range of interest. Only toward the later days

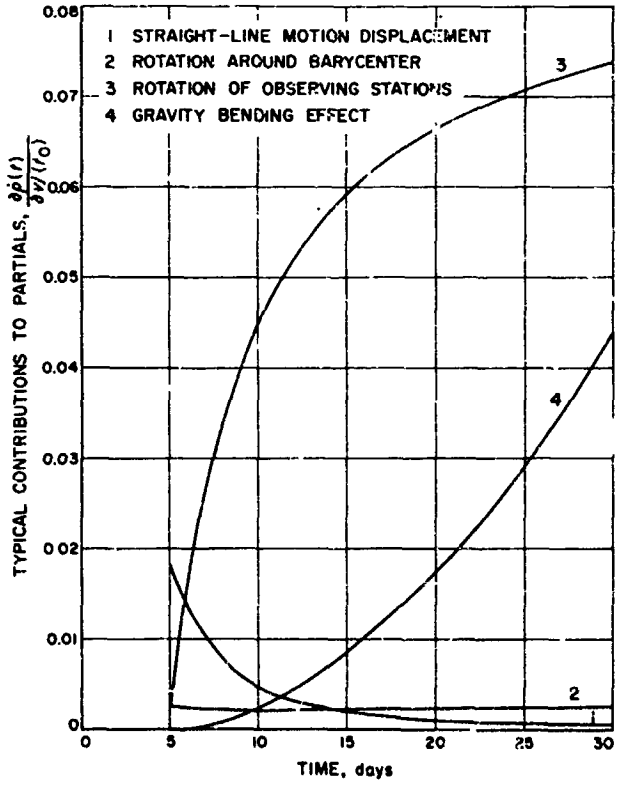

Fig. 15. Typical contributions to the tracking partials vs time

does the gravity bending effect become important, and only right at the beginning is the displacement of the straight-line motion important. Over the large intermediate span of tracking, the rotation of the observing station dominates. A more careful analysis, which separates the contributions of each effect into terms occurring because of the position parallax terms $r_j(t)$ and velocity parallax terms $v_j(t)$, is omitted here. However, such an analysis demonstrates that for each effect the velocity terms are much larger than the position terms and hence determine the overall magnitude of each effect's contribution to the partials. Remember that large contributions to the partials are a necessary *but not sufficient* condition for adequate orbit redetermination, so that this magnitude analysis, though not conclusive, seems to indicate that the dominant effect may well be the rotation of the observing stations, in fact, the velocity parallax arising from that rotation.

Other analytic observations, omitted here for the sake of brevity, can be made which tend to corroborate the indications of the above analysis. The real test of orbit determination knowledge comes, however, when these partials are combined into the covariance matrices of estimated quantities. We, therefore, have constructed a simple computer program which simulates, in a rudimentary fashion, the operation of the JPL Orbit Determination Program. The program, given inputs of the times of the tracking interval, frequency of sampling, $\bar{V}_H$, etc., computes partials arising from typical values of the four effects (averaged over all possible trajectory orientations) and accumulates these partials in a covariance matrix according to

$$\Lambda_v = \sigma_{\dot\rho}^2 \left[\sum_{i=1}^{m} B_i B_i^t \right]^{-1} \tag{9}$$

where

$\sigma_{\dot\rho} \triangleq 0.01$ m/sec = variance of doppler noise

$$B_i^t \triangleq \left[\frac{\partial \dot\rho(t_i)}{\partial v_{p1}(t_0)}, \frac{\partial \dot\rho(t_i)}{\partial v_{p2}(t_0)}, \frac{\partial \dot\rho(t_i)}{\partial v_{p3}(t_0)} \right]$$

$m \triangleq$ number of data points

The program then prints out the covariance matrix of the estimated quantities, which are the velocity components of the probe at time t_0.

The program was constructed so that the four effects could be considered alone, or in any combination; and in fact the position terms or velocity terms from any one effect could be considered separately if so desired. Several runs were made with this program to analyze the orbit determination knowledge accruing from different combinations of the four effects over different tracking intervals. The more important results of these runs are accumulated in Tables 4 and 5. The results can be interpreted as a simple-model simulation of the orbit redetermination process on some sort of typical trajectory, or a

Table 4. Numerical results from the simple-model simulation of the orbit redetermination process (the covariance matrix produced)[a]

Effects included in model[b]	$\sqrt{\text{trace } \Lambda_v}$, m/sec	Resultant covariance matrix, m/sec		
		σ_{v1}	σ_{v2}	σ_{v3}
1	∞	linearly dependent partials		
2	1.82	0.26×10^{-1}	1.25	1.36
3	0.061	0.092×10^{-2}	0.0433	0.0428
4	∞	linearly dependent partials		
1, 2, 3, 4 (all effects)	0.060	0.099×10^{-2}	0.0410	0.0427
3 vel only[c]	0.061	0.092×10^{-2}	0.0433	0.0428
1, 2	1.33	0.23×10^{-2}	0.242	1.30
1, 3	0.060	0.098×10^{-2}	0.0411	0.0428
1, 4	2.22	0.74×10^{-2}	0.56	2.14
1, 3 pos only[d]	0.91	0.24×10^{-2}	0.245	0.874
1, 3 vel only[c]	0.060	0.098×10^{-2}	0.0411	0.0428
1, 4 pos only[d]	16.8	0.95×10^{-2}	0.69	16.8
1, 4 vel only[c]	2.69	0.70×10^{-2}	0.54	2.64

[a]Tracking period: Day 5 to Day 10; doppler noise: $\sigma_{\dot\rho} = 0.01$ m/sec; sampling rate: 1/hr

[b](1) Displacement of the straight-line motion ($\bar{b}$ vector)
(2) Rotation of Earth's center about the barycenter
(3) Rotation of observing stations about the Earth's center
(4) Bending of trajectory due to Sun's gravity

[c]vel only $\triangleq$ only the velocity terms have been included

[d]pos only $\triangleq$ only the position terms have been included

Table 5. Numerical results from the simple-model simulation of the orbit redetermination process (compilation of $\sqrt{\text{trace } \Lambda_v}$ for different tracking periods and combinations of effect)[a]

Tracking period	$\sqrt{\text{trace } \Lambda_v}$, m/sec				
	1, 2, 3, 4[b] (all effects)	3	3 vel only	1, 4	1, 2
(a) Day 3 to Day 8	0.045	0.046	0.046	2.34	1.33
(b) Day 5 to Day 10	0.060	0.061	0.061	2.72	
(c) Day 10 to Day 15	0.096	0.096	0.096	2.18	
(d) Day 5 to Day 20	0.021	0.021	0.021	0.254	
(e) Day 5 to Day 35	0.011	0.012	0.012	0.192	

[a]Doppler noise: $\sigma_{\dot\rho} = 0.01$ m/sec; sampling rate: 1/hr

[b]See Footnote b in Table 4, above.

more complete check upon the "proximity to linear dependence" of the partials over the tracking period.

In Table 4, results of the simulation of tracking from 5 to 10 days are shown for different combinations of the four effects which are coded at the bottom of the table. The first important conclusion to be drawn from this tabulation is that the quality of the orbit redetermination is almost solely determined by the contributions from the rotation of the observing stations. Notice that the A_1 trace and the separate σ's are about as small when this rotation effect is considered alone as when all four effects are considered together. Furthermore, when the $\bar{b}$ displacement terms are included with the observing station rotation, the results are practically identical to the inclusion of all effects. The other combinations of effects yield results which are orders of magnitude worse than the station rotation effect, and are clearly not crucial to the orbit redetermination process.

The relative importance of position parallax from the $r_j(t)$ terms and the velocity parallax from the $v_j(t)$ terms was considered for station rotation effects and later on for several combinations of effects. The inclusion of only the velocity terms is designated by the abbreviation "vel only." As is clear from the tabulated results, the velocity parallax terms are by far the most important contributions. In the case of the observing stations rotation, the position parallax terms yield results an order of magnitude worse than the total effect. The velocity parallax terms dominate the total effect to such an extent that when considered separately, they provide results identical to the total effect. The velocity parallax phenomena, discussed earlier in this article, is clearly of paramount importance in the orbit redetermination process we have investigated.

Table 5 shows selected results from runs which were made over different tracking intervals. Runs a, b, and c each simulated 5 days of tracking, but used different starting times. Runs b, d, and e each started on Day 5, but then tracked for different lengths of time up to 30 days. For each of these tracking periods, the rotation of the observing stations (Effect 3) continues to dominate the redetermination process; moreover, the velocity parallax terms continue to dominate the total contribution of this effect. Notice that for every early tracking (3 to 8 days) and for later tracking (5 to 35 days) this one effect does not account for all of the orbit determination knowledge. A careful analysis at these points shows that the inclusion of the $\bar{b}$ displacement of the straight-line motion accounts for the discrepancy (to our significant digits) early in the flight; and the inclusion of gravity bending effects accounts for the discrepancies later in the tracking interval. These trends are compatible with Fig. 15, which showed the magnitude of contribution to the partials over the tracking interval.

Our two conclusions from this simulation study, i.e., the importance of velocity parallax terms and the dominance of the station rotation effect, are compatible with each other. The stations rotate about the Earth with a velocity of 0.40 km·sec, whereas the Earth moves about its barycenter with a velocity of only 0.013 km/sec, the gravity bending effect creates only small velocities except after long tracking periods >30 days, and the $\bar{b}$ displacement creates no velocity contributions. Therefore, if the velocity terms really determine the orbit, we would expect the station rotation effect to dominate the orbit redetermination process, as it does.

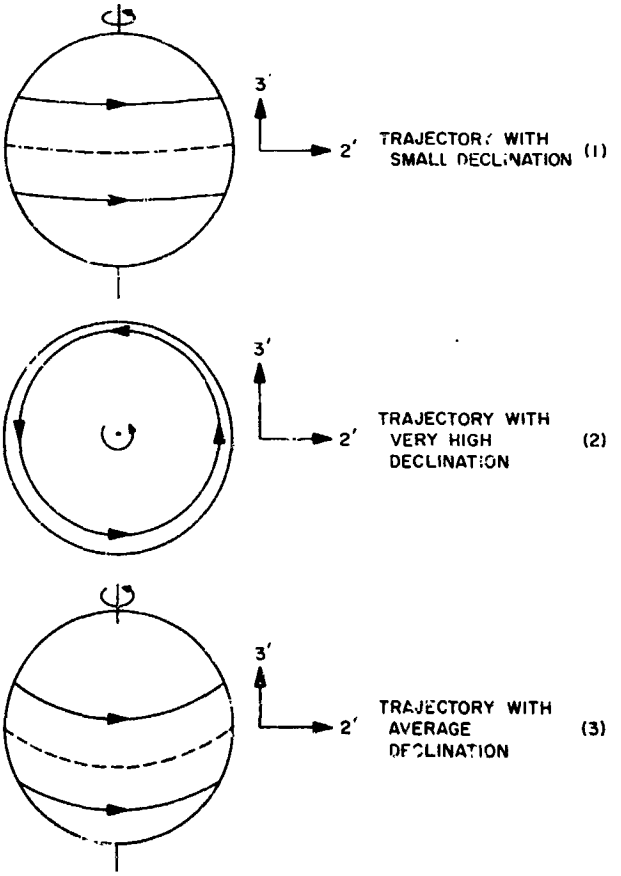

Fig. 16. Views of the tracking stations from the asymptotes of trajectories with different declinations

5. Comparison with Orbit Determination Program Results

In Part 4, above, it was demonstrated that the crucial factors in orbit redetermination are the velocity components of the observing stations in the 2 and 3 directions. The 2 and 3 directions are, by definition, perpendicular to the outgoing asymptote of the near-Earth hyperbola, and the 2 direction lies in the plane of that hyperbola. Fig. 16 illustrates three views of the Earth taken from different near-Earth trajectories: the first view shows the Earth from a trajectory with a very small declination of the outgoing asymptote, the second view shows the Earth from a trajectory with a very high declination, and the third view shows the Earth from a trajectory with an average declination. Note that the views are shown back along the 1 direction, the direction of the outgoing asymptote. The 2′ and 3′ directions are constructed in the plane of the figures such that the 3′ direction is vertical. The true 2 and 3 directions, as defined previously, will lie in this same plane at some angle to 2′ and 3′, and will be determined by the near-Earth plane of motion. Now, observe that the velocity of the observing stations in View (1) has almost no component in the 3′ direction; while the velocity of this same station in View (2) has substantial components in both the 2′ and 3′ directions. As shown in Fig. 17, the magnitude of the station's velocity that the probe "sees" in the 3′ direction will be proportional to the absolute value of the sine of the declination of the outgoing asymptote. Thus, for trajectories with small declinations there will be some direction, namely 3′, in which the velocity of the observing stations will not be able to contribute to the tracking partials; and we, therefore, should obtain poor orbit determination knowledge in that direction. This effect was simulated on the rudimentary program described previously, and the results displayed large uncertainties in the velocity component in a direction in the 2-3 plane, in particular, the 3′ direction. We similarly expect that the JPL Orbit Determination Program will furnish poor orbit determination knowledge for trajectories with small declinations of the outgoing asymptote.

In order to verify this prediction, two classes of trajectories were selected from past orbit determination studies which were conducted using identical tracking periods, physical constant uncertainties, etc. The first class of trajectories was a group of three trajectories studied for the 1969 Mars orbiter opportunity. One of these trajectories, a Type II transit,[1] displayed poor orbit determination characteristics, and though several possible explanations were advanced, the cause of these bad characteristics was never satisfactorily explained. This trajectory had a declination of the outgoing asymptote equal to 9.2 deg while the declinations of the two trajectories studied concurrently were −33.7 and −49.8 deg. By referring back to the computer output, it was possible to calculate the square root of the trace of Λ_r as a function of time, i.e., the root-sum-square (RSS) 1-σ uncertainties of the velocity components being estimated. This quantity is plotted as a function of time in Fig. 18 for each of the three trajectories. The trajectories suggest a

[1]A Type II trajectory is one in which the heliocentric angle traversed by the spacecraft from launch to encounter is between 180 and 360 deg.

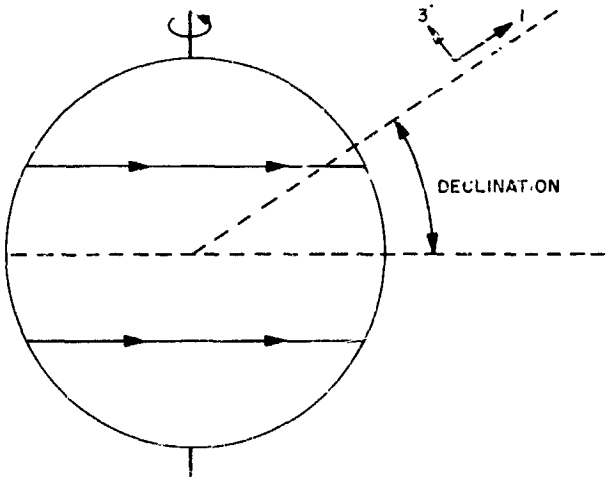

Fig. 17. Side view of the declination of the asymptote and the tracking station geometry

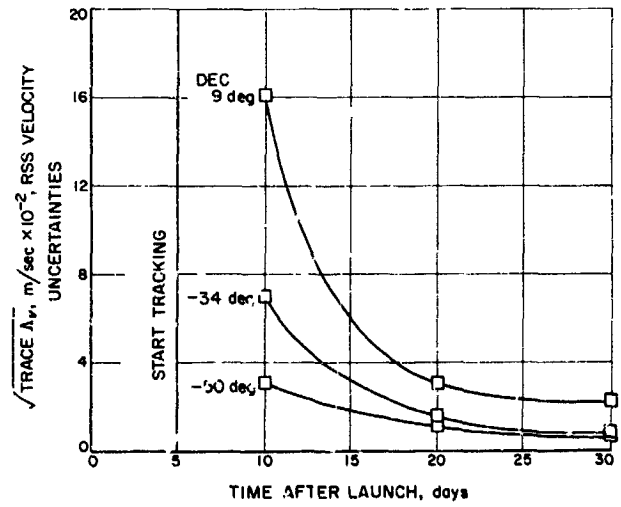

Fig. 18. 3 Mars 1969 trajectories ($\sqrt{\text{trace } \Lambda_r}$ vs time)

correlation between small declinations (absolute magnitude) and poor orbit redetermination knowledge. Fig. 19 plots the same data in a different form. The square root of the trace of Λ_v is plotted as a function of the absolute value of the sine of the declinations for 10, 20, and 30 days after launch. These curves again suggest that a correlation does, in fact, exist between the declination of the outgoing asymptote and the orbit redetermination knowledge.

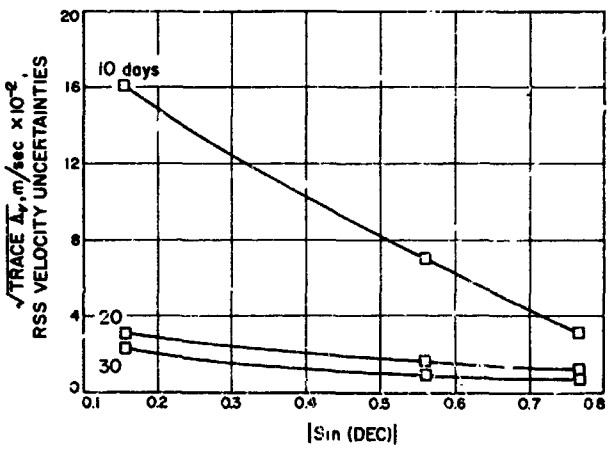

Fig. 19. 3 Mars 1969 trajectories ($\sqrt{\text{trace } \Lambda_v}$ vs |sine of the declination|)

The second class of trajectories consisted of 7 Mars trajectories, one of which was representative of each launch opportunity from 1964 to 1977, inclusively. Table 6 presents the 7 trajectories, their declinations, and the square root of the trace Λ_v evaluated at 10, 20, 30, and 50 days after launch (tracking began at 5 days).

Table 6. $\sqrt{\text{trace } \Lambda_v}$ or $\sqrt{\sigma_{v1}^2 + \sigma_{v2}^2 + \sigma_{v3}^2}$ at 10, 20, 30, and 50 days after launch for 7 Mars trajectories[a]

Mars opportunity	Declination of the outgoing asymptote, deg	$\sqrt{\text{trace } \Lambda_v}$, m/sec × 10^{-3}			
		10 days	20 day	30 days	50 days
1964	13.54	24.4	14.7	10.3	9.20
1971	−20.60	10.3	5.90	5.32	3.33
1966	−20.78	17.0	6.80	4.74	1.78
1973	27.68	9.06	4.94	4.24	2.84
1969	−43.43	9.88	5.08	3.51	2.04
1975	47.27	9.75	4.30	3.52	2.29
1977	49.38	7.30	3.91	3.16	1.87

[a]Tracking begins at 5 days

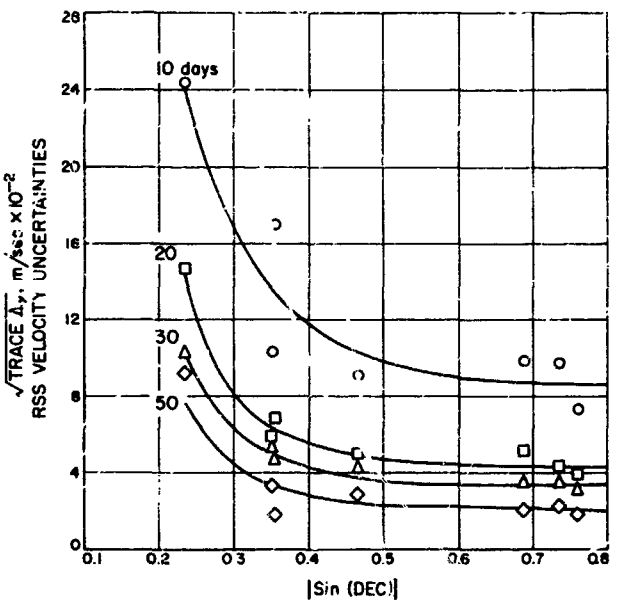

Fig. 20. 7 Mars trajectories (1964–1977) ($\sqrt{\text{trace } \Lambda_v}$ vs |sine of the declination|)

Fig. 20 plots this data showing trace Λ_v as a function of |sine of the declination| for each of the evaluation times. This plot also confirms the high correlation with declination, particularly at 20 and 30 days from launch. Irregularities seem to occur at 10 days (i.e., after only 5 days of tracking) and at 50 days (45 days of tracking). This leads us to suspect that the position parallax effect may still be important after 5 days of tracking, and that the gravity bending effect begins to be important by 50 days from launch. This would be consistent with previous conclusions about the relative importance of the different effects as a function of time. Further investigation of the orbit determination results for both these classes shows that when the declination become small, it is in fact the previously described component of velocity which is difficult to determine. The observable evidence from these trajectories thus seems to corroborate the predictions presented earlier in this study on the basis of the simple-model simulation of orbit redetermination. (This second class of orbit determination runs used different data weights and/or physical constant uncertainties than the first class, so that efforts should *not* be made to compare results between the two classes.)

The phenomena cited above, that trajectories with small declinations of the outgoing asymptote display poor orbit redetermination characteristics, can have important consequences for interplanetary missions. If we require the

ability to redetermine the orbit quickly after the first maneuver so that an early accurate second maneuver can be made, we may be forced to exclude trajectories with small declinations. This suggests a potential constraint to be placed on future interplanetary trajectories. If such a constraint should prove necessary and/or desirable, it should be defined only after a more exhaustive study of the problems arising from trajectories with small declinations.

6. Conclusions

An analytical simple-model investigation of the orbit redetermination process following the first midcourse maneuver indicates that there are four effects which contribute to the orbit determination knowledge. These four effects are: (1) the $\bar{b}$ vector displacement of the straight-line motion of the spacecraft away from the barycenter, (2) the rotation of the Earth's center about the barycenter, (3) the rotation of the observing stations about the Earth's center, and (4) the bending of the spacecraft's trajectory by the gravitational field of the Sun. These effects contribute to the orbit determination knowledge because of the conventional position parallax they exhibit, but more important, because of the velocity parallax caused by the relative velocity of the probe and observing station. Analytic studies indicate that the rotation of the observing stations, and in particular the velocity parallax of that rotation, actually dominates the orbit redetermination process. This leads us to expect that the JPL Orbit Determination Program will furnish poor orbit determination knowledge on trajectories with small declinations of the outgoing asymptote, and this expectation is corroborated by the observed evidence of past orbit determination studies. Further orbit redetermination studies will be necessary to determine exactly how these phenomena will affect the trajectory selection criteria.

C. First- and Second-Sum Numerical Integration

J. D. Anderson

1. Introduction

With the construction of step-by-step numerical integration procedures in extended precision, it becomes necessary to use higher order formulas if the interval of the integration table is to remain reasonably constant as the precision is increased. Therefore, the first- and second-sum formulas used for many years in celestial mechanics are developed here in terms of the backward differences and are carried to the seventh order in the differences or equivalently to the ninth order in the step size h.[5] Both predictor and corrector formulas are given. Also, the formulas are expressed in terms of antecedent values of the acceleration according to a development carried out by Herrick (Ref. 5). It is therefore possible to integrate a set of second-order differential equations without resorting to the construction of a difference table. The antecedent-function formulas are given for all orders from two to nine in the step size h.

Many of the formulas given here are not available in the literature and thus they are useful for studies requiring higher order differences than are usually published. It should be pointed out that the method of generating the formulas is standard and that in fact the coefficients can be generated by a computer program to any order of interest. However, the coefficients are computed only within the precision carried in the machine. This has been done at JPL for the second-sum predictor and corrector to the fifteenth difference (Ref. 6, pp. 109–110) and the resulting formulas have been used to generate the standard planetary ephemerides over the past three years. Also, these formulas are coming into use in all other JPL double-precision orbital calculations. Of course, in practice any form of the first- and second-sum formulas requires a procedure to start the table of differences. Such a procedure is given in Ref. 6, pp. 34–35.

2. Second-Sum Integration

The generating function for the second difference $\nabla^2 x_{n+1}$ in terms of the backward differences $\nabla^n \ddot{x}_n$ in the preceding values of the second derivatives is given by (Ref. 7, Eq. 5.5.12)

$$\nabla^2 x_{n+1} = h^2 (1-\nabla)^{-1} \left[\frac{\nabla}{-\ln(1-\nabla)} \right]^2 \ddot{x}_n \qquad (1)$$

Similarly, the corrector formula for $\nabla^2 x_n$ is given by (Ref. 7, Eq. 5.5.11)

$$\nabla^2 x_n = h^2 \left[\frac{\nabla}{-\ln(1-\nabla)} \right]^2 \ddot{x}_n \qquad (2)$$

In both formulas the size of the integration step from x_n to x_{n+1} is given by h.

[5] Note that Kulikov (Ref. 4) has given the second-sum formula in terms of central differences to the twelfth order in h.

The function in Eq. (2) is now expanded to the ninth order in ∇. First of all, define

$$f(\nabla) = \left[\frac{\nabla}{-\ln(1-\nabla)}\right]^2 \tag{3}$$

The function $-\ln(1-\nabla)$ can be expanded in the well known form

$$-\ln(1-\nabla) = \nabla + \frac{1}{2}\nabla^2 + \frac{1}{3}\nabla^3 + \frac{1}{4}\nabla^4 + \cdots \tag{4}$$

and

$$\frac{-\ln(1-\nabla)}{\nabla} = 1 + \frac{1}{2}\nabla + \frac{1}{3}\nabla^2 + \frac{1}{4}\nabla^3 + \cdots \tag{5}$$

Define

$$\varepsilon = \frac{1}{2}\nabla + \frac{1}{3}\nabla^2 + \frac{1}{4}\nabla^3 + \cdots \tag{6}$$

Then

$$f(\nabla) = (1+\varepsilon)^{-2} \tag{7}$$

or

$$f(\nabla) = 1 - 2\varepsilon + 3\varepsilon^2 - 4\varepsilon^3 + \cdots \tag{8}$$

The expansion is carried out by forming $\varepsilon^2, \varepsilon^3, \varepsilon^4, \cdots, \varepsilon^9$ to order ∇^9 and then by collecting the coefficients of each order in ∇ according to Eq. (8). The necessary arithmetic has been done independently by R. K. Russell and the author, and we are reasonably certain of the accuracy of the coefficients. The result is

$$\begin{aligned}\left[\frac{\nabla}{-\ln(1-\nabla)}\right]^2 = {} & 1 - \nabla + \frac{1}{12}\nabla^2 + 0\nabla^3 - \frac{1}{240}\nabla^4 - \frac{1}{240}\nabla^5 \\ & - \left(\frac{221}{252}\right)\left(\frac{1}{240}\right)\nabla^6 - \left(\frac{190}{252}\right)\left(\frac{1}{240}\right)\nabla^7 \\ & - \left(\frac{9829}{11{,}400}\right)\left(\frac{190}{252}\right)\left(\frac{1}{240}\right)\nabla^8 \\ & - \left(\frac{8547}{11{,}400}\right)\left(\frac{190}{252}\right)\left(\frac{1}{240}\right)\nabla^9 - \cdots\end{aligned} \tag{9}$$

It is necessary to multiply the above series by $(1-\nabla)^{-1}$ in order to obtain $\nabla^2 x_{n+1}$ as given by Eq. (1). Note that

$$(1-\nabla)^{-1} = \sum_{n=0}^{\infty} \nabla^n \tag{10}$$

The product of the two series, Eqs. (9) and (10), is given by

$$\begin{aligned}(1-\nabla)^{-1}\left[\frac{\nabla}{-\ln(1-\nabla)}\right]^2 = {} & 1 + 0\nabla + \frac{1}{12}\nabla^2 + \frac{1}{12}\nabla^3 + \frac{19}{240}\nabla^4 \\ & + \frac{18}{240}\nabla^5 + \frac{17 + \frac{31}{252}}{240}\nabla^6 + \frac{16 + \frac{93}{252}}{240}\nabla^7 \\ & + \frac{15 + \frac{10871}{15120}}{240}\nabla^8 + \frac{14 + \frac{17444}{15120}}{240}\nabla^9 + \cdots\end{aligned} \tag{11}$$

The series of Eq. (11) can be substituted into Eq. (1) to yield the formula for $\nabla^2 x_{n+1}$. Similarly, the series of Eq. (9) when substituted into Eq. (2) yields the formula for $\nabla^2 x_n$. In order to obtain formulas for x_{n+1} and x_n, the operator ∇^{-2} is applied to the series for $\nabla^2 x_{n+1}$ and $\nabla^2 x_n$, essentially to the series of Eqs. (11) and (9), respectively. The resulting expression for x_{n+1} is transformed to x_n by replacing n by $n-1$ in Eq. (1). Thus, the predictor formula is given by

$$\begin{aligned}x_n = h^2\Bigg[& \nabla^{-2} + \frac{1}{12}\nabla^0 + \frac{1}{12}\nabla + \frac{19}{240}\nabla^2 \\ & + \frac{18}{240}\nabla^3 + \frac{17 + \frac{31}{252}}{240}\nabla^4 + \frac{16 + \frac{93}{252}}{240}\nabla^5 \\ & + \frac{15 + \frac{10871}{15120}}{240}\nabla^6 + \frac{14 + \frac{17444}{15120}}{240}\nabla^7 + \cdots\Bigg]\ddot{x}_{n-1}\end{aligned} \tag{12}$$

and the corrector formula as generated by Eq. (2) is

$$\begin{aligned}x_n = h^2\Bigg[& \nabla^{-2} - \nabla^{-1} + \frac{1}{12}\nabla^0 - \frac{1}{240}\nabla^2 \\ & - \frac{1}{240}\nabla^3 - \left(\frac{221}{252}\right)\left(\frac{1}{240}\right)\nabla^4 - \left(\frac{190}{252}\right)\left(\frac{1}{240}\right)\nabla^5 \\ & - \left(\frac{9829}{11{,}400}\right)\left(\frac{190}{252}\right)\left(\frac{1}{240}\right)\nabla^6 \\ & - \left(\frac{8547}{11{,}400}\right)\left(\frac{190}{252}\right)\left(\frac{1}{240}\right)\nabla^7 - \cdots\Bigg]\ddot{x}_n\end{aligned} \tag{13}$$

Eqs. (12) and (13) can be expressed in better forms for computation. The predictor formula is

$$x_n = h^2\left[\nabla^{-2} + \frac{1}{12}\nabla^0 + \frac{1}{12}\nabla + \frac{19}{240}\nabla^2 + \frac{18}{240}\nabla^3 + \frac{4315}{60,480}\nabla^4 + \frac{4125}{60,480}\nabla^5 + \frac{237,671}{3,628,800}\nabla^6 + \frac{229,124}{3,628,800}\nabla^7 + \cdots\right]\ddot{x}_{n-1} \quad (14)$$

while the corrector formula is given by

$$x_n = h^2\left[\nabla^{-2} - \nabla^{-1} + \frac{1}{12}\nabla^0 - \frac{1}{240}\nabla^2 - \frac{1}{240}\nabla^3 - \frac{221}{60,480}\nabla^4 - \frac{190}{60,480}\nabla^5 - \frac{9829}{3,628,800}\nabla^6 - \frac{8547}{3,628,800}\nabla^7 - \cdots\right]\ddot{x}_n \quad (15)$$

The accuracy of the above two formulas when applied to types of equations encountered in celestial mechanics is under investigation by C. J. Devine (*SPS 37-31*, Vol. IV, pp. 17–18 and *SPS 37-32*, Vol. IV, pp. 12–18). The formulas are carried to the fourteenth difference with the coefficients determined numerically.

3. First-Sum Integration

In addition to the position coordinates (x, y, z) in the integration of the equations of motion, the velocity coordinates $(\dot{x}, \dot{y}, \dot{z})$ are often required also. Of course, this is always the situation for velocity-dependent accelerations. The first backward difference $\nabla\dot{x}_{n+1}$ is given by Milne (Ref. 8, Eq. 20.3).

$$\nabla\dot{x}_{n+1} = h\left[\nabla^0 + \frac{1}{2}\nabla + \frac{5}{12}\nabla^2 + \frac{9}{24}\nabla^3 + \frac{251}{720}\nabla^4 + \frac{475}{1440}\nabla^5 + \frac{19,087}{60,480}\nabla^6 + \frac{36,799}{120,960}\nabla^7 + \frac{1,070,017}{3,628,800}\nabla^8 + \cdots\right]\ddot{x}_n \quad (16)$$

Apply the operator ∇^{-1} to Eq. (16) and replace n by $n-1$.

$$\dot{x}_n = h\left[\nabla^{-1} + \frac{1}{2}\nabla^0 + \frac{5}{12}\nabla + \frac{9}{24}\nabla^2 + \frac{251}{720}\nabla^3 + \frac{475}{1440}\nabla^4 + \frac{19,087}{60,480}\nabla^5 + \frac{36,799}{120,960}\nabla^6 + \frac{1,070,017}{3,628,800}\nabla^7 + \cdots\right]\ddot{x}_{n-1} \quad (17)$$

This is the predictor formula for $\dot{x}_n$.

To obtain the corrector formula, the expression for $\dot{x}_n$ as given by Milne (Ref. 8, Eq. 20.5) is used.

$$\nabla\dot{x}_n = h\left[\nabla^0 - \frac{1}{2}\nabla - \frac{1}{12}\nabla - \frac{1}{24}\nabla^3 - \frac{19}{720}\nabla^4 - \frac{27}{1440}\nabla^5 - \frac{863}{60,480}\nabla^6 - \frac{1375}{120,960}\nabla^7 - \frac{33953}{3,628,800}\nabla^8 - \cdots\right]\ddot{x}_n \quad (18)$$

Again apply the ∇^{-1} operator to obtain the required formula.

$$\dot{x}_n = h\left[\nabla^{-1} - \frac{1}{2}\nabla^0 - \frac{1}{12}\nabla - \frac{1}{24}\nabla^2 - \frac{19}{720}\nabla^3 - \frac{27}{1440}\nabla^4 - \frac{863}{60,480}\nabla^5 - \frac{1375}{120,960}\nabla^6 - \frac{33953}{3,628,800}\nabla^7 - \cdots\right]\ddot{x}_n \quad (19)$$

4. Antecedent-Function Formulas

It is always possible to replace formulas involving backward differences of a function by equivalent formulas in terms of antecedent values of the function. First of all, it is convenient to replace the resulting predictor-corrector formulas of the preceding two sections by the following forms.

$$\frac{1}{h^2}x_i = \Sigma^2\ddot{x}_i + \frac{1}{12}\ddot{x}_{i-1} + \frac{1}{12}\delta\ddot{x}_{i-3/2} + \frac{19}{240}\delta^2\ddot{x}_{i-2} + \frac{18}{240}\delta^3\ddot{x}_{i-5/2} + \frac{4315}{60,480}\delta^4\ddot{x}_{i-3} + \frac{4125}{60,480}\delta^5\ddot{x}_{i-7/2} + \frac{237,671}{3,628,800}\delta^6\ddot{x}_{i-4} + \frac{229,124}{3,628,800}\delta^7\ddot{x}_{i-9/2} \quad (20)$$

$$\frac{1}{h^2}x_i = \Sigma^2\ddot{x}_{i+1} - \Sigma\delta\ddot{x}_{i+1/2} + \frac{1}{12}\ddot{x}_i - \frac{1}{240}\delta^2\ddot{x}_{i-1} - \frac{1}{240}\delta^3\ddot{x}_{i-3/2} - \frac{221}{60,480}\delta^4\ddot{x}_{i-2} - \frac{190}{60,480}\delta^5\ddot{x}_{i-5/2} - \frac{9829}{3,628,800}\delta^6\ddot{x}_{i-3} + \frac{8547}{3,628,800}\delta^7\ddot{x}_{i-7/2} \quad (21)$$

$$\frac{1}{h}\dot{x}_i = \Sigma\dot{x}_{i-1/2} + \frac{1}{2}\ddot{x}_{i-1} + \frac{5}{12}\delta\ddot{x}_{i-3/2} + \frac{9}{24}\delta^2\ddot{x}_{i-2} + \frac{251}{720}\delta^3\ddot{x}_{i-5/2} + \frac{475}{1440}\delta^4\ddot{x}_{i-3} + \frac{19,087}{60,480}\delta^5\ddot{x}_{i-7/2} + \frac{36,799}{120,960}\delta^6\ddot{x}_{i-4} + \frac{1,070,017}{3,628,800}\delta^7\ddot{x}_{i-9/2} \quad (22)$$

$$\frac{1}{h}\dot{x}_i = \Sigma\ddot{x}_{i-1/2} - \frac{1}{2}\ddot{x}_i - \frac{1}{12}\delta\ddot{x}_{i-1/2} - \frac{1}{24}\delta^2\ddot{x}_{i-1} - \frac{19}{720}\delta^3\ddot{x}_{i-3/2} - \frac{27}{1440}\delta^4\ddot{x}_{i-2} - \frac{863}{60{,}480}\delta^5\ddot{x}_{i-5/2} - \frac{1375}{120{,}960}\delta^6\ddot{x}_{i-3} - \frac{33{,}953}{3{,}628{,}800}\delta^7\ddot{x}_{i-7/2} \quad (23)$$

The notation used here is consistent with that found in the astronomical literature. The $\delta^n\ddot{x}_k$ indicates the nth difference of the function $\ddot{x}$ on the kth line of the integration table. It can be related to antecedent values of the function by the following formula:

$$\delta^n\ddot{x}_k = \sum_{m=0}^{n} (-1)^n \binom{n}{m} \ddot{x}_{2+n/2-m} \quad (24)$$

Now Eq. (24) can be substituted into Eqs. (20)–(23) to yield the required antecedent-function formulas.

a. Second-sum predictor. The second-sum predictor is obtained by substituting Eq. (24) into Eq. (20).

$$\frac{1}{h^2}x_i = \Sigma^2\ddot{x}_i + \frac{1}{12}\ddot{x}_{i-1} + \frac{1}{12}\sum_{m=0}^{1}(-1)^m\binom{1}{m}\ddot{x}_{i-1-m} + \frac{19}{240}\sum_{m=0}^{2}(-1)^m\binom{2}{m}\ddot{x}_{i-1-m} + \frac{18}{240}\sum_{m=0}^{3}(-1)^m\binom{3}{m}\ddot{x}_{i-1-m} + \frac{4315}{60{,}480}\sum_{m=0}^{4}(-1)^m\binom{4}{m}\ddot{x}_{i-1-m} + \frac{4125}{60{,}480}\sum_{m=0}^{5}(-1)^m\binom{5}{m}\ddot{x}_{i-1-m} + \frac{237{,}871}{3{,}628{,}800}\sum_{m=0}^{6}(-1)^m\binom{6}{m}\ddot{x}_{i-1-m} + \frac{229{,}124}{3{,}628{,}800}\sum_{m=0}^{7}(-1)^m\binom{7}{m}\ddot{x}_{i-1-m} \quad (25)$$

Now perform all of the sums in Eq. (25).

Depending on what order difference is taken into account in simplifying the coefficients of $\ddot{x}_{i-1-m}$, a number of formulas are generated (cf. Ref. 5, p. 129). Let N be the highest order difference included. Then

$$(N=0) \qquad x_i = h^2\left\{\Sigma^2\ddot{x}_i + \frac{1}{12}\ddot{x}_{i-1}\right\} \quad (26)$$

$$(N=1) \qquad x_i = h^2\left\{\Sigma^2\ddot{x}_i + \frac{1}{12}(2\ddot{x}_{i-1} - \ddot{x}_{i-2})\right\} \quad (27)$$

$$(N=2) \qquad x_i = h^2\left\{\Sigma^2\ddot{x}_i + \frac{1}{240}(59\ddot{x}_{i-1} - 58\ddot{x}_{i-2} + 19\ddot{x}_{i-3})\right\} \quad (28)$$

$$(N=3) \qquad x_i = h^2\left\{\Sigma^2\ddot{x}_i + \frac{1}{240}(77\ddot{x}_{i-1} - 112\ddot{x}_{i-2} + 73\ddot{x}_{i-3} - 18\ddot{x}_{i-4})\right\} \quad (29)$$

$$(N=4) \qquad x_i = h^2\left\{\Sigma^2\ddot{x}_i + \frac{1}{60{,}480}(23{,}719\ddot{x}_{i-1} - 45{,}484\ddot{x}_{i-2} + 44{,}236\ddot{x}_{i-3} - 21{,}716\ddot{x}_{i-4} + 4315\ddot{x}_{i-5})\right\} \quad (30)$$

$$(N=5) \qquad x_i = h^2\left\{\Sigma^2\ddot{x}_i + \frac{1}{60{,}480}(27{,}844\ddot{x}_{i-1} - 66{,}109\ddot{x}_{i-2} + 85{,}536\ddot{x}_{i-3} - 63{,}046\ddot{x}_{i-4} + 24{,}940\ddot{x}_{i-5} - 4125\ddot{x}_{i-6})\right\} \quad (31)$$

$$(N=6) \qquad x_i = h^2\left\{\Sigma^2\ddot{x}_i + \frac{1}{3{,}628{,}800}(1{,}908{,}311\ddot{x}_{i-1} - 5{,}392{,}566\ddot{x}_{i-2} + 8{,}697{,}225\ddot{x}_{i-3} - 8{,}536{,}180\ddot{x}_{i-4} + 5{,}061{,}465\ddot{x}_{i-5} - 1{,}673{,}526\ddot{x}_{i-6} + 237{,}671\ddot{x}_{i-7})\right\} \quad (32)$$

$$(N=7) \qquad x_i = h^2\left\{\Sigma^2\ddot{x}_i + \frac{1}{3{,}628{,}800}(2{,}137{,}435\ddot{x}_{i-1} - 6{,}998{,}434\ddot{x}_{i-2} + 13{,}508{,}829\ddot{x}_{i-3} - 16{,}555{,}520\ddot{x}_{i-4} + 13{,}080{,}805\ddot{x}_{i-5} - 6{,}485{,}130\ddot{x}_{i-6} + 1{,}841{,}539\ddot{x}_{i-7} - 229{,}124\ddot{x}_{i-8})\right\} \quad (33)$$

In the integration of the five outer planets, Eckert, Brouwer, and Clemence used this form of the second-sum method with $N = 9$ (Ref. 9, p. XI). They did not use a corrector formula.

b. Second-sum corrector. The pattern for obtaining the corrector is similar to that shown in the previous dis-

cussion. The result of substituting Eq. (24) into Eq. (21) and performing the sums is the following.

$$(N=0) \qquad x_i = h^2\left\{\Sigma^2\ddot{x}_{i+1} - \Sigma\ddot{x}_{i+1/2} + \frac{1}{12}\ddot{x}_i\right\} \tag{34}$$

$$(N=1) \qquad x_i = h^2\left\{\Sigma^2\ddot{x}_{i+1} - \Sigma\ddot{x}_{i+1/2} + \frac{1}{12}\ddot{x}_i\right\} \tag{35}$$

$$(N=2) \qquad x_i = h^2\left\{\Sigma^2\ddot{x}_{i+1} - \Sigma\ddot{x}_{i+1/2} + \frac{1}{240}(19\ddot{x}_i + 2\ddot{x}_{i-1} - \ddot{x}_{i-2})\right\} \tag{36}$$

$$(N=3) \qquad x_i = h^2\left\{\Sigma^2\ddot{x}_{i+1} - \Sigma\ddot{x}_{i+1/2} + \frac{1}{240}(18\ddot{x}_i + 5\ddot{x}_{i-1} - 4\ddot{x}_{i-2} + \ddot{x}_{i-3})\right\} \tag{37}$$

$$(N=4) \qquad x_i = h^2\left\{\Sigma^2\ddot{x}_{i+1} - \Sigma\ddot{x}_{i+1/2} + \frac{1}{60{,}480}(43{,}15\ddot{x}_i + 2144\ddot{x}_{i-1} - 2334\ddot{x}_{i-2} + 1136\ddot{x}_{i-3} - 221\ddot{x}_{i-4})\right\} \tag{38}$$

$$(N=5) \qquad x_i = h^2\left\{\Sigma^2\ddot{x}_{i+1} - \Sigma\ddot{x}_{i+1/2} + \frac{1}{60{,}480}(4125\ddot{x}_i + 3094\ddot{x}_{i-1} - 4234\ddot{x}_{i-2} + 3036\ddot{x}_{i-3} - 1171\ddot{x}_{i-4} + 190\ddot{x}_{i-5})\right\} \tag{39}$$

$$(N=6) \qquad x_i = h^2\left\{\Sigma^2\ddot{x}_{i+1} - \Sigma\ddot{x}_{i+1/2} + \frac{1}{3{,}628{,}800} \times (237{,}671\ddot{x}_i + 244{,}614\ddot{x}_{i-1} - 401{,}475\ddot{x}_{i-2} + 378{,}740\ddot{x}_{i-3} - 217{,}695\ddot{x}_{i-4} + 70{,}374\ddot{x}_{i-5} - 9829\ddot{x}_{i-6})\right\} \tag{40}$$

$$(N=7) \qquad x_i = h^2\left\{\Sigma^2\ddot{x}_{i+1} - \Sigma\ddot{x}_{i+1/2} + \frac{1}{3{,}628{,}800} \times 229{,}124\ddot{x}_i + 304{,}443\ddot{x}_{i-1} - 580{,}962\ddot{x}_{i-2} + 677{,}895\ddot{x}_{i-3} - 516{,}840\ddot{x}_{i-4} + 249{,}861\ddot{x}_{i-5} - 69{,}658\ddot{x}_{i-6} + 8547\ddot{x}_{i-7})\right\} \tag{41}$$

c. First-sum predictor. The first-sum predictor is given by Eq. (22). In terms of antecedent values of the acceleration it takes on the following forms for $N = 0, 1, 2, \cdots, 7$.

$$(N=0) \qquad \dot{x}_i = h\{\Sigma\ddot{x}_{i-1/2} + 1/2\ddot{x}_{i-1}\} \tag{42}$$

$$(N=1) \qquad \dot{x}_i = h\left\{\Sigma\ddot{x}_{i-1/2} + \frac{1}{12}(11\ddot{x}_{i-1} - 5\ddot{x}_{i-2})\right\} \tag{43}$$

$$(N=2) \qquad \dot{x}_i = h\left\{\Sigma\ddot{x}_{i-1/2} + \frac{1}{24}(31\ddot{x}_{i-1} - 28\ddot{x}_{i-2} + 9\ddot{x}_{i-3})\right\} \tag{44}$$

$$(N=3) \qquad \dot{x}_i = h\left\{\Sigma\ddot{x}_{i-1/2} + \frac{1}{720}(1181\ddot{x}_{i-1} - 1593\ddot{x}_{i-2} + 1023\ddot{x}_{i-3} - 251\ddot{x}_{i-4})\right\} \tag{45}$$

$$(N=4) \qquad \dot{x}_i = h\left\{\Sigma\ddot{x}_{i-1/2} + \frac{1}{1440}(2837\ddot{x}_{i-1} - 5086\ddot{x}_{i-2} + 4896\ddot{x}_{i-3} - 2402\ddot{x}_{i-4} + 475\ddot{x}_{i-5})\right\} \tag{46}$$

$$(N=5) \qquad \dot{x}_i = h\left\{\Sigma\ddot{x}_{i-1/2} + \frac{1}{60{,}480}(138{,}241\ddot{x}_{i-1} - 309{,}047\ddot{x}_{i-2} + 396{,}502\ddot{x}_{i-3} - 291{,}754\ddot{x}_{i-4} + 115{,}385\ddot{x}_{i-5} - 19{,}087\ddot{x}_{i-6})\right\} \tag{47}$$

$$(N=6) \qquad \dot{x}_i = h\left\{\Sigma\ddot{x}_{i-1/2} + \frac{1}{120{,}960}(313{,}281\ddot{x}_{i-1} - 838{,}888\ddot{x}_{i-2} + 1{,}344{,}989\ddot{x}_{i-3} - 1{,}319{,}488\ddot{x}_{i-4} + 782{,}755\ddot{x}_{i-5} - 258{,}968\ddot{x}_{i-6} + 36{,}799\ddot{x}_{i-7})\right\} \tag{48}$$

$$(N=7)\quad \dot{x}_i = h\Big\{\Sigma\ddot{x}_{i-1/2} + \frac{1}{3{,}628{,}800}(10{,}468{,}447\ddot{x}_{i-1} - 32{,}656{,}759\ddot{x}_{i-2} + 62{,}820{,}027\ddot{x}_{i-3} - 77{,}035{,}235\ddot{x}_{i-4} + 60{,}933{,}245\ddot{x}_{i-5} - 30{,}239{,}397\ddot{x}_{i-6} + 8{,}594{,}089\ddot{x}_{i-7} - 1{,}070{,}017\ddot{x}_{i-8})\Big\} \tag{49}$$

d. First-sum corrector. Eq. (24) substituted into Eq. (23) yields the first-sum corrector in terms of antecedent values of the acceleration.

$$(N=0)\quad \dot{x}_i = h\{\Sigma\ddot{x}_{i+1/2} - 1/2\ddot{x}_i\} \tag{50}$$

$$(N=1)\quad \dot{x}_i = h\Big\{\Sigma\ddot{x}_{i+1/2} + \frac{1}{12}(-7\ddot{x}_i + \ddot{x}_{i-1})\Big\} \tag{51}$$

$$(N=2)\quad \dot{x}_i = h\Big\{\Sigma\ddot{x}_{i+1/2} + \frac{1}{24}(-15\ddot{x}_i + 4\ddot{x}_{i-1} - \ddot{x}_{i-2})\Big\} \tag{52}$$

$$(N=3)\quad \dot{x}_i = h\Big\{\Sigma\ddot{x}_{i+1/2} + \frac{1}{720}(-469\ddot{x}_i + 177\ddot{x}_{i-1} - 87\ddot{x}_{i-2} + 19\ddot{x}_{i-3})\Big\} \tag{53}$$

$$(N=4)\quad \dot{x}_i = h\Big\{\Sigma\ddot{x}_{i+1/2} + \frac{1}{1440}(-965\ddot{x}_i + 462\ddot{x}_{i-1} - 336\ddot{x}_{i-2} + 146\ddot{x}_{i-3} - 27\ddot{x}_{i-4})\Big\} \tag{54}$$

$$(N=5)\quad \dot{x}_i = h\Big\{\Sigma\ddot{x}_{i+1/2} + \frac{1}{60{,}480}(-41{,}393\ddot{x}_i + 23{,}719\ddot{x}_{i-1} - 22{,}742\ddot{x}_{i-2} + 14{,}762\ddot{x}_{i-3} - 5{,}449\ddot{x}_{i-4} + 863\ddot{x}_{i-5})\Big\} \tag{55}$$

$$(N=6)\quad \dot{x}_i = h\Big\{\Sigma\ddot{x}_{i+1/2} + \frac{1}{120{,}960}(-84{,}161\ddot{x}_i + 55{,}688\ddot{x}_{i-1} - 66{,}109\ddot{x}_{i-2} + 57{,}024\ddot{x}_{i-3} - 31{,}523\ddot{x}_{i-4} + 9976\ddot{x}_{i-5} - 1375\ddot{x}_{i-6})\Big\} \tag{56}$$

$$(N=7)\quad \dot{x}_i = h\Big\{\Sigma\ddot{x}_{i+1/2} + \frac{1}{3{,}628{,}800}(-2{,}558{,}783\ddot{x}_i + 1{,}908{,}311\ddot{x}_{i-1} - 2{,}696{,}283\ddot{x}_{i-2} + 2{,}899{,}075\ddot{x}_{i-3} - 2{,}134{,}045\ddot{x}_{i-4} + 1{,}012{,}293\ddot{x}_{i-5} - 278{,}921\ddot{x}_{i-6} + 33{,}953\ddot{x}_{i-7})\Big\} \tag{57}$$

N65-32414

D. The Determination of a Density Function—An Exercise in the Application of Integral Transforms

C. B. Solloway

1. The Problem

The following problem arose practically in connection with the operational characteristics of a star-tracker device. Given the marginal density function $g(x)$ of a two-dimensional distribution, known to be independent in polar coordinates and uniform in the polar angle θ, determine the probability density function $p(r)$ of the radius vector $r = (x^2 + y^2)^{1/2}$.

Solution. We have

$$\int_x^\infty g(\xi)\,d\xi = 2\int_0^{\pi/2}\int_{x/\cos\theta}^\infty \frac{p(r)}{2\pi}\,dr\,d\theta \qquad x>0 \tag{1}$$

Differentiating both sides with respect to x, we obtain

$$g(x) = \frac{1}{\pi}\int_0^{\pi/2} p\left(\frac{x}{\cos\theta}\right)\frac{1}{\cos\theta}\,d\theta.$$

and making the substitution $r = x/\cos\theta$ yields

$$g(x) = \frac{1}{\pi}\int_x^\infty \frac{p(r)}{(r^2-x^2)^{1/2}}\,dr \tag{2}$$

Eq. (2) is a (singular) integral equation for $p(r)$.

Taking Fourier cosine transforms of both sides, we obtain after interchanging the order of integration

$$\bar{g}(\omega) = \int_0^\infty g(x)\cos\omega x\,dx = \frac{1}{\pi}\int_0^\infty\int_0^r p(r)\frac{\cos\omega x}{(r^2-x^2)^{1/2}}\,dx\,dr$$
$$= \frac{1}{2}\int_0^\infty p(r)J_0(r\omega)\,dr \qquad (3)$$

which shows that $2\bar{g}(\omega)$ is the Hankel Transform of $p(r)/r$, with the kernel $rJ_0(r\omega)$. The inversion theorem for this transform yields

$$\frac{p(r)}{r} = 2\int_0^\infty \bar{g}(\omega)\,\omega J_0(r\omega)\,d\omega$$
$$= 2\int_0^\infty\int_0^\infty \omega g(x)\cos\omega x J_0(r\omega)\,d\omega\,dx \qquad (4)$$

when we substitute the expression for $\bar{g}(\omega)$ from Eq. (3). Interchanging the orders of integration of Eq. (4) and integrating by parts (assuming $g'(x) = dg/dx$ exists), we have

$$p(r) = -2r\int_0^\infty\int_0^\infty g'(x)\sin\omega x J_0(r\omega)\,d\omega\,dx$$
$$= -2r\int_r^\infty \frac{g'(x)}{(x^2-r^2)^{1/2}}\,dx \qquad (5)$$

since the integrated part vanishes at the endpoints. This integral (being singular) does not lend itself to numerical computation An alternate form utilizing the cumulative density function is

$$1 - p(r) = \int_r^\infty p(\xi)\,d\xi = \int_r^\infty -2g'(x)(x^2-r^2)^{1/2}\,dx$$
$$= 2\int_r^\infty \frac{xg(x)\,dx}{(x^2-r^2)^{1/2}} \qquad (6)$$

the last assuming that $\lim_{x\to\infty} xg(x) = 0$.

2. Examples

1. Let $g(x) = \dfrac{1}{(2\pi)^{1/2}\sigma}e^{-x^2/2\sigma^2} \qquad -\infty < x < \infty$

Substituting into Eq. (5) yields

$$p(r) = \frac{+2r}{(2\pi)^{1/2}\sigma}\int_r^\infty \frac{x}{\sigma^2}\frac{e^{-x^2/2\sigma^2}}{(x^2-r^2)^{1/2}}\,dx \qquad (7)$$

The substitution $x^2 = r^2 + y^2$ reduces the integral to

$$p(r) = \frac{2re^{-r^2/2\sigma^2}}{\sigma^2}\int_0^\infty \frac{e^{-y^2/2\sigma^2}}{(2\pi)^{1/2}\sigma}\,dy = \frac{re^{-r^2/2\sigma^2}}{\sigma^2} \qquad (8)$$

the so-called Rayleigh distribution.

2. Let $g(x) = \dfrac{1}{2}e^{-|x|} \qquad -\infty < x < \infty$

Again substituting in Eq. (5) yields

$$p(r) = r\int_r^\infty \frac{e^{-x}}{(x^2-r^2)^{1/2}}\,dx \qquad (9)$$

The substitution $x = r\cosh\theta$ reduces the integral to

$$p(r) = r\int_0^\infty e^{-r\cosh\theta}\,d\theta = rK_0(r) \qquad (10)$$

where $K_0(r)$ is the modified Bessel function of the third kind of zero order. It is well known that $K_0(r) > 0$ and easily verified that

$$\int_0^\infty rK_0(r)\,dr = 1$$

Acknowledgment. The author is indebted to E. S. Davis of JPL Section 344 for bringing the problem to his attention.

E. Symmetrization of the Two-Body Problem

R. Broucke

1. Introduction

The purpose of this article is to describe a change of variables for the perturbed two-dimensional two-body problem that transforms the equations of motion to a new form which presents greater simplicity than the usual equations.

The change of variables we use consists of a transformation of the spatial variables x, y, together with a change of the independent variable t. The coordinate transformation is the ordinary transformation to parabolic coordinates, and the independent variable (time) is replaced by another variable which is essentially equivalent to the eccentric anomaly. This change of variables was used previously by several authors [e.g., Levi-Civita (Ref. 10)],

essentially for the regularization of the circular restricted three-body problem. A. Wintner (Ref. 11) also used this transformation for the solution of the non-perturbed two-body problem in a context which had no connection with the three-body problem.

The main effect of this change of variables is to transform the two-body problem into the two-dimensional harmonic oscillator (with or without perturbations). Thus we have a problem which has a very simple solution in sine and cosine terms (when no perturbations are present). In other words, we have transformed a problem with an inverse-square-law central-force field to another problem with a central force which is directly proportional to the distance. Of course, this last problem belongs to the list of those central-force-field problems which are integrable, as has been shown by many authors [e.g., Whittaker (Ref. 12)]. But the important fact here is that the familiar denominators $1/r^2$ in the two-body force are replaced by the factor r, and this greatly simplifies and symmetrizes the equations and their solutions. The simplicity of the new problem comes solely from the fact that the parabolic coordinates transform the two-body problem to a problem in which the two variables have been uncoupled, i.e., they transform a system with two degrees of freedom into two systems with one single degree of freedom.

In the perturbed two-body problem, this symmetrization also simplifies many of the equations. We can observe this in the development of the special perturbation techniques (e.g., the Encke method and the variation-of-rectangular-parameters method). The Encke method takes a particularly simple form: it can be applied without solving Kepler's equation or any other transcendental equation equivalent to Kepler's equation. It is also interesting to develop the corresponding variation-of-rectangular-parameters method, since there seems to be a tendency now to use rectangular coordinate perturbation techniques in trajectory calculations. Several authors (Refs. 13–16) claim that their formulation is completely general, but this seems not to be true, since the singularity $r = 0$ is still present in their equations. This singularity is not present in the perturbation equations that use parabolic coordinates. In several practical cases, such as atmospheric drag perturbations, for instance, it is worthwhile to remove the singularity $r = 0$. In the case of atmospheric drag, the difficulty with the classical two-body equations comes from the fact that the satellite passes through the regions with maximum density at periapsis, where the perturbations are strongest, with the largest velocity, and this results in a loss of precision when numerical integrations are done with constant steps. In the symmetric formulation, however, the satellite crosses the high-density region in a much smoother way (nearly in a rectilinear path with a constant velocity, at least when the eccentricity tends to unity).

The equations we present for the perturbed problem can also be applied easily when the perturbations are the gravitational forces from extra bodies. In this way we are able to regularize the collision with the central body in the restricted n-body problem ("restricted" is used here in the sense that the body whose motion is studied is a massless particle). This regularization presents two essential facts which are not common in most previous works on regularization. First of all, this regularization is not related to any rotating coordinate system, but can be done as well (and often in a more simple way) in a fixed direction frame as in a rotating frame. On the other hand, the method can be applied independently of the existence of an energy integral, simply by replacing the energy integral by a differential equation giving the variation of the energy. Only in a few particular cases has a regularization been described for a system without the Jacobi integral (Ref. 17).

The formulation we present here is completely general and as a possible application we developed the regularized equations for the general restricted three-body problem (where the two main masses may describe elliptic, hyperbolic, or parabolic orbits) and also for a four-body problem which has been used by a few authors as a model for the Sun–Earth–Moon system (Ref. 18).

The theory is described here only for the two-dimensional case; however, everything can be generalized to the three-dimensional case, for instance by using the osculating plane of motion defined by the two variables I and Ω (inclination and longitude of the node).

2. The Two-Body Problem

Let us write the two differential equations of motion of a satellite of negligible mass in the perturbed force field of a central body of mass m:

$$\frac{d^2x}{dt^2} = -m\frac{x}{r^3} + P_x \tag{1}$$

$$\frac{d^2y}{dt^2} = -m\frac{y}{r^3} + P_y \tag{2}$$

where (P_x, P_y) are the components of the perturbing force, and where

$$r^2 = x^2 + y^2 \tag{3}$$

Multiplying Eqs. (1) and (2) by dx/dt and dy/dt, respectively, and adding them, we obtain

$$\frac{1}{2}\left[\left(\frac{dx}{dt}\right)^2 + \left(\frac{dy}{dt}\right)^2\right] - \frac{m}{r} = \int_0^t \left(P_x \frac{dx}{dt} + P_y \frac{dy}{dt}\right) dt + E_0 \tag{4}$$

which we shall call the "energy equation" (E_0 is an integration constant).

3. Parabolic Coordinates

We define the parabolic coordinates (ξ, η) by the equations

$$x = \xi^2 - \eta^2 \tag{5}$$

$$y = 2\xi\eta \tag{6}$$

We have then

$$r = \xi^2 + \eta^2 \tag{7}$$

and we shall also define a transformation of the independent variable t by the differential relation

$$dt = r\,ds \tag{8}$$

We shall use two derivative symbols: a prime for the t-derivative and a dot for the s-derivative. For any variable F we may then write

$$F' = \frac{1}{r}\dot{F} \tag{9}$$

$$F'' = \frac{1}{r^3}[r\ddot{F} - r\dot{F}] = \frac{1}{r^3}[r\ddot{F} - 2(\xi\dot{\xi} + \eta\dot{\eta})\dot{F}] \tag{10}$$

Thus, for the first derivatives of x, y, and r, we have

$$x' = \frac{2}{r}(\xi\dot{\xi} - \eta\dot{\eta}) \tag{11}$$

$$y' = \frac{2}{r}(\xi\dot{\eta} + \dot{\xi}\eta) \tag{12}$$

$$r' = \frac{2}{r}(\xi\dot{\xi} + \eta\dot{\eta}) \tag{13}$$

and for the second derivatives:

$$x'' = \frac{2}{r^2}(\xi\ddot{\xi} - \eta\ddot{\eta}) - \frac{2}{r^3}(\xi^2 - \eta^2)(\dot{\xi}^2 + \dot{\eta}^2) \tag{14}$$

$$y'' = \frac{2}{r^2}(\xi\ddot{\eta} + \eta\ddot{\xi}) - \frac{4}{r^3}\xi\eta(\dot{\xi}^2 + \dot{\eta}^2) \tag{15}$$

Substituting Eqs. (14) and (15) in the Eqs. of motion (1) and (2) and solving for ξ and η, we obtain

$$\ddot{\xi} - \frac{\xi}{r}\left[\dot{\xi}^2 + \dot{\eta}^2 - \frac{m}{2}\right] = \frac{r}{4}P_\xi \tag{16}$$

$$\ddot{\eta} - \frac{\eta}{r}\left[\dot{\xi}^2 + \dot{\eta}^2 - \frac{m}{2}\right] = \frac{r}{4}P_\eta \tag{17}$$

where we have defined P_ξ and P_η by

$$P_\xi = 2[\xi P_x + \eta P_y] \tag{18}$$

$$P_\eta = 2[-\eta P_x + \xi P_y] \tag{19}$$

In order to obtain a more simple form for the Eqs. of motion (16) and (17), let us first write the energy Eq. (4) in parabolic coordinates. By using Eqs. (11), (12), and (13), we find that

$$\frac{2}{r}\left[\dot{\xi}^2 + \dot{\eta}^2 - \frac{m}{2}\right] = \int_0^s R\,ds + E_0 \tag{20}$$

where the function R is defined by

$$R = (P_\xi\dot{\xi} + P_\eta\dot{\eta}) \tag{21}$$

Using Eq. (20), Eqs. (16) and (17) become

$$\ddot{\xi} = \tfrac{1}{2}(S + E_0)\xi + \frac{r}{4}P_\xi \tag{22}$$

$$\ddot{\eta} = \tfrac{1}{2}(S + E_0)\eta + \frac{r}{4}P_\eta \tag{23}$$

where the function S is defined by the differential equation

$$\dot{S} = R \tag{24}$$

In order to derive the time t from the new variables, we can, by using the Definition (8), write the differential equation

$$\dot{t} = r \tag{25}$$

We can now solve any perturbation problem by integrating numerically the simultaneous Eqs. (22), (23), (24), and (25), or by only integrating the system [Eqs. (22), (23), and (24)] and then solving the Quadrature (25) separately. Eq. (15) is a differential equation which in the perturbed problem corresponds to the energy integral in the non-perturbed two-body problem. The energy E of the satellite, which is a function of t in the perturbed problem, can now be obtained by

$$E = \frac{2}{r}(\dot{\xi}^2 + \dot{\eta}^2) - \frac{m}{r} = S + E_0 \tag{26}$$

The remarkable advantage that the system [Eqs. (22), (23), and (24)] has over the system [Eqs. (1) and (2)] is that the collision singularity, $r = 0$, with the central body has been removed. However, there are other advantages which shall become evident in the following discussion.

4. The Solution of the Non-Perturbed Problem

When both perturbation components (P_x, P_y) and also (P_ξ, P_η) are zero, Eqs. (22) and (23) become

$$\ddot{\xi} = \frac{E}{2}\xi \tag{27}$$

$$\ddot{\eta} = \frac{E}{2}\eta \tag{28}$$

We see that each of these equations has a separate variable, ξ for Eq. (27), η for Eq. (28). Since $E = E_0$ is a constant number, each equation represents the harmonic oscillator, i.e., a problem with a central attractive force proportional to the distance (let us suppose that $E < 0$). The solution of Eqs. (27) and (28) may be written in terms of circular functions:

$$\xi = \xi_0 \cos \sigma s + \dot{\xi}_0 \frac{\sin \sigma s}{\sigma} \tag{29}$$

$$\eta = \eta_0 \cos \sigma s + \dot{\eta}_0 \frac{\sin \sigma s}{\sigma} \tag{30}$$

where we have defined

$$\sigma = \left(-\frac{E}{2}\right)^{1/2} \tag{31}$$

Eliminating s from Eqs. (29) and (30), we obtain a second-degree equation in (ξ, η) which represents a conic centered at the origin (an ellipse when $E < 0$). Thus, one of the effects of the parabolic coordinates is to transform the two-body conic solution centered at one focus to another conic solution centered at the geometric center of the conic. This results in greater symmetry in the equations.

Let us designate by α and β the semi-major and semi-minor axis of the ellipse in the parabolic plane (ξ, η), and let us define a, e, and ε by

$$a = \frac{\alpha^2 + \beta^2}{2} \tag{32}$$

$$e = \frac{\alpha^2 - \beta^2}{\alpha^2 + \beta^2} \tag{33}$$

$$\varepsilon = \frac{1}{\alpha}(\alpha^2 - \beta^2)^{1/2} \tag{34}$$

The parameter ε is the eccentricity of the ellipse with semi-axes α and β. If we take the particular solution

$$\xi = \alpha \cos \sigma s = [a(1 + e)]^{1/2} \cos \sigma s \tag{35}$$

$$\eta = \beta \sin \sigma s = [a(1 - e)]^{1/2} \sin \sigma s \tag{36}$$

in the (ξ, η) plane, we have in the (x, y) plane the corresponding solution

$$x = a(\cos 2\sigma s - e) \tag{37}$$

$$y = a(1 - e^2)^{1/2} \sin 2\sigma s \tag{38}$$

$$r = a(1 - e \cos 2\sigma s) \tag{39}$$

$$dt = 2\left(\frac{a^3}{m}\right)^{1/2}(1 - e \cos 2\sigma s)\, d(\sigma s) \tag{40}$$

Thus, we have the well-known elliptic solution with semi-major axis a and eccentricity e. Integrating Eq. (40), we obtain Kepler's equation

$$t - t_0 = \left(\frac{a^3}{m}\right)^{1/2}(2\sigma s - e \sin 2\sigma s) \tag{41}$$

Thus, the quantity $2\sigma s$ is exactly the eccentric anomaly On the other hand, in parabolic coordinates (ξ, η) the period of the motion is (for the variable s)

$$T_{sP} = \frac{2\pi}{\sigma} \tag{42}$$

while in Cartesian coordinates (x, y) the period is only half of T_{sP}:

$$T_{sC} = \frac{2\pi}{2\sigma} = \frac{\pi}{\sigma} \tag{43}$$

In other words, the Keplerian ellipse is described twice when one single revolution is described in the parabolic plane. The two closest approach and two farthest departure points in the parabolic plane correspond to periapsis and apoapsis, respectively. Comparing Eqs. (33) and (34), we conclude that both ellipses have simultaneous zero eccentricity or unit eccentricity. In the case of unit eccentricity, Eqs. (35) and (36) show that at collision the motion in the (ξ, η) plane goes through the origin (which is a stable equilibrium solution) with a finite non-zero velocity.

5. The Perturbation Equations in Parabolic Coordinates

We shall now come back to the perturbed problem, and derive the so-called rectangular variation of parameters equations, as has been done by Pines, Battin, Kizner, Goodyear, and probably other authors (Refs. 13, 15, 16, and 19).

In order to shorten the notations, we define a few two-dimensional vectors:

$$\vec{\xi} = (\xi, \eta), \qquad \vec{\xi}_0 = (\xi_0, \eta_0) \tag{44}$$

$$\dot{\vec{\xi}} = (\dot{\xi}, \dot{\eta}), \qquad \dot{\vec{\xi}}_0 = (\dot{\xi}_0, \dot{\eta}_0) \tag{45}$$

$$\vec{P} = (P_\xi, P_\eta) \tag{46}$$

The Eqs. (22) and (23) can now be written in the form

$$\ddot{\vec{\xi}} = \frac{1}{2} E \vec{\xi} + \frac{r}{4} \vec{P} \tag{47}$$

while the solution [Eqs. (29) and (30)] of the non-perturbed problem is

$$\vec{\xi} = \vec{\xi}_0 \cos \sigma s + \dot{\vec{\xi}}_0 \frac{\sin \sigma s}{\sigma} \tag{48}$$

$$\dot{\vec{\xi}} = -\vec{\xi}_0 \, \sigma \sin \sigma s + \dot{\vec{\xi}}_0 \cos \sigma s \tag{49}$$

This solution may be considered valid in the elliptic, hyperbolic, parabolic, and rectilinear cases, for all values of s, with the simple condition that hyperbolic trigonometric functions be used when $E > 0$ and σ is imaginary. For many forms considered by previous authors, the equations are not valid for all times t, because the singularity $r = 0$ has not been removed.

We define the "perturbation derivatives" of $\vec{\xi}$ and $\dot{\vec{\xi}}$ by

$$\left(\frac{d\vec{\xi}}{ds}\right)_P = 0 \tag{50}$$

$$\left(\frac{d\dot{\vec{\xi}}}{ds}\right)_P = \frac{r}{4} \vec{P} \tag{51}$$

in accordance with Eq. (47), and the perturbation derivative of E by

$$\left(\frac{dE}{ds}\right)_P = \left(\frac{dS}{ds}\right)_P = R = (\vec{P} \cdot \dot{\vec{\xi}}) \tag{52}$$

in accordance with Eqs. (21), (24), and (26).

To find the perturbation derivatives of $\vec{\xi}_0$ and $\dot{\vec{\xi}}_0$, we first solve Eqs. (48) and (49) with respect to these two quantities:

$$\vec{\xi}_0 = \vec{\xi} \cos \sigma s - \dot{\vec{\xi}} \frac{\sin \sigma s}{\sigma} \tag{53}$$

$$\dot{\vec{\xi}}_0 = \vec{\xi} \sigma \sin \sigma s + \dot{\vec{\xi}} \cos \sigma s \tag{54}$$

Taking the derivatives of the preceding equations, we obtain the final perturbation equations

$$\left(\frac{d\vec{\xi}_0}{ds}\right)_P = \frac{R}{4}\left[\vec{\xi} s \frac{\sin \sigma s}{\sigma} + \frac{\dot{\vec{\xi}}}{\sigma^2}\left(s \cos \sigma s - \frac{\sin \sigma s}{\sigma}\right)\right] - \frac{r \sin \sigma s}{4\sigma} \vec{P} \tag{55}$$

$$\left(\frac{d\dot{\vec{\xi}}_0}{ds}\right)_P = \frac{R}{4}\left[-\vec{\xi}\left(s \cos \sigma s + \frac{\sin \sigma s}{\sigma}\right) + \dot{\vec{\xi}} s \frac{\sin \sigma s}{\sigma}\right] + r \frac{\cos \sigma s}{4} \vec{P} \tag{56}$$

These equations can be applied, with a few precautions, even when $\sigma = 0$, if we set

$$\tau = \sigma s \tag{57}$$

and if we introduce the auxiliary functions of τ,

$$T(t) = \frac{\sin \tau}{\tau} = 1 - \frac{\tau^2}{3!} + \cdots \tag{58}$$

$$U(t) = \frac{1}{\tau^2}\left(\frac{\sin \tau}{\tau} - \cos \tau\right) = \frac{2}{3!} - \frac{4\tau^2}{5!} + \cdots \tag{59}$$

$$V(t) = \left(\frac{\sin \tau}{\tau} + \cos \tau\right) = 2 - \frac{2\tau^2}{3} + \cdots \tag{60}$$

It is also remarkably easy to develop the analog of the Encke method in the parabolic variables. For this purpose, let us consider the non-perturbed reference solution $\vec{\xi}_r$ and the deviation $\delta\vec{\xi}$ due to the perturbations. The true perturbed solution is then given by

$$\vec{\xi} = \vec{\xi}_r + \delta\vec{\xi} \tag{61}$$

$$E = E_0 + \delta E \tag{62}$$

For the reference solution, we have

$$\vec{\xi}_r = \vec{\xi}_0 \cos \sigma s + \vec{\dot{\xi}}_0 \frac{\sin \sigma s}{\sigma} \tag{63}$$

$$\dot{\vec{\xi}}_r = \frac{E_0}{2}\vec{\xi}_r \tag{64}$$

Taking the second derivatives of Eqs. (61) and (62), we obtain directly the differential equations for $\delta\vec{\xi}$ and δE:

$$\delta\ddot{\vec{\xi}} = \frac{E}{2}\delta\vec{\xi} + \frac{\delta E}{2}\vec{\xi}_r + \frac{r}{4}\vec{P} \tag{65}$$

$$\delta\dot{E} = R = (\vec{\dot{\xi}} \cdot \vec{P}) \tag{66}$$

These equations can now be integrated numerically, using the values given by Eqs. (61), (62), (63), and (64) for the right-side members E and ξ.

6. Application to the Atmospheric Drag Perturbations

In the physical coordinates (x, y), we have the perturbation acceleration $\vec{X} = (P_x, P_y)$:

$$\vec{X} = -\frac{B}{2}\rho(r)\, v\vec{x}' \tag{67}$$

where B is the drag coefficient, $\rho(r)$ the atmospheric density, and v the magnitude of the velocity. The corresponding perturbation acceleration in the parabolic coordinates (ξ, η) is

$$\vec{P} = -2B\rho v\vec{\dot{\xi}} \tag{68}$$

where v is given by

$$v = \frac{2}{r}\left[(\xi^2 + \eta^2)(\dot{\xi}^2 + \dot{\eta}^2)\right]^{1/2} \tag{69}$$

The term which is needed for the integration of the differential equations is exactly

$$\vec{F} = \frac{r}{4}\vec{P} = -B\rho\left[r(\dot{\xi}^2 + \dot{\eta}^2)\right]^{1/2}\vec{\dot{\xi}} \tag{70}$$

N65-32416

F. Quantum Mechanics and Stochastic Processes

R. W. Davies and H. Lass

In recent years there have been various attempts to obtain a better understanding of the Schrödinger wave equation on the basis of hydrodynamical analogies.[6] In this article we will obtain a connection between the Schrödinger wave equation and a partial differential equation which arises from a discussion of stochastic processes.

First we derive the stochastic differential equation

$$\frac{\partial^2\rho}{\partial t^2} = \frac{\partial^2}{\partial x^2}(\rho\bar{v}^2) - \frac{\partial}{\partial x}(\rho\bar{a}) \tag{1}$$

The elements of Eq. (1) will become clear as we proceed to its derivation. Let us consider an ensemble of curves $x = \phi(t, \alpha)$. The parameter α, which may be multidimensional, is determined from a probability density function. Each choice of α determines a member of the ensemble. We are interested in obtaining an expression for the density function $\rho(x, t)$ such that $\rho(x, t)\,dx$ represents the probability that at time t the value of $\phi(t, \alpha)$ lies in the range $(x, x + dx)$.

Consider the integral

$$F(x,t) = \int_{-\infty}^{x}\int_{-\infty}^{\infty} \delta[X - \phi(t,\alpha)]\, p(\alpha)\, d\alpha dX$$

$$= \int_{-\infty}^{\infty}\int_{-\infty}^{x} \delta[X - \phi(t,\alpha)]\, p(\alpha)\, dX d\alpha \tag{2}$$

with δ the Dirac delta function. Now

$$\int_{-\infty}^{x} \delta[X - \phi(t,\alpha)]\, dX = \begin{cases} 1 \text{ for } \alpha \text{ such that } \phi(t,\alpha) < x \\ 0 \text{ for } \alpha \text{ such that } \phi(t,\alpha) > x \end{cases} \tag{3}$$

Hence

$$F(x,t) = \int_S p(\alpha)\, d\alpha \tag{4}$$

[6] Bohm, D., *Physical Review*, 1952; Bohm, D. and Vigier, J. P., *Physical Review*, 1954; Madelung, Z., *Physik*, 1926; Moyal, J. E., *Proceedings of the Cambridge Philosophical Society*, 1949; Schenberg, M., *Nuovo Cimento*, 1954; and Takabaysai, T., *Progress of Theoretical Physics* (Japan), 1952.

with S the set of α for which $\phi(t,\alpha) < x$. Thus $F(x,t)$ is the distribution function associated with $\rho(x,t)$, i.e., $\rho(x,t) = \partial F/\partial x$, which yields

$$\rho(x,t) = \int_{-\infty}^{\infty} \delta[x - \phi(t,\alpha)]\, p(\alpha)\, d\alpha \tag{5}$$

Next let us consider the speed $v = \dot{x} = d\phi(t,\alpha)/dt$. If $\rho(x,t;v,t)\,dx\,dv$ represents the joint probability that $\phi(t,\alpha)$ lies in the range $(x, x+dx)$ and $\dot{\phi}(t,\alpha)$ lies in the range $(v, v+dv)$, it can be shown that

$$\rho(x,t;v,t) = \int_{-\infty}^{\infty} \delta[x - \phi(t,\alpha)]\, \delta[v - \dot{\phi}(t,\alpha)] \times p(\alpha)\, d\alpha \tag{6}$$

Of particular interest is the conditional probability that $\dot{\phi}(t,\alpha)$ lies in the range $(v, v+dv)$ given that $\phi(t,\alpha) = x$. From Bayes' postulate,

$$\rho(v,t|x,t) = \frac{\rho(x,t;v,t)}{\rho(x,t)} \tag{7}$$

and the mean-square speed of all curves passing through x at time t is given by

$$\overline{v^2(x,t)} = \frac{1}{\rho(x,t)} \int_{-\infty}^{\infty} \dot{\phi}^2(t,\alpha)\, \delta[x - \phi(t,\alpha)] \times p(\alpha)\, d\alpha \tag{8}$$

Similarly, the mean acceleration of all curves passing through x at time t is given by

$$\overline{a(x,t)} = \frac{1}{\rho(x,t)} \int_{-\infty}^{\infty} \delta[x - \phi(t,\alpha)]\, \ddot{\phi}(t,\alpha) \times p(\alpha)\, d\alpha \tag{9}$$

From Eqs. (8) and (9) we obtain

$$\frac{\partial^2}{\partial x^2}(\rho\bar{v^2}) - \frac{\partial}{\partial x}(\rho\bar{a}) = \int_{-\infty}^{\infty} [\dot{\phi}^2(t,\alpha)\, \delta''(x - \phi(t,\alpha)) - \ddot{\phi}(t,\alpha)\, \delta'(x - \phi(t,\alpha))]\, p(\alpha)\, d\alpha \tag{10}$$

Differentiating Eq. (5) twice with respect to t yields Eq. (1) by making use of Eq. (10). The reader is referred to a paper by J. E. Moyal in the *Journal of the Royal Statistical Society*, Vol. XI, 1949, for a different derivation of Eq. (1).

It is also a simple matter to derive the equation of continuity

$$\frac{\partial \rho}{\partial t} + \frac{\partial}{\partial x}(\rho\bar{v}) = 0 \tag{11}$$

We now show that the time-varying one-dimensional Schrödinger wave equation can be put into the same form as Eq. (1), with $\rho = \Psi\Psi^*$, such that Ψ is a solution of

$$H\Psi = i\hbar \frac{\partial \Psi}{\partial t}$$

$$H = -\frac{\hbar^2}{2m}\frac{\partial^2}{\partial x^2} + V \tag{12}$$

and Ψ^* is the complex conjugate of Ψ, satisfying

$$H\Psi^* = -i\hbar \frac{\partial \Psi^*}{\partial t}$$

V is the classical potential function.

From Eq. (12) we have

$$i\hbar\left[\Psi^* \frac{\partial \Psi}{\partial t} + \Psi \frac{\partial \Psi^*}{\partial t}\right] = -\frac{\hbar^2}{2m}\left(\Psi^* \frac{\partial^2 \Psi}{\partial x^2} - \Psi \frac{\partial^2 \Psi^*}{\partial x^2}\right) = -\frac{\hbar^2}{2m}\frac{\partial}{\partial x}\left(\Psi^* \frac{\partial \Psi}{\partial x} - \Psi \frac{\partial \Psi^*}{\partial x}\right) \tag{13}$$

or

$$\frac{\partial \rho}{\partial t} + \frac{\partial}{\partial x}\left[\frac{\hbar}{2im}\left(\Psi^* \frac{\partial \Psi}{\partial x} - \Psi \frac{\partial \Psi^*}{\partial x}\right)\right] = 0 \tag{14}$$

Eq. (14) is the well-known continuity equation of quantum mechanics. Comparing Eqs. (11) and (14) leads to the result

$$\rho\overline{v(x,t)} = \frac{\hbar}{2im}\left(\Psi^* \frac{\partial \Psi}{\partial x} - \Psi \frac{\partial \Psi^*}{\partial x}\right) \tag{15}$$

A further time derivative of Eq. (14), along with Eq. (12), yields

$$\frac{\partial^2 \rho}{\partial t^2} = \frac{1}{m}\frac{\partial}{\partial x}\left(\rho \frac{\partial V}{\partial x}\right) - \frac{\hbar^2}{4m^2}\frac{\partial^4 \rho}{\partial x^4} + \frac{\hbar^2}{m^2}\frac{\partial^2}{\partial x^2}\left(\frac{\partial \Psi}{\partial x}\frac{\partial \Psi^*}{\partial x}\right) \tag{16}$$

Next let us assume that the speed of the particle [now represented by a probability packet given by $\rho(x,t)$] is given by

$$v(x,t) = w(x,t) + u(x,t) \tag{17}$$

with $u(x,t)$ defined as a perturbation whose mean is zero, so that

$$\begin{aligned} \overline{v(x,t)} &= w(x,t) \\ \overline{v^2(x,t)} &= w^2(x,t) + \overline{u^2(x,t)} \end{aligned} \tag{18}$$

with $w(x,t)$ satisfying the continuity equation

$$\frac{\partial \rho}{\partial t} + \frac{\partial}{\partial x}(\rho w) = 0 \tag{19}$$

from Eqs. (11), (14), and (18).

Squaring Eq. (15) yields

$$\rho^2 w^2 = -\frac{\hbar^2}{4m^2}\left[\Psi^{*2}\left(\frac{\partial \Psi}{\partial x}\right)^2 - 2\rho\frac{\partial \Psi}{\partial x}\frac{\partial \Psi^*}{\partial x} + \Psi^2\left(\frac{\partial \Psi^*}{\partial x}\right)^2\right] \tag{20}$$

Furthermore,

$$\left(\frac{\partial \rho}{\partial x}\right)^2 = \Psi^{*2}\left(\frac{\partial \Psi}{\partial x}\right)^2 + 2\rho\frac{\partial \Psi}{\partial x}\frac{\partial \Psi^*}{\partial x} + \Psi^2\left(\frac{\partial \Psi^*}{\partial x}\right)^2 \tag{21}$$

from $\rho = \Psi\Psi^*$, so that

$$\frac{\hbar^2}{m^2}\frac{\partial \Psi}{\partial x}\frac{\partial \Psi^*}{\partial x} = \rho w^2 + \frac{\hbar^2}{4m^2}\frac{1}{\rho}\left(\frac{\partial \rho}{\partial x}\right)^2 \tag{22}$$

Eq. (16) now becomes

$$\begin{aligned} \frac{\partial^2 \rho}{\partial t^2} = \frac{\partial^2}{\partial x^2}\left[\rho\left(w^2 - \frac{\hbar^2}{4m^2}\frac{\partial^2 \ln \rho}{\partial x^2}\right)\right] \\ - \frac{\partial}{\partial x}\left[\rho\left(-\frac{1}{m}\frac{\partial V}{\partial x}\right)\right] \end{aligned} \tag{23}$$

Thus we have obtained Eq. (1) with

$$\begin{aligned} \overline{u^2(x,t)} &= -\frac{\hbar^2}{4m^2}\frac{\partial^2 \ln \rho}{\partial x^2} \\ \overline{a(x,t)} &= -\frac{1}{m}\frac{\partial V}{\partial x} \end{aligned} \tag{24}$$

and we note that $\overline{a(x,t)}$ corresponds to the classical acceleration.

Next we show that Eq. (24) is consistent with the Heisenberg uncertainty principle. Let us assume that $x\rho$ and $\partial\rho/\partial x$ vanish at $x = \pm\infty$. The total perturbation in momentum is given by

$$\Delta^2 p = \int_{-\infty}^{\infty} m^2 \overline{u^2(x,t)}\,\rho(x,t)\,dx \tag{25}$$

Thus

$$\begin{aligned} \Delta^2 p \Delta^2 x &= -\frac{\hbar^2}{4}\int_{-\infty}^{\infty} \rho\frac{\partial^2 \ln \rho}{\partial x^2}\,dx \int_{-\infty}^{\infty} (x-\bar{x})^2\,\rho(x,t)\,dx \\ &= \frac{\hbar^2}{4}\int_{-\infty}^{\infty}\frac{1}{\rho}\left(\frac{\partial \rho}{\partial x}\right)^2 dx \int_{-\infty}^{\infty} (x-\bar{x})^2\,\rho(x,t)\,dx \\ &\geqq \frac{\hbar^2}{4}\left[\int_{-\infty}^{\infty}\frac{\partial \rho}{\partial x}(x-\bar{x})\,dx\right]^2 = \frac{\hbar^2}{4} \end{aligned} \tag{26}$$

by applying the Cauchy-Schwarz inequality and performing an integration by parts on the last integral.

Now we note that Eq. (23) is a nonlinear differential equation in $\rho(x,t)$. In general, it will have a unique solution provided ρ and $\partial\rho/\partial t$ are given at $t = 0$. Since at $t = 0$ we have no reason to believe that the wave packet is moving to the left rather than to the right, we may assume $\partial\rho/\partial t = 0$. The substitution $\rho = \Psi\Psi^*$ reduces Eq. (23) to two linear equations in Ψ and Ψ^*, namely, the Schrödinger wave equations. Previous hydrodynamic analogies discussed by the authors mentioned in Footnote 6 deal chiefly with models yielding a diffusion equation for which $\rho(x,t) \geqq 0$. The mean-square velocity perturbation term

$$-\frac{\hbar^2}{4m^2}\frac{\partial^2 \ln \rho}{\partial x^2}$$

guarantees that the solutions of Eq. (23) are nonnegative.

It is logical to define the mean energy at any time t as

$$E(t) = \int_{-\infty}^{\infty} \rho V dx + \frac{m}{2}\int_{-\infty}^{\infty} w^2 \rho dx - \frac{\hbar^2}{8m}\int_{-\infty}^{\infty} \rho\frac{\partial^2 \ln \rho}{\partial x^2}\,dx \tag{27}$$

with

$$w(x,t) = -\frac{1}{\rho}\int_{-\infty}^{x}\frac{\partial \rho(\xi,t)}{\partial t}\,d\xi$$

The steady-state energy levels are given by

$$E = \int_{-\infty}^{\infty} \rho V dx + \frac{\hbar^2}{8m} \int_{-\infty}^{\infty} \frac{1}{\rho} \left(\frac{d\rho}{dx}\right)^2 dx \qquad (28)$$

If one writes $\rho = |\Psi|^2$, it is a simple matter to show that the value of E as given by Eq. (28) is in agreement with the value of E obtained from

$$-\frac{\hbar^2}{2m}\frac{d^2\Psi}{dx^2} + (V - E)\Psi = 0 \qquad (29)$$

One need only multiply Eq. (29) by Ψ and perform an integration over the range $(-\infty < x < \infty)$ to obtain the desired result.

The mean-square velocity perturbation term may be intimately connected with the study of information theory. In this field the entropy H (mean information per observation) is usually defined by

$$H = -\int_{-\infty}^{\infty} \rho(x) \ln \rho(x)\, dx \qquad (30)$$

which occasionally yields the unsatisfactory result $H < 0$. Let us define H for a continuous density function by

$$H = -\int_{-\infty}^{\infty} \rho(x,t) \frac{\partial^2 \ln \rho(x,t)}{\partial x^2}\, dx \qquad (31)$$

as suggested by the above analysis. Then

$$H = \int_{-\infty}^{\infty} \frac{1}{\rho}\left(\frac{\partial \rho}{\partial x}\right)^2 dx \geqq 0 \qquad (32)$$

provided $\partial\rho/\partial x$ vanishes at $x = \pm\infty$.

References

1. Kevorkian, J., "The Two Variable Expansion Procedure for the Approximate Solution of Certain Non-Linear Differential Equations," *Report No. SM-42620*, Douglas Aircraft Co., Inc., Santa Monica, California, December 3, 1962.

2. Cole, J. D., and Kevorkian, J., "Uniformly Valid Asymptotic Approximations for Certain Non-Linear Differential Equations," *Proceedings of the International Symposium on Non-Linear Mechanics and Non-Linear Differential Equations*, Academic Press, Inc., New York, N.Y., 1961.

3. Shapland, D. J., "Preliminary Investigation of an Unmanned Mission to the Asteroid Belt with Growth Potential for Jupiter Flyby," *Preprint No. 65-35*, American Astronautical Society Symposium on Unmanned Exploration on the Solar System, Denver, Colorado, February 8–10, 1965.

4. Kulikov, D. K., "Integration of Equations of Celestial Mechanics by Cowell's Method with Variable Intervals," *Dynamics of Satellites*, M. Roy, Ed., Academic Press, New York, N. Y., 1963.

5. Herrick, S., "Step-by-Step Integration of $\ddot{x} = f(x, y, z, t)$ Without a Corrector," *Mathematical Tables and Other Aids to Computation*, Vol. 5, pp. 61–67, 1951.

6. Devine, Charles J., *PLOD II: Planetary Orbit Determination Program for the IBM 7094 Computer*, Technical Report No. 33-188, Jet Propulsion Laboratory, Pasadena, California, April 15, 1965.

7. Hildebrand, F. B., *Introduction to Numerical Analysis*, McGraw-Hill, Inc., New York, N. Y., 1956.

References (Cont'd)

8. Milne, W. E., *Numerical Solution of Differential Equations*, John Wiley & Sons, Inc., New York, N. Y., 1953.

9. Eckert, W. J., Brouwer, D., Clemence, D. M., "Coordinates of the Five Outer Planets, 1653-2060," *Astronomical Papers of the American Ephemeris and Nautical Almanac*, Vol. XII, U. S. Government Printing Office, Washington, D. C , 1951.

10. Levi-Civita, "The Restricted Problem of Three Bodies," *Rendiconti Accademia Lincei*, Vol. 5, p. 553–559, 1915.

11. Wintner, A., "Analytical Foundations of Celestial Mechanics," pp. 192–201, Princeton University Press, Princeton, N.J., 1947.

12. Whittaker, E. T., "A Treatise on the Analytical Dynamics of Particles and Rigid Bodies," p. 80, Cambridge University Press, Cambridge, England, 1959.

13. Pines, S., "Variation of Parameters for Elliptic and Near Circular Orbits," *The Astronomical Journal*, Vol. 66, No. 1, p. 5, February 1961.

14. Danby, J. M. A., "Perturbations of the Coordinates in Planetary Theory," *The Astronomical Journal*, Vol. 70, No. 2, p. 155–161, March 1965.

15. Battin, R. H., "Astronautical Guidance," pp. 200–202, McGraw-Hill Company, New York, N.Y., 1964.

16. Goodyear, W. H., "Completely General Closed-Form Solution for Coordinates and Partial Derivatives of the Two Body Problem," *The Astronomical Journal*, Vol. 70, No. 3, pp. 189–192, April 1965.

17. Szebehely, V., and Giacaglia, G. E. O., "On the Elliptic Restricted Problem of Three-Bodies," *The Astronomical Journal*, Vol. 69, No. 3, pp. 230–235, April 1964.

18. Richards, P. B., Russell, L. H., and Cronin, J., "Some Periodic Solutions of a Four-Body Problem," *Icarus*, Vol. 3, No. 5, p. 6, December 1964.

19. Kizner, W., *A Formulation of the Variation of Parameter Equations for Rectangular Elements*, Technical Memorandum No. 312-535, Jet Propulsion Laboratory, Pasadena, California, February 22, 1965.

Erratum

The following correction should be noted for *SPS 37-31*, Vol. IV: on Fig. 2, p. 9, the Chebyshev, even n plot should follow a smooth curve intersecting the 2×10^0 grid on the abscissa at 3.14 on the ordinate. The isolated Chebyshev, even n point should be omitted from the plot.

II. Scientific Programming

A. Numerical Integration over a Family of Ellipses Using a Second-Sum Multi-Step Integrator Employing High-Order Backward Differences

C. J. Devine

1. Introduction

This is a continuation of accuracy studies of a second-sum Adams-type predictor-corrector numerical integrator (subroutines FORTSZ, TREK) that employs high-order backward differences; it has been in use at JPL for the last four years (*SPS 37-31*, Vol. IV; *SPS 37-32*, Vol. IV; a complete description of the integrator is given in Ref. 1). The method of integration and the method of computing the errors will be the same in the present study as the methods used in the above references.

In Part 2 a description of the second-order differential equations to be solved is given, along with the analytical solution of the differential equations from which the true solution was computed for a check of the errors made in the numerical solution. Part 3 presents the detailed derivation of the integration formulas and the method of computing a starting table. The coefficients employed in Eqs. (12), (14), (16), (17), and (18) were computed by a 7094 computer program [coefficients for FORTSZ (CFF)], using 140-bit ($\simeq 42$ decimal place) arithmetic. This program will compute coefficients to any order desired (for a list of coefficients in decimal and octal up to order 15 consult Ref. 1) Part 4 describes the main results of the integration over a family of ellipses determined by the eccentricity e, where e takes on the values 0.1, 0.2, $\cdots$, 0.9.

2. Method

The second-order differential equations to be solved were

$$\ddot{x} = f(x, y) = -(n^2a^3)\,x/r^3 \tag{1}$$

$$\ddot{y} = f(x, y) = -(n^2a^3)\,y/r^3 \tag{2}$$

where $r^2 = x^2 + y^2$.

The integration was done over a family of ellipses determined by the eccentricity e. The initial conditions were

$$x(0) = a(1-e) \qquad \dot{x}(0) = 0$$

$$y(0) = 0 \qquad \dot{y}(0) = a(1-e^2)^{1/2}/(1-e)$$

with $a = 1$, $n = 1$, and $M = 0$. Here, a is the semi-major axis, n is the mean motion defined by $n = 2\pi/P$, where P is the period, and M is the mean anomaly defined by

$$M = nt \tag{3}$$

Then for x, y lying in the orbital plane with the x-axis directed toward pericenter, solutions were given by

$$x = a(\cos u - e) \tag{4}$$

$$y = b \sin u \tag{5}$$

with the first derivatives given by

$$\dot{x} = -an \sin u/(1 - e\cos u) \tag{6}$$

$$\dot{y} = nb \cos u/(1 - e\cos u) \tag{7}$$

where $b = a(1-e^2)^{1/2}$ is the semi-minor axis and u is the eccentric anomaly. The eccentric anomaly is an angle at the center of the ellipse between the line of apsides and the radius of the auxiliary circle through a point that has the same x-coordinate as a given point on the ellipse. The eccentric anomaly u is determined from Kepler's equation

$$f(u) = u - e\sin u - M \tag{8}$$

by a Newton-Raphson iteration as follows:

Given a first approximation to Kepler's equation

$$u = M + e\sin M + \tfrac{1}{2}e^2 \sin 2M \tag{9}$$

computed in single precision, then u is found by iteration, using the Newton-Raphson equation in double precision

$$u_{k+1} = u_k - \frac{f(u_k)}{f'(u_k)} \tag{10}$$

given explicitly as

$$u_{k+1} - u_k = (M - u_k + e\sin u_k)/(1 - e\cos u_k)$$

with a final iteration in extended precision.

Once u has been found, then by substituting in Eqs. (4) through (7), the solutions x, y and their first derivatives $\dot{x}, \dot{y}$ are obtained. Successive time points are computed by incrementing t in Eq. (3).

3. Solution Method

The computer algorithm used to numerically solve this system of second-order differential equations was a multistep method in summed form. It is closely related to the familiar Adams-type methods. The algorithm may be regarded as consisting of two parts: (1) a starting procedure to produce the solution values at the first $m+1$ time points, and (2) a stepping procedure of the predictor-corrector type to advance the solution one time step, making use of the solution at the m immediately preceding points.

In the following discussion the formulas will be given for one variable x only. Identical formulas would be used for y.

The well-known Adams-Moulton corrector formula may be derived as follows, where the Taylor series formula $\exp(hD) = E = (1-\nabla)^{-1}$ is used in the form $D^{-1} = -h/\ln(1-\nabla)$:

$$\begin{aligned}\dot{x}_n - \dot{x}_{n-1} &= \int_{t_{n-1}}^{t_n} \ddot{x}(\tau)\, d\tau = \nabla(D^{-1}\ddot{x}_n) \\ &= \nabla(-h/\ln(1-\nabla))\,\ddot{x}_n \\ &= h\{\nabla/[\sum_{i=1}^{\infty}(\nabla^i/i)]\}\,\ddot{x}_n \\ &= h(\sum_{i=0}^{\infty} b_{i-1}\nabla^i)\,\ddot{x}_n \\ &= h(\nabla^0 - \tfrac{1}{2}\nabla^1 - \tfrac{1}{12}\nabla^2 - \tfrac{1}{24}\nabla^3 - \cdots)\,\ddot{x}_n\end{aligned} \tag{11}$$

The "summed" form of this formula may be derived by writing the left side of Eq. (11) as $\nabla\dot{x}_n$ and then applying the improper operator ∇^{-1} to both sides of the equation:

$$\begin{aligned}\dot{x}_n &= h[-1/\ln(1-\nabla)]\,\ddot{x}_n = h(\sum_{i=-1}^{\infty} b_i\nabla^i)\,\ddot{x}_n \\ &= h(\nabla^{-1} - \tfrac{1}{2}\nabla^0 - \tfrac{1}{12}\nabla^1 - \tfrac{1}{24}\nabla^2 - \cdots)\,\ddot{x}_n\end{aligned} \tag{12}$$

The expression $\nabla^{-1}\ddot{x}_n$, which appears in Eq. (12), is called a first sum of $\ddot{x}_n$ and satisfies the relation

$$\nabla^{-1}\ddot{x}_n - \nabla^{-1}\ddot{x}_{n-1} = \ddot{x}_n \tag{13}$$

So far $\nabla^{-1}\ddot{x}$ has only been defined to within an arbitrary additive constant. The practical use of Formulas (12) and (13) requires that an initial value of $\nabla^{-1}\ddot{x}$ be derived from the given initial value of $\dot{x}$. Details on this point will be deferred to a later paragraph.

A generalization of Formula (12) that gives $\dot{x}_{n-s}$ for arbitrary values of s is obtained as follows:

$$\dot{x}_{n-s} = E^{-s}\dot{x}_n = (1-\nabla)^s\dot{x}_n$$

$$= h\left[-(1-\nabla)^s/\ln(1-\nabla)\right]\ddot{x}_n$$

$$= h\left(\sum_{i=-1}^{\infty} b_i^{(s)}\nabla^i\right)\ddot{x}_n \qquad (14)$$

With $s=-1$ this is a predictor formula, i.e., the summed form of the Adams-Bashforth formula:

$$\dot{x}_{n+1} = h\left(\nabla^{-1} + \tfrac{1}{2}\nabla^0 + \tfrac{5}{12}\nabla^1 + \tfrac{9}{24}\nabla^2 + \cdots\right)\ddot{x}_n$$

With $0 < s < 1$ Formula (14) may be used for interpolation for values of $\dot{x}$ in the interval between t_{n-1} and t_n. Formula (14) will be used with a positive integer value of s as part of the starting procedure to be described below.

A similar formula giving x in terms of the backward difference line at $\ddot{x}_n$ will also be needed. Reducing the order of derivatives in Equation (14) by one, we obtain

$$x_{n-s} = h\left[-(1-\nabla)^s/\ln(1-\nabla)\right]\dot{x}_n \qquad (15)$$

Then replacing $\dot{x}_n$ in Eq. (15) by the right side of Eq. (12), we have

$$x_{n-s} = h^2\left\{(1-\nabla)^s/[\ln(1-\nabla)]^2\right\}\ddot{x}_n$$

$$= h^2\left(\sum_{i=-1}^{\infty} a_i^{(s)}\nabla^i\right)\dot{x}_n \qquad (16)$$

As with Formula (14), the use of appropriate values of s in Formula (16) provides for prediction, correction, interpolation, and starting. In particular, the predictor and corrector formulas are, respectively,

P
$$x_{n+1} = h^2\left(\nabla^{-2} + 0\cdot\nabla^{-1} + \tfrac{1}{12}\nabla^0 + \tfrac{1}{12}\nabla^1 + \tfrac{19}{240}\nabla^2 + \cdots\right)\ddot{x}_n \qquad (17)$$

C
$$x_n = h^2\left(\nabla^{-2} - \nabla^{-1} + \tfrac{1}{12}\nabla^0 + 0\cdot\nabla^1 - \tfrac{1}{240}\nabla^2 - \cdots\right)\ddot{x}_n \qquad (18)$$

The expression $\nabla^{-2}\ddot{x}$ that appears in Formula (16) is called a second sum of $\ddot{x}$. It satisfies

$$\nabla^{-2}\ddot{x}_n - \nabla^{-2}\ddot{x}_{n-1} = \nabla^{-1}x_n \qquad (19)$$

and its initial value must be determined from the given initial value of x.

To step the solution ahead one time step, Formulas (14) and (16) are used with $s=-1$ for prediction and $s=0$ for correction. The method will be said to be of index m if the highest order difference used is $\nabla^m\ddot{x}$.

The computation of the solution at the first $m+1$ time points requires a special starting procedure. Assume that initial conditions x_0 and $\dot{x}_0$ are given at time t_0 and formulas of index m are to be used. The goal of the starting procedure may be regarded as the establishment of the backward difference line at $\ddot{x}_m$. This requires the determination of $m+3$ quantities, namely $\nabla^i\ddot{x}_m$, for $i=-2,-1,0,1,\cdots,m$. An equivalent set of $m+3$ quantities is $\ddot{x}_0,\ddot{x}_1\cdots,\ddot{x}_m$, $\nabla^{-1}\ddot{x}_m$, and $\nabla^{-2}\ddot{x}_m$. The quantity $\ddot{x}_0$ is immediately available since $\ddot{x}_0 = f(x_0)$. The remaining $m+2$ quantities must satisfy the $m+2$ simultaneous equations obtained by using Formula (14) with $n=m$, $s=m$ and Formula (16) with $n=m$, $s=0,1,\cdots,m$. This system of $m+2$ equations is nonlinear if f is nonlinear and thus must in general be solved by some iterative method. The specific organization of the starting procedure used in the subroutines FORTSZ and TREK follows:

(1) Compute an initial estimate for $x_i,\dot{x}_i, i=1,\cdots,m$, using the Taylor series and $x_0,\dot{x}_0$, and $\ddot{x}_0 = f(x_0)$.

(2) Compute accelerations $f(x_i)$ for points $t_1,t_2,\cdots,t_m$.

(3) Compute backward difference line at t_m.

(4) Compute $\nabla^{-1}f(x_m)$, using Eq. (14) with $s=m$.

(5) Compute $\nabla^{-2}f(x_m)$, using Eq. (16) with $s=m$.

(6) Compute new estimates of $x_i, i=1,\cdots,m$, using Eq. (16) with $s=0,1,\cdots,m-1$ and $\dot{x}_i, i=1,\cdots,m$, using Eq. (14) with $s=0,1,\cdots,m-1$.

(7) Go to 2.

The algorithm is complete when the absolute difference between the difference lines of two successive iterations is zero or some arbitrarily small ε.

4. Analysis of Results

The solution errors were computed at each integration point as the magnitude of the difference between computed solutions, x, y, and true values of the solutions computed in extended precision by the method given in Part 2. At approximately every $\frac{1}{10}$ of a cycle, up to p cycles, the maximum error observed in each of these quantities was output. Figs. 1 and 2 indicate the cumulative maximum error at the end of 5 cycles as a function of the eccentricity e, and the step size h, for index $m = 7$ and $m = 14$, respectively. [A formula is said to be of index m if the highest order difference used in Eq. (17) or (18) is $\nabla^m \ddot{x}$.] The ordinate of each graph represents the negative log base 10 of the maximum error up to 5 cycles, and can be interpreted as the number of correct decimal digits in the computed solution. Each curve represents the number of correct digits for a given step size h.

Ellipses considered were those of eccentricity $e = 0.1$, 0.2, 0.3, 0.4, 0.5, 0.6, 0.7, 0.8, and 0.9. For a given eccentricity e, the step sizes used were $h = 2^{-5}, 2^{-6}, 2^{-7}, 2^{-8}$; and for $e = 0.9$, two additional step sizes used were $h = 2^{-9}$, and $h = 2^{-10}$. In general, for a given h and e, the integration maintained a greater degree of accuracy for index $m = 14$ than for index $m = 7$, and in some cases a striking increase of accuracy was acquired by simply increasing the index from $m = 7$ to $m = 14$, i.e., doubling the order of backward differences carried. For example, for $h = 2^{-5}$, or approximately 200 steps per cycle, index $m = 14$ consistently maintained 1 to 4 more decimal digits of accuracy than did $m = 7$, until the integration was done over an ellipse of eccentricity $e = 0.9$, where in both cases the integration was unstable. Here the step size was reduced to $h = 2^{-10}$ for both index $m = 7$ and index $m = 14$. For index $m = 7$, the integration maintained a little less than 7 decimal digits of accuracy, while for index $m = 14$, better than 10 correct digits were maintained, an increase of 3 digits.

5. Conclusion

More extensive tests have been performed for various indexes from $m = 1$ to $m = 19$ with results similar to those previously obtained (see references cited in Part 1). The results, in fact, closely parallel the work done previously over the unit circle. For small eccentricity, say $e \leqq .2$, the eccentricity associated with most of the planets, the results are almost precisely the same as for those done over the unit circle. For large eccentricity, say $e \geqq 0.25$, a smaller step size h is required to obtain the same accuracy; or, in other words, the truncation region has now moved farther to the right. In any case, for a given h, increasing the index m generally gives a corresponding increase in accuracy at no increase in cost (no more derivative evaluations).

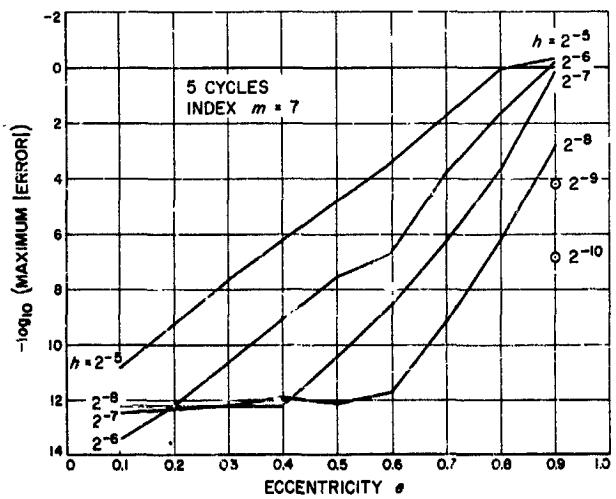

Fig. 1. Cumulative maximum errors as a function of the eccentricity e and the step size h for index m = 7

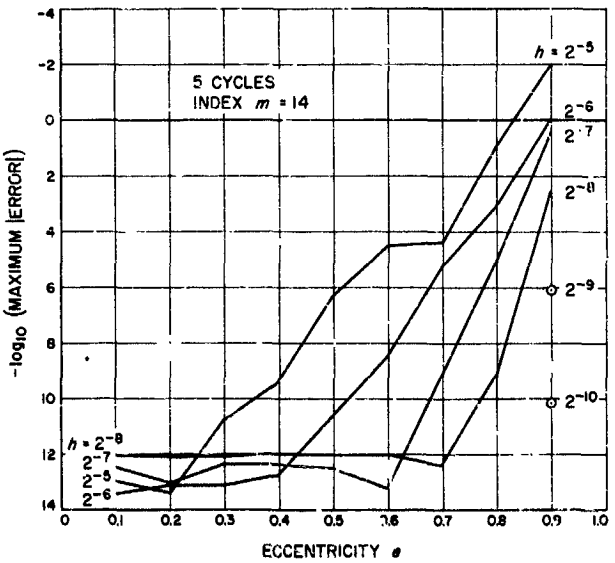

Fig. 2. Cumulative maximum errors as a function of the eccentricity e and the step size h for index m = 14

Reference

1. Devine, C. J., *PLOD II: Planetary Orbit Determination Program for the IBM 7094 Computer*, Technical Memorandum No. 33-188, Jet Propulsion Laboratory, Pasadena, California, April 15, 1965.

III. SFOF and Data Systems Development

A. Bimat Film Processing for *Ranger IX*

F. C. Billingsley

As part of the overall work involved in the digital video data processing activity, we have found it necessary to investigate various film systems and methods of film processing. One of these has been the bimat process recently introduced by the Eastman Kodak Company.

This is a diffusion transfer process which produces simultaneously a positive and a negative. The processing procedure consists of placing an imbibed bimat film in intimate face-to-face contact with the exposed negative material for a suitable length of time to allow the chemical reactions to go to completion. The materials are then separated and each one washed and dried in the normal manner. The bimat film contains the processing chemicals and is damp and slippery to the touch, but contains no free liquids. At this stage of development, the bimat film, which becomes the positive, is available only in transparent material, although it will eventually be available in an opaque material.

Because of the absence of free liquid to fill voids, the laminating process is quite critical. Mark Systems, Inc., of Sunnyvale, California has built for us a batch processor which performs this lamination. Figs. 1 and 2 show the processor loading configuration and the unwinding configuration, respectively (in these photographs the normally transparent bimat material has been replaced by film so that the bimat configuration would be visible). The operation is self-evident from the photographs. After threading of the bimat onto the take-up spindle and the threading

Fig. 1. Bimat processor loading configuration

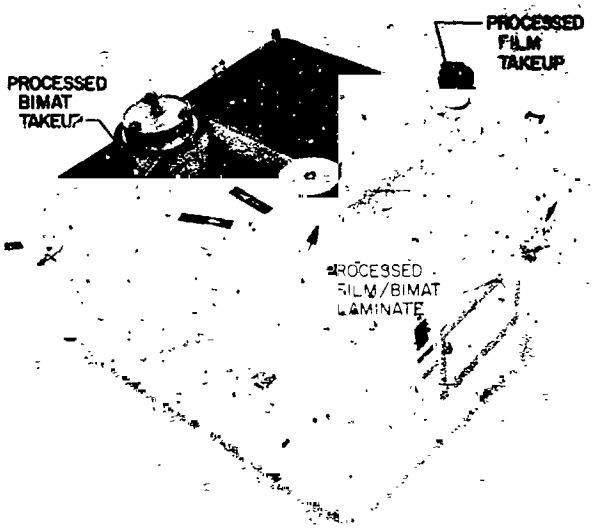

Fig. 2. Bimat processor unwinding configuration

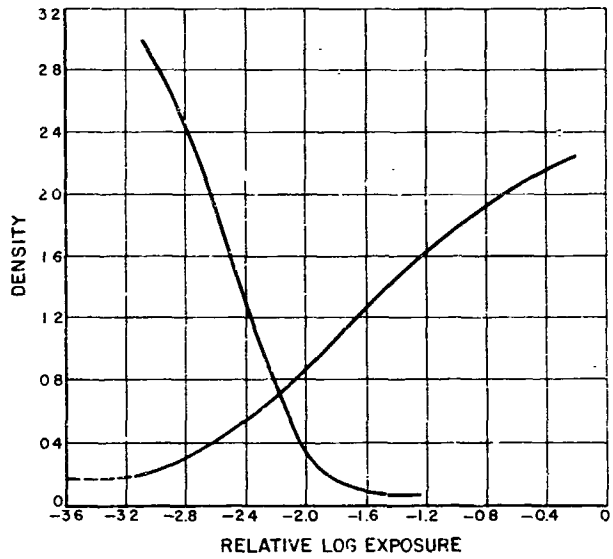

Fig. 3. Density log exposure curves for S0337 film developed with Bimat room temperature

of the film leader in contact with it, an external (light-tight) cover which has been provided may be installed and the lights turned on. (Complete daylight operation may be utilized if the film supply is on a daylight loading spool; otherwise, the film threading must be done in a darkroom.) Running the machine then pulls the bimat and film onto the processing and take-up spindle until the film supply is exhausted, at which time a switch under the end of the film indicator arm turns the motor off. The cover is then left on for the required 15 min of processing, after which time it may be removed in daylight and the film delaminated in the unloading configuration.

It has been found that both the negative and the bimat require much less than the normal amount of washing—2 to 3 min being sufficient. We find that the bimat material takes perhaps three times as long to dry as does the film.

This process was used to supply the science users with dry positive and negative films before 9:00 a.m. the morning of the *Ranger IX* impact. The source data was a magnetic tape recorded in the Telemetry Processing Station from the microwave signal of the pictures which were transmitted on commercial television. This tape was played back twice in the lunar television image converter (Lunar-TIC) to obtain the A and B camera pictures.

The density log exposure curves obtained for this material under these conditions (room temperature processing for 15 min) are given in Fig. 3. These are for the MX615 imbibant, which is not optimum for this film but which was the only one available at the time. Note the sharp toe of the positive curve which necessitates a quite restricted density range in the negative. The video film converter in the Lunar-TIC was adjusted to give a peak negative density equal to 1.2 to avoid washout of the positive. It is expected that with the optimum imbibant MX625 a much wider negative density range will be usable.

The processor was loaned to us by Mark Systems in a precompleted state and has since been returned to them for completion. Due to the precompleted state, some minor mechanical difficulties were encountered which were circumvented for the *Ranger IX* support and which are being cleared up by the manufacturer. Completely satisfactory operation is anticipated upon its return.

The bimat process currently shows the effects of its infancy. Kodak has not yet perfected its packaging techniques, and due to either oxidation or drying-out the material has a limited shelf life even in the unopened package. Several rolls of material which were used about a week after impact showed evidence of deterioration. This begins as a color change in the positive, and with further deterioration development becomes incomplete and a transfer of silver to the positive does not take place. Kodak is presently imbibing the material in New York and can supply it upon several days notice. At this date, due to the deterioration problem, Kodak does not recommend that we store the material more than 2 to 3 weeks

at room temperature before using; however, shelf life at 40 deg is 3 months.

Conclusions:

(1) With proper lamination such as produced by the Mark Systems processor, no difficulty is encountered due to run-out, air bubbles, etc. Short lengths of up to perhaps 3 ft may be laminated with a roller upon a table top, but lengths longer than this should be laminated in the processor.

(2) Although the shelf life of the material is limited at present, Kodak is working to improve this.

(3) Further optimization of the imbibant will allow a greater negative density.

(4) The process as a whole is quite satisfactory and enables the production of a negative in less time than could be accomplished by wet processing and in addition produces a high-quality positive simultaneously.

GUIDANCE AND CONTROL DIVISION

IV. Spacecraft Secondary Power

A. Power Sources

R. A. Boring

1. Solar Thermionic System

Structural environmental testing was performed on a lightweight solar thermionic system which consisted of a 5-ft-D nickel electroformed mirror, tubular aluminum coaxial conductor/generator support, and a mockup generator. The evaluation of this engineering model has shown some design deficiencies in the components; however, preliminary analysis of the test data indicates that lightweight solar thermionic power systems can be designed to successfully meet the dynamic load requirements necessary for space flight qualification.

This model has been subjected to complete environmental tests to JPL Specification GMP-34218-TST, which is essentially the *Mariner C* Solar Panel Type Approved level requirement. The tests at this level revealed no apparent damage to either mirror, conductor support structure, or mockup generator. A further test was conducted to observe the effects of a *Saturn-Centaur* launch acoustic vibration on the thermionic system model. It was after this test that a failure of the mirror-torus attachment was detected. This environmental test program has been discussed in *SPS 37-30*, Vol. IV, pp. 32–41.

2. Environmental Test Results

The Solar Thermionic System environmental test program includes: (1) Magnetic field, low-current tests to determine the design effectiveness of coaxial parallel electrical conductor structural support arms. (2) High current (50 amp, 3.2 v) tests to measure current carrying capabilities for the conductor structural support arms design. (3) Acoustic noise tests to measure structural integrity of the system. (4) Thermal vacuum and shock tests to measure thermal and structural integrity of the mirror, converter, and support arm system. (5) Mechanical vibration, acceleration and shock tests to measure system structural stability and to determine resonances.

The test with an actual generator heated by electron bombardment has been postponed until all the data from these tests can be evaluated and the design can be appropriately modified if required.

a. Magnetic field test results. The system had no measurable perm-field of its own, when measured at 5 ft from the geometric center of the mirror, with the magnetometer on ' milligauss full-scale range. About a 1-milligauss field was induced at 5 ft from the mirror geometric center in the plane of the concentrator. No measurable field is induced from combination parallel coaxial conductor support arms when leads are all identical and ground

loops have been eliminated, allowing the current in both inner and outer conductors to be essentially equal in magnitude and opposite in direction.

It has been estimated that the effect of these magnetic fields on the performance of a spacecraft's attitude control would result in a worst-case torque of 0.003 in.-oz for a near-Earth orbit; i.e., 0.0001 oz on a 30-in. moment arm when the mirror plane is inclined 45 deg to the estimated 0.25 gamma near-Earth magnetic field.

b. High current carrying capability tests. This test was performed in the laboratory with a DC supply delivering 50 amp at 3.5 v to the power takeoff points of the generator support structure. The test setup is shown in Fig. 1. The current flowed through the arms to the cables as shown and through a carbon load. The length of the cables which interconnect the support arms and the load is believed to be representative of the distance which could possibly be realized when the system is attached to a spacecraft. The test indicated the following:

$$V_{in} = 3.5\text{ v} \qquad I_{in} = 50\text{ amp}$$
$$V_{load} = 2.8\text{ v} \qquad I_{load} = 50\text{ amp}$$

This indicates a total voltage drop of 20% of the input. The loss through the support arms alone was 10% of the input, which was the design goal for this model.

c. Acoustic noise tests. The engineering model was mounted, as shown in Fig. 2, in the JPL 960 ft³ reverberant chamber and was subjected to the *Mariner C* Solar Panel Type Approval level (142-db, *Atlas-Agena D*) of acoustic noise. The test was of 90-sec duration with no apparent damage observed during post test inspection of the model. A second test was then performed with the noise amplitude increased 6 db to give 148 db (*Saturn-Centaur* levels) for 90 sec. Post test inspections revealed that the mirror skin-to-torus attachment failed. The failure occurred in the area where the skin is attached to the web (see Fig. 3). Failure was essentially complete around the mirror circumference, with only a few small areas (approximately 3 in. long) remaining attached. The skin did not show evidence of damage although some damage did occur during removal from the chamber. Reason for failure has tentatively been evaluated to be that the area of the web where the failure occurred was relatively thin and the point of attachment was not a smooth radius. It is felt that the sharp bend in the web material was a

Fig. 1. Setup for testing high current carrying capability

Fig. 2. Acoustic noise test setup in reverberant chamber

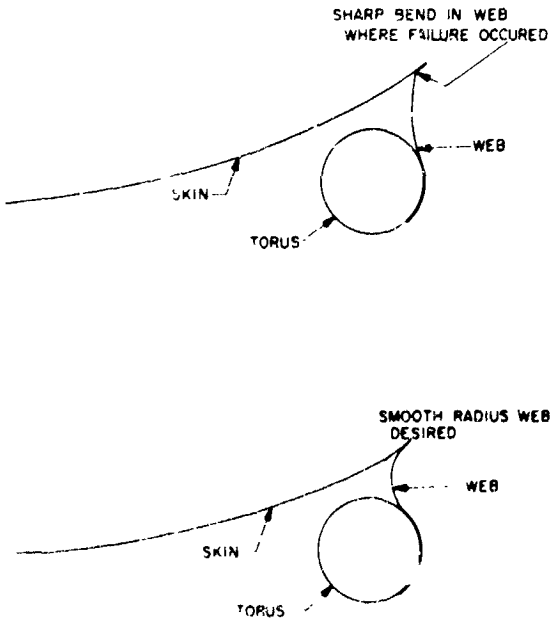

Fig. 3. Mirror skin-to-torus attachment web design

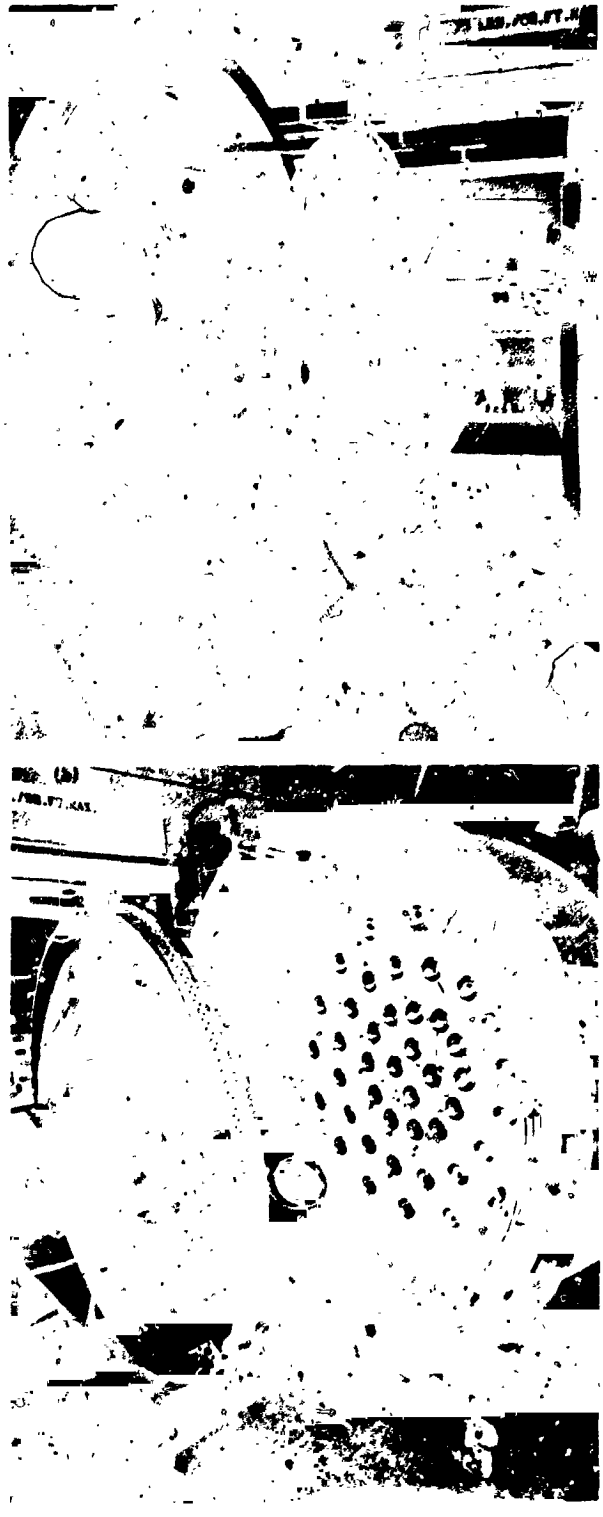

Fig. 4. Vacuum chamber setup for thermal-vacuum tests

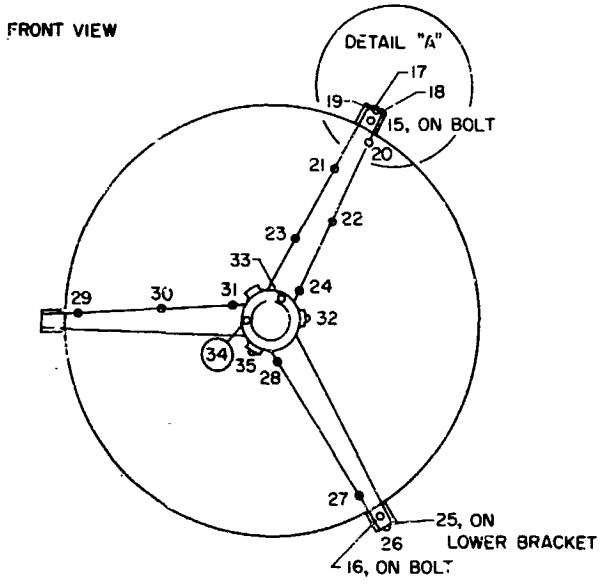

Fig. 5. Locations of thermocouples on reflector for tests

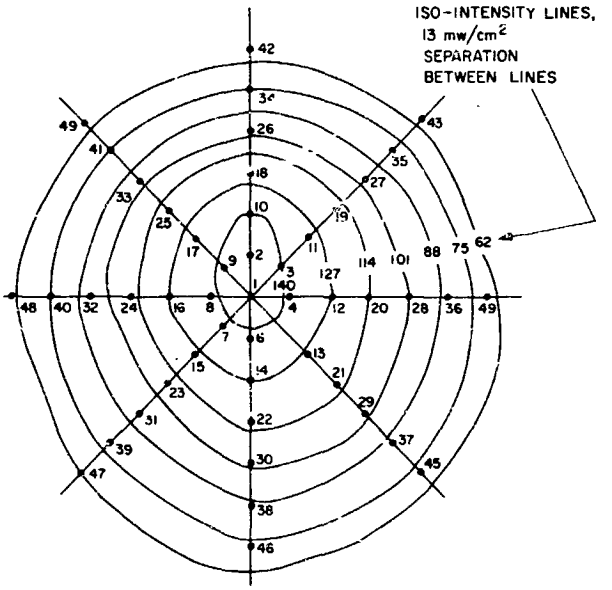

Fig. 6. Lamp beam intensity in test plane

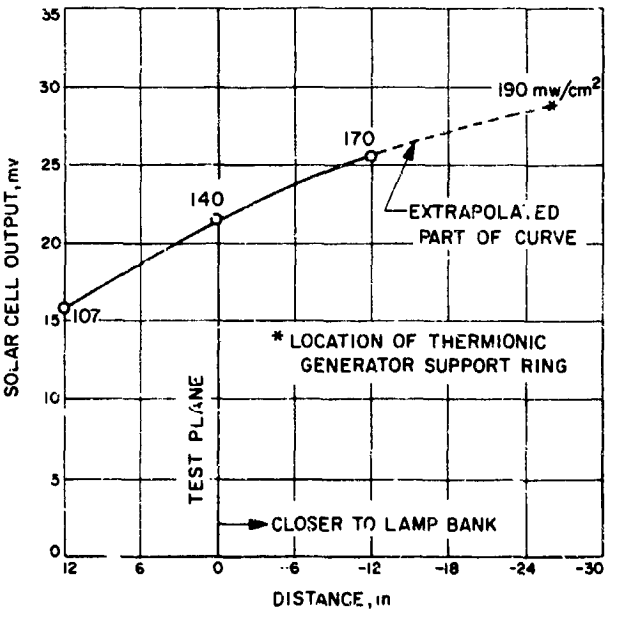

Fig. 7. Beam intensity on central axis in mirror plane

significant factor in this failure. The possibility that the failure was the result of fatigue from the first test has not been discounted and further investigations are continuing to more thoroughly analyze this area.

d. Thermal-vacuum tests. The model was subjected to thermal-vacuum tests in the JPL 7 × 14 ft vacuum chamber. Prior to performing these tests, the mirror torus attachment (as damaged in the previous acoustic tests) was epoxy-bonded to prevent possible gross thermal distortion of the skin and subsequent damage of the support structure due to deflection and concentrated thermal energy. The test setup is shown in Fig. 4(a), (b); in these pictures the epoxy bonding is obvious. Fig. 5 shows the location of the thermocouples, chromel-constantan, on this test model.

The chamber was evacuated with the assistance of the wind tunnel compressors to simulate the *Atlas* launch pressure profile recently applied to *Mariner C* shrouds. The pressure was further reduced and maintained throughout 24 hr of testing at less than 6×10^{-5} torr. The chamber was cooled to −300°F after the chamber reached 1×10^{-4} torr, and the mirror was allowed to cool until a temperature of 32°F was recorded.

The lamp bank shown in Fig. 4(b) was then allowed to irradiate the model with the radial intensities shown in Fig. 6 and also relative to the plane of the mirror as shown in Fig. 7. The temperatures were allowed to stabilize. After 5 hr from pumpdown, the lamps were turned off and the mirror was allowed to cool until a temperature of 32°F was measured (approx 24 min). At this time,

Fig. 8. Axial acceleration test setup with three vibration exciters

the lamps were turned on again, and this condition was held until a total of 24 hr had elapsed. The cold walls were returned to ambient, and the chamber was brought to atmospheric pressure.

No change in the mirror or support arms was noticed during or after the test period. No heavy outgasing nor contamination of the mirror surface or chamber walls was observed. The temperatures ranged from 524°F at point 34 to −23°F at points 11, 12, 13 of Fig. 5 during the stabilized portion of the test. As shown on Fig. 7, the intensity at the support ring (point 34) was approximately 190 mw/cm² while at the same time the intensity at the torus (points 11, 12, 13) was approximately 70 mw cm⁻². The data for this test is presently in the process of being reduced, and only a preliminary analysis has been made.

e. Mechanical vibration tests. In 1961, JPL engineers attempted to test a 5-ft-D mirror to the *Mariner B* vibration levels. The test was never concluded due to deformation of the mirror skin, which is now believed attributable to the shaker fixture design. The setup used for tests prepared this year is shown in Fig. 8. Three vibration exciters are utilized, one at each of the mounting points, which are run in phase for axial acceleration testing. Transverse acceleration tests were also performed, as shown in Fig. 9. Both axial and transverse vibration tests were performed at the *Mariner C* Solar Panel Type approval levels, with the exception that the highest level required of a panel was used for all three axes (X, Y, Z) of the thermionic model system. The repaired mirror noted before was used for initial testing, and a sister mirror similar to the repaired concentrator

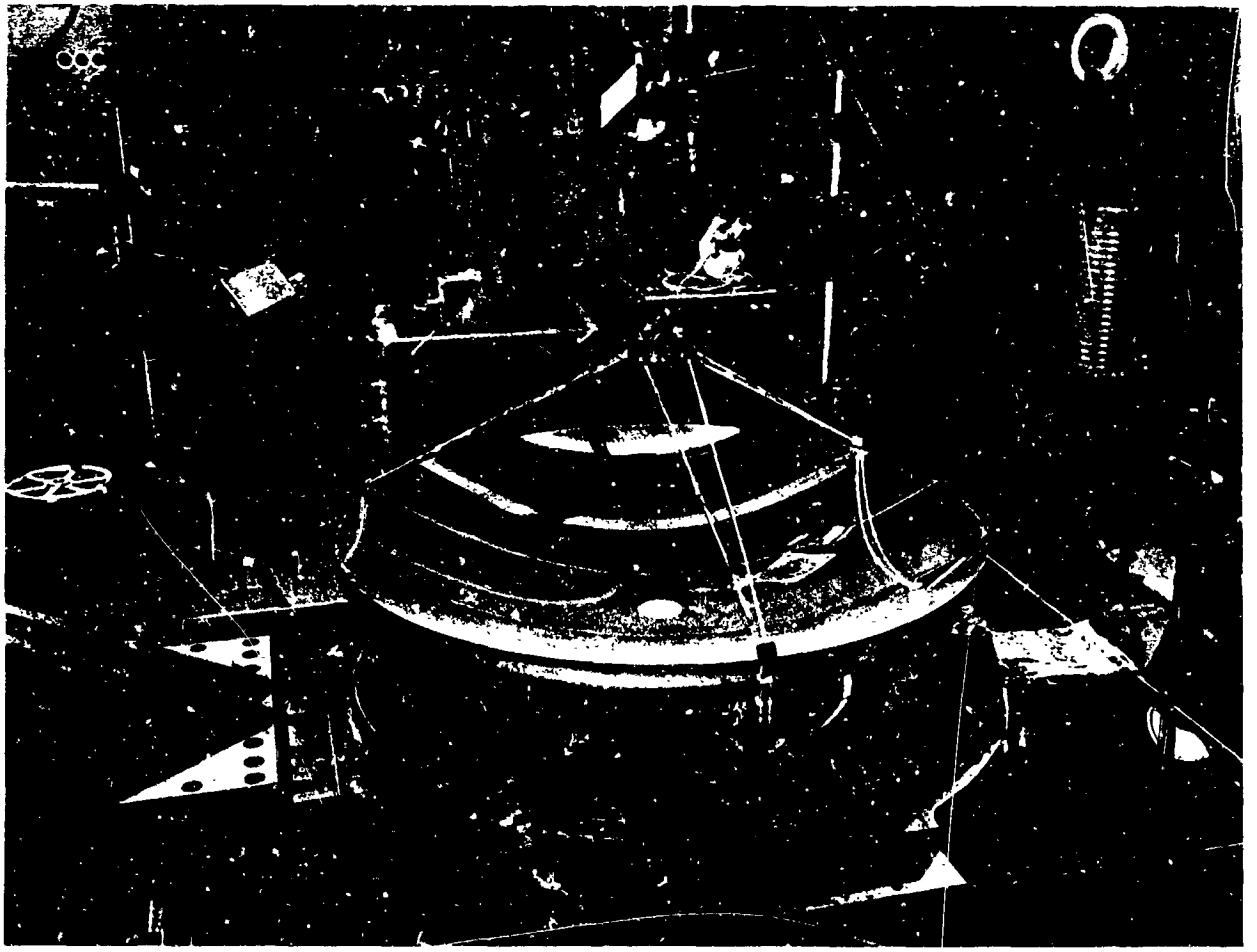

Fig. 9. Transverse acceleration test setup

was used during later phases to determine whether the test data would be reproducible.

Resonant frequencies were observed as follows:

Complete structure	33 cps
Support arms	53 cps
Concentrator	153 cps

These frequencies were repeatable from mirror to mirror and also in both axial and transverse directions. As seen in Fig. 10, after final testing, the mirror and support structure have not degraded significantly from the tests performed, as was the case during previous tests.

A continuation of this program is planned, utilizing improved mirrors and fixed and movable support structures in order to further the engineering evaluation of the mechanical, dynamic and static characteristics of flight-weight solar thermionic power systems.

Fig. 10. Mirror and support structure after final testing

N65-32420

B. Energy Storage

R. Lutwack and G. M. Arcand

1. Development of Separators for Heat Sterilizable Batteries, R. Lutwack

The research work continues in the development of a separator for the Ag-Zn battery that will be capable of withstanding heat sterilization. The work under Contract 951015 with Radiation Applications, Inc., has progressed to the selection of one material for the scale-up phase, and this material is in the process of production. Another contract in which new thermostable polymers will be investigated is being negotiated.

In Contract 951015, the following degrees of completion have been obtained: (1) Forty-four of the fifty-one materials have been prepared, and seven are in process; (2) forty of these have passed satisfactorily the preliminary screening tests of exchange capacity, tensile strength, dimensional stability and resistivity, and five are in process, (3) twenty have undergone thermal sterilization at 145°C, and fifteen are in process; (4) twenty-six are in process of thermal sterilization at 137°C; (5) twenty have undergone in-cell testing, and six are in process.

Analysis of the test results showed that the material prepared from the low-density polyethylene by precrosslinking with an electron beam irradiation to the 70-Mrad level followed by grafting with acrylic acid should be considered for more extensive testing, and accordingly it was selected as one of the two materials to be prepared in the 500 ft² fabrication phase. This decision was made on the basis of results in which 98% of the capacity relative to control cells was obtained on each of the electrical test cycles; the level for satisfactory performance was set at 90%. The preparation of this material is nearly completed.

Nearly identical test results were obtained for a material which was prepared by the same procedure from the low-density polyethylene with the exception that the irradiation level was 50 Mrad. This material has not been selected as yet for the 500 ft² preparation phase; the choice of the second of these materials will be made when a comparison of all samples is possible.

2. Radiation Effects on Battery Behavior, G. M. Arcand

Atomics International has completed its work on the effects of gamma radiation on the behavior of nickel and cadmium electrodes in alkali media. Detailed results are available in the final report (Ref. 1).

a. Experimental. The experimental procedure has been outlined in detail (*SPS 37-31*, Vol. IV, pp. 63–65). The only deviation occurred in two cases where cells were irradiated on open circuit.

b. Results. The average effect of radiation on the capacity of the cadmium electrode is shown in Fig. 11. In

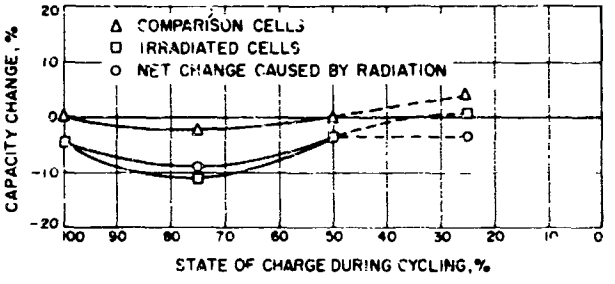

Fig. 11. Capacity loss of cadmium electrode

all cases, the cells were cycled and the total irradiation dose was 8.9×10^7 rads (H_2O). The curve representing the net change is determined by plotting the difference between the comparison cells (operated in a water bath at 45°C) and the irradiated cells. Dashed lines are used between the 50% and 25% states of charge because only two measurements were made at 25%, and experience has shown this to yield insufficient quantitative information.

Table 1 shows the distribution of material loss in compartmented cells. Although all experiments have been duplicated, the results should be treated with caution.

Table 1. Electrode material loss from individual electrodes

Percentage of full charge, %	Number of experiments	Cd electrode loss, mg	Ni electrode loss, mg
100	3	28.9	8.0
75	2	21.0	2.2
50	3	11.1	1.7
25	2	10.7	2.3

The two cells which were irradiated on open circuit showed no significant capacity loss in reference to the comparison cells.

c. Discussion. There is little doubt that the irradiated cadmium electrode loses more capacity than the comparison electrode, although the scatter in data is severe. There also seems little doubt that a maximum loss occurs when the electrodes are cycled about the 75%-of-charge point. This seems true of both irradiated and comparison electrodes.

The data for the 25%-of-charge point are suspect since only two experiments were performed. It is unlikely that cycling about this point would cause an increase in capacity.

The data show that more material is lost from the cadmium electrode than from the nickel. Furthermore, the loss is greatest when the cell is cycled about the 100%-of-charge point, and it levels off around 50%.

None of the observed phenomena have been explained as yet. A literature search is underway which may support certain hypotheses. The investigation has shown that high radiation doses cause partial disintegration of both the cadmium and nickel electrodes and a permanent loss of cadmium electrode capacity. These factors must be considered in any design of Ni-Cd batteries for use in high radiation fields.

3. Thermal Decomposition of AgO and Ag_2O, G. M. Arcand

During work previously reported (*SPS 37-30*, Vol. IV, pp. 31–32), there was visual evidence that the decomposition of Ag_2O occurred primarily on the material surface. This appeared as a layer of silver. In order to check this evidence and to determine the effects of compaction on the decomposition rates, samples were prepared in pellet form.

a. Experimental. All AgO samples were prepared in the laboratory and dried at room temperature in vacuum over P_2O_5. Pellets were prepared from the dried powder in a press such that each weighed about 1.2 g and had a diameter of about 1.27 cm. Some of the first pellets used weighed slightly less than 1.0 g.

Two pellets were placed between Lucite sheets, clamped in position, and placed in a crucible. The arrangement did not permit covering the crucible. All other pellets were placed loose in crucibles, some of which were covered while others were left open.

All samples were placed in a drying oven controlled at 135 ±3°C. Periodically they were transferred directly to a desiccator and allowed to cool for 0.5 hr, after which they were weighed. The samples were returned to the oven immediately after being weighed.

b. Results and discussion. The first pellets treated were placed loose in covered crucibles. These lost weight at about the same relative rate; only one sample will be considered here. This pellet initially weighed 0.9883 g and lost 60 mg in the first 22 hr. Subsequent loss was considerably slower and roughly linear with time. The rate of loss was found to be about 1.2×10^{-3} mg/hr.

The formation of silver is best described with the aid of Fig. 12. It should be noted that dimensions are distorted for clarity; the Ag layer thickness is about 5 μ. The reaction appears to be entirely on the surface of the oxide and primarily on those surfaces exposed to the atmosphere. The bottom of the pellet showed little evidence of metal formation. Where fissures of 0.5 mm or greater width were present, some penetration of metal occurred. There was no such penetration along fine cracks.

Where the pellets were clamped between Lucite plates and heated in an uncovered crucible, the rate of loss was greater, as seen in Fig. 13. The slope of the linear portion of the curve is 4.1×10^{-3} mg/hr. Here the initial sample weight was 1.1586 g, only 0.1903 g greater than that of the pellet described above and not enough different to account for the rate difference. However, the AgO stock was from a new batch which may well account for much of the difference.

Silver metal formed on all surfaces in this case, but those in contact with the Lucite formed less metal. It is reasonable to suspect that Lucite can be oxidized by AgO and Ag_2O at this temperature. Thus the decreased reduction of the oxide caused by covering the surface may be partially counteracted by reduction of the oxide by the Lucite (2). We have no proof of this hypothesis at this time.

Four similar pellets were placed loose in crucibles, two of which were covered. At the end of 89.7 hr, one of the open crucibles was covered and one of the closed crucibles opened. The results are shown in Fig. 14. For convenience, the curves begin after most of the AgO has been converted to Ag_2O. The rate of decomposition of material in the open crucibles is about 5.4×10^{-3} mg/hr, while that in the closed crucibles is about 2.7×10^{-3} mg/hr. Where a crucible was covered at 89.7 hr, the rate decreased and approached that in the closed crucible. Where the crucible was uncovered at 89.7 hr, the data showed a discontinuity which is probably caused by an experimental error. There is no duplicate experiment for comparison, however. After the discontinuity, the rate becomes about 6.5×10^{-3} mg/hr. This is higher than the other values and may be incorrect.

In these last four samples the pellets "exploded" in an annular fashion except that some pieces from the top surfaces were ejected with sufficient force to be lost from the open crucibles. This accounts for the high weight loss from the open crucibles at 19 hr. No effort was made to normalize the values because this unknown loss would have made the results meaningless.

The interesting result which has appeared is the effect on the reaction rate of the presence of a crucible lid. If one assumes the pertinent equation to be

$$Ag_2O = 2Ag + \tfrac{1}{2}O_2$$

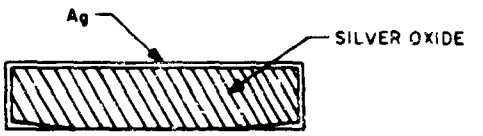

Fig. 12. Silver oxide pellet after heating at 135°C

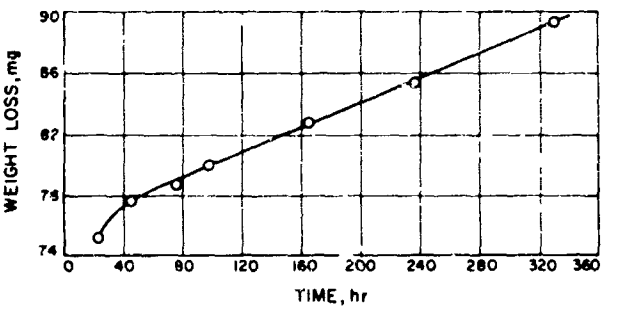

Fig. 13. Weight loss of clamped AgO pellet at 135°C

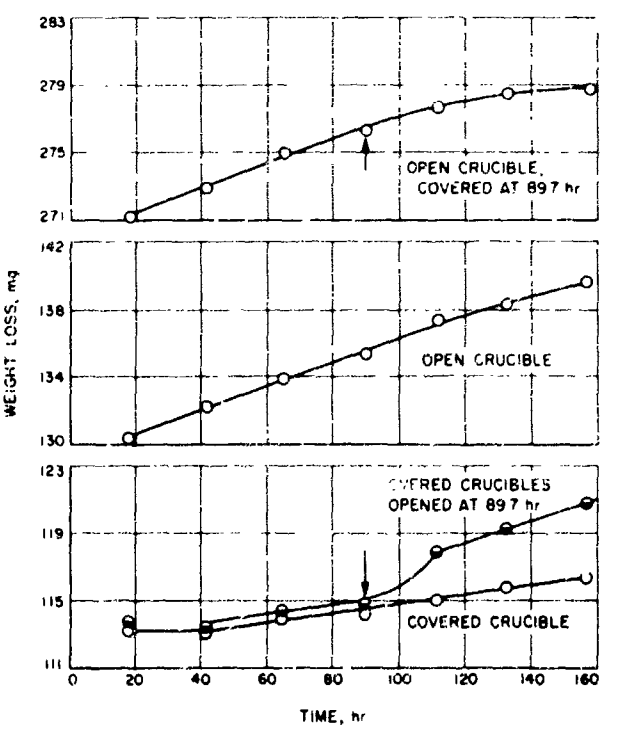

Fig. 14. Weight loss of various AgO pellets at 135°C

one might speculate that the reaction is reversible and that a very small change in oxygen pressure can cause a startling change in reaction rate. There remains a possibility that small amounts of light leaking into the oven catalyze the reaction. Neither hypothesis is satisfying when one considers the magnitudes of pressure change or light involved.

The effects of atmosphere and light on the reaction rate will be determined. No effort has yet been made to relate rate to particle size. One would expect this to be a factor and some support for this is provided by the fact that pellets made from one stock supply decomposed at about one-half the rate of those made from another, all other conditions being the same. The effect of particle size is to be determined. At the present time, commercial Ag_2O powder is being heated in open and closed crucibles to see if the same phenomenon occurs.

C. Electrical Conversion

G. A. Packer

1. Computer Worst-Case Analysis

The computer worst-case analysis effort is being pursued in order to develop an inhouse capability of worst-case circuit analysis for both new and existing circuit designs. JPL's Transient Analysis Generator (TAG) computer program is being utilized for these purposes. Mesa Scientific Corporation has contracted to aid in the development and application of equivalent models of various circuit elements such as transistors, diodes, and magnetic cores. The models will be able to cope with the nonlinear operating regions of these circuit elements. Much progress has been made in the areas of component modeling and verifying. Experimental analysis runs of well-defined circuits have been made in order to explore TAG's capabilities as a circuit analysis tool.

To test the accuracy and efficiency of TAG circuit analysis, an RC ladder circuit of 1, 2, 3, 4, 5, 7, 10, and 15 sections was selected. Solution runs of the 1, 2, 3, 5, and 10 section circuits were completed. The solution run of the 15 section ladder circuit was not completed, as present computer root finding routines which were attempted could not reasonably cope with polynomials of orders higher than 10. Hence no solution run of the 15 section RC ladder circuit could be made. With better root finding routines, analytic accuracy checks of the solutions to RC ladder circuits of more than 10 sections can be accomplished. The results of these runs were compared with hand calculations, employing Laplace transform methods. These comparisons exhibit the accuracy of TAG circuit analysis. The output voltage of the RC ladder circuits ranged from zero to one volt driven by a step function of one volt amplitude. The greatest difference between TAG solutions and analytic solutions was 0.15×10^{-3} volt. The greatest computer time used (including TAG and FORTRAN compilation times as well as input loading and manually mounting the TAG compiler tape) was 7.4 min. This was the time consumed by the 15 section ladder circuit problem. A complete set of DC solutions to a three-stage transistor amplifier has also been completed. Ebers Moll non-linear transistor models were used in generating these solutions. A single transient analysis run of this amplifier was also attempted, but due to poor choice of solution control times no meaningful data was obtained. Under a follow-on contract with Mesa Scientific Corporation, the transient analysis of this amplifier will be completed. A procedure for the evaluation of transistor static parameters was developed, and evaluation of a 2N1016 transistor was made. These parameters were implemented in the TAG program by use of an Ebers-Moll non-linear model, and families of characteristic curves were drawn in by the computer. These curves were compared with those made of an actual 2N1018 on a Tektronix type 575 transistor-curve tracer. The agreement between actual and computer model curves, for both base and collector families, was found to be quite good. A similar procedure for evaluating diode parameters was tried using a Linville Single-L diode model. This is a model developed by Mesa Scientific Corporation which offers a considerable improvement in dynamic fidelity. It makes use of Linville's elements of combinance and storance in a single-L network to model diode reverse recovery. Actual recovery time measurements were made on three different types of diodes, a Westinghouse 479E, a Unitrode UTR22, and a Texas Instruments IN1124.

A single-L diode model was coded for TAG, and a TAG transient response for a similar set of conditions was generated. Since the results agree well with analytic predictions, they can be considered quite satisfactory.

A simple non-linear core model has been programmed and successfully run. This model is based on the present TAG availability of node pair voltage integrals. A more

sophisticated model has been developed and has been undergoing program debugging. This model will be able to account for hysteresis effects, including minor loop operation, as well as time-dependent domain switching effects. Its completion will be accomplished under the follow-on contract with Mesa Scientific Corporation.

References

1. *The Effects of Radiation on Nickel Cadmium Battery Electrodes*, Final Report AI-65-66, Atomics International, Canoga Park, Calif., June 1963–April 1965.

2. Fettes, E. M., *Chemical Reaction of Polymers*, p. 79, John Wiley and Sons Inc., New York, 1964.

V. Spacecraft Control

A. Sun Tracker Control System

T. Kerner

A solar thermionic power system is now under development. In this system a 10-ft parabolic mirror is used to concentrate the Sun's energy at the focal point, where the active elements in the experiment are located. A Sun tracker control system is being designed to keep the parabolic mirror pointed at the Sun to within a 30-sec error. The mirror drive has two degrees of freedom, one in azimuth and one in elevation. For these axes, the two control systems that govern the motions are identical. A block diagram of the mirror control system is shown in Fig. 1.

1. Sun Sensor

The sensor used is characterized by a $V_{out}/\theta_{in} = K_1$ gain. It is sensitive in two axes. A shadow bar is used to control sunlight falling on two cadmium sulfide cells. When the radial toward the Sun makes an angle with the normal to the plane containing the two cells, a differential output voltage is developed that is proportional to that angle.

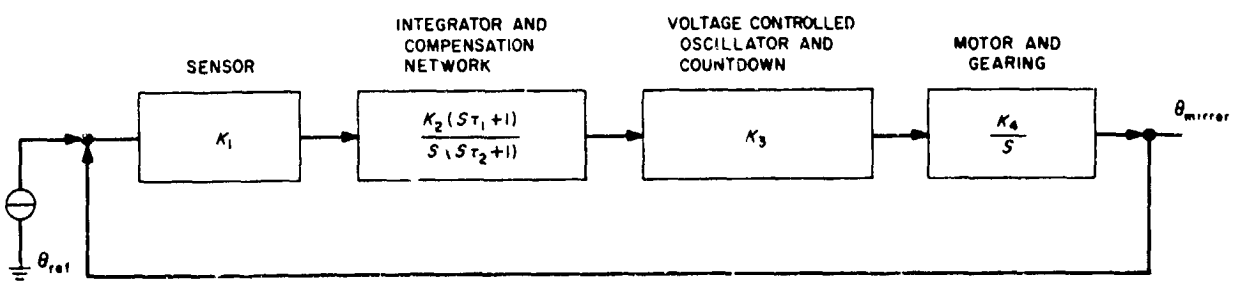

Fig. 1. Sun tracker control system

The output is linear to approximately ±1 deg about the normal. For larger values, the sensor is saturated.

2. Control Circuitry

The integrator and the compensation network are mechanized as shown in Fig. 2. With the assumption that the gain of the amplifier, $-A$, is very large, the transfer function of this configuration is

$$\frac{E_o}{E_s}(s) = \frac{C_1 + C_2}{R_{in}C_1C_2} \times \frac{1}{S} \times \frac{S + \dfrac{1}{R_1(C_1 + C_2)}}{S + \dfrac{1}{R_1C_1}}$$

and its effect is that of an integrator in series with a lead-lag network. The integrator in conjunction with the motor introduces a double pole at the origin in the characteristic equation of the open-loop gain. The double pole characterizes this as a type 2 system with a theoretical zero offset error for a ramp function input. Practically, the drift of the sensor null, the drift of the integrator, the drift of the V_{co}, and outside disturbances all contribute to the tracking error. The zero-pole combination introduced around the operational amplifier in Fig. 2 is used to compensate the double pole at the origin.

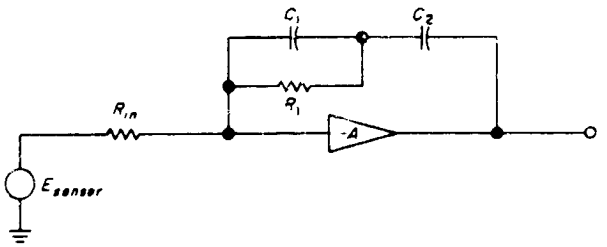

Fig. 2. Integrator and compensation network

The voltage controlled oscillator consists of a unijunction transistor operated as a relaxation oscillator. A variable bias on the input causes a proportional change in the frequency of oscillation. The unijunction transistor oscillates at a quiescent frequency of 960 cps. Four flip-flops are used to count the frequency down to 60 cps. The output and also the output at an angle of 90 deg are introduced into the differential synchronous motor.

3. Control Motor

The differential synchronous motor consists of two synchronous motors with the rotor of one coupled to the stator of the other. For a 60-cps input into both motors, two modes of operation are possible depending upon the phasing. For one phasing arrangement, the output shaft of the motor moves at 7200 rpm, which is twice the synchronous speed of each motor. For a phase reversal on one motor, the output shaft speed goes to zero and the full 1 oz-in. torque is maintained. If the phasing is oriented as in the last-mentioned example and the 60-cps input to one of the motors is frequency-modulated, the resultant motor shaft output is proportional to the modulating signal. This will be the operating mode while tracking. The maximum 7200-rpm output will be used in the slewing mode. The output which is geared down by 300,000 will drive the mirror structure. The use of the differential synchronous motor allows a considerable dynamic range of operation, i.e., a nominal rate of 360 rpm, and a slewing rate of 7200 rpm.

4 Breadboard Model

The system has been breadboarded in the laboratory with some modifications. A diagram of the breadboard circuitry is shown in Fig. 3. The linear sensor is substituted by a potentiometer-generated voltage in the loop, and the gear train driving the mirror has been reduced to a typical one-stage gear train driving a potentiometer.

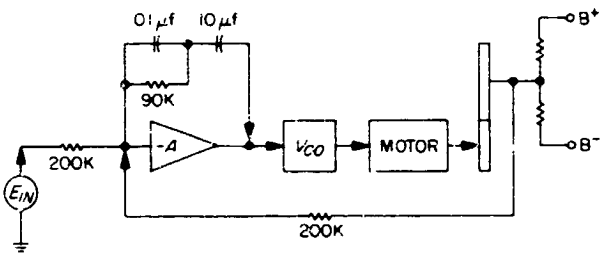

Fig. 3. Sun tracker control network

This has been done with the assumption that the inertia and the friction load of the mirror are negligible as seen by the motor and that only the first gear is significant. Open-loop testing of the V_{co} and motor combination indicated a breakpoint at about 2 cps other than the pole due to the ideal motor. To stabilize the system, the zero has been mechanized at 0.17 cps, and the pole is two decades away at 17.7 cps.

The system performed satisfactorily in the closed-loop configuration. The lead-lag points will be adjusted when the motor is driven into the actual load.

B. A Science Instrument Support Scanning Platform

S. Szirmay

The goal of this effort is to investigate methods of achieving lightweight, low-power, high-reliability scan systems for acquiring, tracking, and scanning planetary bodies from a fly-by or orbiting spacecraft in such a manner as to permit the planet-oriented scientific experiments to meet their objectives.

The platform subsystems will be comprised of a sensor and/or programmer, controller, and actuator. Its performance will be optimized in terms of sensitivity (distance over which it's operable), pointing accuracy, and ability to follow preprogrammed instructions. Fig. 4 shows a block diagram of the platform subsystem.

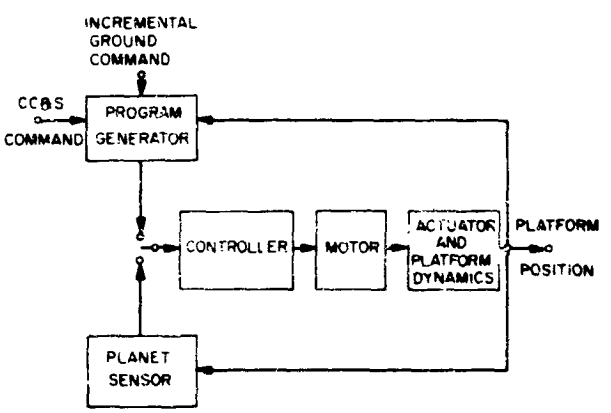

Fig. 4. Scanning platform subsystem

The following are the first iteration constraints placed on the scan platform.

(1) Structure weight, lb

Visual survey	200
Microwave and radar	90
Infrared spectrometer	75
Infrared radiometer	5
Ultraviolet spectrometer	15
Ultraviolet radiometer	4
Total	389
Platform with instruments	480

(2) The moment of inertia of the loaded platform is 265 lb-ft-sec.^{2}

(3) The platform must have a capability of pointing to the planet vertical within 1 deg.

(4) The platform must have a capability of pointing to an arbitrary inertial direction within 1 deg.

(5) The subsystem must see a planet 4 deg to 160 deg continuously.

1. Horizon Sensor

Studies of the sensor area have shown that the use of the infrared horizon in determining the local vertical is superior to other methods. Sensor systems utilizing the infrared horizon have been built and flown successfully.

The Barnes Engineering Company, under contract from JPL, is now developing a lunar and planetary horizon scanner. The details of this device are discussed elsewhere in *SPS 37-33*. The salient features of this horizon scanner are as follows: (1) The scanner has no moving parts. (2) Space and horizon scanning is accomplished by sequential electronic sampling thermopile detectors arranged in linear quadrature array. The scanning geometry is shown in Fig. 5.

The output of the scanner is not yet rigidly defined. The thermopile detectors will be sampled simultaneously from the points *A* and *B* toward each other. For the local vertical, which is not coincident with the vertical as de-

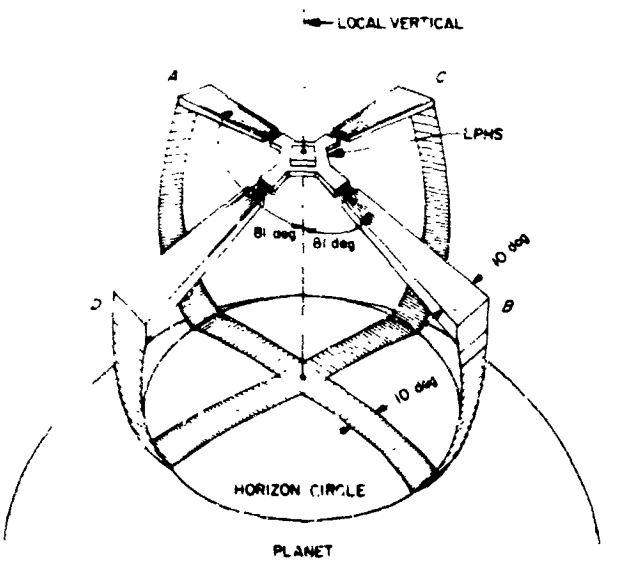

Fig. 5. Horizon scanning geometry

fined by the perpendicular to the plane defined by lines AB and CD, the sampling channel operating from either A or B will be the first to yield an output correspondent to a horizon crossing, the other channel will yield a horizon-crossing indication some time later. This time interval between the two readings is proportional to the deviation of the platform pointing angle from the planets local vertical The error may be presented in either digital or analog form. The scanning period is not yet finalized, but for the purposes of this study it is assumed to be 100 msec.

2. Controller and Motor

Two alternate methods of mechanizing the controller-motor blocks shown in Fig. 4 are being studied. One possible method is to use a stepper motor actuated by a gated clock (Ref. 1); another method being investigated is using a two-phase induction motor.

Figs. 6 and 7 are the block diagram configurations of the two possible schemes. The proposed mechanization of the horizon scanner is such that the error which is the difference between the reference angle and the actual

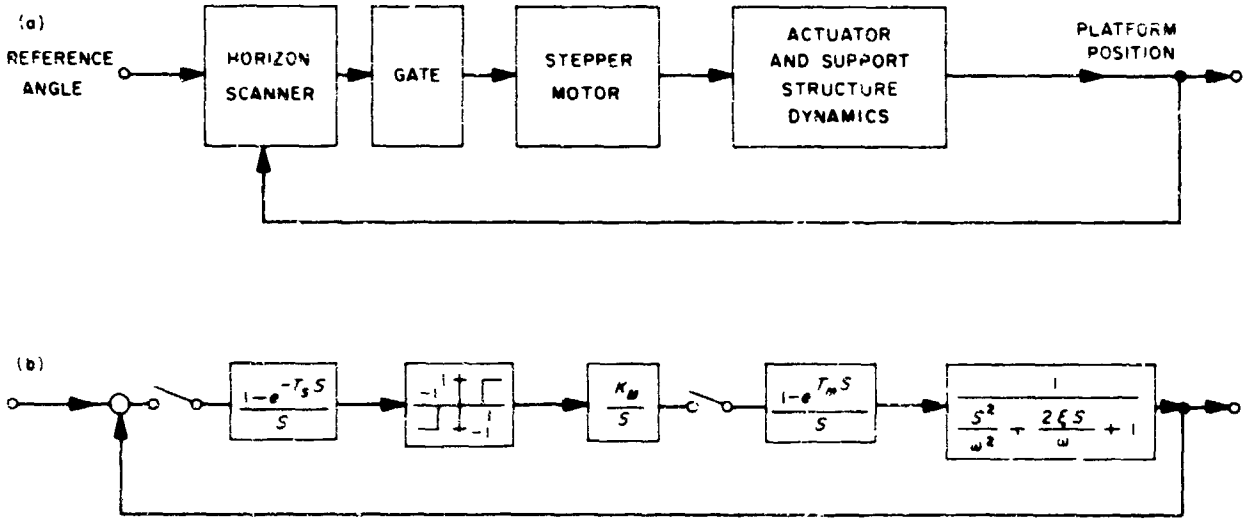

Fig. 6. Platform controlled by stepper motor actuated by a gated clock

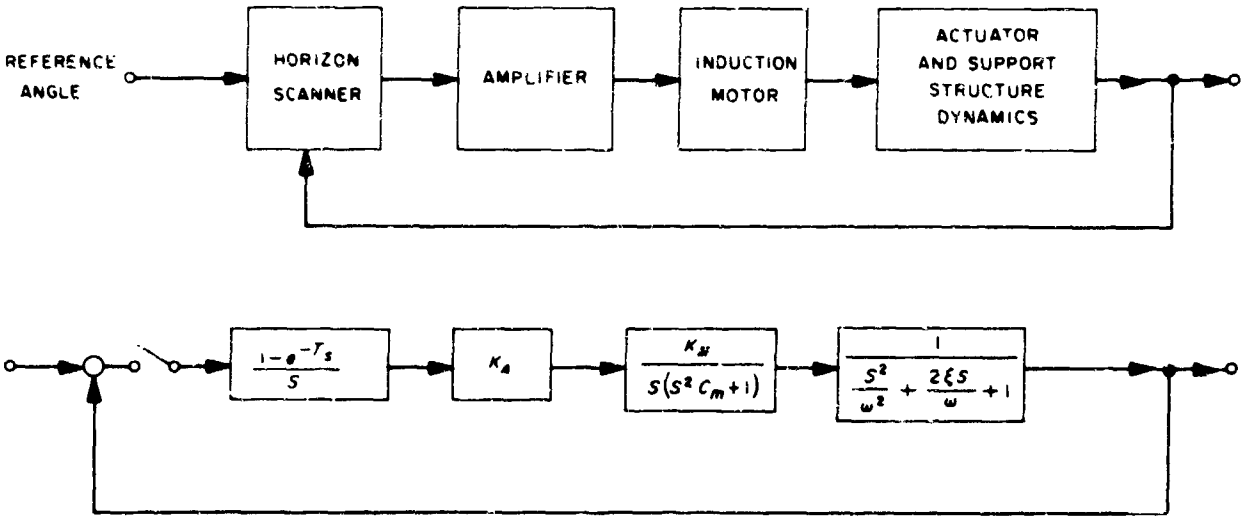

Fig. 7. Platform controlled by two-phase induction motor

angle, is sampled each $T_s = 100$ msec and held with a zero-order hold.

The model for the dynamics is shown in Fig. 8. In Ref. 1 it has been shown that the response of the actuator and the horizon scanner structure can be approximated by a second-order transfer function.

$$\frac{\theta_H}{\theta_M} = \frac{1}{\frac{S^2}{\omega^2} + \frac{2\xi S}{\omega} + 1}$$

where the undamped natural frequency ω and the damping factor ξ are functions of the spring constants K_A, K_B, of the actuator and support structure, C is the coulomb friction, and J_H the inertia of the platform assembly.

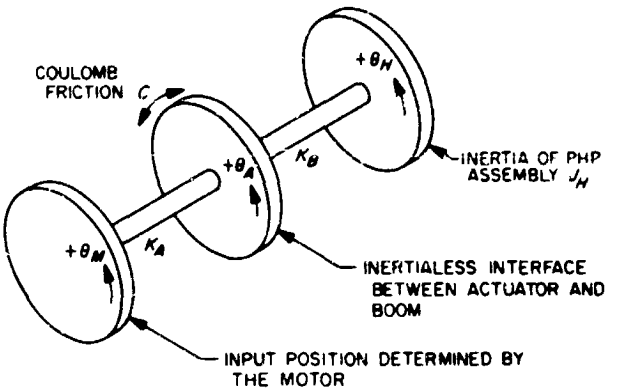

Fig. 8. Horizon scanner dynamics model

Reference

1. Nicklas, J. C., *Analysis, Design, and Testing of a Position Servo Utilizing a Stepper Motor*, Technical Report 32-206, Jet Propulsion Laboratory, Pasadena, Calif., January 25, 1962.

VI. Guidance and Control Research

A. Semiconductor Research

1. Preparation of nπn Structures for the Study of Space-Charge-Limited Current in Silicon

S. Denda* and M-A. Nicolet*

a. Introduction. This report provides information on the preparation of $n\pi n$ structures as required in studies of space-charge-limited current (scle) of electrons in silicon. To provide a good basis of comparison with the theory, the transistorlike structures should satisfy the following requirements: (1) A single-crystal base of known crystallographic orientation, high perfection, and low but homogeneous residual doping; (2) a planar geometry; and (3) abrupt junctions. The first requirement is met by selection of an appropriate single crystal. Crystallographically oriented wafers can then be obtained from it by standard techniques to satisfy the second requirement. Although abrupt junctions are obtained most readily by alloying methods, the present approach uses a diffusion method instead because of the ease with which this method applies to silicon.

b. General considerations on diffusion. Diffusion techniques are classified according to the phase of the sources of impurity as follows: (1) Diffusion from vapor phase into solid, usually called "solid state diffusion." (2) Diffusion from liquid phase into solid, called alloy diffusion. (3) Diffusion from solid phase into solid phase; e.g., grown diffusion.

As a device technology, diffusion from vapor phase has several advantages. It produces a flat, homogeneous and stable junction over the entire surface of the specimen. If desired, masking by a thermally produced oxide layer and subsequent photoengraving can be used to shape the size and form of a junction. Among the various doping agents compatible with this technique, phosphorus has the advantage that (1) solid state diffusion with this element offers no particular difficulties, (2) phosphorus has a high solid solubility in silicon which yields a high impurity concentration at the surface and thus facilitates the approximation of an abrupt junction and problems of ohmic contacting, (3) phosphorus, or P_2O_5, has a high vapor pressure at temperatures as low as 250°C. For these reasons, solid state diffusion of phosphorus was adopted in this work.

*At the California Institute of Technology, performing work supported by the Jet Propulsion Laboratory.

Generally, solid state diffusion in silicon depends critically upon the following processes, most of which still await their detailed technological solution by development and production laboratories:

(1) Lapping and polishing of the silicon surface, with special concern for flatness, roughness and scratches; electropolishing appears as a promising tool.

(2) Chemical etching of the surface to remove the damaged layer produced by the mechanical treatment; this treatment suffers from the fact that it simultaneously deteriorates the flatness.

(3) The presence of localized impurities, such as dust particles on the surface during diffusion, can lead to a localized inversion channel through the junction; this phenomenon, called a "pipe" in Ref. 1, is difficult to avoid but must be absent from integrated circuitry.

(4) Photoresist technique; an increase in resolution is desirable.

(5) Oxide layers and the complicated electronic condition which exists at the Si-SiO_2 interface; these problems are associated with those of impurity segregation and redistribution.

Solid state diffusion produces impurity profiles which are graded unless diffusion times are sufficiently short. Since in the present application steep junctions are to be approximated, the diffusion times should be kept to a minimum. Because of this limitation, the depth of the junction is restricted to a few microns below the surface, which increases the requirement for mechanical perfection of the surface.

c. Theory of diffusion. For planar geometry, the diffusion of atoms in a solid is described (Ref. 2) by the following differential equation:

$$\frac{\partial N}{\partial t} = D\frac{\partial^2 N}{\partial x^2} \tag{1}$$

where N is the concentration of impurity atoms in the crystal, D is the diffusion constant of the impurity under consideration, and x is the distance measured from the surface of the solid into the bulk. The equation can be solved with proper boundary conditions: When diffusion begins at $t = 0$ with a concentration N_s of impurities kept constant at the surface at all times, when the bulk is free of impurities prior to $t = 0$, and when the bulk extends over large distances $x > 0$, the solution is

$$N(x,t) = N_s \operatorname{erfc}\left[\frac{x}{2(Dt)^{1/2}}\right]. \tag{2}$$

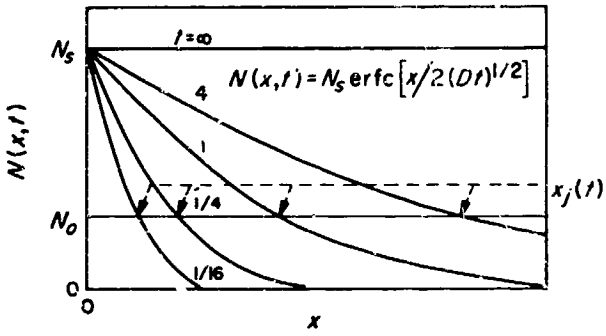

Fig. 1. Impurity distribution in the bulk due to diffusion from a source of constant concentration N_s at the surface, $x = 0$

This solution is sketched in Fig. 1. If the crystal is originally doped with another impurity of concentration N_0 of the opposite type, a *pn* junction will be formed at the point x_j at which $N(x_j, t) = N_0$. Typically, $N_0 << N_s$ and in this case the junction depth is approximately given (Ref. 3) by the simple relationship

$$x_j = 2\left(\ln\frac{N_s}{N_0}\right)^{1/2}(Dt)^{1/2} = k(Dt)^{1/2}. \tag{3}$$

If the total amount of impurity atoms Q diffusing into the solid (and initially deposited on the surface) is kept constant rather than the concentration N_s at the surface, other conditions remaining equal, the solution is

$$N(x,t) = \frac{Q}{(\pi Dt)^{1/2}}\exp(-x^2/4Dt). \tag{4}$$

This solution is sketched in Fig. 2. In this case the junction is located at

$$x_j = 2\left[\ln\frac{Q}{N_0(\pi Dt)^{1/2}}\right]^{1/2}(Dt)^{1/2} \tag{5}$$

which again leads approximately to a dependence

$$x_j = K(Dt)^{1/2} \tag{6}$$

for values of $Q\,(\text{in cm}^{-2}) >> N_0\,(\text{in cm}^{-3})$.

2. Experimental Procedure

a. Sample preparation. The requirements on the mechanical and chemical treatments preceding the diffusion depend on the intended application of the device. The following steps are considered typical and adequate for the study of sclc in silicon:

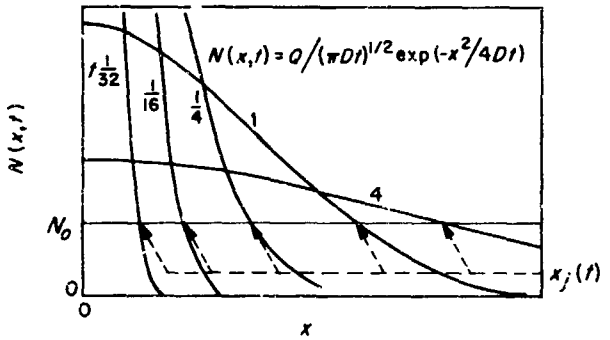

Fig. 2. Impurity distribution in the bulk due to diffusion of a fixed total amount Q of impurity atoms initially present at the surface, $x = 0$

The single crystal is sliced on the diamond saw. Subsequent selective chemical etching revealed that the wafers are oriented in the (111) plane within ± 2 deg. In the case of silicon, however, the crystallographic orientation hardly affects the result of diffusion. The thickness of the wafer is limited to values larger than approximately 0.3 mm by mechanical inaccuracies of the saw. The wafers are then processed on both sides according to the following sequence of steps.

(1) Grinding on 280A-grit emery paper to eliminate coarse grooves and the unevenness of the surface caused by the saw.

(2) Lapping on a flat glass plate with 800-mesh carborundum abrasive and water.

(3) Fine lapping on microcloth with 3200-mesh lapping compound on either a rotating or a stationary plate.

(4) Final polishing on microcloth or Nylon cloth with 1-μ diamond paste or 1-μ aluminum oxide until a mirror-like surface is obtained.

For these operations, thin wafers are mounted with Apiezon wax on a sample holder. The measure of finishing is expressed in terms of "flatness" and "roughness." Steps 1 and 2 develop flatness, while steps 3 and 4 reduce the roughness. For the application envisaged here, smoothness is more important than flatness.

The operations just described leave a mechanically damaged surface layer whose thickness is about 5 to 10 times the size of the grit used. This layer is removed chemically with an etch comprising 5 ppv conc. HNO_3 and 1 ppv conc. HF (called 5-1 etch). The etching rate of the solution depends strongly on the room temperature, the freshness of the reagent, and its total volume. A typical value for silicon is 30 μ/min. It was found that about 40 sec of etching in 30 cc of fresh reagent used at room temperature for one wafer and agitated vigorously yields adequately smooth surfaces. After etching, the wafers are rinsed in succession in water and in deionized water of a resistivity of better than 2 MΩcm.

b. Experimental setup for diffusion. Fig. 3 shows a sketch of the diffusion furnace and the gas system. After final assembly, the whole system is carefully baked out with gas flowing through it and with boats in place at

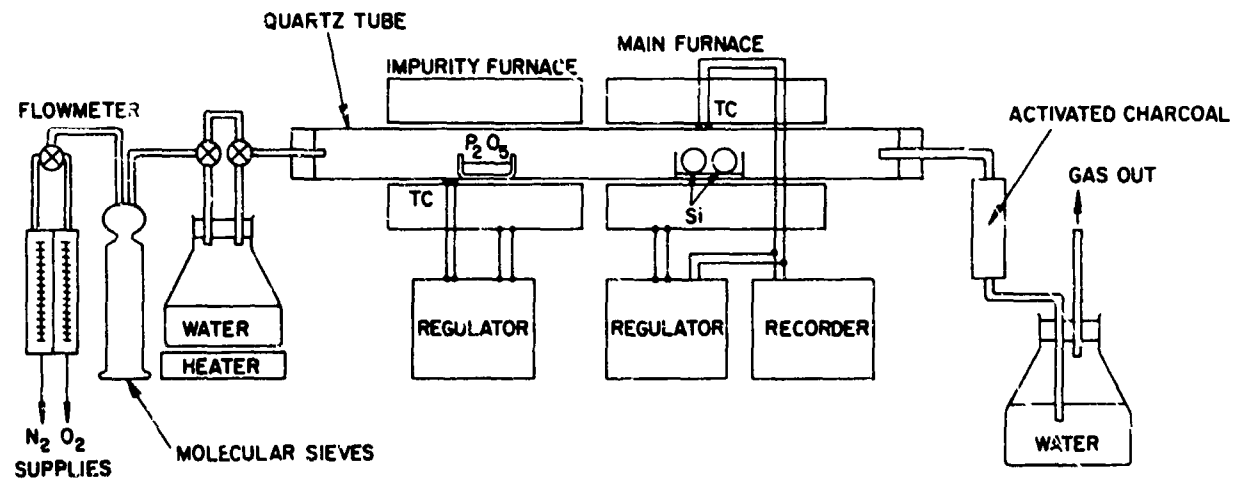

Fig. 3. Sketch of the experimental setup for solid state diffusion of phosphorus into silicon

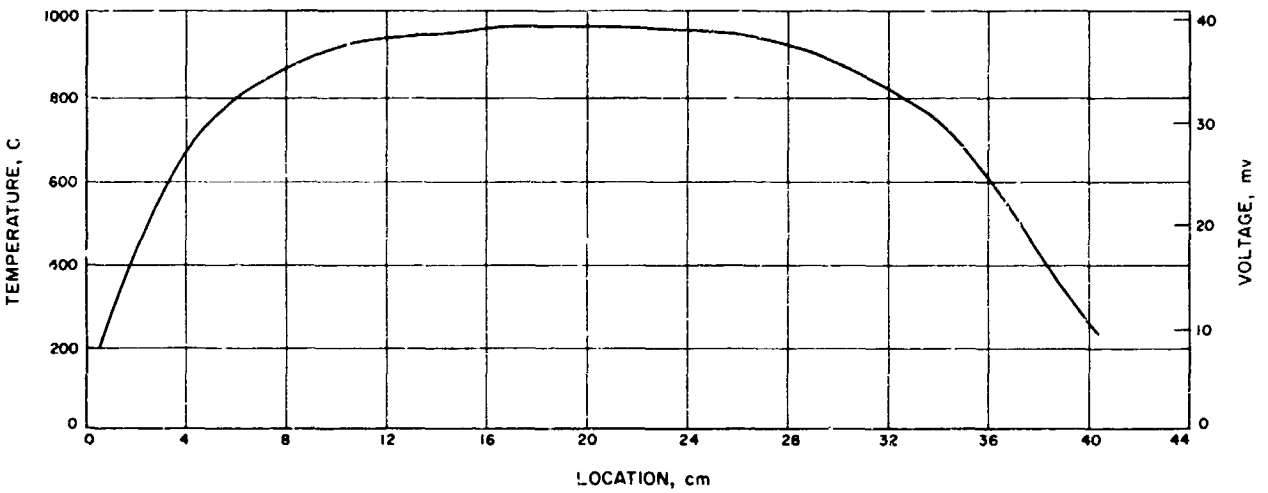

Fig. 4. Temperature distribution along the central axis of the diffusion furnace at steady state

1400°C, for the main furnace, and at 400°C for the impurity furnace, for a total period of 8 hr.

The working length (range of temperature variation $\leq \pm 5\%$) of the main furnace at about 1000°C, as determined by measuring the temperature distribution along the axis of the furnace at steady-state conditions, was found to be at least 10 cm (see Fig. 4). The temperature regulator and the temperature recorder are calibrated with reference to, but including, room temperature.

c. Diffusion procedure. (1) The main furnace is preheated to 1100°C, and the impurity furnace to 250°C; both are held at these temperatures for at least 20 min to assure stationary conditions. (2) Gas flow is adjusted to 1 ft³/hr for N_2 and 0.1 ft³/hr for O_2. (3) A quartz boat loaded with P_2O_5 is inserted into the center of the impurity furnace. (4) The Si wafers are inserted 5 min later on a quartz boat into the main furnace and positioned at the center. Diffusion time is measured beginning with the insertion of the wafer. (5) After the desired diffusion time has elapsed, the power to both furnaces is turned off; they are allowed to cool at their natural rate. (6) The wafers are extracted from the main furnace once its temperature has fallen below 700°C; they reach room temperature in open air. The surface of the wafers generally shows interference colors due to the thin oxide layer formed during diffusion.

d. Physical data on phosphorus diffusion into silicon. The diffusion constant D of P in Si is shown in Fig. 5, which represents (Ref. 4)

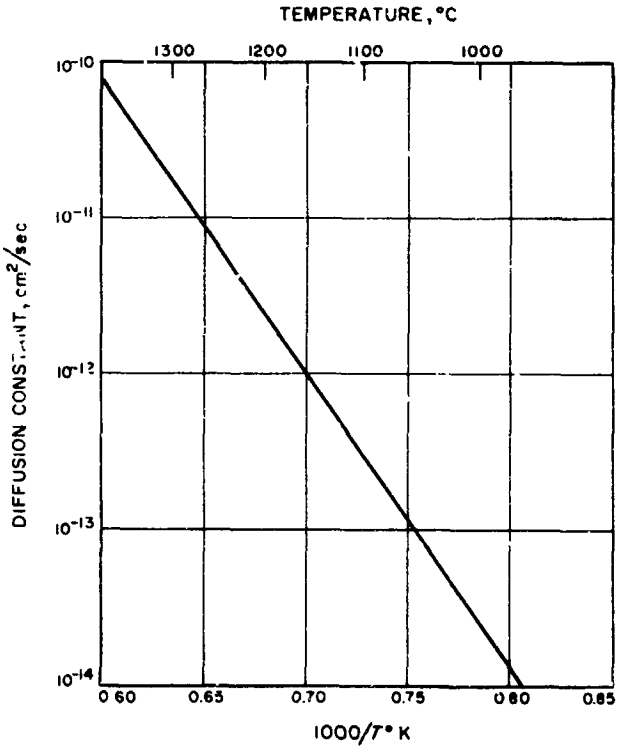

Fig. 5. Diffusion constant D of phosphorus in silicon, Ref. 4

$$D = 10.5 \exp(-42.7 \cdot 10^3\ ^\circ\mathrm{K}/T)\ \mathrm{cm^2\ sec^{-1}} \qquad (7)$$

where T is the diffusion temperature in °K. The solubility of P in Si is given in Fig. 6 and Ref. 5. The vapor

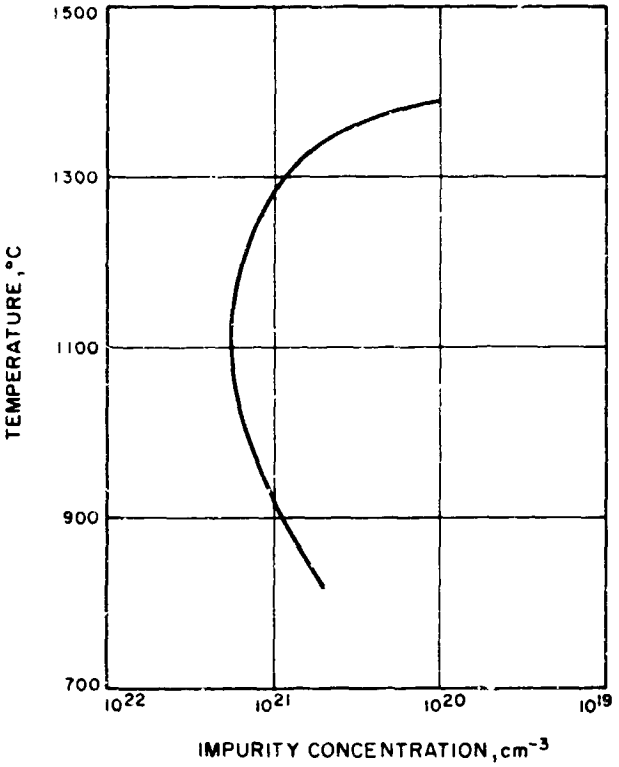

Fig. 6. Solid solubility of phosphorus in silicon, Ref. 5

pressure of P_2O_5 (metastable form) is as follows:

Temperature, °C	Vapor pressure, mm Hg
189	1
236	10
270	40
294	100
336	400
358	760

SiO_2 formation on Si surface is depicted in Fig. 7. Masking effect of SiO_2 for P diffusion is shown in Fig. 8 and Ref. 6.

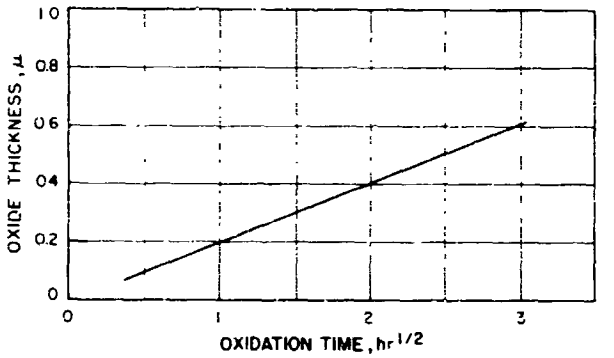

Fig. 7. Formation of SiO_2 on a silicon surface at 1200°C by a flow of O_2 1l/min bubbled through water of 60°C

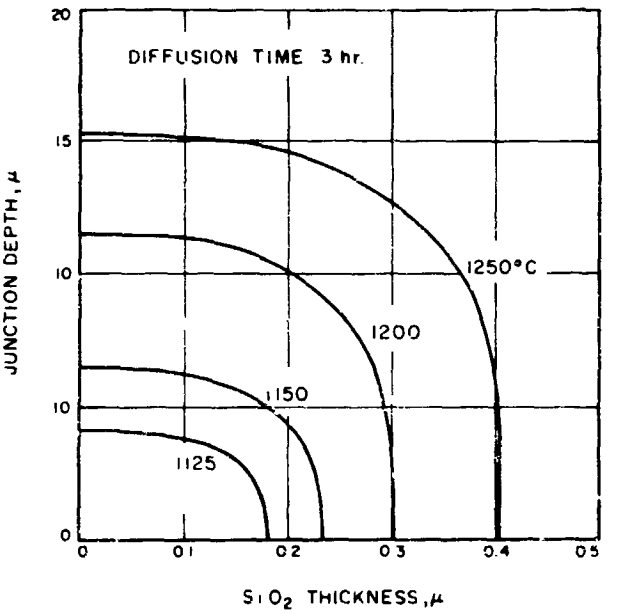

Fig. 8. The effect of a SiO_2 mask on the diffusion of phosphorus into silicon, Ref. 6

3. Evaluation

a. Metallographic observation of the diffused layer. The diffused layer can be observed easily by angle lapping and staining. The sample is waxed to a slightly inclined bottom of a lapping jig and carefully lapped on a glass plate with 1-μ diamond paste. The resulting surface forms a suitably sharp edge with the diffusion surface. The lapped sample is then stained for 15 to 30 sec in a staining etch comprising 30 cc of conc. HF and 1 or 2 drops of conc. HNO_3. Better results can be expected if the wafer surface is illuminated with white light during staining. A photograph of a typical result is shown in Fig. 9. The depth of the junction can be determined with the knowledge of the lapping angle and the photographic amplification factor. In the case shown, the angle is 6°37′, as determined on an interference microscope.

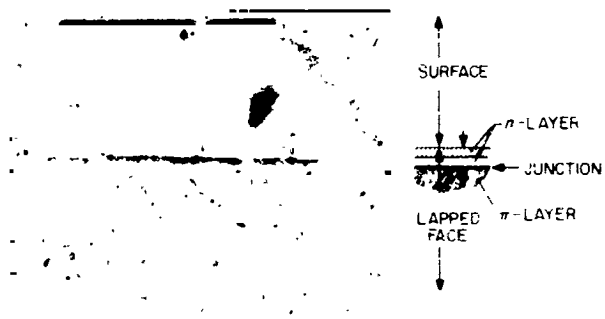

Fig. 9. Display of the junction by angle lapping and staining; sample diffused for 40 min at 1100°C; junction depth 3.4 μ

Fig. 10 shows the dependence of the junction depth measured in this fashion as a function of the square root of the diffusion time obtained in different diffusion operations with wafers of the same bulk material (≈200Ω-cm p-type). The results agree well with the theory; see Eq. (3).

b. Determination of the impurity concentration at the surface. The impurity concentration at the surface can be obtained from measurements of the sheet conductance of the diffused layer if the junction depth and the profile of the impurity distribution are known. The surface conductance can be measured with a four-point probe. From the measured values, the sheet resistivity ρ_s is obtained in ohms as follows:

$$\rho_s = 4.53\,(V_{inner\ probes})/(I_{outer\ probes})$$

The conversion factor 4.53 does not depend upon the dimension of the four-point probe (Ref. 7). Fig. 11 reproduces a chart calculated by Backenstoss (Ref. 8) for an erfc impurity profile. With this chart, the concentration N_s at the surface can be found once ρ_s and x_j are known. The value of N_s obtained in this manner has an estimated error of approximately ±30% due to the cumulated uncertainties in ρ_s and x_j. Table 1 summarizes the results obtained on the samples of Fig. 10.

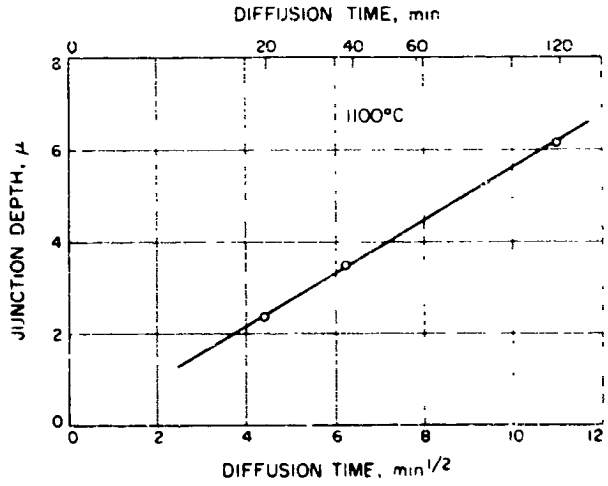

Fig. 10. Experimental dependence of the junction depth on the diffusion time at a constant diffusion temperature of 1100°C

Table 1. Diffusion sample test results

Parameter	No. 1	No. 2	No. 3
t(min)	20	40	120
x_j (μ)	2.4	3.4	6.1
N_s (cm^{-3})	$5 \cdot 10^{19}$	$2 \cdot 10^{20}$	$2 \cdot 10^{20}$

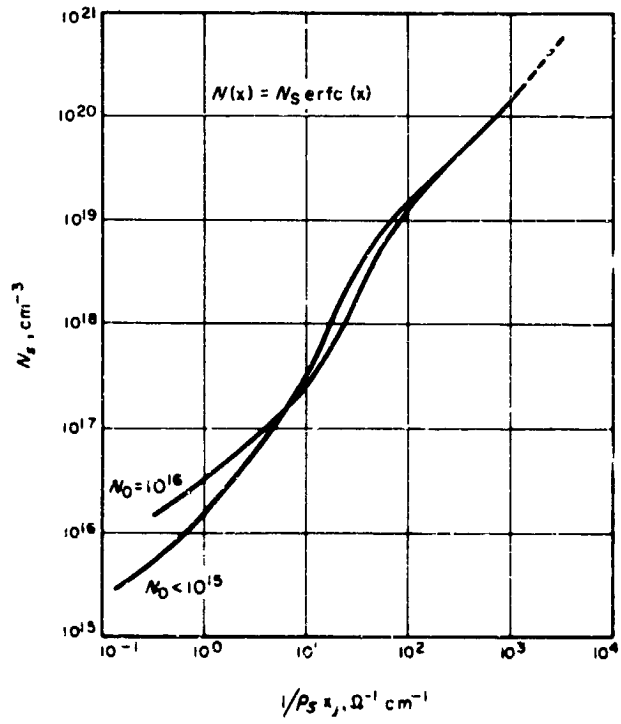

Fig. 11. Evaluation of the surface concentration N_s from values of the junction depth x_j and the sheet resistivity ρ_s for an erfc impurity profile, Ref. 8

c. V-I characteristics. A dot of Apiezon wax about 1 or 2 mm in diameter is applied on one side of a wafer. The sample is then immersed into a 5-1 etch to remove the diffused layer on the remainder of the surface. A mesa junction is formed beneath the area protected by the dot of wax. The sample is then thoroughly rinsed in deionized water and the wax removed. The back side of the sample is abraded with emery paper. Silver is painted on a metal plate serving as electrode. Electrical contact to the mesa is made with a metal point fixed on a micromanipulator. Fig. 12 shows a typical *V-I* characteristic. The reverse resistance exceeds 10 MΩ, and the breakdown voltage is above 200 V. At small forward biases, a short range of negative resistance is sometimes observed, which is caused by a poor quality of the backside contact.

d. Junction capacitance. The voltage dependence of the junction capacitance with backward bias gives information of the impurity distribution. An abrupt junction exhibits a dependence of

$$C = a(V + V_d)^{-1/2} \tag{8}$$

and a linearly graded junction has a dependence of

$$C = b(V + V_d)^{-1/3} \tag{9}$$

where V is the value of the applied reverse bias. For diffused junctions, the dependence often falls in a range between these two limiting cases. An experimental result is shown in Fig. 13. At large reverse biases, $C^{-2} \approx V$. Fig. 14 shows that at low reverse biases

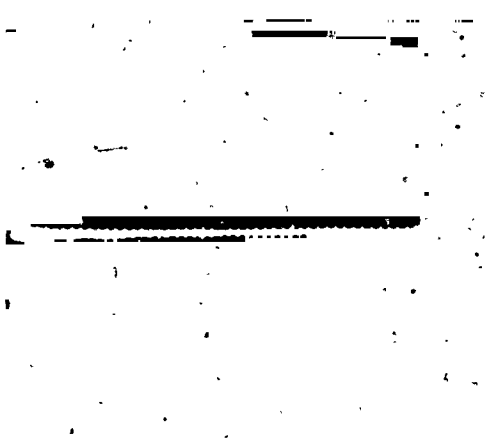

Fig. 12. Typical *V-I* characteristic of a junction; horizontal scale 20 v/div; vertical scale 500 μamp/div; junction area approx 1.0 mm²

$C^{-2} \sim (V + V_d)$, where $V_d = 0.5 \pm 0.1$ v. Using this value, the measured curve of Fig. 13 can be corrected to test. There results a straight line, confirming that Eq. (8) is applicable in this case. This indicates that the junctions obtained in the diffusion process are essentially abrupt, as expected from the short time of diffusion. Measurements with various mesa areas confirmed that capacitances other than that of the junction are negligible

The coefficient a of the above equation has the value

$$a = A\left(\frac{q\epsilon\epsilon_0}{2} \cdot \frac{N_a N_d}{N_a + N_d}\right)^{1/2} \tag{10}$$

where $q = 1.6 \cdot 10^{-19}$ Cb, ϵ is the dielectric constant (12 for Si), $\epsilon_0 = 8.85 \cdot 10^{-14}$ F/cm, N_d is the donor concentration in the n-side of the junction, N_a is the acceptor concentration in the p-side of the junction, and A is the junction area. This expression can be used to estimate the acceptor concentration N_a of the wafer if N_d is much larger than N_a and if Eq. (8) is indeed applicable at large reverse biases; in this case

$$N_a = \frac{2VC^2}{q\epsilon\epsilon_0}. \tag{11}$$

Applied to the results of Fig. 13, this equation yields $N_a = 4.8 \cdot 10^{13}$ cm^{-3}, which corresponds to a resistivity of about 270 Ω-cm. By manufacturer's specification, the crystal used for the wafer has a resistivity of 200 Ω-cm. This value of the doping concentration can be verified in two additional ways. Measurements of the bulk resistivity at room temperature on a bar-shaped sample, from which the diffused surface layers have been lapped off, yield the number of mobile majority charge carriers. From the punch-through voltage of n-π-n structures, the number of ionized acceptors can be deduced. A comparison of the results of these different methods is given in Table 2.

The calculation of V_d using concentrations of 10^{19} cm^{-3} for the n-side and $4.8 \cdot 10^{13}$ cm^{-3} for the π-side (300 Ω-cm resistivity at room temperature) and an intrinsic carrier

Table 2. Comparison of the resistivity values deduced from three different measurements

Parameter	By capacitance, Eq. (11)	By two-point resistivity	By punch-through
N_a (cm^{-3})	$4.8 \cdot 10^{13}$	$4.6 \cdot 10^{13}$	$4.6 \cdot 10^{13}$
Resistivity, Ω-cm	270	296	300

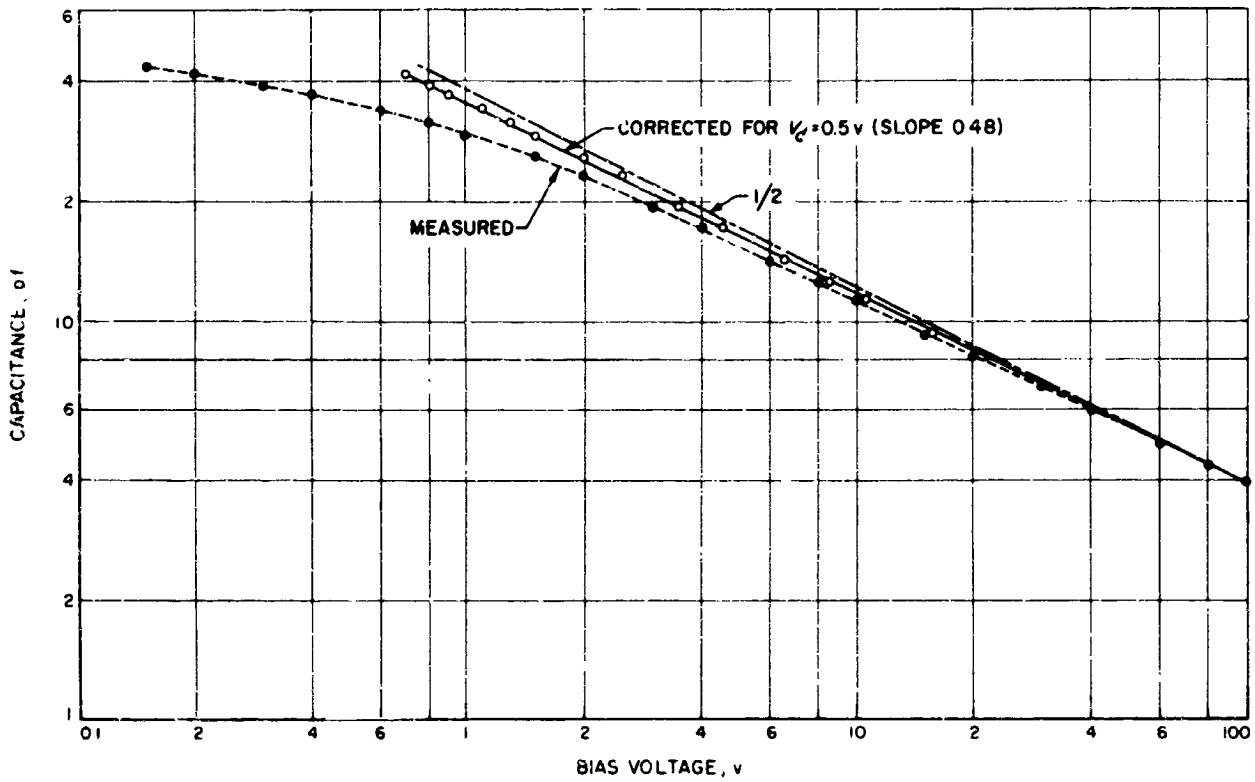

Fig. 13. Dependence of the junction capacitance C on a reverse bias

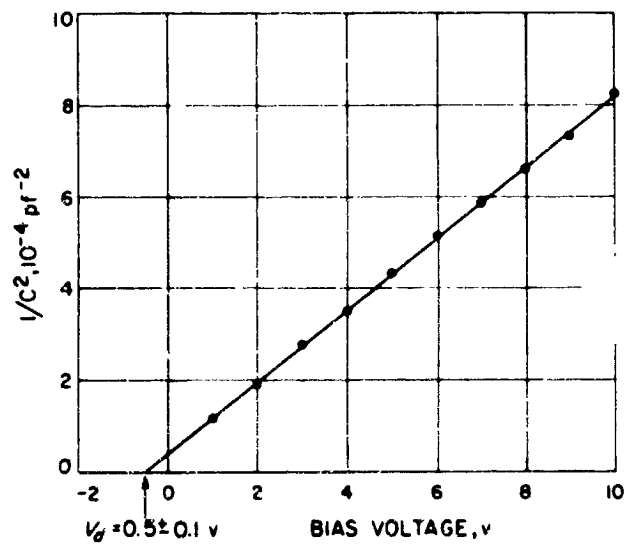

Fig. 14. Dependence of the junction capacitance C on a low reverse bias

density of $1.5 \cdot 10^{10}$ cm^{-3} at room temperature results in a value of 0.70 v for the junction. It is believed that the discrepancy between this value and that obtained from Fig. 14 is due to experimental errors and possibly some uncertainties in the doping profile.

4. Contacts

When electrical contacts are made to the diffused layer with gold wire or gold-plated metal plates applied with moderate pressure, the contact resistance is found to be in the range of a few ohms. At high current densities, this resistance introduces significant and unreproducible errors in the *V-I* characteristic. Mechanically strong and electrically non-rectifying contacts ("ohmic contacts") to the diffusion layer are therefore required. Evaporated aluminum contacts are known to give non-rectifying contacts to *n*-type silicon of less than approximately 10^{-3} Ω-cm. Gold offers similar properties, with the added advantage of an oxide-free metal surface, but its large diffusion constant prohibits extended thermal treatments after its application.

The wafer is placed on a Ta heating strip in a vacuum system. At a pressure of approximately 10^{-6} mm Hg, a gold film of 0.1 to 0.3 μ thickness is evaporated on the wafer, which is kept at a temperature of about 250°C during this process. The temperature is then raised to roughly 350°C and held there for 5 min. To test the electrical quality of this contact, small circular contacts are deposited with a mask. Very little resistance is measured between them. The linearity is excellent. To ascertain that the gold does not penetrate through the junction, the *n*-type diffused lay is etched away between the contacts. A *V-I* characteristic between two contacts equal to that of a reverse-biased junction for both polarities indicates an unperturbed junction under the gold layer.

B. Cryogenics Research

J. T. Harding

1. Analysis of Torques Exerted on a Spherical Superconductor Due to Trapped Flux in an Axially Symmetric Magnetic Field

a. Introduction. This report describes part of a program to analyze the magnetic forces and torques acting on a superconducting sphere which forms the rotor of a cryogenic gyro. An earlier report (*SPS 37-24*, Vol. IV, p. 35) calculated the torques exerted by an axially symmetric magnetic field on a slightly deformed spherical superconductor.

b. Procedure. Here, as in the previous report, the torque on the superconducting sphere is calculated by integrating the Maxwell stress tensor over the surface of the body

$$\mathbf{T} = \iint \mathbf{r} \times \frac{\mathbf{BB} - \frac{1}{2}B^2\mathbf{I}}{\mu_0} \cdot d\mathbf{S}$$

For a sphere $\mathbf{r}$ is also the surface normal so that

$$\mathbf{T} = \frac{1}{2\mu_0}\iint \mathbf{r} \times \mathbf{BB} \cdot d\mathbf{S} \qquad (1)$$

Because of the spherical boundary, it is appropriate to express both the applied and the trapped fields as expansions in sets of Spherical Harmonic functions. The final expression for torque is in the form of products of expansion coefficients of the applied and the trapped fields. Each term may be interpreted as an interaction between a mode of trapped-flux configuration and a corresponding asymmetry in the magnetic field. Since these expressions get increasingly complicated as the order of asymmetry grows, this type of analysis is only useful if the applied field is of a low order of symmetry. Simple examples are illustrated later in *Sect. g*.

c. Spherical harmonics. As in the earlier report, the complete set of Spherical Harmonics (see Fig. 15 for coordinate system),

$$Y_l^m(\mu,\phi) = (-1)^{\frac{1}{2}(m+|m|)}\left[(2l+1)\right.$$

$$\times (l-|m|)!/2(l+|m|)!\left.\right]^{\frac{1}{2}}$$

$$\times P_l^{|m|}(\mu)\, e^{im\phi}/(2\pi)^{\frac{1}{2}} \qquad (2)$$

where

$$P_l^m(\mu) = \frac{1}{2^l l!}(1-\mu^2)^{m/2}\frac{d^{l+m}}{d\mu^{l+m}}(\mu^2-1)^l,$$

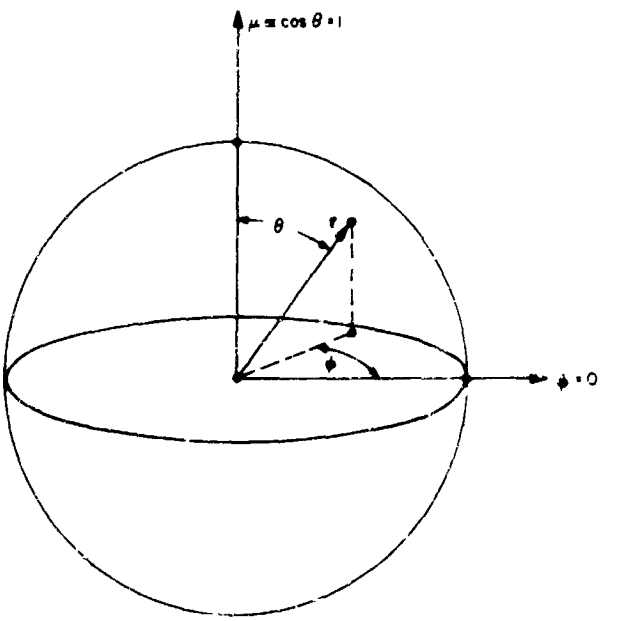

Fig. 15. Coordinates for analysis of magnetic torque

is chosen for representing the factors in the integral for torque because of the following useful properties (Ref. 9, p. 158).

$$(\mathbf{r}\times\nabla)^2 Y_l^m = -l(l+1)Y_l^m$$

$$(\mathbf{r}\times\nabla)_z Y_l^m = imY_l^m \tag{3}$$

$$\iint Y_l^{m*} Y_p^q \, d\mu d\phi = \begin{cases} 1 & \text{if } l=p \text{ and } m=q \\ 0 & \text{otherwise} \end{cases} \tag{4}$$

where the asterisk * denotes a complex conjugate, and boldface type denotes a vector quantity.

$$(\mathbf{r}\times\nabla)_+ = [(\mathbf{r}\times\nabla)_x + i(\mathbf{r}\times\nabla)_y]\, Y_l^m = iG_l^m Y_l^{m+1} \tag{5}$$

where $G_l^m \equiv [(l-m)(l+m+1)]^{1/2}$

$$(\mathbf{r}\times\nabla)_- \equiv [(\mathbf{r}\times\nabla)_x - i(\mathbf{r}\times\nabla)_y]\, Y_l^m = iH_l^m Y_l^{m-1} \tag{6}$$

where $H_l^m \equiv [(l+m)(l-m+1)]^{1/2}$

d. Expressions for $\mathbf{B}$. There are three contributions to the magnetic field $\mathbf{B}$, each of which can be expressed as the gradient of a scalar potential in the region outside the surface of the sphere.

(1) *The applied field*, which is assumed to have axial symmetry, can be represented quite generally by

$$-\mathbf{B}_A = \nabla \sum_l b_l r^l P_l(\mu')$$

(2) *The induced field*, which combines with $\mathbf{B}_A$ to satisfy the boundary conditions, $\mathbf{B}_{normal} = 0$ at the surface of a superconductor, can be represented by

$$-\mathbf{B}_I = \nabla \sum_l a_l r^{-(l+1)} P_l(\mu')$$

The boundary condition becomes

$$-B_{normal} = \frac{\partial}{\partial r}\sum_l (b_l r^l + a_l r^{-(l+1)}) P_l(\mu') = 0$$

at $r = R$, which implies

$$a_l = \frac{l}{l+1} R^{2l+1} b_l \tag{7}$$

(3) *The trapped field* can be thought of as that part of the total field which does not satisfy the boundary condition; i.e.,

$$-\mathbf{B}_T = -\mathbf{B}_{total} + \mathbf{B}_A + \mathbf{B}_I = \sum_{lm} c_{lm} r^{l-1} Y_l^m(\mu,\phi).$$

(Only inverse powers of r are permissible inasmuch as this field has its sources within the ball and will vanish at $r = \infty$.) However, an important assumption is that $\mathbf{B}_T$ is rigidly attached to the sphere and rotates with it while the applied and induced fields are fixed relative to the external current sources that produce the applied field. This assumption is in accordance with observations of superconductors containing trapped flux.

The direction $\mu' = 1$ represents the field symmetry axis. To calculate the torque, all contributions to $\mathbf{B}_{total}$ must be expressed in the same coordinate system. This is easily done with the aid of the "Addition Theorem for Legendre Polynomials" (Ref. 9, p. 161). Let the symmetry axis of the magnetic field, $\mu' = 1$, intersect the $\mu = 1$ axis (fixed in the rotor) at the origin, and let the coordinates of the μ' axis, referred to the μ, ϕ system be given by $\mu = \cos\alpha$ and $\phi = \beta$. Then

$$\left(\frac{2l+1}{4\pi}\right)^{1/2} P_l(\mu') = Y_l^0(\mu') = \left(\frac{4\pi}{2l+1}\right)^{1/2} \times \sum_{m=-l}^{+l} Y_l^{m*}(\cos\alpha,\beta)\, Y_l^m(\mu,\phi)$$

Accordingly

$$-\mathbf{B}_A - \mathbf{B}_I = \nabla \sum_l \frac{4\pi}{2l+1}(b_l r^l + a_l r^{-(l+1)}) \sum_m Y_l^{m*}(\cos\alpha,\beta)\, Y_l^m(\mu,\phi)$$

$$\nabla \sum_{lm} b_{lm}(r)\, Y_l^m(\mu,\phi)$$

where

$$b_{lm}(r) = \frac{4\pi}{2l+1}(b_l r^l + a_l r^{-(l+1)}) Y_l^{m*}(\cos\alpha,\beta) \tag{8}$$

e. Evaluation of the torque. The expressions for torque in Eq. (1) can be written

$$\mathbf{T} = \frac{1}{\mu_0}\iint \mathbf{r} \times (\mathbf{B}_A + \mathbf{B}_I + \mathbf{B}_T)(\mathbf{B}_A + \mathbf{B}_I + \mathbf{B}_T)\cdot d\mathbf{S}$$

$$= \frac{1}{\mu_0}\iint \mathbf{r} \times (\mathbf{B}_A + \mathbf{B}_I + \mathbf{B}_T)(\mathbf{B}_A + \mathbf{B}_I)\cdot d\mathbf{S}$$

$$+ \mathbf{r} \times (\mathbf{B}_A + \mathbf{B}_I)\mathbf{B}_T \cdot d\mathbf{S} + \mathbf{r} \times \mathbf{B}_T\mathbf{B}_T \cdot d\mathbf{S}.$$

The first term is zero because of the superconducting boundary condition $\mathbf{B}(\text{applied} + \text{induced})\cdot d\mathbf{S} = 0$. The third term is zero because the trapped flux cannot exert a net torque on itself. (Note: This choice of grouping of terms greatly shortens the calculation as compared to other possible groupings.) The remaining integrand is evaluated by use of the following relations:

$$-\mathbf{B}_T \cdot d\mathbf{S} = \frac{\hat{c}}{\hat{c}r}\sum_{lm} c_{lm} r^{-(l+1)} Y_l^m r^2 d\mu d\phi$$

$$= \sum_{lm} -(l+1) r^{-l} c_{lm}^* Y_l^{m*}\, d\mu d\phi,$$

(since $\mathbf{B}_T$ is real).

$$\mathbf{r} \times (\mathbf{B}_I + \mathbf{B}_I) = \sum_{pq} b_{pq}(r)\, \mathbf{r} \times \nabla Y_p^q,$$

$$\mathbf{r} \times \nabla = \hat{\mathbf{k}}(r \times \nabla)_z + \hat{\mathbf{i}}\frac{(r \times \nabla)_+ + (r \times \nabla)_-}{2}$$

$$+ \hat{\mathbf{j}}\frac{(r \times \nabla)_+ - (r \times \nabla)_-}{2i}$$

The operator and integral relations, Eqs. (3)–(6), make evaluation of the integrals almost trivial.

$$\mathbf{T} = \frac{1}{\mu_0}\iint \mathbf{r} \times (\mathbf{B}_A + \mathbf{B}_I)\mathbf{B}_T \cdot d\mathbf{S}$$

$$= \frac{1}{\mu_0}\sum_{pq}(p+1) R^p b_{pq}^*(R)\left[\hat{\mathbf{k}} i q c_{pq} + \hat{\mathbf{i}}\frac{i}{2}\right.$$

$$\left. \times (G_p^q c_{p,q-1} + H_p^q c_{p,q+1}) - \frac{\hat{\mathbf{j}}}{2}(G_p^q c_{p,q-1} - H_p^q c_{p,q+1})\right].$$

From Eqs. (7) and (8),

$$b_{pq}^*(R) = \frac{4\pi}{p+1} b_p R^p Y_p^q(\cos\alpha, \beta)$$

Finally, the expression for torque is

$$\mathbf{T} = \frac{4\pi}{\mu_0}\sum_{pq} b_p Y_p^q(\cos\alpha, \beta)\left[\hat{\mathbf{k}} i q c_{pq} + \hat{\mathbf{i}}\frac{i}{2}(G_p^q c_{p,q-1} + H_p^q c_{p,q+1})\right.$$

$$\left. - \frac{\hat{\mathbf{j}}}{2}(G_p^q c_{p,q-1} - H_p^q c_{p,q+1})\right]$$

f. Discussion. Each term in the expression for torque is a product of three factors: the expansion coefficient of the axially symmetric applied field, b_p; the expansion coefficient of the trapped field, c_{pq} or $c_{p,q\pm1}$; and an angularly dependent function Y_p^q. Of particular significance is the fact that the contribution to torque due to a trapped flux component c_{pq} is null if the corresponding applied field component b_p is zero.

g. Example of uniform trapped flux. If a metal becomes superconducting in the presence of a uniform field, but due to absence of a Meissner effect, it fails to exclude flux in the process, a uniform field is "trapped" within the superconductor and it persists after the applied field is removed. In the case of a sphere, the field produced outside, which satisfies the continuity of the normal component of $\mathbf{B}$ on the surface, is given by

$$\mathbf{B}_T\,(r > R) = \frac{R^3}{r^3} B_T(\cos\theta\,\hat{\mathbf{r}} - \tfrac{1}{2}\sin\theta\,\hat{\boldsymbol{\theta}})$$

$$= -\nabla\left[\left(\frac{\pi}{3}\right)^{1/2} R^3 B_T\right] r^{-2} Y_1^0$$

i.e., $c_{10} = (\pi/3)^{1/2} R^3 B_T$, inasmuch as

$$Y_1^0 = \left(\frac{3}{4\pi}\right)^{1/2}\cos\theta$$

The only non-zero terms in torque are

$$\mathbf{T} = \frac{4\pi}{\mu_0} b_1\left[\hat{\mathbf{i}}\frac{i}{2}(G_1^{-1}Y_1^{-1} + H_1^1 Y_1^1) + \frac{\hat{\mathbf{j}}}{2}(-G_1^{-1}Y_1^{-1} + H_1^1 Y_1^1)\right] c_{10}$$

and since

$$Y_1^{\pm1} = \mp\left(\frac{3}{8\pi}\right)^{1/2}\sin\alpha\, e^{\pm i\beta}$$

and

$$G_1^{-1} = (2)^{1/2} = H_1^1$$

$$\mathbf{T} = \frac{2\pi}{\mu_0} b_1 R^3 B_T \sin\alpha\,(\sin\beta\,\hat{\mathbf{i}} - \cos\beta\,\hat{\mathbf{j}})$$

The magnetic dipole moment of the trapped flux is

$$M = \frac{3}{2}\frac{B_T}{\mu_0}\frac{4}{3}\pi R^3$$

while $b_1 = -B_0$, the magnitude of the uniform applied field. Hence,

$$\mathbf{T} = MB_0 \sin\alpha\,(\cos\beta\,\hat{\mathbf{j}} - \sin\beta\,\hat{\mathbf{i}})$$

Table 1. Definitions of symbols

MKS units used throughout

$\mathbf{B}$ = magnetic field (weber/m²)
$\mathbf{B}_A$ = applied field
$\mathbf{B}_I$ = induced field
$\mathbf{B}_T$ = trapped field
$\mu_0 = 4\pi\ 10^{-7}$
$\mathbf{r}$ = radius vector from center of sphere
dS = element of surface area
$\mathbf{T}$ = torque on sphere
R = radius of sphere
$P_p^q(\mu)$ = unnormalized associated Legendre function
$Y_p^q(\mu, \phi)$ = normalized Spherical Harmonic function
a_p = expansion coefficient in scalar potential representing the induced field
b_p = expansion coefficient in scalar potential representing the applied field
c_{pq} = expansion coefficient in scalar potential representing the field due to trapped flux
θ, ϕ = spherical coordinates referenced to rotor
$\mu = \cos\theta$
θ', ϕ' = spherical coordinates referenced to sources of applied field
$\mu' = \cos\theta'$
M = magnetic dipole moment of the trapped flux
α, β = angles relating rotor coordinates and field coordinates
$G_l^m \equiv [(l-m)(l+m+1)]^{1/2}$
$H_l^m \equiv [(l+m)(l-m+1)]^{1/2}$
$i = (-1)^{1/2}$
$\hat{k}$ = unit vector in $\mu = 1$ direction
$\hat{i}$ = unit vector in $\mu = 0, \phi = 0$ direction
$\hat{j}$ = unit vector in $\mu = 0, \phi = \pi/2$ direction
l, m, p, q = summation indices

which is the familiar result for the interaction between a magnetic dipole and a uniform magnetic field. Note carefully the definitions of α and β in determining the vector sense of $\mathbf{T}$.

h. Example of uniform field plus uniform-gradient field. Consider the case of a rotor rotating rapidly in the field $\mathbf{B}_A$, where:

$$\mathbf{B}_A = -\nabla[b_1 r P_1(\mu') + b_2 r^2 P_2(\mu')], \qquad (b_n = 0,\ n > 2)$$

(This is merely a uniform field plus a uniform-gradient field.) If the rotation occurs about the $\mu = 1$ axis of the rotor, the time average torque will involve only that portion of the trapped field which has symmetry about $\mu = 1$, i.e., only the c_{p0} terms. In this case, then, only the uniform and uniform-gradient components, c_{10} and c_{20}, contribute to net torque. This comment is significant because in the present configuration of the cryogenic gyro, the applied field meets this specification. Hence as far as analyzing drift due to trapped flux is concerned, only two parameters relative to trapped flux need be considered. Similar considerations based on the previous analysis of torque due to non-sphericity show that only four parameters defining the rotor surface are sufficient for analyzing drift.

N65-32426

C. Thermionics Research

K. Shimada

1. Self-Excited Oscillations in Cylindrical Cesium Diodes

This report contains the results of investigations of low-frequency oscillations occurring in JPL-built, cylindrical, cesium diodes. Preliminary results for a commercial diode were reported in *SPS 37-30*, Vol. IV, p. 53.

a. Introduction. Natural oscillations in the kilocycle range have been observed in thermionic energy converters and other cesium diodes. They occur spontaneously as oscillations in the current and in the voltage of a diode. Among the various operating parameters of a diode, the emitter temperature, the cesium pressure, and the interelectrode gap are the principal parameters which influence the amplitude and the frequency of the oscillations, and which determine the conditions for the oscillations to exist at all. The results indicate that the oscillations consist of changes in the space-charge distribution when the conditions for neutral emission are nearly satisfied.

b. Measurements. Several glass diodes having pyrex windows were built in the laboratory. One of such diodes is shown in Fig. 16. The electrodes were cylindrical in structure. The emitter was a tungsten wire having a 20-mil diameter and a 2.5-in. length. The collector, which was concentric with the emitter, was constructed in two different dimensions in order to observe the effect of dimensional changes on the oscillations. Except for one diode, the diodes had collectors with an inside diameter of

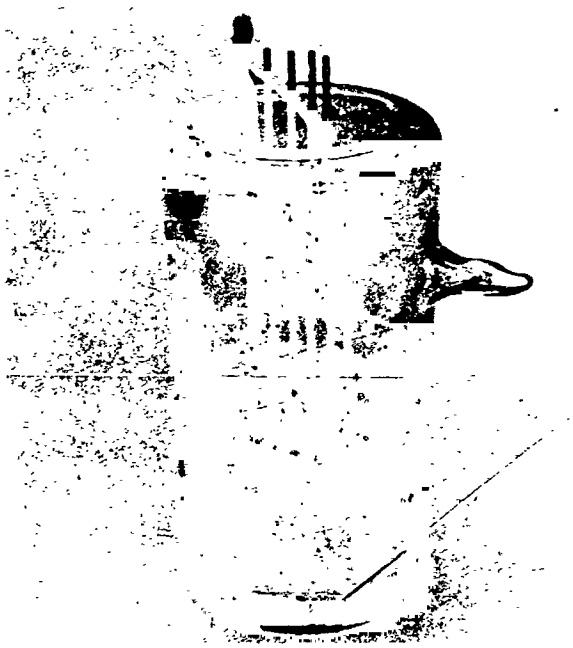

Fig. 16. Experimental diode, W-Ni

approximately 0.5 in. and an axial length of 2 in. One diode had a smaller collector with an inside diameter of approximately 0.25 in. and an axial length of 0.654 in. The collector is centrally located along the length of the emitter. In this diode there was an additional collector of the same dimension located immediately above the central collector in order to facilitate the study of the temperature distribution along the emitter. This diode will be referred to as the small diode in later discussions. The small diode had a tungsten emitter and a tantalum collector. The other diodes had combinations of tungsten for the emitter and tantalum or nickel for the collector; they will be designated as the W-Ta diode and the W-Ni diode. The emitter was directly heated by a half-wave rectified 60 cyc current. The volt-ampere curves were taken by an oscilloscope during the off-cycle of the heating current. True temperatures of the emitter were obtained from the brightness temperatures which were measured at the center of the emitter through the pyrex window by a micro-optical pyrometer. There were temperature variations as large as 300°K along the effective part of the emitter of each of the two large diodes. However, the variations were as small as 20°K along the effective part of the emitter in the small diode.

Vacuum data were taken before cesium was introduced so as to identify the condition of the diodes, especially the emission properties of the emitter surface. A Richardson plot based upon the current density determined from the effective emitter area agreed favorably with the theoretical line for tungsten. After cesium was introduced, the diode was placed in an oven and the cesium reservoir temperature, T_{Cs}, was determined from the equilibrium oven temperature. The cesium pressure is a direct function of the cesium reservoir temperature The diode circuit was completed through a variable-voltage dc power supply and a decade resistance box. The oscillations were observed with an oscilloscope and a spectrum analyzer which were connected across the decade box. A schematic diagram of the circuit which was used is shown in Fig. 17.

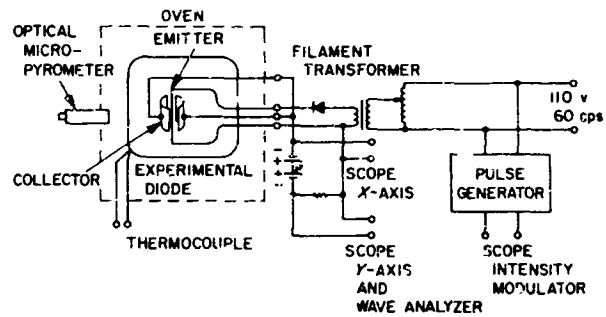

Fig. 17. Schematic diagram of measuring circuit

c. Results. The oscillations were examined with respect to: (1) the conditions for oscillation to occur, (2) the amplitude of oscillation, and (3) the frequency of oscillation. Although oscillations might have occurred when the diode was operated in a glow discharge mode or in an arc mode, as they are known to occur in various discharge devices (Refs. 10–12), the type of oscillation examined here was limited to the plateau part of the volt-ampere curve in its pre-breakdown regime. Typical oscilloscope records are shown in Fig. 18. The first column is for the case of a low emitter temperature, and the second column is for the case of a high emitter temperature. The cesium reservoir temperature was the same for both. In both cases the resistance in series with the diode was 5 ohms. The amplitude of the current oscillation increased as the circuit resistance was decreased, whereas the amplitude of the voltage oscillation across the diode decreased as the resistance was decreased. It was observed that the maxima of the oscillation in current became larger as the resistance was decreased, but the minima remained nearly unchanged. Also, there was a threshold value of resistance below which no recognizable change in oscillation occurred. Circuit resistance did not affect the frequency spectrum as long as the diode was

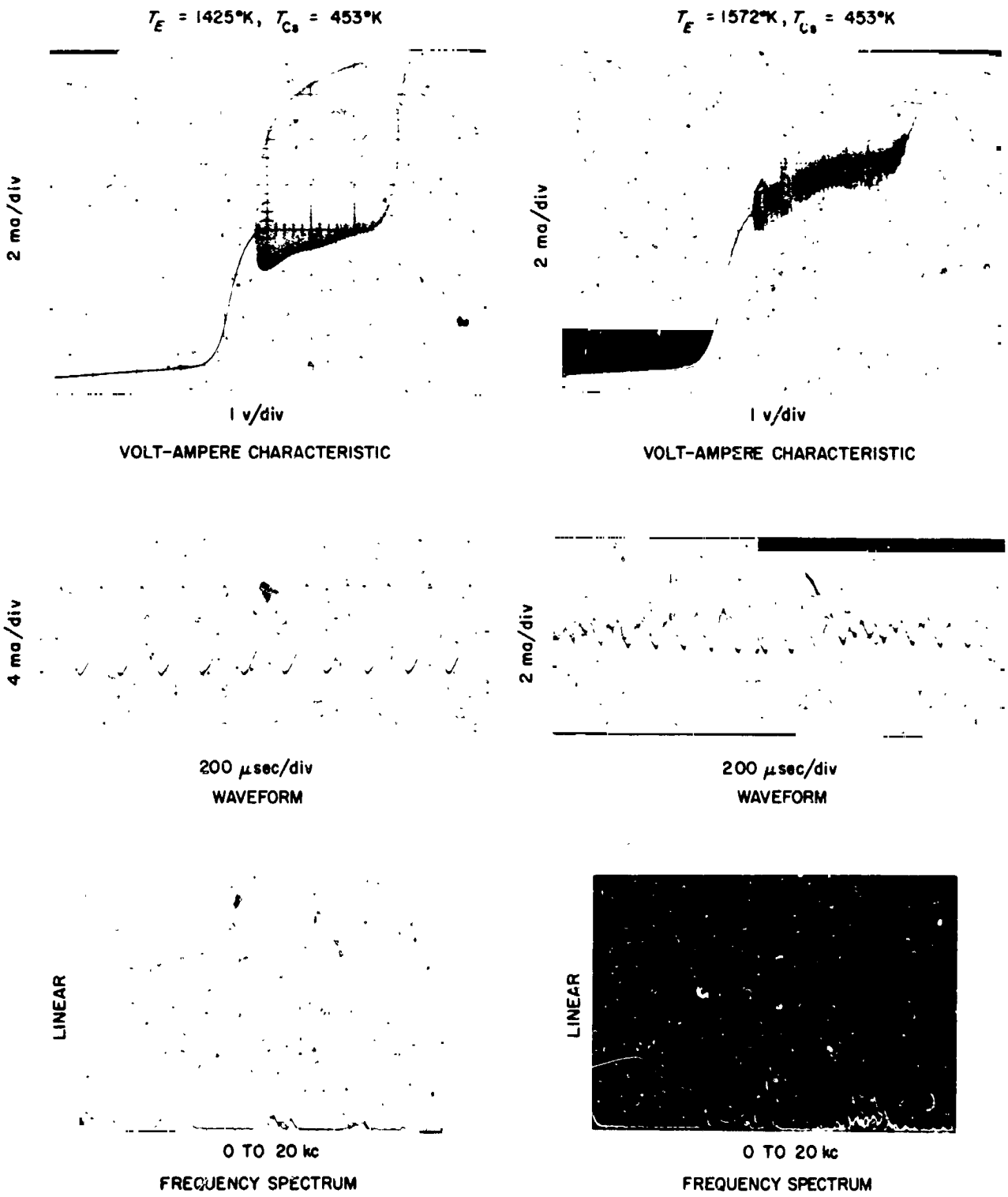

Fig. 18. Typical oscillograms of oscillations

operated at the same operating point on the volt-ampere curve. The frequency spectrum shown was obtained at a voltage across the diode of 1 v. The frequency of the major mode of oscillation was approximately 5 kc for T_E = 1425°K and approximately 7.5 kc at T_E = 1572°K.

Note that the waveform showed amplitude modulation at the higher emitter temperature. This was due to simultaneous oscillations at two closely spaced frequencies as indicated in the spectrum. The modulation effect was rarely observed at lower emitter temperatures, but was almost always observed at higher emitter temperatures in the diodes with large collectors.

Further experiments were performed in order to clarify the modulation effect using the small diode which had two collectors. One collector was located along the center section of the emitter and the other collector was located along the end section of the emitter. Consequently the center collector was subjected to a higher emitter temperature and the end collector was subjected to a lower emitter temperature. First, the frequency spectrum of the oscillation was obtained for each collector current when the diode was operated at a cesium temperature of 182°C and a collector temperature of 1345°C at the center of the emitter. For the center collector, the dominant frequency component was 30 kc, whereas it was 42 kc for the end collector. The waveform of each individual current, for each collector connected separately, did not show the modulation. When both collectors were connected together, the resultant current showed the amplitude-modulated waveform. Also, the frequency spectrum indicated two frequency components, one of which was at 42 kc and the other at 34 kc. Apparently the oscillation in the center collector of 30 kc was pulled to a higher frequency of 34 kc due to the stronger oscillation at 42 kc of the end collector.

d. Conditions for oscillations. The conditions required for oscillations to occur were determined by recording the current through the diode when the voltage across the diode was 1 v. Since the volt-ampere curve showed a plateau region for voltages larger than approximately −0.5 v, the value of current at 1 v was considered to be the "constant" plateau value for that particular temperature combination. In fact the value of current thus determined agreed with the calculated temperature-saturated value if the temperature combination was such that ion rich emission was occurring at the emitter surface. Such current densities were plotted as a function of the inverse emitter temperature for different cesium reservoir temperatures. The Langmuir S-curve type of behavior was

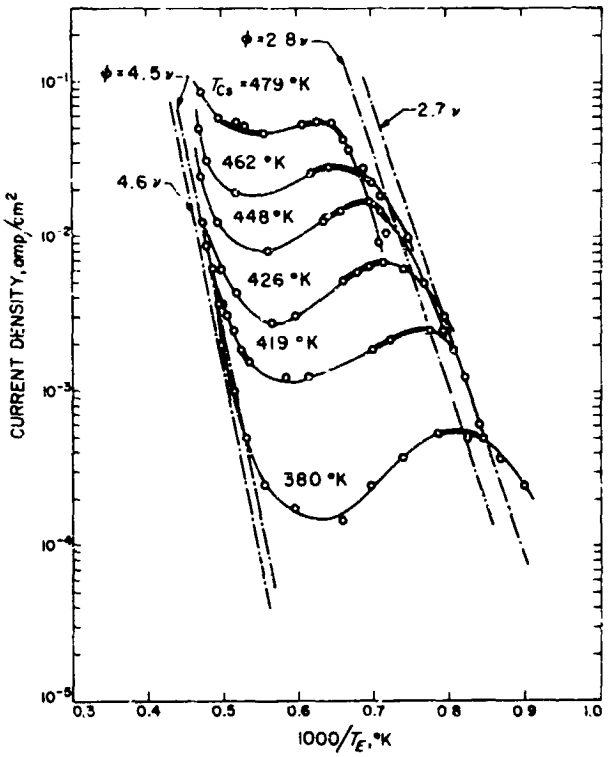

Fig. 19. Regions for oscillation, W-Ni diode

expected. The heavily-lined part of the curves in Fig. 19 shows the average dc current through the diode when oscillations were observed. Note that the average dc current fell short of theoretical values for temperature combinations such that T_E/T_{Cs} was smaller than 3.2.

The ratio of 3.2 corresponded to an effective work function of approximately 2.8 v; this value of work function was also the value required for neutral emission. Neutral emission is defined as the condition under which the number of electrons emitted is related to the number of ions emitted in such a way that the following equation is satisfied in the diode:

$$J_e/J_i = (m_i/m_e)^{1/2}$$

where J is the current density, m is the mass, subscripts e and i represent electron and ion, respectively. This condition results in a neutral space-charge at the emitter surface. Similar results together with the theoretical lines are shown in Fig. 20.

The oscillations did not occur at either too large or too small a cesium reservoir temperature even though the conditions for neutral emission were satisfied. Such limits

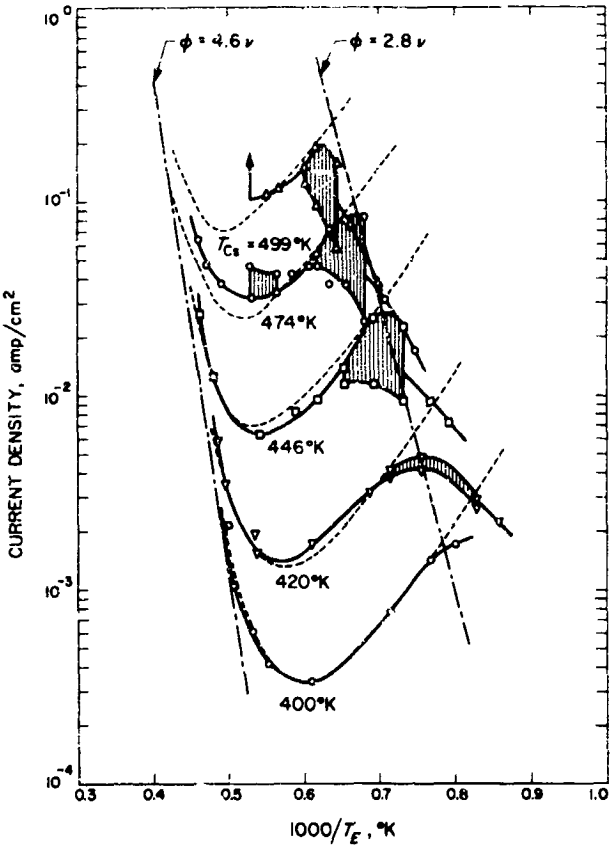

Fig. 20. Amplitude of oscillation, small diode dashed lines are theoretical S-curves based on a bare work function of 4.65 v

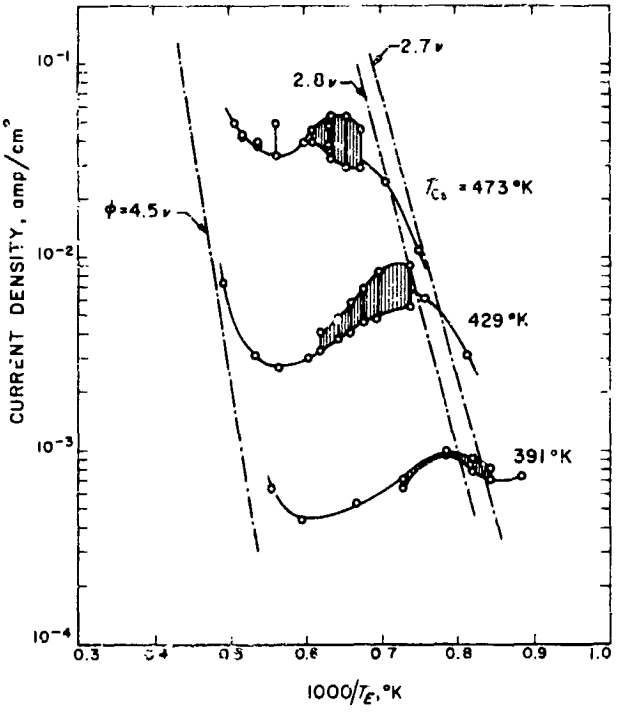

Fig. 21. Amplitude of oscillation, W-Ni diode

were 480°K for a maximum and 370°K for a minimum in the W-Ta diode, as shown in Fig. 17. The upper limit corresponded to a cesium pressure of 9.6×10^{-2} torr where the electron-neutral mean-free-path was approximately 0.1 mm. Since the interelectrode distance was approximately 6 mm for this diode, many collisions were expected at this pressure. This fact was also substantiated by an onset of volume ionization which occurred when the limit was exceeded. The lower limit of T_{Cs} = 370°K corresponded to a current density of the order of 10^{-4} amp/cm². Such a current density is not large enough to form an optimum space-charge for the oscillation to occur. This effect is also seen at T_{Cs} = 400°K in Fig. 20. For the sake of comparison, the interelectrode gap which caused the onset of space-charge effects was examined for a planar diode. It was 0.6 mm when the diode was operated at T_E = 1300°K with a current density of 10^{-4} amp/cm². In view of the cylindrical geometry of the test diode, which had a large potential gradient near the emitter, the onset of space-charge could occur at an actual interelectrode distance of 6 mm instead of 0.6 mm as expected for a planar diode. Summarizing the results, for oscillations to occur it is necessary to have: (1) a space-charge in which collisions are negligible, and (2) the space-charge must be such that near-neutral emission occurs at the emitter surface.

e. Amplitude of oscillation. As was expected, the amplitude in current oscillations increased as the circuit resistance decreased, while the amplitude in voltage oscillations decreased. However, there was a limiting value of resistance, of the order of an ohm, below which no further change in the amplitude of the oscillation occurred. At such a circuit resistance and with a voltage across the diode of 1 v, the maxima and the minima of the oscillating current were recorded. The results are plotted in Fig. 20 and in Fig. 21. For example, at $1000/T_E = 0.73$ and T_{Cs} = 446°K in Fig. 20, the maximum current density was 2.3×10^{-2} amp/cm² and the minimum current density was 9.5×10^{-4} amp/cm². Note that the amplitude of the current oscillation of 1.35×10^{-2} amp/cm² was of the same order of magnitude as the average dc current density. Also note that the maxima followed the theoretical curve for temperature-limited electron emission. It seemed, therefore, that the current conduction was

switching between the temperature-saturated mode and the space-charge-limited mode whenever the oscillation occurred. This type of phenomenon can be visualized as an oscillation in a space-charge minimum in front of the emitter in the motive diagram for the diode. For example, at $1000/T_E = 0.73$ and $T_{Cs} = 446°K$ in Fig. 20, the change in the depth of the space-charge minimum, which resulted in the observed current oscillation, was 102 millivolts. Indeed this amplitude was of the same order of magnitude as the equivalent electron temperature in volts. V_e, determined from $eV_e = kT_E$ at $1000/T_E = 0.73$. It is apparent that the depth of the minimum must be of this order of magnitude, in order for the diode to operate in a space-charge-limited mode.

f. Frequency of oscillation. The temperature dependence of the frequency of oscillation was examined using a frequency spectrum analyzer. The results are presented in Fig. 22. It shows the relationship between the period of the major mode of oscillation and $1000/T_E$ for various cesium reservoir temperatures. At higher cesium reservoir temperatures, the period peaked at some particular emitter temperature, or the frequency was a minimum at that temperature. For example, at $T_{Cs} = 453°K$, the period was the largest at $1000/T_E = 0.68$. It corresponded to a frequency of 5 kc at an emitter temperature of 1470°K. Similar behavior was recognized in a thermionic energy converter of planar geometry, as was reported elsewhere (Ref. 13). It is interesting to note that the emitter temperature where the current along the S-curve became a maximum for that particular cesium reservoir temperature agreed with the point where the period of oscillation was a maximum. Indeed this was the emitter temperature at which perfect neutralization of space-charge occurred at the emitter surface. The fact that the period depended strongly on the cesium reservoir temperature indicated that the period of oscillation was a function of more than only the ion transit time determined by the thermal velocity. Also, it was found that the frequency increased as the voltage across the diode increased. Such a behavior suggested that the frequency of oscillation was also influenced by the electric field intensity. In other words, the dynamics of the ions must be determined from both thermal and electrostatic considerations. The period of oscillation was smaller in the small diode than in the large diode as expected.

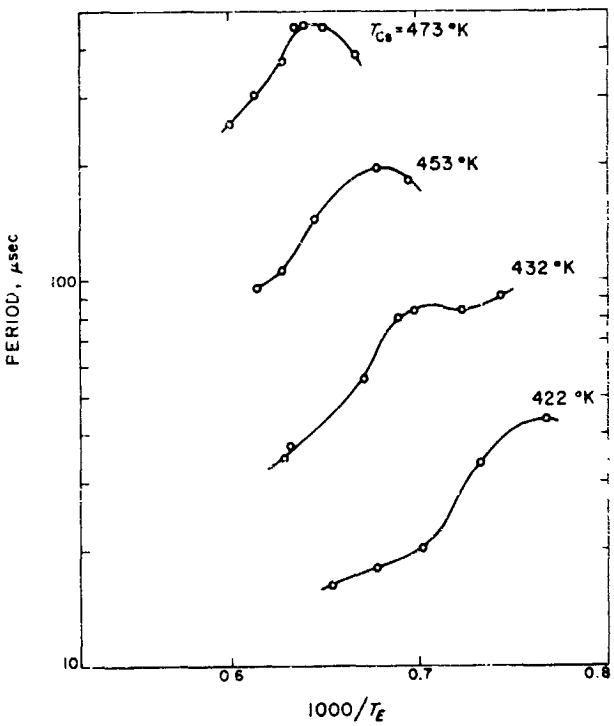

Fig. 22. Fundamental period of oscillation

g. Conclusions. Oscillations in the plateau region of the volt-ampere curve were found to occur when the temperature combinations were such that nearly neutral emission occurred at the emitter surface. This result is in agreement with predictions made by Eichenbaum and others (Refs. 14, 15). The maxima of the current oscillations were limited by the temperature-saturated electron emission, and the minima were limited by the space-charge-limited current conduction. The peak-to-peak amplitude of current oscillation was as large as the average dc current through the diode. The amplitude of the oscillating space-charge minimum, which resulted in current oscillations in the external circuit, was of the order of the equivalent electron temperature in volts. The frequency of oscillation was also strongly governed by the space-charge conditions for neutral emission. The frequency decreased as the cesium pressure increased. The frequency was smaller in a larger diode than in a smaller diode when they were operated at the same cesium pressure. These results suggested a functional dependence between the period of oscillation and the pressure distance product. Further study is required in order to construct a consistent explanation.

References

1. Goetzberger, A., "Impurity-Induced Pipe Through Diffused Layers in Si," *Solid State Electronics*, Vol. 5, pp. 61–70, 1962.

2. Hannay, N. B., *Semiconductors*, p. 222, Reinhold Publishing Co., New York, 1960.

3. Hunter, L. P., *Handbook of Semiconductor Electronics*, pp. 7–19, McGraw-Hill, New York, 1962.

4. Biondi, F. J., *Transistor Technology*, Vol. III, pp. 71, 86, D. Van Nostrand Co., New York, 1958.

5. Trumbore, F. A., "Solid Solubility of Impurity Elements in Ge and Si," *Bell System Technical Journal*, Vol. 39, pp. 205–232, 1960.

6. Allen, R. B., "Effect of Oxyde Layer on the Diffusion of P into Si," *Journal of Applied Physics*, Vol. 31, pp. 334–337, 1960.

7. Smith, F. M., "Measurement of Sheet Resistivities with the Four-Point Probe," *Bell System Technical Journal*, Vol. 37, pp. 711–718, 1958.

8. Backenstoss, G., "Evaluation of the Surface Concentrations of Diffused Layers in Si," *Bell System Technical Journal*, Vol. 37, pp. 699–710, 1958.

9. Goertzel G., and Tralli, N., *Some Mathematical Methods of Physics*, pp. 158, 161, McGraw-Hill Book Company, Inc., New York, 1960.

10. Houston, J. M., *Physical Electronics Conference Report No. 52*, Massachusetts Institute of Technology, 1962.

11. Kayakhanov, V. Ya, Kucherov, R. Ya, and Tatishvili, D. G., *Soviet Phys.-Tech. Phys.*, Vol. 9, p. 256, 1964.

12. Zollweg, R. J., and Gottlieb, M., *Journal of Applied Physics*, Vol. 32, p. 890, 1961.

13. Shimada, K., *Report on the Thermionic Conversion*, Specialist Conference No. 181, 1964.

14. Eichenbaum, A. L., and Hernqvist, K. G., *Journal of Applied Physics*, Vol. 32, p. 16, 1961.

15. Norris, W. T., *Journal of Applied Physics*, Vol. 35, p. 3260, 1964.

ENGINEERING MECHANICS DIVISION

VII. Materials

A. Carbon and Graphite Research

W. V. Kotlensky and D. B. Fischbach

1. Structural Changes Accompanying Creep Deformation of Pyrolytic Carbon

As part of a continuing study of the high-temperature deformation behavior and associated structural changes of pyrolytic carbon, data have been obtained on the structures developed during tensile creep to various elongations at several temperatures. The results show that the same structure is developed at the same strain, regardless of test temperature (at least above 2500°C). In addition, the structure in the basal (substrate) plane is highly anisotropic after moderate amounts of deformation.

Optical polarized light micrographs of etched specimens creep-tested to nominal 10% elongation at three temperatures are shown in Fig. 1. Three orthogonal views of the center of the gauge section are shown for each sample: basal edge parallel and perpendicular to the stress axis, and basal plane surface. Corresponding microstructures are indistinguishable at the three temperatures. The structural parameters determined by X-ray diffraction (preferred orientation, unit cell dimensions) for these three samples were also the same within experimental error. This was an underlying assumption of the method used earlier to analyze data on creep strain as a function of time and temperature (*SPS 37-30*, Vol. IV, pp. 71–72). These results therefore support the validity of that method.

Another striking feature of the micrographs in Fig. 1 is the difference in basal edge configuration viewed parallel and perpendicular to the stress. With no deformation, these two views show the same structure. With deformation, a marked anisotropy in structure is seen. The deformed basal surface also shows deformation features parallel to the stress direction (vertical in the figure). These micrographs were made from adjacent areas of the gauge section for each sample, and only the direction of viewing differs.

The basal plane preferred orientation texture is also highly anisotropic. X-ray preferred orientation measurements on rod-shaped samples cut parallel and perpendicular to the stress axis gave β values of 6.9 and 1.5 deg, respectively. β is a measure of the average misorientation of the basal planes relative to the substrate (*SPS 37-24*, Vol. IV, p. 44).

These structural changes result from dewrinkling of the basal planes. Both the amount of dewrinkling and the anisotropy of the structure are functions of tensile strain, as shown in Fig. 2 and Table 1. In Fig. 2 (top), sample deformed 5%, the cone structure is evident in all three views,

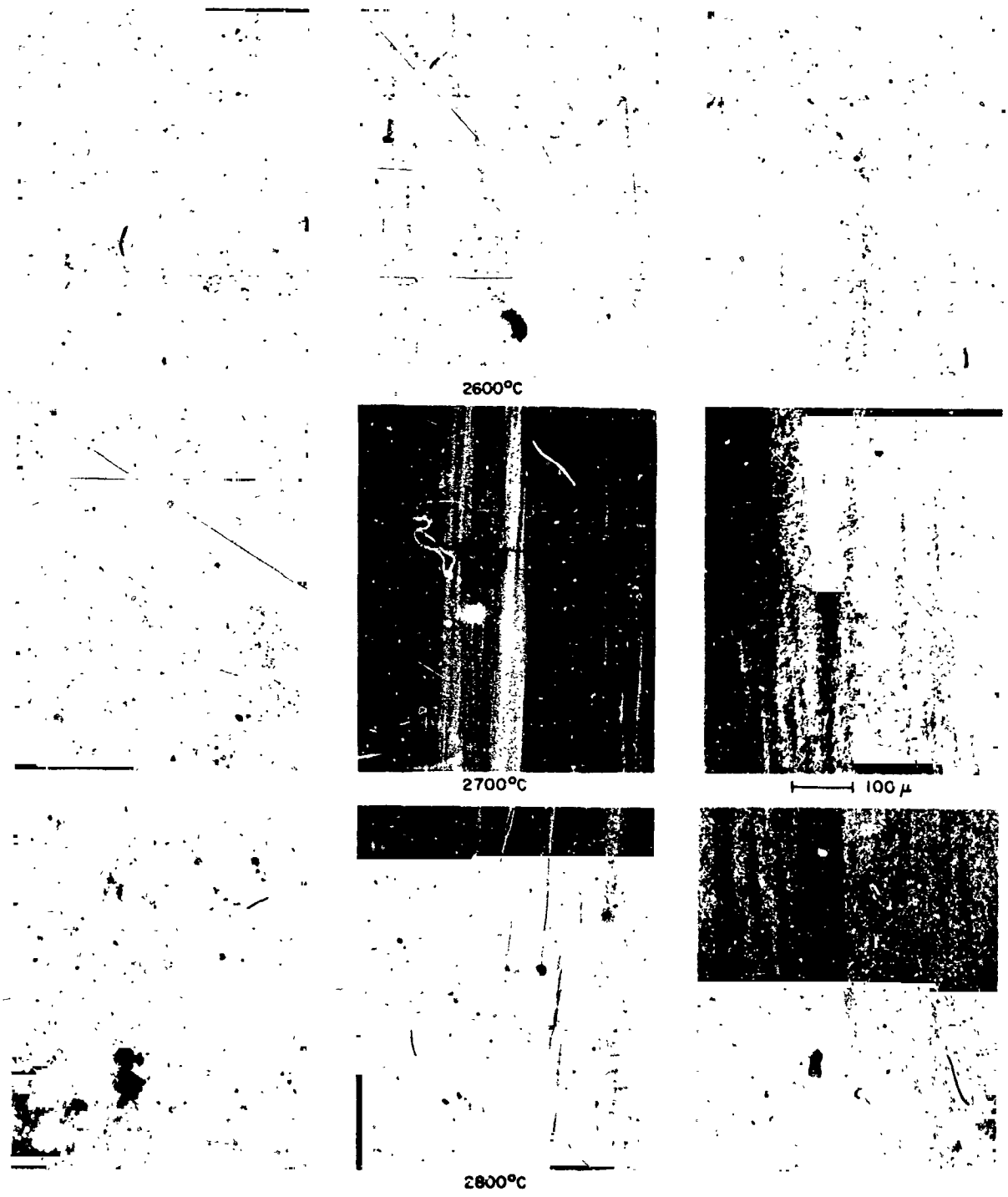

Fig. 1. Microstructures of pyrolytic graphite (Lot 170) after 10% creep deformation at three temperatures

Fig. 2. Microstructures of pyrolytic graphite (Let 170) after various amounts of creep deformation

Table 1. X-ray structural parameters for pyrolytic graphite (Lot 170) deformed by tensile creep

Test temperature, °C	Elongation, %	Preferred orientation parameter		Unit cell dimensions, Å	
		∥ to stress	⊥ to stress	c_0	a_0
As rec'd.	0	22.5	22.5	6.84	2.45
2700	5	17.2	10.4	6.74	2.46
2700	10	6.9	1.8	6.73	2.46
2800	21	2.0	1.1	6.72	2.46

but preferential dewrinkling already is seen in the basal edge viewed parallel to the stress. Moreover, the basal surface shows some distortion of the growth cones in the stress direction. Table 1 shows that an anisotropic orientation texture has developed. Fig. 2 (center), corresponding to 10% elongation, is the same set of micrographs shown in Fig. 1. The microstructural and preferred orientation (Table 1) anisotropy is most pronounced here. Fig. 2 (bottom), sample deformed 21%, shows the microstructure developed in the second stage of deformation. Dewrinkling is nearly complete parallel to the stress and the anisotropy is no longer apparent in the microstructure (though there are differences in the distribution of delamination cracks parallel and perpendicular to the stress). However, as shown in Table 1, there is still a definite anisotropy in the orientation texture.

The degree of graphitization also increases with deformation, as shown by the decreasing value of the unit cell height, c_0, in Table 1. Although this is due in part to different treatment times and temperatures, comparison of undeformed butt sections with deformed gauge section structures indicate a strong influence of deformation on graphitization.

All of the results shown here are for a substrate nucleated pyrolytic carbon. Regeneratively nucleated pyrolytic carbons exhibit similar but less pronounced structural changes on tensile deformation. The wrinkled sheet structure is stabilized in such regeneratively nucleated carbons by soot particles distributed throughout the deposit.

These results are consistent with magnetic susceptibility anisotropy and X-ray observations reported earlier for similar samples (*SPS 37-27*, Vol. IV, p. 29). They show that the conically wrinkled sheet structure of the as-deposited carbon has been transformed by the high-temperature uniaxial creep deformation into a corrugated sheet structure, with the corrugations lying parallel to the stress axis. This is illustrated schematically in Fig. 3.

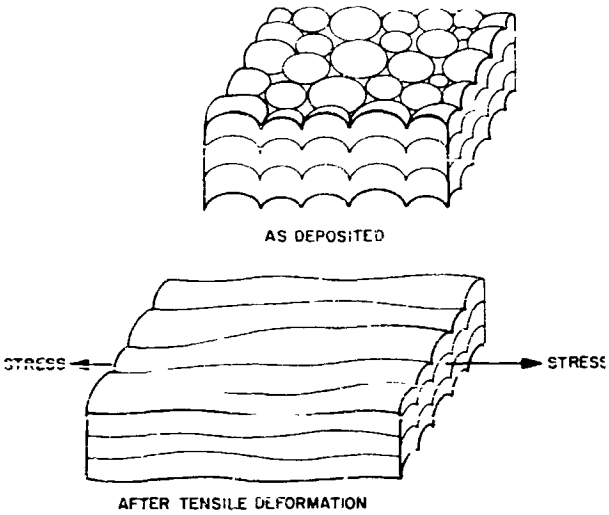

Fig. 3. Schematic representation of the structure of as-received and tensile deformed (first stage) pyrolytic graphite; layer plane traces are shown

Although appreciable dewrinkling occurs perpendicular to the stress, the flattening out of the layers is much more pronounced parallel to the stress, as would be expected. This behavior is characteristic of the first stage ($\lesssim$15% elongation) of tensile deformation of pyrolytic carbons. Deformation occurs by dewrinkling and basal plane shear in this range (Ref. 1). The mechanisms of deformation which operate in the second stage (>15% elongation) have not yet been definitely identified.

2. *Electron Micrography and Fractography of Glassy Carbons*

Studies on the high-temperature mechanical properties of two grades of Japanese glassy carbon (Ref. 2; *SPS 37-27*, Vol. IV, p. 32–33; and *SPS 37-26*, Vol. IV, p. 70) have shown that one (GC-20) exhibits appreciable ductility above 2200°C while the other (GC-30) fails at low elongations, even at high temperatures. The ultimate strengths of both grades are similar. The processing history of these two grades differs only in that GC-20 is treated to a maximum temperature of 2000°C, whereas GC-30 is given an additional treatment at 3000°C. The property differences therefore must result from structural changes resulting from the additional heat treatment received by the GC-30. (Experiments on GC-20 confirmed the influence of heat treatment on the mechanical properties.) On the other hand, densities of the two materials are the same. Differences in X-ray structure also are not

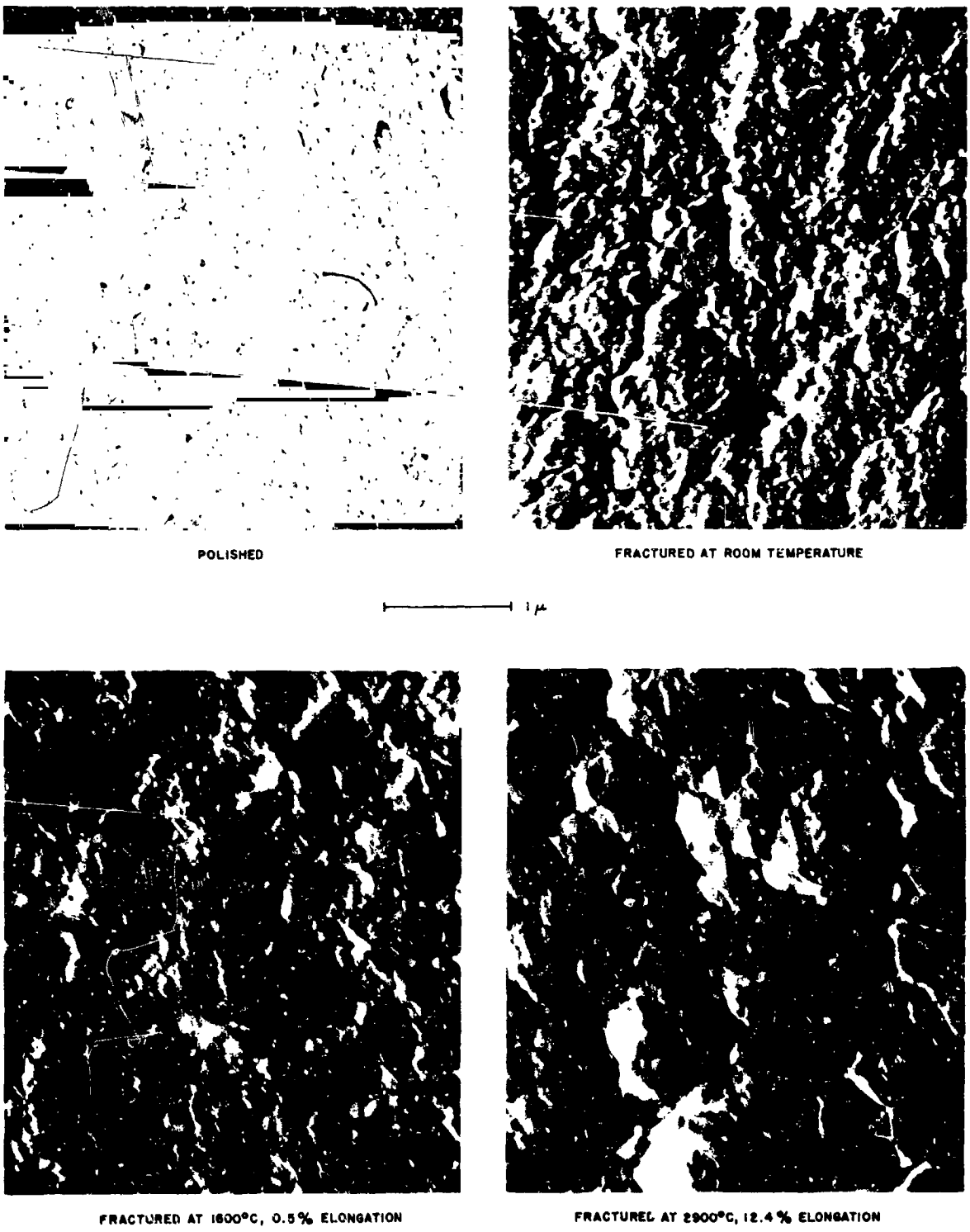

Fig. 4. Electron micrographs of polished and fractured surfaces of GC-20 glassy carbon. Positive two-step replica shadowed, left to right

POLISHED

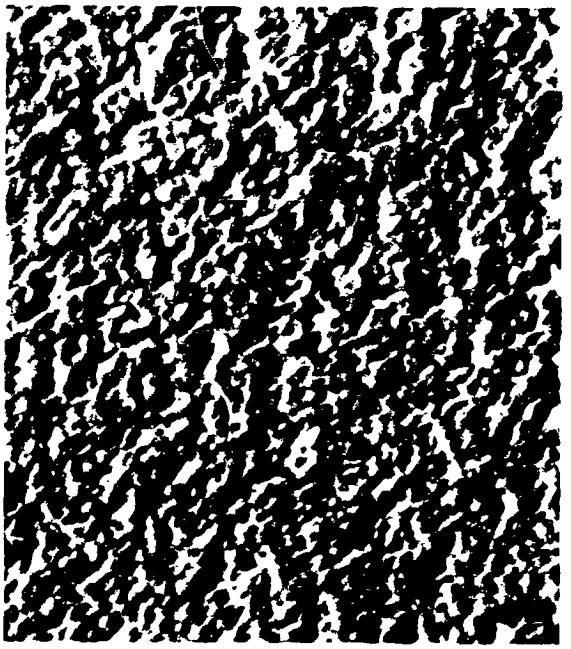

FRACTURED AT ROOM TEMPERATURE

1 μ

FRACTURED AT 1600°C, 0.7% ELONGATION

FRACTURED AT 2900°C, 3.9% ELONGATION

Fig. 5. Electron micrographs of polished and fractured surfaces of GC-30 glassy carbon. Positive two-step replica shadowed, left to right

pronounced—both have small crystallite sizes and turbostratic structures (*SPS* 37-32, Vol. IV). An appreciable difference in microhardness, however, suggests a difference in microstructure, or perhaps internal stresses.

An electron micrographic investigation has been initiated to determine if microstructural differences can account for the difference in mechanical behavior. Shadowed positive carbon replicas[1] (two-step technique) of both polished and fractured surfaces were examined. Electron micrographs[1] are shown in Fig. 4 for GC-20 and Fig. 5 for GC-30. The shadowing direction is from left to right in each case, and the magnification is near the maximum appropriate to the resolution obtainable with this type of replica (Ref. 3).

The polished surfaces of as-received material show a random distribution of fine pits with an average diameter of about 350 Å. If the most sharply defined pits are considered to be pores, the observed pore volume is consistent with the observed bulk density. However, there is an incompletely resolved background structure suggestive of a much higher pore volume. Some of the apparent pore structure may be a polishing or replication artifact (for example, plucking out of small particles). Differences between the GC-20 and GC-30 structures are surprisingly subtle. GC-30 shows more prominent polishing scratches than GC-20, consistent with its lower microhardness. Close examination of the GC-20 micrographs suggests a poorly defined "grain" structure in which pore-free regions about 3000 Å in diameter are delineated by a discontinuous network of pores. This grain structure is less apparent in GC-30, but there appears to be a greater incidence of short chains of adjacent pores in this material. This appearance, to some extent, might be an artifact resulting from polishing scratches.

The appearance of the fracture surfaces, on the other hand, clearly differentiates between GC-20 and GC-30. There is a definite "graininess" in the GC-20 fractures which becomes increasingly well-defined as the temperature of fracture increases from room temperature to 2900°C. A tendency for the "grains" to be bounded by cracks (or grooves) is particularly pronounced in the 2900°C fracture. The appearance of the grains changes, too, from irregular pitted areas delineated by cracks at room temperature to relatively smooth flat-topped plateaus at 1600°C and to convex bumps at 2900°C. In GC-30, on the other hand, the impression of graininess is largely absent. Instead, there is a high density of randomly oriented chains of adjacent pits and microcracks. The length and frequency of occurrence of these features increases with increasing fracture temperature.

These preliminary electron micrographic results show that the differences in high-temperature mechanical properties of GC-20 and GC-30 are associated with marked differences in fracture mode. However, structural features accounting for these differences are not yet clearly identifiable. Further studies on polished (and perhaps etched) surfaces, and on possible replication artifacts will be required before the connection between microstructure and fracture mode can be understood.

[1]Prepared by Shan Research Industries, Inc.

N65-32428

B. Far Infrared Optical Properties of Some Spacecraft Paints

W. M. Hall

Much engineering data have been accumulated on the optical properties of spacecraft finishes in the solar wavelength region and in the infrared wavelength region which covers thermal radiation at room temperature. Any effort to determine solar absorptance or emittance for a very cold surface meets with the fundamental difficulty of lack of data for very cold absorbers or radiators. The basic method of obtaining emittance data is that of spectral measurements of reflectance in the infrared. In order to obtain such data, JPL recently has concluded a brief study contract with the UCLA thermal properties laboratory for measurements of far infrared spectral properties of several common spacecraft paints.

These spacecraft paints and their clear vehicles have been examined for spectral reflectance and transmissivity over a broad spectral range from the near ultraviolet to 60 μ in the infrared. Figs. 6–10 identify the type of paint and display transmittance and reflectance curves for a number of thicknesses of the coating. The transmittance specimens were overlaid on polyethylene film of approximately 38-μ thickness; the reflectance specimens were sprayed on aluminum.

Because of program limitations, only the laminar X-500 clear vehicle (polyurethane) provided a usable set of both transmittance and reflectance data (Figs. 6 and 7). For

[2]Finch Paint and Chemical Co., Torrance, California.

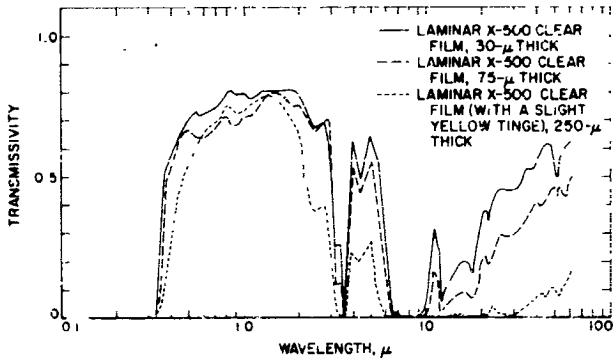

Fig. 6. Transmissivity of laminar X-500 polyurethane clear film

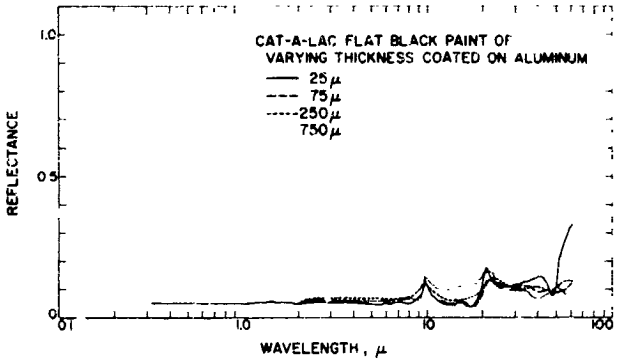

Fig. 9. Reflectance of Cat-a-lac flat black paint on aluminum

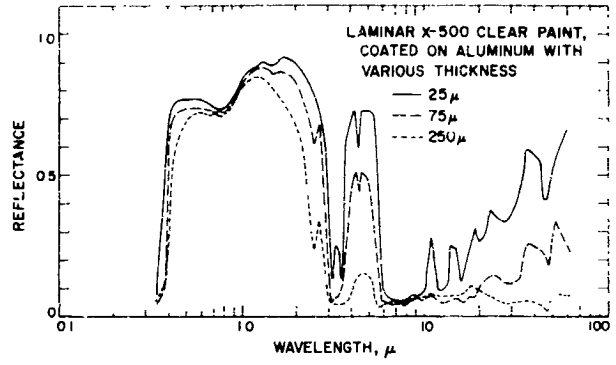

Fig. 7. Reflectance of laminar X-500 polyurethane clear film

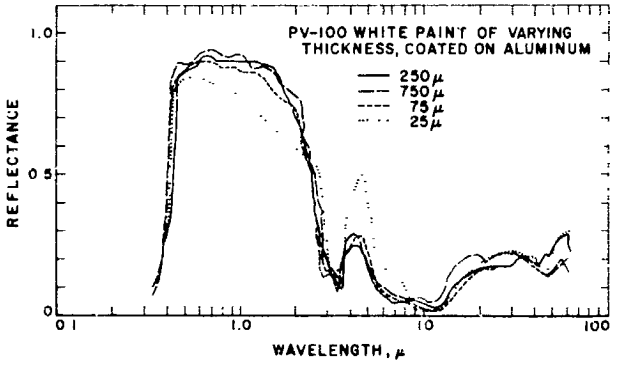

Fig. 10. Reflectance of PV-100 silicone–alkyd white paint on aluminum

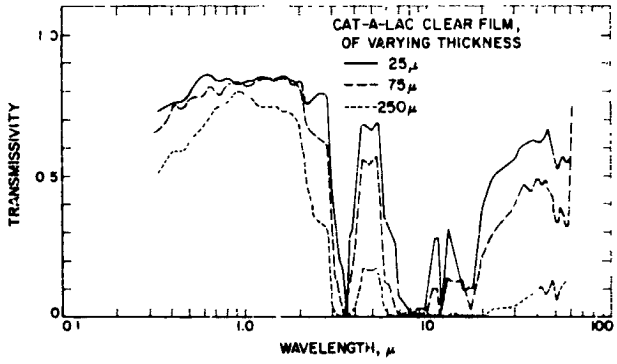

Fig. 8. Transmissivity of Cat-a-lac epoxy clear film

this material it can be seen that spectral bands generally agree and that the absorption coefficient is quite large at long wavelengths, compared to the visible and near infrared region. It can be shown that the spectral structure seen beyond 10 μ is an interference pattern modulating the broad band of transmission. The aluminum-backed reflection sample shows this interference structure most distinctly, as might be expected. The effect of the polyethylene film on the spectral structure is negligible, except for possible interference effects ... can be seen by comparison of the reflectance curve where the spectrally structureless aluminum backing is involved with the transmission curve which includes the polyethylene film.

Figs. 8 and 9 display Cat-a-lac[1] clear vehicle (epoxy) and Cat-a-lac flat black, respectively. For paint thickness 75 μ or greater, this paint is quite black to 60 μ. It would appear that the vehicle is becoming transparent beyond 60 μ with the paint thereby losing its black quality when used on a highly reflecting backing, such as aluminum.

[1]Magna Coatings and Chemical Corp., Los Angeles, California

PV-100[4] (Fig. 10) appears to be a rather structureless grey in the far infrared, with thickness of coating entering only weakly as a parameter.

[4]Vita-Var Co., Newark, New Jersey.

It should be emphasized that these materials were examined at room temperature and that, therefore, the spectral structure shown in the curves would alter in relative intensity of the lines when extreme cooling of the samples occurs.

References

1. Kotlensky, W. V., "Deformation in Pyrolytic Graphite," *Transactions of the Metallurgical Society of AIME*, Vol. 233, pp. 830–832, 1965.
2. Kotlensky, W. V., and Martens, H. E., "Tensile Properties of Glassy Carbon to 2900°C," *Nature* (to be published).
3. Phillips, A., Keriins, V., and Whiteson, B. V., "Electron Fractography Handbook," TR ML-TDR-64-416, Air Force Materials Laboratory, Wright-Patterson Air Force Base, Dayton, Ohio, January 31, 1965.

VIII. Electro-Mechanical Engineering

A. Printed Conductor Assembly Substitution for *Mariner* C Upper Ring Harness

E. R. Bunker, Jr

Based on the original work of substituting a printed conductor ring harness (PCRH) for the *Mariner R*[1] wire cable harness described in *SPS 37-24*, Vol. IV p. 55, a more complex PC assembly has been designed and fabricated in order to determine the feasibility of replacing the two upper ring harnesses and trough assembly in *Mariner C*.[2] This unit now is undergoing tests on the proof test model (PTM). The present trough assembly is shown in Fig. 1, Figs. 2 and 3 are the art work for the two sides of the replacement board. While construction details are similar to those for *Mariner R*, additional features have been included in the design.

1. Design Considerations

Substitution of the PCRH assembly for the upper ring harness and trough assembly requires a minimum of modification of the PTM so that the flight configuration can be restored in the shortest time possible. This was accomplished by the fabrication of suitable jumper cables to provide the interconnections between the PCRH board connectors and the eight bay harness connectors which normally mate to the hard-mounted receptacles on the trough. Originally, the PCRH board was designed to

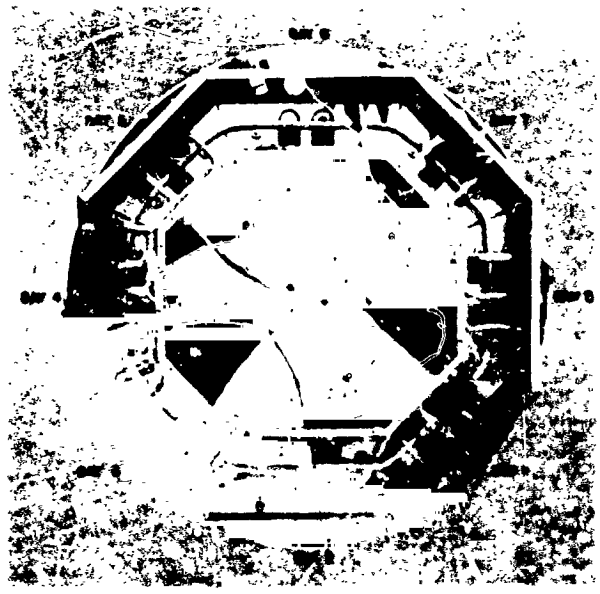

Fig. 1. Top view of upper ring harness assembly, including trough

[1] *Mariner* Venus 1962
[2] *Mariner* Mars 1964

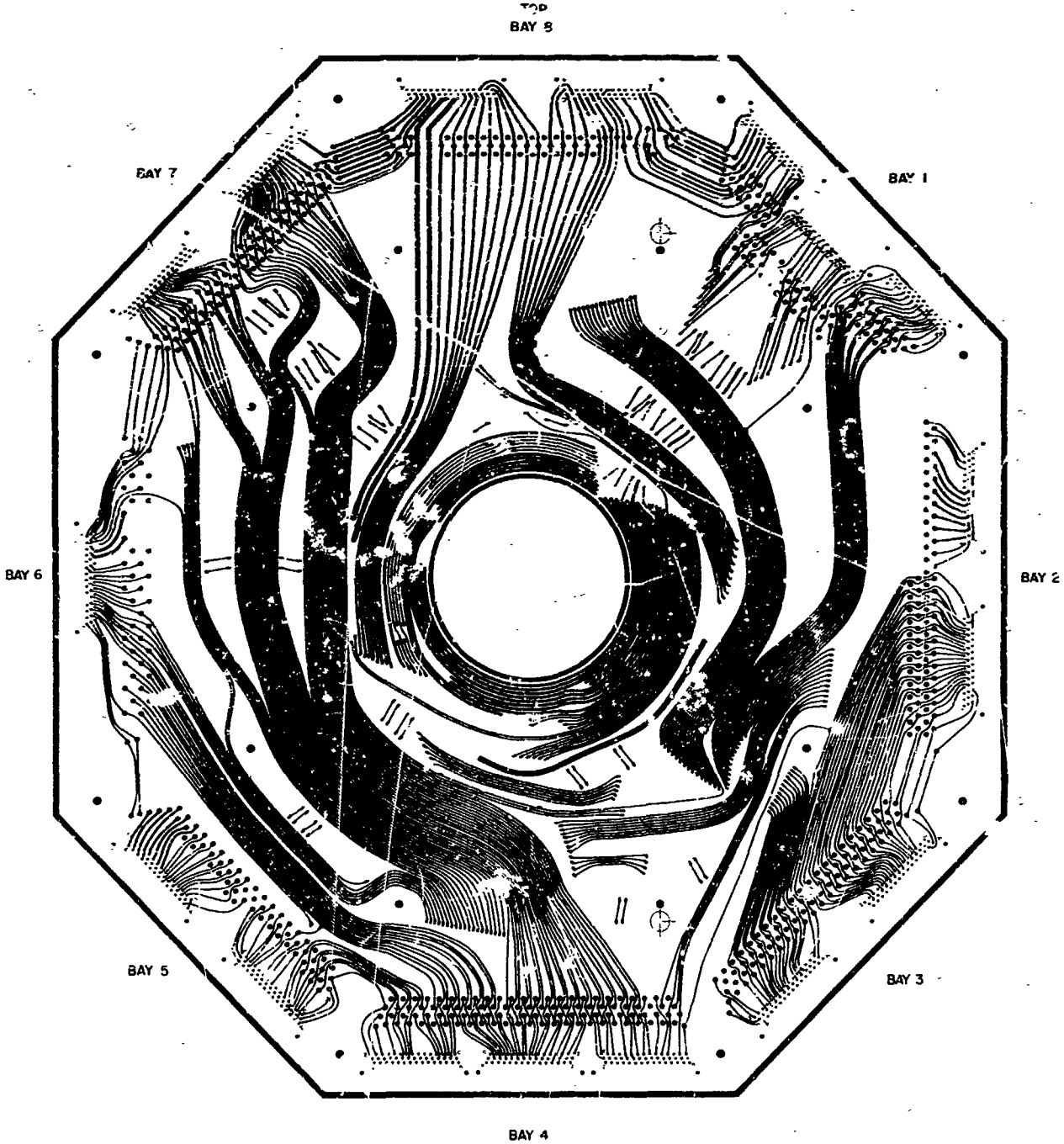

Fig. 2. Layout of top of PCRH

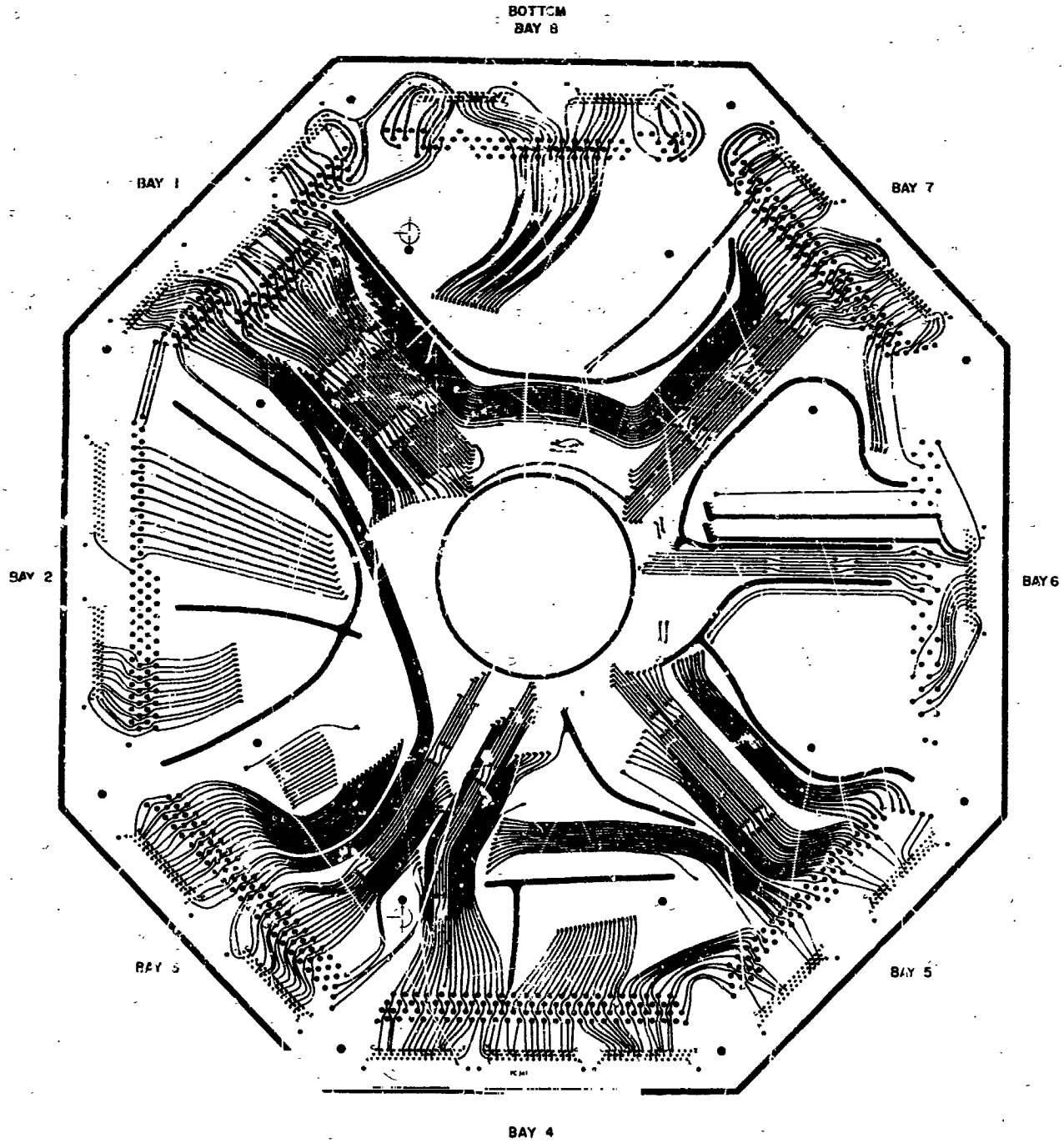

Fig. 3. Layout of bottom of PCRH

utilize the same mounting holes as the trough, which was to be removed; however, it was anticipated that such a removal might become undesirable at a later time. Consequently, the design also allowed the PCRH board to be laid on top of the trough, as the jumper cables were made long enough to reach the bay harness connectors. The printed board was of two-sided rather than multilayer construction.

Wiring changes and shielded wire substitution in noise-sensitive signal circuits during tests will be facilitated by a solder terminal for each conductor, located just inboard from the connectors. Additional shielding of the printed conductors may be possible by use of a conductive coating on plastic tape.

Reliability of the edge connectors used in the *Mariner R* PC board was doubtful, consequently a survey and selection of a more reliable connector appropriate to this application were made.

Transpositions of power conductors from side to side were made to reduce inductive and capacitive coupling into low-level signal circuits.

Pairs of plated-through holes were employed throughout to improve reliability of the transpositions.

Because of the relatively low currents in the power circuits, capacitive rather than inductive coupling between power and signal circuits appears to be the major source of noise. A simple mathematical model was established to provide a quantitative measure of noise susceptibility of each signal circuit. Fig. 4(a) shows the assumed model and Fig. 4(b) is the equivalent schematic.

The equation for the noise susceptibility number S_N is:

$$S_N = 0.54 \frac{LR}{V_s} \qquad \mu v \text{ noise/signal v}$$

where L is a length factor dependent on the number of intervening bays, R is the circuit impedance (resistance) and V_s is the peak signal voltage for 100% of full-scale voltage between the signal conductor and ground. Values of S_N range from 0 to $150 \times 10^3 \mu v/v$ of signal.

The copper conductor width was limited to 0.025 in. minimum, which was required to allow all of the runs to be made to various bays. This width and the thickness of 0.008 in. corresponds in cross-sectional area to a No. 26 wire gauge which is adequate for signal circuits. Power circuits with appreciable current flowing had an increased conductor width so as to obtain a current density of not

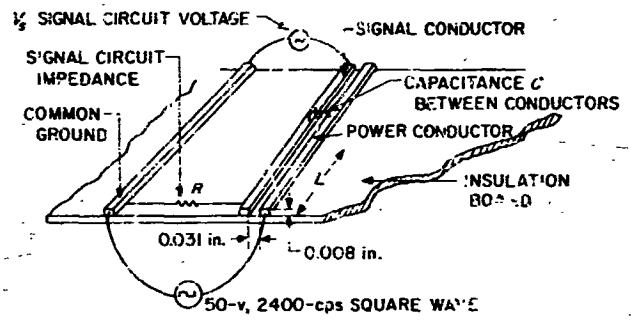

(a) ASSUMED MODEL FOR COMPUTATION OF NOISE SUSCEPTIBILITY NUMBER, S_N

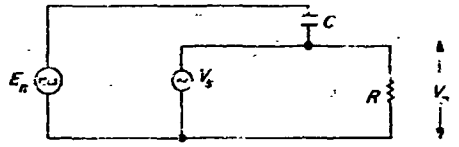

(b) EQUIVALENT SCHEMATIC

Fig. 4. Geometrical model

less than 250 mils²/amp. This kept conductor heating and voltage drops within acceptable limits.

The maximum voltage present in the ring harness is 50-v peak, so corona or arcing in the critical air pressure region will not be a problem. Frequencies range from 0 (DC) to 38.4 kc with a 2400-cps square wave power frequency. Pulse widths occur between 100 msec and 5 μsec at peak voltages of 6 v or greater.

2. Layout

The fundamental problem in layout of the printed circuit ring harness was providing adequate isolation for sensitive low-level lines from adjacent noisy or high-voltage lines, such as the 2400-cps square wave circuits. This was accomplished in the present *Mariner C* upper ring harness by using two harnesses to separate the 2400-cps power sources from other circuits. In a similar manner, the printed conductor ring harness has the 2400-cps square wave power circuits at the center of the board with the low-level circuits near the outer edges as can be seen in Figs. 2 and 3. This enables the power to be supplied to the different bay connectors by radial conductors running from the center, straight out to the appropriate connector. Signal circuits farther out thus cross the power circuits at right angles, minimizing capacitive and inductive coupling. To further reduce pickup, ground conductors were placed adjacent to the 2400-cps power conductors, and power circuits were transposed, with

their respective returns, at regular intervals to the opposite sides of the board.

The 400-cps three-phase sine wave power circuits were routed adjacent to the 2400-cps square wave circuits at the center of the printed conductor ring harness. The 400-cps circuits also have conductors routed radially to the connectors. The remaining circuits were located according to type of circuit (quiet or noisy), and the noise susceptibility number, S_N. Each signal circuit was evaluated using the noise susceptibility number equation, and the resulting S_N numbers were used as a relative indication of susceptibility to stray pickup and noise.

The S_N equation is based on the assumption that all signal circuits were assumed to have equal frequency responses to the induced 2400-cps noise source, i.e., no noise rejection capability inherent in the circuit design was included. Consequently, during layout, considerations of circuit functions and how they varied with respect to time were investigated. For example, the temperature transducer circuits showed a rather high S_N; however, no problem was anticipated because of the 5-cps low-pass filter employed, which is far from the 2400-cps fundamental power frequency. Therefore, the transducer circuits were grouped together without individual shielding.

Based on the required specification tolerances, both the nominal line widths and spacings were 0.031 in. A plated through hole diameter of 0.031 in. was selected as a small, reliable, readily fabricated size. Smaller diameters can be used, but are difficult to fabricate and, therefore, tend to be less reliable. A larger size would use an excessive amount of space. Terminal pads were 0.125 in. in diameter, and the holes in the connector pattern were 0.036 in. An exception was the 0.025-in. line width between the terminals and the connectors, which was required because of the close spacing in the connector circuit pattern. The routing of 0.025-in.-wide circuitry in between connector pins permitted a spacing of 0.027 in. The solder terminals of the connector selected were bent at right angles to the body in a three-layer staggered configuration. This allowed inspection and soldering of the terminals to the PCRH board pads from both sides.

3. Fabrication

Two boards, designated S/N 1 and 2, with the required 8-mil thickness of conductors, were obtained from the vendor. The conductor widths were 25 mils, the lower limit of the tolerance. As mentioned previously, this results in a current density of approximately 250 mils²/amp. A third board (S/N 3), fabricated out of conventional 2-oz double-sided copper printed circuit stock was obtained for comparison. This resulted in the standard conductor thickness of 2.8 mils and conductor widths of approximately 31 mils. Comparison tests are planned to determine if any significant operational difference exists between S/N 3 and S/N 1 or 2. A top view of the first PCRH is shown in Fig. 5. The white-appearing conductors are on the top side, while the black conductors are on the reverse side of the translucent insulating board. Transpositions and circuit runs can be followed readily.

4. Checkout of PCRH

Using the jumper cables, the boards were checked out for continuity and voltage breakdown using the regular QA cable continuity and Megger test set. Updating and corrections were made and the boards retested. During the tests, one of the male pins on a connector broke. Replacement of the entire connector was not as difficult as originally anticipated. The right-angle bends in the connector leads going to the solder pads on the PCRH were cut, facilitating unsoldering of each individual lead. Thus a ganged tool, usually necessary for unsoldering connectors on PCRH boards, was not required.

Arcing between a solder terminal and an adjacent conductor at 500 v was encountered during the hi-pot tests at two places on the PCRH. This was not considered sufficient cause for rejection as the maximum voltage present is 52 v, and the subsequent application of the protective conformal coat would tend to prevent such breakdowns. In future designs this separation would be increased.

5. Tests on PTM

Using the conventional cable harness, more than 100 photographs were taken of the waveforms existing in critical circuits. The PCRH, together with the jumper cables, was installed on top of the cable trough (Fig. 6). After the normal interface checkout to make sure that the connections were identical to the upper ring cable harness, photos of the waveforms of the same circuits were taken, with the identical oscilloscope settings as before.

6. Preliminary Results

An initial comparison of the two sets of photographs shows that in approximately 95% of the circuits, the noise pick up is appreciably *less* with the PCRH as compared to the same circuit using the conventional cable harness. In the remaining 5% of the circuits the induced noise,

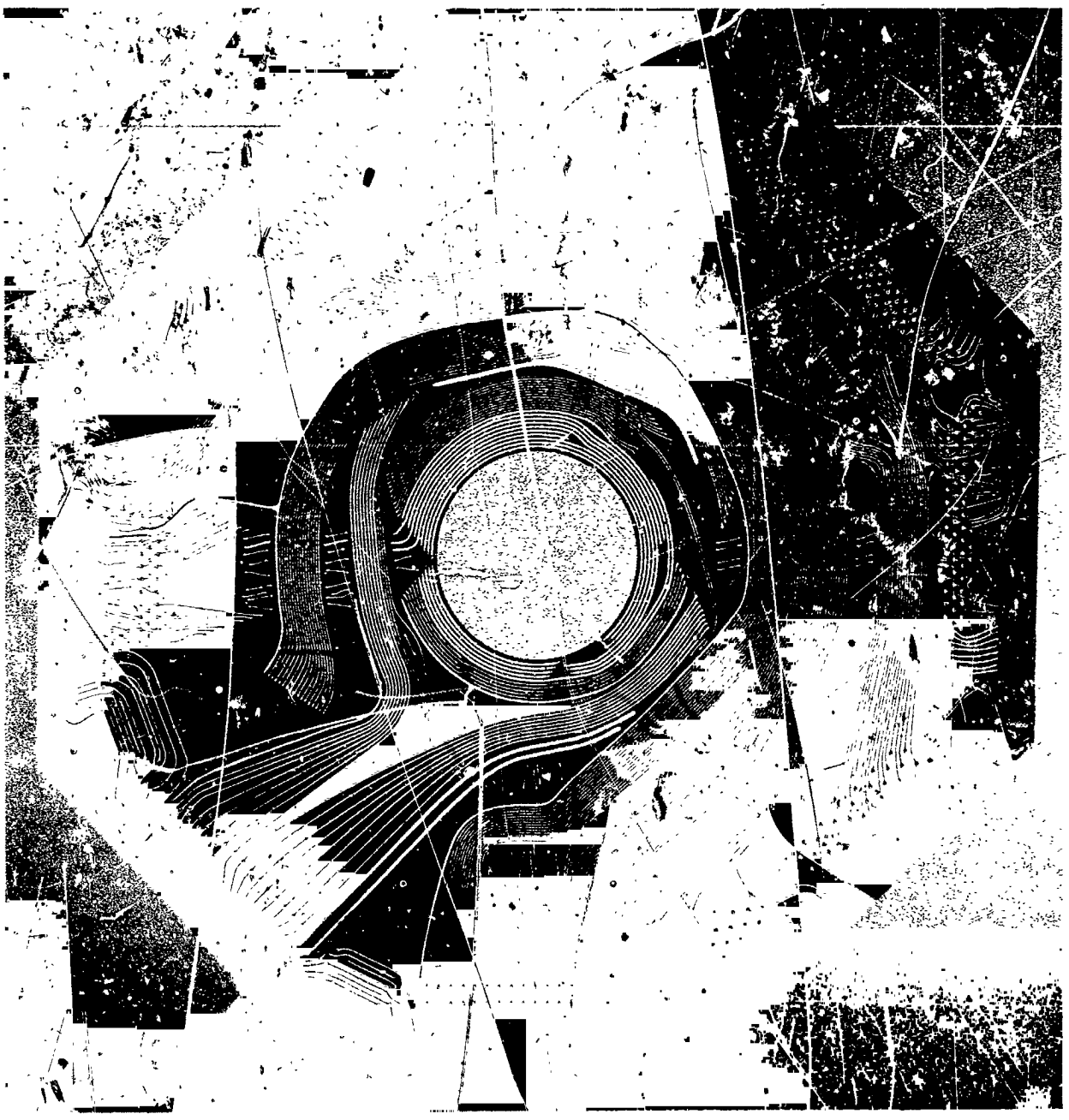

Fig. 5. Top view of fabricated PCRH

mainly from the 2400-cps square wave power circuits, is somewhat greater than in the conventional cable harness, but still well below the specification limit. These tests show that from the electrical performance standpoint, the printed conductor ring harness in its present configuration is a flight-quality item.

Further tests are planned to determine the sources of noise on the PCRH, including the contribution of the jumper cables, which is expected to be appreciable. Comparison of the performances of S/N 1 and 3 will be made to determine the effect of different thicknesses of conductors.

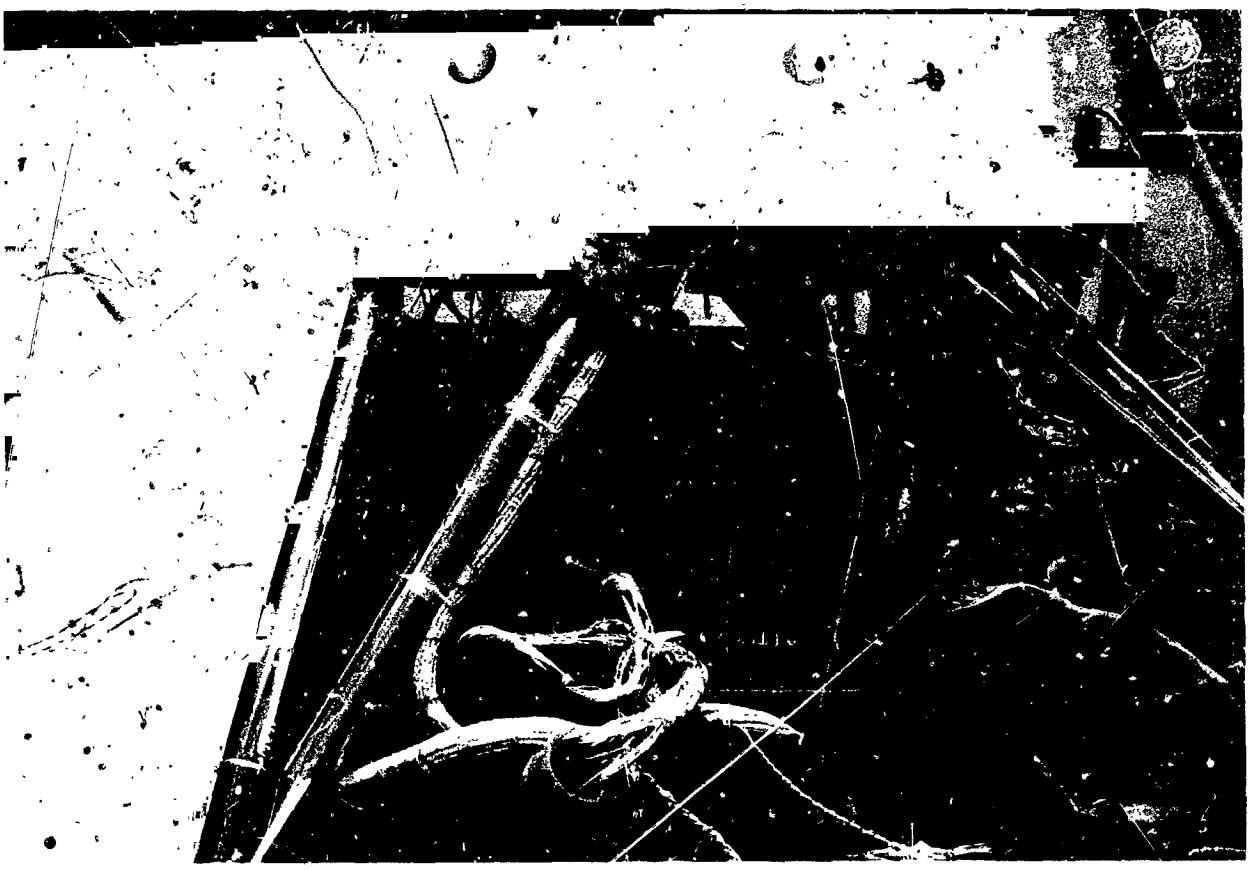

Fig. 6. Installation of PCRH on PTM for tests

Present plans call for a revision of the PCRH air work, incorporating the desired changes, and for obtaining a new board for final tests on the PTM in August.

B. Nonmagnetic Interconnect Material for Welded Modules

R. M. Jorgensen

Since the introduction of welded cordwood techniques for spacecraft packaging, the use of nickel as the interconnect media has been a concern whenever magnetometer experiments are flown. Although some magnetic materials can be tolerated, nickel as it is used in welded cordwood is magnetically "soft," i.e., is easily magnetized and demagnetized, a characteristic causing difficulty with calibration of spacecraft magnetic fields. Because of this, an effort was initiated to develop a nonmagnetic interconnect material that will be interchangeable with nickel in terms of weld joint reliability, the design of welded cordwood modules (both past and future), and interchangeable in terms of the skill and knowledge of assembly technicians so that the introduction of this material will not create new problems in fabrication.

While many materials are nonmagnetic, very few approach nickel in terms of its utility as an interconnect material for welded cordwood. The unique characteristics of nickel that lend themselves to a welding interconnect are:

(1) Thermal and electrical conductivities approximately midway between the extremes of part-lead materials normally encountered: copper (high), and nickel–iron glass sealing alloys (low).

(2) Good ductility properties (i.e., a large elongation).

(3) A large amount of known metallurgy.

(4) Alloying ability with many other materials.

(5) Relative freedom from embrittlement due to heat-affected zones or trace elements.

(6) Availability.

(7) A relatively stable passive oxide coating.

There are several classes of materials which may be investigated to find a nonmagnetic material to replace nickel:

(1) Unalloyed metals of similar electrical and thermal conductivities, specific heat, and melting point.

(2) Readily available binary alloys having the appropriate resistance welding properties. It is hoped that there will be found practical metallurgical knowledge due to wide usage.

(3) Clad materials combining desirable surface properties with necessary bulk or core properties.

(4) Nickel alloyed with elements that depress the Curie point below that anticipated for spacecraft environments.

The latter two approaches involve considerably larger engineering efforts than the first two and will not be reported on here.

An experimental approach to determining the feasibility of materials is based upon choosing the same conductor cross section that has been found to be optimum for nickel and comparing the results obtained to the weldability of nickel (Grade A).

The optimum nickel conductor cross section is 0.010 × 0.030 in. and this size is compatible with 0.017 to 0.040-in. diameter gold plated kovar, 0.016 to 0.030-in. diameter dumet, 0.016 to 0.032-in. diameter nickel, 0.016 to 0.032-in. diameter oxygen-free copper and 0.020 to 0.032-in. diameter ETP copper wires when cross-wire welded. It should be noted that nickel is close to being an ideal material in regard to ductility and freedom from weld zone embrittlement. Therefore, equaling the weldability of nickel may not be easy.

Regarding the first class of materials listed, a pure material or even a binary alloy would be preferred in place of more complex (ternary or quaternary) alloys because it would permit drawing upon a larger potential known metallurgy, at least in the theoretical sense. Practical welding knowledge may or may not exist since this is usually a function of the type and scope of application a particular material sees.

Two unalloyed elements, platinum and palladium, satisfy some of the previously listed characteristics and could be nickel substitutes. Pertinent physical properties are listed in Table 1, compared to two grades of nickel commonly used. The weldability index which approximates a ratio of heat generation capability to heat necessary to reach melting temperature for a given material is also listed.

Table 1. Resistance welding properties of unalloyed nonmagnetic materials

Material, %	Thermal conductivity K_t, cal/cm sec °C	Specific resistivity R, μΩ cm	Melting point F, °F	Specific heat, Btu/lb	Weldability index $R/F K_t$, μΩ sec °C/°F cal
Grade A nickel 99.0	0.15	11.0	2625	0.11	25.2×10^{-3}
Nickel 270 99.95	0.22	7.3	2625	0.109	12.7×10^{-3}
Palladium 99.9	0.17	10.8	2830	0.058	22.4×10^{-3}
Platinum 99.9	0.17	10.6	3220	0.031	18.5×10^{-3}

Both platinum and palladium possess moderate ductility properties but do not have a large known practical metallurgy since they are seldom used as pure metals, but as alloys for a variety of reasons—one being cost. Cost for platinum (99.9%) is approximately $125/oz, and the cost of palladium (99.0%) is about $35/oz. Nickel in ribbon form as used for cordwood modules runs approximately $5/lb or $0.40/oz.

Both platinum and palladium have very stable surfaces and do not tarnish in sulfur-bearing industrial atmospheres, which implies that normally no surface preparation would be necessary for resistance welding purposes.

A practical problem arose in the procurement of the group of materials listed in Table 1. In the case of platinum, the cost proved to be about an order of magnitude greater than palladium when compared on the basis of cost per unit length of conductor. For this reason, platinum was dropped from consideration at this time, the results of the palladium testing serving as a guide as to the desirability of evaluating platinum.

Preliminary welding experiments have revealed that palladium appears to satisfy the requirements of a nickel substitute when compared on the basis of process margins and achievable joint efficiencies. An unanticipated difficulty has arisen in that the technology of etching palladium (for metallographic examination) requires developing, and temporarily welding studies with palladium have been suspended, pending improvements in etching technology.

The second approach, examination of readily available alloys having the appropriate resistance welding properties, also has several potential nickel substitutes. The most obvious selection would be copper alloys with some past satisfactory welding experience. Typically, copper–tin alloys deoxidized with phosphorus (phosphor bronze) and nickel–copper alloys (several are readily available as closely controlled resistance wire) appear suitable. Properties are given in Table 2.

Procurement of materials in Table 2 also provided practical problems. The limiting chemical composition of yellow brass is not sufficient to insure freedom from potential embrittlement problems, and no source was found that could furnish this material with a satisfactory control of trace elements. A similar situation exists in regard to phosphor bronze B although some sources can furnish material with the desired control of trace elements.

Table 2. Resistance welding properties of alloy nonmagnetic materials

	Thermal conductivity, cal/cm sec °C	Specific resistivity, μΩ cm	Melting point F, °F	Specific heat, Btu/lb	Weldability index, μΩ sec °C/°F cal
Grade A nickel (99.0% Ni	0.15	11	2625	0.11	25.2×10^{-3}
Yellow brass 35% Zn, balance Cu	0.27	6.39	1710	0.09	13.9×10^{-3}
Alloy 60 6% Ni, balance Cu	0.22	10	2012	0.09	23.0×10^{-3}
Phosphor bronze B 92% Cu, 8% Sn	0.15	13.3	1880	0.09	48.2×10^{-3}
Alloy 90 11.5% Ni, balance Cu	0.13	15	2030	0.09	51.0×10^{-3}
Alloy 180 23% Ni, balance Cu	0.09	30	2090	0.09	169×10^{-3}

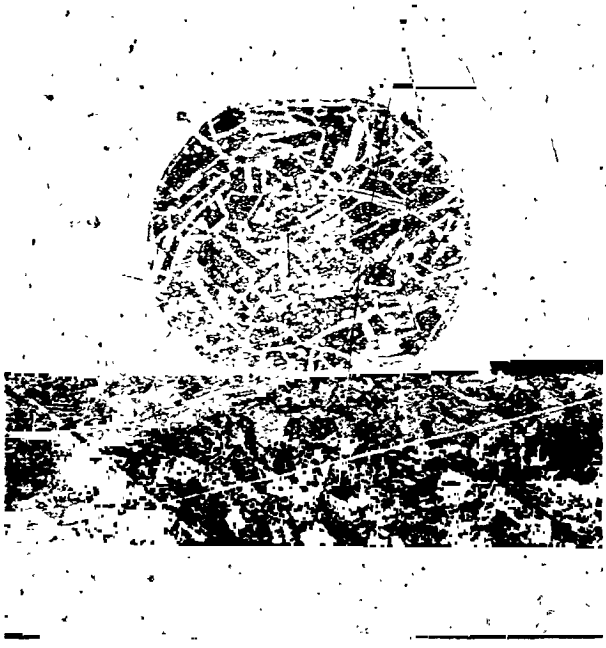

Fig. 7. Transistor lead (0.017-in. diameter gold plated kovar) welded to 0.010 × 0.030-in. Grade A nickel

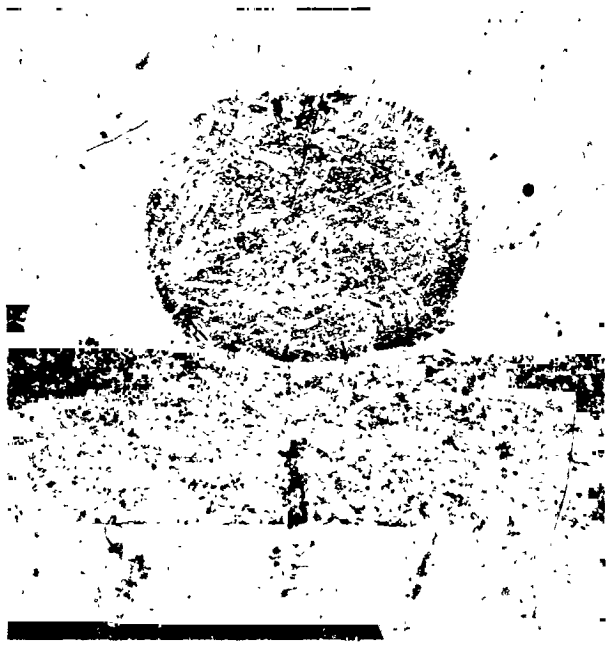

Fig. 8. Transistor lead (0.017-in. diameter gold plated kovar) welded to 0.010 × 0.030-in. Alloy 90

Preliminary experiments with the nickel–copper alloys have revealed that Alloy 60 (6% Ni, balance Cu) does not provide a satisfactory welding process when welded to 0.017-in. diameter gold plated kovar, although for other materials and sizes tested, the results may be acceptable. Alloy 90 (11.5% Ni, balance Cu) has given the best results so far, satisfying both the 0.017-in. diameter gold plated kovar and the 0.032-in. diameter tinned copper which are the extremes of conductor welding difficulties. Work is in progress to determine the weldability of Alloy 90 and Alloy 180 (23% Ni, balance Cu) to other materials and wire sizes.

Fig. 7 is a photomicrograph of 0.017-in. diameter gold plated kovar welded to 0.010 × 0.030 Grade A nickel. Fig. 8 is a photomicrograph of 0.017-in. diameter gold plated kovar welded to 0.010 × 0.030 Alloy 90. The degree of grain growth in the round lead is very similar in both welds, indicating comparable welding conditions. Fig. 9 is a photomicrograph of 0.025-in. diameter tinned ETP copper welded to 0.010 × 0.030 Grade A nickel. Fig. 10 is the same lead welded to 0.010 × 0.030 Alloy 90. The heat-affected zone in these two welds is similar although the degree of penetration of the ribbon is less for the Alloy 90 weld, which is desirable.

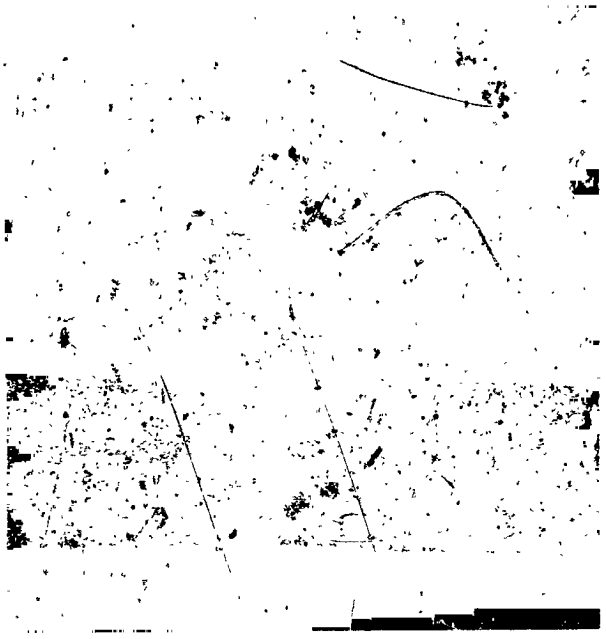

Fig. 9. Tinned ETP copper (0.025-in. diameter) welded to 0.010 × 0.030-in. Grade A nickel

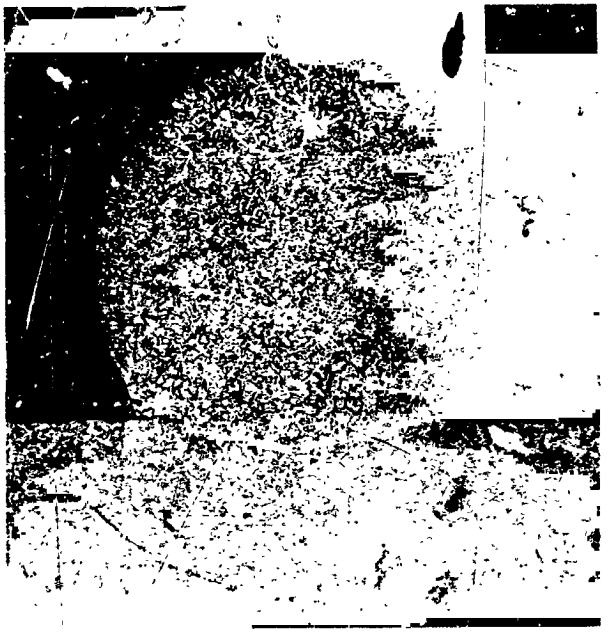

Fig. 10. Tinned ETP copper (0.025-in. diameter) welded to 0.010 × 0.030-in. Alloy 90

IX. Lunar Spacecraft Development

A. High Impact Technology

J. L. Adams

This report summarizes accomplishments in the JPL high impact program during the past two months.

1. Ruggedized Gas Chromatograph

Component tests have continued during this period. In order to examine the behavior of several transistor types under impact, four each of Texas Instrument 2N930, 2N2605, 2N3350, 2N2432, 2N3329, Fairchild 2N3117 and Solid State Products 2N2843 transistors were mounted in a block of aluminum. The transistors were rigidly mounted and oriented so that during impact one of each type would be impacted with the leads trailing, one with the leads leading, and two axially in normal directions. The block was first impacted at 4400 *g* from 105 ft/sec with no failures. An impact at 6300 *g* from 110 ft/sec failed one of the TI 2N3329 transistors which was mounted axially to the impact. An impact at 7400 *g* from 185 ft/sec failed one of the TI 2N930 and one of the TI 2N3350 transistors which were mounted axially to the impact. An impact at 9100 *g* from 175 ft/sec failed one Fairchild 2N3117 transistor mounted axially to the impact. A final impact at 10,000 *g* from 175 ft/sec caused no failures.

All failures occurred at the bond between the lead wires and the semiconductor chip. All failed transistors were replaced with ones of the same type before the next test was conducted. For the last two tests the block was rotated from its orientation for the first three tests in order to test the various individual transistors in various planes. During the last three tests, three TI 2N3609 transistors were included. No failures of this particular device occurred. Additional tests exposed Goodall 617-G-1, 1-μf, 10%, 50-v Mylar capacitors to 10,000 *g* from 200 ft/sec. No failures occurred.

Fig. 1 is an exploded view of a spring-operated sample valve developed for the gas chromatograph. This device

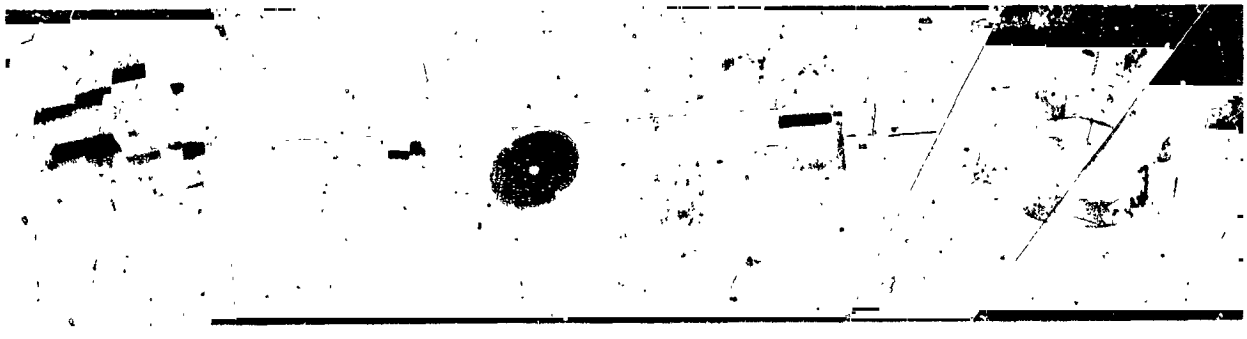

Fig. 1. High impact sample valve

is a three-position rotary gas valve used to interconnect the sample source, the carrier gas, the vacuum line from the jet pump, the sample loop, and the analysis line in various combinations. The valve is powered by a "spirator" spring which stores sufficient energy for 45 cycles (15 complete gas analyses). The unit weighs ½ lb and can be triggered by a small solenoid. It has successfully withstood impacts of 5000 *g* from velocities in excess of 100 ft/sec and should survive 10,000 *g* from 200 ft/sec with no major problems.

2. Ruggedized S-Band Transmitter

Dummy crystal units produced under contract with Valpey-Fisher Co. were impact-tested in order to investigate sealing techniques. The crystal cases consisted of two ceramic discs joined by solder which was applied to treated chamfers on the edges of the discs. Some of the solder surfaces were treated with a vapor-deposited chrome–silver coating and some of them were treated with a fired moly-manganese coating. All units survived 10,000 g from 200 ft/sec, both axially and radially with no detectable seal degradation.

3. Batteries

Table 1 summarizes various tests performed on battery cells during the reporting period. In all cases the cells were completely supported in a rigid (typically ⅜-in. wall aluminum) fixture. The impact directions referred to are shown in Fig. 2. The arrows represent the direction of the accelerations (opposite to the direction of preimpact velocity). The plates are parallel to the *BA* plane. In

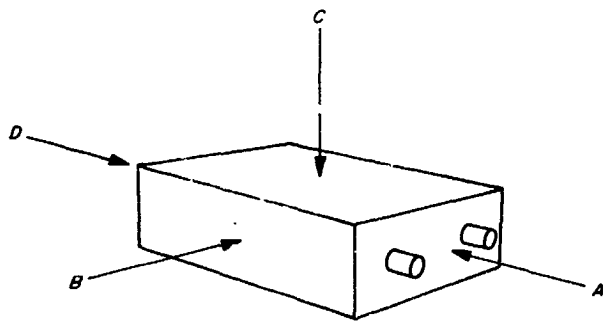

Fig. 2. Battery impact directions

Table 1. Summary of battery cell tests

Battery	Condition	Potting	Impact direction	g level	ΔV, ft/sec	Comments
Eagle-Picher model 25-65 silver zinc	Uncharged	Silastic	C	4,800	145	Slight visible plate damage. No shorting. Plates buckled.
	Uncharged	Silastic	D	4,800	145	
Eagle-Picher model 25-65	Charged	Silastic	C	3,900	130	
	Charged	Silastic	C	4,600	152	
	Charged	Silastic	C	5,750	148	No detectable degradation.
	Charged	Silastic	C	8,220	149	
	Charged	Silastic	B	3,700	135	
	Charged	Silastic	B	5,700	150	Case split, one plate buckled. Discharge cycle showed almost full capacity.
Eagle-Picher model 25-65	Charged	Epon 815	B	7,000	148	No detectable degradation.
	Charged	Epon 815	B	8,800	142	Case cracked and separated from potting, plates crushed, internal short.
Yardney YS 20 silver cad cell	Charged	Silastic	C	7,400	166	No detectable degradation.
	Charged	Silastic	B	7,200	167	No detectable degradation.
	Charged	Silastic	B	10,800	169	Case cracked. Electrically O.K.
Yardney YS 20 silver cad cell	Charged	Silastic	B	7,600	174	Case cracked. Electrically O.K.
Whittaker P.S.D. 201171 sealed silver cad cells (2 potted in fixture)	Charged	Epon 815	B	8,400	161	Case cracked. Electrically O.K.
MA-C ESB cell	Charged	Epon 815	D	5,400	158	Case cracked; internal shorting.
Whittaker P.S.D. CD-3 sealed silver cad cells (2 potted in fixture)	Charged	Epon 815	B	10,800	174	No detectable degradation.
	Charged	Epon 815	D	10,000	170	No detectable degradation.

general, the direction *A* is most severe and *D*, *B*, and *C* follow in order of decreasing severity.

4. Mechanisms

A series of five tests was performed as part of an investigation of the behavior of gears under impact. In each test, two 96-tooth, ⅛-in.-wide gears were meshed, one rigidly fixed to the testing fixture and the other eccentrically weighted so as to produce approximately 0.65 in.-oz of torque in a 1 *g* field. The direction of impact was such that the torque value would be approximately equal to the *g*-loading times the 0.65 in.-oz value.

In the first test, both gears were stainless steel and the impact level was 5800 *g* from 170 ft/sec. Fellows Red Line tests showed no detectable damage to the rotating gear and a maximum tooth-to-tooth error of 0.0006 in. in the fixed gear. Test 2 duplicated Test 1 and resulted in no detectable damage to the rotating gear and a maximum tooth-to-tooth error of 0.0005 in. in the fixed gear. Test 3 was run with a fixed 2024 aluminum gear and a rotating 2024 aluminum gear. At an impact of 5900 *g* from 165 ft/sec, the fixed gear showed a maximum tooth-to-tooth error of 0.0022 in. and the rotating gear a maximum tooth error of 0.0022 in. In Test 4, a rotating stainless steel gear was meshed with a fixed aluminum gear and impacted at 6000 *g* from 170 ft/sec. Red Line results showed no detectable damage to the stainless steel gear and 0.002 maximum tooth-to-tooth error in the aluminum gear. Test 5 meshed a rotating aluminum gear with a fixed stainless steel gear. No damage could be detected to the steel gear and a maximum tooth-to-tooth error of 0.003 appeared in the rotating aluminum gear. The impact level was 6,000 *g* from 170 ft/sec. These test results are slightly inconsistent, both with theory and among themselves. Further analysis is being performed.

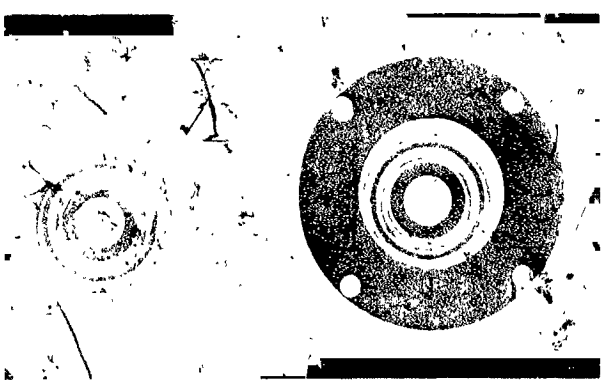

Fig. 3. Prototype bearing spring mount

Fig. 3 shows a prototype spring mount for a rotating element bearing. This mount is a six-degree-of-freedom spring which is stiff enough (approximately 25,000 lb/in. axially and radially) to maintain alignment, yet soft enough to deflect during an impact so that bearing loads will not become high enough to damage the bearing. A 4-oz rotating mass with a 0.002 clearance in its housing was supported between two lightweight ball bearings (Microtech Mc814SSR 25L10) in these spring mounts. The unit survived impacts of 10,000 *g* from 200 ft/sec with no detectable damage. The major loads, of course, were taken out by bottoming elsewhere in the assembly (as, in this case, between the rotor and the housing).

5. Miscellaneous

A program is under way to investigate the effects of high impact upon cordwood electronic packaging. Blocks of Stycast 1090 potting compound, the size and shape of cordwood modules, have been tested both unweighted and weighted under various impacts with various mountings. In general, the potting itself apparently can withstand impacts on the order of 10,000 *g* and support the required component masses, providing that the modules are supported rigidly on at least one side. A representative welded cordwood module (the *Mariner* Mars 1964 gyro switch control) has survived impacts of 10,000 *g* from 200 ft/sec in three principal directions with no apparent degradation when mounted in a rigid fixture.

6. Test Equipment

Fig. 4 shows the 22-in. bore compressed air gun in its present state. Work is proceeding on mounting, debugging, and pressure-testing the gun.

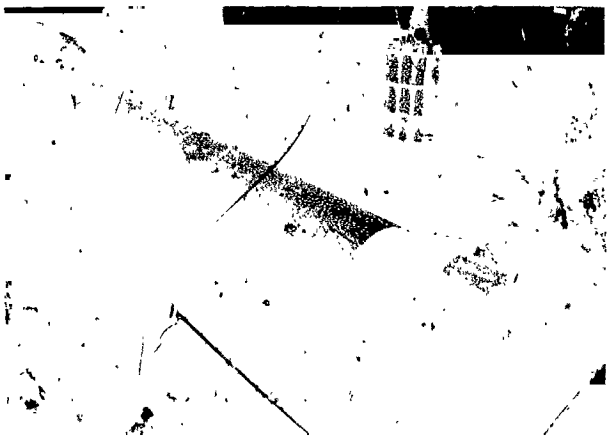

Fig. 4. 22-in. bore compressed air gun

X. Applied Mechanics

A. Heating–Cooling Time for a Planetary Lander Survival Payload

J. Hultberg

A survival sphere for a planetary lander is protected by an energy absorber which may make the sterilization time very long. The method described here is most suitable for calculation of the transient heat-up and cool-down time associated with a survival payload with a low thermal resistance, in comparison to the thermal resistance of the surrounding energy absorber. Fig. 1 shows the nomenclature for the survival sphere.

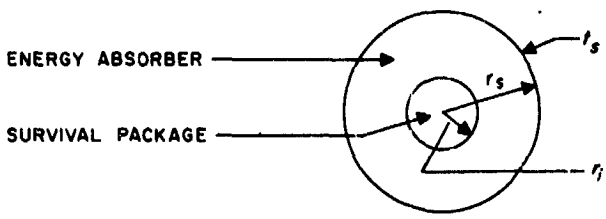

Fig. 1. Cross section of a hard-impact survival sphere

The heat transferred from the outer surface of the energy absorber to the survival payload is

$$dq = K(t_s - t)\,d\theta \tag{1}$$

where

q = rate of heat flow

K = conductance

t_s = temperature of the surface of the sphere

t = temperature of the survival payload

θ = time

Since temperature gradients in the survival payload are small in comparison to the temperature gradients in the surrounding material, the change in temperature caused by heat transfer to the survival payload is given by

$$dq = C\,dt \tag{2}$$

where C is the heat capacity of the survival payload

$$C = \int_V c_p \rho \, dV \tag{3}$$

where

c_p = specific heat

ρ = density

V = volume

Eqs. (1) and (2) may be combined and integrated to give

$$\ln\left(\frac{t_s - t}{t_s - t_i}\right) = -\left(\frac{K}{C}\right)\theta \tag{4}$$

where t_i is the initial temperature of the survival payload.

For various values of (K/C) the results are shown in Fig. 2. The analysis is not valid for short times when the temperature gradients in the survival payload must be considered.

The conductance may be evaluated by considering the heat conduction equation for a sphere

$$q = -kA\frac{dt}{dr} = -k\,4\pi r^2 \frac{dt}{dr} \tag{5}$$

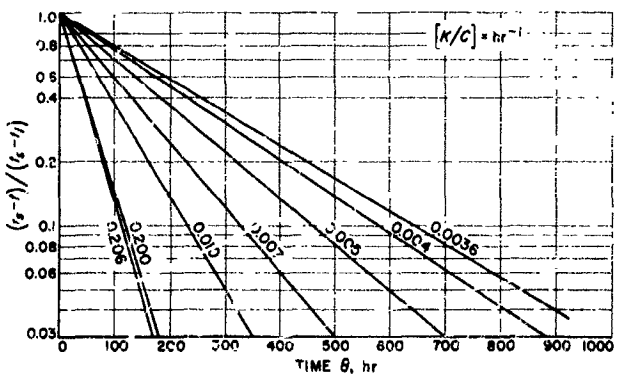

Fig. 2. Time-temperature history of a survival sphere for various values of K/C

This may be integrated between the outer radius and the inner radius to give

$$q = 4\pi k \frac{t_i - t_s}{\frac{1}{r_i} - \frac{1}{r_s}} \quad \text{or,} \quad = \frac{4\pi k}{\frac{1}{r_i} - \frac{1}{r_s}}. \tag{6}$$

Thus, when the properties and geometry are given, the time-temperature history may be calculated.

A numerical example is given for illustration. It is desired to find the time-temperature history for the heating of a lander survival payload from an ambient temperature at 15 to 130°C with an outside surface temperature at 135°C. Balsa wood 15-in. thick with a thermal conductivity of 0.0225 Btu/hr ft°F, density of 7 lb_m/ft^3, and specific heat of 0.327 Btu/lb_m °F covers the survival package. The survival payload has a diameter of 15 in., an average density of 50 lb_m/ft^3 and an average specific heat of 0.25 Btu/lb_m °F.

The geometry and properties above give a value for K/C equal to 0.206 if the heat capacity of the insulation is neglected and a value of 0.0036 if the entire heat capacity of the energy absorber is combined with the heat capacity of the survival payload. The time-temperature heating curve is shown in Fig. 3 for both cases. As an example, the time required to reach 125°C is 100 hr in the former case and 700 hr in the latter case. For the case combining the heat capacity of the survival payload and the energy absorber, the heating curves are shown for three different surface temperatures. Higher surface temperatures greatly decrease heating times; the time to reach 125°C in the latter case is reduced from 700 to 370 hr when the surface temperature is raised from 135 to 165°C. From Fig. 3 the time above a certain temperature may be estimated.[1]

For cool down, the time-temperature curves are calculated in the same manner as shown by Eq. (4). Thus, the cool-down time of the survival payload from 130 to 15°C with a surface temperature of 10°C is the same as the heating time from 15 to 130°C with a surface temperature at 135°C. The effect of conducting leads running into the survival payload should be noted. A large conducting path to the survival payload would have the effect of reducing the sterilization time considerably. In the above example, the time to reach a temperature would be reduced by 20% if a ¼-in.-diameter copper wire were placed through the energy absorber.

[1]It should be noted that a formula presenting an exact solution for the geometry considered here is presented in "Conduction of Heat and Solids," Second Edition, p. 351, by H. S. Carslaw and J. C. Jaeger, Clarendon Press, Oxford, England, 1959.

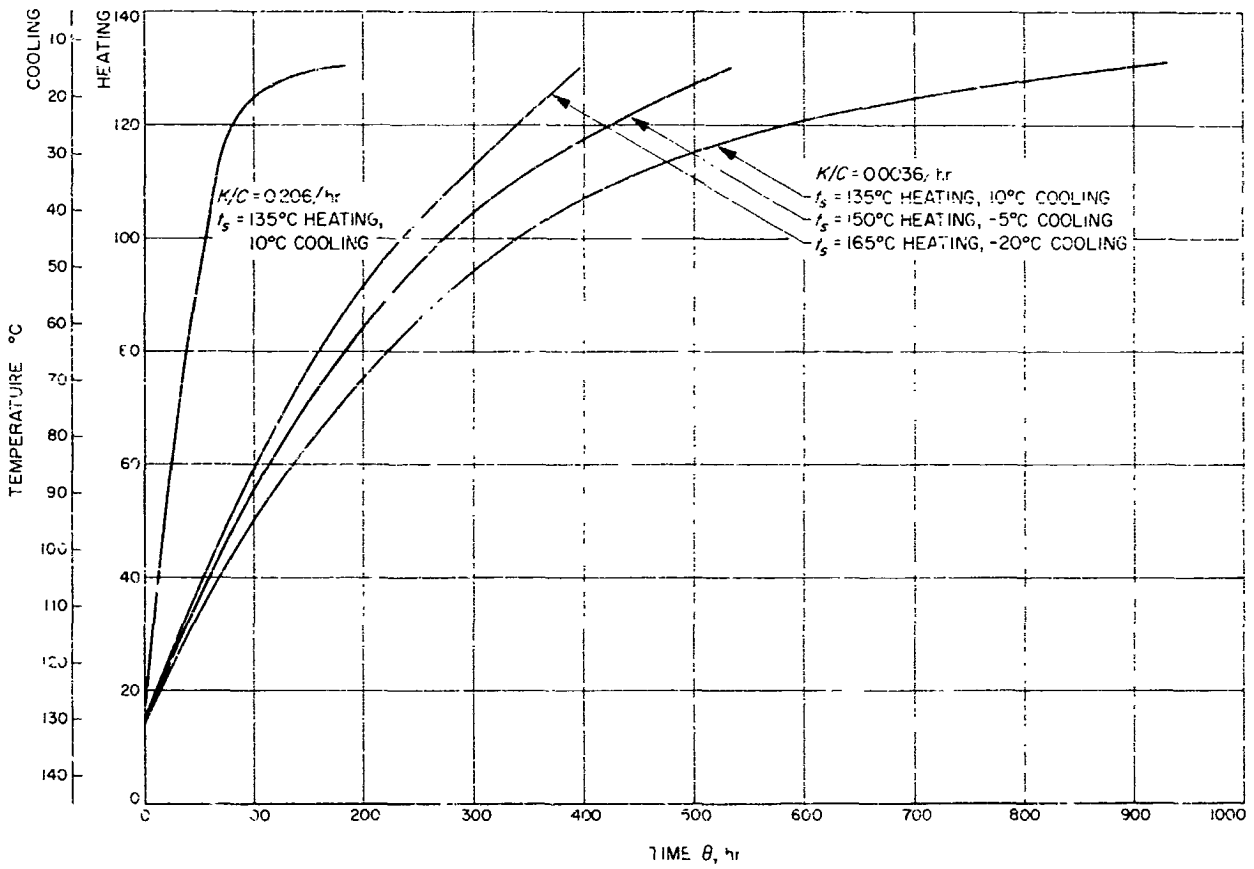

Fig. 3. Time-temperature history for a survival sphere

B. Analysis of Equilibrium Shock-Layer Radiation for Atmospheric Entry to Mars

F. Wolf and J. Spiegel

As part of a continuing analysis of theory and experimentation for equilibrium shock-layer radiation expected during Martian entry, it has become apparent that currently used experimental techniques result in data obtained at density levels much higher than for expected entry conditions. When acceptable agreement is obtained by a number of experimental techniques in the near future, it should be possible to verify theoretical methods at the higher pressure levels. For example, good agreement between theory and experiment has been shown for the Martian velocity range in Ref. 1. However, as the experimental results become available at much lower densities, it is necessary to predict equilibrium radiation at true entry density conditions either by use of theoretical density dependence or by a density dependence obtained from test results at relatively high pressures. In this summary some significant aspects of the theoretical method are presented.

The gas radiance of mixtures simulating the Martian atmosphere was calculated from Ref. 2, except for some modifications to the CN f-number, and the equilibrium chemical composition of these mixtures at elevated temperatures, supplied by the JPL Thermochemistry and Normal Shock Program (Ref. 3). Fig. 4 shows total equilibrium radiation intensity of a 30% CO_2–70% N_2 mixture behind the normal shock as a function of the free-stream density with the flight velocity as a parameter.

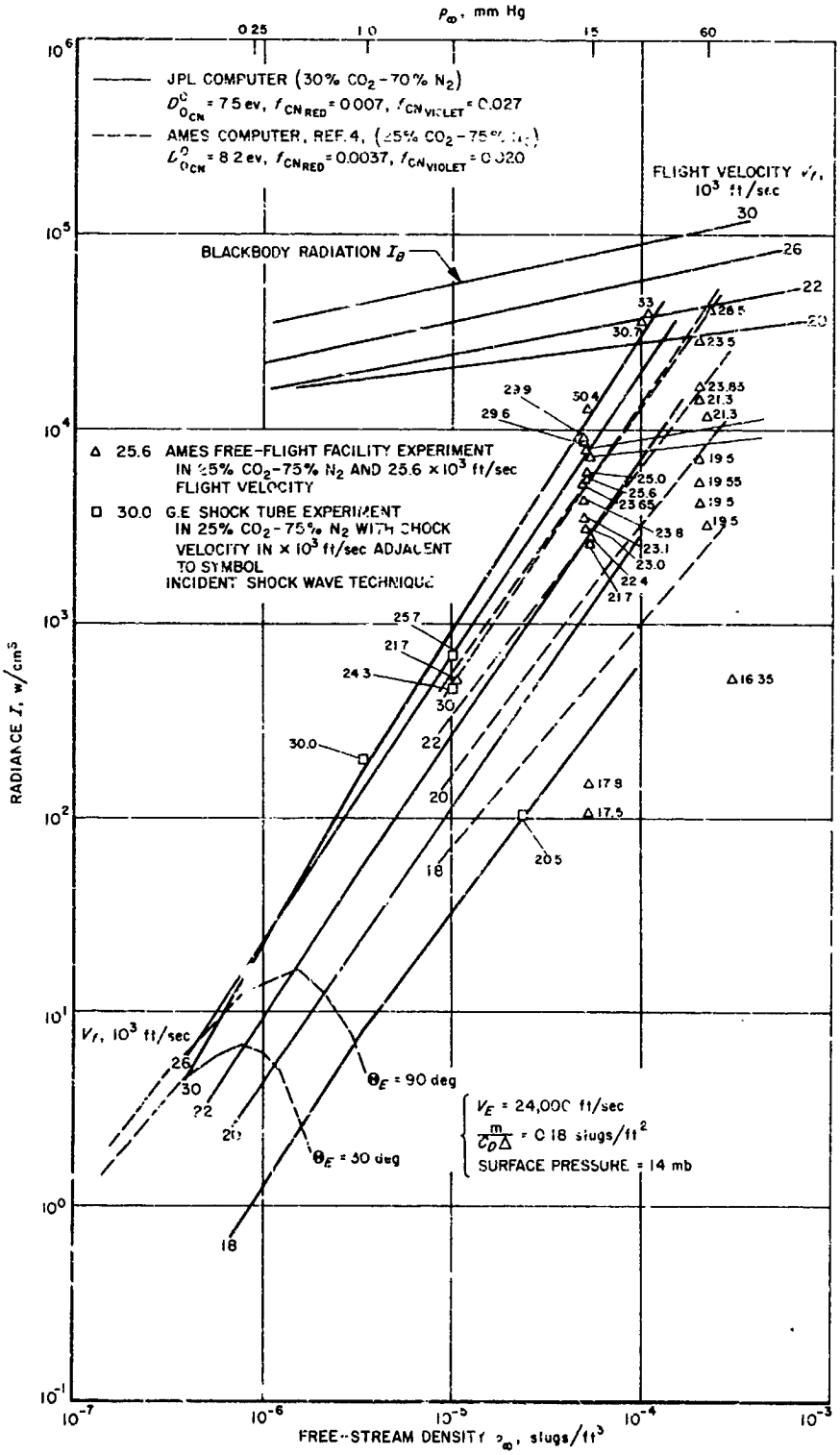

Fig. 4 Free-flight gas radiance of 30% CO_2–70% N_2 versus free-stream density

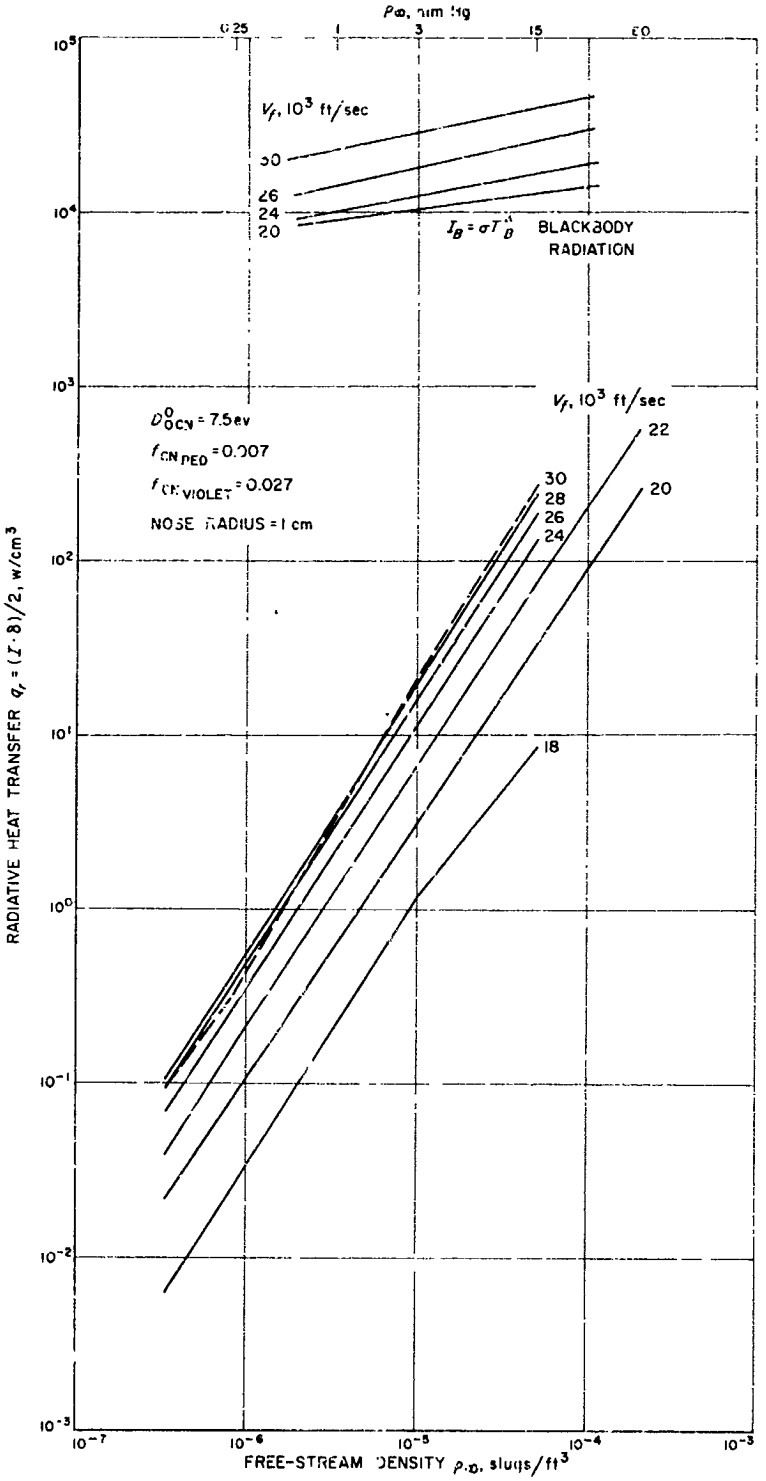

Fig. 5. Radiant heat transfer to stagnation region for 30% CO_2–70% N

The solid lines are computed JPL values as a function of free-stream density, with the free-flight velocity from 18 to 30 × 10^3 ft/sec as a parameter. The set of dashed lines represents the corresponding Ames calculations for a slightly different mixture (25% CO_2–75% N_2) and a CN radical contribution, determined by a higher energy of dissociation ($D^0_{0_{CN}} = 8.2$ ev) which results in higher CN concentration.

Also, slightly lower CN_{violet} oscillator strength ($f_{CN_{violet}} = 0.020$) was used by Ames as compared to the JPL inputs. Generally, the Ames total radiance levels agree with JPL calculations in the region of 22000 ft/sec flight velocity, while being lower at higher velocities and vice versa. The different values of the energy of dissociation used in the two sets of calculation would contribute to these trends. This will be substantiated by further JPL calculations where only $D^0_{0_{CN}}$ is varied.

The experimental data shown on Fig. 4 comes from shock-tube and free-flight tests, as indicated. In the lower left of the figure are two representative entry trajectories in the form of point sequences of atmospheric pressure and velocity for entry angles of 30 and 90 deg. It is apparent that most of the experimental data so far obtained are for much higher densities than these tentative entry conditions would require. Thus it seems desirable to determine gas radiation intensities at much lower free-stream pressure than presently, with the objective of validating the theoretical predictions in a region more comparable to prototype flight conditions.

The total radiative heat transfer of a plane parallel layer of gas, neglecting self-absorption and stimulated emission, is approximated by the quantity

$$q_r = \frac{I \cdot \delta}{2}$$

where δ represents the thickness of the shock layer and q_r is commonly accepted as the total equilibrium radiative energy to the stagnation region of a blunt body. This quantity is shown in Fig. 5 for a mixture of 30% CO_2 and 70% N_2, calculated with the same set of radiation input data as in Fig. 4. It is apparent that the density dependence of q_r changes relatively little over the range of densities which covers the shock tube experimental conditions down to actual free-flight density levels.

The lines marked I_B represent blackbody radiation intensity on the radiation emitted by an optically opaque gas, again with the free-flight velocity as the parameter. This intensity is the upper limit for radiative energy transfer to the body surface and the difference between q_r and I_B is a measure of the optical "thinness" of the shock layer for the assumed nose radius, 1 cm.

The density dependence of equilibrium radiance I and the radiative heat transfer q_r as obtained from the average slope of the lines in Figs. 4 and 5 over a wide density range is plotted in Fig. 6. It can be seen that in the Mars entry velocity range the power n varies significantly with flight velocity. Converting from radiance to radiative heat transfer tends to raise n slightly. The reason for the difference between the JPL and Ames calculations has not been specifically identified at this time, but will be examined soon.

In summary, it appears necessary to compute equilibrium radiation at much lower density than where experimental data exist. The simple procedure of normalizing to free-stream density appears to introduce some problems. Although at a fixed velocity, density dependence of radiation is acceptable for engineering estimates. The density dependence with velocity is significant. For more exact heat transfer predictions, a simple exponential density dependence should not be used.

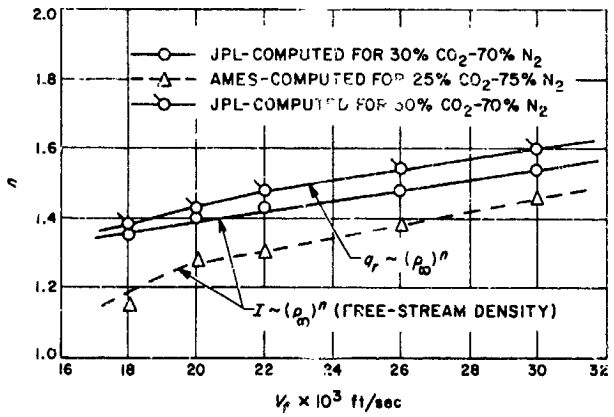

Fig. 6. Density dependence of radiance and radiation heat transfer

References

1. Arnold, J. O., Reis, V. H., and Woodward, H. T., "Theoretical and Experimental Studies of Equilibrium and Non-Equilibrium Radiation to Bodies Entering Postulated Martian and Venusian Atmospheres at High Speeds," presented at the Second AIAA Aerospace Sciences Meeting, New York, New York, January 25–27, 1965.

2. Kivel, B., and Bailey, K., "Tables of Radiation from High Temperature Air," AVCO Research Report No. 21, AVCO Corp., Everett, Massachusetts, December 1957.

3. Horton, T. E., "The JPL Thermochemistry and Normal Shock Computer Program," Technical Report No. 32-660, Jet Propulsion Laboratory, Pasadena, California, November 1, 1964.

4. Williams, M. J., and Treanor, C. E., "A Method for Calculating Diatomic Spectra Using a Digital Computer," CAL Report No. QM-1626-A-5, Cornell Aeronautical Laboratory, Inc., Buffalo, New York, May 1962.

ENGINEERING FACILITIES DIVISION

XI. Instrumentation

A. A Pressure Telemeter for Wind Tunnel Free Flight Pressure Measurement

R. G. Harrison, Jr.

1. Introduction

Pressure telemeters are being used at JPL's aerodynamics facilities to study interference free pressure data on models projected into free flight by a pneumatic launch mechanism.

A wind tunnel test program has been conducted at JPL (Ref. 1) to develop the pressure telemetry technique. The pressure measurements in this program were limited to the base pressures of 10- and 15-deg half angle cones. Model bodies were made of plastic with steel noses, to prevent melting during flight.

An attempt was made to catch the model at the end of the flight. When it was not caught it was totally destroyed, except for the telemeter. The telemeter was generally recoverable due to the protection given by the lucite insert (Fig. 1). Protection while on the launch gun was provided by a heat shield (Fig. 2) and a cooling gas. The cooling requirements were that the model not be distorted by heat and the pressure telemeter not be taken outside its operating temperature range. The heat shield also provided the model nose support and protected it from buffeting when the wind tunnel was started.

About 15 min was required to bring the wind tunnel up to operating pressure and temperature, and usually by that time the telemeter had stabilized and was ready for free flight measurement. Then the model nose support was withdrawn, reference pressure measured, heat shield raised, and the model launched into free flight. The telemeter was designed to function, uneffected, over the wide ranges of pressures, temperatures, and accelerations encountered during launch and free flight.

2. Telemeter Performance

The pressure telemeter full scale pressure measurement capabilities are limited by the bandwidth capabilities of the receiver used. In this case, 200 kc. Three sensitivities were produced: 1 mm Hg = 20, 40 or 80 kc.

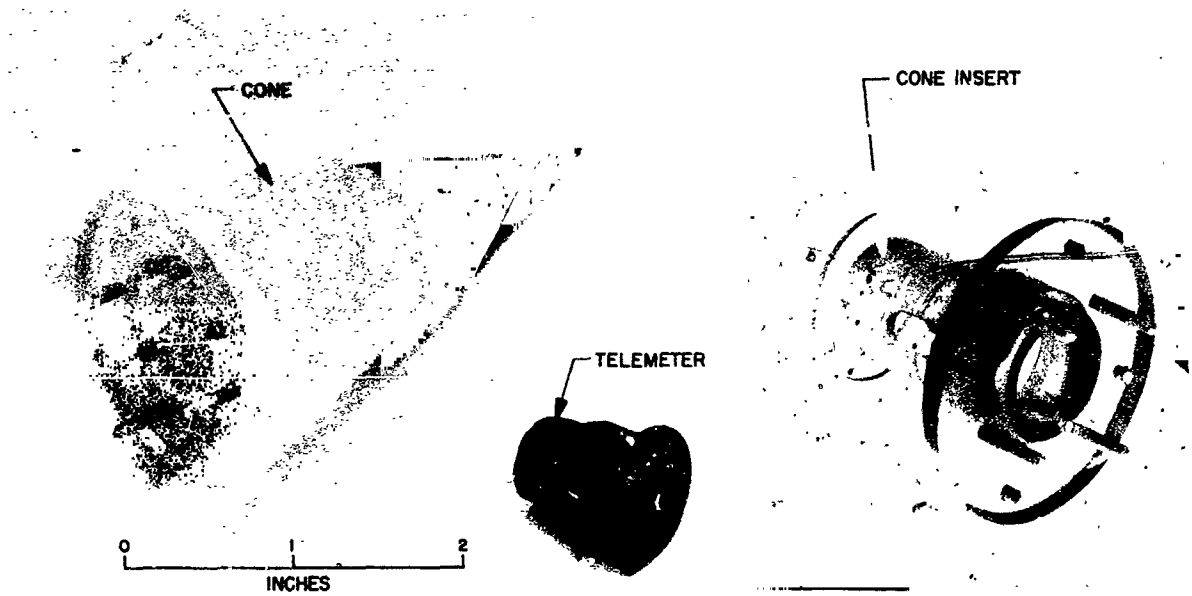

Fig. 1. Free flight telemeter model

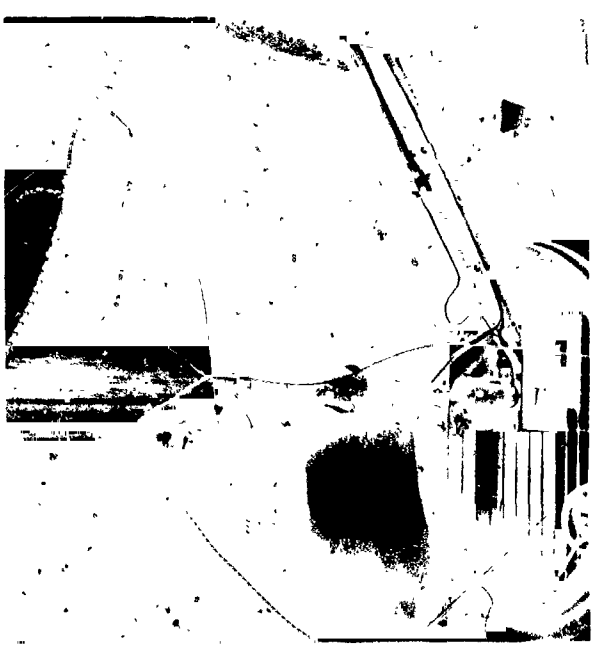

Fig. 2. Launch gun and heat shield

The pressure telemeters were insensitive to the accelerations encountered in the wind tunnel. At 25 *g*'s there were no measurable effects on the instrumentation used for data recording. This was determined by firing a model with a telemeter into a padded box with the pressure port sealed and the acceleration computed. This exercise was repeated with several models of various sensitivities.

The oscillator stability was found to be 0.001% of the oscillator frequency over a period of 30 min. For a period of 1 min the stability was found to be 0.5% of 200 kc. This was determined with the pressure telemeter pumped down in a bell jar, to eliminate atmospheric disturbances, and the oscillator frequency monitored with a Hewlett Packard Model 524B electronic counter. For periods of time comparable to free flight periods no deviations could be recorded.

The rise time capabilities of the pressure telemeters are 0.5 msec or better without tubing or a bypass capacitor on the tuners discriminator output. The diaphragm of the pressure sensor vibrates at its natural frequency for about 6.0 msec, when a sharp pressure pulse is applied. Rise times were determined by using a small shock tube to generate the pressure pulse.

The pressure telemeter thermal stability was thoroughly investigated and found to be quite good for the stable test times required. A temperature increase of 100°F, with an ambient pressure of 14 psi, produced a

2.7% increase in the oscillator frequency. The time interval between the temperature increase and the start of the oscillator frequency shift was 3 min. The telemeter could be exposed to 800°F for at least 10 sec before an oscillator shift began. These thermal stability measurements were made in a well regulated electric oven. An investigation of the effects of thermal shock was performed in the same manner with no effects noted. The 100°F temperature rise also produced a 0.1% change in the full scale calibration of the pressure telemeter. There were few or no changes in the performance of the telemeter over a temperature range of 30 to 200°F.

The pressure telemeter is a differential transducer that can be subjected to an overpressure of 50 psi without damage or change in performance. The reference pressure is obtained by a very slow leak into the large volume of the reference side of the sensor. This leak rate can be easily adjusted to provide stable measurement times as long as 5 sec at atmospheric pressure. As the ambient pressure goes down, this time can be increased.

The diaphragm natural frequencies are from 20 to 27.5 kc, depending upon the assigned diaphragm thickness and tension.

3. Pressure Telemeter Design and Construction

The primary performance requirement of the pressure telemeter was stability and consistent operation. Next was simplicity of assembly and operation. Special techniques and materials were avoided as much as possible, and the number of components were held to a minimum.

A colpitts oscillator (Fig. 3) was used because of its insensitivity to variations of the circuit components other than the tank circuit. The telemeter, ready for assembly, consists of four major components: a printed circuit inductor, a pressure sensitive capacitor, a battery, and all other circuit components in a microminiature package of pellet type construction (Ref. 2) (Fig. 4).

The characteristics and technique of fabrication of the pressure sensor were determined empirically for the most part, due to the uncertainties of determining mathematically the characteristics of very thin metal diaphragms under tension (Fig. 5). Before assembly of the sensor the diaphragm was examined for proper tension by pumping down the reference side and measuring the focal length of the concave surface. For example, a focal length of 1.3 in. at a pressure of 14 psi (atmospheric pressure at

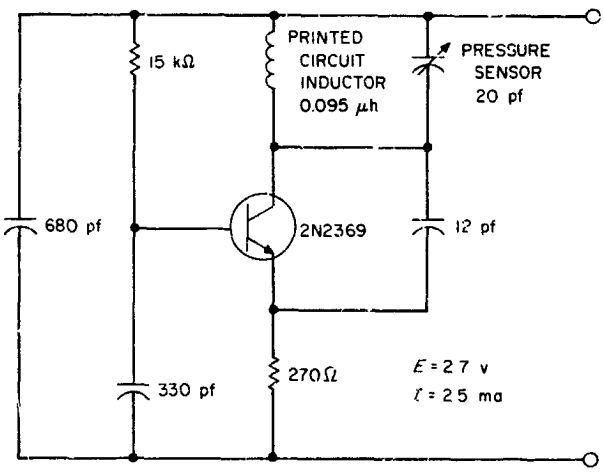

Fig. 3. Schematic diagram of telemeter oscillator

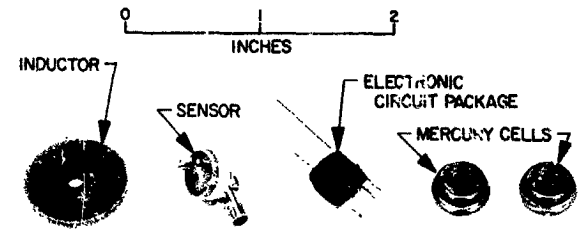

Fig. 4. Telemeter components

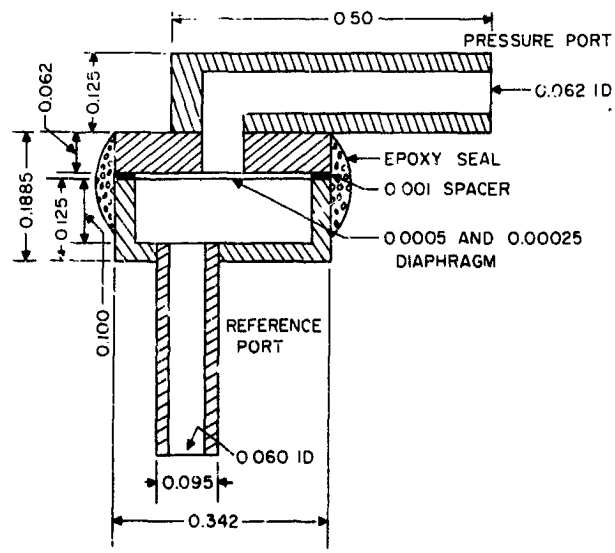

Fig. 5. Pressure sensor

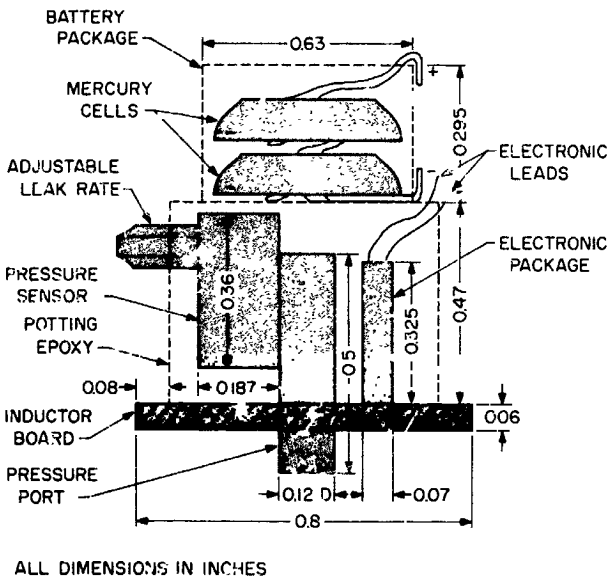

Fig. 6. Pressure telemeter components layout

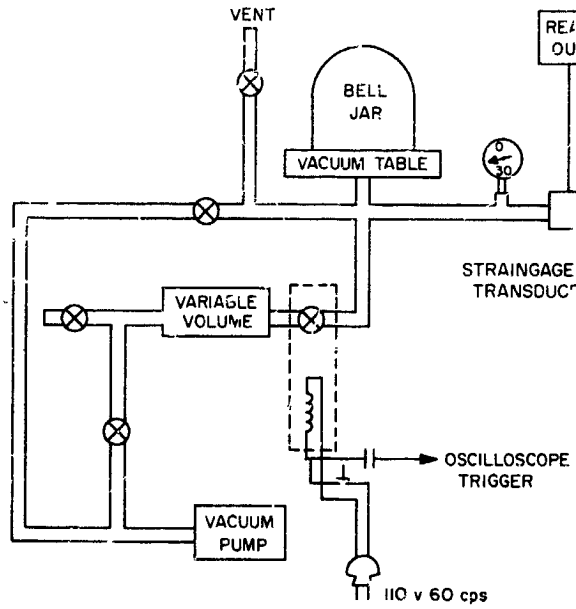

Fig. 7. Calibration system

JPL is usually very close to 14 psi) would, at final assembly of the pressure telemeter, provide a sensitivity of 20 kc ±10% for a pressure difference of 1 mmHg. Two diaphragm thicknesses were used, with variations in tension, to provide a selection of sensitivities.

After assembly of the sensor, it was checked for proper capacitance on a Q-meter and attached to the inductor, where the tank circuit was checked for proper resonant frequency with a grid-dip oscillator. The microminiature circuit was then attached, and the pressure telemeter checked for proper operation before potting. The resonant frequency of the circuit changes very little after potting. The mercury cells are attached with a hard sealing wax, and they can be changed in a matter of minutes if necessary. Extreme toughness of the potting material enabled the telemeter to survive high temperatures and high velocity impact. The pressure telemeter is 0.80 in. long, 0.80 in. in diameter at the inductor end and 0.50 in. in diameter at the battery end (Fig. 6). Total weight is ⅛ oz. Useful battery life averages about 20 hr providing ample time for calibration and wind tunnel operations. Most battery failures occur during calibration. It has been noted that a ΔT of 100°F will produce a change in battery voltage of about 1%.

4. Calibration

The pressure telemeter was placed in a bell jar (Fig. 7) and pumped down to simulate approximately, the wind

Fig. 8. Typical calibration pulse; ΔP = 200μ Hg; X = 20 msec/cm; Y = 50 mv/cm

tunnel static pressure. A strain gauge transducer a readout, with a scale factor of 5 μ per division, was zer at this condition. The frequency modulated (FM) tu was adjusted to center frequency and the output of discriminator displayed on the Y axis of an oscillosco A small volume of gas was admitted to the bell jar ca ing a sharp pressure step. The calibration system rise ti was about 10 msec.

The sweep of the oscilloscope was triggered at the sa time the gas was admitted and to record the frequer shift of the pressure telemeter. The strain gauge press transducer reading was then recorded to provide a pr sure measurement corresponding to the voltage measu

ment on the oscilloscope (Fig. 8). To record a pressure decrease a large volume at vacuum was opened to the bell jar, causing a sharp pressure decrease.

The telemeters have been found to be linear in the area of interest, and no change in the calibration slope occurs in going from a pressure increase to a pressure decrease (Fig. 9). The leak rate of the sensor was adjusted at the beginning of the calibration. After calibration the pressure telemeter was ready for use in the wind tunnel, or it could have been stored for a time without a change in calibration.

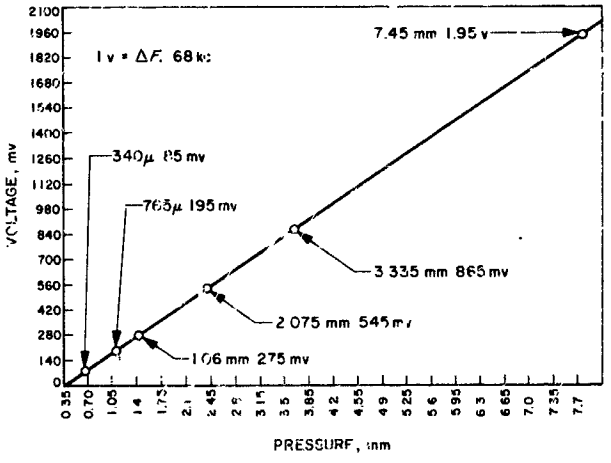

Fig. 9. Telemeter calibration curve

5. Recording Instrumentation

A standard McIntosh FM tuner Model MR71 was used to receive the pressure telemetry. It had been realigned to tune through 98 to 118 Mc. The tuner has a 200-kc bandwidth, a flat top response and a useable sensitivity of 2 μv. The output of the discriminator was a dc voltage coupled to the input of a Dynamics dc amplifier Model No. 6122. The two dc voltage outputs of the amplifier were coupled to a 3-kc response galvanometer in a CEC recording oscillograph and to a Tektronix 545 oscilloscope (Fig. 10).

The antenna used was a λ/2 loop placed in one window of the test section. Antenna orientation was extremely critical; however, once properly located it was possible to have nearly perfect reception throughout the test area. This was determined by mapping the antenna pattern with a telemeter. The most troublesome areas were the window edges. A Fastax camera was used to provide optical data for each flight (Ref. 5).

6. Technique of Operation and the Problems Encountered

Free flight techniques have been developed successfully at other facilities (Ref. 4); and, in many respects they are similar to the JPL program. Launching hardware (Ref. 5) (Fig. 2) is not described in detail other than to mention its place in the time sequence (Fig. 11) of operation.

When the wind tunnel was ready for data, the tuner and scopes were zeroed and triggers set. Then, a reference base pressure was recorded on the wind tunnel data system. Immediately after recording the reference pressure, the heat shield was raised. A switch closure at the top of the heat shield travel started the Fastax camera, and an event timer on the camera started the recording oscillograph. A second event timer started the launch gun and triggered the oscilloscopes. The pressure telemeter performed properly with few exceptions. A number of data runs were lost for a variety of reasons.

Improper timing and poor antenna patterns at the beginning of the test program accounted for many of the lost data. When these problems were solved it was discovered that an unsatisfactory dew point was producing poor data. Other runs were lost because of improper cooling and subsequent damage to the model, battery failure in the telemeter, shorted sensor in the telemeter, and power line loading caused a tuner shift. Most of the data curves of the lost runs indicated that the pressure telemeter functioned properly, but the relationship to the initial reference pressure recorded was lost. The faulty antenna system, of course, did not produce a normal curve (Fig. 12). A total of 134 flights were accomplished with 12 pressure telemeters.

7. Conclusion

On the basis of the results (Ref. 1) (Fig. 13) of the pressure telemetry development program in the hypersonic wind tunnel, the pressure telemeter is considered to be operational and capable of producing valid data.

In future wind tunnel tests the wind tunnel data system will be fully utilized to achieve greater accuracy. Data acquisition in general will be improved. No special instrumentation or training is required to use the pressure telemeter. The capabilities of the telemetry system can be immediately improved by obtaining tuners with wider bandwidths than those used in the development program.

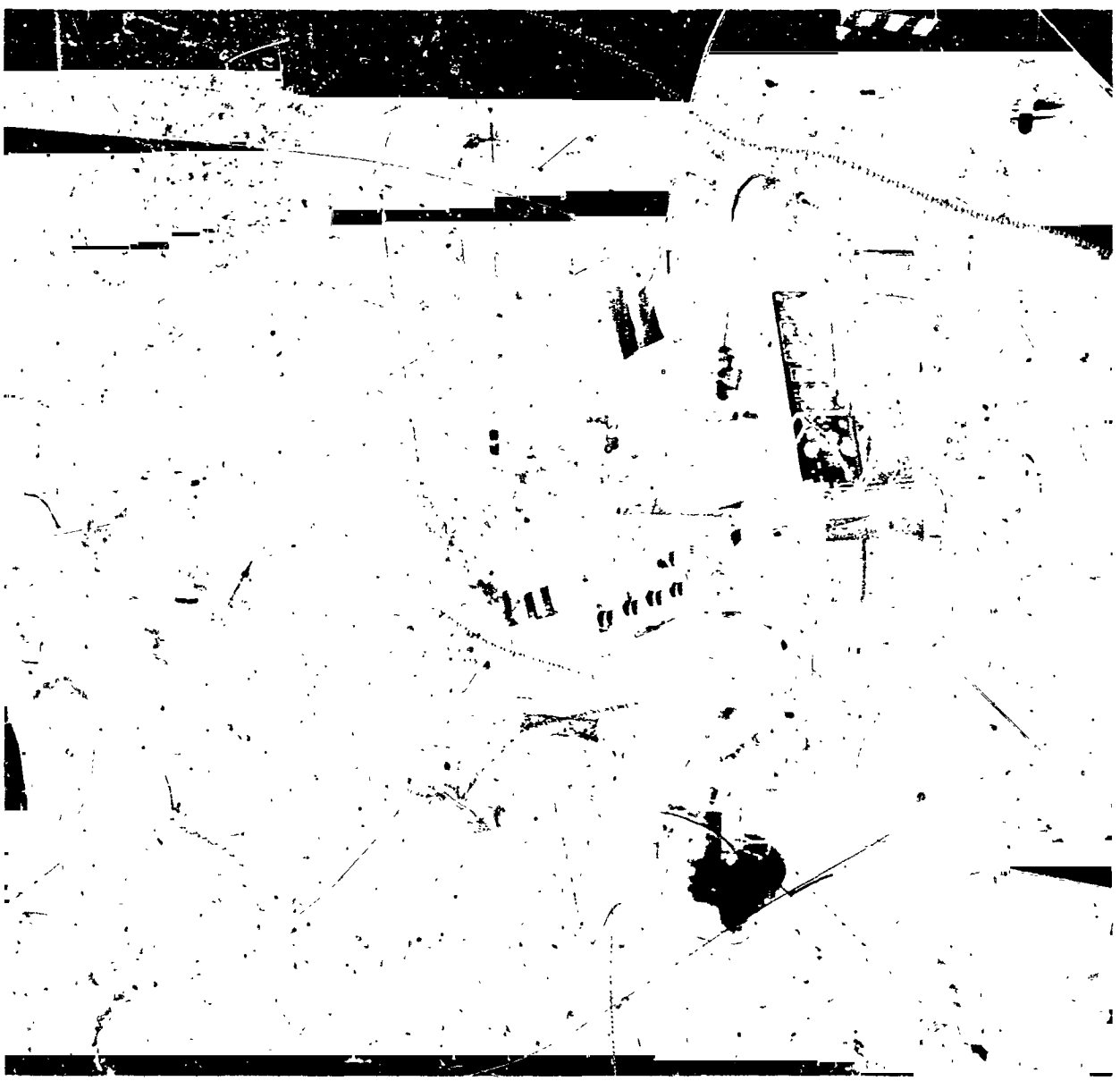

Fig. 10. Tunnel installation of instrumentation

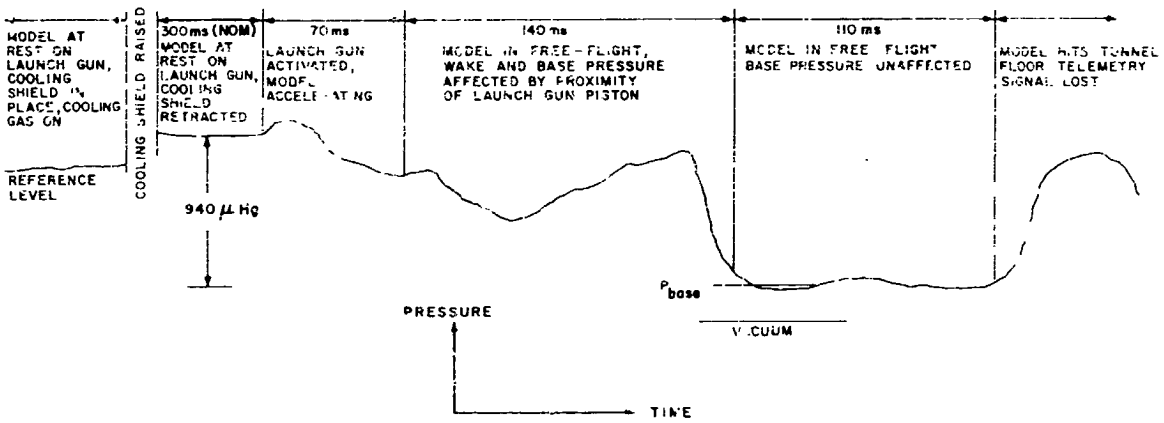

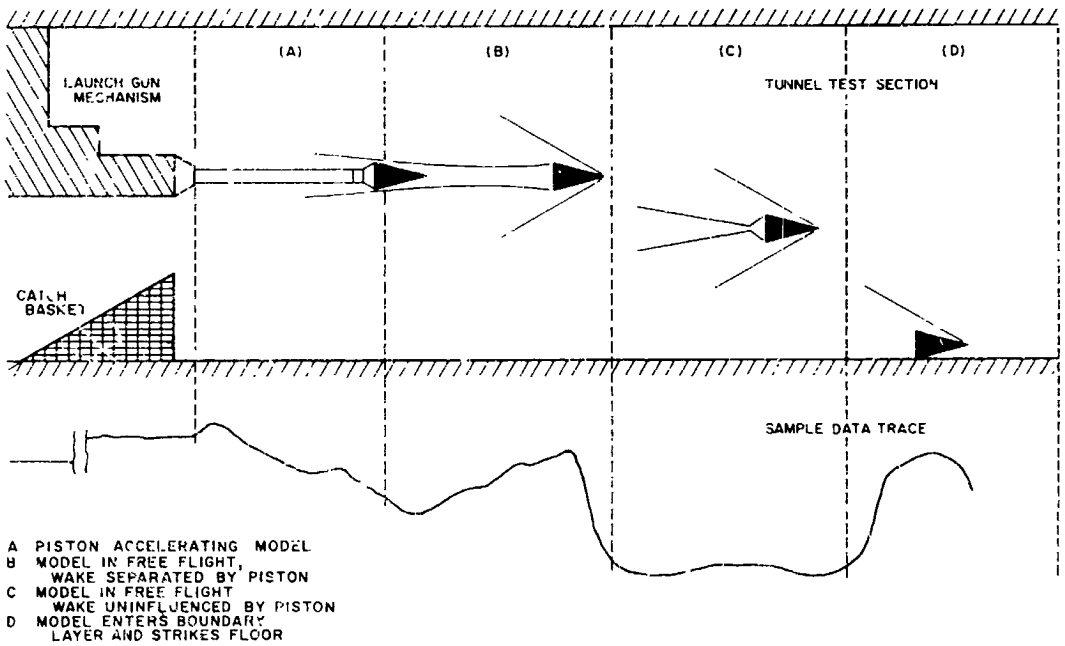

Fig. 11. Examples of timing and model position on data trace

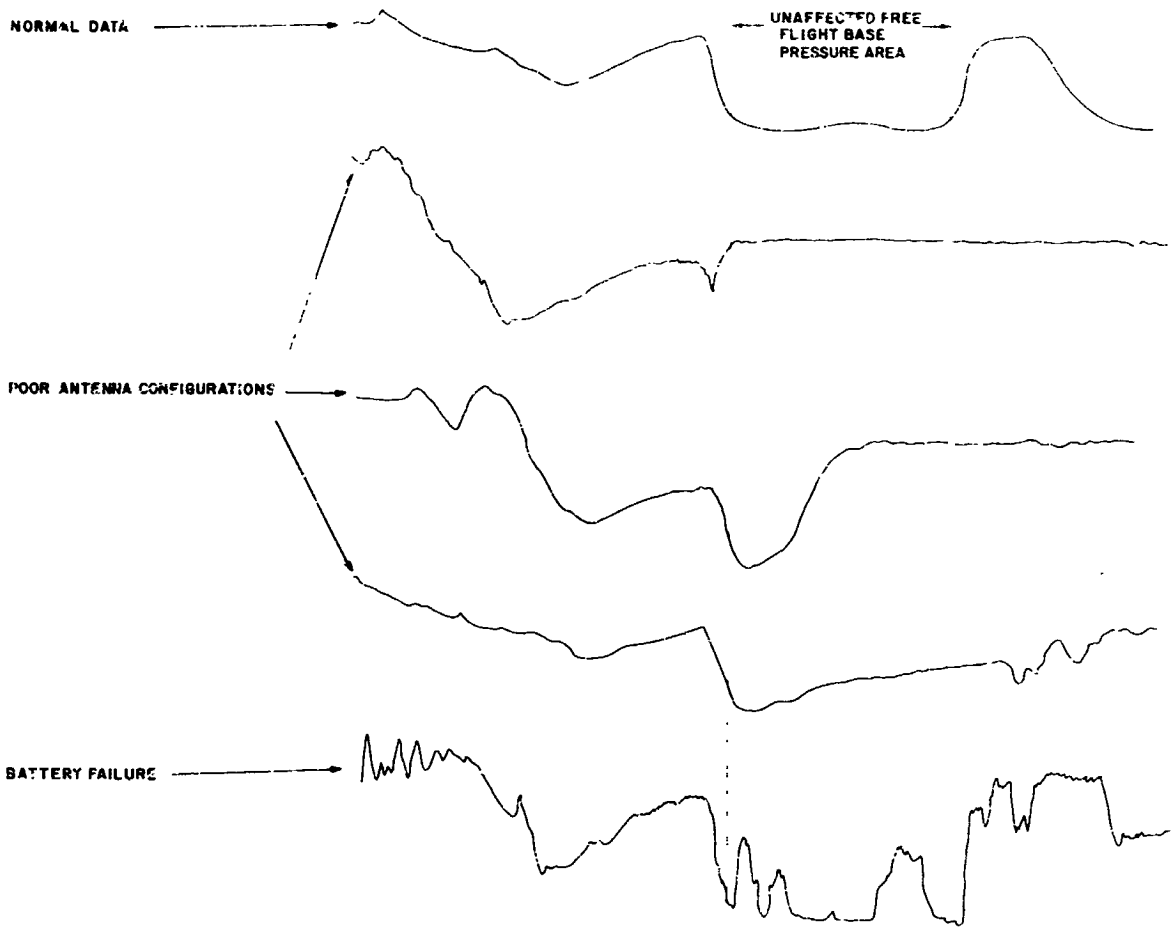

Fig. 12. Examples of good and bad data curves

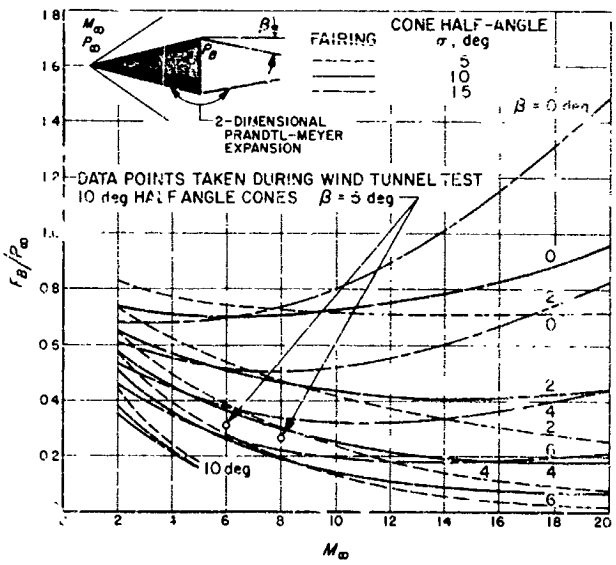

Fig. 13. Ratio of cone base pressure to free stream static

B. A Raster Generator for Use in the Measurement of Shock Velocities

A. P. Horne

1. Introduction

The JPL hypervelocity laboratory uses a raster presentation of time-related data on an oscilloscope as a means of measuring shock speed at various points in an arc-driven shock tube. The reason for the use of a raster presentation, rather than a normal time base, is that it is necessary to measure the time between three pairs of pulses, with high resolution and accuracy, where each pair of pulses is separated by 20 to 30 μsec, and the first pair is separated from the third pair by several hundred microseconds. This presents a conflicting requirement of high resolution and relatively long total display time.

2. Initial Raster and Equipment

The raster generator previously used was a rack-mounted, vacuum tube unit that provided for a display having a maximum resolution of 2.5 μsec/cm. It was used in conjunction with a Tektronix Type 545 oscilloscope. This particular oscilloscope was used because it had the widest bandwidth horizontal deflection amplifier available.

The raster presentation was formed by combining a triangular horizontal deflection voltage, provided by the raster generator, with a linear ramp vertical deflection voltage, provided by the MAIN SWEEP SAWTOOTH output of the oscilloscope.

In addition, z-axis markers were provided by a blocking oscillator. Fig. 14 is a sketch showing the form of the previous raster. Fig 15 is a block diagram of how it is obtained.

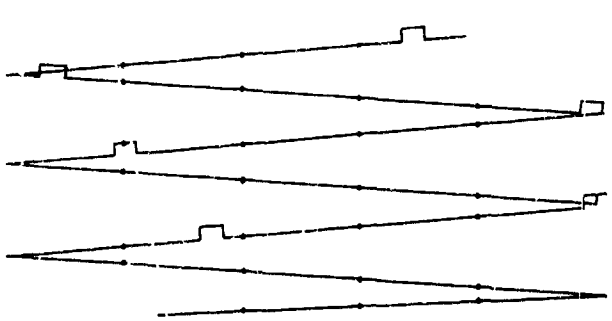

Fig. 14. Original raster, 25μsec/sweep with 5-μsec markers

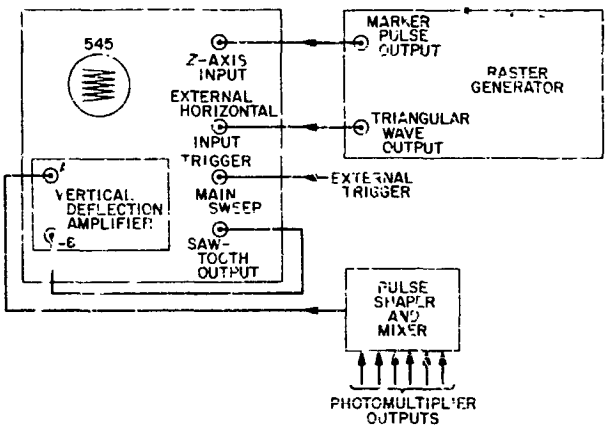

Fig. 15. Block diagram showing how original raster was developed

A raster of this form has several drawbacks. One is that it requires modifications of the oscilloscope it is used with. The reason for these modifications is that the raster generator is external to the oscilloscope and requires connections to internal portions of the oscilloscope. This is an undesirable situation.

Another, and the most important, limitation resulted from the nature of this type of raster. If a longer time must be monitored, as in the case of a slow shock speed, one of two alternatives must be taken. One is to slow the sweep speed down. This will result in a proportional loss of resolution. The other is to reduce the slope of the ramp input to the vertical amplifier of the oscilloscope. The result of doing this is shown in Fig. 16. If a data pulse

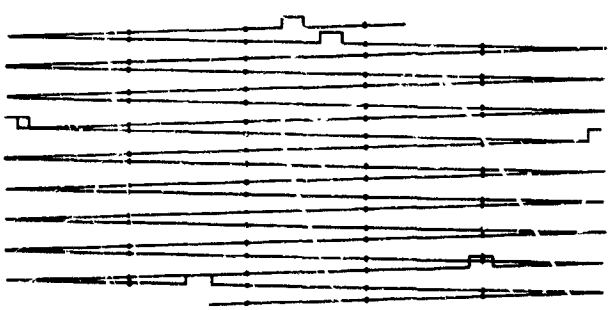

Fig. 16. Original raster, 25μsec/sweep with 5-μsec markers, showing result of reduced slope of ramp input to vertical amplifier of oscilloscope

should occur near the end of a sweep it would be impossible to tell whether the pulse occurred on the upper sweep or on the lower sweep. Obviously, large ambiguities could develop.

A third limitation resulted from the method of introducing the triangle deflection voltage to the horizontal deflection plates of the oscilloscope. The triangular wave output of the raster generator was connected to the EXTERNAL HORIZONTAL INPUT terminal of the oscilloscope. The fastest sweep speed available from the previous unit was 2.5 μsec/cm and was provided by a triangle wave having a period of 50 μsec. To reproduce such a triangle wave with good linearity requires an amplifier having at least a 2-Mc bandwidth. The horizontal deflection amplifier of the Tektronix Type 545 oscilloscope has a bandwidth of approximately 1 Mc. This narrow bandwidth causes turn-around and phase-shift distortion of the triangle waveform resulting in unsatisfactory linearity of the time base. Any attempt to obtain higher resolution with the previous raster by decreasing the period of the triangle wave would be unsuccessful because the 1-Mc bandwidth would introduce excessive distortion. Disregarding this limitation it would still be unsatisfactory to try to obtain better resolution by merely decreasing the period of the triangle wave because it would then be impossible to monitor a sufficiently long time. A factor contributing to this is that the Tektronix Type 545 oscilloscope has only 4-cm vertical deflection. This would limit the maximum number of sweeps per raster to about twenty.

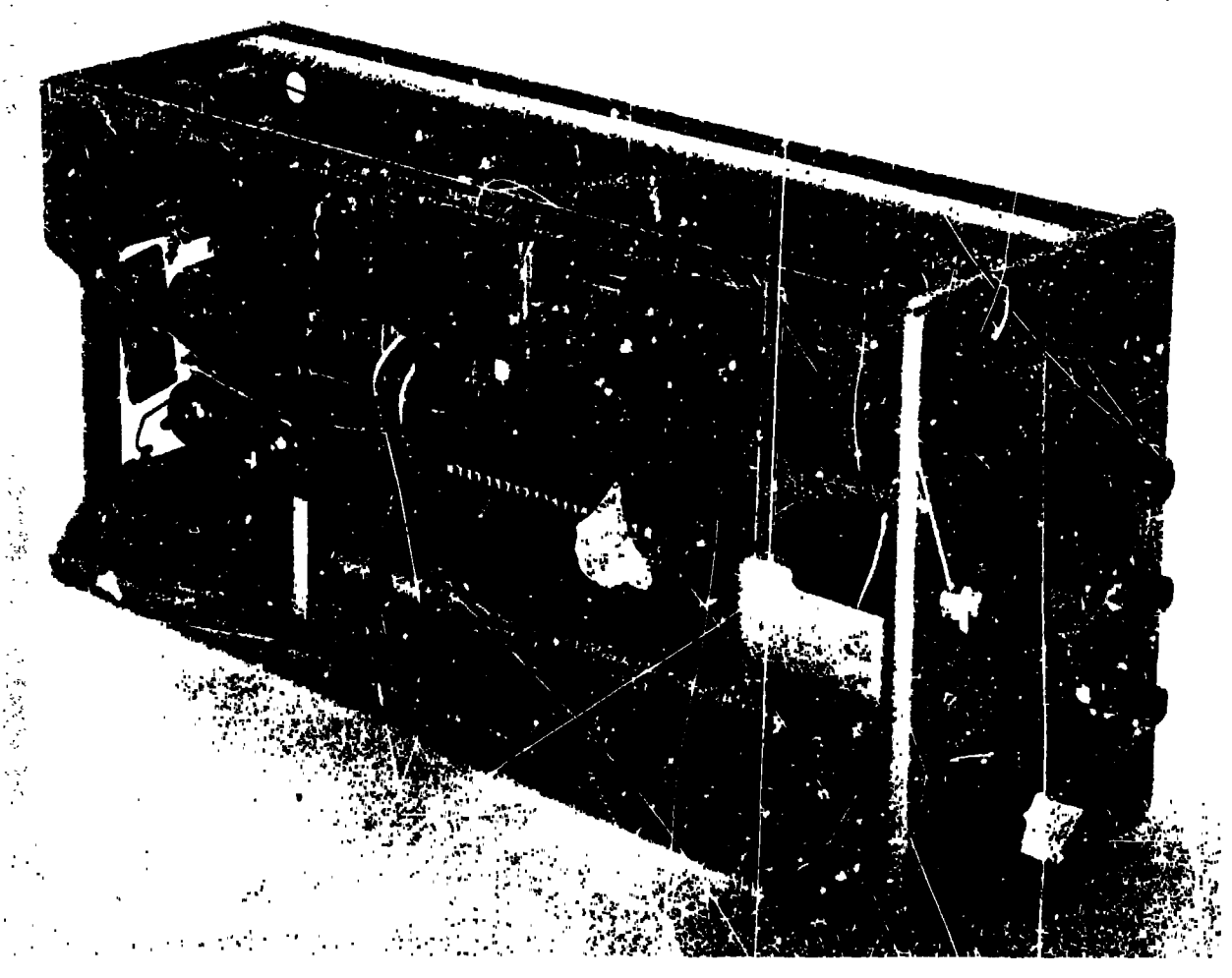

Fig. 17. New raster plug-in unit

3. Modified Raster and Equipment

These limitations are overcome by the system to be described. This system is based upon the use of a Tektronix Type RM561A oscilloscope. Several reasons for choosing this oscilloscope are: 8-cm vertical deflection; direct connection to deflection plates available on plug-in connector; dual-channel vertical amplifier available with less than 35-nanosec rise-time; and requires only 7 in. of rack space.

It was possible to build a complete solid-state raster generator, including a wide-band deflection amplifier, on a blank chassis plug-in unit for a Type RM561A oscilloscope. No modifications to the oscilloscope were necessary because all waveforms needed to produce a complete raster presentation are generated by this new unit (Figs. 17 and 18).

The output amplifier is similar to the output amplifier of the Type 3A1 preamplifier manufactured by Tektronix. It has a bandwidth of 10 Mc. This allows a triangle waveform with a period of only 10 μsec, to be used without introducing turn-around or phase-shift distortion, thus providing a factor-of-five increase in resolution of the time base.

If the vertical deflection were still derived from a linear ramp it would be impossible to display a sufficiently long time base with a sweep speed of 5 μsec/sweep. To eliminate this problem, it was necessary to generate a staircase waveform that is synchronized with the triangle waveform. By replacing the linear ramp with the staircase, a raster similar to Fig. 19 is formed. (In this unit the markers are vertical pips rather than the z-axis modulation used in the previous system.)

It is the use of a staircase waveform that makes this unit unique. The staircase has a rise-time of only 40 nanosec. Its amplitude is fixed, so the gain of the vertical amplifier is varied to control the vertical distance between sweeps. The gain can be reduced to provide as many as eighty sweeps, spaced 1 mm, or increased to provide as few as four sweeps, spaced 2 cm. It is the resolution of the cathode ray tube that limits the maximum number of sweeps to eighty.

To make the unit more versatile, five sweep rates are provided. Each one is derived from a crystal controlled oscillator with a stability of ±0.003% over the temperature range of 20 to 60°C. The feedback networks and crystals are switched to allow the use of one oscillator instead of one crystal oscillator and a series of frequency dividers, providing a large reduction in parts count.

The five sweep rates are

Sweep rate, μsec	Marker interval, μsec
5	1
10	2
20	4
50	10
100	20

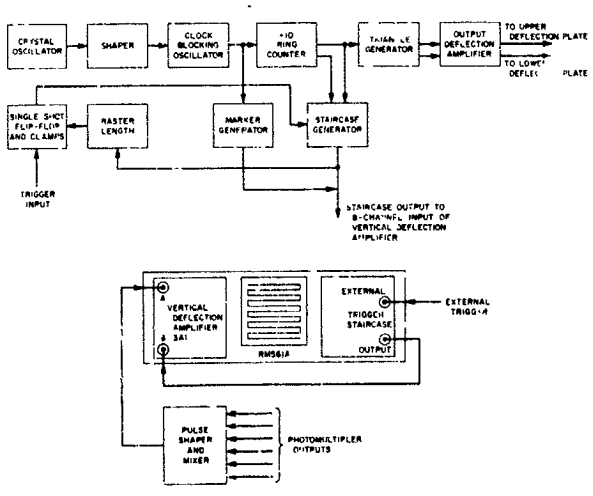

Fig. 18. Block diagram showing how new raster was developed

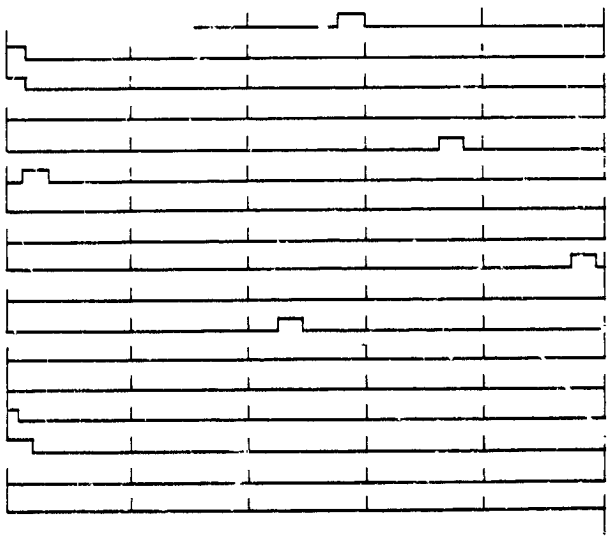

Fig. 19. New raster, 20μsec/sweep with 4-μsec markers

These rates allow monitoring of from 400 μsec, with a resolution of ½ μsec/cm on the fastest sweep rate, to 8 msec, with a resolution of 10 μsec/cm on the slowest sweep rate. Nonlinearity of the generated time-base is less than 0.6% for any sweep rate.

Since the event being monitored is of a transient nature, several additional features were incorporated into this unit. Provisions were made to externally trigger the raster in a "single shot" mode. This is necessary because the display must be photographed for analysis and multiple rasters on one photo would be undesirable. A raster length circuit is also included for a similar reason. If the display is allowed to deflect off-screen, flare-back occurs and fogs the photograph. The trigger can be armed remotely, as well as locally. Also, there are provisions for remote indication of the ready condition.

References

1. Welton, J. T., *Free Flight Telemetry Testing in the Jet Propulsion Laboratory Wind Tunnels*, Technical Report No. 32-775, Jet Propulsion Laboratory, Pasadena, California (to be published in June 1965).
2. Electrolab Electronics Corporation, EXI Division, Los Angeles, California.
3. Dayman, Bain Jr., *Optical Free-Flight Wake Studies*, Technical Report No. 32-364, November 1, 1962.
4. McDevitt, J. B., Harrison, D. R., Lockman, W. K., *Measurement of Pressures and Heat Transfer by FM Telemetry from Free-Flying Models in Hypersonic Tunnel Streams*, NASA, Ames Research Center, Moffett Field, California. Presented at the First International Congress on Instrumentation in Aerospace Simulation Facilities, Paris, 28 and 29 September, 1964.
5. Holway, H. P., Herrera, J. G., Dayman, B. Jr., *A Pneumatic Model Launcher for Free-Flight Testing in a Conventional Wind Tunnel*, Technical Memorandum No. 33-177, Jet Propulsion Laboratory, July 30, 1964.

PROPULSION DIVISION

XII. Solid Propellant Engineering

A. Arc-Imaging Furnace Ignition Test Facility

L. Strand

Solid propellant ignition test programs are being carried on with a newly operational ignition test facility. The system is basically an ignition research model of the A. D. Little arc-imaging furnace. This furnace combines a high-intensity radiation source with an optical system for re-imaging the radiant energy onto a propellant sample. The radiation source is a 10-kw (normal power level) to 20-kw (maximum power level) carbon arc struck between two 10-mm carbon rods. The tail flame plasma is concentrated by a ring of impinging air jets located on the anode holder (Fig. 1). The concentration of the tail flame allows the arc to be focused at the re-imaging source. A magnetic field surrounding the anode stabilizes the arc by rotating the plasma stream. During operation of the furnace, the anode and cathode are each continuously fed by a two-speed motor so as to maintain a constant arc position and arc current. The position of the anode is optically controlled by a photocell sensor that detects the magnitude of the arc illumination. The output of this sensor controls a relay which, in turn, calls for fast or slow feed operation of the feed motor. The cathode feed rate is governed by the magnitude of the arc current across the electrodes.

Fig. 2 is a schematic of the re-imaging optical system. The radiant energy of the arc is collected on a 21-in. D ellipsoidal mirror projected onto a similar mirror, and then re-imaged on the propellant sample. An electronically controlled camera type shutter is located at the intermediate focus position. This shutter has opening and closing times of approximately 6 msec. When the shutter is closed, a douser protects the shutter from the arc. The douser opens and closes immediately prior to and after the opening and closing of the shutter. Attenuation screens of descending mesh size are placed between the douser and the shutter to control the intensity of the re-imaged radiation. Maximum re-imaged radiation densities of the furnace averaged over a 9.5-mm diameter image are approximately 150 cal/cm²-sec at the 150-amp normal arc current level and 240 cal/cm²-sec at the 300-amp maximum arc current level.

Fig. 1. Anode and cathode and holders

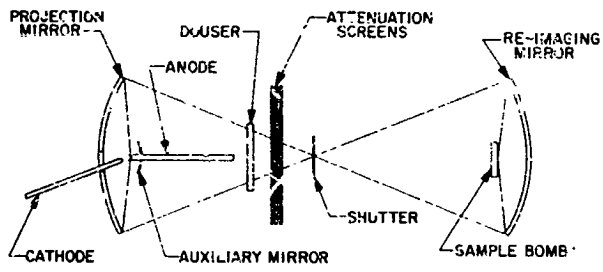

Fig. 2. Arc-imaging furnace optical system

1. Ignition Test Equipment

The ignition test equipment for this furnace, including the previously mentioned douser and shutter, were fabricated from United Technology Center supplied designs. Fig. 3 shows, left to right, the 0.5-in. D by 0.100-in. thick propellant sample used in ignition testing, the back side of a sample holder with a propellant sample in place, the copper cup calorimeter used to measure the intensity of the radiation, and one of the 0.5-in. ID by 3-in. long Lucite tubes that enclose each of the five sample holders and the calorimeter in the multiple bomb test assembly. Fig. 4 shows five sample holders and the calorimeter mounted in the upper plate of the bomb assembly, and Fig. 5 shows the six enclosure tubes mounted on the plate. The multiple bomb test assembly and sample positioner are shown in Fig. 6. The re-imaging mirror is also shown to the right of the assembly. Vernier control of the sample position is provided in three axial directions. The assembly can be pressurized and purged with nitrogen, oxygen or a combination of both, and can also be vented to an evacuated surge tank. Succeeding bombs are brought into test position by manually turning the bomb assembly.

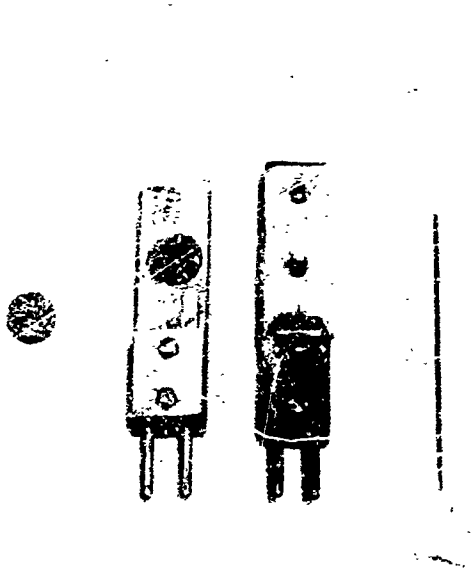

Fig. 3. Propellant sample holder and calorimeter

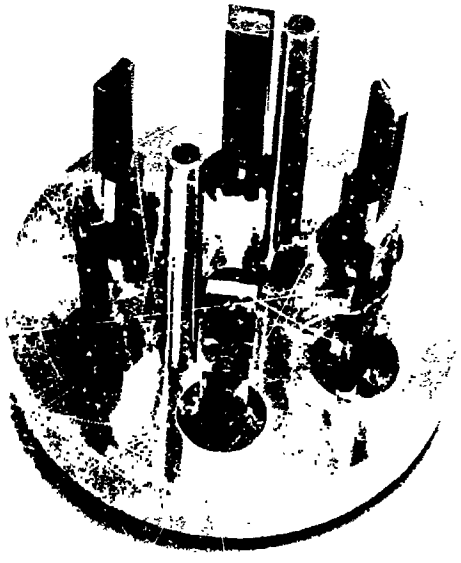

Fig. 4. Mounted propellant sample holders

One of the two photodiodes presently used to view the surface of the propellant sample under test is shown mounted to the right of the bomb assembly in Fig. 6. This rear diode views the sample from a normal direction. The second diode views across the front surface of the sample and is hidden by the bomb assembly in Fig. 6.

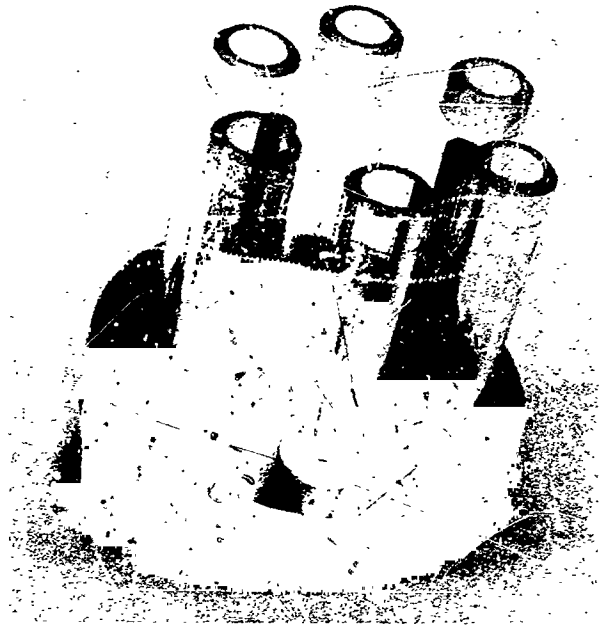

Fig. 5. Mounted enclosure tubes

A third diode is shown mounted on the upper left-hand corner of the sample positioner. This diode is aligned on the optical centerline of the furnace passing through the shutter. The electrical signal of this diode is used to determine the open time of the shutter and, therefore, the propellant sample irradiation time.

The calorimeter used is of the thermal mass, or slope, type (Ref. 1). The receiver is a spherical copper cup with an inner radius of 0.55 cm and an inner height of 0.15 cm. The inner surface is blackened with electro-deposited platinum black. A 0.1-mm D copper-Constantan thermocouple is silver-soldered to the back side of the receiver near one edge to measure the temperature rise. The receiver is mounted on Bakelite posts for thermal insulation. An aperture shield of silver-plated copper sheet, 0.025 cm thick, is mounted in front of the concave surface to limit the intercepted area of the beam of radiant energy. The edges of the 0.135-cm diameter aperture hole have been honed sharp. The shield is mounted 0.025 cm from the rim of the receiver with the line connecting the center of the receiver and the center of the aperture parallel to the optical axis of the system. The physical constants of the copper receiver are

m = mass = 0.30 g

C_p = specific heat = 0.093 cal/g-°C

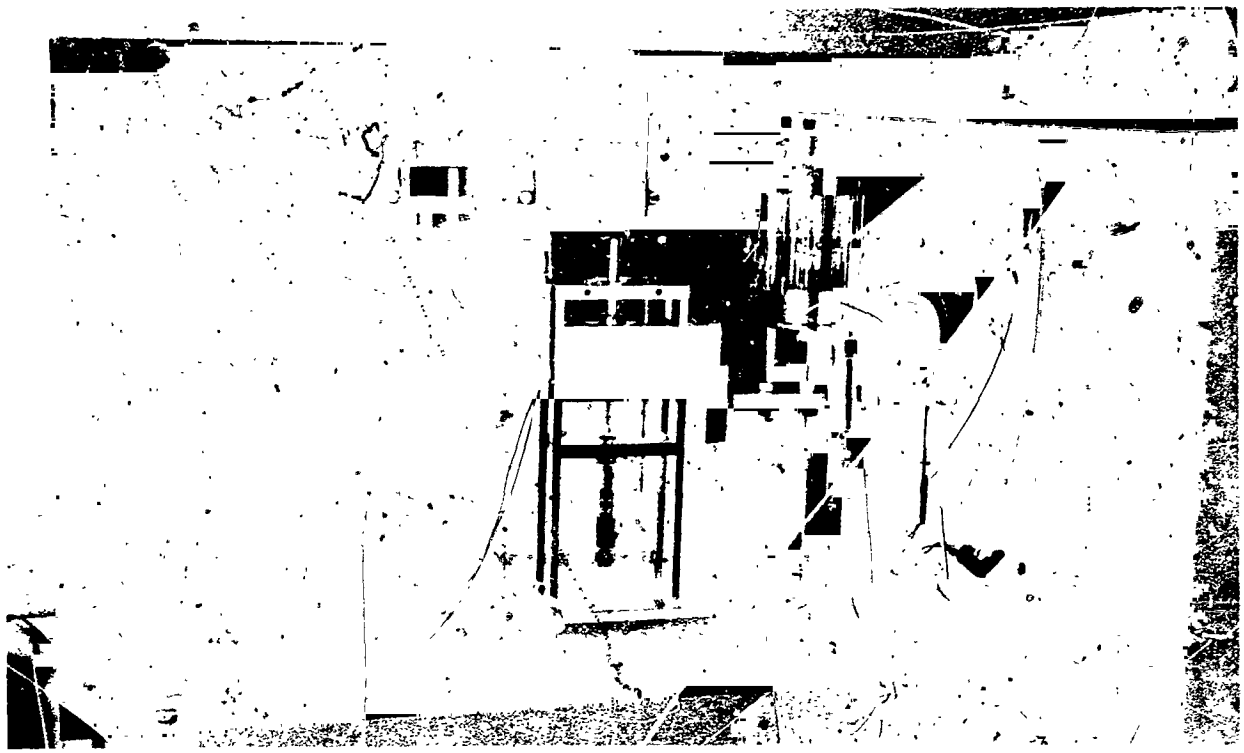

Fig. 6. Multiple bomb test assembly and sample positioner

Neglecting heat losses, if the gradient across the receiver thickness is small, and if the difference between the temperature measured at the edge of the receiver and the average temperature is small, the average heat flux density I_a at the aperture over an aperture area A_a is given over any time interval Δt by

$$I_a = \frac{m C_p}{a A_a}\left(\frac{\Delta T}{\Delta t}\right) \quad (1)$$

where ΔT is the increase of average temperature of the receiver and a is the receiver absorptivity (assumed equal to 1). Knowing the receiver physical constants and the aperture area, the heat-flux density of a pulse of radiant energy is obtained by measuring the slope of the calorimeter temperature-time curve on an oscillograph. In Ref. 1 it is shown that the assumptions of negligible heat loss and uniform receiver temperature are valid under practical test conditions.

2. Control System

Fig. 7 is an over-all view of the arc-imaging furnace installation. The arc housing unit, shown close-up in Fig. 8, is located at the far left of Fig. 7. The housing holds the electrodes, their feed systems, blowers, the projection mirror, and the douser. All controls for starting and striking the arc, correcting electrode positions, and stopping the arc are contained on the housing. Both housing doors have interlocks to shut off the arc if they are opened during operation of the arc. The panel below and to the left of the housing contains the main power switch and switches for the cooling water pump (located below the housing) and the blower.

Located to the right of the arc housing is the housing for the shutter, sample positioner and multiple test bomb assembly, and the re-imaging mirror.

The environmental system control panel is mounted to the right of the arc imaging furnace. Solenoid valves are used throughout in the gas lines.

The instrumentation control chassis (Fig. 9) is located in the console to the right of the environmental system control panel. All instrumentation lines have been wired into the adjacent instrumentation room amplifier-recorder system (Fig. 10) pending completion of the arc furnace recorder system. The chassis contains the circuitry for controlling the douser, shutter, and oscillograph operations and the mechanical and electronic timer circuits.

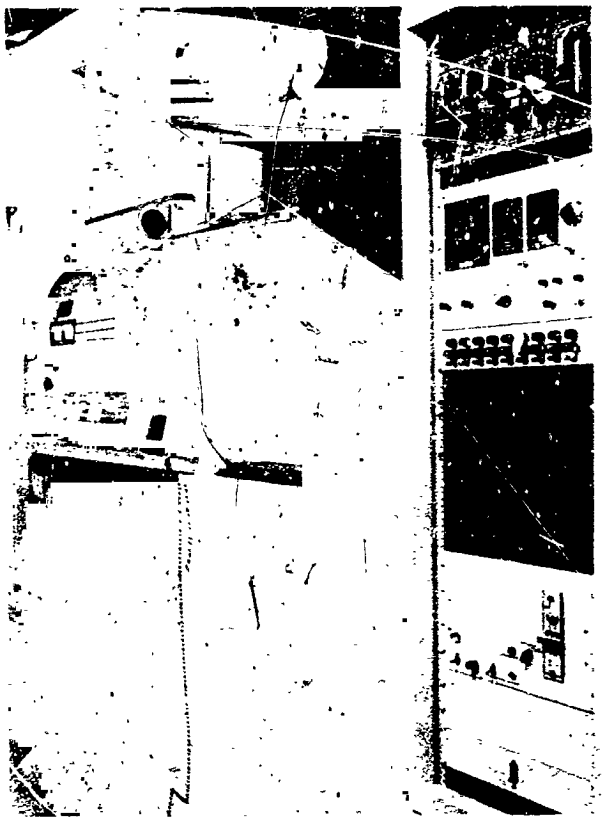

Fig. 7. Arc-imaging furnace installation

The timer circuits allow accurate control of the radiation exposure times. The electronic timer has two ranges: 15 to 100 msec and 100 to 500 msec. The mechanical (manual) timers are used for exposure ranges of 0.5 to 1 sec and 1 to 15 sec. Three other modes of exposure duration can be used:

(1) Manual, in which the douser and shutter are closed by pushing the remote control switch shown wrapped around the bomb pressure gages in Fig. 7.

(2) Light, in which termination of radiation occurs automatically when the photodiodes detect increased radiation from the ignition process.

(3) Fuse, in which the burning through of a fuse wire mounted across the front of the propellant sample terminates the exposure.

Pushing the *close shutter* switch will terminate exposure under any operation mode. The shutter may be opened without going through the test sequence by pushing the *open shutter* switch. The test sequence is initiated by pushing the *operate* switch. In sequence the recorder starts, the douser and shutter open and then close (the period of exposure is dependent upon which termination mode the stop mode switch is set), and the recorder stops. As a means of protecting the shutter, the arc current is automatically stopped if the douser should fail to close following closure of the shutter.

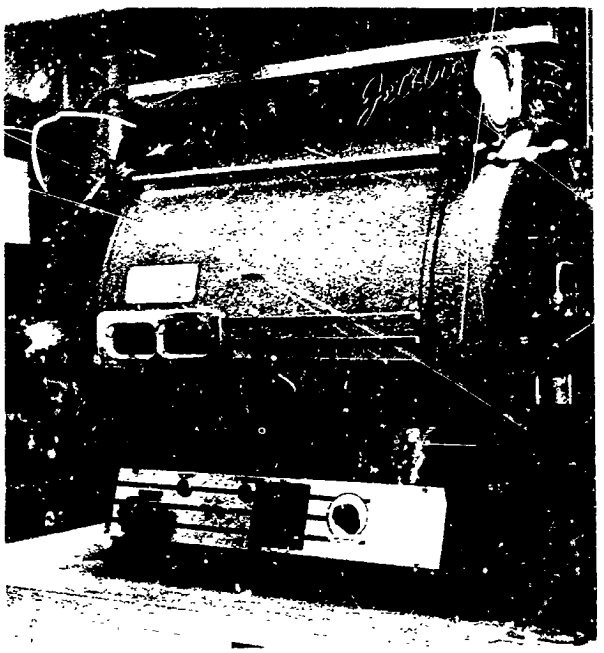

Fig. 8. Arc housing unit

3. Calorimeter Calibration and Focal Volume Mapping

It is seen from Eq. (1) that, knowing the physical constants of the copper receiver and the aperture area, calorimeter calibration consists of determining the inches of deflection of the oscillograph per degree of receiver temperature rise. This was done by two different methods. Method 1 consisted of placing the calorimeter with aperture removed into an oven and raising the temperature to 161 ±1°F. The increased output of the oscillograph was recorded for each of the usable amplifier gain settings and oscillograph sensitivity values. Then °C/in. deflection was computed for each amplification used. The second method consisted of connecting a millivolt source of 0.25% estimated accuracy to the calorimeter leadwire. For each oscillograph amplification, inputs of 0, 0.40, 0.80, 1.00, 1.20, 1.60, and 2.00 mv were imposed on the recording system. Millivolts input per inch of recorder deflection was calculated for each millivolt input. The computed average of the values for each amplification was multiplied by the °C/mv constant for a copper-Constantan thermocouple (20 to 50°C) yielding °C/in.

Fig. 9. Instrumentation control chassis

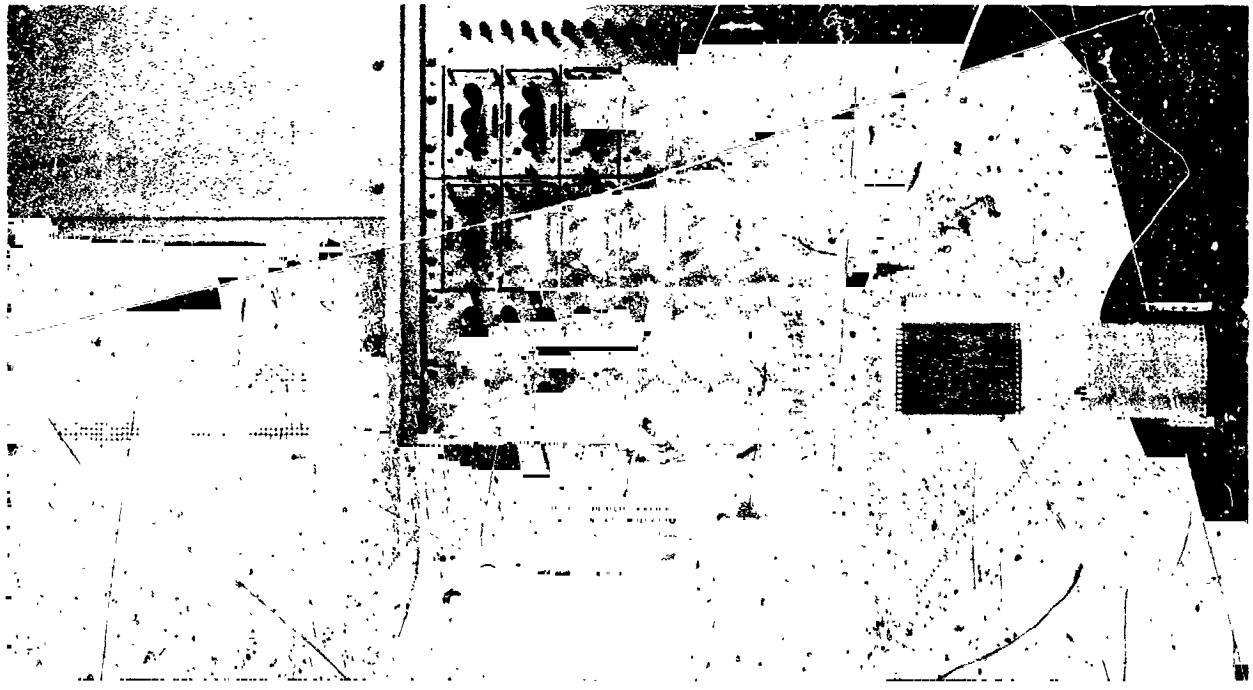

Fig. 10. Amplifier recorder system

deflection. The average difference in the calibration values obtained using the two methods was less than 0.75%.

The re-imaged radiant energy is nearly identical in shape to the arc source itself. It is, therefore, not a point source, but a volume of energy called the focal volume. The focal volume center is the region of maximum energy. The flux profiles in the axial, horizontal, and vertical directions were determined by traversing the focal volume with a water-cooled CFR-1A circular foil radiometer. The electrical output of the copper-Constantan differential thermocouple in this instrument is linearly proportional to the incident radiant flux density and is independent of the temperature of the cooling water. The calorimeter's small 0.9-mm diameter receiving area and 10-msec time constant allow it to measure local flux densities within the focal volume. In addition to the calibration provided by the manufacturer, the calibration constant (cal/cm²-sec per millivolt output) for the JPL instrument was determined by the U.S. Naval Radiological Defense Laboratory.

Fig. 11 is a graph of the flux density divided by the maximum flux density versus distance from the center of the focal volume along the three axes. The physical position of the center point will shift slightly with the small excursions of the electrodes from their mean position. For accurate ignition testing, the sample positioner must be set so that the calorimeter aperture is centered to measure the radiant flux density at the focal volume center. Propellant ignition delay depends not upon the magnitude of the average flux incident upon the propellant surface, but upon the maximum flux intensity incident.

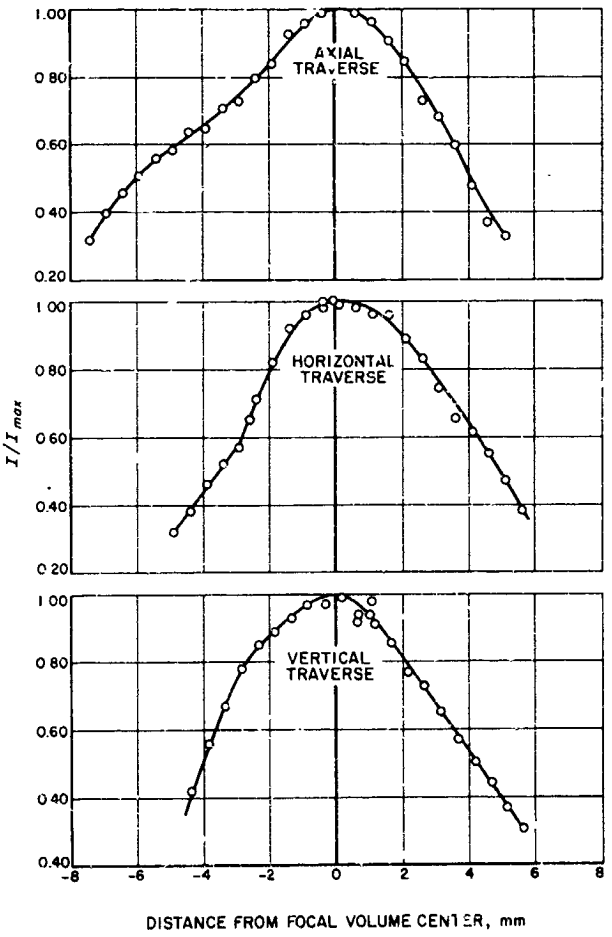

Fig. 11. Focal volume flux profiles

4. Test Procedure and Results

The ignition delay time of a propellant at a given heat flux level and chamber pressure is defined as the minimum irradiation time required to initiate self-sustained combustion, i.e., ignition. A propellant has been characterized as to its ignitability when a log–log plot of ignition delay time versus heat flux has been determined experimentally for the chamber pressure of interest. Fig. 12

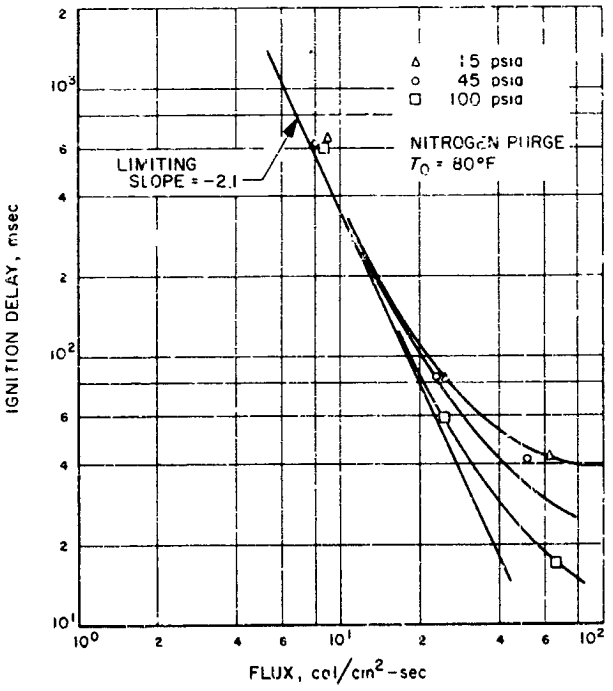

Fig. 12. Ignition delay versus flux for NOTS A-87 composite propellant

shows such a characterization for a Naval Ordnance Test Station composite solid propellant, A-87. It was determined by JPL as a participant in the Interlaboratory Solid Propellant Ignition Exchange Program.

The following standard procedure has been arrived at for determining the ignition delay time at a given nominal flux intensity level. Attenuation screens are inserted in the furnace to attenuate the radiation to the desired level at the re-imaging focus. The furnace has been previously optically aligned (mirrors positioned) so that the re-imaged focus lies on the furnace optical axis. Electrodes are placed in their holders and positioned to their proper spacing. Five loaded propellant sample holders and the bomb calorimeter are inserted into the upper plate of the multiple bomb, and the bomb is assembled with the calorimeter in test position. After measuring the barometric pressure, instrumentation and valve power are switched on and the bomb gage pressure is adjusted to the desired value. The instrumentation panel stop mode switch is set on *electronic* mode and the electronic timer is set to the correct calorimeter irradiation time interval for the irradiation flux level. The interval must be long enough to allow the slope of the oscillograph calorimeter trace to be accurately measured, but short enough to avoid damaging the calorimeter. All furnace switches are turned on, and the arc is struck. When the arc is operating stably, as indicated by the on-and-off flickering of the electrode feed lights (fast and slow drive speeds) and the stabilizing of the arc current at the correct level, the test sequence is initiated. At the conclusion of the test sequence the arc is shut off to avoid overheating and damaging the douser. The multiple test bomb is rotated to the first propellant sample, the instrumentation panel stop mode switch set to the *timer* or *electronic* mode, the respective timer set to the desired irradiation time interval, and the procedure repeated. If ignition occurs, a shorter irradiation time is chosen, and the test procedure is repeated with the second propellant sample. Testing is continued at successively shorter irradiation time intervals until no ignition occurs. When all five propellant samples in the multiple bomb have been used in a test, the radiation intensity is again measured with the calorimeter. The multiple bomb is then disassembled, loaded with five new samples, reassembled, and testing is resumed. Testing is continued at decreasing irradiation time intervals until the oscillograph traces of the two photodiodes viewing the propellant sample show that ignition occurs just following closure of the shutter (Fig. 13). A test is then run at a slightly lower irradiation time interval. If no ignition occurs, the arc is restruck, the intensity is measured with the calorimeter, two additional tests are run in rapid succession at the previous time

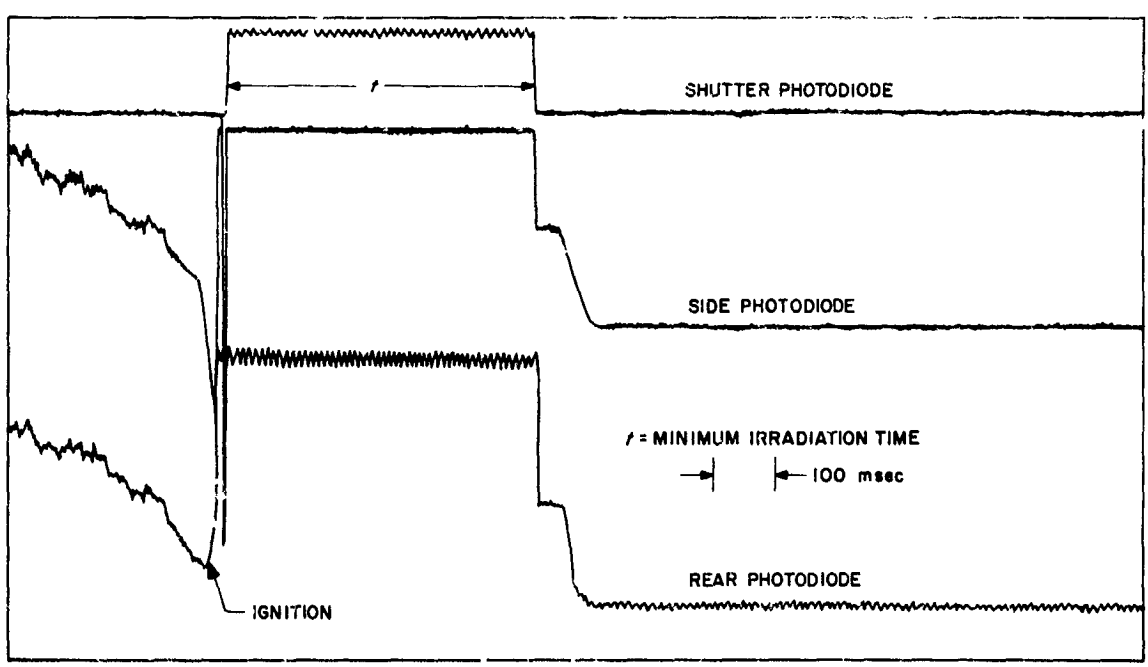

Fig. 13. Oscillograph trace of arc-imaging furnace ignition test

interval to verify it as the minimum irradiation time for ignition (ignition delay time), the intensity remeasured with the calorimeter, and the arc shut off.

With increasing experience it is believed that this arc-imaging furnace installation will become an increasingly more useful research tool.

Reference

1. Beyer, R. B., McCulley, L., and Evens, M. W., "Measurement of Energy Flux Density Distribution in the Focus of an Arc Image Furnace," *Applied Optics*, Vol. 3, No. 1, January 1964.

XIII. Polymer Research

A. Some Characteristics of a Miniature Stress Transducer

A. San Miguel and R. H. Silver

A miniature stress transducer has been developed at JPL (Refs. 1 2) to measure the internal stress fields in solid propellant. Work is currently under way to establish the general characteristics as well as to define the realm of practical application of this transducer.

The concept of directly measuring individual principal stresses within a material is relatively novel. To qualify a device to accomplish this task, it must be demonstrated that the advantages to its use outweigh the inherent disadvantages. Basic questions that must satisfactorily be resolved evolve from the inclusion problem, the packaging function, temperature interaction; and finally, whether stress or strain should be considered as the argument of the transducer output function.

1. The Inclusion Problem

The true inclusion problem consists of determining the disturbing influence of a relatively rigid particle in an otherwise continuous stress field. The importance of the inclusion problem usually centers around the crack initiation phenomena, which eventually manifests itself in macro-structural material failure. Our interest in the inclusion problem will be limited to an attempt to assess the interaction between the miniature stress transducer and the surrounding elastomeric medium, and the influence of one transducer on another when three are employed in a rosette configuration. Fig. 1 illustrates the nominal stress raisers created by the rigid transducer rosette which is embedded in a low modulus polyurethane binder, and which, it may be seen, does create a perturbation in the stress field. Further studies are currently under way to quantize the inclusion effect by photoelastic stress-freezing, a phenomenon which allows a three-dimensional stress analysis analogous to classical two-dimensional photoelastic stress analysis.

2. The Packaging Function

The sensing element of the miniature stress transducer is a piezoresistive *p*-type silicon splinter presumably having a (111) crystallographic orientation. This splinter is commercially available with dimensions of approximately 0.0005 × 0.005 in. rectangular cross-section and 0.040 in. over all length. This element is quite fragile in itself. Hence one objective of packaging is to protect the splinter from directly applied environmental loading. A second objective of the packaging is to limit the dimensional changes of the splinter, thereby greatly increasing the range of stress which may be applied to the element

Fig. 1. Embedded stress transducer rosette

without fracturing it. A third objective of packaging is to provide an electrical contact, as well as an application flexibility for bracing and recording wires.

The phenomenon of piezoresistance allows a great degree of freedom with regard to packaging design. Essentially, one stress-sensitive axis of the splinter is packaged so that it is aligned with the stress axis to be measured. A synopsis of the pertinent construction and theory is found in Ref. 2.

The general constitutive equations for silicon (Eq. 2 of Ref. 2) are based on the assumption that commercially available silicon splinters belong to a cubic class such as a diamond cubic and zinc-blende structure. It can be shown (Ref. 5) that a maximum longitudinal piezoresistive coefficient can be obtained in silicon along the (111) direction. A pertinent relationship to consider (Ref. 6) is what may be called the "General-Orientation-Uniaxial" Piezoresistance Design Equation. If the conditions that

$$i'_2 = i'_3 = \tau'_{23} (= \sigma_{23}) = \tau'_{13} (= \sigma_{13}) = \tau'_{12} (= \sigma_{12}) = E'_2 = E'_3 = 0$$

(Eq. 2 of Ref. 2) are imposed on a splinter in the (111) orientation, then

$$\frac{E'_1}{i'_1 \rho_0} = \frac{\rho}{\rho_0} = 1 + \pi'_{11}\sigma_1 + \pi'_{12}\sigma_2 + \pi'_{13}\sigma_3 \qquad (1)$$

or

$$\frac{\Delta\rho}{\rho_0} = \pi'_{11}\sigma_1 + \pi'_{12}\sigma_2 + \pi'_{13}\sigma_3$$

where

$$\pi'_{11} = \pi_{11} - 2(\pi_{11} - \pi_{12} - \pi_{44}) \times [(l_1 m_1)^2 + (m_1 n_1)^2 + (n_1 l_1)^2]$$

$$\pi'_{12} = \pi'_{13} = \pi_{12} + (\pi_{11} - \pi_{12} - \pi_{44}) \times [(l_1 l_2)^2 + (m_1 m_2)^2 + (n_1 n_2)^2] \qquad (2)$$

Here

E'_1 = the electric field component along the length of the splinter

i'_1 = the current component along the length of the splinter

$\Delta\rho$ = resistivity change along the length of the splinter

π'_{11} = resistivity change along the splinter length as a result of a longitudinal stress on the splinter

π'_{12}, π'_{13} = resistivity change along the splinter length as a result of a lateral stress on the splinter

σ_1 = longitudinal stress on splinter

σ_2, σ_3 = lateral stress on splinter

τ'_{23}, τ'_{13} = shear stress on splinter

Eq. (2) indicates that if the crystallographic piezoresistive coefficients are known, as well as the splinter orientation, then a set of coefficients pertinent to a given splinter may be evaluated. At present the crystallographic coefficients for the p-type silicon splinters used in this study are unknown. However, the direction cosines l_1, m_1, n_1, which commercial sources strive for (assuming that silicon strain gages of maximum sensitivity are being manufactured), are (referring to Fig. 2) given in Table 1.

The angles and rotations of Fig. 2 can best be understood by a description of the operations used to perform a transformation from axes (x,y,z) to axes (x',y',z'): (1) Start

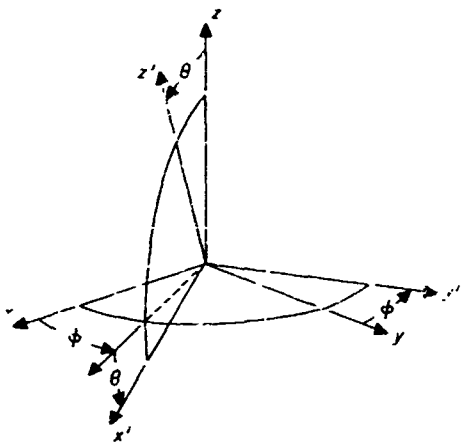

Fig. 2. Transformation from axes (x, y, z) to axes (x', y', z')

with the axes coinciding, x' with x, y' with y, and z' with z. Rotate the primed axes through an angle ϕ about the z axis. This determines the final position of y', which remains in the (x,y) plane at an angle ϕ from y. (2) Rotate the primed axes through an angle θ about the y' axis, while keeping y' fixed. The z' axis is then at an angle θ with the z axis. (Note that x', z and z' are all in the same plane, since all are perpendicular to y'.) The final angle between x and x' is $\cos^{-1}(\cos\theta\cos\phi)$.

It is obvious that the direction cosines of the x' axis along (111) are

$$l_1 = \cos\theta\cos\phi = \sqrt{\frac{1}{3}}$$

$$m_1 = \cos\theta\sin\phi = \sqrt{\frac{1}{3}} \qquad (3)$$

$$n_1 = -\sin\theta = -\sqrt{\frac{1}{3}}$$

Further analysis (Ref. 5) shows that

$$\cos^2\phi = \sin^2\phi = \frac{1}{2}$$

Hence

$$\cos^2\theta = \frac{2}{3}\ ;\ \sin^2\theta = \frac{1}{3} \qquad (4$$

Having established what the direction cosines *should* b for commercially available silicon splinters, the transduce packaging arrangements can be set

The applicability of the above theory to the stress trans ducer design can be illustrated in the following manner In Ref. 5 the values for a particular p-type silicon ar listed as

$$\rho = 7.8\ \text{ohm-cm},\ \pi_{11} = 6.6 \times 10^{-12}\ \text{dynes/cm}^2,\ \pi_{12}$$

$$= 1.1 \times 10^{-12}\ \text{dynes/cm}^2$$

and $\pi_{44} = 138.1 \times 10^{-12}$ dynes/cm^2. These values were incorrectly stated in Ref. 2, since they were obtained from Ref. 7, which is in error. The results of either Ref. 2 or 7 were not affected by the error. In any event, using the values of direction cosines in Table 1 together with the above listed π_{ij}'s, the oriented π'_{ij}'s can be computed and are found to be

$$\pi'_{11} = 93.6 \times 10^{-12}\ \text{dynes/cm}^2,\ \pi'_{12} = \pi'_{13}$$

$$= -44.5 \times 10^{-12}\ \text{dynes/cm}^2$$

Fig. 3 illustrates data obtained by direct "dead-weight" loading, both in the longitudinal and lateral directions of the transducer. This experiment consists of applying a load directly to the transducer. Needless to say, the data are relatively consistent, despite the inherent experimental difficulties encountered. A pertinent observation is that

$$\left(\frac{\pi'_{12}}{\pi'_{11}}\right)\ \text{experimental} = -0.45 \qquad \text{as compared to}$$

$$\left(\frac{\pi'_{12}}{\pi'_{11}}\right)\ \text{theoretical} = -0.48$$

This comparison indicates that the direction of this study program is a reasonable one.

Table 1. Direction cosines for maximum longitudinal sensitivity along (111)

	x	y	z	x	y	z	x	y	z
x'	l_1	m_1	n_1	$\cos\theta\cos\phi$	$\cos\theta\sin\phi$	$-\sin\theta$	$\sqrt{\frac{1}{3}}$	$\sqrt{\frac{1}{3}}$	$\sqrt{\frac{1}{3}}$
y'	l_2	m_2	n_2	$-\sin\phi$	$\cos\phi$	0	$-\sqrt{\frac{1}{2}}$	$\sqrt{\frac{1}{2}}$	0
z'	l_3	m_3	n_3	$\cos\phi\sin\theta$	$\sin\phi\sin\theta$	$\cos\theta$	$\sqrt{\frac{1}{6}}$	$\sqrt{\frac{1}{6}}$	$\sqrt{\frac{2}{3}}$

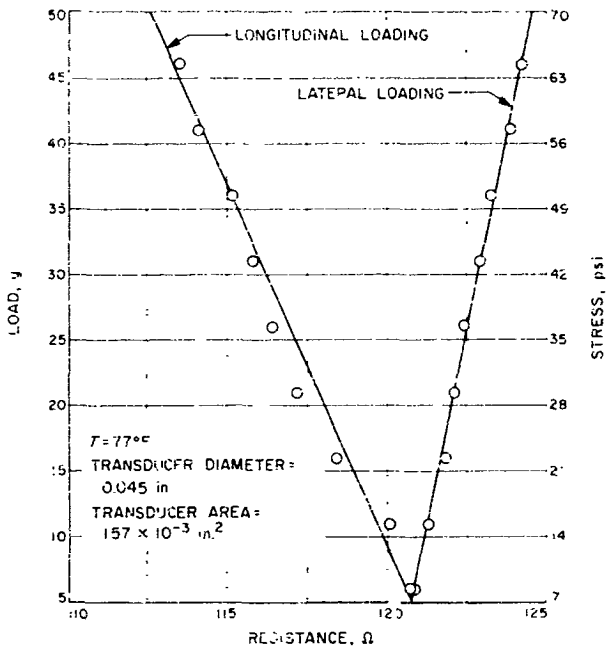

Fig. 3. Direct dead-weight transducer calibration

3. Temperature Interactions

The effects of temperature on the miniature stress transducer can be examined by observing the isolated splinter and comparing these observations with the over-all transducer response for various loadings and temperatures.

The circuitry employed for observing transducer response as a function of temperature is shown in Fig. 4. This circuit exhibits reasonable output linearity. The bridge is balanced by adjusting the variable resistor in parallel with the stress transducer so that the parallel resistance (transducer and variable resistance) equals 75 Ω. The current is then adjusted so as to cause a 100-mv potential across the parallel resistance. Fig. 4 also exhibits the actual calibrated output that was used to measure resistance changes of the order of 60 Ω.

An isolated silicon splinter was heated from 80 to 150 F and exhibited only a 1.6-Ω resistance change. This relatively low resistance change (for a stress transducer) was probably a consequence of high doping of the splinter (and hence low resistivity). The commercial suppliers of the splinter indicated that the resistivity of the splinter is of the order of 0.02 Ω-cm. The coefficient of expansion for the splinter was also indicated as being approximately 2.5×10^{-6} in./in./°F (Ref. 8).

This splinter was packaged (i.e., made into a transducer (Ref. 2), and placed at the center of a cubical mold together with a thermocouple located 0.25 in. from the stress transducer. A polyurethane resin was cast into the mold at a temperature of about 140°C and cured for 15 hr at 145°F. The temperature of the cured polyurethane resin with the embedded stress transducer and thermocouple was then brought down to room temperature in the period of 1 hr. The output of the thermocouple and stress transducer is shown in Fig. 5 as a function of time. The significant observations are: (1) Residual

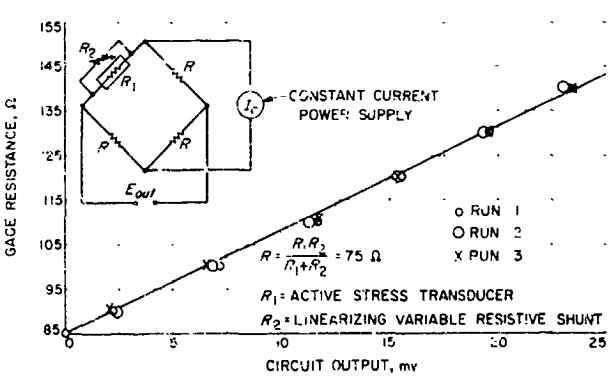

Fig. 4. Transducer electrical circuitry schematic and standard calibration curve

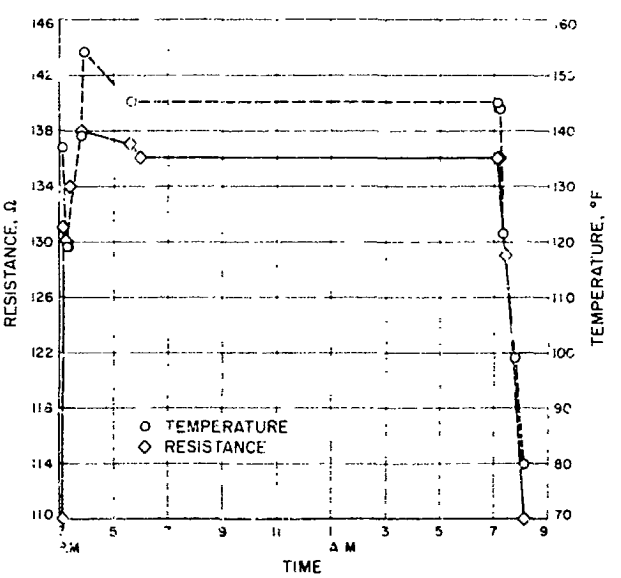

Fig. 5. Curing cycle response of transducer

stresses did not occur as a consequence of curing and the thermal cycle, since the resistance of the transducer returned to its initial 110 Ω. (2) Transducer drift did not occur for a period of 13 hr at 145°F. (3) The transducer is temperature-sensitive in a nearly linear relationship. These observations indicated that the embedding of similar miniature stress transducers in polyurethane binder does not give rise to serious residual stress concentrations (Fig. 1). It also appears that the stress transducer can readily survive the curing cycle of many solid propellants. Finally, the temperature sensitivity of the transducer must be due to the difference of the coefficients of expansion of the Teflon packaging material (approximately 0.5×10^{-6} in./in./°F), the silicon splinter (approximately 1.3×10^{-6} in./in./°F), and the polyurethane resin (approximately 1.3×10^{-4} in./in./°F). Thus the transducer should be calibrated in solid propellant as a function of temperature to establish the portion of output due to temperature.

Finally, Fig. 6 illustrates the relationships among compressive stress of the polyurethane block containing the miniature stress transducer, the resistance change of the stress transducer, and the temperature of the transducer. The slopes of the stress-input/resistance-output curves are approximately the same. The shift of each curve is due to differences in thermal coefficients as discussed. With calibration curves such as shown in this figure, the stress state within solid propellants could be measured by separating out the temperature contribution to the transducer output.

4. Stress or Strain Transducers

It has been shown that the response of one transducer can be characterized by Eq. (1). However, if three such transducers are positioned within a material along the three principal stress directions, the three principal

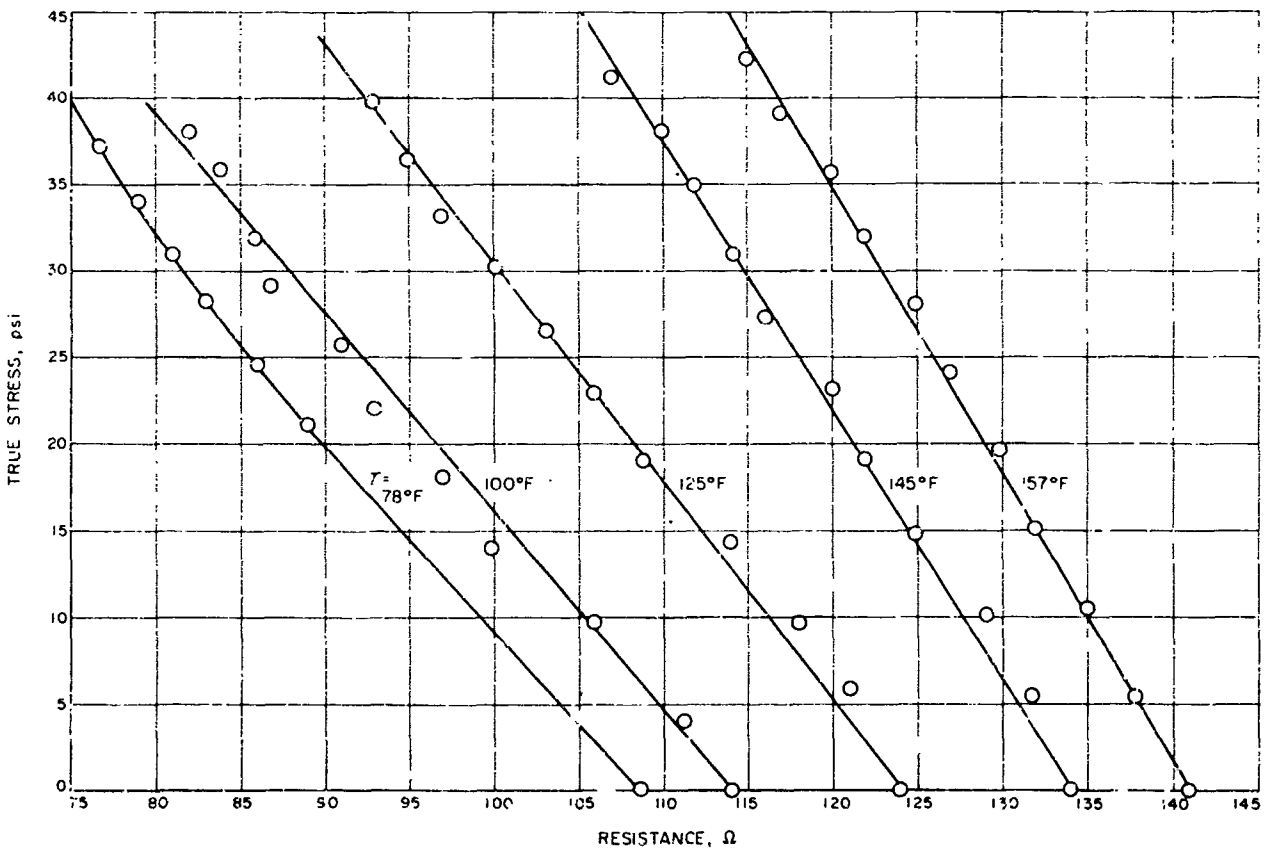

Fig. 6. Compressive stress-temperature-resistance response of transducer

stresses within a point region of propellant can be evaluated by the following three equations:

$$\frac{\Delta\rho_1}{\rho_0} = A\sigma_1 + B\sigma_2 + B\sigma_3 \text{ (Transducer 1)}$$

$$\frac{\Delta\rho_2}{\rho_0} = B\sigma_1 + A\sigma_2 + B\sigma_3 \text{ (Transducer 2)} \qquad (5)$$

$$\frac{\Delta\rho_3}{\rho_0} = B\sigma_1 + B\sigma_2 + A\sigma_3 \text{ (Transducer 3)}$$

Note that symmetry of $\pi'_{12} = \pi'_{21}$ means that only two coefficients are required [Eq. (1)]. Another assumption is that the three transducers have the same piezoresistive properties. Thus it is shown that the three principal stresses can reasonably be measured within elastomers or solid propellant, provided that the stress rosette is oriented along the three principal directions of stress. It is obvious that a stress field gradient within the volume containing the rosette would introduce error. However, Fig. 1 indicated that such a gradient may not exist for several types of stress fields. The strains experienced at some distance away from the transducer can easily be 20%, as was the case for the above-mentioned polyurethane resin. The only way this transducer could be used to measure finite solid propellant strains would be to require that the solid propellant constitutive relationship between stress and strain be known *a priori*. Such relationships are not yet in existence. One objective in developing a miniature stress transducer is to provide a tool with which to establish such material property constitutive equations for solid propellants.

References

1. San Miguel, A., and Silver, R. H., "Radial Stress Measurements in Solid Propellant Grains." *Bulletin of the Third Meeting of ICRPG Working Group on Mechanical Behavior*, November 15, 1964, SPIA, Johns Hopkins University, Applied Physics Laboratory, Silver Spring, Md.

2. San Miguel, A., and Silver, R. H., "On the Construction and Theory of a Miniature Stress Transducer to Measure Radial Stress in Propellant Grains." *Technical Report No. 32-643*, Jet Propulsion Laboratory, Pasadena, Calif., February 15, 1965.

3. Muskhelisnvili, N. I., *Some Basic Problems of the Mathematical Theory of Elasticity*, 2nd English Edition, Noordhoff, Groningen, 1963.

4. Radok, J. R. M., "Effects of Stress Raisers in Linear Viscoelastic Bodies;" *Fracture Processes in Polymeric Solids*, B. Rosen, Ed., Interscience Publishers, New York, N. Y., 1964.

5. Mason, W. P., and Thurston, R. N., "Use of Piezoresistive Materials in the Measurements of Displacement, Force and Torque," *Journal of the Acoustical Society of America*, Vol. 29, No. 10, pp. 1096–1101, October 1957.

6. Pfann, W. G., and Thurston, R. N., "Semiconducting Stress Transducers Utilizing the Transverse and Shear Piezoresistance Effects," *Journal of Applied Physics*, Vol. 32, No. 10, pp. 2008–2019, October 1961.

7. O'Regan, R., "Development of the Semiconductor Strain Gage and Some of Its Applications," *Semiconductor and Conventional Strain Gages*, M. Dean, Ed., Academic Press, New York, N. Y., 1962, p. 247.

8. Dorsey, J., *Semiconductor Strain Gage Handbook*, Sect. I, Electronics Div., Baldwin-Lima-Hamilton Corp., Waltham, Mass.

XIV. Research and Advanced Concepts

A. O-Ring–Alkali Metal Compatibility

W. Phillips

A series of eleven O-ring materials were exposed to static potassium at 300°F for 500 hr (Fig. 1). Buna N was the only material which retained its initial shiny, smooth, and elastic characteristics. Six other O-rings remained in fairly good condition, retaining their smooth surface and elasticity. These were: polyacrylic, butyl, silicone, fluoro-silicone, natural rubber, and nitrile MIL-P5315A. The neoprene was attacked, and the acrylate was completely destroyed. The Teflon and Buna S were hardened and roughened, respectively.

An identical series of rings was exposed to solid lithium at the same temperature. The five rings shown in Fig. 2 were hardened and attacked. These were Buna N, acrylic, Buna S, neoprene, and nitrile MIL-P5315A. The silicone rubber ring was completely destroyed and not recovered. The butyl ring was softened to a plastic unusable state. The remaining rings—polyacrylate, natural rubber, Teflon, and fluoro-silicone—appeared in satisfactory condition. Another series of O-rings are currently in test at 450°F in molten lithium.

Table 1. Summary of O-ring–alkali metal compatibility

Numb	Compound	Condition after potassium exposure[a]	Condition after lithium exposure[a]
1	Buna N	Very good	Hardened
2	Acrylate	Destroyed	Hardened
3	Buna S	Surface roughness	Hardened
4	Polyacrylic	Good	Good
5	Neoprene	Attacked	Hardened
6	Natural rubber	Good	Good
7	Silicone	Good	Destroyed
8	Teflon	Hardened	Good
9	Butyl	Good	Softened
10	Fluoro-silicone	Good	Good
11	Nitrile MIL P5315A	Good	Hardened

[a]Exposures were at 300°F for 500 hr. The potassium was molten and the lithium solid at this temperature.

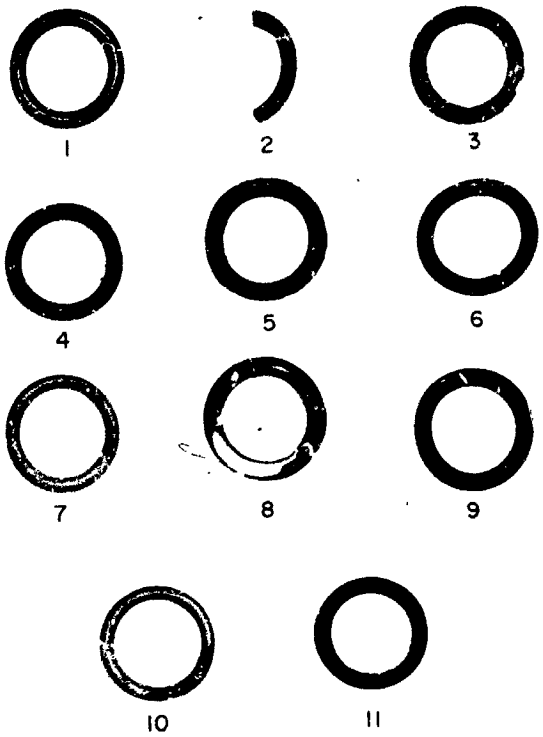

Fig. 1. O-rings after exposure to potassium at 300°F for 500 hr

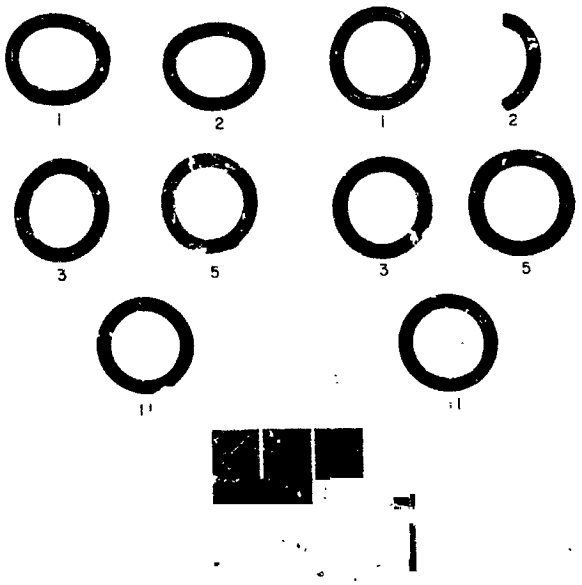

Fig. 2. O-rings on left attacked by contact with solid lithium at 300°F for 500 hr compared to those exposed to potassium

B. Axisymmetric Steady Flow of a Swirling Compressible Fluid Through a Convergent-Divergent Nozzle Without External Heat Transfer

P. F. Massier

1. Introduction

Axisymmetric swirling flow through a nozzle may occur, for example, in the exit nozzle of an arc jet or in the exit nozzle of a vortex tube. For the case of an arc-jet nozzle, swirling flow may have a significant influence on the heat flux to the nozzle wall, in particular in the convergent portion, as was shown in Ref. 1. In order to gain a better understanding of the flow field which in turn influences convective heat transfer, an investigation of ambient temperature swirling flows through nozzles was initiated in conjunction with present ionized gas-flow experiments. The steady swirling motion of a real fluid that flows through an axisymmetric convergent-divergent nozzle is three-dimensional and viscous. Because of the complexity associated with the mathematics required to describe a real flow of this type, the analysis presented is one in which numerous assumptions are made in order to greatly simplify the approach.

Preliminary experiments have been performed with argon at approximately ambient temperature using the apparatus configuration shown in Fig. 3. The measurements that were made—namely, the temperature and radial static pressure distribution along the end wall located upstream of the nozzle inlet, the static pressure distribution along the nozzle wall, the average inlet gas temperature, and the mass flow rate—were used in the analysis to establish quantities that were not measured, such as the axial and tangential components of the

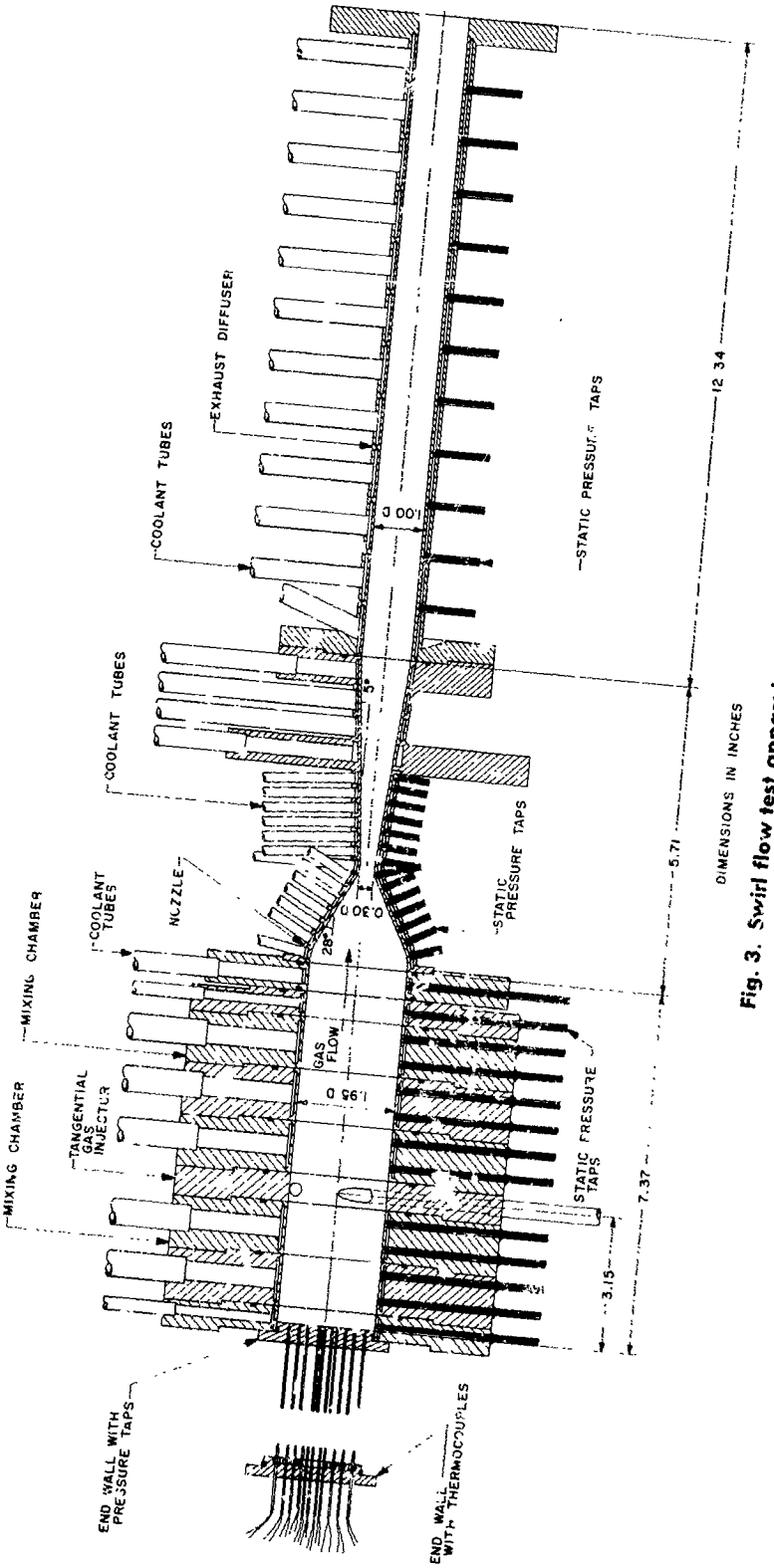

Fig. 3. Swirl flow test apparatus

velocity. Experimental results are shown for one test in which the stagnation pressure was 15.2 psia. For this test the injection velocity into the mixing chamber, which was tangential, was 136 ft/sec. The gas was injected through four 0.250-in.-D holes spaced 90 deg apart. On the end wall the diameter of the five pressure taps nearest the centerline was 0.011 in., and for the remaining holes the diameter was 0.013 in. The length-to-diameter ratios were approximately 5 for the smaller diameter holes and 3 for the larger holes. The diameter of the pressure tap holes on the nozzle was 0.019 in., and the length-to-diameter ratio of these holes ranged from 4 to 25.

The analytical problem is analogous to, but more general than, plane one-dimensional flow through a nozzle. That is, as in plane one-dimensional flow, the radial component of the velocity is neglected and the axial velocity distribution is considered to be uniform at any given plane normal to the nozzle axis. Unlike plane one-dimensional flow, however, both the tangential and axial components of the velocity are taken into account. The experimental tangential velocity distributions were determined from the temperature and static pressure measurements along the end wall, and as a consequence of the analysis were taken to be the same at the nozzle inlet. As established by numerous other investigations of flows in vortex tubes, two flow regions were found to exist. Near the centerline the swirling flow rotates with a velocity distribution similar to that of a solid body, and in the outer annulus the velocity distribution is similar to that of a potential vortex. A transition occurs between the two swirling flow regions. Although it is primarily the injection technique and the viscosity that cause the fluid to form two regions in which the tangential velocity distributions are different, the expansion process through the nozzle is assumed to be reversible and adiabatic both in the core and in the outer annulus. The decrease in pressure along the flow direction, resulting from the expansion process, is associated with an increase only in the axial component of the velocity. Hence, the tangential velocity component is a unique function of radius throughout the nozzle and is not a function of axial position.

2. Major Assumptions

The general equations of motion (Ref. 2) are simplified into a set of equations that may be used in both the annulus and the core of the swirling flow by introducing the following general assumptions:

(1) No body forces exist.

(2) The flow is steady.

(3) The radial component of the velocity is negligible.

(4) The distribution of the axial velocity component is uniform at any plane normal to the axis.

(5) The flow is axially symmetric.

(6) The gas is perfect; therefore,

$$p/\rho = RT \tag{1}$$

$$c_\rho = \text{constant}$$

(7) The fluid is nonviscous.

(8) The flow is adiabatic.

Perhaps the most restrictive and nonrealistic of these assumptions is that the radial component of the velocity is neglected. A radial velocity component must exist in the flow field whenever the walls of a duct converge or diverge, as they do in a nozzle. This can have a significant influence on some of the flow variables, such as static pressure and mass flux (Ref. 3). However, since plane one-dimensional flow theory has been used with considerable success to establish relationships among the flow variables for nonswirling axial flow in convergent divergent nozzles, the radial velocity component in swirling flow is not considered in the present investigation. Besides these assumptions and those stated in the introduction, additional assumptions are discussed throughout the analysis.

3. Simplified Equations of Motion

The equations that result by introducing the eight assumptions listed in the previous section into the equations of motion are as follows:

Continuity:

$$\frac{\partial(\rho w)}{\partial z} = 0 \tag{2}$$

Radial momentum:

$$\frac{\rho v^2}{r} = \frac{\partial p}{\partial r} \tag{3}$$

Tangential momentum:

$$\rho w \frac{\partial v}{\partial z} = 0 \tag{4}$$

Axial momentum:

$$\rho w \frac{\partial w}{\partial z} = -\frac{\partial p}{\partial z} \tag{5}$$

Energy:

$$\rho C_p \frac{\partial T}{\partial z} = \frac{\partial p}{\partial z} \tag{6}$$

4. The Flow Field at the Nozzle Inlet

The experimental tangential velocity distribution at the nozzle inlet was determined from the temperature and static pressure measurements along the end wall which was located upstream of the nozzle inlet, as shown in Fig. 3. The validity of this method is established by use of Eqs. (2) and (4). The product ρw is a constant between the end wall and the nozzle inlet as established by Eq. (2), because the diameter in this region is constant. Also, ρw is not zero; therefore, by Eq. (4)

$$\frac{\partial v}{\partial z} = 0 \tag{7}$$

Hence, the tangential velocity is independent of axial position and, therefore, can depend at most only on the radial coordinate. This condition is a consequence of the nonviscous and axial symmetry assumptions and of neglecting the radial velocity. The fact that the tangential velocity v does depend on the radius is established by Eq. (3).

In order to evaluate the tangential velocity, both the density and radial static pressure gradient must be known at each radial position. The end wall static-pressure distribution is shown in Fig. 4, and the pressure gradient distribution, as determined graphically from the pressure

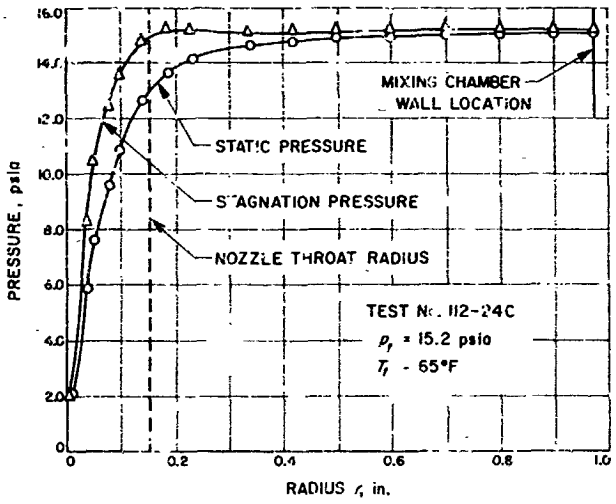

Fig. 4. Static and stagnation pressure distributions at the nozzle inlet for argon flow with swirl

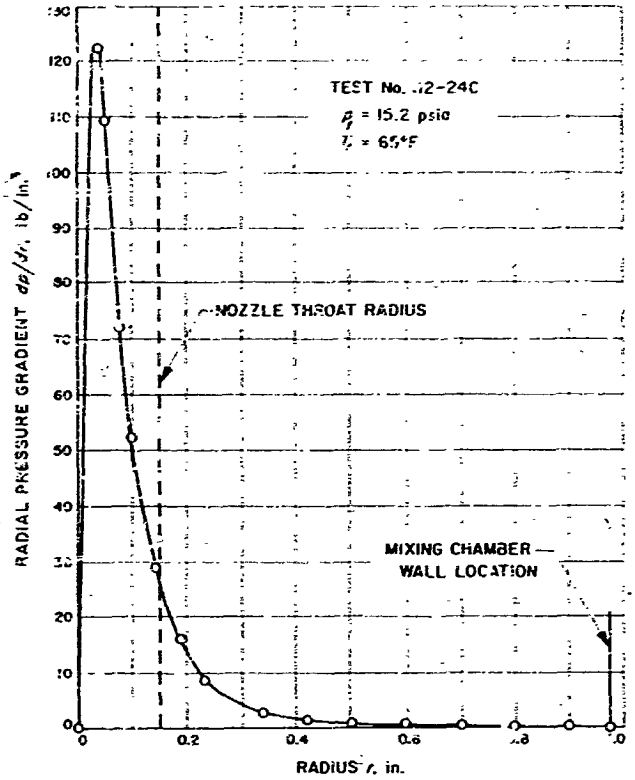

Fig. 5. Radial pressure-gradient distribution along the end wall for argon flow with swirl

distribution plotted on a greatly expanded scale, is shown in Fig. 5. The density was obtained by iteration with the use of Eqs. (1) and (3) as well as Eqs. (8) and (9) that follow:

$$(T_p - T) \equiv K(T_t - T) \tag{8}$$

$$(T_t - T) = \frac{v^2}{2g\,c_p} \tag{9}$$

Eq. (8) is a definition of a recovery factor for thermocouples. For these tests bare wire thermocouples were installed through the end wall, which, according to Ref. 4, have a recovery factor of about 0.65. Eq. (9) is a form of the energy equation. It does not contain other velocity components, because at the end wall the tangential velocity probably dominates the other possible components, at least for the purpose of evaluating the temperature in this manner. The iteration procedure was initiated by assuming the thermocouple temperature to be the static temperature in Eq. (1). The temperature distributions obtained by this procedure are shown in Fig. 6, and the tangential velocity distribution is shown in Fig. 7.

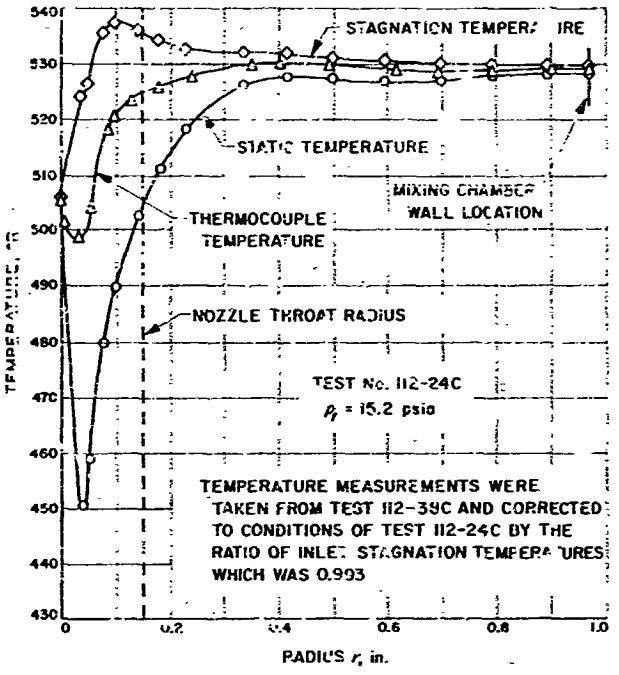

Fig. 6. Gas temperature distributions for argon flow with swirl

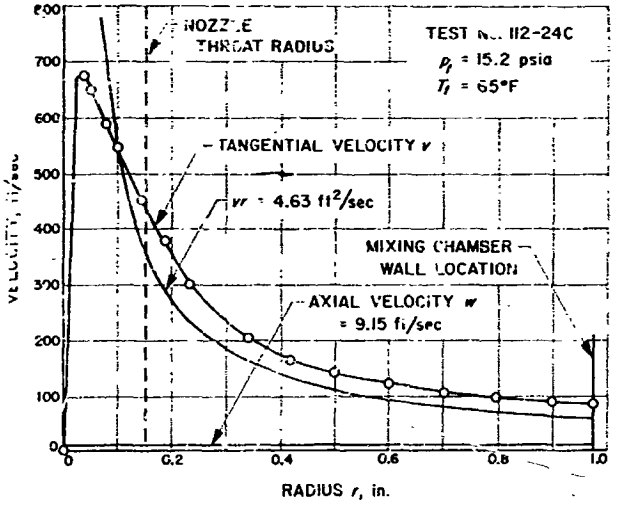

Fig. 7. Velocity distributions at the nozzle inlet for argon flow with swirl

Actually, two tests at nearly the same stagnation temperature and pressure were performed to obtain these results, one with an end wall that contained static pressure taps and the other with an end wall that contained thermocouples. An adjustment was made for the slight difference in inlet temperature as indicated in the note in Fig. 6, and a similar adjustment was made for the pressure. The stagnation pressure was computed using the following equation:

$$p_t = p + \frac{\rho V^2}{2g} \tag{10}$$

This pressure distribution is shown in Fig. 4.

It is apparent in Fig. 6 that energy transfer occurred within the vortex, since the stagnation temperature is not uniform. All the temperatures at the centerline are the same because the velocity there is taken to be zero.

The tangential velocity distribution of a potential vortex (vr = 4.63 ft²/sec) is shown in Fig. 7 for comparison with the experimental results. The constant was arbitrarily chosen to match one of the data points. It is apparent that in the outer part of the vortex the tangential velocity distribution is more nearly that of a potential vortex than it is of a solid-body type of rotation which approximates the distribution in the core. Subsequent tests not shown in which the peak tangential velocity has shifted to a larger radius indicate the solid-body type of rotation in the core more clearly. In addition to the tangential velocity Fig. 7 also shows the axial component of the velocity at the nozzle inlet which was determined from the following form of the continuity equation

$$\dot{m} = \rho_{avg} A_c w \tag{11}$$

The average density across the cross-section at the nozzle inlet was evaluated graphically by use of the end wall measurements, and it is of course assumed that at the nozzle inlet the axial velocity is uniform.

5. The Flow Field in the Nozzle

In the nozzle the same conditions apply with respect to the tangential velocity as between the end wall and the nozzle inlet; that is, v is a function of the radius only as shown by the experimental data in Fig. 7. As a consequence, the flow expansion process resulting from the axial pressure gradient influences only the axial component of the velocity and the values of the thermodynamic properties. The axial velocity is assumed to be uniform at any cross-section in the nozzle. The radial static pressure distribution normalized to the measured value at the wall is assumed to be identical from the centerline to the local wall radius at all axial positions including the end wall. As a consequence, it was possible to establish average values of the density at all axial locations where wall

static pressures were measured by use of graphical integration of one curve of density ratio (ρ/ρ_{st}) versus A_c. The axial velocity distribution in most of the convergent part of the nozzle was then computed with the use of Eq. (11). In order to evaluate the average density it was necessary to determine the density at the wall. This was done by assuming an isentropic expansion (not one-dimensional) from the stagnation conditions determined by end wall measurements at the local nozzle wall radius to the measured static pressure on the nozzle wall. For this purpose the following equation was used:

$$\rho_{st} = \frac{p}{RT_t}\left(\frac{p_t}{p_w}\right)^{\frac{\gamma-1}{\gamma}} \tag{12}$$

For argon $\gamma = 1.67$. The axial velocity was then added vectorally to the tangential component in order to obtain the resultant velocity V. This procedure was followed for the first six data points beginning at the nozzle inlet shown in Fig. 8.

Beginning with the seventh data point from the inlet Eq. (13) was used to compute the resultant velocity

$$V = \sqrt{\frac{2g\gamma RT_t}{(\gamma-1)}\left[1-\left(\frac{p}{p_t}\right)^{\frac{\gamma-1}{\gamma}}\right]} \tag{13}$$

This equation applies for an isentropic (not one-dimensional) expansion from the stagnation condition to the measured static pressure on the nozzle wall. The axial velocity was then obtained from the resultant velocity and the tangential velocity. The nozzle was divided into two regions in this manner, because near the inlet the pressure ratio was not sufficiently accurate to obtain good results from Eq. (13). Furthermore, in the divergent region the accuracy of the average density was believed to be less than that of the velocity determined by Eq. (13). Between axial distances of 1.6 and 2.0 in. the velocities determined by these two methods agreed within 10%.

In Fig. 8 it is apparent that in most of the convergent part of the nozzle the tangential velocity is considerably larger than the axial component; whereas, in the divergent part, the axial component clearly dominates the tangential. The ratio of these two velocities (tangential divided by axial) is shown in Fig. 9, where it is very evident that the flow field in the convergent portion is dominated by the swirl.

Since this investigation was initiated as a result of an observed significant effect on nozzle heat flux resulting from swirling flow (Ref. 1), it is appropriate to also consider the mass flux, which is a major parameter that influences convective heat transfer. In Fig. 10 the ratio of mass flux with swirl to that without swirl at approximately the same stagnation pressure is shown as a function of axial distance along the nozzle. It can be seen that in the convergent portion the mass flux with the amount of swirl present, as discussed, is much larger than when swirl is not present; hence, the convective heat flux would be expected to be much higher with swirl.

Since the velocities and mass fluxes discussed were obtained from the static pressure measurements along the nozzle wall they are the values in the free stream at the edge of a presumably thin boundary layer. The variables at the edge of the boundary layer are among the important ones that influence the convective heat flux

6. Relevance of These Results to Those of the Heat-Transfer Tests

The heat-transfer tests of Ref. 1 were conducted with a nozzle that had convergent and divergent half angles of 10 deg and a throat diameter of 0.6 in., which is a different configuration from that of this nozzle (Fig. 8). Furthermore, the heat-transfer tests were conducted at a lower pressure, higher temperature, and with a cathode, anode and different tangential injector in the system. The differences in configuration would certainly have an effect on the flow field as would the gas properties; however, it is believed that qualitatively the trend in mass flux ratio indicated by Fig. 10 was present when the heat-transfer tests were performed. It is anticipated that additional cold flow tests will be conducted which more nearly represent the configuration used for the heat-transfer tests.

7. Conclusions

The combination of the analysis and the experimental results indicate that the swirling flow through a nozzle consists of essentially two types of swirling regions. A core exists in which the tangential velocity distribution is approximately that of solid body rotation, that is, v/r = constant. In the outer annulus the tangential velocity distribution is more nearly that of a potential vortex; that is, vr = constant. A consequence of the analysis based on the simplifying assumptions is that the tangential component of the velocity depends only on the radial coordinate and not on the axial coordinate. Hence the expansion process results in an increase of only the axial component of the velocity.

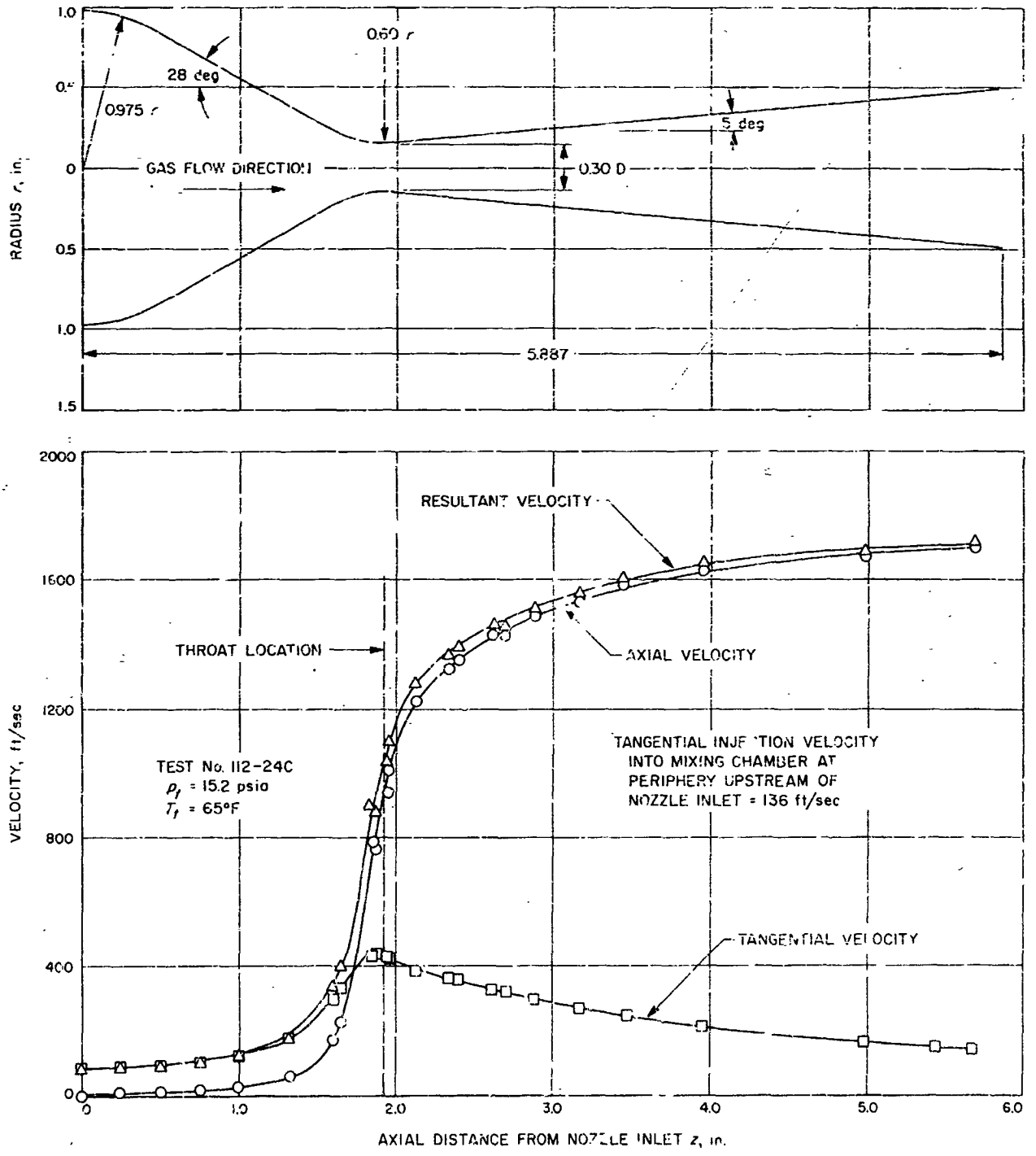

Fig. 8. Velocity distributions along the nozzle for argon flow with swirl

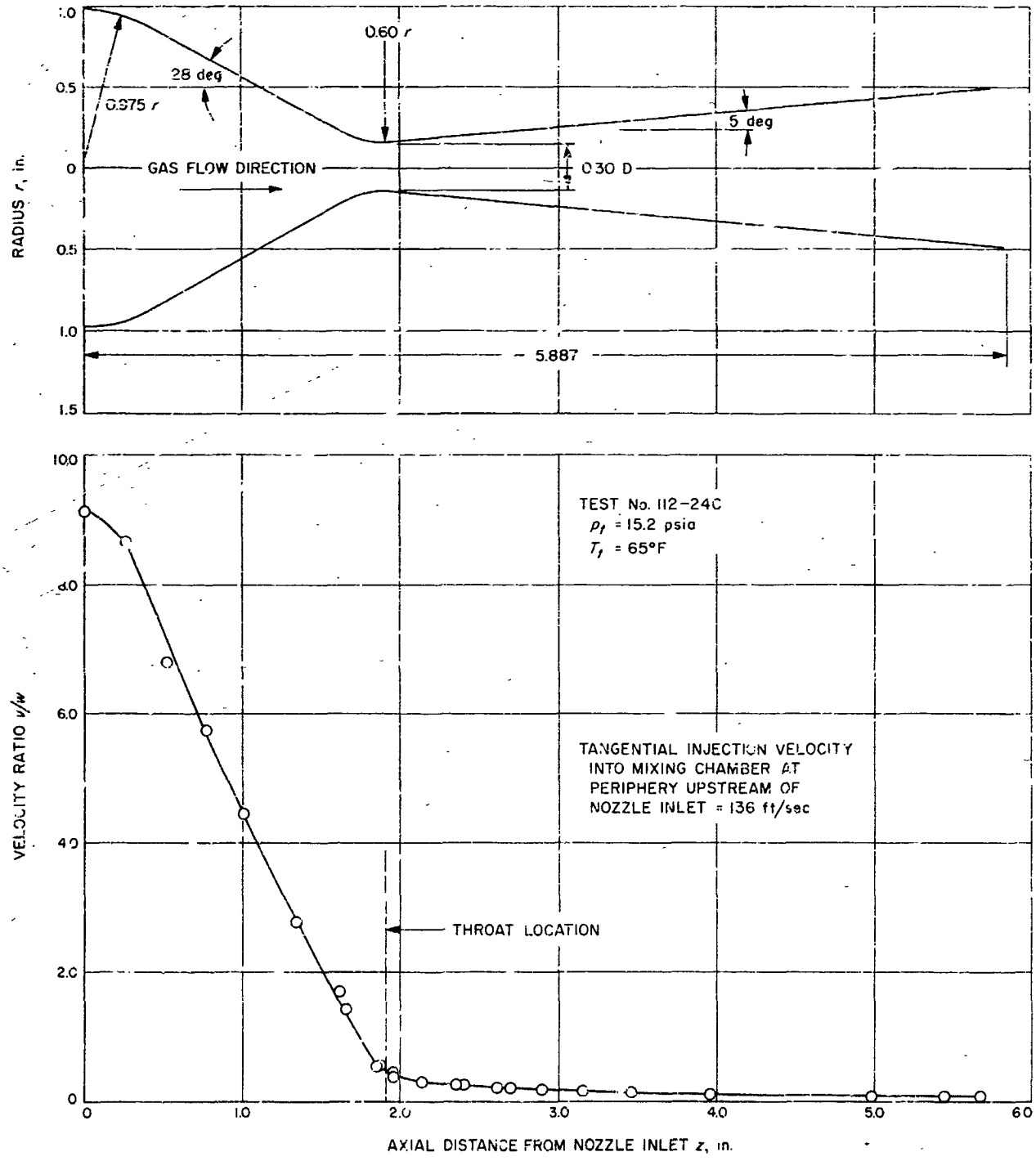

Fig. 9. Ratio of tangential to axial velocity distribution along the nozzle for argon flow with swirl

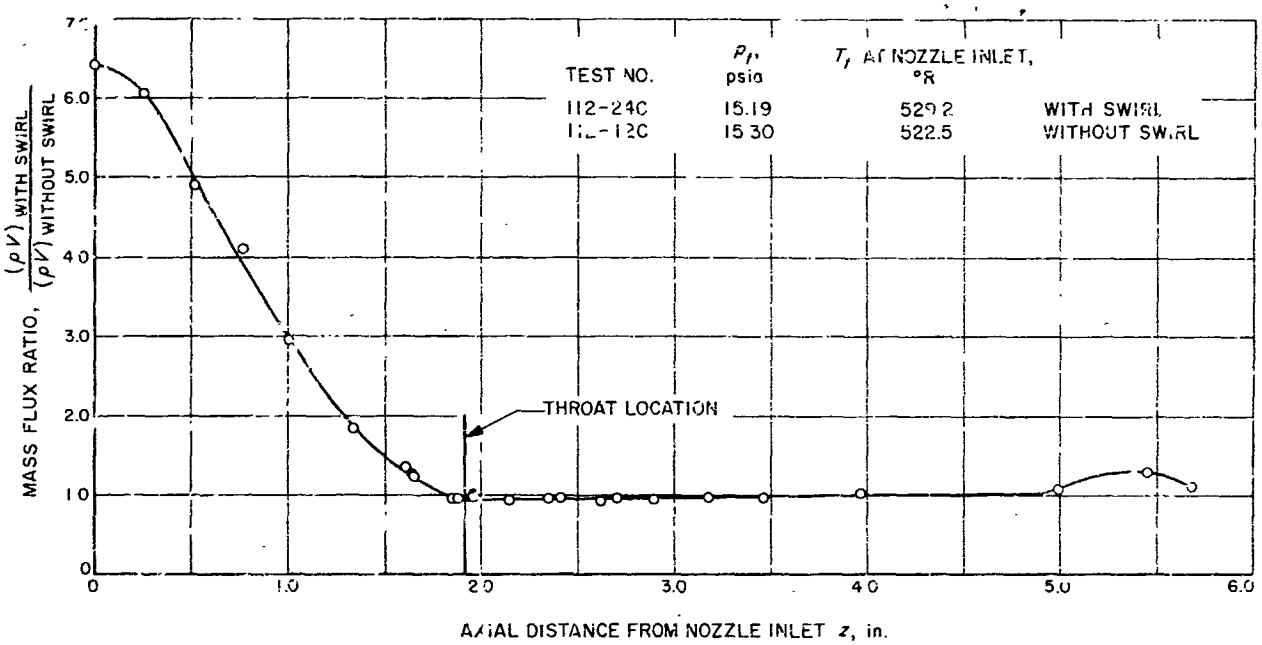

Fig. 10. Ratio of mass flux with swirl to mass flux without swirl near the wall of the nozzle

For the amount of swirl injected in the test analyzed the tangential velocity dominated the axial velocity in most of the convergent part of the nozzle; whereas, the axial component dominated in the divergent part. Also, in the convergent part of the nozzle the mass flux near the wall for flow with swirl was much higher than for flow without swirl, but this effect diminished as the flow progresssed along the nozzle. This high local mass flux with swirl undoubtedly was the major factor that influenced the previously observed high heat flux for an approximately similar flow condition.

A definition of terms used in this section appears in the following table.

Definition of Terms

A	cross sectional area	T_t	stagnation temperature
c_p	specific heat at constant pressure	V	resultant velocity
D_{th}	nozzle throat diameter	v	tangential component of velocity
g	gravitational constant	w	axial component of velocity
K	constant = 0.65	z	axial coordinate
$\dot{m}$	mass flow rate	γ	specific heat ratio
p	static pressure	ρ	static density
p_t	stagnation pressure		
r	radial coordinate	*Subscripts*	
R	gas constant	w	condition at the nozzle wall or outer periphery
T	static temperature	avg	average conditions
T_p	thermocouple temperature		

C. Liquid MHD Power Conversion

D. Elliott, D. Cerini, R. Eddington, L. Hays and E. Weinberg

The long lifetimes required of electric-propulsion powerplants make nonrotating cycles attractive. A nonrotating powerplant under investigation at JPL is the liquid magnetohydrodynamic system shown schematically in Fig. 11. In this cycle a fluid, such as cesium, circulates in the vapor loop and causes a liquid metal, such as lithium, to circulate through an MHD generator in the liquid loop. The cesium leaves the radiator as condensate, flows through an EM pump to the mixer, vaporizes on contact with the lithium, atomizes and accelerates the lithium in the nozzle, separates from the lithium in the separator, and returns to the radiator. The lithium leaves the separator at high velocity (typically 500 ft/sec), decelerates through the production of electric power in the MHD generator, and leaves the generator with sufficient velocity (typically 300 ft/sec) to return through a diffuser to the reactor, where the lithium is reheated.

Results of nozzle, separator, and diffuser investigations, and estimates of cycle performance were presented in Ref. 5, and DC generator experiments were reported in Ref. 6. Further electrical and hydraulic investigations were discussed in Refs. 7–11 and are continuing.

1. Wall Shear in Two-Phase Flow

Wall shear stress has been determined for two different liquid volume ratios in two phase flow of the type leaving the separator in an MHD conversion system. The results suggest a simple relationship for predicting the wall shear.

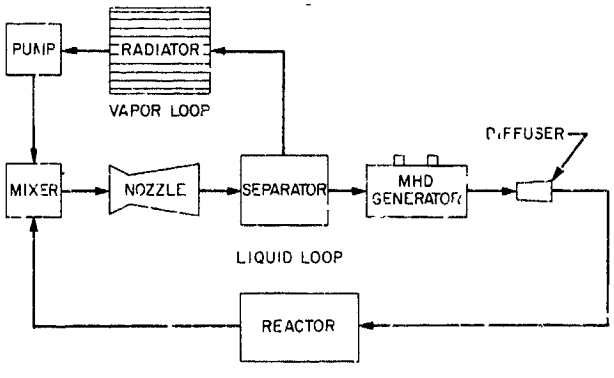

Fig. 11. Liquid MHD power conversion cycle

The injector of the supersonic two-phase tunnel described in Ref. 8 was attached to a 15-in.-long duct of 0.75- × 1.95-in. cross-section. The assembly was mounted on a thrust stand with a digital thrust-measuring system indicating to tenths of a pound. Two phase flow of 0.5 liquid volume fraction was injected at velocities from 146 to 330 ft/sec at atmospheric pressure. Sections of duct approximately 2 in. long were removed between thrust measurements and wall shear stress τ_w was determined from

$$\tau_w = \frac{\text{thrust increase}}{\text{wall area removed}} = \frac{\Delta F}{\Delta A}$$

From a previous, less accurate, experiment of this type, wall shear results corresponding to a liquid volume fraction of 0.35 were also available.

By computing τ_{w_L} corresponding to a completely water-filled duct at the same flow velocity, the ratio τ_w/τ_{w_L} was determined for each velocity and plotted versus liquid volume fraction for the two groups of data. The results are shown in Fig. 12. Comparison with a straight line between zero (wall shear with pure gas would be 0.0013 τ_{w_L} or essentially zero) and 1.0 shows that the simple relationship

$$\tau_w = \tau_{w_L} \times \text{liquid volume fraction}$$

can be conservatively used for predicting wall shear in a high-velocity homogeneous two-phase flow of this type.

The above relationship is equivalent to utilizing the mixture density (ρ = liquid density × liquid volume fraction, ignoring gas density) of the two-phase flow and calculating the shear stress as though the mixture were a single-phase medium. If friction factors for the experiments are computed based on mixture density and plotted versus Reynolds number based on mixture density and liquid viscosity, the results for the 0.5-volume fraction case (Fig. 13) fall within 10% of the Prandtl-von Kármán resistance law.

2. AC Generator End Effects

A method has been found for minimizing the end losses in AC induction generators by adding compensating poles to cancel the flux changes at zero slip and thus achieving, in a one-wavelength generator, substantially the "infinite length" efficiency. An experimental 5-kw one-wavelength generator using this method is being fabricated. This generator will have an efficiency of only about 40%, but the desired efficiency level of 60 to 70% appears attainable at the 300-kw level, as discussed later.

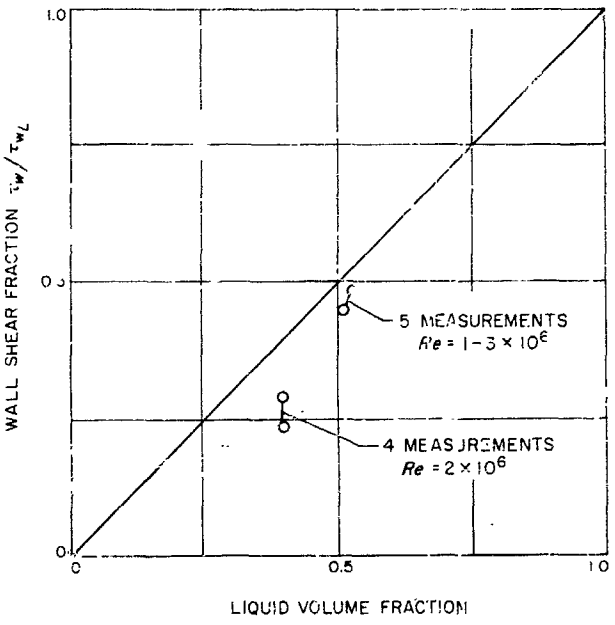

Fig. 12. Variation of wall shear with liquid volume fraction in two-phase flow

Two AC generator geometries are of interest for a full-scale conversion system; the annular generator (Fig. 14) which would be used in conjunction with a conical separator (Ref. 5) and the flat generator (Fig. 15) which would be used with a two-dimensional separator (Ref. 11)

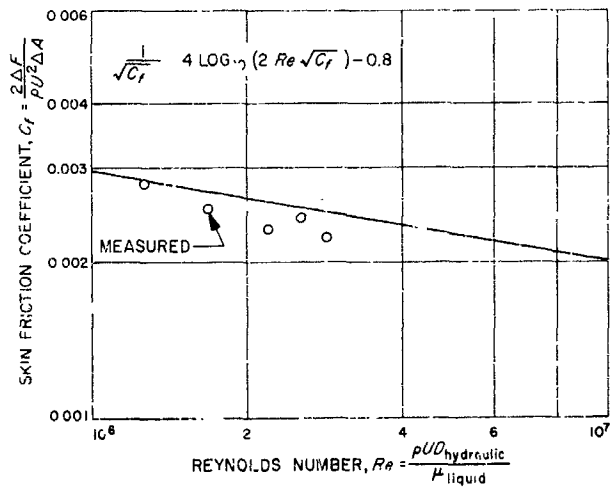

Fig. 13. Comparison of measured friction factor based on mixture density with Prandtl-von Kármán law (liquid volume fraction = 0.5)

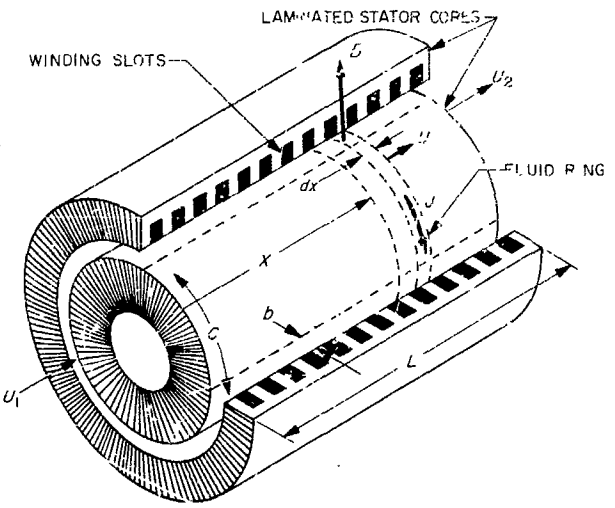

Fig. 14. Annular AC generator

In the annular generator the liquid metal enters a channel of circumference c, matching the circumference of the exit of the separator cone, and of gap b, matching the thickness of the liquid film leaving the separator. The inlet velocity is U_1. Within the generator the liquid passes through a traveling-wave magnetic field, radially directed, produced by polyphase windings in slots in the inner and outer laminated stators. The field travels more slowly than the fluid and induces circumferential currents in it. The currents produce two effects: (1) they retard the fluid and (2) they induce voltages in the windings to provide the desired AC power output. Due to the retarding force the fluid decelerates, in length L, to velocity U_2 at the generator exit. The gap b increases to accommodate the decreased velocity while maintaining constant pressure as dictated by cycle considerations. The circumference c also increases as the channel follows the angle of the separator exit.

The operation of the generator is entirely equivalent to that of a squirrel-cage induction motor, with the squirrel-cage rotor replaced by the liquid metal.

In the flat generator (Fig. 15) the channel is rectangular with conducting side plates. The circumference c is replaced by the distance between the side plates. Here, the currents in the fluid flow into and out of the conducting side plates, instead of closing on themselves as in the annular generator. Within the fluid, however, there is no difference in behavior between the two generators, and performance is the same provided the annual generator has no net current flowing around its circumference, a case excluded by the side plates in the flat generator.

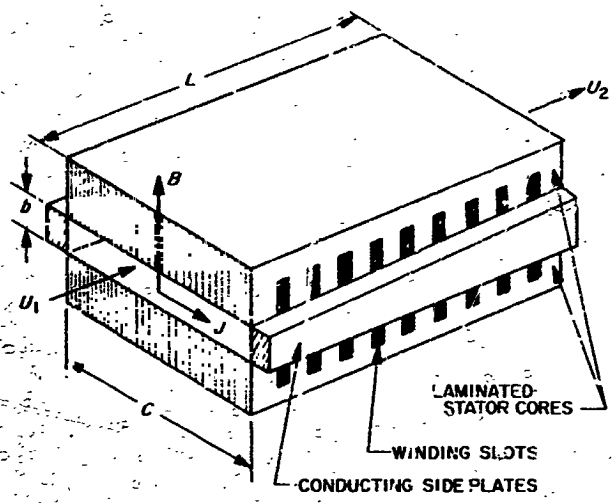

Fig. 15. Flat AC generator

Two requirements on liquid-metal AC generators are apparent at the outset. First, the large friction loss in high-velocity liquid flow dictates that the generator length be as short as possible. Since this length is determined by the magnetic field available to provide the necessary velocity change, the field must, ideally, reach full amplitude at the inlet of the generator and remain constant throughout its length, limited only by saturation of the iron. Second, the amount of copper must be minimized to provide maximum iron length fraction for maximum channel field at saturation, and, since each pole requires the same ampere-turns, this means that the fewest possible poles (two poles = one wavelength) should be used. Two poles are the fewest that can be employed without an external magnetic return path or power output pulsation and that number, therefore, is the obvious choice.

The use of a constant-amplitude traveling magnetic field introduces a potentially serious loss mechanism which can be visualized by following a particular fluid ring through an annular generator, as illustrated in Fig. 16. For simplicity, the circumference and fluid velocity will be assumed constant.

Consider, first, the case of zero slip, i.e., the fluid velocity U equal to the wave velocity U_w, and consider a ring located at a zero field point as shown. As the ring moves into the generator at position (a) it initially has no flux linking it, since all the iron is to the right. But as the ring moves further into the generator, for example one-quarter of the way, as at position (b), the ring becomes linked by the flux from the downward half pole

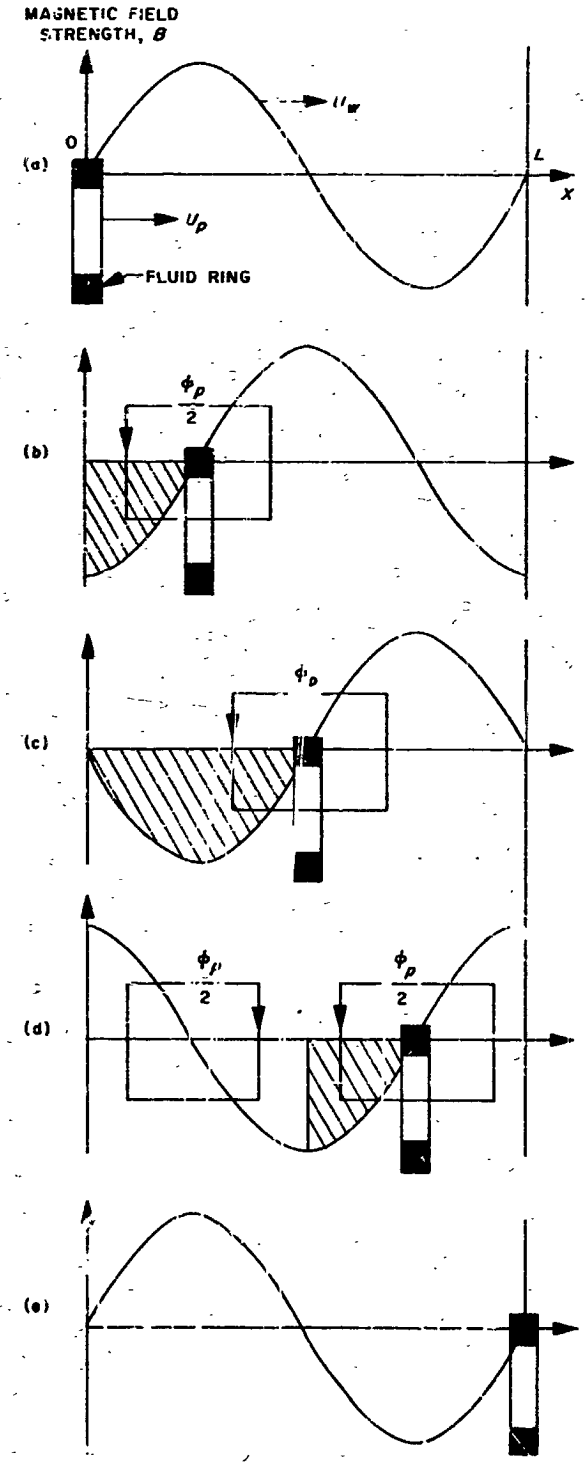

Fig. 16. Changing flux linkages through a fluid ring traveling at wave speed in an annular generator. Shaded area represents the flux linking the ring

which has entered between the ring and the entrance (one pole of flux = ϕ_p). When the ring reaches the middle of the generator; position (c), it has become linked by one full pole of flux. As the ring proceeds further, an upward pole moves into the generator and provides a return path for some of the flux which had been linking the ring. At the three-quarter point, position (d), only a half pole of flux still links the ring, and as the ring reaches the exit, position (e), the flux linking the ring has returned to zero.

When other rings are followed through the generator it is found that the amount of flux linking each ring depends on the ring position relative to the wave, but that the *rate of change* of flux for all rings at a given instant of time is the same. Thus a traveling-wave magnetic field bounded by fixed ends induces circumferential currents in the fluid even at zero slip. It can be shown that the currents produced by this effect, and the resulting ohmic heating losses, are greater than can be tolerated. In fact, the maximum efficiency attainable subject to this effect, neglecting reaction fields due to the fluid current, is 17%, originally shown by Blake in Ref. 12.

This result seems, at first glance, inconsistent with the relatively good efficiencies, as high as 45%, obtained with traveling-wave induction pumps which are constructed like the flat generator of Fig. 15. The explanation is that the side plates block any net circumferential currents. An AC voltage appears between the side plates instead, producing shunt end currents as in a DC generator. But for channel lengths greater than about four times the channel width, as has been the case with pumps, the shunt end losses are only about 20% or less, especially when further reduced by the customary "grading" of the magnetic field amplitude at the ends.

The side-plate remedy is probably not adequate for high-velocity liquid-metal generators, because the length is limited by friction to no more than twice the width, while the efficiencies needed would require, for a constant-amplitude wave, lengths greater than four times the width.

Several treatments of the finite-length annular induction generator have been published. Pierson and Jackson (Refs. 13 and 14) solved the case of finite winding length and infinite iron length. This analysis, applied to two-pole generators suitable for a 300-kw system, showed efficiencies no higher than 20%[1]. Peschka, Kelm, and Engeln (Ref. 15) solved the semi-infinite case and showed efficiencies of 70 to 80%, without friction, at the conditions of interest; Ref. 15 does not present sufficient detail to permit locating the discrepancy relative to Refs. 13 and 14, and the favorable results must be held in question. Schwab (Ref. 16) solved the problem closest to the practical case, that of both finite-length winding and iron, but presented no efficiency results. Sudan (Ref. 17) analyzed the finite winding, infinite-iron case with results equivalent to Pierson's and Jackson's and also showed the possibility of a winding distribution which would eliminate the end effects. The latter is probably related to the compensating pole scheme discussed below.

Although differences and discrepancies between the various published analyses and scarcity of performance calculations based on them, cloud the picture somewhat, it seems clear that the basic finite-length AC generator has unacceptable losses and must be modified. The modification that seems most promising is to add "compensating poles" at each end of the generator, as illustrated in Fig. 17. These compensating poles operate as follows:

As the fluid ring considered in Fig. 16 enters the generator, the sinusoidally excited compensating poles are synchronized to provide a downward half pole of flux linking the ring. At position (b) the compensating pole flux goes through zero, leaving the downward half pole of flux from the traveling wave linking the ring. As the ring reaches the halfway point, position (c), the compensating poles provide an upward half pole of flux which cancels half of the traveling wave pole linking the ring, so that the net flux is still only half a pole. This process continues through positions (d) and (e), with the compensating poles always adding or subtracting enough flux to hold the flux through the ring constant at half a pole.

When other rings at different positions relative to the traveling wave are followed through the generator, it is found that the flux linkage is different for each ring, but remains constant throughout the traveling wave region. Thus, no current is induced at zero slip and ideal "infinite length" conditions have been restored in the traveling wave region.

The cost of this remedy is the additional friction and electrical losses in the compensating pole regions. However, induced currents can be minimized by vanes or flow-splitting pins in these regions, and the capture slot and diffuser regions already present can be made the locations for the compensating pole field, requiring little or no additional duct friction.

[1] Analysis made by E. S. Pierson and W. D. Jackson of Massachusetts Institute of Technology.

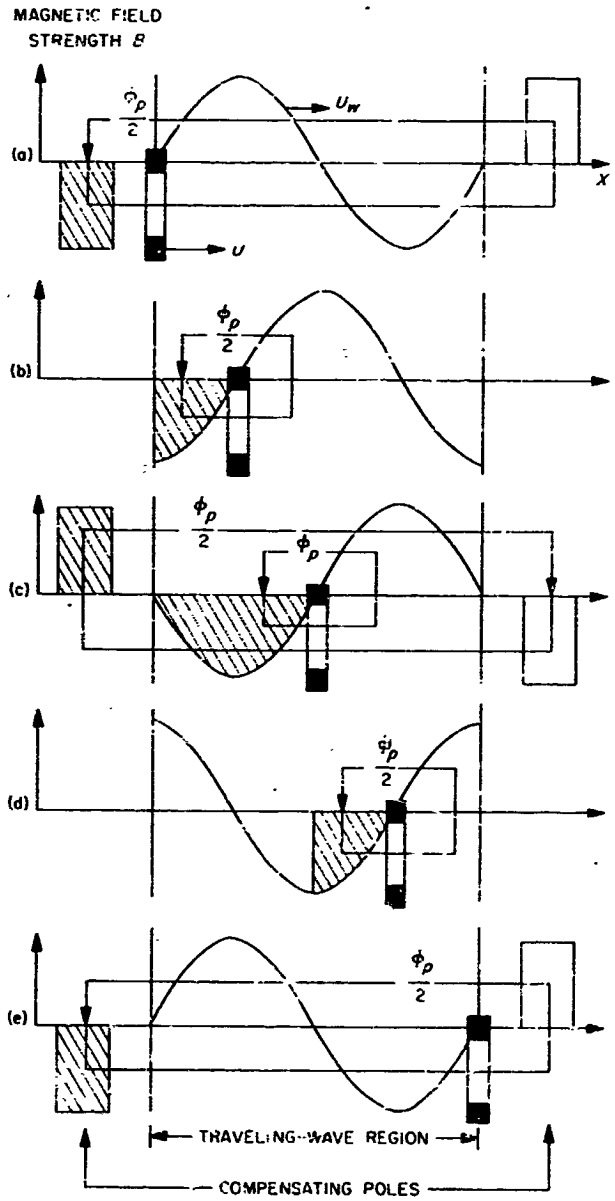

Fig. 17. Constancy of flux linkage through a fluid ring when compensating poles are added

3. Limiting Performance of AC Generators

With end effects removed from the traveling wave region, the limiting performance capability of AC generators can readily be determined.

Referring to Fig. 14, consider the fluid ring of length dx at distance x from the inlet, traveling at velocity U. Let B be the RMS field and J be the RMS current density at that position. The electrical retarding force on the ring is

$$BJbcdx$$

and the friction retarding force is

$$\rho U^2 C_f c dx$$

where ρ is the fluid density and C_f is the skin-friction coefficient. At constant pressure the momentum equation is, therefore

$$\dot{m}\, dU = -(BJb + \rho U^2 C_f)c dx \tag{1}$$

where $\dot{m}$ is the mass flow rate,

$$\dot{m} = \rho U b c \tag{2}$$

The ohmic heating power in the ring is

$$\frac{J^2 bc}{\sigma} dx$$

where σ is the electrical conductivity.

The electric output power dP_e from the ring must equal the difference between the power extracted from the fluid, by electrical retarding force, and the ohmic heating loss. Thus, the energy equation is

$$dP_e = \left(BJbU - \frac{J^2 b}{\sigma}\right) c dx \tag{3}$$

Substituting dx from Eq. (1) and employing Eq. (2) to eliminate (b), the increment of power output obtained for a given increment of velocity change is

$$dP_e = -\dot{m}U\left[\frac{1 - \frac{J}{\sigma BU}}{1 + \frac{\rho^2 U^3 C_f c}{BJ\dot{m}}}\right] dU \tag{4}$$

The maximum possible generator output occurs when the expression in the brackets is maximized at each point by optimizing the current density through proper variation of the slip. Differentiating the bracketed expression and equating to zero, the optimum current density is

$$J_{opt} = \frac{\rho U^2 C_f}{Bb}\left[\sqrt{1 + \frac{\sigma B^2 b}{\rho U C_f}} - 1\right] \tag{5}$$

The variation of current density required by Eq. (5) is a steady decrease from the inlet to the exit

Substituting Eq. (5) into Eq. (4), integrating from U_1 to U_2 to obtain the total power output, and dividing

by the fluid power input $\dot{m}(U_1^2 - U_2^2)/2$, the generator efficiency is

$$\eta = \frac{1}{1-\left(\frac{U_2}{U_1}\right)^2}\left\{\left[\frac{\sqrt{1+\frac{S_1}{C_f}}}{2}-1\right]\left[\frac{\sqrt{1+\left(\frac{S_1}{C_f}\right)\left(\frac{U_1}{U_2}\right)^2}-2}{\sqrt{1+\frac{S_1}{C_f}}-2}\left(\frac{U_2}{U_1}\right)^2-1\right]\right.$$

$$+\left[\frac{\sqrt{1+\frac{S_1}{C_f}}-1}{\frac{S_1}{C_f}}\right]\left[\frac{\sqrt{1+\left(\frac{S_1}{C_f}\right)\left(\frac{U_2}{U_1}\right)^2}-1}{\sqrt{1+\frac{S_1}{C_f}}-1}\left(\frac{U_2}{U_1}\right)^4-1\right]$$

$$\left.+\frac{S_1}{2C_f}\log_e\left[\frac{\sqrt{1+\frac{S_1}{C_f}}+1}{\sqrt{1+\left(\frac{S_1}{C_f}\right)\left(\frac{U_1}{U_2}\right)^2}+1}\left(\frac{U_1}{U_2}\right)\right]\right\} \tag{6}$$

where S_1 is the magnetic force coefficient at the inlet defined by

$$S_1 = \frac{\sigma B^2 b_1}{\rho U_1} \tag{7}$$

Eq. (6) gives the maximum possible efficiency, considering friction and ohmic heating losses, attainable with a constant-pressure MHD generator operating at uniform field amplitude and constant fluid properties. It applies to both AC and DC generators, with B referring to the RMS field in the AC case and the steady field in the DC case.

Integrating Eq. (1) between $x = 0$ and $x = L$, using the optimum current density from Eq. (5), the generator length is

$$\frac{LC_f}{b_1} = \sqrt{\frac{C_f}{S_1}}\log_e\left[\frac{\sqrt{1+\left(\frac{S_1}{C_f}\right)\left(\frac{U_1}{U_2}\right)^2}+\sqrt{\frac{S_1}{C_f}\left(\frac{U_1}{U_2}\right)^2}}{\sqrt{1+\frac{S_1}{C_f}}+\sqrt{\frac{S_1}{C_f}}}\right] \tag{8}$$

Fig. 8 presents efficiencies calculated from Eq. (6) as a function of magnetic force coefficient divided by skin-friction coefficient for generator velocity ratios U_2/U_1 from 0.4 to 0.8, the range of practical interest. It is seen that the ratio S_1/C_f must be at least 10 to provide the desired efficiencies of 60% or more.

For a 300-kw(e) cesium-lithium MHD conversion system the approximate generator operating conditions are:

$\dot{m}$ = 130 lb/sec

U_1 = 500 ft/sec

U = 300 ft/sec

ρ = 27.2 lb/ft³ (lithium)

$\sigma = 2.0 \times 10^4$ mho/cm

c = 27 in. (annular generator)

c = 9 in. (flat generator)

b_1 = 0.05 in. (annular generator)

b_1 = 0.15 in. (flat generator)

C_f = 0.0032

For the annular generator at 10 kgauss RMS field, a value difficult but probably possible to attain, the value of S_1/C_f is 12, and the corresponding efficiency in Fig. 18 is 0.63. With a two-dimensional separator and a flat generator a threefold increase in S_1 is obtained, raising the efficiency to 0.76.

As described in Ref. 11, it has been found possible to achieve a twofold reduction in skin-friction coefficient by injecting gas between the liquid and the wall. If this can be achieved in the flat generator with no sacrifice in field strength from the wider gap, then S_1/C_f can be increased to 72 and the efficiency raised to 0.83.

Boundary injection of gas would not only reduce the skin-friction coefficient but also flatten the velocity profile which, if unchanged from the fully developed turbulent profile, would actually set a limit of about 80% on generator efficiency, regardless of S_1/C_f. Inherent in the upper end of the curves in Fig. 18, therefore, is the requirement for at least partial detachment of the liquid from the channel walls. This technique, partially demonstrated in the tests reported in Ref. 11, appears essential for high efficiency.

Fig. 19 shows how the generator efficiency varies with the length parameter LC_f/b_1. The efficiency is 1.0 at zero length, requiring infinite field, and decreases with increasing length (and decreasing field requirement) until the length is reached at which the required velocity reduction is achieved by friction alone, at zero field.

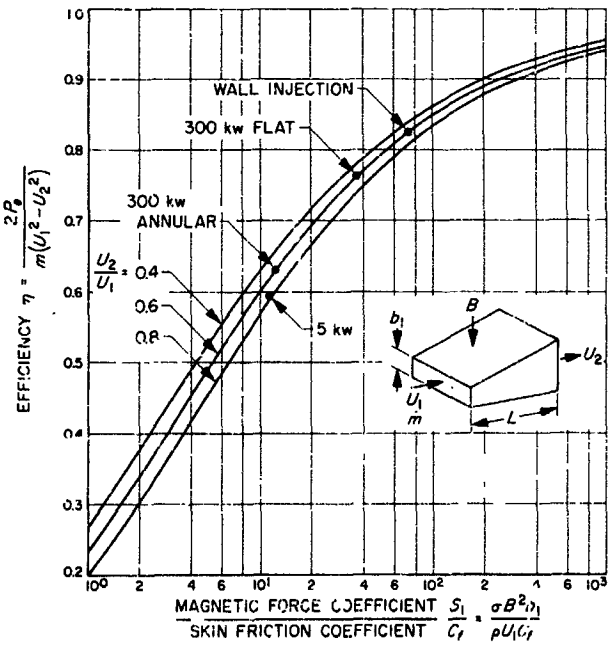

Fig. 18. Limiting efficiency of constant-pressure MHD generators

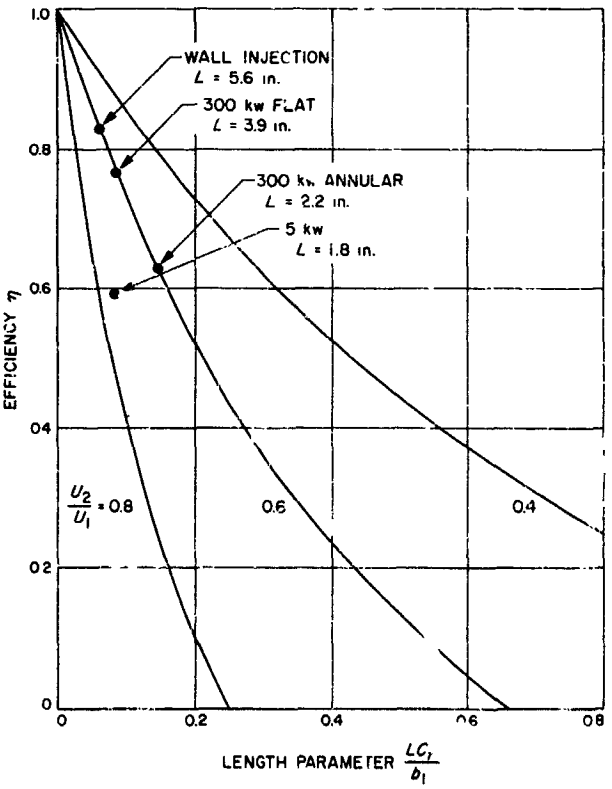

Fig. 19. Effect of length on limiting efficiency of constant-pressure MHD generators

The lengths for the various 300-kw generators are also indicated. These vary from 2.2 to 5.6 in. The corresponding operating frequencies for a two-pole generator range from about 2000 to 700 cps.

The efficiencies given by Figs. 18 and 19 include only friction and fluid ohmic heating losses. Losses due to boundary layer, compensating poles, windings, and iron core will reduce these efficiencies by 10 to 30 percentage points. Therefore, probably only the flat version of the 300-kw generator, with wall injection, can be expected to achieve a net efficiency of 60% or more.

4. Experimental AC Generator

A flat AC generator is being fabricated for testing with NaK in the facility previously used for the DC generator tests (Ref. 6). For simplicity, the generator will operate at constant velocity with power derived from pressure drop. The tests are intended to verify predicted efficiency and demonstrate stable operation and start-up with capacitor excitation. The dimensions and nominal operating conditions of the experimental AC generator are as follows:

length of traveling-wave region L	= 1.8 in.
total length L_t	= 3.6 in.
width c	= 1.6 in.
channel gap b	= 0.1 in.
fluid velocity U	= 250 ft/sec
flow rate $\dot{m}$	= 15.2 lb/sec
wave velocity U_w	= 190 ft/sec
slip $s = \dfrac{U - U_w}{U_w}$	= 0.3
frequency f	= 1280 cps
RMS field $\mathcal{B}$	= 6400 gauss
pressure drop (traveling-wave region) Δp	= 210 psi
input power (traveling-wave region) $\dfrac{\dot{m}\Delta p}{\rho}$	= 11.4 kw
predicted power output (traveling-wave region) P_e	= 4.9 kw
efficiency (traveling-wave region) η $\dfrac{4.9}{11.4}$	= 0.43

A constant-pressure generator of the same power input and mean velocity would have $U_2/U_1 = 0.75$ and $S_1/C_f = 11$. These conditions are indicated in Figs. 18 and 19, showing that the 5-kw experimental generator operates near the conditions of interest for a 300-kw annular generator.

The difference between the Fig. 18 efficiency of 0.59 and the predicted net efficiency of 0.43 is due to the winding and core losses. The compensating poles are expected to consume an additional 0.44 kw of the output power and require 0.9 kw more input power due to additional electrical retarding force, reducing the over-all efficiency to 0.36. If vane friction, possibly not required in a conversion system, is added, the efficiency is lowered to 0.32; if all the additional duct friction, certainly not required in a conversion system, is added, the final efficiency is 0.26.

Comparing Fig. 18 with the predicted performance of the experimental generator, it is evident that AC generators have potentially high efficiency, provided numerous parasitic losses can be minimized. Studies are in progress to determine the extent of the latter in a 300-kw generator. Studies are also continuing on DC generators in the light of recent improvements in inverters (Ref. 18) which may permit operation at lower voltages than previously thought possible.

5. Cesium-Lithium Erosion Loop

Work is continuing on the lithium pump acceptance test. Bakeout of the vacuum chamber at temperatures ranging from 400 to 800°F was accomplished. The Cb-1Zr pump loop was installed in the chamber and all welds were field annealed at 2200°F for 1 hr with tantalum heaters.

Wedge-shaped specimens, representing separator tips, have been mounted downstream of the impinging lithium jet orifices for preliminary erosion evaluation. The specimens include Cb-1Zr, thoriated tungsten, zirconium carbide, tantalum carbide, and titanium carbide. Field welding of the stainless steel loop connections and loading system is now being conducted.

A computer stress analysis has been completed for the final configuration of the 2000°F cesium-lithium erosion loop. All stresses are lower than the design value of cold-set stress (10,000 psi) and limiting creep stress under hot conditions (2000 psi). No design modifications appear necessary. Fabrication of the lines has been initiated, and they are being assembled on the final support frame of the loop.

6. Cycle Analysis

All cesium-lithium two-phase nozzle cases have been computed for the temperature range 1800 to 2200°F, and potassium-lithium computations are in progress. The single-component program has been completed, and computations are being made for potassium. No other working fluids appear to offer advantages over these for liquid MHD systems in this temperature range.

Upon completion of the nozzle computations, the cycle efficiencies and radiator areas of both separator and condenser cycles will be computed. The results will yield refinement of prediced conversion system performance, provide a consistent set of comparisons between the various cycles that have been proposed, and establish the optimum operating conditions toward which to orient the experimental work.

D. Zero Gravity Feed System for Mercury Ion Engines

T. D. Masek and D. J. Kerrisk

1. Introduction

The mercury bombardment ion engine has demonstrated a performance level sufficiently encouraging to warrant its further consideration for mission applications. To make a valid evaluation, however, requires that this thrustor be operated in a configuration that approximates the requirements of an actual spacecraft. This implies that the thrustor must be operated with a zero-gravity propellant feed system and an automatic-control system. Neither of these has been developed at this time. A number of feed-system studies have been made at various laboratories, but little usable hardware has evolved (Refs. 19–27).

In line with previous work on the mercury bombardment engine (Refs. 28, 29), the Applications Study Group is investigating the problem of the zero-gravity mercury feed system. The present concept is based on an expanding-diaphragm-type expansion system, which forces liquid mercury through a valve to a porous matrix vaporizer, a flowmeter, and a high-voltage isolator. The isolator permits the feed system to operate at spacecraft ground and reduces mounting and high-voltage isolation problems. A schematic diagram of the system under investigation is shown in Fig. 20. Fig. 21 is a conceptual design complete thrustor module using this feed system. In the present study, attention is being concentrated on the tankage and expulsion system, the vaporizer and the isolator. In the following discussion these components will be treated individually.

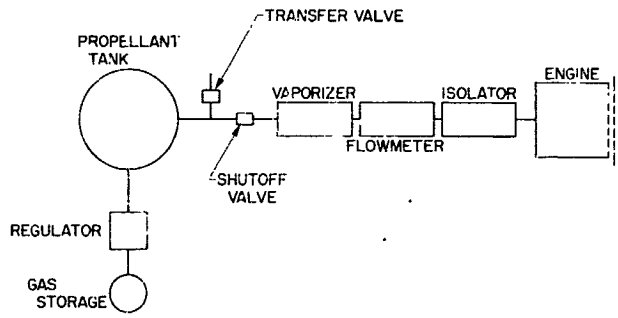

Fig. 20. Zero-gravity feed system

2. Feed System Concept

The mercury ion engine requires a propellant flow rate on the order of 10^{-3} g/sec, regulated to a few percent. The method used here to accomplish this makes use of the sensitivity of the flowrate to vaporizer temperature, temperature gradient and liquid mercury pressure.

The pressure, temperature, and mass flowrate of vapor through a system of capillaries can be related by

$$\left(\frac{M}{\dot{m}^2}\frac{P}{kT}-\frac{1}{P}\right)\frac{dP}{dx}+\frac{128\mu l}{D^2\dot{m}}=-\frac{1}{T}\frac{dT}{dx}$$

where

P = pressure, dynes/cm²

T = temperature, °K

M = atomic mass, g

$\dot{m}$ = mass flowrate, g/cm²-sec

μ = viscosity, poise

l = capillary length, cm

D = capillary diameter, cm

x = normalized distance along capillary

This equation shows the relative effects of temperature and pressure on mass flowrate through a sintered porous plug. Assuming that the pressure at the inlet to the vaporizer is the equilibrium vapor pressure corresponding to the inlet temperature, that the outlet pressure is negligible, and that the temperature distribution is given

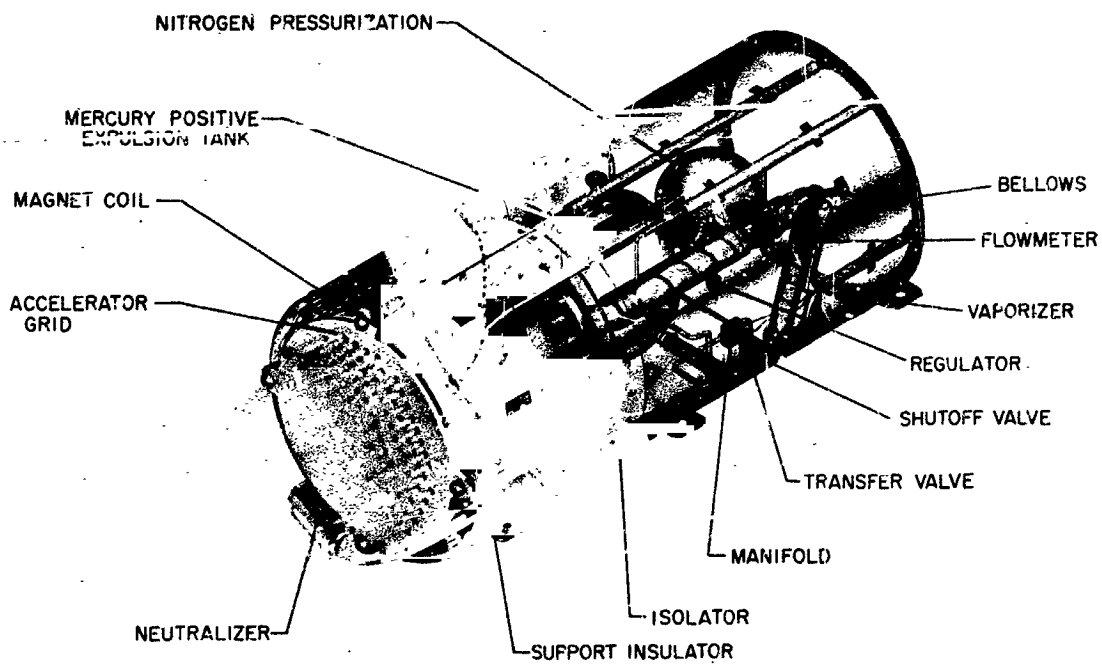

Fig. 21. Mercury positive expulsion system

by $T = T_0 (1 + \alpha x)$, where T_0 is the inlet temperature, and α is a constant, $\dot{m}$ was calculated for various values of T_0, and α and is plotted in Fig. 22. Values of the other parameters are noted on the figure. The mass flowrate is more sensitive to changes in inlet temperature than to changes in the temperature gradient. At 350°C the rate of change of flow due to a ΔT_0 is 9.1×10^{-5} g/sec-°C but the change due to a change in outlet temperature with the inlet temperature held constant is 7.9×10^{-6} g/sec-°C. It seems likely that once the operating temperature range is chosen, T_0 will be used to control the flowrate, because of the higher sensitivity. Without an elaborate heating system, the temperature distribution of the vaporizer will also change slightly with changes in T_0. This distribution change should not affect the flowrate control.

The liquid pressure will be an important factor if liquid enters the vaporizer. The flowrate is inversely proportional to the vapor path length but depends exponentially on the temperature of the liquid-vapor interface, since this temperature determines the vapor pressure. Small changes in liquid pressure could move the position of the interface and could significantly affect the flowrate if the vaporizer temperature is not uniform.

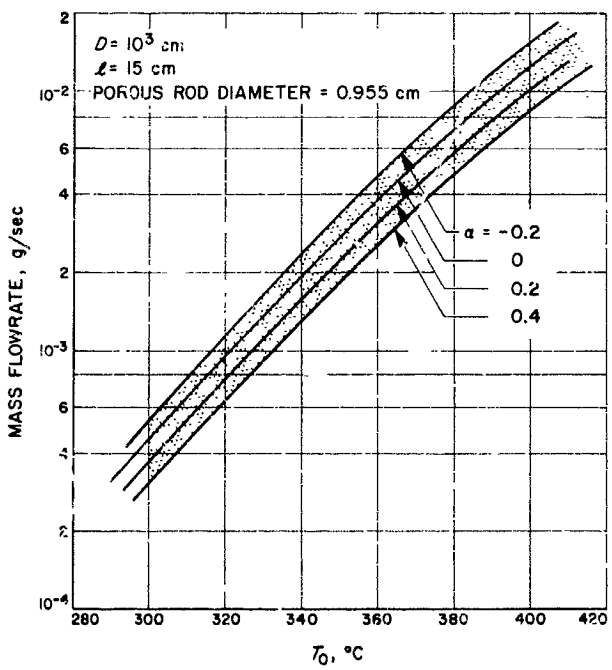

Fig. 22. Mass flow rate as a function of vaporizer inlet temperature for various values of α

Surface tension forces require pressures on the order of 10 psia in the liquid to force it into the vaporizer. The vaporizer could be more easily controlled if the liquid pressure were kept below the surface tension force limit, and the liquid-vapor interface were maintained at the inlet to the vaporizer. Variations in the liquid pressure would then have little effect on the mass flowrate. System operation with the liquid-vapor interface at the entrance and in the vaporizer is discussed in Section 6.

The liquid mercury pressure was of some concern in the previous discussion because of the characteristics of the expulsion system being studied. The metal diaphragms tested thus far expand in a nonuniform manner and experience a sudden expansion after about 10% expulsion. The expansion causes a rapid pressure increase in the mercury liquid. If the liquid is in the vaporizer (i.e., if the liquid pressure exceeds the surface tension pressure) a serious problem could occur, since liquid mercury could then be pushed completely through the vaporizer. This is due to the relatively low impedance of the vaporizer to liquid flow. Operation with the liquid at the vaporizer entrance would not be seriously affected by this transient, unless it exceeded the surface tension and mercury was forced into the vaporizer. The effects of pressure transients on the system will be investigated in this study.

The isolator being used is described in detail later and is the same type being used at the Lewis Research Center[2]. Isolators tested thus far are laboratory models, and further work is required to design and build a more compact type.

3. Positive Expulsion System

In the present investigation, metal and elastomeric diaphragms are being evaluated. Each type shows promise for use in a spacecraft-type system but both have a number of problems in construction and operation.

a. Metal diaphragm system. The diaphragms being tested are 0.003-, 0.004- and 0.005-in. thick 300 series stainless steel. They are convoluted initially and are expanded with gas pressure to form a hemisphere. When placed back to back in a spherically shaped tank, expansion forces the propellant out of the tank. A typical unexpanded diaphragm is shown in Fig. 23. Fig. 24 shows a set of expanded diaphragms. The wrinkles seen result in a slight loss of expulsion efficiency. Expulsion test

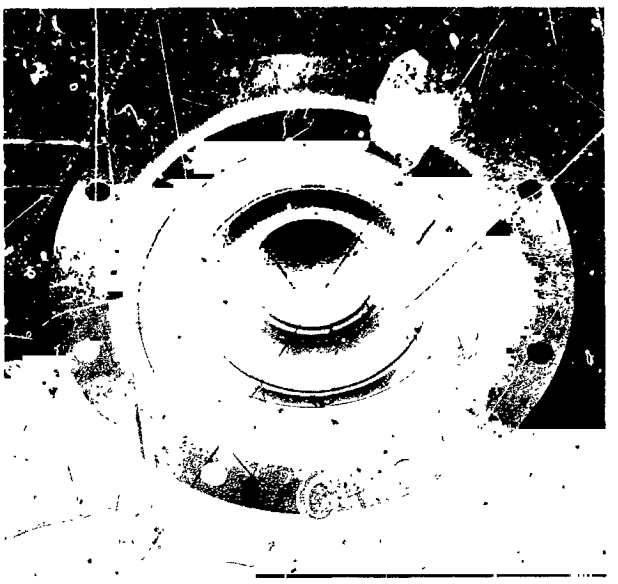

Fig. 23. Typical unexpanded diaphragm

results are summarized in Table 2. The low efficiencies for the thinner diaphragms are the result of a poorly sized tank. That is, the expanded diaphragms did not fill the tank.

Laboratory tests thus far have used a bolted tank which consists of two hemispherical sections and a center flange. The flange is equipped with a knife edge which crushes the diaphragms and provides a liquid and gas seal. The bolted tank is shown in Fig. 25. The laboratory

Table 2. Metal diaphragm tests

Expellant	Thickness of stainless steel diaphragm, in.	Efficiency, %	Maximum expulsion pressure, psig
Water	0.005	9[illegible]	131.6
		[illegible].5	134.4
		94.4	133.4
		94.5	98.5
		94.0	98.5
Cesium		97.5	110
		96.5	110
		97.0	125
		97.0	125
Water	0.004	92.3	125
		88.7	125
	0.003	9[illegible].5	115
		91.2	115

[2]Private communication with P. D. Reader, Lewis Research Center.

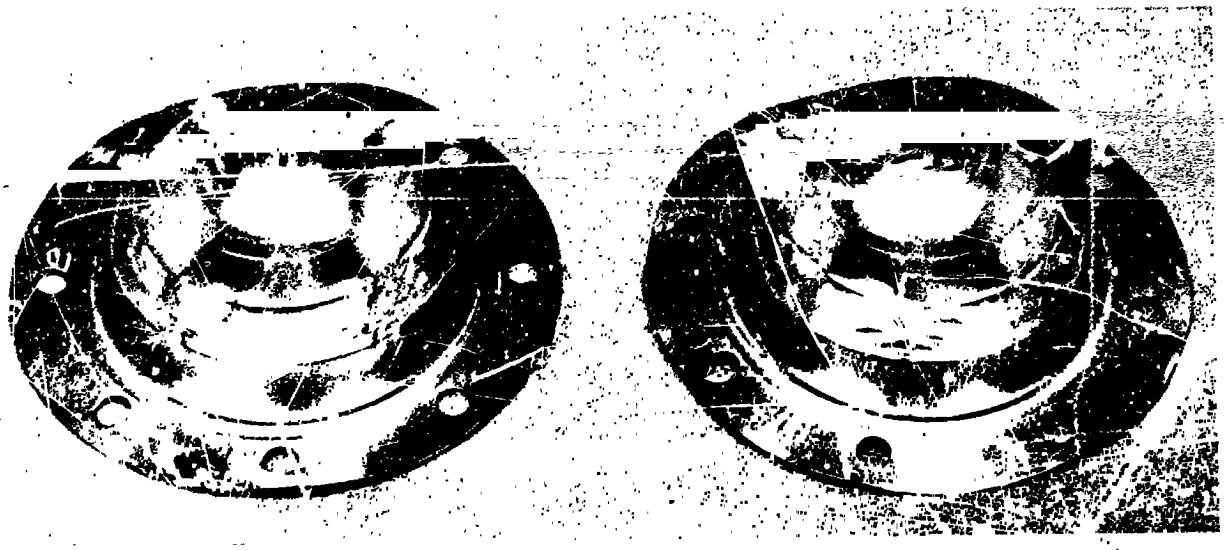

Fig. 24. Expanded diaphragms

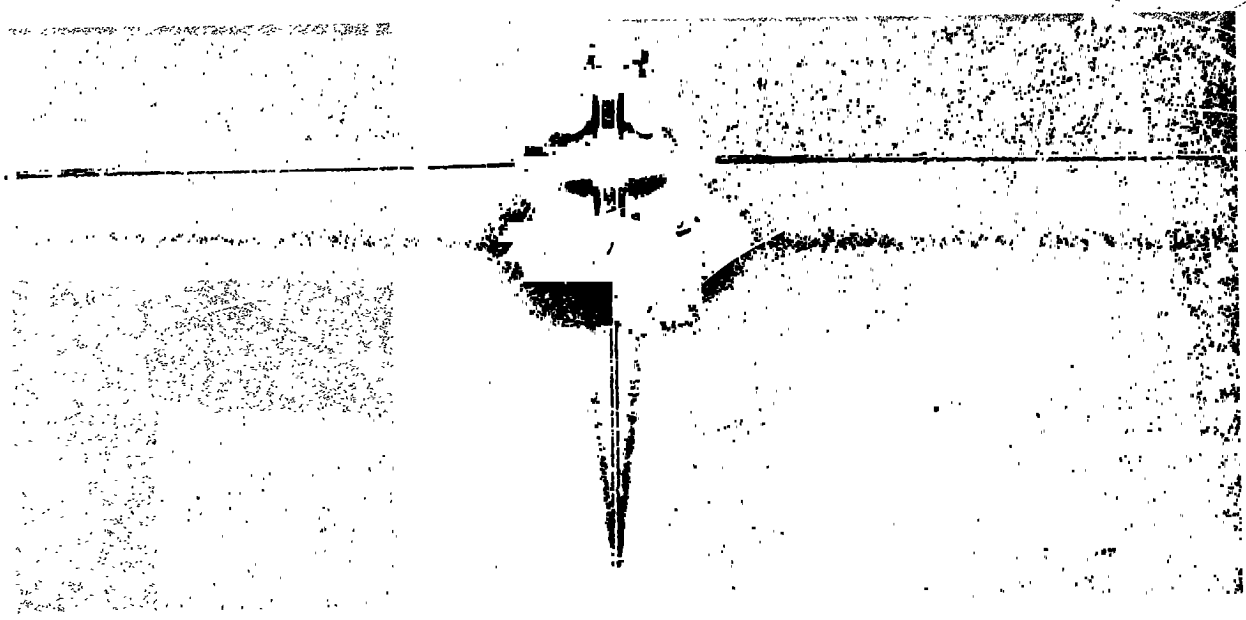

Fig 25. Mercury positive expulsion tank, bolted construction

tank weighs about 5 lb when empty and is far too heavy for spacecraft application. An all-welded tank is shown in Fig. 26 and weighs 0.47 lb. This is 8% of the filled tank weight and is near flight weight.

b. Rubber diaphragm system. A rubber diaphragm system is being studied because of the expulsion-rate control problem with metal diaphragms. The elastomers are expected to provide a more uniform expulsion rate, due to their linear expansion with pressure.

Several rubber materials have been given preliminary water tests to determine expulsion efficiency and pressure requirements. The materials tested were neoprene, butyl, SBR, EPR and Nevea rubber. A summary of the water tests performed to date is shown in Table 3. The

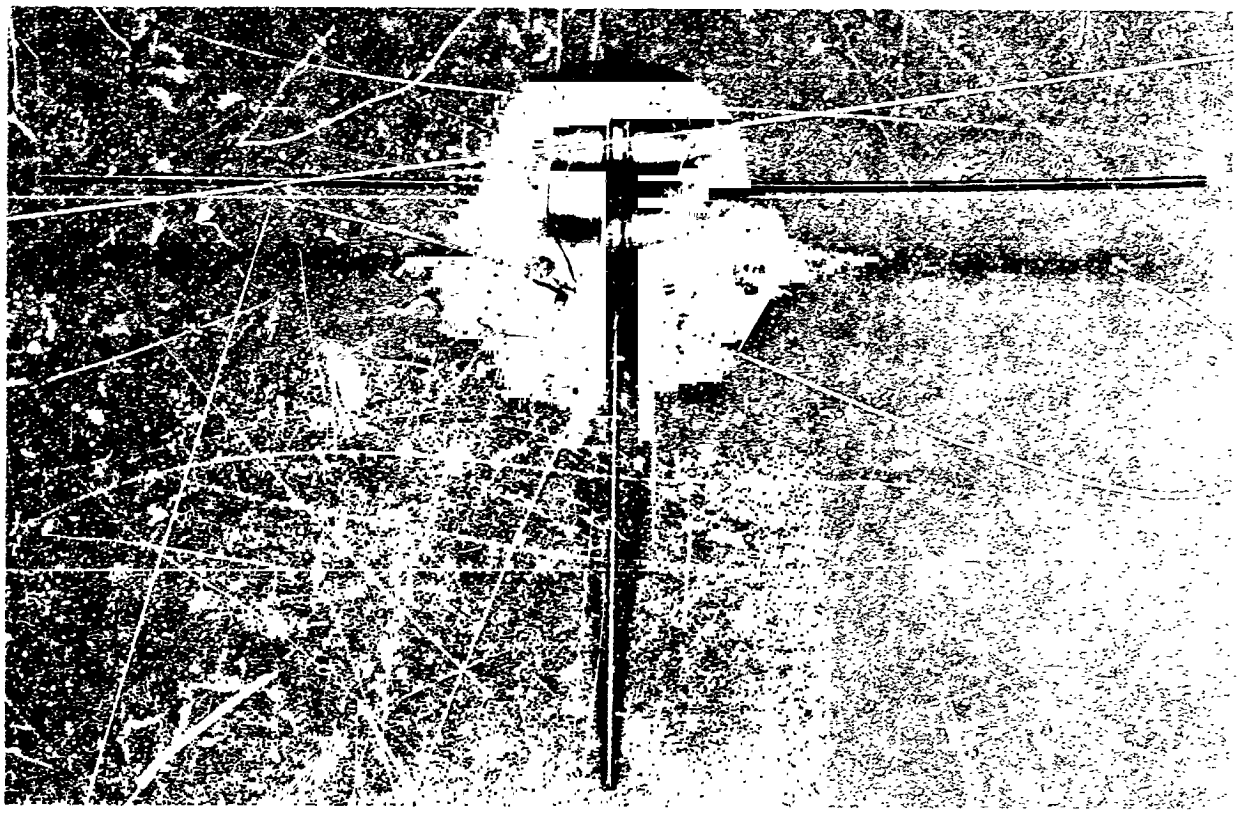

Fig. 26. Mercury positive expulsion tank, welded construction

excellent efficiency of this type of diaphragm is quite encouraging. These tests were performed in the tank shown in Fig. 25.

The use of the elastomeric diaphragms poses a serious problem of tank weight, because of the necessity to use a bolted construction. To get around this problem, filament-wound fiberglass tanks have been fabricated in which rubber diaphragms are integrally contained. These tanks, which have approximately eight times the capacity of the welded tank, weigh about 2 lb. A small fiberglass gas pressurization tank and a propellant tank are shown in Fig. 27. This system has not been tested at the present time.

Table 3. Rubber diaphragm tests

Expellant	Diaphragm	Maximum expulsion pressure, psi	Thickness
Water	EPR	3.5	0.052
	Nevoc	2.7	0.035
	Neoprene	6.3	0.045
	Butyl	Burst at 5.00	0.043
	SBR	Burst at 10.0	0.063

Fig. 27. Fiberglass pressurization tank and propellant tank

4. Propellant Vaporizer

The vaporizer being studied as described in Section 2, is a sintered 316 stainless steel rod, 50% dense, welded in a stainless tube. A heater of nickel thermal coat is wrapped on the tube to provide the desired temperature distribution. Thermocouples and a heat shield are then attached. A vaporizer with heater, thermocouples and flanges is shown in Fig. 28. The length of this particular vaporizer is 6 in.

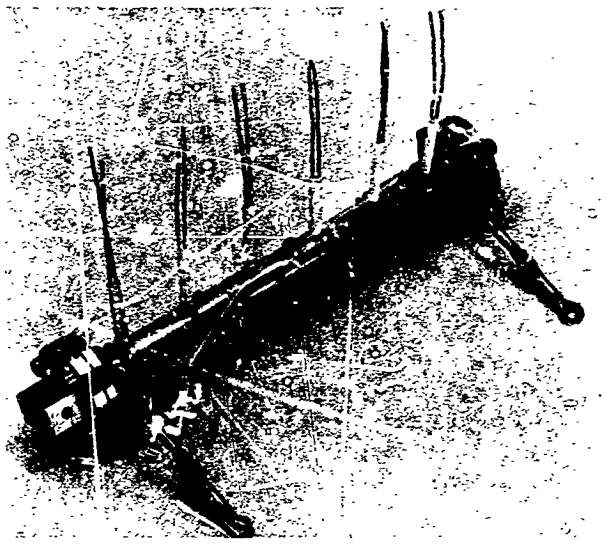

Fig. 28. Typical vaporizer with heater coil and thermocouples

Porous rods of 30, 40, and 50% of theoretical density stainless steel have been evaluated. The 30 and 40% materials were found to be too porous for this system; liquid could be forced through them by relatively low (< 3 psi) pressure, due to low surface-tension forces. The 50% dense materials have performed best thus far; however, more dense materials are being considered to provide better flowrate control characteristics. The control of vapor flow as a function of vaporizer temperature and liquid pressure is currently being investigated.

Vaporizer temperature versus heating power for a 50% dense vaporizer is plotted in Fig. 29 for the hot end upstream and downstream. The difference between the curves is a result of different heat-transfer rates. When operated with the cold end upstream, liquid had to be forced into the vaporizer to provide the desired flowrate. This provided a large path for heat conduction. With the hot end in the upstream position, liquid mercury did not

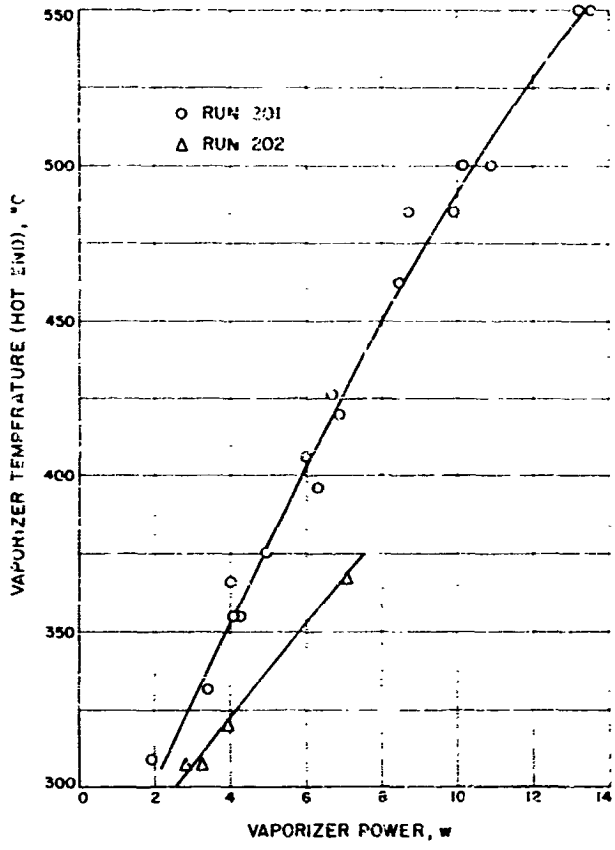

Fig. 29. Vaporizer heating power versus temperature

enter the vaporizer, and the heat conduction path was considerably reduced. Typical steady-state temperature profiles are shown in Fig. 30.

Additional studies must be performed to determine the minimum vaporizer length and optimum temperature distribution for control purposes. However, it now appears that the vapor flowrate is not extremely sensitive to temperature distribution and is primarily controlled as expected by the temperature of the liquid-vapor interface.

5. Isolator

The mercury bombardment ion engine operates at a high positive voltage in order to accelerate and focus an ion beam. Since it is convenient to have the feed system at spacecraft ground, three problems arise: (1) a portion of the feed line must be a good insulator and must withstand temperatures high enough to prevent propellant condensation, (2) the pressure of the mercury vapor in the isolator must be such that a high voltage breakdown

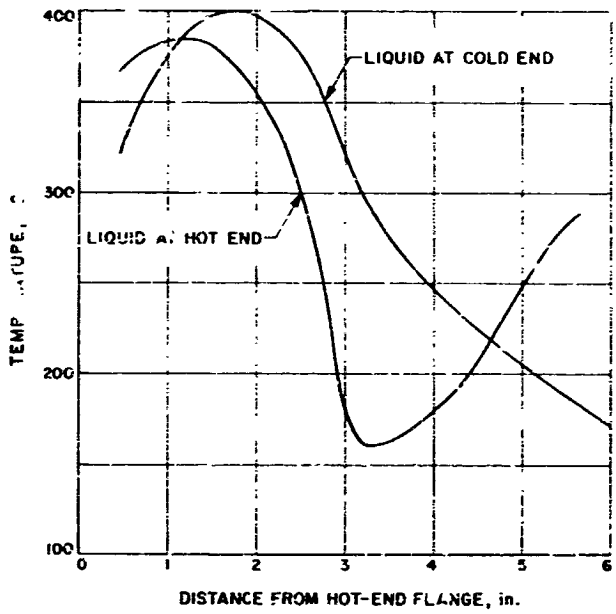

Fig. 30. Observed vaporizer temperature distribution

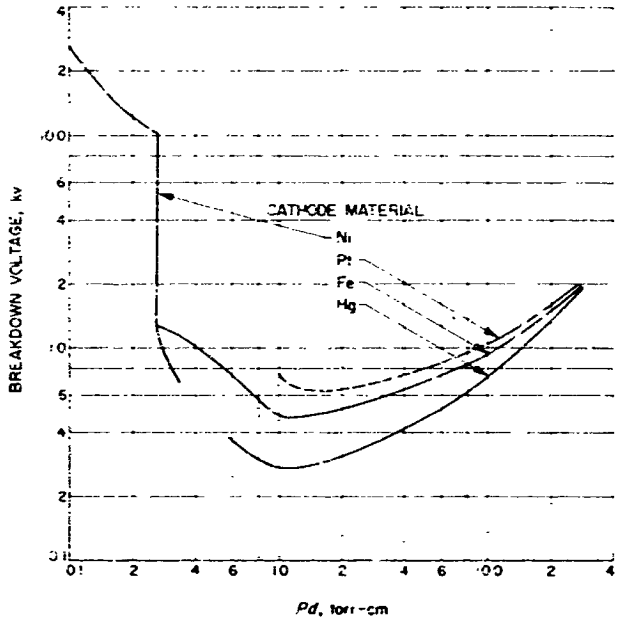

Fig. 31. Breakdown voltage versus *Pd*

will not occur, and (3) the plasma in the engine must be bounded to restrict ion currents from flowing through the plasma to ground.

The first problem is easily solved with a glass or ceramic tube. The tube can be heated to prevent condensation, with the required temperature depending on the pressure in the isolator. Initially a glass tube approximately 1.5-in. ID was chosen, based on isolators used at Lewis Research Center. The pressure in the isolator was calculated to be about 10^{-3} torr. At this pressure, a temperature greater than ambient should prevent condensation. In the experiments reported, the isolator heater was operated in series with the rest of the feed-line, which, due to its smaller diameter (0.5 in.) and consequently higher average pressure, had to be maintained at a higher temperature to prevent mercury condensation. The actual isolator temperature was 200°C.

The second problem, that of a high voltage breakdown, can be investigated with the use of Paschen curve data (Ref. 30). Fig. 31 is a plot of breakdown voltage against *Pd*, where *P* is the pressure and *d* is the spacing between electrodes (in this case, ends of the isolator). Using 10^{-3} torr and 5 kv, an isolator of any convenient length is operable, since *Pd* will be to the left of the minimum on the curve for *d* less than 300 cm. A length of 10 in. was chosen initially; however, a much shorter length should work just as well.

The last problem is also easily solved with the use of a fine mesh screen placed in the isolator. Tests have indicated that the screen can be operated at engine potential or left "floating." The screen provides a boundary for the plasma and the sheath formed restricts the plasma from propagating upstream. A screen rolled into the form of a cone is being used for this purpose. The glass isolator with a heater and thermocouples are shown in Fig. 32. This isolator, used in the initial tests, broke near one of the metal seals. A boron nitride element was then fabricated, which is shown in Fig. 33. The plasma boundary screen and details of the heater can also be seen in this figure. The BN isolator is 1.25-in. ID.

6. System Operation

The system presently being tested is shown on the vacuum tank header in Fig. 34. Initial tests indicate that the system operates as expected. However, sufficient operational time has not been logged to determine quantitative information about the control functions required.

The expulsion tank with metal diaphragms performed as expected, although some extraneous problems were introduced when operating the system on a daily rather than a continuous basis. The gas expulsion pressure was reduced at the end of each day to eliminate any possibility of pushing liquid through the vaporizer. This

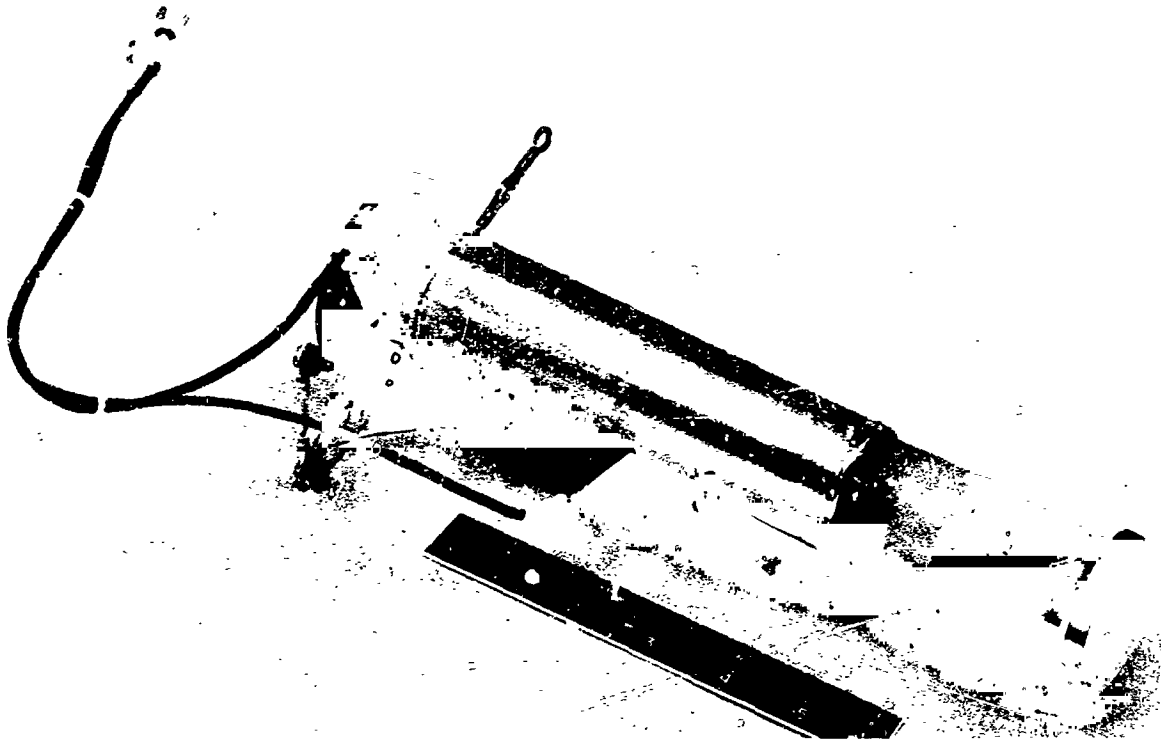

Fig. 32. Glass isolator with heater and thermocouples

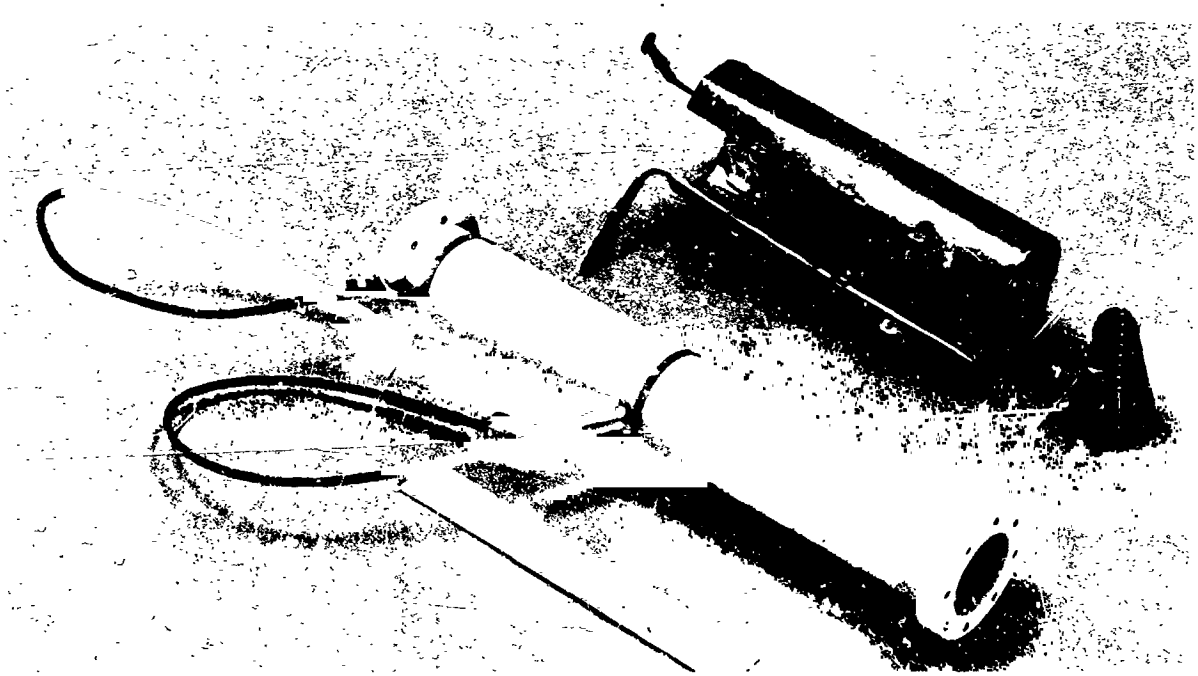

Fig. 33. Boron nitride isolator

Fig. 34. Mercury positive expulsion system mounted on tank header

cycling caused a diaphragm to crack, and the first run had to be terminated.

During this first run, the vaporizer was operated with the hot end upstream and with the liquid-vapor interface at the vaporizer inlet. The vaporizer temperature was found to control the flowrate quite adequately. The liquid pressure had little effect, as one might expect from the discussion in Section 2. An automatic controller was used to maintain the desired temperature at the upstream end of the vaporizer.

A second run is currently being made with new diaphragms and with the vaporizer hot end downstream and liquid in the vaporizer in order to evaluate the problems arising when the liquid-vapor interface is inside the vaporizer. In this mode, the flowrate has been difficult to control with either temperature or pressure, due to their interaction. Conclusive data are not yet available on the operation of the system in this mode.

The isolators (glass and boron nitride) operated properly to as high a voltage as needed—4.5 kv. Breakdown did occur when the flowrate was excessive during several startups; however, steady-state operation was completely stable.

Table 4. Engine and feed system operating conditions

Engine	Run 1	Run 2	Run 3	Run 4	Run 5	Run 6
V^+, kv	2.0	2.0	2.50	2.5	2.7	2.7
V^-, kv	3.0	3.5	3.0	3.0	3.0	3.0
I^+, ma	400	460	500	522	550	580
I^-, ma	3.3	3.6	3.8	3.8	4.5	5.0
Arc current, A	10	12.0	13.5	13.7	14.0	14.0
Arc voltage, v	35.0	36.0	36.0	37.5	35.0	34.0
Cathode power, w	0	0	0	0	0	0
Magnet power, w	32	41	38	39.5	29.5	29.5
Beam power, kw	0.88	0.91	1.24	1.30	1.47	1.55
Total power, kw (including feed system)	1.22	1.44	1.82	1.91	2.05	2.12
Feed System						
Vaporizer power, w	4.9	6.0	6.0	6.0	5.7	5.9
Isolator heater, w	28.0	28.0	28.0	28.0	28.0	28.0
Expulsion pressure, psia	18.1	20.1	20.8	19.9	6.7	4.5
Liquid Hg pressure, psia	3.3	2.8	2.7	2.6	5.8	5.4
Performance						
η_{power}, %	65.0	63.5	68.4	68.0	71.8	73.0
I_{sp}[a], sec	4450	4450	4970	4970	5180	5180
Power/thrust, kw/lb	151	155	161	162	158	155

[a] Uncorrected for propellant utilization.

The system operation in the first tests is presented in Table 4. The engine data is included for completeness, although the engine operation has not been specifically described in this report.

Several modifications are anticipated from the system performance to date. The vaporizer and isolator can apparently be made shorter, at least by a factor of two. A vaporizer of 60% dense material is being planned to aid in controlling the flowrate. The gas pressurization problem is being studied to make the liquid pressure control automatic as is necessary for spacecraft operation. Tests will also continue on the rubber diaphragms to determine their applicability.

From the results to date, the system being studied appears to be worth further investigation. With some modifications and additions, this system gives promise of becoming a reliable and controllable feed system for spacecraft application.

References

1. Massier, P. F., "Heat Transfer to Convergent-Divergent Nozzles From Ionized Argon," *SPS 37-24*, Vol. IV, pp. 105–108, Jet Propulsion Laboratory, Pasadena, California, December 31, 1963.
2. Pai, S., *Viscous Flow Theory, I—Laminar Flow*, pp. 36, 38, 43, D. Van Nostrand Company, Inc., Princeton, New Jersey, 1956.
3. Back, L. H., Massier, P. F., and Gier, H. L., *Comparisons of Experimental With Predicted Wall Static-Pressure Distributions in Conical Supersonic Nozzles*, Technical Report No. 32-654, Jet Propulsion Laboratory, Pasadena, California, October 15, 1964.
4. Volluz, R. J., Handbook of Supersonic Aerodynamics, Wind Tunnel Instrumentation and Operation, NAVORD Report 1488, Vol. 6, Section 20, p. 297, January 1961.
5. Elliott, D., Cerini, D. J., and Weinberg, E., *Investigation of Liquid MHD Power Conversion*, Third Biennial Aerospace Power Systems Conference, Philadelphia, Pa., September 1–4, 1964, AIAA Paper No. 64-760.
6. Elliott, D., "DC Liquid Metal Magnetohydrodynamic Power Generation," *Sixth Symposium on the Engineering Aspects of Magnetohydrodynamics*, University of Pittsburgh, Pittsburgh, Pa., April 21–22, 1965, pp. 49–59.
7. Elliott, D., Cerini, D., Hays, L., O'Connor, D., and Weinberg, E., "Liquid MHD Power Conversion," *SPS 37-28*, Vol. IV, pp. 86–92, Jet Propulsion Laboratory, Pasadena, California, August 31, 1964.
8. Elliott, D., Cerini, D., and Eddington, R., "Liquid MHD Power Conversion," *SPS 37-29*, Vol. IV., pp. 106–115, Jet Propulsion Laboratory, Pasadena, California, October 31, 1964.
9. Elliott, D., Cerini, D., Hays, L., and Weinberg, E., "Liquid MHD Power Conversion," *SPS 37-30*, Vol. IV, pp. 116–119, Jet Propulsion Laboratory, Pasadena, California, December 31, 1964.
10. Elliott, D., Cerini, D., Hays, L., and Weinberg, E., "Liquid MHD Power Conversion," *SPS 37-31*, Vol. IV, pp. 186–191, Jet Propulsion Laboratory, Pasadena, California, February 28, 1965.

References (Cont'd)

11. Elliott, D., Cerini, D., and Hays, L., "Liquid MHD Power Conversion," *SPS 37-32*, Vol. IV, pp. 134–141, Jet Propulsion Laboratory, Pasadena, California, April 30, 1965.

12. Blake, L. R., "Conduction and Induction Pumps for Liquid Metals," *Proceedings of the Institute of Electrical Engineers*, London, Vol. 104A, July 1956, pp. 49–63.

13. Pierson, E. H., *The MHD Induction Machine*, Thesis, Massachusetts Institute of Technology, Cambridge, Mass., September 1964.

14. Jackson, W. D., and Pierson, E. S., "The Magnetohydrodynamic Induction Machine of Finite Length," *Research on New Concepts in Energy Conversion*, Quarterly Progress Report No. 4, Research Laboratory of Electronics, Massachusetts Institute of Technology, Cambridge, September 15, 1964, pp. 6–17.

15. Peschka, W., Kelm, S., and Engeln, F., "Penetration Effects in the MHD Induction Engine of Semi-Infinite Length," *International Symposium on Magnetohydrodynamic Electrical Power Generation*, Paris, France, July 6–10, 1964.

16. Schwab, B., "Theory of Annular Electromagnetic Pumps and Comparison with Experiments," *Liquid Metal Colloquium of the European Society of Atomic Energy*, Aix-en-Provence, September 30–October 2, 1963, AEC Translation No. 6383.

17. Sudan, R. N., "Interaction of a Conducting Fluid Stream with a Traveling Wave of Magnetic Field of Finite Extension," *Journal of Applied Physics*, Vol. 34, No. 3, March 1963, pp. 641–650.

18. Lingle, J. T., and Jenson, K. J., *Low Input Voltage Conversion*, Quarterly Progress Report No. 1, March 1 to May 31, 1964, Honeywell, Inc., Ordnance Division, Hopkins, Minnesota.

19. Barcatta, F. A., Daley, H. L., Firestone A. H., and Forrester, A. T., "Zero Gravity Feed Systems for Cesium Ion Rocket Engines," AIAA Preprint 63027, 1963.

20. Samuel, W. A., "Research and Development of Propellant Feed Systems for Ion Engines," MSA Research Corp., Final Contract Report, NAS 8-2589, 1963.

21. Thompson, L. M., "Welded Metal Bellows, A Reliable Positive Expulsion Device for Liquid Propellants," AIAA Preprint 64-264, 1964.

22. Lawlor, P. J., and Montgomery, K. M., "Research and Development of Propellant Feed Systems for Ion Engines," Thompson Ramo Wooldridge, Inc., Final Contract Report, Contract NAS 8-2525, 1964.

23. Krivetsky, A., and Bauer, W. H., Loucks, H. L., Podlog, J., Robinson, J. V., and Walters, W. H., "Research On Zero-Gravity Expulsion Techniques," Bell Aerosystems Co., Final Contract Report, Contract NASR-44, 1962.

24. Atkins, J. H., "Research and Development of Propellant Feed Systems for Ion Engines," National Research Corp., Final Contract Report, Contract NAS 8-1619, 1961.

25. Tepper, F., "Research and Development of Propellant Feed System for Ion Engines," MSA Report, Contract NAS 1617, September 6, 1961.

References (Cont'd)

26. Lawlor, P. T., and Muller, M. W., "Literature and Industrial Survey and Outline of Experimental Test Program for Development of Ion Propellant System," Thompson Ramo Wooldridge, Inc., Interim Report No. 1, TRW No. 512-007946-88, Contract AF 33(616)-7219, 1960.

27. Montgomery, K. M., "Porous Matrix Phase Separator Evaluation," Thompson Ramo Wooldridge, Inc., Contract NAS 3-2518, 1964.

28. Kerrisk, D. J., and Masek, T. D., "Effects of Plasma Nonuniformity on Grid Erosion in an Electron Bombardment Ion Engine," AIAA Preprint, 64-688, 1964.

29. Strickfaden, W. B., and Geiler, K. L., "Probe Measurements of the Discharge of an Operating Electron Bombardment Engine," *AIAA Journal*, Vol. 1, pp. 1815–1823 (1963).

30. Landolt-Bornstein, *Physikalisch-Chemische Tabellen*, IV Band, Technik, 3 TEIL.

XV. Liquid Propulsion

A. Advanced Liquid Propulsion Systems

R. N. Porter, D. D. Evans, W. H. Tyler, W. F. MacGlashan, and O. F. Keller

1. Introduction

The Advanced Liquid Propulsion Systems (ALPS) program is investigating selected problems generated by spacecraft operational requirements for propulsion systems capable of high inherent reliability, long-term storage in space, multiple start in free fall (zero-gravity), and engine throttling. The solutions proposed to satisfy these requirements have been incorporated into the ALPS system.

Periodic reports in the *SPS*'s (starting with *SPS 37-8*) describe the progress of work on the various parts of the ALPS system. Recent accomplishments are outlined below. These include an investigation of the reactions between nitrogen tetroxide and hydrazine, firing tests of several ablative thrust chambers, work on a method for locating pinholes in metal foils, high- and low-temperature tests of a tank and expulsion diaphragm assembly, and results of a metallographic examination of an aluminum propellant tank which has been subjected to a long-term storage test with hydrazine.

2. Injector Development,[1] D. D. Evans

a. Introduction. The nitrogen tetroxide–hydrazine (N_2O_4–N_2H_4) propellant combination exhibits an extremely rapid liquid-phase reaction rate. This factor requires the utilization of special techniques to accomplish liquid phase mixing, since the rapid reaction tends to disrupt the mixing process with a resultant decrease in performance of some injectors. Previous attempts physically to increase the mixing of a doublet element were described in *SPS 37-22, 24,* and *28,* Vol. IV; and Ref. 1 contains the results of these and other related experiments. Since these physical methods were unsuccessful, it was decided to attempt to find a chemical inhibitor for the N_2O_4–N_2H_4 reaction. Such an inhibitor presumably would allow mixing to be accomplished before sufficient energy could be released to disrupt the impingement process. *SPS 37-29,* Vol. IV described the results of an investigation into ignition delay inhibitors.[1] To summarize, it was found that the ignition delay time could be varied over a range of 0.8 to 4.2 msec by the use of additives to the fuel, including such compounds as fluorobenzene and triethylborate (the value for the delay time without inhibitors was 2.6 msec). However, it was found that these inhibitors had little effect on the mixing

[1] This work and the work described herein was performed under contract to JPL by Dynamic Science Corp., Monrovia, Calif.

process when subjected to rocket engine testing in the 2000-lb thrust standard test engine; experimental combustion efficiency remained unchanged from the case without additives.

The decision was then made to pursue this chemical approach further in three phases: Phase I being to determine the temperature, and measure the heat evolved in the first step of the nitrogen tetroxide–hydrazine reaction through the use of differential thermal analysis techniques; Phase II being to examine the infrared spectrum of any solid phase thus formed in order to identify any intermediate species which may be present in the reaction; and Phase III being to determine the effects of various surface-active agents on the miscibility of N_2O_4 and N_2H_4 by photographing the dropwise addition of the oxidizer into the fuel. This report will summarize the results of the investigations performed in the three phases described above. A comprehensive report is now under preparation and will be published in the near future.

b. Differential thermal analysis. Differential thermal analysis (DTA) of the N_2O_4-N_2H_4 reaction system was made using the apparatus shown in Fig. 1. The reaction was run in an all glass system in which the reactor and reference bulb were immersed in the same low-temperature environment. The temperature of the calorimeter was controlled by bubbling nitrogen gas through liquid nitrogen and then into the calorimeter. An electrical heater on the inlet tube allowed the cold nitrogen to be warmed at a uniform rate. The thin-walled reactor and reference bulb were plated with a platinum film and the thermocouples soldered to the surface of the glass to insure intimate contact. In a typical experiment, measured quantities of reactants were condensed into the reactor with liquid nitrogen. The liquid nitrogen was removed from the Dewar and a flow of cold nitrogen gas was started immediately. The output voltage of the thermocouples on the reactor and differential between the reactor and reference cell were measured on a potentiometer. The current on the heater winding was increased

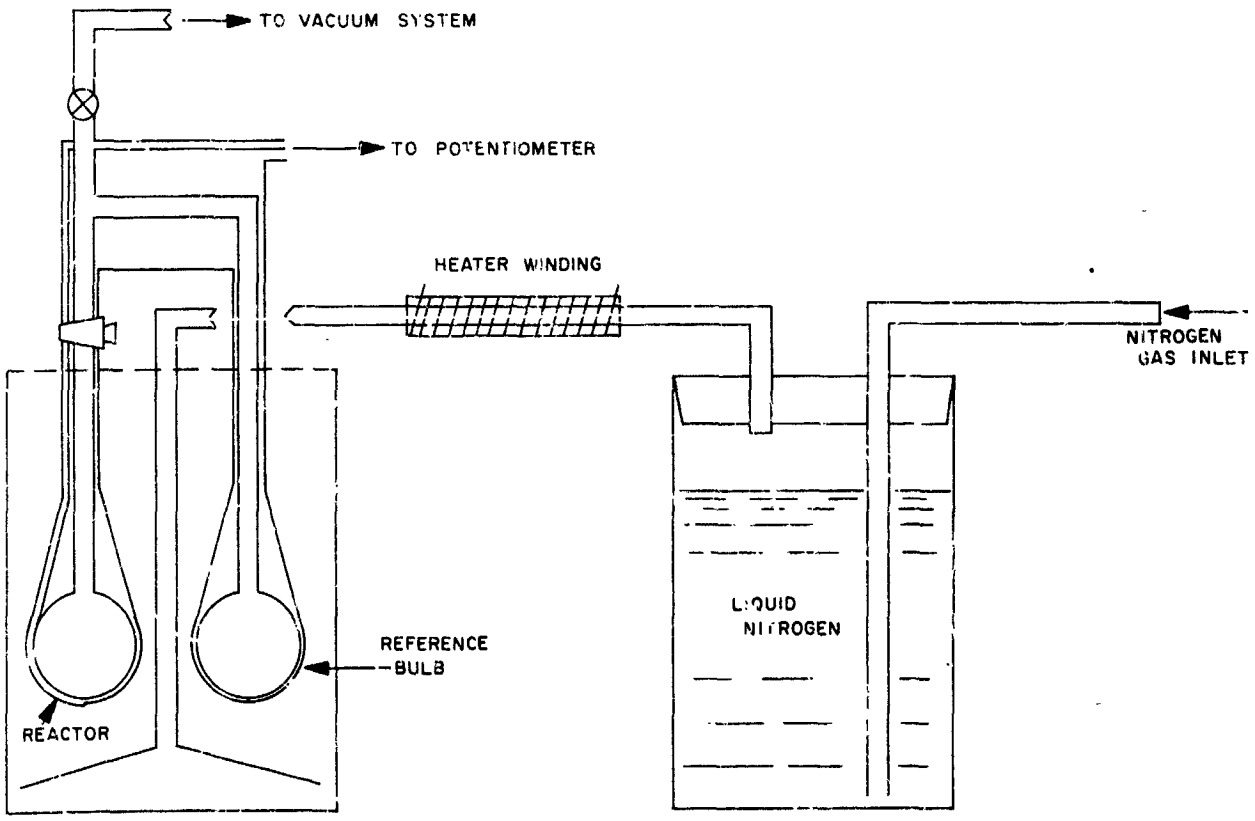

Fig. 1. Differential thermal analysis apparatus

slowly as required to obtain the desired increase in temperature.

A number of DTA experiments were conducted. The results of one of these experiments are given in Fig. 2. In the lower plot the potentiometer reading, obtained from a differential thermocouple located on the sample bath and reference bulb, is recorded as a function of time. The data obtained are positive when the sample bulb is at a higher temperature than the reference bulb. The upper curve in this figure shows the temperature of the reactor with time. This was obtained from a standard thermocouple attached to the bulb containing the N_2O_4–N_2H_4 mixture. By alternating readings it was possible to obtain both bulb temperature and differential temperature curves during the same run. Note that the point of inflection of the DTA curve (labeled "A") occurred at a temperature of −58°C. The broad base on this curve and the small rise occurring on the trailing edge of the main peak are attributed to either a nonuniform

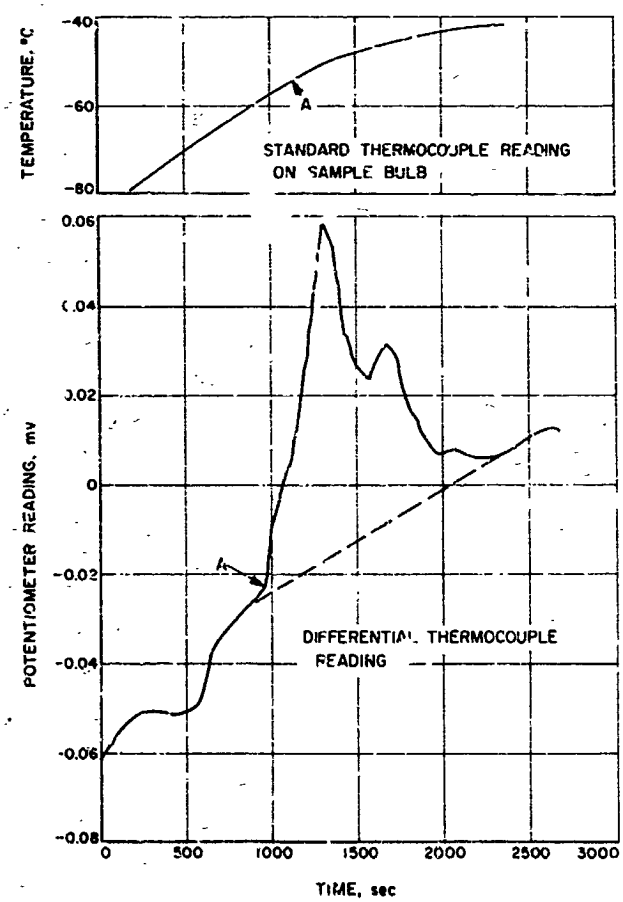

Fig. 2. DTA Experiment 19

reaction or to poor heat transfer to the thermocouple junction. Using the initial temperature rise as a measure of the energy released, a value of about 1 kcal is calculated, if one assumes reaction of all the N_2O_4 present in the reactor. This represents the minimum amount of heat liberated from this reaction. No evidence of exothermic reaction was obtained at temperatures below −58°C.

c. Infrared techniques. Low-temperature infrared spectra were obtained in a specially constructed low-temperature infrared cell. A liquid-nitrogen–cooled sodium chloride window was used to view the sample. Calibrations were accomplished with pure N_2H_4 and N_2O_4 in order to learn how much material was required to give a spectrum of optimum intensity. After initial calibrations were accomplished, infrared spectra of nitrogen tetroxide–hydrazine mixtures were obtained at low temperatures. A total of about 150 spectra were taken in a series of experiments aimed at distinguishing the minimum reaction temperature and identifying intermediates and products of the reaction. In the procedure used on these experiments, N_2O_4 and N_2H_4 were first condensed on the sodium chloride window at liquid nitrogen temperature (−196°C), and then were warmed slowly as spectra were recorded in rapid succession. The first evidence of new species being formed was obtained during a test at −133 to −124°C, when several new peaks were observed in the spectra. Further progressive changes were evident in spectra up to a temperature of −43°C. No further spectral changes were noticed at temperatures below room temperature, but the over-all intensity of the spectrum decreased somewhat.

In order to establish if the reaction occurring at −133°C represented an adduct formation or a reaction, it was deemed advisable to measure and identify the volatile gases from the reaction. Of the possible gases that could be obtained, all but ammonia have vapor pressures sufficiently high to be pumped from the reaction system for analysis and measurement at the temperatures where reaction first occurs (−133°C). The high sensitivity of the infrared for ammonia insures that it would be observed in the solid phase if it were present. In order to conduct a gas analysis the reaction was allowed to proceed in a glass bulb to which a thermocouple had been attached. The N_2O_4 and N_2H_4 were condensed in a tube in layers at −196°C. The bulb was then warmed slowly while gases were pumped continuously using a Toepler pump. Gases were pumped into an infrared cell, where their volume was determined, and infrared spectra were obtained. The spectrum obtained corresponds to that of nitrous oxide (N_2O). The gas from this cell was then

transferred directly into a mass spectrometer for analysis, and the presence of a substantial quantity of N_2O in the product gas was confirmed by a large parent peak at mass 44. In addition, residual peaks at mass 30 and 28 indicated presence of NO and N_2. The major part of the gas was collected at a temperature above −110°C.

More quantitative experiments were conducted in which the nonvolatile and volatile products at various temperatures were measured and identified. The results are shown in Table 1. This table shows the quantities of gases given off at each temperature, and identifies each gas. The formation of the large quantity of N_2O in the reaction at −50°C shows that the principal reaction occurred between −126 and −50°C. It is of interest that the reactions occurring at temperatures above −50°C involve liberation of only trace amounts of additional gases.

In one of the low temperature experiments, it was observed that crystals of a solid material had formed in the bulb. A melting point determination was conducted with the sample, and the material was melted in the range of 66.3 to 73.0°C. Of the possible products that could be formed in the reaction, only hydrazinium nitrate (mp. 71°C) fits the observed melting points of the crystals. The presence of hydrazinium nitrate was subsequently confirmed by infrared analysis.

From the accumulated infrared data it is concluded that the low temperature reaction between N_2O_4 and

Table 1. Gas evolution from the low temperature reaction of N_2O_4–N_2H_4

Temperature, °C	Gas evolved, millimoles × 10^{-2}		Species found
	Non-condensable[a]	Condensable[a]	
−126	0.13		NO, N_2
		10.3	NO_2, N_2O
−50	0.52		N_2
		30.5	N_2O, NO_2 + unknown
−30	0.25		N_2
		0.27	NO_2
+25	0.02		N_2
		0.16	NO_2
Total gas evolved	0.92	41.2	

[a] At −196°C in the LN_2 trap.

N_2H_4 forms an intermediate adduct, which in turn reacts at about −50°C to form an intermediate species capable of reverting to hydrazinium nitrate, nitrous oxide, and traces of nitric oxide and nitrogen. To balance an equation in which N_2O and hydrazinium nitrate are formed from N_2O_4 and N_2H_4 requires ammonia as another reaction product, viz.

$$N_2O_4 + 2\,N_2H_4 \rightarrow N_2H_5NO_3 + N_2O + NH_3$$

Curiously, ammonia has never been observed as a product in any of the reactions. An unidentified material having a vapor pressure of about 42.5 mm at −111.8°C was observed, however. This material appeared on the gas chromatogram after N_2O (retention time, 18 min).

d. Miscibility experiments. High-speed motion pictures were taken of the dropwise addition of N_2O_4 to N_2H_4, with and without additives. The purpose of these experiments was to find a miscibility agent for the two propellants. The technique of Weiss and Klusmann (Ref. 2) was used. The procedure involves the use of a high-speed camera operating at 4000 to 5000 frames/sec to photograph the N_2O_4 drops as it falls through a 1-in. column of hydrazine. The apparatus utilizes a condenser system of lenses for back-lighting the sample tube. The yellow color defined the N_2O_4 drop, which is easily distinguished on color film. This method also provided a qualitative measure of the reactivity of the propellant. It is thought that either an increase in miscibility between the two propellants, or a substantial decrease in the initial reaction rate, might be beneficial in solving the problem of the rapid reaction disruption, the stream impingement and mixing process. Visual observation appeared to be the quickest method for study of this phenomenon.

Initial tests were conducted with pure N_2O_4 being added to hydrazine containing 16% water. This propellant combination was chosen for testing because it had shown evidence of solving the stream disruption process in previous tests at JPL (Ref. 1). These photographs did not indicate increased miscibility, but showed instead an apparent decrease in the rate of reaction between the two propellants. No evidence was obtained of increased miscibility between the two reactants for any of the additives tried. However, apparent differences in reactivity were observed.

Although only qualitative estimates could be made of the relative reaction rates, it appeared that four types of reactions were occurring. These are shown in Table 2.

Table 2 Effect of additives on N_2O_4–N_2H_4 reaction

Additive in N_2O_4	Additive in hydrazine (% by weight)	Type of reaction[c]
None	None	A
None	16% H_2O	B
None	16% H_2O 8% KOH	B
None	1% Santomerse (Monsanto Chemical Co.)	C
None	1% Alkaterge A (Hercules Powder Co.)	C
None	1% FC-126 (Minnesota Mining and Mfg. Co.)	C
None	Oronite NI-O (California Chemical Co.)	C
None	Oronite NI-W	C[a]
1% I_2	None	—[b]
16% H_2O	1% Oronite NI-O	C
1% I_2	1% Oronite NI-O 16% H_2O	D

[a] Possible increase in solubility.

[b] Ignited.

[c] Type A: Rapid reaction which vaporizes N_2O_4 at surface of contact and causes N_2O_4 drop to be thrown out of the chamber.

Type B: Similar to A, except that reaction time appears slower.

Type C: Slow reaction time and evidence of more extensive reaction between N_2O_4 and hydrazine, resulting in violent interaction.

Type D: Reactants are in contact; reaction is mild with relatively slow "boiling" of N_2O_4.

All of the additives in the hydrazine appeared to decrease the rate of initial reaction. The most dramatic change in reaction rate appeared when 1% iodine was added to the N_2O_4, and a mixture of 1% Oronite NI-O and 16% water was added to the hydrazine. In this case two liquids actually remained in contact while reacting and did not tend to blow apart as normally observed. Subsequent experiments with these same compounds revealed that the water content could be reduced to 2% and the same slow-reaction effect could be obtained. The presence of iodine in the N_2O_4–N_2H_4 system was predicted to decrease the reaction rate, since the reaction was thought to proceed by a free-radical mechanism, and iodine is known to suppress this mechanism. Surprisingly, however, the ignition delay time with normal N_2H_4 was shortened when the iodine was added to the N_2O_4, and in the droplet experiment very rapid reaction and ignition occurred.

On the basis of the above results it was judged to be worthwhile to make rocket motor firings at the 2000-lb thrust level, utilizing the same apparatus as used in previous experiments, wherein the stream separation phenomenon had been observed (Ref. 1). Tests were conducted with 1% I_2 in the N_2O_4 and with 1% Oronite NI-W and 1% Oronite NI-O in hydrazine containing 2% H_2O. Only a slight effect (2% higher c^*) was observed with the propellants containing additives, as compared to previous tests with neat propellants. This approach was not pursued further, since the performance gains were so slight.

e. Conclusions. The data obtained in the work reported here is consistent with the fact that nitrogen tetroxide–hydrazine impinging jets are subject to disruption by the rapid reaction occurring at the interface between the two propellants. The principal factors which cause this phenomenon are believed to be: (1) the rapid reaction rate between N_2O_4 and N_2H_4, resulting in rapid heat evolution and the generation of a large gas volume, and (2) the immiscibility of the two reactants.

Although these factors are closely related, it appears that miscibility is a major factor. Photographic studies showing the dropwise addition of N_2O_4 to N_2H_4 indicate that the two materials are completely immiscible. None of the pictures, with or without additives, gave any indication of even partial miscibility of the two compounds. Additives to promote miscibility still cannot be ruled out as possible solutions to this problem. However, mixing processes are generally considered to be relatively slow, even with miscible materials, and even improved miscibility may not overcome the rapid rate of reaction at the liquid-liquid interface.

As reported above, the reaction between nitrogen tetroxide and hydrazine can occur at a temperature as low as −133°C. From measurements of the gas evolved at this temperature, it appears that this initial reaction involves adduct formation between N_2O_4 and N_2H_4. The fact that no measurable heat is evolved in this initial reaction tends to support this view. A further reaction, involving heat evolution occurs at about −58°C. These reactions were carried out under conditions where the rate of temperature rise could be carefully controlled. Thus heat generated by the reaction was quickly dissipated, and intermediates such as hydrazinium nitrate were capable of being isolated. Under actual conditions in an engine, these initial reactions would occur very rapidly. Not only would the initial reactions occur rapidly, but the heat evolved in these reactions would effectively increase the reaction temperature. On this basis, it is estimated that the reaction between hydrazine and nitro-

gen tetroxide would go to completion on contact. Since the stoichiometric reaction between these two propellants involved one mole of N_2O_4 plus two moles of N_2H_4 going to three moles of gaseous N_2 plus four moles of H_2O, while evolving approximately 2 kcal/mole, it is not surprising that the bulk of the liquid can be diverted by relatively small surface interaction.

It is difficult to conceive of a chemical approach which would solve this problem. It does not appear possible to prevent adduct formation or decomposition by the use of additives. It is possible that the rate of decomposition of intermediates such as hydrazinium nitrate could be altered chemically. The most promising method of improving rocket engine performance thus appears to be injector design. It is important that the surface-to-volume ratio is as large as possible, so that essentially all of the liquid is contacted, thus small diameter jets or sheets of liquid appear optimum for this propellant system.

These results do appear applicable toward our understanding of ignition phenomenon. The so-called ignition-spike problem may well be related to this set of reactions wherein explosive compounds such as hydrazinium nitrate are formed on the interior wall of the rocket motor during the preignition period. Compounds such as these could then detonate when the temperature increases during the ignition process. This could well lead to the extreme pressure excursions which have been encountered with propellant systems of this general class.

3. Thrust Chamber Development, W. H. Tyler

The ALPS program has recently completed evaluation test firings of five 100-lb thrust ablative thrust chamber assemblies. These chambers were obtained from five different industrial suppliers and were tested as a partial assessment of the current state of the art in the design and fabrication of ablative chambers in a size range which was compatible with an injector used in previous pyrolytic graphite tests.

Each supplier was responsible for his own design, i.e., determining the materials and fabrication techniques which would best satisfy the operating and design conditions specified. The only dimensions specified were those of the interior contour and chamber-to-injector attachment provisions. Unspecified dimensions were left to the discretion of the supplier. In addition, the total assembly weight was not to exceed 5 lb nor produce an outside wall temperature in excess of 400°F during the test firing.

The evaluation firings were conducted at ambient pressure and temperature with the ALPS MOD IV injector. This injector has demonstrated reproducible performance and heat-flux distribution with N_2O_4–N_2H_4 propellants and has produced predictable erosion of both ablative and pyrolytic graphite thrust chamber throats (Refs. 3 and 4). The tests were run at a nominal nozzle stagnation (effective chamber pressure ($P_{c_{eff}}$) of 150 psia and a propellant mixture ratio of 1.2. The characteristic velocity c^*, averaged 5500 ft/sec. Flow rates were nearly constant, despite changes in nozzle throat area during the firings. Each chamber was fired uninterruptedly until either (1) the chamber pressure dropped below 120 psia, (2) the outside wall temperature exceeded 400°F, or (3) an extraordinary change in axial or side thrust occurred.

A general description of each chamber, listed by manufacturer, is presented below:

(1) *Aerojet-General Corporation (AGC).* One-piece ablative chamber; throat insulator and exit cone made of edge oriented high-silica tape and rubber modified phenyl-silane resin; SiC throat insert; glass filament overwrap.

(2) *AVCO Corporation (AVCO).* Composite of silica-reinforced precharred epoxy Novolac; light weight insulator of silica fibers, resin, and phenolic microballoons; SiC throat insert, encased in an aluminum shell.

(3) *H. I. Thompson Fiber Glass Co. (HITCO).* Ablative chamber liner and throat, molded carbon-phenolic resin surrounded by Refrasil-paper phenolic insulator; glass filament overwrap; no throat insert.

(4) *Magnesium Aerospace Products, Inc. (MAP).* Molded one piece, including throat section inner liner of SiC-ZrC, binary film-coated carbon-particle-reinforced phenolic ablative structure surrounded by insulating layers, titanium shell.

(5) *Thompson Ramo Wooldridge, Inc. (TRW).* Inner chamber liner of oriented chromic oxide-coated silica-cloth reinforcement; molybdenum throat insert with a proprietary coating; insulating layers; outer stainless steel pressure shell.

Preliminary results of the test firings are presented in Table 3. Fig. 3, a typical plot of a chamber pressure versus run time, explains the nomenclature used in Table 3. This plot is generally representative of all of the tests. The time to start of pressure decay and time to 120 psia is shown as T_1 and T_2 and is tabulated for

Table 3. ALPS ablative chamber data

Manufacturer	Initial steady-state chamber pressure $P_{c_{eff}}$, psia	Mixture ratio $\dot{W}_{ox}/\dot{W}_f$	Time to start of P_c decay,[a] T_1, sec	Time to P_c = 120 psia,[a] T_2, sec	Slope of P_c decay, psi/sec	Maximum temperature during test, °F	Maximum temperature post run, °F
AGC	149	1.24	125	154	0.4	530 at 154 sec	475 at 450 sec
AVCO	150	1.2	300	590	0.1	405 at 590 sec	412 at 610 sec
HITCO	156	1.2	7	23[b]	1.75	67 at 23 sec	250 at 28 sec
MAP	163	1.22	11	31	1.45	254 at 57 sec	571 at 111 sec
TRW	148	1.18	160	510	0.09	240 at 510 sec	340 at 940 sec

[a] Refer to Fig. 3 for explanation of these parameters.
[b] Attachment flange failed.

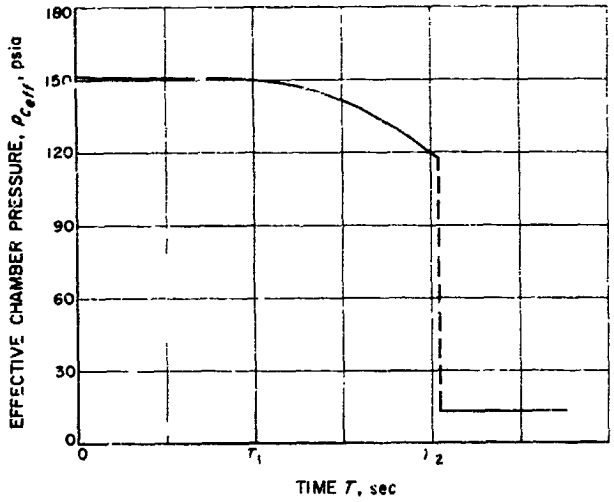

Fig. 3. Typical plot of chamber pressure as a function of test duration for ablative chamber tests

all of the tests in Table 3. The outside wall temperatures were recorded from thermocouples bonded to the outside of each chamber at several different locations.

All five tests were terminated due to decrease in chamber pressure. For four of the tests, this decrease was either the result of throat erosion or gas leakage around the throat insert. In one case, the chamber-injector mounting flange attachment failed permitting the chamber to separate from the injector terminating the test.

Although the test results shown in the table are not encouraging, it should be realized that the test conditions were quite severe for ablative-type chambers, since the chamber pressure was 150 psia and no film or fuel-rich "barrier" cooling was used.

A detailed examination and analysis of the chambers and the test results are in progress. These results will be published in a forthcoming formal report.

4. Bladder Development, *W. F. MacGlashan*

Laminates of Teflon and aluminum foil are being used in the construction of expulsion bladders. Since pinholes in the aluminum foil would destroy the impermeability of the laminate, a means of detecting these holes is necessary.

A method for detecting pinholes in aluminum foil by using photographic printing paper is being developed. The method consists of directing a strong light toward the sheet of aluminum foil which is backed by photographic printing paper. The foil and paper are separated by a piece of glass. The edges are secured to exclude stray light and to hold the foil, paper, and glass securely together. The light is played in a grid pattern across the surface so that the rays passing through pinholes strike the paper behind the foil. The glass separator permits the diverging rays to amplify the hole image on the paper. When developed, the location of pinholes is indicated by black spots on the paper. An apparent draw-

back of this method is that the holes must not be tortuous paths if light is to pass through.

The investigation is continuing with the intent of: determining the minimum size and shape holes that can be photographically detected; the correlation, if any, between the permeability of the foil and the apparent relative magnitudes of the holes indicated by the photographic images; and the correlation between the abundance of holes and the foil thickness.

5. Generant Tank and Cell Development, O. F. Keller

All previously reported expulsion tests of the ALPS generant tank and diaphragm assembly were carried out at ambient temperature using distilled water as the test fluid (*SPS 37-22, 37-24,* and *37-32,* Vol. IV). Recently, expulsion tests have been made at temperatures ranging from 40 to 100°F. For high-temperature environmental testing, the water expulsion test facility was equipped with a heater (visible on the right side in Fig. 4). A television camera (seen in the left foreground) was used for remote observation of the volumetric tank during environmental and high-pressure expulsion testing. The titanium generant tank (partially visible behind the television camera) was mounted in a protective wood cradle.

Fig. 4. Water expulsion tests facility equipped for water expulsion testing at high temperature

Three expulsion tests were made following 24-hr conditioning periods during which the final generant tank temperatures ranged from 92 to 108°F; distilled water temperatures during these tests ranged from 96 to 110°F. One of the above tests was made with two steps and restarts during the run. An additional expulsion test was made following a 72-hr conditioning period during which the final generant tank temperature was 102°F; the final distilled water temperature, 105°F. One expulsion test was also made following a 24-hr conditioning period at approximately 40°F. In all cases the tank outlet was downward.

Expulsion appeared to be normal in all of the above environmental tests. Prior to the low-temperature expulsion test, however, an increase in pressure drop was noted in transferring the distilled water from the volumetric tank to the titanium generant tank, possibly indicating a stiffening of the elastomeric diaphragm at the 40°F temperature level. Any increase in pressure required for deforming the diaphragm at 40°F was not noticeable during the low-temperature expulsion test.

6. Materials Compatibility, R. N. Porter

A long-term compatibility test of a flight-weight fuel tank fabricated of Type 2014 aluminum has been accomplished. All instrumentation, the vent valve, and all fittings were of aluminum or stainless steel and all seals were Teflon. The tank was cleaned by first rinsing with trichloroethylene, then thoroughly washing with a commercial aviation-type detergent, rinsing with distilled water, pickling with an acid solution, washing again with a detergent rinsing with distilled water, and drying with nitrogen gas. The tank was placed in direct sunlight at Edwards Test Station. On July 27, 1960, after being leak-tested to 25 psig with nitrogen gas, the tank was filled with approximately 2750 lb of hydrazine, which left about 20% of the tank volume for ullage. The ullage was pressurized to 5 psig with nitrogen gas.

Tank pressure, liquid temperature, and ambient temperature were recorded three times each working day for the first seven months, once each working day for the next nineteen months, and after that no records were

kept. The recorded tank pressures ranged from 0 to +5 psig as the recorded ambient temperature varied from +13 to +116°F, and the recorded liquid temperature varied from −27 to +100°F. It is not clear whether these pressure variations were due strictly to the temperature changes alone; the pressure gauge resolution was only ±0.5 psi, which could be the cause of some scatter in the data. Further complications, such as the possibility of leakage, decomposition of the hydrazine and dissolving of the decomposition products (nitrogen, hydrogen and ammonia) into the hydrazine, make it difficult to interpret the data.

Hydrazine samples for analysis were withdrawn from the middle of the tank through a standpipe and from the bottom of the tank every two weeks for the first year, once each month for the following six months, and then once each six months for the remainder of the test. Although the first samples, taken on August 8, 1960, contained a very small amount of black residue analyzing high in aluminum, iron, and copper, the subsequent samples were clear, with no noticeable solid matter. The analyses made during the first 3 yr indicated the liquid was 98.7 to ±0.5% hydrazine, using an analytical procedure which has a resolution of about ±0.5% hydrazine. A sample taken five months before the end of the test period was approximately 97.0% hydrazine, and at the end of the test the liquid contained approximately 96.5% hydrazine. It is assumed that the change reflects an increase in the amount of dissolved ammonia; unfortunately, the ammonia content was not analyzed. On May 6, 1964, the hydrazine was drained into carefully cleaned hydrazine storage drums.

After being drained, the tank was purged with warm nitrogen to dry it out. Several weeks later it was flushed with a small amount of water and cut open for inspection. Many areas of the internal surface appeared to be discolored; the colors of the splotches were randomly almost white, yellow gray, blue gray, and green gray. Samples were taken from locations typifying the different surface conditions.

Some of the samples were made into metallographic specimens. Examination showed that the degree of corrosion varied considerably from area to area and that the severest attack was limited to discrete spots rather than covering extensive areas. In no case did the pits exceed a depth of 0.002 in. Although the exact corrosion mechanism was not determined, it was judged that the magnitude of the corrosion was minimal and not detrimental to the tank. The discoloration was not indicative of the severity of the corrosion, but corrosion was more prevalent in the discolored areas than in the normally colored areas. The cause of the discoloration was not determined.

Other samples were subjected to tensile yield strength and tensile ultimate strength tests. The results indicated that the material of the tank was slightly less strong than the strength reported in the literature for new 2014-T6 aluminum alloy and stronger than reported for 2014-T4. From these data and the results of an extensive hardness survey it was hypothesized that the tank was not in the T6 condition, as supposed, but rather was solution-treated and then allowed to age-harden at room temperature to the T4 condition.

From this test, it was concluded that tanks of 2014-T4 aluminum alloy are essentially unaffected by long-term (up to at least 3 yr) contact with anhydrous hydrazine, with temperatures varying between 30 and 100°F. The evaluation of the effect of such a storage environment on hydrazine was in the final stages in this reporting period. Firing tests, ignition lag tests, analysis of the final composition, and physical properties measurements were being performed with the hydrazine which was drained from the tank.

References

1. Johnson, B. H., "An Experimental Investigation of Combustion Effects on the Mixing of Highly Reactive Liquid Propellants," Technical Report No. 32-689, Jet Propulsion Laboratory, Pasadena (to be published).

2. Weiss, H. G., and Klusmann, E. B., *Journal of American Chemical Society*, Vol. 84, p. 4993, 1962.

References (Cont'd)

3. Tyler, W. H., "Thrust Chamber Development," *SPS 37-28*, Vol. IV, pp. 81–83, Jet Propulsion Laboratory, Pasadena, Calif., August 31, 1964.

4. Rowley, R. W., Tyler, W. H., "The Effect of Injector Design on Thrust-Chamber Erosion," paper presented at AIAA Propulsion Joint Specialist Conference, U.S. Air Force Academy, Colorado Springs, Colorado, June 14–18, 1965.

SPACE SCIENCES DIVISION

XVI. Lunar and Planetary Instruments

A. pH Instrument Development

J. R. Clark

In most physiological monitoring or detection systems presently under development, the measurement of hydrogen ion concentration (pH) is required. The "Wolf Trap" effort at the University of Rochester monitors changes in pH of inoculated test cells as an aid in detecting bacterial growth. The Multivator at Stanford University uses pH instrumentation for similar reasons. In the Biosatellite Project, the pH of primate urine is monitored to detect changes in the acid–base balance for a better understanding of the prolonged weightlessness problem. It is also well-known that aqueous chemical reactions that might be used in an automated biological laboratory would proceed only under conditions of controlled pH. For these reasons, circuitry is being developed at JPL for the measurement of hydrogen ion concentration.

1. Electrode System

a. Glass electrode. Other than the inconvenient hydrogen electrode standard, the glass electrode is primarily used for pH measurement. In a simplified form, it consists of a thin glass bulb in which an electrode is immersed in a solution of constant pH. When the bulb is placed in the test solution, the potential at the glass-bulb–test-solution interface is a direct function of the pH of the test solution. The change in potential due to a change in pH is given by

$$\frac{\Delta E}{\Delta \mathrm{pH}} = \frac{2.303RT}{F}, \qquad (1)$$

where 2.303 is the natural logarithm to common logarithm conversion factor, R is the universal gas constant T is the absolute temperature, and F is the Faraday. Representative values at four different temperatures are given below:

T, °C	$\Delta E/\Delta$pH, mv
0	54.19
25	59.15
60	66.10
100	74.03

b. Measurement errors. When a reference electrode is placed in the test solution for electrical contact, the actual voltage measured between the glass and the reference electrode is the algebraic sum of several potentials developed at other glass–liquid interfaces. Most of these are negligibly small or are constant with respect to changing pH and temperature; thus, they can be calibrated out of the system.

The one characteristic of glass electrodes which makes measurement of the pH potential difficult is the high glass-bulb resistance. This resistance is a function of the material and geometry of the glass bulb or membrane, as it is sometimes called; e.g., the bulb resistance of Corning Glass Works Type 015 glass will vary from 1000 MΩ at 10°C to 1 or 2 MΩ at 50°C, and Leeds & Northrup Co. Type 399 glass will vary from about 500 to 1 MΩ over the same temperature range. Therefore, the measuring circuitry must be such that this kind of source impedance contributes negligible error to the signal output. Source resistances of this magnitude are also very sensitive to electrostatic pickup and electrode leakage paths. This problem is minimized by completely sealed and internally shielded glass electrodes. The sealed construction eliminates the surface leakage paths.

The glass electrode does exhibit measurement errors which depend on the pH and temperature of the test solution and the glass bulb material. Under conditions of high temperature with high or low pH, ions other than hydrogen may take part in the electrode process. The error voltage of the Corning Glass Works Type 015 electrode is p in strong solutions of alkali hydroxides. This error is termed alkaline error and can require a correction factor as high as 1 pH unit to be added to the indicated value. The sodium ion error is another important error factor to consider when working with high pH values. The error potential is generated due to sodium ions present in the test solution and sodium dioxide in the glass material of the bulb. In this pH region (pH>9), a correction factor is added to the indicated pH. For Corning Glass Works Type 015 glass, this factor is about 0.2 pH for an indicated pH of 10. However, Beckman Instruments, Inc., Type E glass makes sodium ion errors almost negligible below a pH of 12 at 25°C.

When investigating electrodes for space application, sterilization must be considered. This does not appear to be a difficult problem, even if presently developed glass and reference electrodes are used. Standard laboratory electrodes have been subjected to repeated sterilization cycles with some slight change in $\Delta E/\Delta pH$. Beckman Instruments, Inc., has under development an electrode system which can operate in a zero gravitational field.

2. Amplifier Design

a. Approach. The approach to the measurement of hydrogen ion concentration uses shunt voltage feedback around an operational amplifier. This type of feedback allows the pH-measuring electrodes to work into a higher input impedance when the system is at null. The equivalent circuit in Fig. 1 is used to derive basic design relationships. The source resistance, R_s, in series with the voltage generator, e_{pH}, is used as the equivalent circuit for the measuring electrodes.

It can be shown that the transfer relationship between e_0 and e_{pH} is given by

$$\frac{e_0}{e_{pH}} = \frac{-R_L(R_0 + AR_i)}{R_0R_s + R_iR_0 + R_0R_L + R_sR_L + R_iR_L(1 + A)} \tag{2}$$

where R_s is the electrode source resistance, R_0 is the output impedance of the amplifier, R_L is the load resistance, R_i is the input impedance of the open loop amplifier, and A is the amplifier gain. In order to arrive at design criteria for the parameters A and R_i, R_L is assumed to become arbitrarily large. Then, Eq. (2) can be written as

$$\frac{e_0}{e_{pH}} = \frac{-(R_0 + AR_i)}{(R_0 + R_s) + R_i(1 + A)} \tag{3}$$

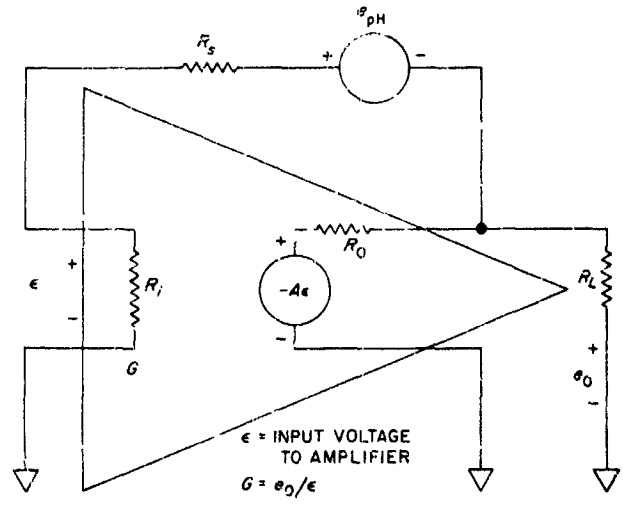

Fig. 1. Feedback configuration

The next valid assumptions are that $AR_i \gg R_s$ and $R_s \gg R_{in}$. Then, Eq. (3) reduces to

$$\frac{e_o}{e_{pH}} = \frac{-1}{\frac{R_s}{AR_i} + \frac{1+A}{A}} \tag{4}$$

Eq. (4) shows the addition of an error term which is dependent on A and R_i. This means that the accuracy of the pH measurement will depend on the inequalities:

$$R_i > R_s/A \tag{5}$$

$$A > 1 \tag{6}$$

b. Description. The amplifier configuration is illustrated in Fig. 2, which shows a mechanical chopper feeding a high-impedance field-effect transistor stage. The output of this input stage drives a conventional AC amplifier. This particular mechanical chopper was chosen because of the low offset voltage, low leakage paths, high insulation resistance, and low noise characteristics. The chopper can and has been subjected to sterilization (145°C for 36 hr) with no noticeable defects. It is realized that, from a reliability standpoint, solid-state components are much preferred over mechanical components. However, at the time of the amplifier design, the solid-state chopper could not compare with the mechanical chopper. In addition to the reliability disadvantage, the chopper requires about 230-mw driving power.

A synchronous detector transforms the AC amplifier output to the proper polarity DC, which provides the input signal for the output integrator. The resistance–capacitance of the integrator and the input filter is used to set response time and output noise level.

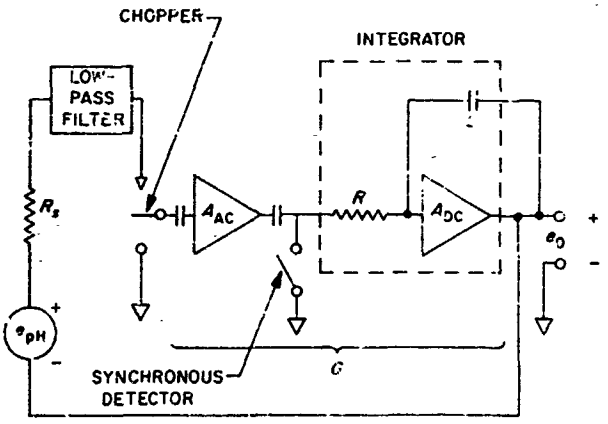

Fig. 2. pH Amplifier configuration

A Wien bridge oscillator operating at 400 cps drives a Class B push–pull amplifier from which chopper drive and synchronous detector reference signals are derived. The amplifier, power supply, and pH calibrating and indicating circuitry were assembled to provide a complete pH-measuring instrument. The unit (Fig. 3) is now under evaluation in the laboratory.

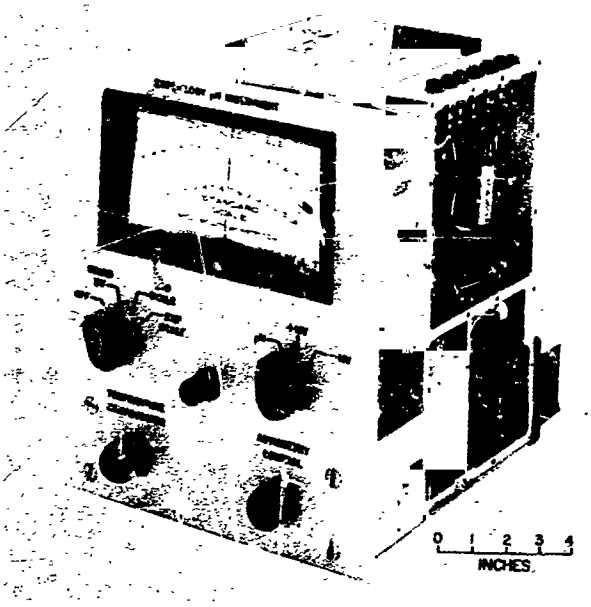

Fig. 3. pH Instrument

c. Performance. Table 1 shows how system offset voltage varies with temperature T and R_s. It can be seen that the system offset voltage is reasonably stable with T, but that some limit must be set on R_s for a given measurement accuracy. If T is known, then larger values of R_s could perhaps be tolerated.

Table 1. Variation of system offset voltage with T and R_s

T, °C	Offset voltage, mv		
	$R_s = 10^8$	$R_s = 10^9$	$R_s = 10^{10}$
−20	1.2	−3.5	−12
−5	1.2	−3.0	−11
20	1.3	−2.6	−8
40	1.4	—	—
65	1.0	−3.0	−10

The AC gain was measured to determine the amplifier's immunity to DC offsets at the input to the integrator for various values of R_s. This was accomplished using the diagram shown in Fig. 4. If A_{AC} is the gain of the AC amplifier times the chopper and demodulator efficiency, A_{DC} is the integrator DC gain, and e_D is the disturbance or demodulator offset voltage, then

$$\frac{e_D}{e_o} = \frac{1 - A_{AC} A_{DC}}{A_{DC}} \approx A_{AC} \quad (7)$$

where e represents incremental voltage changes. This ratio is given below for three different values of R_s:

R_s	e_o/e_o
10^8	−200
10^9	−36
10^{10}	−4.4

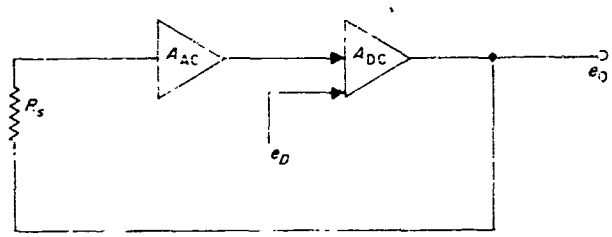

Fig. 4. AC Gain measurement diagram

3. Conclusions

This development effort has shown that pH measurement can be accomplished using all solid-state circuitry and a mechanical chopper. In the future, attempts will be made to eliminate the mechanical chopper by using some of the more recently developed semiconductor devices. This will result in simplification of the circuitry and a substantial reduction in required power.

XVII. Space Instruments

A. Ultimate Sensitivity of Imaging Devices

L. R. Malling

1. Space-Camera Sensitivity

The function of a TV space camera is to relate an electrical current to a photometric function derived from the planetary surface. The relationship so established is valid until, with decreasing illumination, the signal is degraded with noise. The ultimate sensitivity is determined by statistical quantum relationships. Frequently, the quantum noise is overshadowed by thermal noise, thus permitting the sensitivity to be evaluated from purely thermal noise considerations.

Because of the increasing diversity of space-camera technology, sensitivity comparisons must be made between widely differing imaging concepts. These systems may be categorized into two broad areas: (1) photostorage with beam-scanning readout, as represented by the vidicon and image-orthicon families; and (2) non-storage photocell readout with mechanical, electronic, or mechanico-electronic scanning, as represented by photographic-film scanning and the image dissector.

Irrespective of the sensor employed, an optico-electronic conversion must be performed to translate the optical image into a signal current with time as the axis. Signal current is derived from electronic charges produced at the photosensitive surface by the impact of photons. Depending on the type of imaging device, either the photons release electrons in the form of an electrical current or the electrons are stored to produce a charge. In the latter case, the signal current is that produced by a discharge of the stored charge. The magnitude of the current in each case is determined by the number of photons/sec arriving at the photosensor. The photon arrival is a function of the illumination, conventionally expressed in ft-c.

2. The Candle

Although the candle, as a measure of illumination intensity, has had an historic background in photometry, it cannot be considered a particularly appropriate standard for space science. The candle has been defined as the luminous intensity of $\frac{1}{60}$ cm^2 of a blackbody radiator maintained at the temperature of solidification of platinum, 2045°K. The extremely red-oriented nature of the emission is illustrated in the normalized curve of Fig. 1, which is derived from Wien's law.

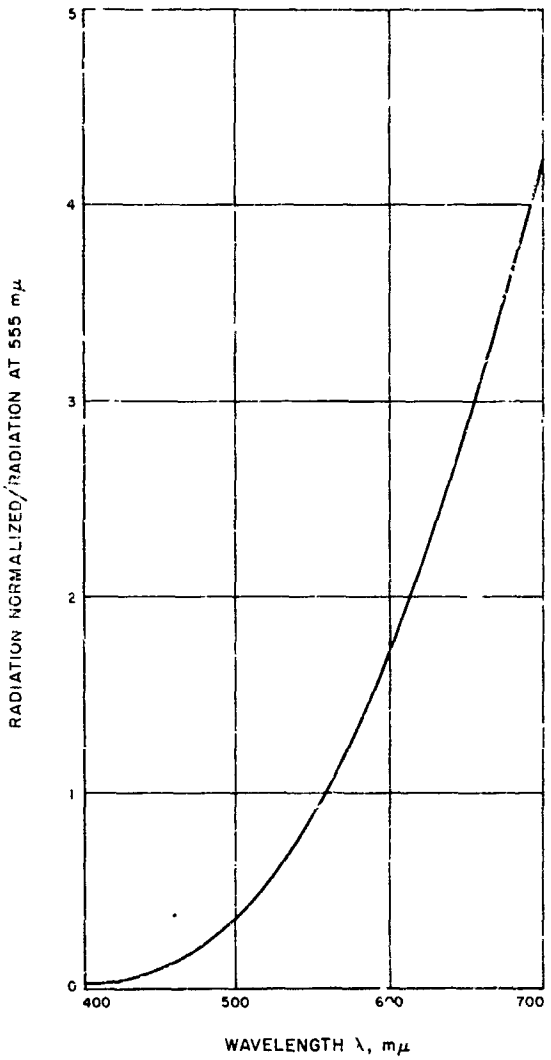

Fig. 1. Spectral distribution for the standard candle

From Wien's law, the energy radiated within a bandwidth of 1 mμ is

$$E_\lambda = \frac{C_1\lambda^{-5}}{\epsilon^{C_2/\lambda T}} \text{ ergs/sec/cm}^2.$$

Equivalent blackbody temperatures of interest to space science are those of the Earth, 6000°K; the Moon, 5500°K; Mars, 3000°K; and test illuminant A, 2848°K (*SPS 37-28*, Vol. IV, pp. 95–100). The energy radiated by a blackbody at 555 mμ is plotted over a range of temperatures, 2000 to 6000°K, in Fig. 2. The spectral distributions vary widely, but essentially equal-energy white occurs at 5500°K.

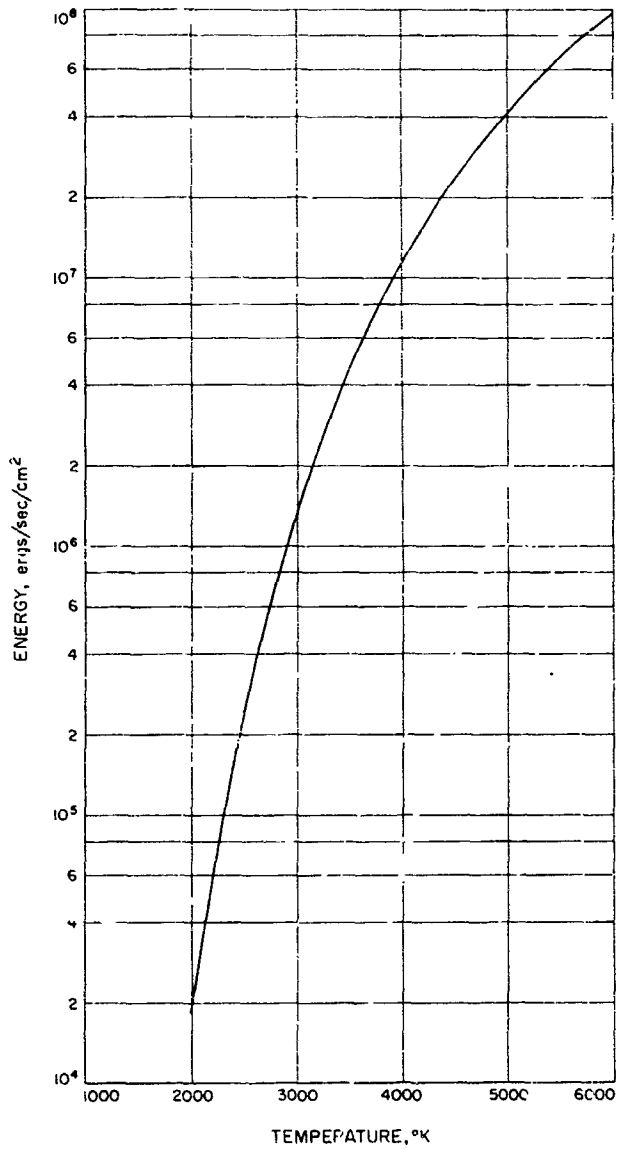

Fig. 2. Energy radiated by a blackbody in the interval of 559.5 to 560.5 mμ

3. *The Eye*

The sensitivity of the eye has a Gaussian-type distribution over the visual band as shown in Fig. 3, where the ordinate is the illumination observed at each wavelength in mμ intervals for constant power input. The area under the curve represents 1 lu of radiation over the visual band. For computational purposes, the bandwidth may be defined as 260 mμ, ranging from 430 to 690 mμ, beyond which the sensitivity drops to less than 1%. An ideal

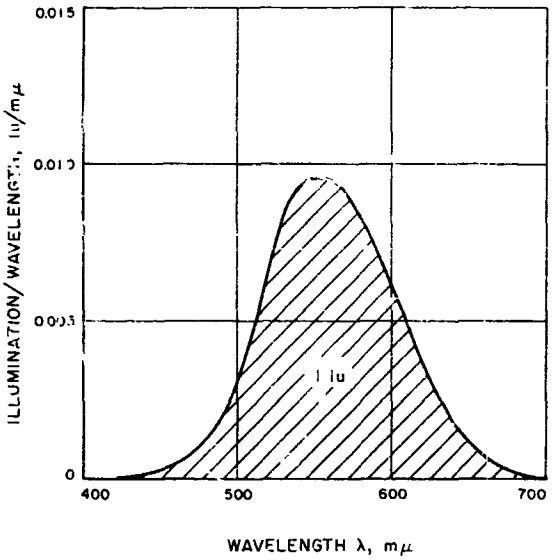

Fig. 3. Brightness distribution to the eye for an equal-intensity white source radiating 14.1 μw/mμ

photosensor will have a response identical to that defined for the eye, or filters may be inserted to match the eye response.

4. Photon Energy

The photon energy from Einstein's law is $e_p = h\nu$ ergs, where h = Planck's universal constant = 6.63×10^{-27} ergs and ν = frequency, cps. The photon energy is plotted in Fig. 4 over the visual band with wavelength, rather than frequency, as the abscissa. For equal-energy white, an average value is $e_p = 3.6 \times 10^{-12}$ ergs at 555 mμ or 545 teracycles.

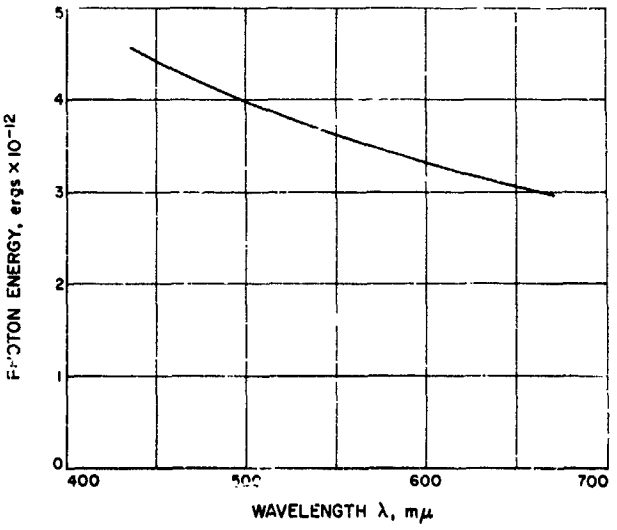

Fig. 4. Photon energy vs wavelength

The photosensor current will be determined by the product of its spectral response S_λ and the spectral distribution E_λ of the source; i.e., the photo-electric current

$$i_p = k \sum_{430}^{690} S_\lambda E_\lambda .$$

This has been estimated for three blackbody temperatures of interest in Fig. 5. Note the progressive shift toward the red with decreasing temperature.

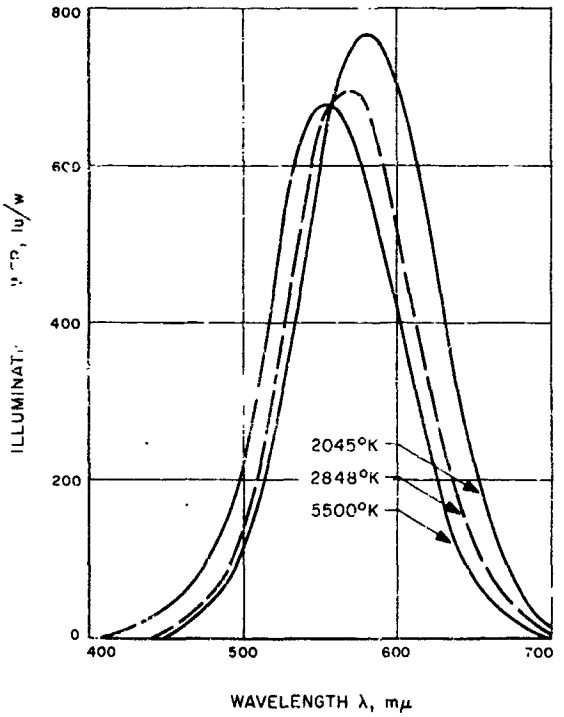

Fig. 5. $E_\lambda S_\lambda$ for different blackbody temperatures (illuminance equalized at λ = 555 mμ)

A ft-c is defined as 1 lu of light flux distributed evenly over unit area at unit distance from a 1-c power source. The power required to produce 1 lu of brightness to the eye at each wavelength increment is shown in Fig. 6. An average value produced by integration is $(W_\lambda)_{ave}$ = 3.67 mw/lu/mμ. If the source is equal-energy white, 5500°K, then the total energy radiated for 1 lu over the visible band is $E_{tot} = 3.67 \times 10^4$ ergs/sec. To produce 1 lu of flux over unit area, W_λ = 14.1 μw must be radiated at each wavelength increment over the visual band.

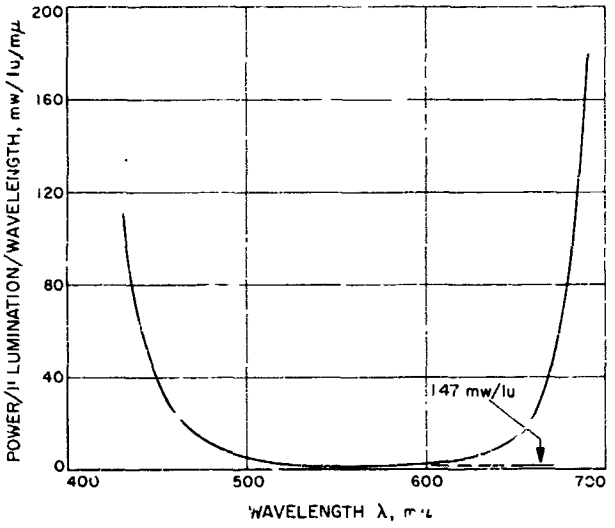

Fig. 6. Radiant power required for 1-lu intensity

5. Quantum Yield

The quantum yield is the number of photo-electrons produced by the incident photons. With an ideal 1:1 relationship, i.e., one electron excited for each photon, the number of photo-electrons produced for an equal-energy-white source having an illumination intensity of 1 ft-c is

$$n = \frac{E_{tot}}{e_p} = \frac{3.67 \times 10^{4}}{3.6 \times 10^{-12}} = 1.02 \times 10^{16} \text{ electrons/sec.}$$

The electron charge $e = 1.6 \times 10^{-19}$ coulombs, and, since $i = dq/dt$, 1 amp = 1 coulomb/sec = 6.24×10^{18} electrons/sec. Thus, for a photocathode surface with a typical quantum efficiency $\eta = 10\%$, the photocurrent

$$i_p = \eta ne = 0.1 \times \frac{1.02 \times 10^{16}}{6.24 \times 10^{18}} = 164\ \mu\text{A/lu.}$$

A value of 150 μA/lu is frequently assumed.

It should be recognized that, for a photostorage tube, the signal current cannot be estimated directly from the μA/lu figure. With photostorage, it is effectively multiplied by the ratio of the charge and discharge times of the storage element as determined by the exposure and the beam-scanning velocity.

If the equal-energy source is replaced by Illuminant A, the effective energy radiated over the visual band is modified. Integration of the curves of Fig. 5 indicates that the effective radiation from Illuminant A is 0.99 times that from the equal-energy source. Also, at the lowered temperature, the average power emitted is reduced to $(W_\lambda)_{avg} = 0.95$ times the nominal value at 555 mμ. However, in terms of the photo-electron population, this is compensated by a decrease in photon energy (Fig. 4) due to the shift of the major portion of the emission into the red region. Accordingly, for Illuminant A,

$$n = \frac{1.02 \times 0.95}{0.90} \times 1.01 \times 10^{16}$$

$$= 1.08 \times 10^{16} \text{ electrons/sec/ft-c,}$$

which is not too different from the value of 1.02×10^{16} achieved for an equal-energy-white source. By similar reasoning, the photo-electron population for the equivalent blackbody temperature of the standard candle, 2045°K, is

$$n = \frac{1.02 \times 1.35}{1.18} \times 1.14 \times 10^{16}$$

$$= 1.33 \times 10^{16} \text{ electrons/sec/ft-c.}$$

To verify the latter value, a second approach is made, starting with the definition of the standard candle. The candle has also been defined in terms of the luminous intensity achieved by a complete radiator operating at 2045°K for which 60 units of intensity/cm² is specified. The ft-L, a unit of illuminance equal to $1/\pi$ c/ft², is the luminance of a surface emitting 1 lu/ft². At 2045°K, $E_{555} = 2.4 \times 10^{4}$ ergs/sec from Fig. 2. Hence, for 1 lu radiated from the specified body,

$$E_{555} = 1/\pi \frac{2.4 \times 10^{4}}{60} \text{ ergs/sec} = 12.7\ \mu\text{w.}$$

From the spectral distribution curve of Fig. 1, the average power radiated $(W_\lambda)_{avg} = 17.1$ μw, distributed over a waveband (as indicated in Fig. 5) of 240 mμ. Hence, the total power radiated $W_{tot} = 17.1 \times 240 = 4.1$ mw for 1 lu emitted. For this value, the photon population

$$n = \frac{4.1 \times 10^{-4} \times 10^{7}}{3.4 \times 10^{-12}} = 1.30 \times 10^{16} \text{ photons/sec/ft-c,}$$

or 1.30×10^{16} photo-electrons/sec/ft-c for unity quantum yield. As expected, this is almost identical to the value of 1.33×10^{16} obtained by the first method. Estimates of photon concentration taken from several sources have been tabulated for comparison in Table 1.

6. Ultimate Sensitivity

The ultimate resolution of an imaging system is determined from the sine-wave response and the noise-power per unit bandwidth. For space photography, the minimum acceptable picture quality is taken as peak signal/

Table 1. Estimates of photon concentration in 1 ft-c of illuminance

Method	Subject	Temperature, °K	n, photons/sec/ft-c × 10^{11}
—[a]	Photon evaluation	5 00	1.02
—[b]	Vidicon	2870[f]	16.00
—[a]	Photon evaluation	2848	1.08
—[c]	Vidicon	2780	1.22
—[a]	Photon evaluation	2045	1.33
—[d]	Photon evaluation	2045	1.30
—[c]	Vidicon	—[g]	2.00

[a]Determined from the defined sensitivity of the eye, lu/w.
[b]Gebel, R. K. H., "The Potentialities of Electronically Scanned Photoconduction Image Detectors for Astronomical Uses," *Advances in Electron Physics XVI*, Academic Press, New York, 1962.
[c]Mengert, P., *Noise Limited Resolution of Low Light Level Camera Tubes*, Dalmo-Victor Company, Belmont, California, September 16, 1963.
[d]Determined from the definition of the standard candle
[e]Redington, R. W. "Maximum Performance of High-Resistivity Photoconductors," *Journal of Applied Physics*, Vol. 29, No. 2, February 1958.
[f]Over 290- to 1500-mμ band.
[g]Not stated.

rms noise = 20 db or signal/noise (S/N) = 10. The peak signal to be considered is the signal derived from an elemental area of the photosensitive surface equal to one picture element, ΔA. Non-storage and storage devices must be considered separately. For an evenly illuminated photosurface, the photo-electron population of the individual elements will contain minor perturbations. The variations may be due to either non-uniform arrival of photons or non-uniform excitation of electrons. The phenomena are associated with the law of rare events in a large population and are described by a Poisson distribution. In the Poisson distribution, the standard deviation is equal to the mean.

Assuming sinusoidal spatial illuminance of maximum contrast and of frequency contained within the camera resolution capability and the system bandwidth B, the peak photocurrent $i_p = n_e e$, where n_e is the photo-electron population of a ΔA picture element produced by an exposure at the incident illumination and e is the electron charge. From Poisson's law, the rms noise current $\bar{i}_n = 2e\bar{i}_p B$, where $\bar{i}_p$ is the average current and, hence, the expected deviation. Thus, for a non-storage device,

$$S/N = \frac{n_e e}{(2ei_p B)^{1/2}} = \left(\frac{n_e}{B}\right)^{1/2}.$$

For storage devices, there is an effective multiplication of the signal current. This is due to the fact that electrons are stored during a relatively long exposure time and discharged by the scanning beam in a much shorter interval t, where t is the time taken to scan one ΔA element. The signal current $i_s = Q/t = n_e e/t$; hence, for a storage target, $S/N = (2n_e)^{1/2}$. The system is generally designed so that $B = 1/2t$.

Ultimate sensitivity of the slow-scan vidicon. The quantum efficiency of a photoconductor has been expressed as $\eta \leqslant \tau/\tau_r$, where τ = lifetime of the photocharge and τ_r = relaxation time = ϵ_r/σ. The permittivity ϵ_r and the conductance σ define the relaxation characteristics of the target or photosurface. Space TV cameras must operate with extremely long frame times because of communication limitations. In addition, relative motion requires that the exposure time t_{exp} be short compared to the frame time T_f; typically, $t_{exp} \leqslant T_f/100$. As problems arise in extending τ_r, there is a tendency for $\tau \to \tau_r$, and the quantum efficiency is consequently high. This is quite unlike the case of the broadcast vidicon, where, to avoid shading problems, τ_r is made very much longer than the frame time so that $\eta \leq 1\%$. With the slow-scan vidicon, τ_r becomes sufficiently high, with a target resistivity of 10^{14} Ω-cm^{-1}, that the photoconductor essentially behaves as an insulator. The result is that, at low illumination levels, the signal current is almost a linear function of brightness and, unlike the case of the broadcast vidicon, is relatively independent of target voltage over the operating range (Figs. 7 and 8).

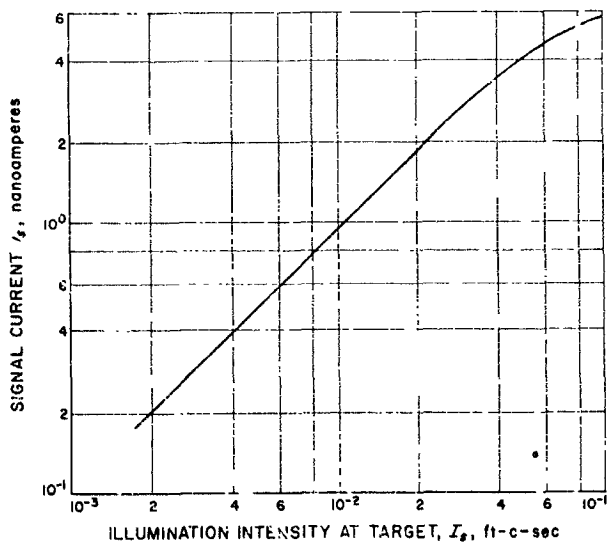

Fig. 7. Transfer characteristics of a slow-scan vidicon (B = 7 kc)

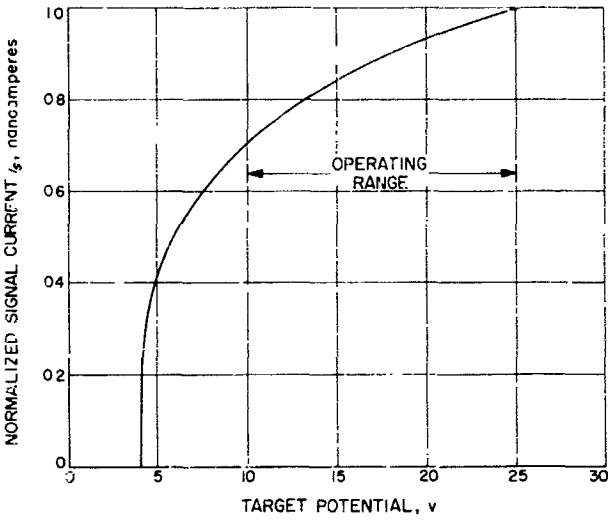

Fig. 8. Normalized signal current vs target potential for an illumination of 0.C5 ft-c-sec

Typical characteristics and operating parameters were assumed for a General Electrodynamics Corp. slow-scan vidicon (Type 1351B). In determining τ, the measured signal decay was 0.5 over a period of 48 sec, so that $\epsilon^{-48/\tau} = 0.5$ or $\tau = 69$ sec. Determining τ_r, the dark current $i_d = 1$ nanoampere at $E_T = 10$ v, from which the target resistivity $R_T = E_T/i_d = 10^{10}$ Ω. The surface area = 3.75 cm², so that unit resistivity $R = 3.75 \times 10^{10}$ Ω/cm². The capacitance C of the surface is estimated at 4500 $\mu\mu$f/cm², hence, $\tau_r = RC = 3.75 \times 10^{10} \times 4.5 \times 10^{-9} = 168$ sec. The expected quantum efficiency is thus $\eta = 69/168 = 40\%$.

With an illumination intensity at the target of $I_s = 0.01$ ft-c-sec arriving from Illuminant A, 2848°K, and an image area = 0.275×0.22 in.² scanned by 200 lines (line time $t_l = 14.4$ msec), the element area $\Delta A = 1.5 \times 10^{-6}$ in.², and the time to scan the element $t_a = 72 \times 10^{-6}$ sec. The photo-electron population for the element $n_a = 0.4 \times 1.06 \times 10^{16} \times 1 \times 10^{-2} \times 1.5 \times 10^{-6} \times 1/144 = 0.44 \times 10^6$. The stored charge $Q_a = n_a e = 0.70 \times 10^{-13}$ coulombs. Hence,

$$i_s = \frac{dQ_a}{dt} = \frac{0.7 \times 10^{-13}}{72 \times 10^{-6}} \times 10^9 = 0.97 \text{ nanoamperes.}$$

From Fig. 7, the measured $i_s = 0.95$ nanoamperes, which indicates substantial agreement in view of the many possible perturbations in the value of i_s that are difficult to include in estimates (e.g., light losses due to reflection and absorption, and residual charges remaining after scanning and non-ideal spectral response which raise or lower estimates of i_s).

Ignoring amplifier noise, the ultimate sensitivity for the storage vidicon is expressed by $S/N = (2n_a)^{1/2} = (0.74 \times 10^6)^{1/2} = 850$. This is completely obscured by the white noise of the amplifier for which (with operating values of $B = 7$ kc, $R = 0.5$ MΩ, and $T = 300$°K)

$$\bar{i}_n^2 = \frac{4KTB}{R} = \frac{4 \times 1.37 \times 10^{-23} \times 300 \times 7000}{0.5 \times 10^6}$$

$$= 2.3 \times 10^{-22} \text{ amp.}$$

Therefore, $i_n = 2.7 \times 10^{-2}$ nanoamperes, allowing for a measured 5-db noise figure. This makes the effective $S/N = 0.9/(2.7 \times 10^{-2}) = 33$ db. The measured value at this illumination level was $S/N = 30$ db. As always experienced with vidicon operation, the white amplifier noise completely overshadows the quantum noise. Based on a permissible $S/N = 20$ db, the quantum noise alone would permit pictures to be resolved at an illumination level of 0.0003 ft-c-sec, as opposed to the 0.003-ft-c-sec limitation determined by the amplifier performance.

7. Summary

The photon population for a given luminous intensity has been estimated by means of two separate concepts of the lumen. A useful approximation for space science is 1 ft-c = 1.1×10^{16} photons/sec.

From the photon concentration on the picture element, the ultimate sensitivity may be expressed by quite simple equations: for non-storage devices as $S/N = (n_a/B)^{1/2}$, and for storage devices as $S/N = (2n_a)^{1/2}$.

The quantum efficiency of the slow-scan vidicon, $\eta = 40\%$, is seen to be much greater than is generally supposed and approaches that of the best photoconductive cells. As with the broadcast vidicon, early experimental samples exhibited a sensitivity that later units could only marginally exceed because of the fundamental relationship $\eta = \tau/\tau_r$, established by the camera system restraints.

XVIII. Space Instrument Systems

A. Vibration Testing of a Tape Recorder Designed for Spacecraft Data Storage Applications

W. G. Clement

Vibration stressing of a miniature tape transport intended for data storage applications in spacecraft was recently completed. The unit tested was a Kinelogic Corp., "isoelastic" drive, reel-to-reel design (Fig. 1). This transport occupies a standard 6- × 6-in. module, weighs 2.5 lb, and is intended for hard-mounting in the spacecraft; a 468-ft tape is driven at 15 in./sec with less than 3-w input to the drive motor. The unit was previously described in *SPS 37-25*, Vol. IV, pp. 225, 226.

The purposes of the tests were to reveal whatever mechanical weaknesses might exist in the transport and to indicate possible design improvements to be incorporated into subsequent units. Determination of the degree of damage sustained by the mechanism during a particular vibration stress (except for visually obvious damage) was exceedingly difficult because of the very slight damage, if any at all, that occurred. Several new testing techniques for detecting performance degradation were developed.

1. Testing Procedures

The following nine vibration stresses were imposed:

(1) *Mariner C* (*Mariner* Mars 1964) type-approval level (16.4 *g* burst), Plane 2.

(2) *Mariner C* type-approval level, Plane 1.

(3) *Mariner C* type-approval level, Plane 3.

(4) 9-*g*-rms sinesweep, 30 to 2000 cps, Plane 3. Resonances indicated at 713 cps (45 *g*), 1063 cps (76 *g*), and 2025 cps (106 *g*); dwell at each for 6 min.

(5) 9-*g*-rms sinesweep, 40 to 2000 cps, Plane 3.

(6) 9-*g*-rms sinesweep, 40 to 2000 cps, Plane 3.

(7) 9-*g*-rms sinesweep, 40 to 2000 cps, Plane 1. Resonance indicated at 683 cps; dwell at 683 cps for 30 min.

(8) 9-*g*-rms sinesweep, 40 to 2000 cps, Plane 2. Resonance indicated at 760 cps (48 *g*); dwell at 760 cps for 30 min.

(9) 9-*g*-rms sinesweep, 40 to 2000 cps, Plane 3. Resonance indicated at 726 cps; dwell at 726 cps for 20 min.

Fig. 1. Tape transport

Each of six different tests was performed initially and after each vibration stress imposed on the tape transport. These tests are discussed below:

Test 1. The minimum start voltage for a 15-in./sec tape speed was measured in each direction of tape travel.

Test 2. The maximum breakaway torque at the capstan was measured in each direction with a torque watch.

Test 3. Mechanical vibration of the transport while running was measured with a General Radio Co. Type 1553A vibration meter. A measurement was made for each direction of tape travel at 3.75- and 15-in./sec tape speeds. A range of readings was recorded after 2-min observations in each mode of operation. The transport was placed in a styrofoam mounting block during the measurements to avoid resonant amplifications from outside structures.

Test 4. Tape motion jitter (instantaneous speed variation) was measured at 15 and 3.75 in./sec in each direction of tape travel. For the 15-in./sec measurement, a 10-kc square wave was recorded on the tape. This signal was played back through a level detector and displayed on an oscilloscope, and the leading edge of the reconstructed square wave was photographed. A 1-min exposure was made to include many cycles of the played-back signal and, hence, the maximum motion variation occurring. For the 3.75-in./sec measurement, a 1-kc square wave was recorded, and the played-back signal was handled in a similar fashion. Fig. 2 shows two typical leading-edge photographs.

Test 5. Start and stop times in each direction at each speed were measured by observing the time–amplitude characteristic of the signals recorded on the tape. Typical 15-in./sec start and stop characteristics are shown in Fig. 3.

Test 6. Cogging of the motor (*SPS 37-26*, Vol. IV, pp. 136, 137), as reflected in a cyclic speed variation of the tape, was measured by observing the corresponding cyclic variation of the played-back signal amplitude. Measurements were made at the low speed (3.75 in./sec) only, since cogging is predominantly a low-speed (low-drive-frequency) phenomenon. The motor cogging effect may be seen in Fig. 4.

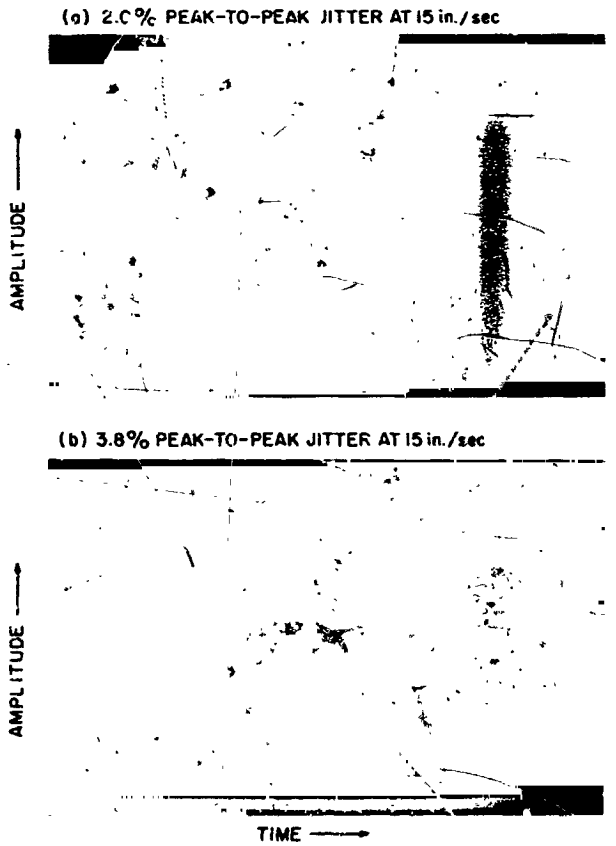

Fig. 2. Typical jitter oscillograms

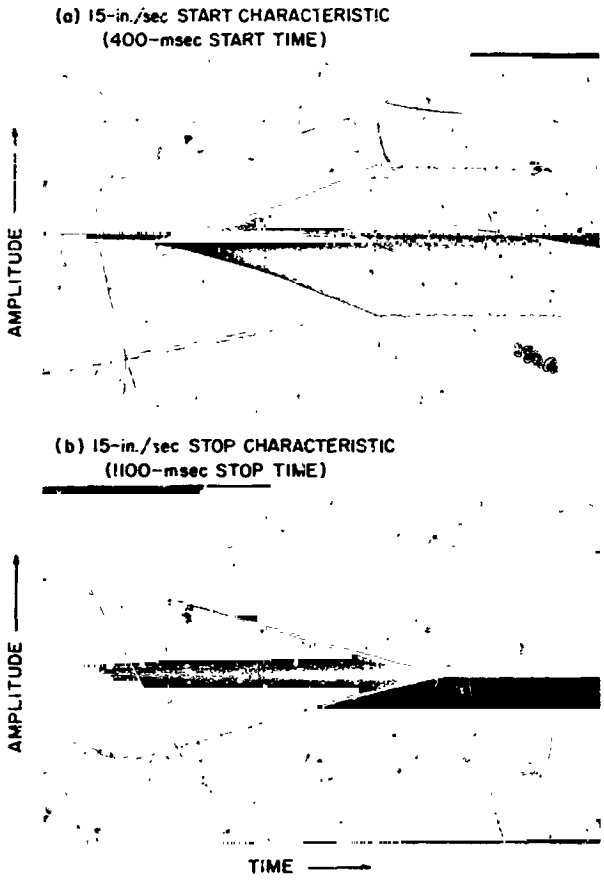

Fig. 3. Typical start and stop characteristics

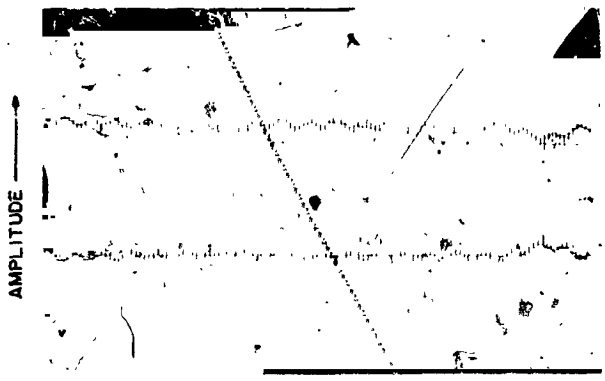

Fig. 4. Motor cogging effect at 3.75-in./sec tape speed (100-cps motor excitation frequency)

2. Results

An effort was made to display the test results in a manner which would indicate progressive damage, or the lack thereof, to the transport mechanism. Data plots are shown in Figs. 5 through 11, where the progression of the tests through the nine vibration stresses is indicated along the horizontal axis by t_a through t_i. It may be noted in Fig. 5 that the minimum voltage to start the tape moving at 15 in./sec showed an increasing trend at first and then remained almost constant throughout the subsequent cycles of vibration stress. Breakaway torque values shown in Fig. 6 followed approximately the same trend, as expected. The trend of torque values is less definite than that of starting voltage values and probably indicates that the latter is a more sensitive indicator of degradation of the transport mechanism.

It is difficult to discern any significant trend in the vibration characteristics depicted in Fig. 7. Levels of vibration and audible noise are typically high for rotating assemblies utilizing preloaded ball-bearings. Eleven such assemblies are contained in the test transport, and the noise and vibration levels may have been sufficiently high

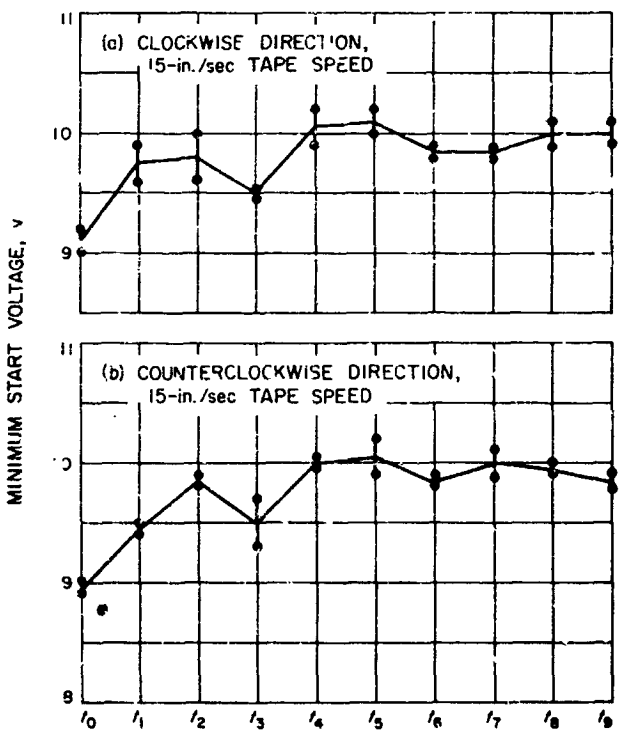

Fig. 5. Test 1, start voltage

initially to mask any degradation effects produced by the vibration stress.

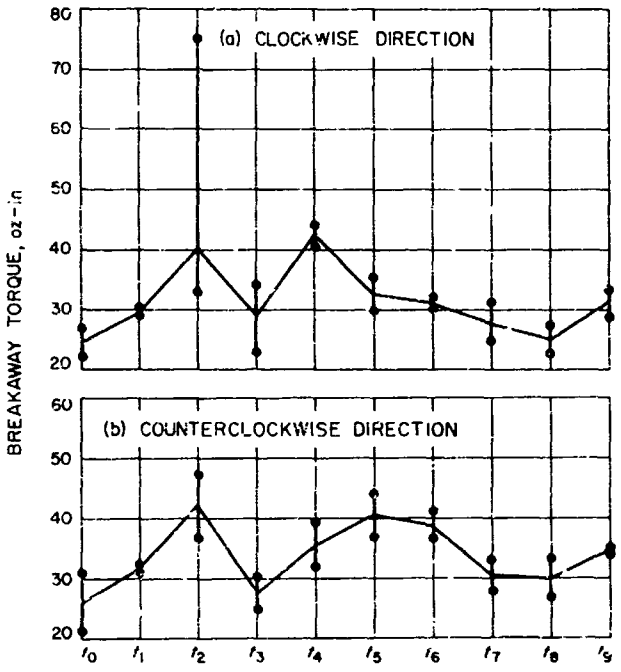

Fig. 6. Test 2, breakaway torque

Tape motion jitter would normally be expected to increase with increased bearing damage. As may be seen in Fig. 8, low-speed jitter did show an increasing trend and possibly indicates a slight degree of bearing damage. The trend is less discernible for high-speed jitter, and one might conclude that the inertia of the various rotating assemblies was sufficient to mask the slight increase in jitter discernible at the low speed, where rotational inertia effects were much less significant.

Start and stop times are generally considered fairly sensitive indications of increased (or decreased) friction in a mechanism, and it is probably significant that, in these tests, no appreciable changes were observed (Figs. 9 and 10). While the start time showed a slight decrease, indicating a reduction of friction with vibration stress, a corresponding increase in stop time was not indicated. Moreover, the results of Test 1 (Fig. 5) indicate, if anything, an increase in friction.

Low-speed cogging characteristics are shown in Fig. 11. It appears safe to conclude that no trend is indicated by the data taken. The method of measurement does not seem to be a particularly sensitive one; furthermore, the validity of the assumption that there is any correlation between bearing damage and low-speed cogging is questionable.

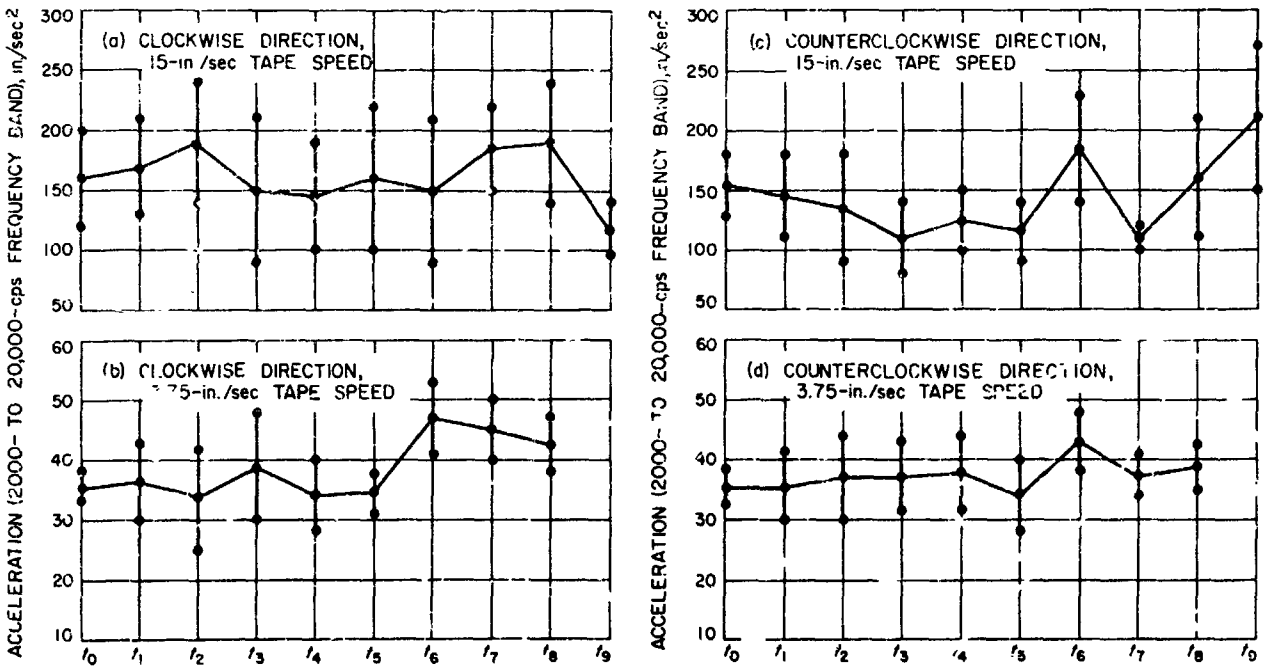

Fig. 7. Test 3, vibration

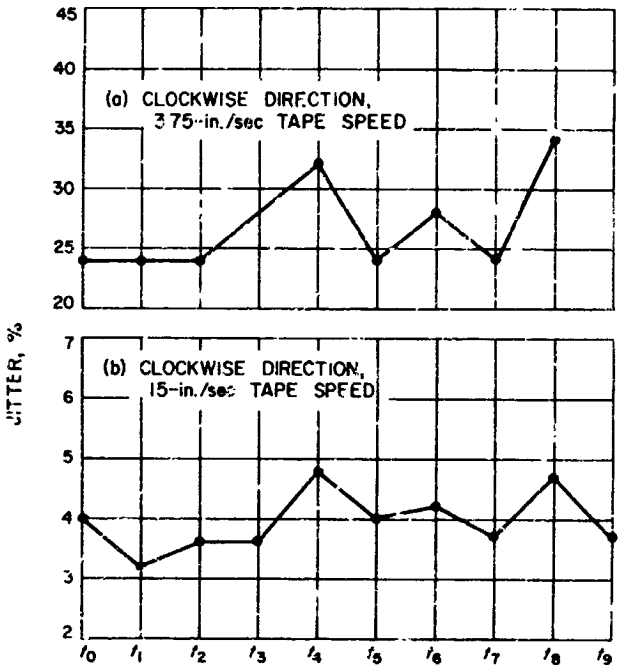

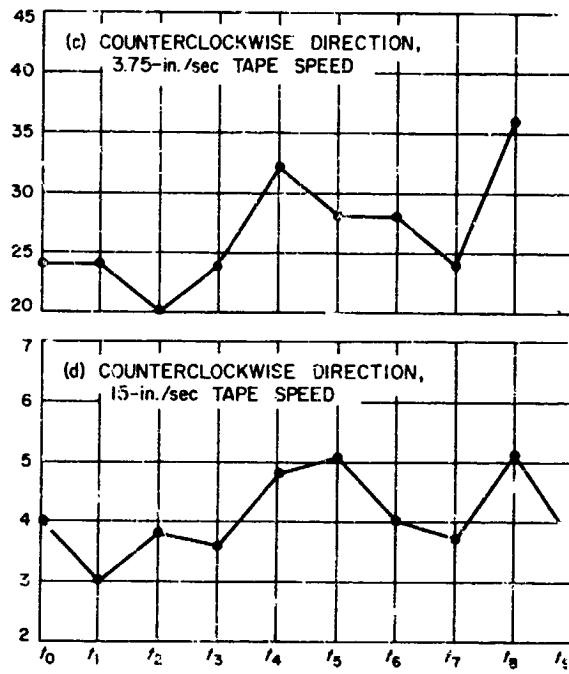

Fig. 8. Test 4, jitter

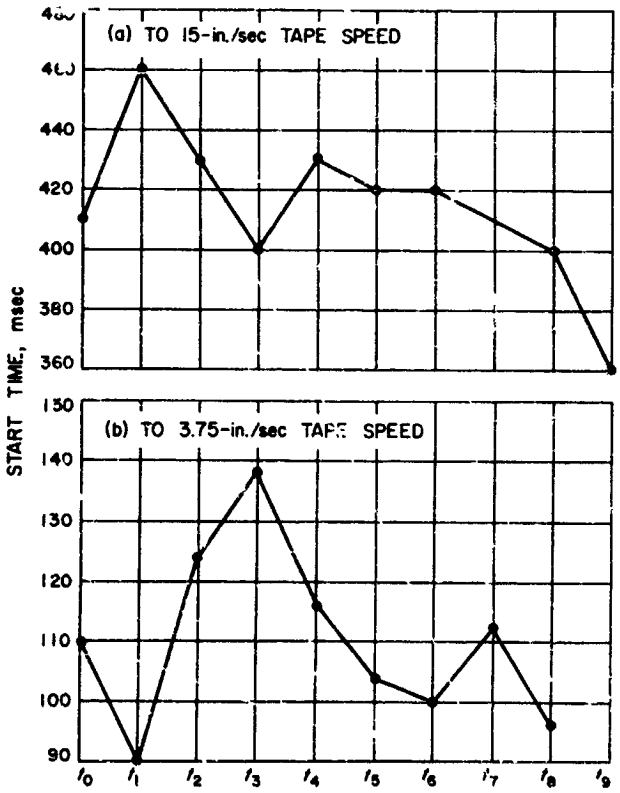

Fig. 9. Test 5, start time

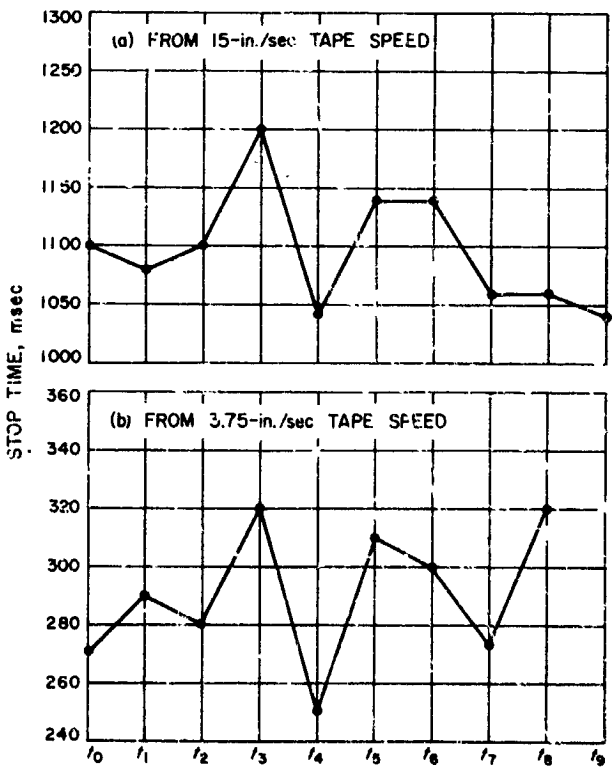

Fig. 10. Test 5, stop time

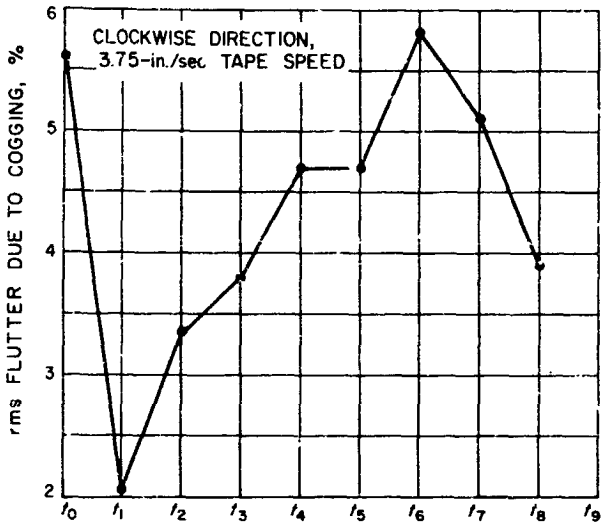

Fig. 11. Test 6, cogging

3. Conclusions

The particular recorder mechanism tested did not exhibit significant performance degradation as a result of the standard JPL *Mariner C* type-approval vibration stress levels. Although structural resonances existed for excitation frequencies between 40 and 2000 cps, 30-min "dwells" at these frequencies did not significantly degrade the mechanism.

The merit of designing such mechanisms with low-mass bearing-supported elements is implicit. Minimum start-voltage and start- and stop-time measurements were probably the most sensitive mechanical performance degradation criteria used in this test program and should be considered for use in future tests of this nature.

B. A Device for Measuring the Static Friction (Stiction) Between Magnetic Tape and Heads

W. G. Clement

During tests on the rocket-radar recorder in late-1963, the following problem was uncovered: When the recorder remained in a dormant condition at an elevated temperature, the tape tended to adhere to the heads, thus jeopardizing the recorder's startup capability[1]. This sticking tendency would sometimes manifest itself after only a few hours of dormancy at near-ambient temperatures. Photomicrographs of both head and tape after one such test revealed that the sticking had occurred only between the tape and the brass "bracket" region of the head, and not at all in the magnetic (nickel-iron) region. This observation added emphasis to the desirability of obtaining a more suitable head-bracket material[2]. Therefore, a program was initiated at the Applied Magnetics Corporation for the evaluation of various materials with regard to static friction characteristics, as well as characteristics relating to thermal coefficient and wear.

As a result of further recorder-dormancy tests and the subsequent study of the heads and tapes, the following hypothesis was advanced: Under the influence of elevated temperatures and in the presence of oxygen (air), certain organic compounds present in the tape's binder system tend to break down into lower molecular weight species which are "tacky." The brass portion of the head may also be a factor in this process, since copper and copper alloys react readily with certain halogenated compounds, often found in tape dispersions, to cause corrosion and material breakdown. Such reactions result in the adherence phenomenon observed.

On the basis of this hypothesis, it was concluded that three steps could be taken to minimize the problem:

(1) Since oxygen and oxidation are not factors in space, they should be eliminated from the tests.

(2) Tape should be preconditioned (cured) by heat and vacuum to drive off the residual volatiles which, if allowed to remain, could react with the head-bracket material.

(3) Consideration should be given to selecting a head-bracket material having a minimum tendency to react with the tape compounds.

Work was started at the Kinelogic Corporation to determine a suitable tape conditioning schedule, and tests were initiated to determine the effect of a dry-nitrogen

[1]Concurrent with the discovery of this problem at JPL, reports were received from industry indicating concern by other project groups about the same phenomenon (Ref. 1).

[2]Some of the previously known deficiencies of brass brackets were poor wear characteristics and an incompatible thermal coefficient.

atmosphere on the sticking phenomenon. The work previously initiated to find a more suitable head-bracket material continued.

Prior to this time, most of the tests were made with Memorex Corp Type 62L and Minnesota Mining & Mfg. Co. (3M) Type 991 tapes. At this time, however, 3M Type 951 tape in ¼-in width became available. Its characteristics, especially short wavelength response and physical durability, seemed particularly appropriate for spacecraft applications; thus, from this point on, stiction tests and curing efforts were performed with this tape. Stiction tests revealed that this new tape tended to adhere to the heads somewhat less tenaciously than either the 62L or 991 tapes; however, the problem remained essentially the same.

Efforts to cure 951 tape by continuously cycling it back and forth on a recorder in a vacuum (about 10^{-5} torr) at temperatures up to 80°C met with moderate success after it was discovered that the elements of sliding friction, especially heads, had to be eliminated from the tape path during this process. Cured tape was successfully transported in a sealed rocket radar recorder after a dormancy period of 32 days at 55°C and again after 8 days at 65°C. Testing of this particular specimen of tape was then discontinued, since the recorder was needed for the high-altitude rocket-radar project at JPL.

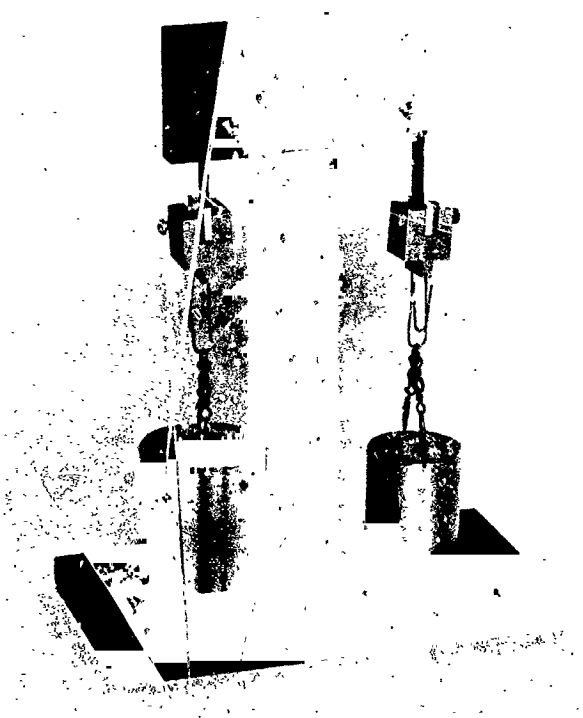

Fig. 12. First test fixture for measuring static friction between heads and tape

In evaluating various head-bracket materials at Applied Magnetics, it was initially assumed that the characteristics of a given tape would be uniform and that static-friction measurements after a 4-hr soak at an elevated temperature would provide a valid basis for comparison of bracket materials. Tests were conducted using the test fixture shown in Fig. 12. The resulting data exhibited poor repeatability. The frictional characteristics of a given specimen of tape appeared to vary not only from reel-to-reel, but also within a reel between two points no more than 1 in. apart. This lack of tactile uniformity in the tape was felt to be attributable to inadequate processing and served to support the premise that a more thorough cure of the tape was required. In any case, it seemed obvious that, before valid head-material evaluation could proceed, tape characteristics would have to be better controlled and/or defined. Accordingly, efforts at Applied Magnetics to evaluate the frictional aspects of head materials were diverted to a study of the tape problems. Two projects were initiated: (1) the design and construction of a static-friction test device which would embody more adequate control of environment[1] and measurement, and (2) a study to obtain quantitative information on a suitable tape curing process.

Experiments were conducted to establish the amount of outgassing of a tape specimen undergoing vacuum and temperature treatment as a possible criterion for determining adequate cure and presumably, therefore, uniform frictional characteristics. Weight loss measurements were also made in an effort to establish an alternate criterion. Some data on outgassing rate versus time of cure were obtained. Short-term dormancy tests were conducted which established that a curing process significantly reduced the static friction. However, at this time, the 3M Company announced the removal of 951 tape from the market due to problems of manufacturing control. All work at JPL on 951 tape was therefore immediately discontinued. However, the design and construction of a more suitable friction tester continued. This device and some of the test results obtained are described herein.

[1]It was felt that, among other factors, humidity variations had affected the results of previous tests.

1. Description of Test Device

Friction testers for magnetic tape have been constructed and used to obtain valid test data (Refs. 2–5). Such devices generally embody a tape transport with suitable modifications. Usually, the primary interest is in running friction. However, with static friction as a primary consideration, it was felt that the frictional characteristics of bearings, motors, clutches, brakes etc., typically embodied in such tape transports introduce unknown and variable contributions into the test results, especially under conditions of heat soak, and that a new device should be designed and constructed which would not only be reasonably free of such spurious contributions, but would also be a simpler and more appropriate device.

The test rig is shown in Fig. 13. The test head is mounted on a cantilever spring, to which strain gages are attached for measuring the flexure. A thermocouple is embedded in the head for temperature monitoring and control. The tape to be tested is secured at the upper end to a solenoid and at the lower end to a weight. In this way, constant tape tension is maintained. The operation of the solenoid which pulls the tape over the head is controlled by means of a motor-driven rheostat. The entire test device, including a suitably controlled heater, is placed in a bell jar, and tests are performed in a nitrogen atmosphere. The steps followed in performing a test are as follows:

(1) A test head is installed at the tip of the cantilever and is then carefully cleaned to remove any contaminants, including body fluids from handling.

(2) A length of the test tape is clamped in place at both ends and carefully cleaned.

(3) The bell jar is placed over the assembly, and the enclosure is purged and back-filled with dry nitrogen. A slight negative differential pressure is maintained in order to keep the bell jar sealed.

(4) Friction between the head and tape is measured by energizing the solenoid motor and then recording on a chart recorder the deflection of the cantilever.

(5) The heat is turned on and maintained for the desired soak period.

(6) At the end of the soak period, the heat is turned off; when the head temperature has dropped to ambient room temperature, the friction measurement, Step (4), is repeated.

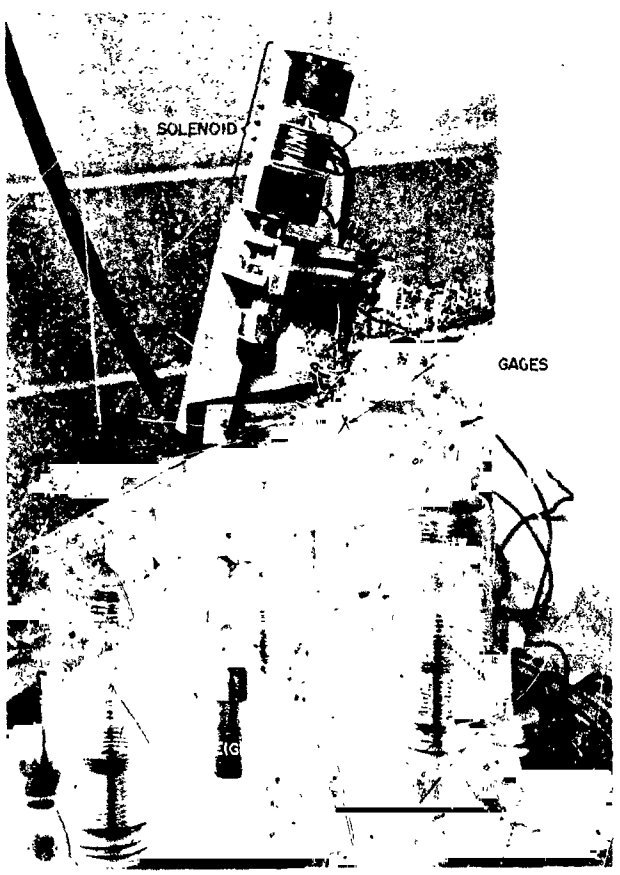

Fig. 13. Final static-friction test rig

2. Test Results

Some of the more interesting test data obtained to date are given in Table 1, which indicates the apparent desirability of monel and/or brass for head-bracket material, as opposed to inconel, manganese–bronze, aluminum–bronze, or 310 stainless steel, and the merit of CEC/EK tape[1], as compared with three other types (two other brands).

3. Conclusions

A suitable test rig for determining the static friction characteristics of various tapes and head materials has been developed. With some refinements in procedure, it is anticipated that measurements will be repeatable within 20%. Use of this test rig is continuing in an effort to determine the effects on static friction of soak time, soak

[1]CEC/EK tape is an Eastman Kodak Co. tape marketed by the Consolidated Electrodynamics Corp.

Table 1. Stiction test results for various head-bracket materials and tape samples[a]

Item	Preheat stiction, g, for indicated test				Postheat stiction, g, for indicated test				Increase, %				
	1	2	3	4	1	2	3	4	1	2	3	4	Average
Head-bracket materials[b]													
KR Monel	70	75	60	85	100	100	160	155	43	33	167	83	82
Inconel	55	55	45	50	270	175	110	130	390	220	145	160	229
Manganese-bronze	60	50	50	40	240	210	235	205	300	320	370	410	350
310 Stainless steel	60	40	40	45	200	80	90	110	230	100	125	140	149
Aluminum-bronze	60	40	40	45	210	190	290	240	250	375	630	430	421
Brass	110	95	95	90	165	135	180	120	50	42	47	33	43
Tape samples[c]													
CEC/EK	50	50	45	50	85	90	90	85	70	80	100	60	78
3M 991	70	75	60	85	110	100	160	155	43	33	167	83	82
3M 951[d]	65	80	85	85	300	190	255	240	310	137	200	182	182
Memorex 62L	65	80	50	50	140	165	135	195	115	106	170	225	154

[a]Soak time: 10 hr; soak temperature: 75°C.
[b]Tested against 3M 991 tape.
[c]Tested against KR-monel.
[d]From manufacturer's defective lot.

temperature, tape tension, tape pretreatment, and tape wrap-angle.

It is interesting to consider the possible validity of stiction testing as a criterion for determining a tape's wear resistance quality. Nesh and Brown (Ref. 6) have conjectured that a greater degree of cross-linking in the polymer chain of a given tape sample may provide greater wear resistance. Their approach to a determination of this degree of cross-linking and, hence, wearability is a measurement of the tape's solvent resistance. It would appear that a static-friction test after an appropriate heat soak may also yield a measure of the degree of cross-linking in the polymer structure.

References

1. Collum, R. C., Jr. (Collins Radio Co.), and Bryant, P. M. (Leach Corp.), *Apollo Spacecraft Data Storage System*, paper presented at the National Telemetry Conference, Los Angeles 1964.
2. Scheiman, J., *Method for Measuring and Varying Friction in Magnetic Recording*, Final Report for Laboratory Project 5942-4, Material Laboratory, New York Naval Shipyard, December 22, 1958.
3. *Magnetic Tape Study*, Final Report for Contract DA18-119-SC-42, General Kinetics, Inc., Arlington, Virginia, January 31, 1960.
4. Spratt, H. G. M., *Magnetic Tape Recording*, Second Edition, D. Van Nostrand Company, Inc., New York, pp. 162, 163.

References (Cont'd)

5. Engels, E., Jr., and Cooper, L. R., *An Evaluation of the Physical and Magnetic Characteristics of Thirteen Instrumentation Quality Magnetic Recording Tapes*, Air Force Flight Test Center, Edwards Air Force Base, California, Air Research and Development Command, U.S. Air Force, August 1957.

6. Nesh, F., and Brown, R. F., Jr., "A Study of the Chemical and Physical Properties of Magnetic Recording Tape," National Bureau of Standards, *IRE Transactions on Audio*, May–June 1962.

XIX. Lunar and Planetary Sciences

A. Further Antenna Pattern Measurements in the 13-mm Microwave Band on the Goldstone Space Communications Station 30-ft Antenna

M. L. Kellner

The Goldstone Space Communications Station 30-ft precision antenna was used in December 1964 and January 1965 for radiometric observations of Jupiter in the 13-mm microwave band. Azimuth and elevation antenna patterns were obtained to evaluate the feed–antenna combination for beamwidth, symmetry, and sidelobe structure information. Patterns were also rerun at the frequencies and on-axis feed position used during the radiometric observations of Venus (*SPS 37-29*, Vol. IV, pp. 122–126) to refine the values obtained at that time.

1. Implementation

The patterns were obtained with an arrangement identical to the one utilized previously: a boresighting transmitter at Tiefort Mountain, and the radiometer used for the planet observations as receiver. Figs. 1 and 2 show the boresighting bench which was used as the transmitter. This is a slightly modified version of the unit used in the Venus experiment (*SPS 37-29*). In this unit, a backward-wave oscillator, with a maximum power output of approximately 40 mw, is used as an RF signal source. It is followed by an isolator, a level-setting attenuator, a waveguide switch that permits the power to be routed into a load when desired, a directional coupler that feeds a precision wavemeter and temperature-compensating bolometer for frequency and power monitoring, two attenuators, and a standard gain horn. One

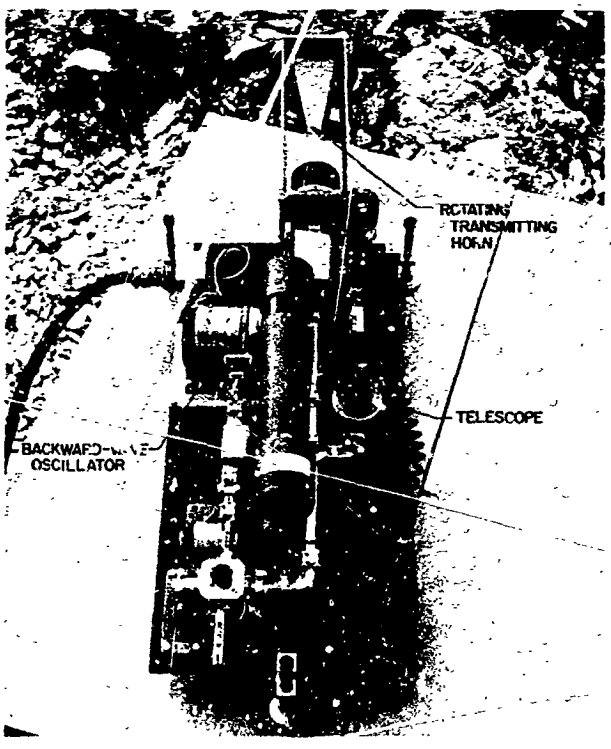

Fig. 1. Boresighting bench

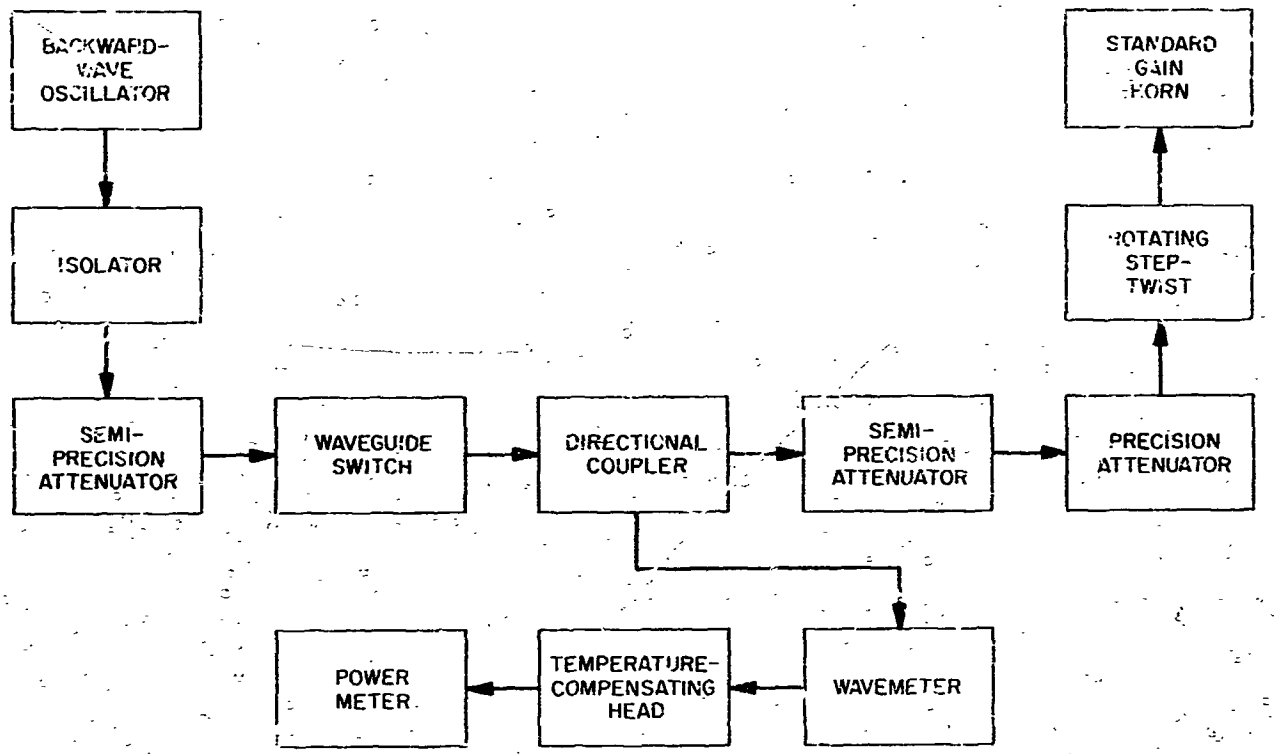

Fig. 2. Boresighting bench block diagram

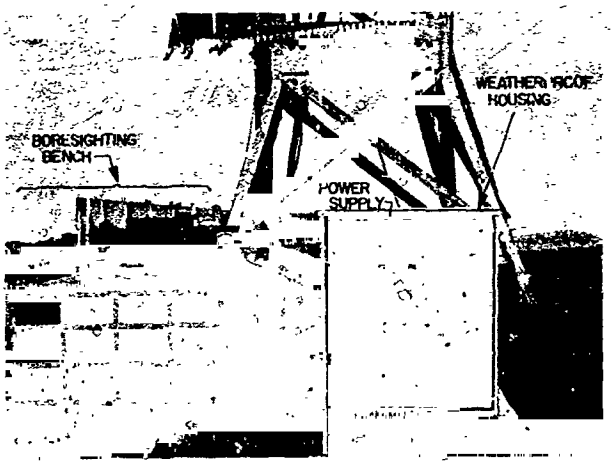

Fig. 3. Boresighting bench and associated equipment in transmitting position

of the two attenuators before the horn was a precision attenuator to permit accurate power output level changes for linearity calibration purposes. A rotating step-twist was incorporated in the standard-gain-horn mounting structure to allow rapid polarization changes of the transmitted signal. Fig. 3 shows the boresighting bench and associated equipment in the transmitting position.

All of the components, with the exception of the backward-wave oscillator power supply and power meter and an electronic prime power regulator, were mounted on a ½-in. aluminum plate for rigidity. Three leveling screw-jacks on the plate permitted fine adjustment of the output beam position. A telescope was also mounted on the plate for visual collimation of the output beam.

The radiometer receiver local oscillator and the boresighting bench used identical backward-wave oscillators and power supplies. After 1 hr of warmup time, both systems were extremely stable; there was a direct correlation of frequency setting between the systems, enabling very accurate pattern measurements.

2. Procedure and Results

The first step in the measurement procedure was to properly focus the feedhorn on the antenna. This was accomplished at 23.8 Gc by observing the on-axis feed

position yielding maximum output consistent with lowest sidelobes and symmetry from the radiometer when the antenna was pointed at the boresight bench at Tiefort Mountain. All power levels and the radiometer performance were carefully monitored during this and subsequent measurements.

With the feed locked in proper position, the antenna was computer-controlled to scan in both elevation and azimuth at a rate of 0.005 deg/sec. The recorder was operated at a 60-mm/min rate, yielding a calibration of 0.005 deg/mm on the chart. Two types of patterns were run in this manner. The first type was obtained by setting the radiometer gain so that the peak output on-axis was several db below compression. This allowed the main antenna lobe to be recorded in detail, but the dynamic range was insufficient to see the sidelobe structure. The second type of pattern was run by allowing the recorder to become saturated on the main antenna lobe by increasing the gain. The sidelobes were then recorded with better detail.

Figs. 4 and 5 show the patterns obtained at 20.6 Gc. The main characteristics at this frequency are summarized below:

Scan plane	3-db Beamwidth, deg	6-db Beamwidth, deg	First sidelobe, db
Azimuth	0.108	0.141	−18.0
Elevation	0.135	0.189	−12.0

Patterns were obtained at 20.6, 21.0, 21.5, 22.0, 22.5, 23.0, 23.5, and 24.0 Gc using the same technique. The patterns shown in Figs. 4 and 5 are representative of those for all the frequencies.

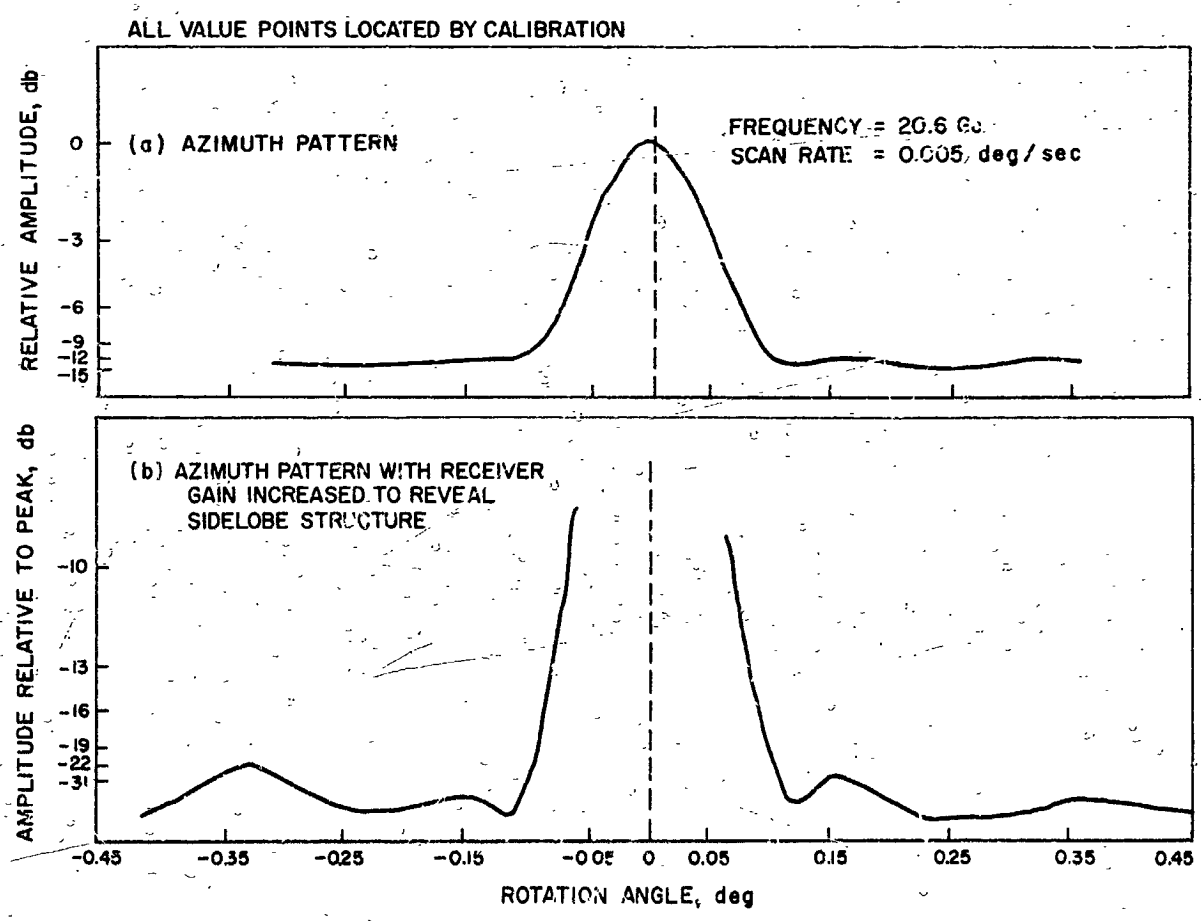

Fig. 4. Azimuth antenna patterns at 20.6 Gc on the Goldstone 30-ft antenna

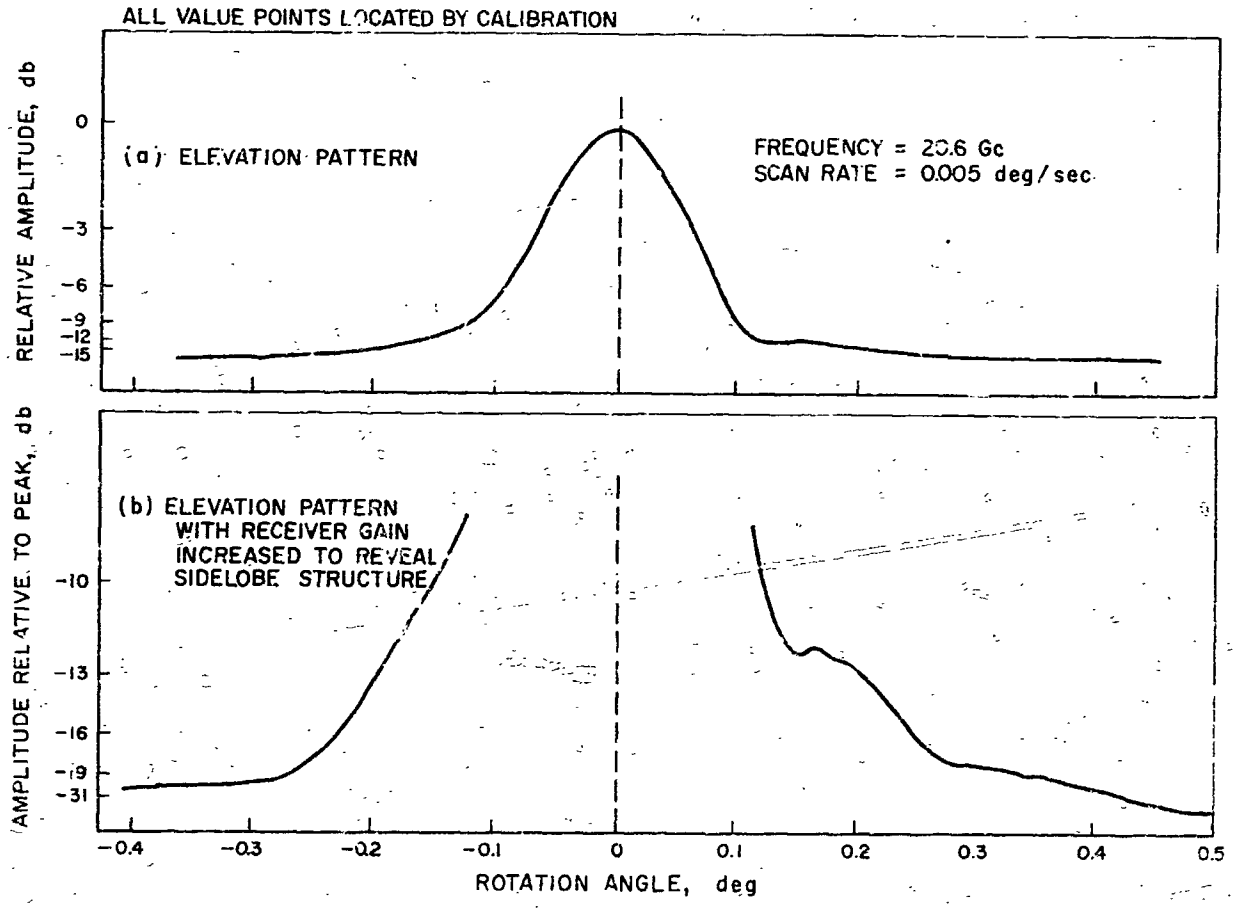

Fig. 5. Elevation antenna patterns at 20.6 Gc on the Goldstone 30-ft antenna

XX. Physics

A. Theory of Ionization of Atomic Systems by High-Intensity Radiation

O. von Roos

Experiments have been reported (Refs. 1–3) of the generation of plasmas in gases of H_2, He, Ar, and N_2 by pulsed ruby laser light (intensity of the order of 10^7 to 10^8 w/cm^2). Theories have been advanced (Refs. 4 and 5) to explain the electron generation by a direct ionization of the neutral gas molecules by means of multiple photon absorption. It is, of course, true that ionization cross-sections may become large enough once the molecule is excited sufficiently high that only a one- or two-photon absorption suffices to lift the electron into the continuum (Ref. 6). However, it is quite a different matter to excite the electron from the ground state. For hydrogen, for instance, we would need about 10 photons of the ruby laser light to even lift the electron into the first excited (2P) state, and we will see that the cross-section for this process is prohibitively small.[1] It seems, therefore, that an explanation for the experimental findings (Refs. 1–3) rests with the "microwave breakdown process," i.e., the assumption of the presence of at least one free electron originally (Refs. 3 and 7). In the following discussion, we develop a theory of the above processes in perturbation theory, the latter being valid for intensities as high as 10^{11} w/cm^2.

[1] It is small not only because so many photons are involved but also because of the small phase space available. For a truly sharp bound state as the final state, the transition rate would be exactly zero.

1. Wave Function of the Electron

The Schrödinger equation for a one-electron system under the influence of a circularly polarized monochromatic plane wave of frequency w_0 is:

$$(H_0 + H_1)\psi = i\hbar\dot{\psi}, \tag{1}$$

with

$$H_0 = -\frac{\hbar^2}{2m}\nabla^2 + \phi(r), \tag{2}$$

$$H_1 = ie\epsilon\hbar\left[\cos k_0(z-ct)\frac{\partial}{\partial x} + \sin k_0(z-ct)\frac{\partial}{\partial y}\right]. \tag{3}$$

Here, ϵ is the parameter (Ref. 8):

$$\epsilon^2 = \frac{4\pi e^2 \bar{n}}{m^2 c^2 w_0}, \tag{4}$$

and the electromagnetic wave propagates in the z-direction. In Eq. (1), the well-known A^2 term has been omitted since it only gives rise to an irrelevant phase factor in the case of circularly polarized light. Expanding the wave function ψ in the complete set belonging to H_0, we have for the expansion coefficients:

$$i\hbar\,\dot{a}_l(t) = \sum_m < l \mid H_I \mid m > \exp(i w_{lm} t)\, a_m(t) \quad (5)$$

Under the assumptions that the electromagnetic field is switched on at $t = 0$, say, and that the electron was in the ground state, we have

$$a_l(0) = \delta_{l0}\,, \quad (6)$$

as the initial condition.[2]

Defining the operators

$$D^{\pm} = \frac{c}{2}\left[\exp(\pm i k_0 z)\frac{\partial}{\partial x} \mp i\frac{\partial}{\partial y}\right] \quad (7)$$

and performing a Laplace transformation on the expansion coefficients $a_l(t)$:

$$a_l(s) = \int_0^{\infty} \exp(-st)\, a_l(t)\, dt\,, \quad (8)$$

we find, by using Eqs. (3), (5), and (6), that

$$s a_l(s) - \delta_{l0} = \epsilon \sum_m \{ < l \mid D^+ \mid m > a_m(s + i w_0 - i w_{lm}) + < l \mid D^- \mid m > a_m(s - i w_0 - i w_{lm}) \}\,. \quad (9)$$

We are solving Eq. (9) by an iteration, treating ϵ as the expansion parameter:[3]

$$a_l(s) = \sum_{\alpha=0}^{\infty} \epsilon^{\alpha} a_{l;\alpha}(s)\,. \quad (10)$$

We immediately have:

$$a_{l;0}(s) = s^{-1}\delta_{l;0}\,, \quad (11)$$

and, for $\alpha > 0$, the recursive equation:

$$s a_{l;\alpha}(s) = \sum_m \{ < l \mid D^+ \mid m > a_{m;\alpha-1}(s + i w_0 - i w_{lm}) + < l \mid D^- \mid m > a_{m;\alpha-1}(s - i w_0 - i w_{lm}) \}\,. \quad (12)$$

From Eqs. (11) and (12), we obtain the first-order correction:

$$a_{l;\alpha}(s) = < l \mid D^+ \mid 0 > s^{-1}(s + i w_0 - i w_{l0})^{-1} + < l \mid D^- \mid 0 > s^{-1}(s - i w_0 - i w_{l0})^{-1} \quad (13)$$

Eqs. (13) and (12) then lead to the second-order correction $a_{l;2}(s)$, etc. We will not include here any of the higher-order terms, since they rapidly become more and more involved. However, we do wish to show how any contribution of an arbitrary order (α, say) toward the expansion coefficient $a_l(s)$ can be constructed. This can be accomplished with Feynman diagrams, but, since in our case these diagrams are somewhat different[4], it is worthwhile to give the results here. The contribution to $a_l(s)$ in order α [i.e., the quantity $a_{l;\alpha}(s)$] consists of a sum of exactly 2^{α} terms, each of which can be uniquely represented by a diagram. Each diagram consists of a horizontal line to which are attached exactly α vertical lines, some from above (called positive lines, whose intersection with the horizontal line is called a positive vertex) and some from below (called negative lines, whose intersection with the horizontal line is called a negative vertex) in arbitrary order. If there are α_+ positive lines and α_- negative lines, we have $\alpha_+ + \alpha_- = \alpha$, and the total number of such diagrams is

$$N(\alpha_+) = \alpha!\,(\alpha_+!\,(\alpha - \alpha_+)!)^{-1}\,.$$

Since any number of positive lines is allowed, we have altogether

$$\sum_{\alpha_+=0}^{\alpha} N(\alpha_+) = 2^{\alpha} \quad (14)$$

diagrams. A few examples are shown below:

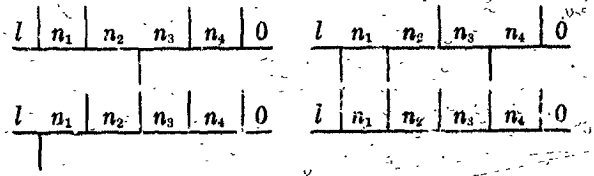

[2] In Eq. (5) and the following, l or m, etc., signifies a collection of quantum numbers, and all summations extend over the complete set of eigenfunctions of H_0, including, of course, the continuum states. $w_{lm} = \hbar^{-1}(E_l - E_m)$ is simply the Bohr frequency.

[3] This is allowed even for the highest laser intensities presently available (Ref. 7).

[4] There are no internal lines and a different propagator.

The rules for associating to each diagram a definite contribution to the amplitude $a_{l;n}(s)$ are the following: For each positive vertex joining the two parts of the horizontal line labeled n_j and n_{j+1} (see examples), write the expression $< n_j | D^+ | n_{j+1} >$. Likewise, for a negative vertex, write $< n_j | D^- | n_{j+1} >$. For that part of the horizontal line which is labeled n_j, write the "propagator" $(s - iw_{in_j} + i\alpha_j w_\alpha)^{-1}$, where the number α_j is equal to the sum of all positive vertices *minus* the sum of all negative vertices which are to the left of the "propagator." Finally, multiply all terms together and sum over all labels (quantum numbers), except those of the open ends. According to these rules, the diagrams on the right-hand side above give rise to

$$\sum_{n_1,\ldots,n_4} < l | D^- | n_1 > \; < n_1 | D^- | n_2 > \; < n_2 | D^- | n_3 >$$

$$\cdots < n_4 | D^- | 0 > s^{-1} (s - iw_\alpha - iw_{i_1})^{-1}$$

$$\times (s - 2iw_\alpha - iw_{i_{n_2}})^{-1} (s - iw_\alpha - iw_{i_{n_3}})^{-1}$$

$$\times (s - 2iw_\alpha - iw_{i_{n_4}})^{-1} (s - iw_\alpha - iw_{i_1})^{-1} \qquad (15)$$

and

$$\sum_{n_1,\ldots,n_4} < l | D^+ | n_1 >$$

$$\cdots < n_4 | D^- | 0 > s^{-1} (s + iw_\alpha - iw_{i_{n_1}})^{-1}$$

$$\times (s + 2iw_\alpha - iw_{i_{n_2}})^{-1} (s + 3iw_\alpha - iw_{i_{n_3}})^{-1}$$

$$\times (s + 4iw_\alpha - iw_{i_{n_4}})^{-1} (s + 5iw_\alpha - iw_{i_1})^{-1} \qquad (16)$$

respectively.

The wave function of the electron is finally given by

$$\psi(\mathbf{r}, t) = \sum_l \sum_\alpha \epsilon^\alpha \frac{1}{2\pi i} \int ds \exp(st) a_{l;\alpha}(s) \psi_l(\mathbf{r}) \times \exp\left(-\frac{it}{\hbar} E_l\right). \qquad (17)$$

2. Transition Probability Per Second Due to Incident Radiation

In order to find the transition probability per second due to the incident radiation, we proceed as follows: Since, by Eq. (17), the wave function of the electron contains an admixture of continuum states, we project on an arbitrary continuum state ψ_n for example. This gives from Eq. (17):

$$< n | \psi(\mathbf{r}, t) > = \sum_\alpha \epsilon^\alpha \frac{1}{2\pi i} \int ds \exp\left(st - \frac{it}{\hbar} E_n\right) a_{n;\alpha}(s) \qquad (18)$$

The transition probability per second into the continuum state characterized by the collection of quantum numbers n is then given by:

$$A(n) = \lim_{t \to \infty} \frac{d}{dt} | < n | \psi(\mathbf{r}, t) > |^2. \qquad (19)$$

Let us assume that the relationship

$$Nw_\alpha - w_{n\alpha} = 0 \qquad (20)$$

is satisfied for a certain integer N and that no such relationship is possible for any integer smaller than N. Physically this means that it takes at least N photons of the incident radiation to ionize the atomic system.[2] From our diagrammatic expansion, we know that the lowest order in which the term $(s - iNw_\alpha - iw_{n\alpha})^{-1}$ can arise is of the Nth-order and it is precisely this term which gives rise to a non-vanishing contribution in Eq. (19). But, in Nth-order there is only one diagram with the "propagator" $(s - iNw_\alpha - iw_{n\alpha})^{-1}$, and that is the one with only positive vertices. We now have in Nth order

$$< n | \psi(\mathbf{r}, t) > = \epsilon^N (2\pi i)^{-1} \int ds \exp\left(st - \frac{it}{\hbar} E_n\right) \times \sum_{n_1,\ldots,n_{N-1}} < n | D^+ | n_1 > \cdots < n_{N-1} | D^+ | 0 > s^{-1} \times (s - iw_\alpha - iw_{n_1})^{-1} \cdots (s + i(N-1)w_\alpha - iw_{n_{N-1}})^{-1} (s + iNw_\alpha - iw_{n\alpha})^{-1}. \qquad (21)$$

There are $(N + 1)$ simple poles in the s-plane, and the integration over s is relatively easy. Because of Eq. (20) and the asymptotic limit $t \to \infty$ in Eq. (19), it is easy to see that only the poles at $s = 0$ and $s = i(w_{n\alpha} - Nw_\alpha)$

[2] We specifically exclude a resonance condition of the type $Nw_\alpha - w_{n'} = 0$, where n' specifies any bound state. Cases like this can be handled according to Ref. 7 and do not lead to any interesting effects as far as ionization is concerned (see also Ref. 6).

contribute. Leaving out all irrelevant phase factors we now obtain:

$$<n\,\epsilon\,(\mathbf{r},t)> \sim \epsilon^N \sum_{n_1 \cdots n_{N-1}} <n\,D\,n_1> \cdots <n_{N-1}\,D\,0>\,(w_n - w_{n_1 N})^{-1}(2w_n - w_{n_2 N})^{-1} \cdots \left[(N-1)\,w_n - w_{n_{N-1} N}\right]^{-1} \frac{1-\exp\left[it(w_{nN} - Nw_n)\right]}{w_n - Nw_n}, \tag{22}$$

from which we have, using Eq. (19):

$$A(n) = 2\pi\epsilon^{2N} \sum_{m_1 \cdots m_{N-1}} |<n\,D\,m_1> \cdots <m_{N-1}\,D\,0>\,(w_{n_1 N} - (N-1)\,w_n)^{-1} \cdots (w_{n_{N-1} N} - w_n)^{-1}|^2 \times \delta(Nw_n - w_{nN}). \tag{23}$$

Specifying the quantum numbers n by E, l, m, where E is the energy of the continuum and l and m are the angular momentum quantum numbers, and using continuum wave functions which are normalized in the energy scale (Ref. 9), we find for the transition probability per second of a transition from the ground state to a continuum state (ionization) by the simultaneous absorption of N photons of frequency w_n:

$$A(E; l, m) = \frac{1}{2Ry}\,\epsilon^{2N} \left| \sum_{n_1 \cdots n_{N-1}} <E; l, m\,|D|\,n_1> \cdots <n_{N-1}\,|D|\,0>\,(w_{n_1 N} - (N-1)\,w_n)^{-1} \times (w_{n_2 N} - (N-2)\,w_n)^{-1} \cdots (w_{n_{N-1} N} - w_n)^{-1} \right|^2, \tag{24}$$

where Ry = Rydberg frequency $= 3.3 \times 10^{15}$ sec^{-1}. A crude estimate of the magnitude of A can easily be given by replacing the intermediate frequencies $w_{n_j N}$ by a mean value $\overline{w}$. In that case, using a sum rule, we obtain from Eq. (24):

$$A(E) \approx \frac{1}{2Ry}\,\epsilon^{2N} \left| <E; l, m\,|(D)^N|\,0> \right|^2 \prod_{j=1}^{N-1} (\overline{w} - jw_n)^{-2}. \tag{25}$$

To estimate the magnitude of Eq. (25), let us apply it to the ionization of hydrogen from its ground state with ruby laser light of frequency $w_n = 3 \times 10^{15}$ sec^{-1}. The magnitude of various matrix elements $<n|D|m>$ is $(mc^2/\hbar)\,\alpha$, where α is the fine structure constant (see Footnote 5). The number of photons absorbed simultaneously is at least $N = 7$ in this case. We obtain, therefore,

$$A(E) \approx \frac{1}{2Ry} \left(\epsilon \frac{mc^2}{\hbar}\,\alpha\right)^{14} \prod_{j=1}^{6} (\overline{w} - jw_n)^{-2}. \tag{26}$$

Estimating $\overline{w} = 10^{15}$ sec^{-1}, we obtain the result that ϵ must be 10^{-3} in order that $A = 10^{7}$ sec^{-1}, a truly small ionization probability. But, in order to produce this low ionization rate, the laser beam intensity must have the staggering value of $I = 10^{13}$ w/cm^2. The estimate is conservative since the values of the matrix elements are usually smaller than those adopted here. Also, since the two-photon ionization of excited hydrogen has been calculated exactly (Ref. 6), it is possible to check the estimate given here; it turns out that the estimate leads to the right order of magnitude in that case.

N65-32449

B. Interaction of Intense Electromagnetic Beams with Electron Beams

M. M. Saffren

Recently several authors (Refs. 10–12) have studied the interaction of a single intense light beam with a free electron, the electron being allowed to move with relativistic speed. Von Roos (Ref. 13) has proposed a method to treat the interaction of an intense beam with a bound electron. We propose a perturbation method for handling the problem of bound and free electrons which utilizes the Feynman propagator in the perturbation expansion of the electron wave function. In our method, there appears to be no problem with the boundary conditions at infinity. The method allows us to write explicitly the S matrix in any particular order of the fine structure constant without first solving an initial-value problem. Moreover, we have no difficulty in treating problems in which there is more than one intense beam present.

Along with all other authors, we assume that the intense radiation field may be regarded as unquantized. This has been justified in detail by Frantz (Ref. 14), but is more or less simply a consequence of the fact that the probability of a photon being either radiated into or absorbed from a beam is proportional (roughly) to the number of photons already present in the beam. We now assume $S_F(x, y)$ to be the Feynman propagator (Ref. 15)

for either a free particle or a particle bound by a time-independent potential. The wave function for such a particle now perturbed by a radiation field A may be written as Ψ, and Ψ is the solution of (Ref. 15):

$$\Psi(z) = \psi_i(z) + \int d^4x\, S_F(z,x)\, W[A(x)]\, \Psi(x), \quad (1)$$

where, for fermions,

$$W(A) = ieA = ie\,\gamma_\mu A^\mu,$$

$$\gamma_\mu = \text{dirac matrices}, \quad (2)$$

and, for scalar particles,

$$W(A) = ie\,[A^\mu \partial_\mu + \partial_\nu A^\nu] + e^2 A^\mu A_\mu, \quad (3)$$

and $\psi_i(z)$ is the initial state of the particle.

We now split A into two parts: (1) A_0, the field due to the intense beam; and (2) a, the field of any other photons that are either absorbed or emitted by the electron. The electron wave function in the presence of this combined field (radiation corrections aside) is obtained as usual by iterating Eq. (1). Thus [dropping the integral sign in Eq. (1) and continuing to do so below], we obtain to third order in the fine structure constant.

$$\begin{aligned}\Psi = \psi_i &+ S_F W(A_0)\,\psi_i \\ &+ S_F W(A_0)\, S_F W(A_0)\,\psi_i \\ &+ S_F W(a)\,\psi_i \\ &+ S_F W(A_0)\, S_F W(a)\,\psi_i \\ &+ S_F W(a)\, S_F W(A_0)\,\psi_i \\ &+ S_F W(A_0)\, S_F W(A_0)\, S_F W(a)\,\psi_i \\ &+ S_F W(A_0)\, S_F W(a)\, S_F W(A_0)\,\psi_i \\ &+ S_F W(a)\, S_F W(A_0)\, S_F W(A_0)\,\psi_i \\ &+ \text{etc.}\end{aligned}$$

A scattering matrix element is then

$$S_{fi} = \langle \psi_f \mid \Psi \rangle,$$

where ψ_f is a state of the particle in the time-independent potential that corresponds to the propagator S_F. The matrix element is

$$\begin{aligned}S_{fi} = \delta_{fi} &+ \langle \psi_f \mid S_F W(A_0) \mid \psi_i \rangle \\ &+ \langle \psi_f \mid S_F W(a) \mid \psi_i \rangle \\ &+ \langle \psi_f \mid S_F W(A_0)\, S_F W(A_0) \\ &+ S_F W(A_0)\, S_F W(a) \\ &+ S_F W(A_0)\, S_F W(a) \\ &+ S_F W(a)\, S_F W(A_0) \mid \psi_i \rangle \\ &+ \langle \psi_f \mid S_F W(A_0)\, S_F W(A_0)\, S_F W(a) \\ &+ S_F W(a)\, S_F W(A_0)\, S_F W(A_0) \\ &+ S_F W(A_0)\, S_F W(a)\, S_F W(A_0) \\ &+ S_F W(a)\, S_F W(a)\, S_F W(A_0) \\ &+ S_F W(a)\, S_F W(A_0)\, S_F W(a) \\ &+ S_F W(A_0)\, S_F W(a)\, S_F W(a) \\ &+ S_F W(A_0)\, S_F W(A_0)\, S_F W(A_0) \\ &+ S_F W(a)\, S_F W(a)\, S_F W(a) \mid \psi_i \rangle .\end{aligned}$$

As is easily verified, this expansion corresponds to the usual Feynman expansion. The matrix elements can be calculated using the usual Feynman rules, except that now, in each term in which an "intense photon" A_0 appears, the term is to be multiplied by the square root of the number of photons in the beam as many times as A_0 appears. This is nearly the result found by Frantz, who used more formal methods. The agreement is, in fact, complete, except for diagrams where the electron radiates another photon into the beam made up of such photons. For intense beams, however, the difference is negligible.

We are presently calculating the radiation from a particle subject to the field of two intense beams. We have already calculated the cross-section for frequency doubling when a single intense beam is incident upon a free particle. Up to terms that are third order in the fine structure constant, the result is in agreement with previous calculations (Refs. 10–12).

References

1. Meyerand, R. G., and Haught, A. F., *Physical Review Letters*, Vol. 11, p. 401, 1963.

2. Damon, E. K., and Tomlinson, R. G., *Applied Optics*, Vol. 2, p. 546, 1963.

References (Cont'd)

3. Minck, R. W., *Journal of Applied Physics*, Vol. 35, p. 252, 1964.
4. Bunkin, F. V., and Prokhorou, A. M., *Soviet Physics JETP*, Vol. 19, p. 739, 1964.
5. Tozer, B. A., *Physical Review*, Vol. 137, p. A1665, 1965.
6. Zernik, W., *Physical Review*, Vol. 135, p. A51, 1964.
7. Wright, J. K., *Proceedings of the Physical Society of London*, Vol. 84, p. 41, 1964.
8. Von Roos, O., *Physical Review*, Vol. 137, p. A358, 1965.
9. Bethe, H. A., and Salpeter, E. E., *Quantum Mechanics of One and Two Electron Atoms*, Academic Press, New York, 1957.
10. Brown, L. S., and Kibble, T. W. B., *Physical Review*, Vol. 133, p. A705, 1964.
11. Goldman, I. I., *Physics Letters*, Vol. 8, p. 103, 1964.
12. Fried, Z., and Eberly, J. H., *Physical Review*, Vol. 136, p. B871, 1964.
13. Von Roos, O., *Physical Review*, Vol. 135, p. A43, 1964.
14. Frantz, L. M., *Physical Review*, Vol. 134, p. B1419, 1964.
15. Feynman, R. P., *Quantum Electrodynamics*, W. A. Benjamin, Inc., New York, 1961.

XXI. Chemistry

A. Urinary "Free" Corticosteroids by a Simple Clinical Method

A. J. Bauman

Biosatellite monkey experiments require a simple method for continuous instrumental monitoring of urinary corticosteroids because emotional stress in primates is reflected in increased urinary corticosteroid excretion. However, the recovery of urinary steroids is the weakest feature of contemporary steroid analysis (Ref. 1). The steroids are excreted as very complex mixtures of sulfuric acid esters or glycosides of D-glucuronic acid. The analysis and clinical significance of these conjugates is as yet not well developed (Ref. 2). Ordinarily, the conjugates are hydrolyzed enzymatically — a lengthy and uncertain step (Ref. 3) — and the free steroids are then partitioned into organic solvents. The steroids are subsequently resolved by analytical sequences, e.g., thin-layer chromatography (TLC) followed by gas-liquid-partition chromatography (GLPC) (Refs. 4 and 5). Because of the uncertainty and complexity of instrumenting such an operational sequence we decided to examine a typical simple clinical method for "free" urinary corticosteroids.

Dörner and Stahl's recent fluorometric method (Ref. 6) for "free" cortisol plus corticosterone begins with a successive extraction of urine with petroleum ether and methylene chloride. The latter extract is treated with ethanol/sulfuric acid and the acid phase examined fluorometrically. The results are presented in terms of an internal standard of cortisol. In our hands the method was simple and reliable. We obtained a linear fluorescence peak yield at 530 mμ activation for 0-5 μg of cortisol in an Aminco-Bowman instrument. However, TLC examination of the extracts by Bennett's procedure (Ref. 7) showed that no cortisol or corticosterone was present.

One liter of quick-frozen urine from a single male person (about ⅔ of a 24-hr sample) was quickly thawed and divided into two equal parts. Cortisol (40 μg) was added to one part. The samples were then put through the Dörner-Stahl procedure, this being a 100-fold scaleup in size. If we assume that 1500 ml was a fair 24-hr urine sample, their method gives a value of 227 μg of cortisol plus corticosterone for the total sample. We concentrated the extracts to dryness in the cold under nitrogen, obtaining about 33 mg (33,000 μg) of a yellow oil with an odor like that of maple syrup from each. The samples were dissolved in chloroform/methanol 4/1 volume/volume and spotted as 1-μl spots onto a silica gel G TLC plate. Fig. 1 shows the visual appearance of the plate after spraying with 50% sulfuric acid and heating. Though 1200 μg of sample was applied, we see no cortisol and corticosterone. One could easily see 0.05 μg of cortisol

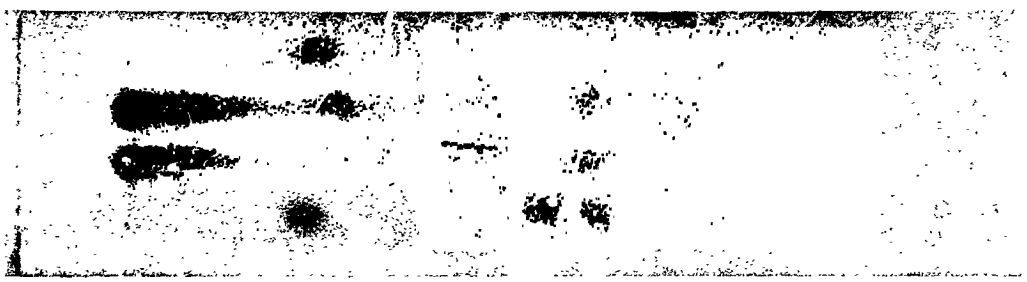

SYSTEM: ETHYL ACETATE/CHLOROFORM/WATER, 9/10/1 BY VOLUME
ADSORBENT: SILICA GEL G UNIPLATE
1. CORTISOL, CORTICOSTERONE; 2 μg EACH; 1-μl SPOTS
2. DÖRNER-STAHL EXTRACT; 1200 μg; 40 μg OF ADDED CORTISOL
3. DÖRNER-STAHL EXTRACT; 1200 μg
4. ESTRONE, ESTRADIOL, ESTRIOL; 2 μg EACH

Fig. 1. Thin-layer chromatograms of urinary extracts

as an olive green spot in visible light or 0.001 μg of cortisol as a blue fluorescent spot under long wave ultraviolet. The 1200 μg of sample should contain at least 1% of a "normal" 24-hr yield of cortisol, or 0.05 μg (Ref. 8). The main body of the extract is very likely a mixture of bile acids — the material at the origin — which fluoresce blue under ultraviolet (Ref. 5). The material which moves with estrone is cholesterol on the basis of infrared and other spray reagents. It seems likely that no free corticosteroids exist in urine and that clinical methods like this one are measuring other classes of compounds.[1]

N65-32451

B. Soil Studies — Microflora of Desert Regions. VII. Abundance of Chemical Elements in an Area of Soil at White Montain Range, Califorina

R. E. Cameron and G. B. Blank

1. Introduction

Soil composition on our planet is dependent upon the geochemistry of surface materials that are exposed to the atmosphere and also upon the influence of organisms. In terrestrial desert areas, organisms are not a principal factor in soil formation and therefore contribute negligibly to soil composition (Ref. 9). It can also be expected that in a more severe desert environment, such as Mars, where aridity may be more extreme, that the soil composition will be primarily mineral. In general, the lower the moisture content of a soil, the fewer the numbers and the less the activity of the soil microflora (Ref. 10). As a consequence, there is a limited organic matter content in desert soils. Although varying proportions of mineral matter are present in different kinds of terrestrial soils, approximately 98 to 99.5% or more of desert soils is of a mineral nature, the remainder being organic matter, which also includes biota (Ref. 11). However, the amounts, distribution, relative abundance, and availability of chemical elements in the soil environment are of vital importance to organisms.

From the viewpoint of extraterrestrial investigations these chemical elements will be in association and interaction with possible endemic organisms or organic residues. An analysis for various elements will therefore be indicative of the extraterrestrial chemical environment in which life might occur or with which organic matter may be complexed. Analyses for C and N are especially important in this respect.

On a geochemical basis, the biophile elements, or those which tend to be associated with organisms, are also the elements which accumulate in soils that are the most affected by organisms (Ref. 12). In terrestrial soils, these include essential major elements, C, H, O, P, K, N, S, minor elements, Ca Fe, Mg, and trace elements, Mn, Fe, Zn, Cu, Mo, Co, and V. Additional biologically associated

[1]Vandenheuvel, W. A., personal communication.

elements include Na, Cl, I, Ag, Ni, Au, Be, Cd, Se, Tl, Sn, Pb, and As. These latter elements may be needed in such minute quantities by organisms that their essentiality has been difficult to assess. The biophile elements do not include Si or Al, and these two elements, plus O, Fe, Ca, Na, K, and Mg, constitute almost 99% of the Earth's crust (Ref. 12).

The average content of chemical elements has been determined for a number of different zonal soils (Ref. 13). These are primarily agricultural soils developed optimally under favorable environmental influences. This article compares the relative abundances and distribution of elements in a relatively arid area of soil of the same genesis and morphology with chemical abundance of elements in agricultural soils and of biological materials.

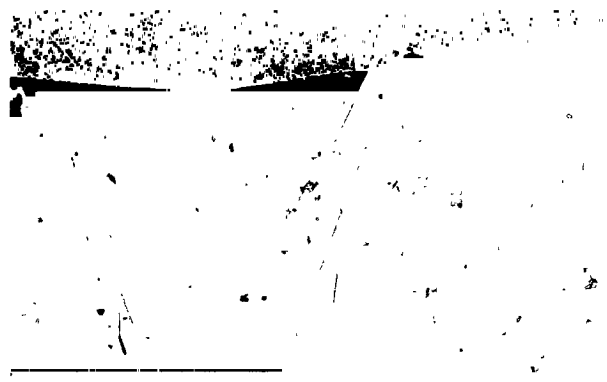

Fig. 2. Soil field plot at White Mountain Range, California (elevation 12,400 ft)

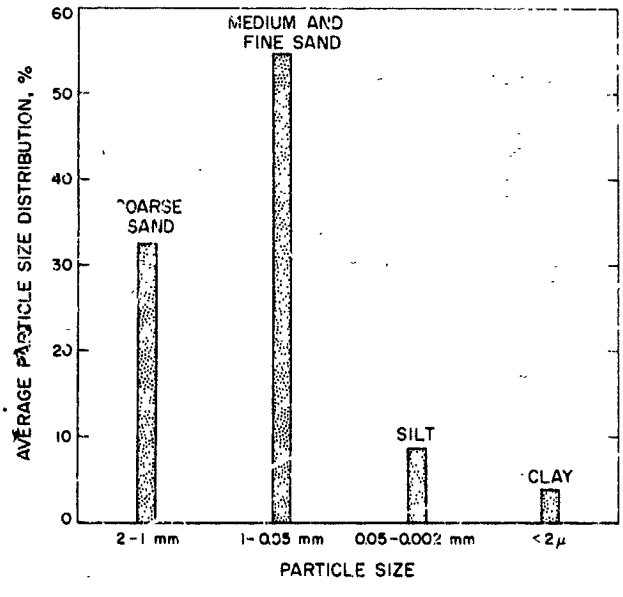

Fig. 3. Average particle size distribution for 18 White Mountain Range field plot soils

2. Materials and Methods

a. Soil description. Within an alpine field plot of 24 ft on a side, 18 samples of naturally air-dry soil were collected from the surface 1-in. (Fig. 2). All of these soils were light yellowish brown (6/4 10YR), of medium bulk density (1.51 g/cm³), loamy sand in texture, and predominately of material ranging from 0.05 to 2 mm in particle size (Fig. 3). All of these soil samples had saturated pH values between 6.1 to 7.0, and Eh values of +450 to +550 mv. Cation exchange values were between 7 to 10 meq/100 g of soil. Organic matter content ranged from 3.5 to 9.0% with an average value of 5.0%. Mineral components of these soils consisted primarily of quartz, plagioclase (albite, anorthite), K-feldspar (orthoclase, microcline), and possibly amphibole and muscovite (Fig. 4).[2] Microbiological data on these 18 samples were reported previously (Ref. 14).

b. Analyses. All soil samples were passed through a 2-mm sieve (#10 mesh) and an aliquot powdered by mortar and pestle for subsequent chemical analyses.

For spectro-chemical analyses, 10 mg of soil was mixed with powdered graphite and ignited with a dc arc. Calibrations were obtained for a photographic emulsion response curve. Photographic spectrograms for the unknown soils were placed in the ARL projector comparator-densitometer, and characteristic lines of the elements determined by comparison with the master spectrogram (Ref. 15).[1] The dc arc is the most convenient method for obtaining a general survey of the inorganic composition of soils.

Other analyses were performed for C, H, N, P, and S. Oxygen values were calculated. C, H, and N were determined by ignition in Coleman C-H and N analyzers as described previously (Ref. 11).[4] S and P were determined on $HClO_4$ extracts. Sulfur was determined by the methylene blue method and P by the molybdenum blue method (Ref. 16).[5]

[1]Analysis by Neil Nickle, JPL Lunar and Planetary Science Section.

[2]Analyses by Pacific Spectro-Chemical Laboratory, Los Angeles, California.

[4]Analyses by Elek Microanalytical Laboratories, Torrance, California.

[5]Analyses by Edward S. Babcock and Sons, Riverside, California.

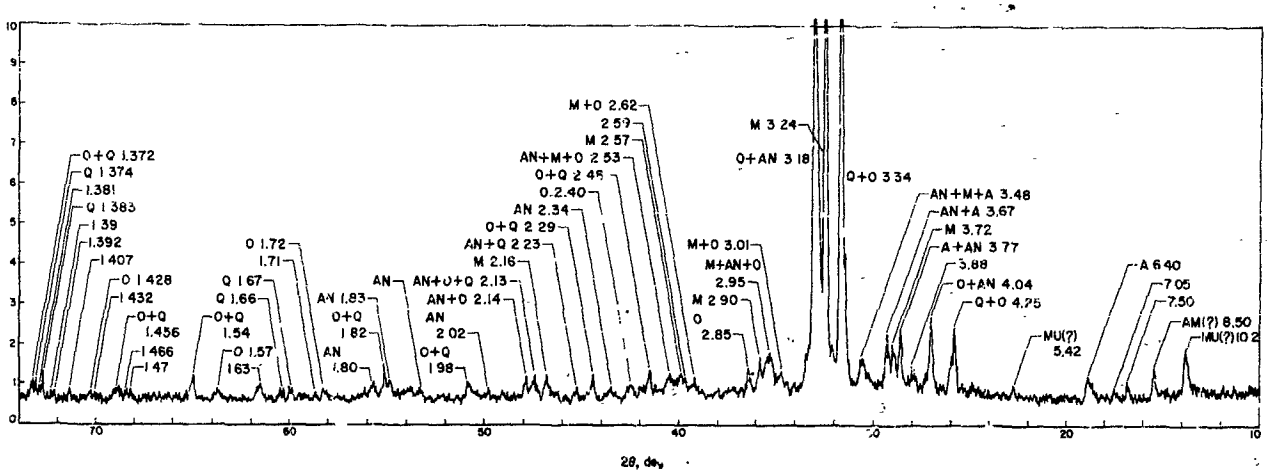

Fig. 4. X-ray diffraction curve for Sample 3 in White Mountain Range soil field plot (Q = quartz, O = orthoclase, M = microcline, MU = muscovite, A = albite, AM = amphibole, AN = anorthite)

3. Results and Discussion

a. Chemical abundance. Chemical abundance of individual elements obtained by various analyses are shown in Table 1. These elements include, in decreasing order or abundance, O, Si, Al, K, Na, Fe, Ca, Mg, C, Ti, H, Mn, N, P, Sr, Ba, Zr, Cr, V, Ga, Cu, S, Ni, B, and Co. Other elements as Sb, As, Be, Bi, Au, Ag, Pb, Sr, Mo, and Zn, would have to be above 5 to 1000 ppm, in order to be detected at these spectrographic sensitivities.

Average abundances of the 25 chemical elements are plotted in decreasing order of abundance in Figs. 5 and 6. These average abundances, while similar to those for typical zonal soils, are, in other cases, more similar to

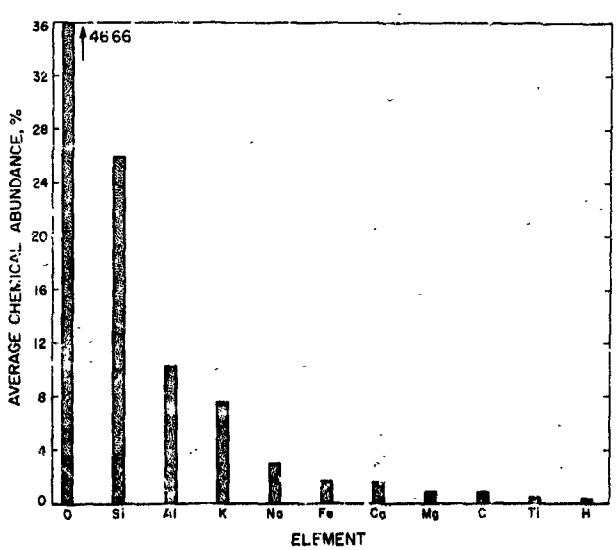

Fig. 5. Average chemical abundance of elements for 18 White Mountain Range field plot soils (major elements)

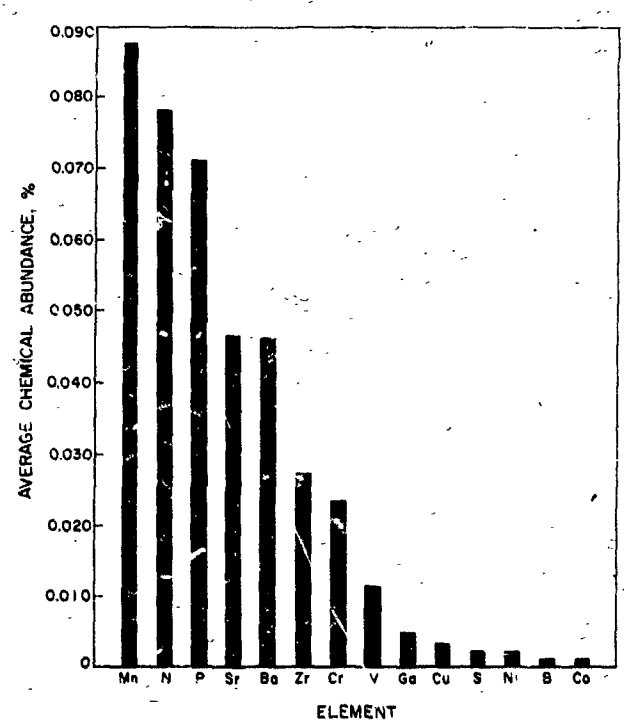

Fig. 6. Average chemical abundance of elements for 18 White Mountain Range field plot soils (minor elements)

Table 1. Chemical abundance of elements for 18 White Mountain Range field plot soils

Sample	Element, total % by wt																							
	O	Si	Al	K	Na	Fe	Ca	Mg	C	Ti	H	Mn	N	P	Sr	Ba	Zr	Cr	V	Ga	Cu	S	Ni	B	Co
1	47.05	28	9.7	6.4	2.4	2.0	1.7	1.24	0.71	0.44	0.28	0.078	0.087	0.07	0.042	0.05	0.016	0.012	0.013	0.0038	0.0021	0.002[illegible]	0.0016	0.0010	0.0003
2	47.33	28	11.0	9.2	3.2	1.6	1.9	0.97	0.73	0.48	0.28	0.069	0.061	0.07	0.038	—	0.011	0.032	0.011	0.0042	0.0037	0.0037	0.0013	0.0010	0.0003
3	4[illegible].59	26	12.0	7.0	2.4	1.9	2.0	1.0	0.90	0.46	0.26	0.074	0.070	0.07	0.061	0.13	0.028	0.031	0.012	0.0043	0.0015	0.0039	0.0023	0.0010	0.0040
4	46.58	27	9.2	7.9	2.9	1.9	1.6	1.1	0.94	0.38	0.28	0.087	0.076	0.06	0.056	0.05	0.055	0.011	0.009	0.0060	0.0017	0.0030	0.0025	0.0010	0.0003
5	45.65	26	10.0	9.8	3.2	1.3	1.4	0.91	0.67	0.41	0.27	0.076	0.056	0.08	0.043	0.05	0.023	0.040	0.012	0.0054	0.0045	0.0027	0.0020	0.0010	0.0003
6	45.90	27	11.0	6.2	2.9	2.6	1.5	0.95	0.86	0.41	0.27	0.110	0.078	0.07	0.058	0.05	0.018	0.008	0.009	0.0046	0.0028	0.0023	0.0023	0.0010	0.0048
7	46.91	28	11.0	4.9	2.0	1.9	1.3	1.5	1.20	0.51	0.32	0.120	0.090	0.08	0.041	0.05	0.025	0.028	0.011	0.0045	0.0027	0.0016	0.0026	0.0010	0.0059
8	45.41	27	9.6	8.0	3.3	1.7	1.7	0.91	1.22	0.40	0.36	0.091	0.090	0.07	0.050	0.05	0.019	0.009	0.011	0.0046	0.0031	0.0017	0.0017	0.0010	0.0003
9	50.06	26	10.0	6.0	2.1	1.6	1.5	0.78	0.92	0.40	0.30	0.090	0.072	0.07	0.039	—	0.041	0.008	0.012	0.0047	0.0021	0.0016	0.0016	0.0010	0.0003
10	48.32	26	10.0	6.1	2.8	2.1	1.4	0.93	1.04	0.50	0.31	0.120	0.107	0.08	0.034	0.05	0.041	0.041	0.015	0.0044	0.0041	0.0016	0.0032	0.0010	0.0003
11	46.08	27	10.0	8.2	3.3	1.5	1.5	0.96	0.56	0.39	0.22	0.081	0.049	0.06	0.055	—	0.011	0.007	0.012	0.0051	0.0028	0.0027	0.0022	0.0010	0.0005
12	43.54	24	11.0	10.0	3.9	1.7	2.1	0.95	1.21	0.47	0.33	0.098	0.100	0.08	0.063	0.05	0.027	0.045	0.011	0.0044	0.0038	0.0023	0.0024	0.0010	0.0003
13	47.33	25	9.4	8.3	3.3	2.0	1.5	0.87	1.07	0.45	0.033	0.070	0.083	0.07	0.051	0.05	0.057	0.048	0.012	0.0059	0.0029	0.0013	0.0031	0.0010	0.0003
14	47.41	27	9.7	7.2	3.2	1.4	1.3	0.70	1.11	0.29	0.31	0.062	0.068	0.08	0.042	0.05	0.019	0.012	0.010	0.0046	0.0027	0.0016	0.0022	0.0020	0.0003
15	46.25	26	11.0	7	8.3	1.7	1.2	0.98	1.00	0.45	0.30	0.098	0.074	0.05	0.051	0.05	0.031	0.045	0.013	0.0046	0.0029	0.0007	0.0017	0.0010	
16	46.39	26	9.0	8.1	3.7	1.3	2.3	0.84	1.24	0.44	0.032	0.084	0.063	0.07	0.033	0.05	0.022	0.012	0.010	0.0039	0.0024	0.0016	0.0021	0.0010	
17	46.43	23	10.0	9.9	4.5	1.5	1.8	0.90	0.89	0.46	0.028	0.071	0.068	0.07	0.041	0.05	0.014	0.010	0.010	0.005[illegible]	0.0027	0.0015	0.0029	0.0010	0.0003
18	47.67	26	10.0	6.4	3.1	2.2	1.5	1.1	0.93	0.39	0.30	0.096	0.074	0.08	0.039	0.05	0.035	0.022	0.012	0.0052	0.0033	0.0010	0.0020	0.0010	0.0005
Average	46.67	26	10.3	7.6	3.1	1.8	1.6	0.96	0.95	0.43	0.10	0.088	0.078	0.07	0.047	0.05	0.027	0.023	0.011	0.0048	0.0031	0.0021	0.0021	0.0011	0.0010
Range	6.52	5	3.0	3.1	2.5	0.9	1.9	0.80	1.29	0.22	0.14	0.058	0.058	0.03	0.030	0.13	0.046	0.041	0.006	0.0022	0.0042	0.0030	0.0019	0.0010	0.0059
Standard deviation	1.37	1	0.8	1.5	0.6	0.3	0.3	0.17	0.20	0.05	0.03	0.017	0.015	0.01	0.009	0.03	0.014	0.015	0.002	0.0006	0.0010	0.0085	0.0005	0.0002	0.0018
Standard error	0.98	1	0.6	1.2	0.5	0.3	0.3	0.10	0.16	0.04	0.03	0.014	0.012	0.01	0.007	0.02	0.011	0.014	0.001	0.0005	0.0007	0.0068	0.0004	0.0001	0.0012

amounts found in various ultrabasic, basic, intermediate, acid, or sedimentary rocks (Ref. 13).

b. Major soil elements. The oxygen content in these soils was the same as the average oxygen content of the Earth's crust, 46.5% (Ref. 12) or of intermediate rocks (Ref. 13). The oxygen content was lower than that of agricultural soils, which is 49.0%. The average Si content was 26%. This amount compares closely to an average of 27.6% in the Earth's crust, or 26% in intermediate rocks. Typical agricultural soils have a higher average Si content.

The average abundance of Al in the Earth's crust is 8.1%. Approximately 10% Al occurs in sedimentary rocks. The average Al content for these soils, 10.3%, was therefore representative of Al in sedimentary rocks, and 3% higher than that for typical agricultural soils.

The highest Fe content of the 18 samples was 2.6%, with an average of 1.8%. This average is about three times less than the average for zonal soils, and more closely approximates that found in acid rocks. The average abundance of iron in well-developed surface soils is usually less than the average of 5.1% found in the Earth's crust.

Ca and K each have approximately the same abundance in well-developed soils — an average of 1.36%. Average Ca content of these 18 soils was 1.6%, less than that found in calcareous desert soils (Ref. 11), and about half of the average content of the Earth's crust.

The K content was exceptionally high for all 18 soils. The average was 7.6%, and would be indicative of the relatively large amount of K-feldspars and plagioclase present.

Na and Mg are the two remaining elements, along with O, Si, Al, Fe, Ca, and K, that constitute almost 99% of the Earth's crust. In typical agricultural soils, both Na and Mg average 0.63%, approximately four times less than their average in the Earth's crust or intermediate rocks. The Na average for these soils was high, 3.1%. Magnesium was slightly above the average for zonal soils, with an average of 0.96%.

C is not a major element in the chemical composition of the Earth's crust, and its abundance in zonal soils averages 2.0%, compared to an average of 0.04% occurring in the Earth's crust and in most rocks. For 18 soils, the average C content was 0.95%, and nearly all in the organic form. In southwestern U.S. desert soils, the mean value for C more nearly approaches a lower value of 0.15% (Ref. 11).

c. Minor and trace elements in soils. In general, other elements may or may not show deviations from their average content in rocks. Hydrogen analyses are infrequently reported for soils. S and P, while of biological importance, may show little or no difference in abundance in soils compared to rocks (Refs. 12 and 13).

Average P content of these 18 soils was 0.07%, and compares favorably with 0.08% for typical agricultural soils. The average S content was 0.002%, compared to averages in well-developed soils of 0.08%. Other biologically important elements, Mn, Cu, Co, V, and B in these soils, had approximately the same abundance as for typical soils.

For life detection purposes, N content of soils ranks in importance with C. Average content of N for well-developed soils is 0.1% and compares favorably with the N content of the 18 White Mountain field plot soils, 0.078%. This is approximately ten times the amount of N found in Southwestern U.S. desert soils (Ref. 11). Most of the N was organic, although some was in the form of NH_4^+ and NO_3^-.

4. Concluding Remarks

A comparison of chemical abundance of 25 elements was made for 18 samples from the surface of a relatively arid soil field plot at the White Mountain Range, California. In decreasing order of abundance, these elements included O, Si, Al, K, Na, Fe, Ca, Mg, C, Ti, H, Mn, N, P, Sr, Ba, Zr, Cr, V, Ga, Cu, S, Ni, B, and Co. For zonal agricultural soils the average order of abundance of chemical elements shows some variations, and in decreasing order of abundance, these were O, Si, Al, Fe, C, Ca, K, Na, Mg, H, Ti, N, Mn, S, P, Ba, Sr, Zr, Cr, V, Ga, Ni, Cu, B, and Co.

There was actually little deviation in the abundance of any element from the 18 samples analyzed from the soil field plot. Variation in the chemical abundance of elements was also comparable to the small variability found for numbers of microflora from the same field plot (Ref. 14). However, additional information is needed for more typical desert soils, especially for soils from different, but adjacent ecosystems, and from various depths of soil.

All chemical elements were in sufficient abundance for microbial activities. Although the total abundances of Fe, Na, and K showed substantial differences compared to typical well-developed zonal agricultural soils, there was no apparent effect on the numbers and kinds of microflora found in the soils. Proximate analyses for Na and K on soil extracts, and their subsequent determination by flame photometry, indicated that "available" Na and K were "normal" for soils.[a]

Acknowledgment. Appreciation is given to Dr. Nello Pace and his staff at the White Mountain Research Station for use of facilities, equipment, and permission to establish an experimental soil field plot.

C. Theory of the Low-Temperature Chromatographic Separation of the Hydrogen Isotopes

J. King, Jr. and S. W. Benson

1. Introduction

A new electrostatic theory has been developed which quantitatively explains the gas-solid chromatographic separation of the hydrogen isotopes at low temperatures. All of the hydrogen isotopes, including the ortho-para derivatives, are separable in a variety of chromatographic columns, such as, alumina (Al_2O_3) (Refs. 17 and 18), molecular sieves (Ref. 19), and glass containing a high percentage of SiO_2 (Ref. 20).

It is obvious from the separation of the ortho- and para-species that there must be some type of hindered rotation on the surface since these species differ only in their rotational energies (Ref. 21). We suggest that hindered rotation results from the difference in α_η and $\alpha_\perp$, the parallel and perpendicular components of the molecular polarization of the isotopes. We propose to show that the attraction of the isotopic gases to the surface arises from the electric-field-induced dipole interactions. The energy of this interaction is given by

$$\Phi_{ads} = -\frac{\alpha}{2} E_z^2 \tag{1}$$

where α is the polarizability of the adsorbed molecule and E_z is the electric-field intensity normal to the surface. Since α_η is one and a half times larger than $\alpha_\perp$ (Ref. 22), the stable configuration of the molecule on the surface is with its internuclear axis perpendicular to the surface plane. Thus, E_z acts parallel to the internuclear axis.

2. Theory

When the molecule goes from the gaseous to the adsorbed state, there is a corresponding change of two degrees of freedom. One translational degree of freedom in the gas phase becomes, on adsorption, a vibration normal to the surface plane, and a gas-phase rotation becomes a hindered rotation on the surface.

The energies of the molecules can be obtained by solving the Schrödinger equation for the Hamiltonian (Ref. 23),

$$H = \frac{P_x^2}{2M} + \frac{P_y^2}{2M} + \frac{P_z^2}{2M} + \frac{P_\theta^2}{2I} + \frac{P_\phi^2}{2I\sin^2\theta} + \Phi(z,\theta) \tag{2}$$

where M is the mass of the molecule, I, the moment of inertia, and $\Phi(z,\theta)$ is the potential energy of interaction of the molecule with the surface. The equation can be solved if the vibrational and rotational motions are separable. Under these conditions, the viorational energy is simply that of harmonic motion normal to the surface and is given by

$$E_v^n = \left(n + \frac{1}{2}\right) h\nu \qquad n = 0, 1, 2 \cdots \tag{3}$$

where ν is the vibrational frequency.

The rotational energy is obtained from a solution of the differential equation (Ref. 24)

$$\frac{d}{d\eta}\left[(1-\eta^2)\frac{d\Theta}{d\eta}\right] + \frac{8\pi^2 I}{h^2} \times \left[E_{v,\phi} - V_0(1-\eta^2) - \frac{m^2 h^2}{(1-\eta^2)8\pi^2 I}\right]\Theta = 0 \tag{4}$$

where η is cos θ, Θ is a function only of the angle θ that the molecular axis makes with the normal to the surface, and V_0 is the value of the barrier height in energy units. The other symbols have their usual meanings. Eq. (4) must satisfy the condition that Θ be bounded and single-valued at $\eta = \pm 1$. Solutions to Eq. (4) with these boundary conditions have been tabulated by Stratton et al (Ref. 25).

[a]Analyses by Lois Taylor, JPL Chemistry Section.

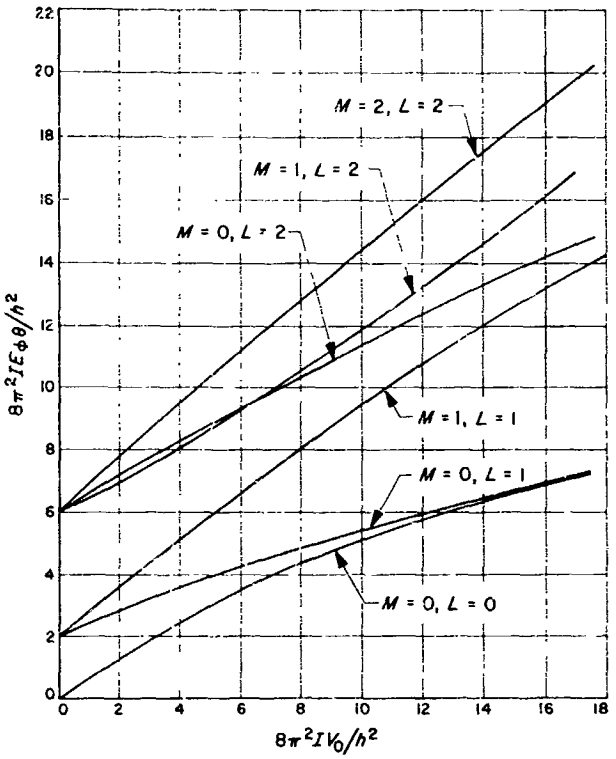

Fig. 7. Rotational energy as a function of barrier height V_0

Fig. 7 shows the first six rotational states of the hindered rotor as a function of barrier height V_0.

The vibrational energies of the adsorbed molecules are obtained from the total potential function. The attractive term in this potential is given by Eq. (1).

$$\Phi_{att} = -\alpha \frac{E_z^2}{2} \tag{5}$$

The characteristic feature of all the adsorbents used in the separation of the hydrogen isotopes is the presence of strong surface electric fields. The strong fields are caused primarily by vacancies in the crystal lattices. All defect structures such as 3-2 or 3-4 lattices must have these vacancies in order to maintain charge neutrality.

The structure, shown in Fig. 8, has these vacancies and represents a simple model of an Al_2O_3 surface. It consists of the {100} plane of a cubic closest packing array of oxygen ions in which the Al^{+3} ions are located in the interstices with every third positive site unoccupied.

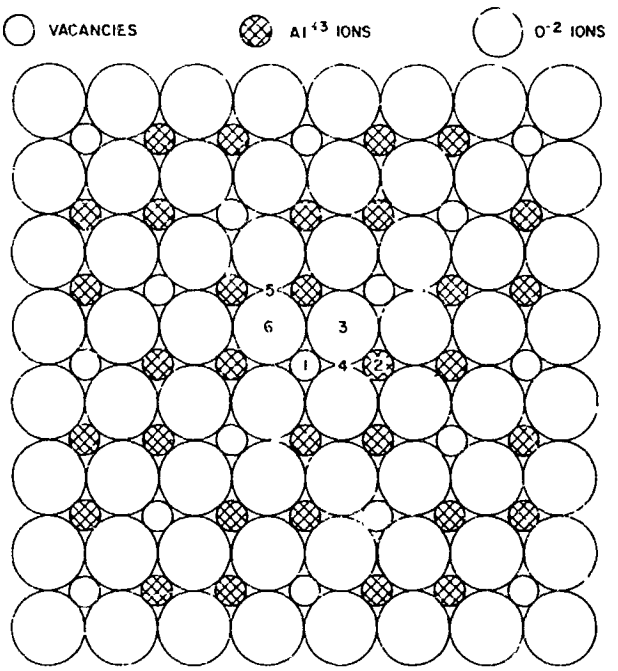

Fig. 8. The {100} surface plane of the Al_2O_3 lattice

We have utilized this surface to determine the field intensity over different surface sites by summing, with the aid of a 7094 IBM computer, the contribution each ion makes to the electric field.

The electric fields over different surface sites as a function of the perpendicular distance from the surface are plotted in Fig. 9. The curves in Fig. 9 originate at their geometric distance of closest approach, which is obtained by assuming hard spheres and taking the O^{-2} diameter to be 2.80 Å. As can be seen from Fig. 9, there are rather strong fields between the Al^{+3} sites and also over the O^{-2}, which has two vacancies as its nearest neighbors. The fields over the other sites are relatively weak.

We find from our calculations that the field intensity over each site can be expressed empirically as a reciprocal power of the distance z_i from the median plane of the ion

$$E_{z_i} = \frac{D_i}{z_i^m} \tag{6}$$

where i denotes a particular site. Then from Eq. (1)

$$\Phi_{att} = -\frac{\alpha D_i}{2 z_i^m} \tag{7}$$

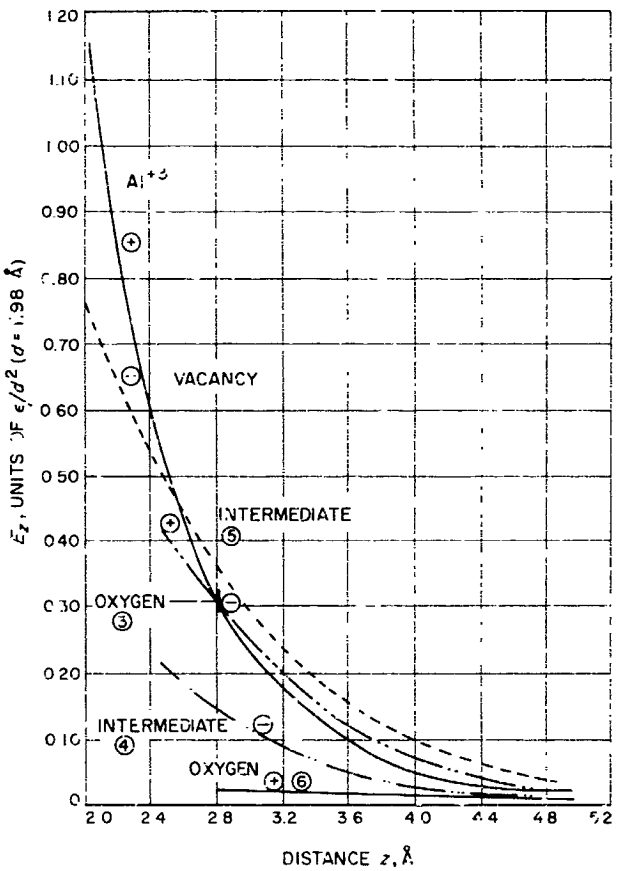

Fig. 9. The electric-field intensities over different surface sites as a function of the distance z

The repulsive term can also be expressed as a reciprocal power of z, making the total potential.

$$\Phi_T = -\frac{\alpha D_i}{2z_i^m} + \frac{B_i}{z_i^n} \tag{8}$$

At the equilibrium distance z_0, where $(\partial \Phi/\partial z_i) = 0$,

$$B_i = \frac{\alpha}{2}\frac{m}{n} D_i z_0^{n-m}$$

The total potential is then

$$\Phi_i = -\frac{\alpha}{2}\frac{D_i}{z_i^m}\left[1 - \frac{m}{n}\left(\frac{z_0}{z_i}\right)^{n-m}\right] \tag{9}$$

The potential has its minimum value Φ_0 at $z_i = z_0$, or

$$\Phi_0 = -\frac{\alpha}{2}\frac{D_i}{z_0^m}\left[\frac{n-m}{n}\right] \tag{10}$$

The vibrational force constant and zero point energy are then given by

$$k = -\frac{mn\Phi_0}{z_0^2} \tag{11}$$

and

$$E_v^0 = \frac{1}{2}h\nu = \frac{h}{4\pi}\left(\frac{k}{M}\right)^{1/2} = \frac{h}{4\pi z_0 M^{1/2}}\left[-mn\Phi_0\right]^{1/2}$$
$$= \frac{h}{4\pi z_0 M^{1/2}}\left[\frac{\alpha D_i m(n-m)}{2z_0^m}\right] \tag{12}$$

where M is the total mass

The ratio of the elution time from a chromatographic column of Gas 2 to some reference Gas 1 can be expressed as a function of the corresponding free energy change.

$$\frac{t_2 - t_0}{t_1 - t_0} = \exp\left[-\left(\frac{\Delta F_2 - \Delta F_1}{RT}\right)\right]$$
$$= \exp\left[-\left(\frac{\Delta A_2 - \Delta A_1}{RT}\right)\right] = s \tag{13}$$

where t_0 is the elution time of a reference gas not adsorbed on the column, and ΔF and ΔA refer to the change in the Gibbs and Helmholtz free energies, respectively. The ratio of the elution times defines the separation factor s.

From statistical thermodynamics,

$$\Delta A_i = -RT \ln \frac{Q_{g-i}}{Q_{a-i}} = -RT \ln Q_{R-i} \tag{14}$$

where the Q's are the corresponding molar partition functions. Therefore,

$$s = \frac{t_2 - t_0}{t_1 - t_0} = \frac{Q_{R-2}}{Q_{R-1}} \tag{15}$$

For an adsorbed molecule with two degrees of translation freedom, one hindered rotation, one free rotation, and one vibration normal to the surface, the partition function is given by

$$Q_{a-i} = g_n Q_{a-i}(t)\, Q_{a-i}(r)\, Q_{a-i}(v)\, e^{-E_i^0/RT} \tag{16}$$

where g_n is the nuclear spin degeneracy, E_i^0 is the zero point energy of the absorbed molecule, and $Q_{a-i}(t)$, $Q_{a-i}(r)$, and $Q_{a-i}(v)$ are molar partition functions for translation, rotation, and vibration, respectively. For two degrees of freedom, $Q_{a-i}(t)$ is given by

$$Q_{a-i}(t) = \frac{1}{N!}\left(\frac{2\pi m_i kT}{h^2}\right)^N \tag{17}$$

where τ is the surface area. For rotation

$$Q_{a\text{-}i}(r) = \left[\Sigma_j\, g_j \exp\left[-(E_i^j - E_i^0)/kT\right]\right]^N \qquad (18)$$

where g_j is the degeneracy of the j^{th} rotational level and E_i^j is the corresponding energy. For harmonic vibration normal to the surface,

$$Q_{a\text{-}i}(v) = \left[1 - \exp\left(\frac{-h\nu_i}{kT}\right)\right]^{-N} \qquad (19)$$

where ν_i is the vibration frequency and h is Planck's constant.

In the gas phase with three degrees of transitional freedom

$$Q_{g\text{-}i} = g_n\, Q_{g\text{-}i}(t)\, Q_{g\text{-}i}(r) \qquad (20)$$

$$Q_{g\text{-}i}(t) = \frac{1}{N!}\left[\frac{(2\pi M_i RT^{3/2}V}{h^3}\right]^N \qquad (21)$$

and

$$Q_{g\text{-}i}(r) = \left[\sum_J (2J+1)\exp\left(\frac{-J(J+1)\,h^2}{8\pi^2 I_i kT}\right)\right]^N \qquad (22)$$

where I_i is the moment of inertia and V is the gaseous volume.

The heat necessary to vaporize the gases from the surface is given by

$$\Delta H_{vap} = -\Phi_0 - E_{a\text{-}vib} - E_{a\text{-}r_\perp} + E_{g\text{-}trans} + E_{g\text{-}rot} + P\Delta V \qquad (23)$$

The first three terms represent the energies the molecule has on the surface while $E_{g\text{-}trans}$ and $E_{g\text{-}rot}$ are the gas-phase translational and rotational energies, respectively. The $P\Delta V$ work necessary to remove the molecule from the surface is just RT for an ideal gas.

4. Results of Discussion

We use the formulas of the preceding sections to calculate the separation factors for the ortho- and para-derivatives as a function of the barrier height. The results are plotted in Fig. 10

The experimentally determined separation factor for ortho- and para-hydrogen is 1.20 (Ref. 17). Using this value, we find from Fig. 10 that a barrier of 0.7 kcal is sufficient to explain the separations. Since this barrier height is accounted for by the difference in $\alpha_\parallel$ and $\alpha_\perp$, we use Eq. (1) to determine the surface electric field needed

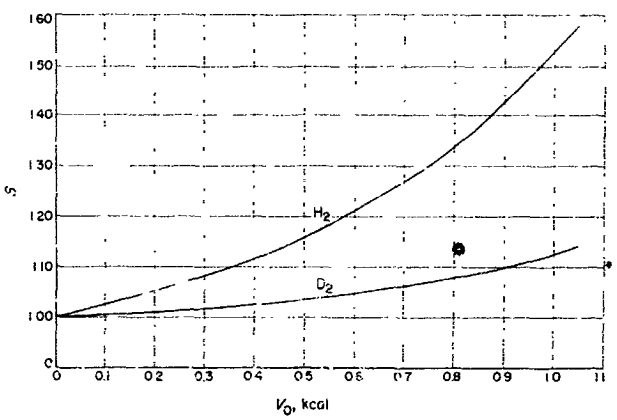

Fig. 10. The ortho-para separation factors for hydrogen and deuterium as a function of barrier height at 77.4°K

to produce the barrier. For a barrier height of 0.700 kcal/mole, we find

$$E_z = 2.04 \times 10^8 \text{ v/cm} \qquad (24)$$

We then determine the distance the molecule must be from the surface to experience an electric field of this magnitude over a particular adsorption site. If the adsorption occurs over a vacancy, from Fig. 9,

$$z_v = 2.40 \text{ Å}$$

and over an Al^{+3} site

$$z_{Al^{+3}} = 2.47 \text{ Å}$$

We are therefore in the region where the field is essentially the same over both highly active sites.

In all probability both types of sites are involved in the separation at 77°K. However, we can use the distance dependence of the electric field to ascertain if adsorption over one particular site is more compatible with experimental observations.

It is obvious from Eqs. (10) and (23) that the calculated heats of adsorption are functions of the type of adsorption sites. Since from Fig. 9 the electric field over an Al^{+3} site varies as $z^{-7/2}$ and that over a vacancy as $z^{-5/2}$, m in Eq. (6) becomes 7 and 5, respectively.

We have calculated heats of adsorption over both active sites for values of 9, 12, and 15 for the repulsive exponent n in Eq. (8). The (5-12), (7-12), and (5-9) potentials gave values compatible with the experimentally determined values. This comparison is made in Table 2.

Table 2. A comparison of heats of adsorption

Heat of adsorption	p-H_2	o-H_2	HD	o-D_2	p-D_2
$-\Delta H(Al_2O_3)$, kcal/mole					
Observed[a]	1.40	1.55	1.51	1.58	1.65
Calculated (5-12)	1.25	1.41	1.41	1.45	1.58
$-\Delta H(SiO_2)$, kcal/mole					
Observed[b]	0.77	0.93	0.92	1.00	1.09
Calculated (7-12)	0.88	1.03	1.04	1.07	1.20
Calculated (5-9)	0.91	1.07	1.05	1.08	1.20

[a]Ref. 17.
[b]Ref. 20.

There is little to choose between the conditions $m = 7$, $n = 12$, and $m = 5$, $n = 9$. Since a $1/z^9$ repulsive potential has been shown to be compatible with experimental values for the alkali halides, it would be rather surprising if the repulsion on the surface varied as $1/z^{15}$ or some larger reciprocal power of z. On this basis, we have calculated separation factors for the two conditions $m = 5$, $n = 9$, and $m = 5$, $n = 12$, and compared them with available experimental data in Table 3. In Table 3 the equilibrated H_2, D_2, and T_2 species are compared where

$$q_{e\text{-}H_2} = 3q_{o\text{-}H_2} + q_{p\text{-}H_2} \quad (25)$$

$$q_{e\text{-}D_2} = 6q_{o\text{-}D_2} + 3q_{p\text{-}D_2} \quad (26)$$

$$q_{e\text{-}T_2} = 10q_{o\text{-}T_2} + 6q_{p\text{-}T_2} \quad (27)$$

We see from Table 3 that the $1/z^{12}$ repulsive potential leads to large separation factors, indicating that the $1/z^{15}$ potential would produce even larger factors. A comparison of the values in Table 3 tends to support a (5-9) potential for the interaction. If, as suggested by Moore and Ward, the separation factors increase with column activity, then the (5-12) potential might be applicable, since we have chosen as our model a surface with the highest possible activity. It is necessary to have experimental data on such a surface in order to make an accurate comparison.

D. Polarization Effects in the Chromatographic Separation of the Rare Gases on an Alumina Column

J. King, Jr.

1. Introduction

The rare gases have been separated on an Al_2O_3 column in order to further investigate the role electrostatic forces play in gas-solid chromatographic separations. King and Benson[1] were the first to show the importance of polar-

[1]King, J., Jr., and Benson, S. W., *The Journal of Chemical Physics* (in press); also the preceding *SPS* article: C. Theory of the Low-Temperature Chromatographic Separation of the Hydrogen Isotopes.

Table 3. Chromatographic data for the isotopes

Isotope	S_i (experimental; King[a]), t_i/t_{H_2}	S_i (experimental; M. and S.[b]), t_i/t_{H_2}	S_i (experimental; M. and W.[c]), t_i/t_{H_2}	S_i (calculated; $m=5$, $n=9$), t_i/t_{H_2}	S_i (calculated; $m=5$, $n=12$), t_i/t_{H_2}
e-H_2	1	1	1	1	1
HD	1.14	1.22	1.09	1.31	1.50
HT	1.23	1.42	1.20	1.52	1.92
e-D_2	1.38	1.49	1.26	1.70	2.15
DT	–	1.85	1.45	2.05	2.75
e-T_2	1.58	2.08	1.66	2.10	2.93

[a]Ref. 18.
[b]Ref. 20.
[c]Ref. 17.

ization forces in the low-temperature chromatographic separations of the hydrogen isotopes on an alumina column. By calculating the electric field over the {100} plane of an Al_2O_3 surface, it was shown that the separations were caused by the interactions of the polarizable hydrogen isotopes with the surface electric field. From a detailed analysis of the interactions chromatographic separations were calculated which were in agreement with those observed.

For the diatomic hydrogen isotopes there is a change of two degrees of freedom in going from the free gaseous state to adsorption on the surface. One translational degree of freedom in the gas phase becomes, on adsorption, a vibration normal to the surface, and a gas-phase rotation becomes a hindered rotation on the surface. The barrier to rotation on the surface was shown to arise from the difference in the parallel and perpendicular components of the molecular polarizabilities of the isotopes.

Since the rare gases are monatomic, there is a change of only one degree of freedom in going from the gaseous to the adsorbed state. A translation in the gas phase becomes, on adsorption, a vibration normal to the surface. This change allows the measured retention times on a chromatographic column to be logarithmically related to the polarizabilities of the gases. Since methane is a regular tetrahedron whose polarizability is isotropic, it should freely rotate on the surface and show adsorption properties similar to the rare gases. It is therefore included in this work.

2. Experiment

The column material was 30–40-mesh activated alumina from Matheson, Coleman, and Bell. The column was constructed of 7-mm Pyrex tubing 18 ft long and coiled to fit into a constant temperature apparatus containing a heater. The material was packed into the column by applying compressed air at the inlet, a vacuum at the outlet, and by vibrating the column by means of a drill motor.

The packed column was heated at 450°C for 72 hr while being flushed with preheated helium gas in order to eliminate physically adsorbed water from the surface. After cooling, the column was maintained at 25°C with a helium flow rate of 180 ml/min.

A Loenco Model 15A gas chromatograph was used to detect the effluent gases.

All the rare gases were Airco reagent grade. Reagent grade methane was obtained from the Matheson Company and was used without further purification. The gases were mixed manometrically, and 0.2 ml of the mixture was passed through the column.

3. Theory

In gas-solid chromatography, there is an array of adsorption sites within the column with a moving concentration zone consisting of adsorbed gas in dynamic equilibrium with gas in the vapor phase. Gas molecules do not move down the column when adsorbed, whereas in the vapor phase they move at the same rate as the carrier gas. Therefore, the linear velocity of migration of any gas down the column is

$$U = U_g \frac{N_g}{N_g + N_a} \tag{1}$$

where

N_g = number of moles in gas phase

N_a = number of moles adsorbed

and U_g is the linear velocity of the carrier gas.

The equilibrium constant for adsorption is

$$K_a = \frac{N_a}{N_g} \tag{2}$$

and substituting this into Eq. (1) gives

$$U = U_g \frac{1}{K_a + 1} \tag{3}$$

but

$$U = \frac{l}{t_R} \text{ and } U_g = \frac{F_c}{a} \tag{4}$$

where t_R = retention time of gas in column, l = packed length of column, F_c = flow rate of carrier gas, and a = interstitial area of column.

Then

$$t_R = \frac{la}{F_c}(1 + K_a) \tag{5}$$

Since the gases spend most of their time in the adsorbed phase, $K_a >> 1$ and

$$t_R = \frac{la}{F_c} K_a \tag{6}$$

From thermodynamics,

$$K_c = e^{-\frac{\Delta F}{kT}} \tag{7}$$

where ΔF = the free energy change accompanying desorption from the solid. Therefore,

$$t_R = \frac{La}{F_c} e^{-\frac{\Delta F}{kT}} = \frac{La}{F_c} e^{\frac{\Delta S}{k}} e^{-\frac{\Delta H}{kT}} \tag{8}$$

since

$$\Delta F = \Delta H - T\,\Delta S \tag{9}$$

where ΔH is the heat of adsorption and ΔS is the entropy change.

From statical thermodynamics, the entropy change can be expressed as a function of the molecular partition functions.

$$\Delta S_i = Nk \ln q_{i\text{-}a}/q_{i\text{-}g} + NkT \frac{d}{dT} \ln q_{i\text{-}a}/q_{i\text{-}g} \tag{10}$$

where q_a, the partition function for the adsorbed molecule, is the product of the partition function for vibration normal to the surface and the partition function for two degrees of unhindered translation parallel to the surface. Therefore,

$$q_a = q_{a\text{-}t}\, q_{a\text{-}v} = \left(\frac{2\pi MkT}{h^2}\right) \sigma \frac{\exp(-h\nu/2kT)}{1-\exp(-h\nu/kT)} \tag{11}$$

where M is the molecular weight, σ the surface area, and ν is the frequency of harmonic vibrations normal to the surface. Since

$$\nu = \frac{1}{2\pi}\left(\frac{f}{M}\right)^{1/2} \tag{12}$$

where f is the force constant, $kT >> h\nu$ at room temperature, and the exponentials in Eq. (11) can be expanded.

$$\frac{\exp(-h\nu/2kT)}{1-\exp(-h\nu/kT)} = \frac{kT}{h\nu} = \frac{2\pi kT\, M^{1/2}}{hf^{1/2}} \tag{13}$$

The translational partition functions in the gas phase q_g is for three degrees of translational freedom and is given by

$$q_g = \left(\frac{2\pi MkT}{h^2}\right)^{3/2} V \tag{14}$$

where V is the gaseous volume.

Therefore,

$$\ln \frac{q_g}{q_a} = \ln\left(\frac{2\pi kT}{f}\right)^{1/2} \frac{\sigma}{V} \tag{15}$$

$$\Delta S = \frac{Nk}{2}\left[1 + \frac{\ln 2\pi kT\, e^2}{fV^2}\right] \tag{16}$$

The entropy change is independent of the molecular mass and is rather insensitive to small differences in the force constant since it appears in the logarithmic expression. Thus, the entropy change for all the gases should be essentially the same.

The heat of adsorption ΔH is exactly the negative of the heat necessary to vaporize the molecule from the surface. For adsorbed molecules, the heat of vaporization is given by

$$\Delta H_{vap} = -\Delta H_a = -\Phi_0 - E_{a\text{-}rib} - E_{a\text{-}trans} + E_{g\text{-}trans} + P\Delta V \tag{17}$$

where Φ_0 is the value of the interaction potential of the molecules with the surface at the equilibrium distance. The first three terms represent the energies the molecules have on the surface while $E_{g\text{-}trans}$ is the gas phase translational energy.

For ideal gases,

$$E_{g\text{-}trans} = 3/2RT \tag{18}$$

$$E_{a\text{-}trans} = E_{a\text{-}rib} = P\Delta V = RT \tag{19}$$

Therefore,

$$-\Delta H_a = -\Phi_0 + \frac{RT}{2} \tag{20}$$

The potential depth Φ_0 is the quantity through which the polarizabilities of the gases are related to their retention times on a chromatographic column. It has been shown by King and Benson[1] that a consideration of the total interaction potential between the adsorbed molecules and the surface electric field leads to the following relationship between Φ_0 and α, the polarizability.

$$\Phi_0 = -\frac{\alpha}{2}\frac{D_1}{z_0^m}\left[\frac{n-m}{m}\right] \tag{21}$$

where D_1 is a proportionality constant between the surface electric field and the distance z_0 that the molecules

[1]See preceding *SPS* article: C. Theory of the Low-Temperature Chromatographic Separation of the Hydrogen Isotopes.

are from the surface. The quantities m and n, respectively, refer to the reciprocal powers of the attractive and repulsive terms in the overall potential expression.

If this value of Φ_s is substituted in Eq. (20), the heat of adsorption becomes

$$-\Delta H_c = \frac{a}{2}\frac{D_1}{z_0^2}\left[\frac{n-m}{n}\right] + \frac{RT}{2} = aC_1 + \frac{RT}{2} \tag{22}$$

where C_1 is a constant whose value depends on the type of interaction potential between the molecules and the surface.

Using Eqs. (3), (16), and (22) the retention time expression for the gases in the column is

$$\ln t_{R_i} = \ln\frac{ta}{F_c} + \frac{NR}{2}\left[1 + \ln\frac{2\pi RT\sigma^2}{fV^2}\right] + a_iC_1 + \frac{kT}{2} \tag{23}$$

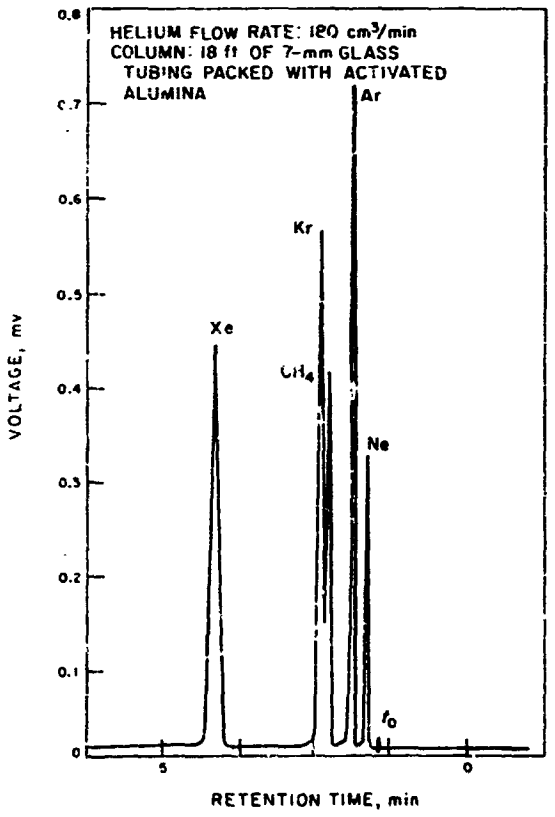

Fig. 11. Chromatogram of 0.2-ml sample of the rare gases and methane

4. Results and Discussion

If the retention times of the rare gases are determined under conditions of constant temperature and constant carrier gas flow, the theory predicts that a plot of $\ln t_R$ versus α_i should yield a straight line.

Fig. 11 is a chromatogram of a mixture of the rare gases, including methane, on an Al_2O_3 column. The retention times, corrected for gas hold-up time in the column,

Table 4. Chromatographic data and polarizabilities

	Ne	Ar	Kr	CH_4	Xe
t_R, min	1.68	1.80	2.18	2.30	4.03
α, (Å³)[a]	0.39	1.63	2.46	2.60	4.00

[a]Ref. 26.

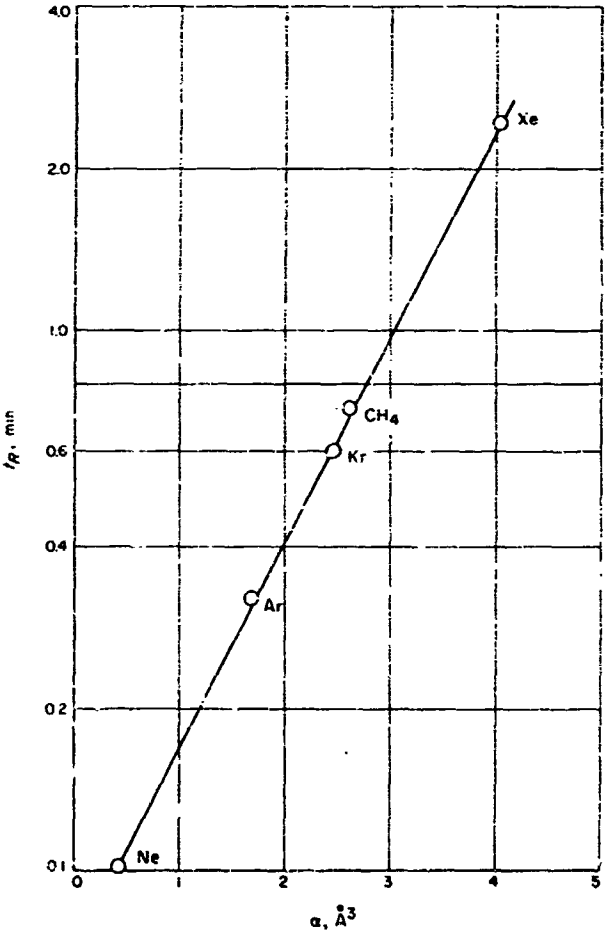

Fig. 12. Retention times vs polarizabilities

are given in Table 4 along with the known polarizabilities. Fig. 12 shows a plot of the corrected retention times of the gases as a function of their respective polarizabilities. The resulting straight line is convincing evidence that polarization forces are primarily responsible for the physical adsorption of gases on defect structures, like Al_2O_3.

It is obvious from Eq. (23) that gas-solid chromatography can be used to compare electric-field strengths on different adsorbents since C_1, the slope of the curve in Fig. 12, is a function of the electric fields on the surface. Also, if the total interaction potential between the molecules and the surface is specified, the vibrational force constants can be obtained and the intercept of the curve in Fig. 12 allows the surface area to be determined.

This investigation, therefore, shows a new approach in the utilization of gas-solid chromatography for the investigation of gas-solid interactions. Future investigations will involve the chromatographic separation of the rare gases on other defect solids, such as Fe_2O_3 and Fe_3O_4, in order to study the relative strengths of their surface electric fields.

E. Photolysis of Low Concentrations of Nitrogen Dioxide at 3660Å

J. King, Jr.

1. Introduction

The photolysis of nitrogen dioxide at 3660Å was first studied at trace concentrations by Ford and Endow (Ref. 27), who determined the quantum yield Φ in nitrogen at one atmosphere pressure. They worked at concentrations below 4×10^{-7} moles/liter and found the average quantum yield for the disappearance of NO_2 to be 0.600 molecule/quanta.

Ford and Jaffe (Ref. 28) in a later investigation studied the photolysis at higher concentrations, also in an atmosphere of nitrogen. At concentrations above 2.5 mm of NO_2 pressure they found that the quantum yield approached 2.0, which agrees with other investigators of the NO_2 photolysis (Refs. 29, 30, and 31). However, at low NO_2 concentrations the quantum yield approached zero, which was in disagreement with the data of Ford and Endow. The two sets of data could be compatible only if the quantum yield were to go through a minimum value as the NO_2 concentration approached zero. Since the data of Ford and Jaffe did not go below 5×10^{-6} moles/liter, the present work was undertaken in order to bridge the gap between 4×10^{-7} and 5×10^{-6} moles/liter and to ascertain if there was a minimum in the value of the quantum yield as the NO_2 concentration approached zero.

2. Experiment

A Perkin-Elmer 421 infrared spectrophotometer equipped with twin long-path optical cells was used as the analytical instrument. The optical layout of one of the cells is shown in Fig. 13. The optical path length could be changed from 4 to 40 m by varying the number of reflections between M_5, M_6, and M_7. The reference optics were enclosed in a metal can which was maintained under high vacuum. The source of 3660Å radiation was four Westinghouse 360-BL fluorescent lamps, which were arranged concentrically with the upper half of an 82-liter Pyrex cylinder enclosing the sample optics. Quantities of NO_2, which had been purified by the method of Harris et al (Ref. 32) and stored as a white solid at −195°C, were introduced into the cell from an inlet system of known volume. The concentration of NO_2 in the inlet system was determined spectrophotometrically by allowing the gas to equilibrate between the inlet system and a quartz cell which was designed to fit directly into a Cary Model 11 recording spectrophotometer.

Linde high-purity extra-dry nitrogen was passed through Ascarite, $CaSO_4$, $Mg(ClO_4)_2$, and activated charcoal at dry ice temperature. The pressure of the nitrogen in the cell was read on a Wallace and Tiernan gauge and was maintained at one atmosphere.

The time of the irradiations was automatically controlled by a Gra-Lab universal timer.

3. Results

The infrared spectra of NO_2 shows a strong dependence on added inert gas pressure. This pressure dependence is not well understood although it has been studied by several investigators (Refs. 33, 34, and 35). In Fig. 14 is displayed a typical infrared spectra of NO_2 with and without added N_2. The intensity was found to be independent of N_2 pressure above 600 mm.

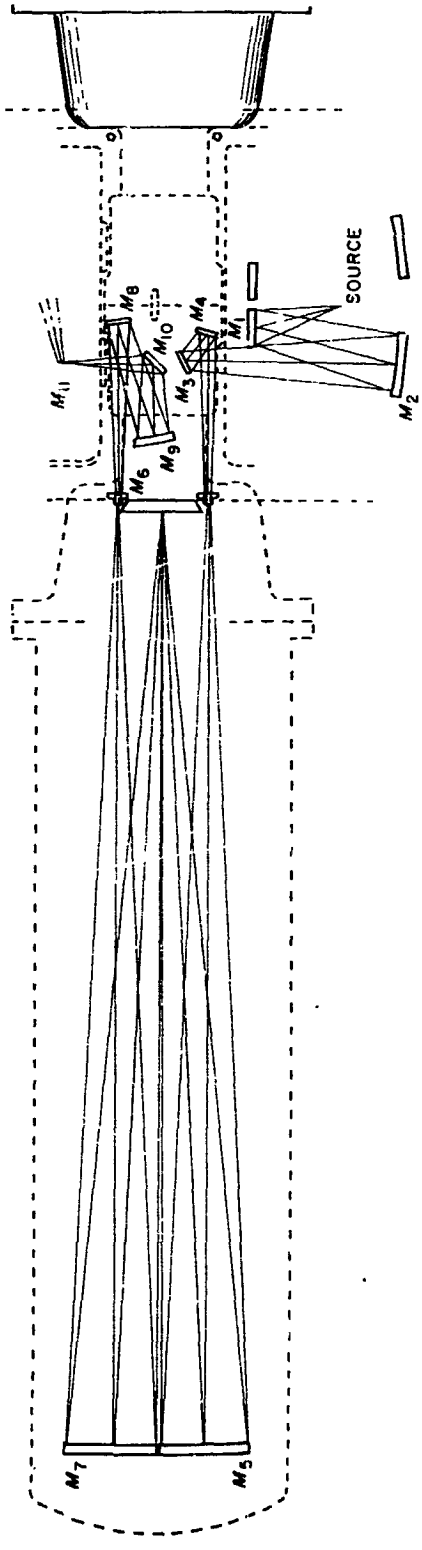

Fig. 13. Optical layout of the long-path cell

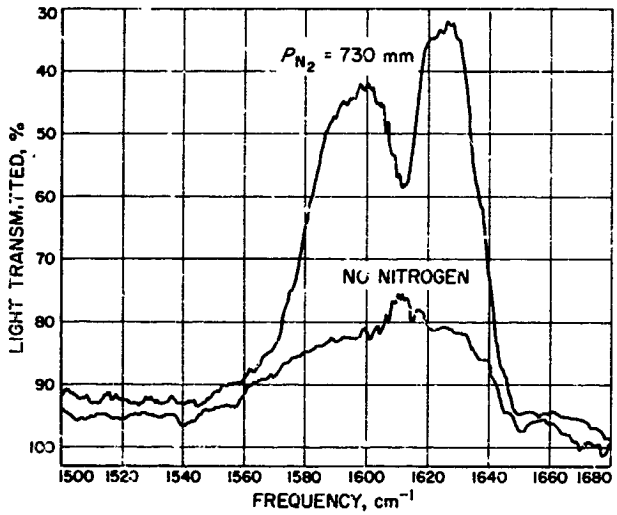

Fig. 14. Infrared spectra of nitrogen dioxide (NO_2 pressure is 7.37 μ; instrument is set for 40 m)

The relative quantum yield for NO_2 disappearance, based on the quantum yield of Ford and Endow at trace concentrations, was determined in the following way.

At trace concentrations where only a small fraction of the light is absorbed (Ref. 27),

$$I_a = K I_0 (NO_2) \qquad (I)$$

where K is the absorption cross-section, i.e., cm²/molecule. By definition, the quantum yield is

$$\Phi = \frac{d\,NO_2/dt}{I_a} = \frac{d\,NO_2/dt}{K I_0 (NO_2)} \qquad (II)$$

The disappearance of NO_2 as a function of time was determined in the long-path cell at the average concentration used by Ford and Endow, i.e., 6×10^{-4} mm; and by using their value for the quantum yield $\Phi = 0.60$, KI_0 was calculated. This value was then used to calculate the quantum yields at higher NO_2 concentrations.

The quantum yields, determined in this way, are given in Table 5 and plotted as a function of NO_2 concentration in Fig. 15. The results show the quantum yield to be essentially constant over the pressure range studied. This does not agree with the data of Ford and Jaffe, although their data at low pressures of NO_2, as noted by the authors, are subject to rather large errors because of the small concentration changes which they measured.

Table 5. Relative quantum yields of NO_2 disappearance in photolysis at 3660Å

P_{NO_2}, mm × 10²	$\Delta P/\Delta t$, mm/sec × 10³	I_A, 10³	Φ
0.600	0.544	0.906	0.600
1.55	1.40	2.34	0.598
9.93	9.07	14.99	0.605
11.80	10.0	17.82	0.562
13.38	11.80	20.20	0.585
22.50	20.10	33.98	0.592
48.11	42.60	72.65	0.587
50.7	44.50	75.56	0.582
53.5	47.50	80.79	0.588
78.8	70.5	118.9	0.593
101.0	90.0	152.5	0.592
109.5[a]	98.0	165.34	0.595

[a]This is the maximum NO_2 concentration which could be photolyzed with the instrument set for 4 m.

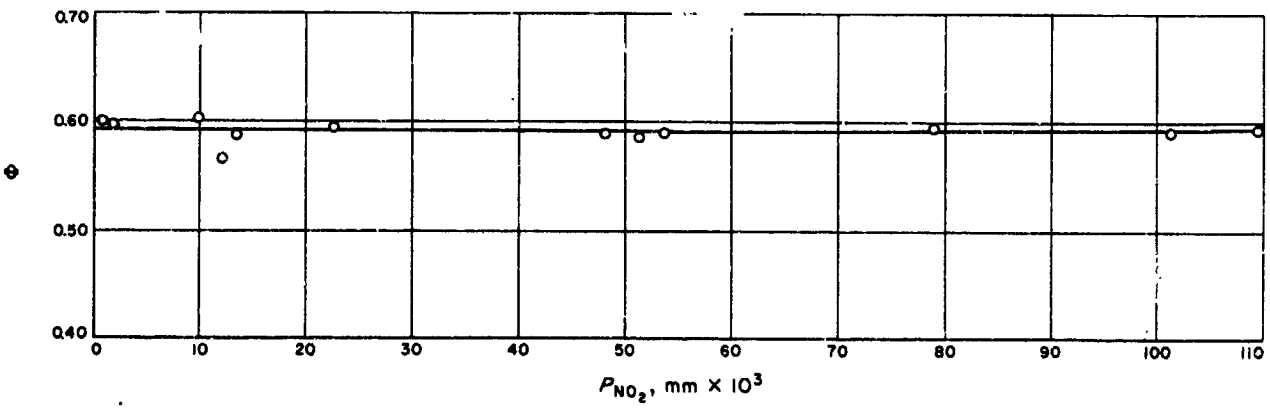

Fig. 15. Quantum yield vs P_{NO_2} from infrared studies

If a plot is made of the present data, along with the data of Ford and Jaffe above 0.4 mm of NO_2 pressure where their data is more reliable, the curve in Fig. 16 is obtained. This curve shows the quantum yield to be independent of the NO_2 pressure below 0.45 mm but rises rapidly with pressure above this value.

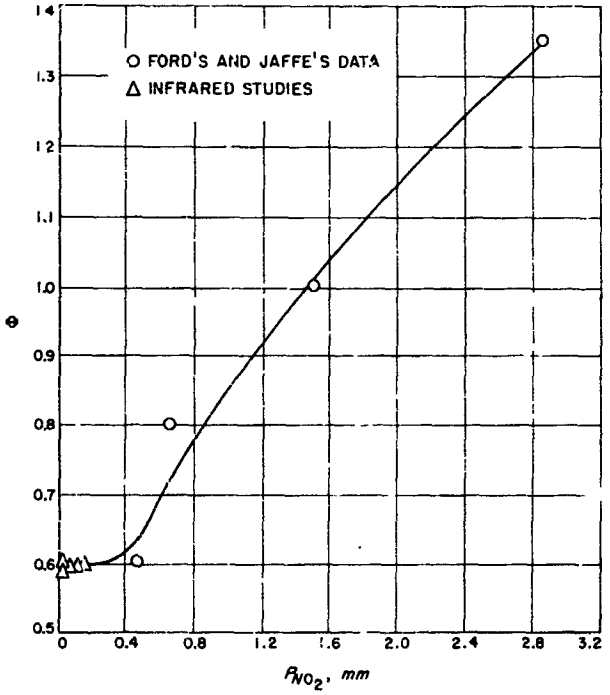

Fig. 16. Quantum yield vs P_{NO_2}

4 Discussion

Neither the mechanism proposed by Ford and Endow (Ref. 27) nor that suggested by Ford and Jaffe (Ref. 28) can explain the observed behavior of the curve in Fig. 16. The mechanism proposed by the former investigators is

$$NO_2 + h\nu \rightarrow NO + O \quad (1a)$$

$$O + O_2 + M \rightarrow O_3 + M \quad (2a)$$

$$O + NO_2 + M \rightarrow NO_3 + M \quad (3a)$$

$$O + NO_2 \rightarrow NO + O_2 \quad (4a)$$

$$O + NO + M \rightarrow NO_2 + M \quad (5a)$$

$$NO_3 + NO \rightarrow 2\,NO_2 \quad (6a)$$

$$O_3 + NO \rightarrow NO_2 + O_2 \quad (7a)$$

where M denotes an inert gas, such as N_2.

If steady-state conditions are assumed for NO_3 and atomic oxygen, this mechanism leads to the following expression for the reciprocal of the overall quantum yield for the disappearance of NO_2.

$$\frac{1}{\Phi_{NO_2}} = \frac{1}{2} + \frac{k_{(3a)}(M)}{2k_{(4a)}} + \frac{k_{(5a)}(NO)(M)}{2k_{(4a)}(NO_2)} + \frac{k_{(2a)}(O_2)(M)}{2k_{(4a)}(NO_2)} \quad (III)$$

Under the conditions of no added NO and O_2, Eq. (III) reduces to

$$\frac{1}{\Phi_{NO_2}} = \frac{1}{2} + \frac{k_{(3a)}(M)}{2k_{(4a)}} \quad (IV)$$

or

$$\Phi_{NO_2} = \frac{2k_{(4a)}}{k_{(4a)} + k_{(3a)}(M)} \quad (V)$$

Eq. (V) accounts for the independence of the quantum yield at trace concentrations but does not explain the NO_2 pressure dependence at higher concentrations.

At higher concentrations, the mechanism proposed by Ford and Jaffe is

$$NO_2 + h\nu \rightarrow NO + O \quad (2b)$$

$$O + NO_2 \rightarrow NO + O_2 \quad (3b)$$

$$O + NO_2 \rightarrow NO_3^* \quad (4b)$$

$$NO_3^* \rightarrow NO_2 + O \quad (5b)$$

$$NO_3^* + NO_2 \rightarrow NO_2 + O_2 + NO \quad (6b)$$

$$NO_3^* + M \rightarrow NO_3 + M \quad (7b)$$

$$NO + NO_3 \rightarrow 2\,NO_2 \quad (8b)$$

Again, assuming steady state for O, NO_3, and NO_3^*, the quantum yield expression is

$$\Phi = \frac{2k_{(3b)}k_{(5b)} + k_{(6b)}(k_{(3b)} + k_{(4b)})(NO_2) + k_{(3b)}k_{(7b)}(M)}{k_{(3b)}k_{(5b)} + (k_{(3b)} + k_{(4b)})[k_{(6b)}(NO_2) + k_{(7b)}(M)]} \quad (VI)$$

Although this mechanism explains the observed fact that the quantum yield approaches 2 at very high NO_2 concentrations, it is not consistent with the data in Fig. 16. In Fig. 16 there is an apparent inflection point at approximately 0.45 mm of NO_2 pressure. Eq. (VI) does not satisfy the mathematical condition for an inflection point since there is no value of NO_2 pressure which allows $d^2\Phi/dp^2_{NO_2}$ to be zero. One possible cause for the disagreement between Eq. (VI) and the data in Fig. 16 is that the scatter in the

data at the low concentrations does not allow a differentiation between a small but finite slope or a line with zero slope. However, in order for the curve to have a finite slope at the low concentration and still agree with the present infrared data, the lower points from Ford's and Jaffe's data must be considered unreliable and eliminated. Since the concentrations represented by these points are beyond the range of the present experimental apparatus, the reliability of the points could not be checked.

Since the calculated quantum yields of the present investigation are based on the results of Ford and Endow, the value of the intercept in Fig. 16 is relative and could be in error. In order to check this possibility an independent determination of the quantum yield at the low concentrations is being undertaken using azomethane as an actionometer.

F. On the Correlation of Geminal and Vicinal Nuclear Magnetic Resonance Spin-Spin Coupling Constants with Substituent Electronegativities

S. L. Manatt and D. D. Elleman

1. Introduction

There is presently considerable interest in what electronic and structural factors determine the magnitudes and relative signs of geminal nuclear magnetic resonance proton-proton spin-spin couplings. The initial theoretical attempts to describe this coupling by Karplus and coworkers (Ref. 36)

have been shown experimentally to be insufficient in several respects. First, the effect of the adjacency to a methylene group of substituents containing π-electron centers was not accounted for, although subsequently Grant proposed a semiempirical theory which remedied this (Ref. 37). Also, the effect on the geminal coupling due to electron withdrawal by electronegative substituents was not accounted for. Probably the most dramatic failing is the fact that the theory predicted a positive sign for the geminal coupling in a sp^3 hybridized methylene group, whereas there is overwhelming evidence that this coupling is negative (Refs. 38, 39, and 40).

We chose to study the signs and magnitude of the coupling constants in styrene oxide (I) (*SPS 37-17*, Vol. IV), styrene imine (II), and styrene sulfide (III) (*SPS 37-22*, Vol. IV) for several reasons. First, structural information from other methods (Ref. 41) suggests that the H—C—H angles in these three molecules are about the same (approximately 116 deg); thus, perhaps any differences in the geminal couplings could be attributed to substituent effects. The H_2—C—C angles in I and II are very similar and that in III is only slightly less,[a] and the changes of the vicinal couplings in at least I and II may reflect mainly electronic rather than steric substituent effects.

2. Discussion

Several correlations have been described which attempt to relate magnitudes of couplings to substituent electronegativities (*SPS 37-24*, Vol. IV and Refs. 43-49). All these treatments have used plots of coupling constants versus electronegativity to derive a linear correlation. It would seem that a multiplicity of substituent effects influences these couplings and that the most important effect appears to be that of electronegativity. It has been pointed out (*SPS 37-24*, Vol. IV) that in systems containing π-electron centers adjacent to a —CH—CH_2— fragment, two classes of π-electron effects appear to be distinguishable. In addition, in the case of oxiranes much better correlation between substituent electronegativity and coupling constants is arrived at if groups containing π-electrons adjacent to the —CH—CH_2— fragment are not used to establish the correlation line. The deviations for the latter type of substituents then provide a measure of the magnitude of these special electronic effects which must not contribute significantly to the determination of the electronegativity of a substituent, which itself should be directly related to thermochemical properties. It should be pointed out, as discussed elsewhere (*SPS 37-24*, Vol. IV), that π-electron effects exist for both vicinal and geminal proton-proton couplings, a fact which has not been noted previously. More detailed discussions of the multiplicity of substituent effects on geminal and vicinal

[a] Estimated to be 158.1 ±0.5, 159.4, and 151.7 deg, respectively, from data in Ref. 42.

couplings will be deferred at present. The main point we wish to make here is that the linear correlation between vicinal and geminal proton-proton couplings and substituent electronegativities for substituents which do not have the possibilities of bringing into play electronic effects not measured by bond-energy quantities may be much better than previously thought. Some evidence supporting this viewpoint will now be presented.

Some time ago, Muller and Pritchard (Ref. 50) discussed the correlation of the ^{13}C—H coupling in substituted methanes with s character of the carbon orbital and the C—R bond distance in a three-parameter equation. Looking at the same data, we feel that perhaps a simpler relation exists, i.e., $J_{^{13}C-H} = A + BE_R$, where A and B are positive constants and E_R is the substituent electronegativity, provided that R is not a group which can participate in special electronic effects not measurable from thermochemical data. Fig. 17 shows the ^{13}C—H data for CH_3CH_3, CH_3NH_2, CH_3OH, and CH_3F plotted against the Huggins electronegativities (Ref. 51). An excellent straight line can be drawn through the points for R = —CH_3, —NH_2, and —OH, while the point for R = —F appears to deviate very slightly. More careful measurements of these ^{13}C—H couplings might be worthwhile to establish unequivocally whether the very good line determined by the three points —CH_3, —NH_2, and —OH is not an artifact and the deviation of the point for —F is real. There are several pieces of evidence (Refs. 52 and 53) that —F should deviate, i.e., have certain capacities for electronic effects not measured by thermochemical properties.

We have found another case where a set of molecules all having similar geometry but differing only in a substituent give a good linear plot between Huggins electronegativities and the ^{13}C—H coupling. In Fig. 17 there is a good linear relation for the case of the three-membered ring compounds, cyclopropane, ethylene imine, and ethylene oxide. This linear plot is derived from experimental data reported to be less in error (±0.5 cps) (Refs. 54 and 55) than that for the substituted methanes (±1 cps) (Ref. 50). These linear correlations are both excellent for the two sets of three points for the substituents involving C, N, and O atoms. As is shown in Fig. 17, the points for styrene sulfide and methyl sulfide fall considerably off

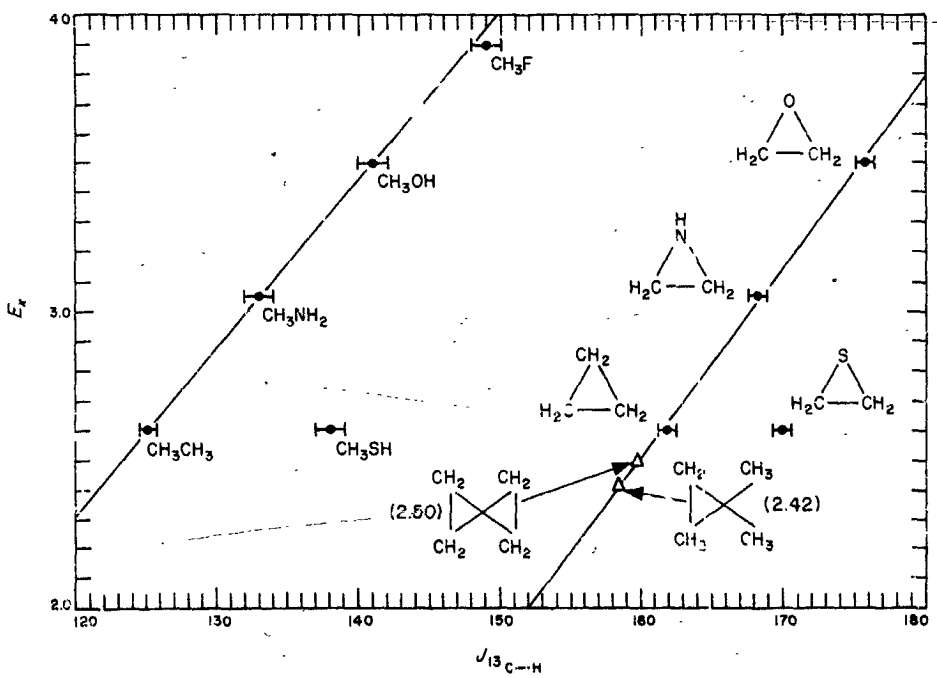

Fig. 17. Plot of $J_{^{13}C-H}$ versus E_R, the Huggins' electronegativity, for some substituted methanes and some three-membered ring compounds (the △'s represent predicted electronegativities based on $J_{^{13}C-H}$ for the substituents —C△ and —C(CH₃)₂)

the two correlation lines determined by the first row elements, thus indicating contributions to the ^{1}C—H couplings of about +9 and −13 cps, respectively, in these latter molecules above those predicted by a linear correlation with electronegativity.

It would seem reasonable that, for systems with substituents whose spin coupling contributions are derived only from electronic effects measured by electronegativity, it should be possible from measured ^{13}C—H couplings to derive an appropriate group electronegativity. *A priori* we would expect this to be possible for alkyl groups and substituents which do not contain π-electrons. We have taken the recent ^{13}C—H data (Ref. 55) for 1,1-dimethylcyclopropane and spiropentane and derived an electronegativity for the

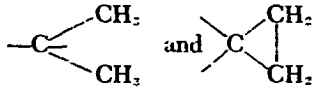

substituents in a three-membered ring, as indicated in Fig. 17.

As was discussed above, linear correlations between substituent electronegativity and geminal and vicinal couplings have been suggested. In Fig. 18 we have taken the data for the vicinal (*cis* and *trans*) couplings for the cyclopropanes mentioned above, ethylene imine (Ref. 54) and ethylene oxide (Ref. 54), and plotted them versus the Huggins electronegativity (Ref. 51). For the former two compounds this electronegativity was determined from Fig. 17. A rather satisfactory linear relation is evident. The points for ethylene sulfide are also shown in Fig. 18. As in the case of the ^{13}C—H coupling, the points for the vicinal couplings in this molecule deviate significantly from the linear correlation. Also shown in Fig. 13 are the data for styrene oxide, styrene imine, and styrene sulfide. The data for the former two would appear to determine lines parallel to but slightly displaced from those determined for the unsubstituted molecules. The points for the sulfur analogue III again deviate.

In the case of the geminal coupling, values for ethylene oxide,[19] 1,1-dimethylcyclopropane (Ref. 55), and spiropentane (Ref. 55) are available. The difference between the geminal couplings in ethylene oxide and styrene oxide is very small. We have plotted the five points for ethylene

[19]Derived from the observation of certain weak transitions in a sample of ^{13}C-enriched material (Manatt, S. L., unpublished work).

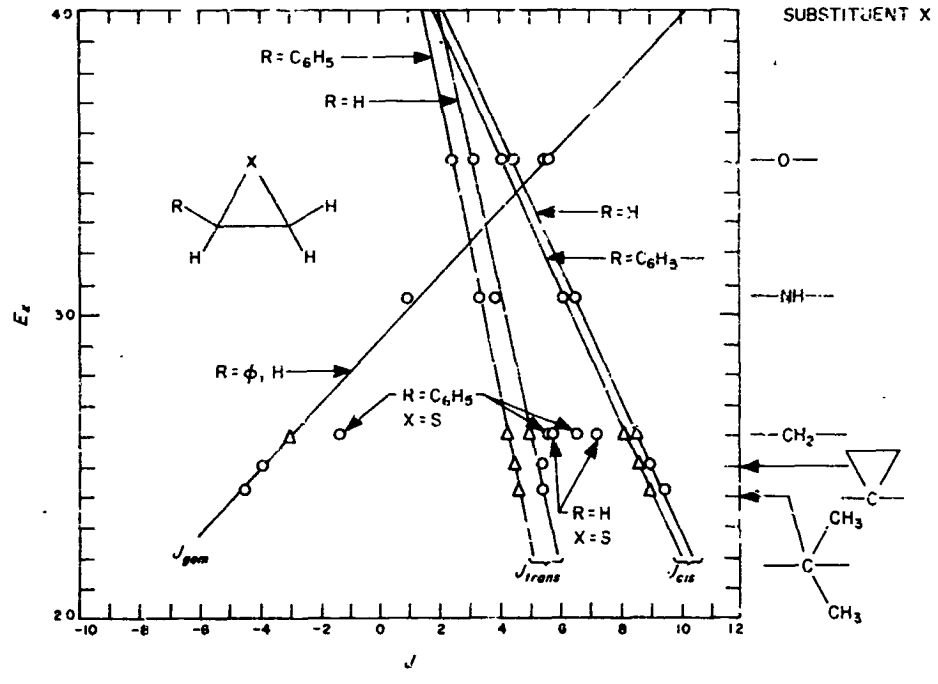

Fig. 18. Plot of vicinal coupling and the geminal coupling versus E_x, the Huggins electronegativity, for a series of three-membered ring compounds (the △'s represent certain predicted couplings)

oxide, the two cyclopropanes mentioned above, styrene oxide, and styrene imine, and they determine a rather satisfactory straight line. Again the sulfur analogue's geminal coupling deviates from this linear relation.

The discussion and coupling constant data above indicate that the linear correlation between geminal and vicinal proton-proton couplings in rigid systems and Huggins electronegativities (Ref. 51) is better than previously indicated (*SPS 37-17*, Vol. IV and Ref. 47). It is then possible to predict with some reasonable confidence the values for certain couplings heretofore unobserved or undetermined. Previously, Mortimer in his analysis of the ^{13}C satellite spectrum of ethylene imine could not determine the proton-proton geminal coupling (Ref. 54); from Fig. 18 this coupling is estimated to be about $+1$ cps. Similarly, for cyclopropane itself the geminal and the two vicinal couplings are predicted to be -3.0, $+8.5$ (*cis*), and -5.0 cps (*trans*), respectively. Assuming that the points for the vicinal couplings for styrene oxide and styrene imine determine lines parallel to those of the unsubstituted molecules, the vicinal couplings for phenylcyclopropane are predicted to be -4.3 (*trans*) and $+8.2$ cps (*cis*). The geminal coupling is estimated to be about -2.7 cps. There are still two more vicinal couplings in this molecule whose values may be estimated from other data (Refs. 55 and 56) to be $+10.5$ and $+7.5$ cps. Table 6 summarizes predictions from Fig. 18 for this latter molecule and several other molecules whose nuclear magnetic resonance spectra have not been analyzed.

Fig. 17 shows that the ^{13}C—H coupling in the substituted methanes is only slightly more strongly dependent on substituent electronegativity than the ^{13}C—H coupling in the three-membered cyclics. Comparing the plots in Figs. 17 and 18, it is obvious that of the four types of couplings we have discussed the ^{13}C—H coupling is much more strongly dependent on the electronegativity. The *trans*-vicinal couplings are the least strongly dependent on electronegativity, while the *cis*-vicinal couplings are only slightly more dependent than the latter. The geminal coupling is more dependent on substituent electronegativity than the vicinal couplings. Also, the dependence is of opposite sense to that for the vicinal couplings. As is evident from these linear correlations with electronegativity, both vicinal couplings and the geminal coupling in the simple three-membered cyclics we have discussed are linearly related to the respective ^{13}C—H couplings (Ref. 57). As the appropriate ^{13}C—H couplings become available for the unsymmetric substituted derivatives, such as styrene oxide, styrene imine, and phenylcyclopropane, it will be interesting to see if any degree of generality exists for this type of relation. There should be different ^{13}C—H couplings in the three-membered ring of these latter derivatives for each C—H bond (Ref. 42).

Table 6. Summary of couplings constants predicted from Fig. 18

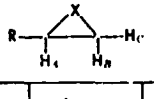

R	X	J_{tr}, cps	J_{cis}, cps	J_{gem}, cps
H	$-CH_2-$	+8.5	+5.0	−3.0
C_6H_5-	$-CH_2-$	+8.2	+4.3	−3.0
C_6H_5-		+8.5	+4.5	−4.1
C_6H_5-		+9.1	+4.6	−4.5

3. Conclusion

In the foregoing analysis we have attempted to demonstrate for one series containing three-membered ring molecules that there appears to exist a very simple linear relation between geminal and vicinal proton-proton couplings and the Huggins electronegativity (Ref. 51) (or a related quantity derived from ^{13}C—H couplings) and that this relation is better than previous similar correlations would lead one to believe. The reason for the scatter in the previously offered correlations is the fact that certain substituents possess electronic interactions, which we shall term "extra-electronic effects," whose presence does not contribute measurably to the determination of bond energies from which electronegativities are derived, but whose presence does provide additional possibilities for the propagation of nuclear spin-spin coupling. This may mean that in *many cases the ^{13}C—H coupling does not directly measure the percentage s character in a carbon bonding orbital when a carbon atom is substituted by one of the type of substituents capable of "extra-electronic effects."* This same conclusion has also been reached by Karabatsos (Ref. 58), who suggests that the breakdown of the simple correlation stems from spin-dipole and/or electron-orbital contributions to the ^{13}C—H coupling. However, Pople's recent theoretical treatment of the coupling between directly bonded atoms suggests that these two contributions will both be zero if one of two coupled nuclei is hydrogen (Ref. 59). On this basis, it would seem that the deviations from a simple correlation of ^{13}C—H coupling with *s* character observed may well

arise through a Fermi contact mechanism involving electrons of substituent atoms or groups. A theoretical consideration of this possibility could be fruitful.

Deviation from a simple correlation can probably *a priori* be expected for substituents with π-electrons, second and higher row elements, and fluorine atoms in close proximity to a set of coupled nuclei. Possibly low-lying excited states and/or d-orbital participation contribute to these effects for second and higher row elements. The nature of these electronic effects in the case of fluorine appears rather obscure

The manner in which the relation between coupling constants and electronegativity has been discussed here could serve as a basis for making a separation between contributions to spin-spin coupling due to factors depending on bond strength and those derived from several extra-electronic effects; these points are being further investigated.

G. The ^{19}F NMR Spectra of the Trifluoroacetates of Poly (Alkylene Oxides)[11]

S. L. Manatt, D. D. Lawson, and J. D. Ingham

1. Introduction

Studies reported previously (*SPS 37-31*, *37-26*, and *37-24*, Vol. IV) have shown that ^{19}F nuclear magnetic resonance (NMR) spectroscopy can be used effectively to establish the molecular structure of terminal hydroxyl groups of polyalkylene oxides. The end-group structure is most significant because it is generally the most reactive chemical site for polymer modification or degradation, both of which qualify the applicability of polymers for solid propellants or spacecraft components.

One of the significant results stemming from our previously reported work on poly(propylene oxides) (PPO) was that these polymers possess two distinct types of secondary hydroxyl end-groups (*SPS 37-24*, Vol. IV). This fact was established through the study of the ^{19}F NMR spectra of the ditrifluoroacetate (DTFA) esters of these polymers The DTFA esters, which are readily prepared by trifluoroacetylation with trifluoroacetic anhydride, exhibit a doublet ^{19}F fluorine spectrum with a splitting of 1.9–2.2 cps (depending on the solvent) at 56.4 Mc. The fact that the members of the doublet are not of equal intensity suggests that the observed structure does not originate from long range ^1H-^{19}F spin-spin coupling between the ^{19}F nuclei of the TFA group and the proton five bonds removed. Strong irradiation of the ^1H spectrum at 60 Mc with greater than 10 milligauss of power failed to remove the doublet structure. The ^{19}F spectra of these polymer DTFA esters at 94.1 Mc showed a doublet splitting of about 3 cps (*SPS 37-31*, Vol. IV). The ^{19}F NMR chemical shifts of nuclei are linearly dependent on field strength so this result together with the result from the double resonance experiment unequivocally demonstrate the presence of two magnetically non-equivalent types of hydroxyl end-groups for these polymers. We have discussed two possible origins for these two types of secondary hydroxyl end-groups (*SPS 37-26* and *37-24*, Vol. IV). First, the methyl group of the propylene oxide monomer units adjacent to the terminal monomer units could be α or β to the terminal ether linkage to give a positional isomerization. In the case of positional isomerization this difference could originate from the several pathways available in the initial polymerization steps. Alternately, the doublet ^{19}F NMR signals for these DTFA esters could originate from the various combinations of asymmetric carbon atoms in the two terminal monomer units of the two ends of the polymer chain. In this case the difference in concentration of the two types of TFA groups in the product from the base-catalyzed polymerization of racemic propylene oxide suggests a small but significant amount of stereoselectivity in the polymerization.

We have now distinguished between these two possibilities in three ways. Previously (*SPS 37-26*, Vol. IV), we described the preparation of a polymer of racemic propylene oxide initiated with sodium n-propoxide. This material yielded a TFA ester which exhibited two ^{19}F NMR peaks (2.1-cps splitting) of equal intensity. This result suggests that the two types of hydroxyl end-groups present in PPO materials prepared by basic catalysis originate from the asymmetric carbon atom of the monomer units. We now wish to describe two additional experiments bearing on this same problem which lend further support for this explanation for the two types of end-groups we have detected in PPO polymers.

[11]Joint contribution with the JPL Polymer Research Section, Propulsion Division.

2. ^{19}F NMR Spectrum of DTFA of Poly[(+)-*l*-propylene oxide]

If the doublet structure observed for the DTFA's of racemic PPO liquid polymers arises from the asymmetric centers in the monomer units, apparently one of the two signals corresponds to *dl* and *ld* type end-group diads while the other signal corresponds to *ll* and *dd* type end-group diads. Confirmation for this explanation could be obtained from study of the DTFA of optically active PPO where we would expect to observe a singlet ^{19}F NMR signal. In addition, from the optically active polymer unequivocal identification of which signal corresponds to which end-group diad would be obtained.

Therefore, (+)-*l*-propylene oxide was prepared. First, the corresponding optically active glycol was obtained, converted to the bromohydrin, and then dehydrobrominated to the epoxide (Ref. 60). The epoxide was polymerized according to the method of Price (Ref. 61). The polymerization conditions were adjusted on the basis of recent kinetic studies (Ref. 62) to give a molecular weight of ~2000. The DTFA was prepared, and from the fluorine analysis a molecular weight of 1690 was calculated. This ester gave a single sharp ^{19}F NMR signal (Fig. 19a) superimposible on admixture with the high-field member of the doublet of an atactic PPO–2000 DTFA ester (Fig. 19b). This result firmly establishes that *the ^{19}F NMR doublet for the secondary TFA esters of poly(propylene oxide) arises from the asymmetric center in the monomer units.* Thus Structures I and III represent the *dl* and *dd* end-group diads which yield TFA esters with the highest field ^{19}F NMR signals, and Structures II and IV represent the *dl* and *ld* diads which fall at lower magnetic field.

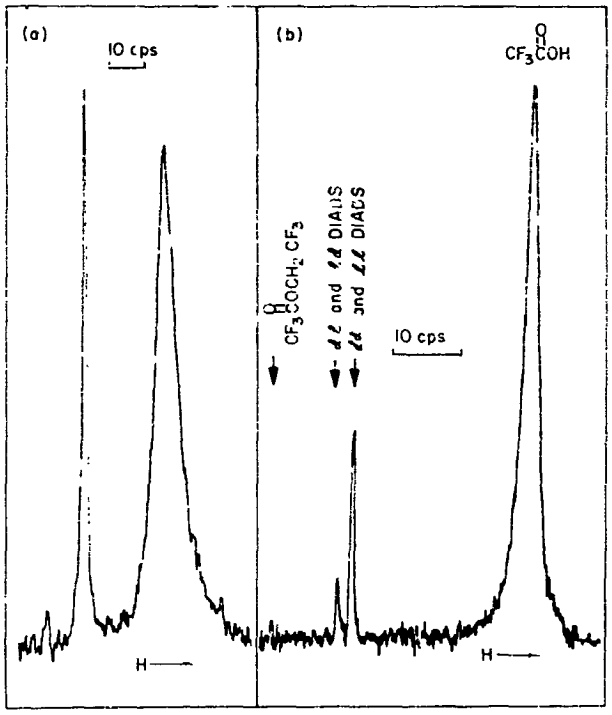

Fig. 19. ^{19}F NMR spectra at 56.4 Mc of DTFA esters: (a) poly(*l*-propylene oxide) in mixture of trifluoroacetic acid, benzene, and CF_3CH_2OH; (b) mixture (80:20) of esters of poly(*l*-propylene oxide) and a liquid poly(*d*,*l*-propylene oxide) (molecular weight 2000) in same solvent system

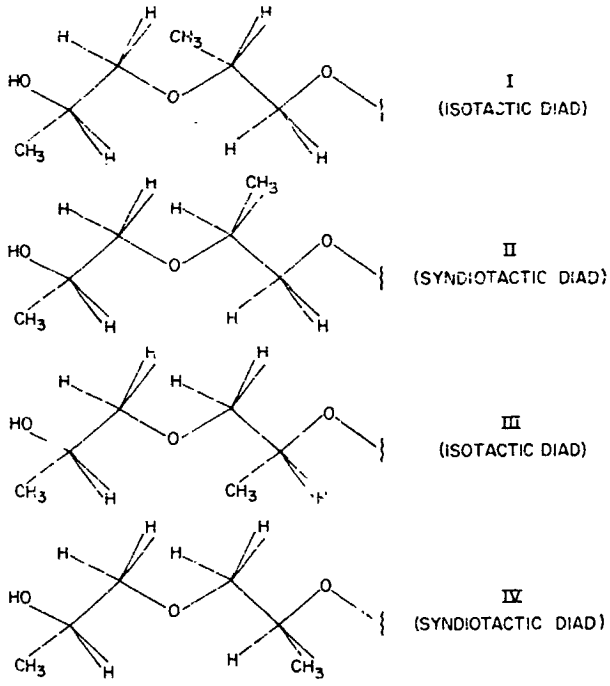

If the chain adds monomer units in the polymerization at both ends then Diads III and IV may not be present; we have not yet demonstrated to what extent this is the case.

3. Degradation of High-Molecular Weight PPO

It is well known (Ref. 61) that a ferric chloride-propylene oxide catalyst is capable of converting *d*,*l*-propylene oxide into a high molecular weight polymer which is a mixture of crystallines and amorphous materials. The exact structure of these materials is still in

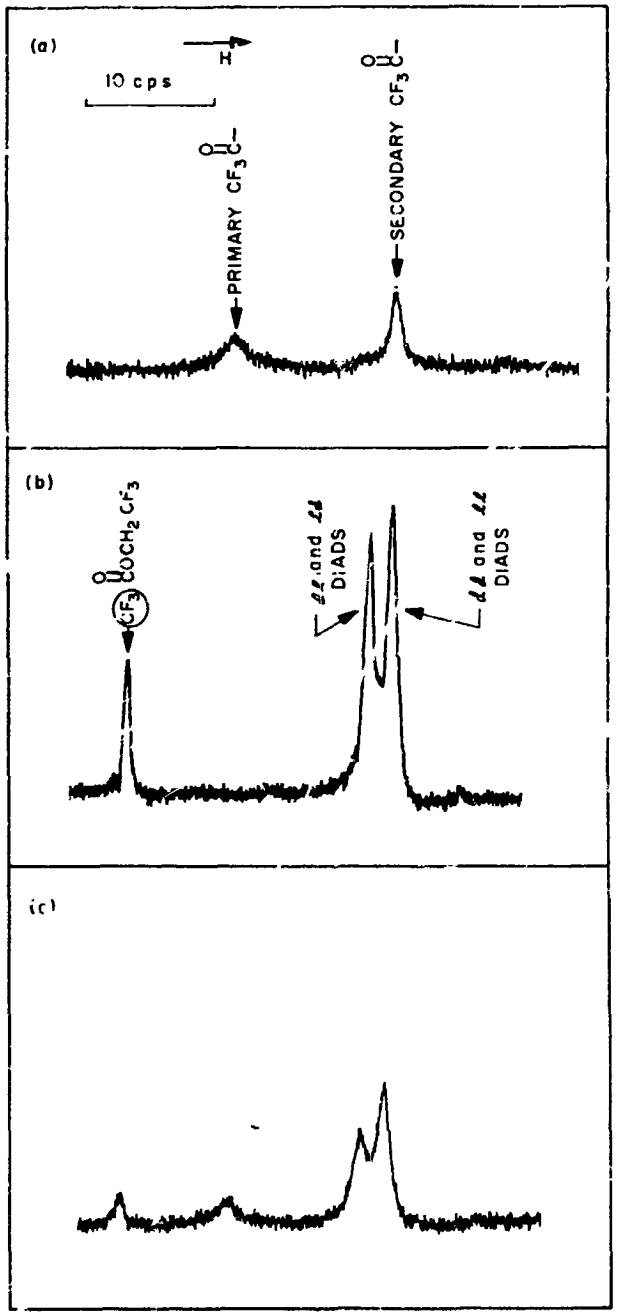

Fig. 20. ^{19}F NMR spectra at 56.4 Mc of DTFA esters: (a) ester of degradation product from hydrobromic acid cleavage of high molecular weight poly(*d*, *l*-propylene oxide) prepared with $FeCl_3$ catalyst in CF_3CH_2OH; (b) esters of liquid poly(*d*, *l*-propylene oxide) with molecular weight about 2000 in same solvent; (c) spectrum of mixture of (a) and (b)

some doubt. We felt that random degradation of such a high molecular weight PPO polymer followed by trifluoroacetylation of the degradation product and study of the ^{19}F NMR spectrum of these esters would reveal useful information concerning the structure of these PPO polymers.

A sample of waxy polymer prepared with a ferric chloride catalyst (Ref. 61) was degraded by boiling concentrated hydrobromic acid to give a very viscous slightly yellow oil. Trifluoroacetylation gave a less viscous TFA ester which exhibited a singlet ^{19}F signal (Fig. 20a)[12] for a secondary TFA group along with a broader signal (Fig. 20a) at the right chemical shift position for primary TFA groups. The single secondary TFA signal was superimposible on admixture with the high-field member of the DTFA doublet of a low molecular weight liquid PPO (compare Figs. 20b and 20c). The broadening exhibited in the spectra shown in Fig. 20 is due to a small amount of paramagnetic iron ions which could not be removed by the aqueous washings employed in the isolation of the degradation product.

Conclusion

The three results described in some detail above demonstrate that the asymmetric carbon atoms present in the propylene oxide monomer units are the origin of the doublet ^{19}F NMR signals observed for the TFA esters of the PPO polymers we have studied. We have identified the high-field member of the doublet as belonging to the isotactic diad end-group units. Furthermore, our results suggest that the polymers obtained by ferric chloride catalyzed polymerization of racemic propylene oxide are primarily isotactic (i.e., chains of all *l* and all *d* monomer units). A recent X-ray study of the crystal structure of *d,l*-poly(propylene oxide) could not distinguish between the latter structure and a syndiotactic structure (Ref. 64). It also appears, as evidenced from the inequality of the concentrations of the two types of secondary hydroxyls present in the atactic PPO, that a certain degree of stereoselectivity exist in the polymerization of racemic propylene oxide with basic catalysts.

Thus, using the NMR techniques described above and in previous reports (*SPS 37-31*, *37-26*, and *37-24*, Vol. IV), we have obtained important information, which heretofore was unknown or has been the subject of considerable

[12]These frequency sweep ^{19}F spectra were taken with the field frequency lock system previously described in Ref. 63. The lock signal was derived from 7–10% added 1,1,2,2-tetrafluoro-1,2-dibromoethane whose signal is conveniently downfield about 700 cps from the region of interest.

controversy, on the structures of one type of poly(alkylene oxide) polymer. In addition, the technique which we have developed has proved, from an analytical chemistry standpoint, to be a convenient means of determining the relative amounts of various types of hydroxyl end-groups present in poly(alkylene oxides). It appears that this technique should be of significant value in predicting the reactivity and applicability of these polymers for propellants and spacecraft materials.

H. The Microwave Spectrum of 2,3-Dicarbahexaborane(6)

R. L. Poynter and R. A. Beaudet

1. Introduction

The relatively new field of carbon-boron chemistry has shown extensive activity in the past few years. The synthesis of a number of relatively new compounds has produced a number of questions concerning their unusual stability and speculation concerning their geometric structures and chemical bonding. These compounds appear to have carbon and boron bonded together in an unusual fashion. Onak, Williams, and Weiss (Ref. 65) and Shapiro, Good, and Williams (Ref. 66) have synthesized several compounds which have been the subject of recent structural analyses. 2,4 dicarbaheptaborane(7), $C_2B_5H_7$, has been studied by Beaudet and Poynter (Ref. 67), while dihydrocarborane, or 2,3-dicarbahexaborane(8) with an empirical formula $C_2B_4H_8$, has been studied by Boer, Streib, and Lipscomb (Ref. 68). One of the other compounds in this interesting series is 2,3-dicarbahexaborane(6), which has the empirical formula $C_2B_4H_6$ (Ref. 66). The structures of these two molecules are quite different, despite the fact that they both have the same number of carbon and boron atoms. Dihydrocarborane contains two bridge-bonded hydrogen atoms with an icosohedral cap of B_4C_2 consisting of a B apex atom and a five-membered C_2B_3 ring. On the other hand, the present work shows that $C_2B_4H_6$ has the form of a bipyramid with a trapezoidal base consisting of a four-membered C_2B_2 ring, and two symmetrically located apex B atoms. In both molecules the two carbon atoms are adjacent to each other and located in the base ring. This study was stimulated by the desire to better understand the physical basis for the chemical behavior of the more elementary members of this series of compounds.

2. Experimental Methods

The microwave spectrometer which was used in this study has been described in previous reports (Ref. 69). A 10-mg sample of the 2,3-dicarbahexaborane(6) was obtained on loan from Professor T. Onak. This sample was used as obtained without further purification. Because of the difficulties of obtaining this sample, it was divided into two aliquot portions, one of which was stored for safety. Frequency measurements were made by interpolation receiver methods, using as standard frequencies the harmonics of a microwave multiplier chain which was controlled with the output signal from an HP Model 104 AR quartz oscillator. This oscillator was in turn calibrated against a National Atomichron and the National Bureau of Standard's broadcasting station WWV.

3. Rotational Spectrum

To obtain initial predictions of the rotational spectrum, estimates of the bond distances and angles were made using the published data on $C_2B_4H_8$ and $C_2B_5H_7$ (Refs. 67 and 68). Such predictions indicated that the 2,3-dicarbahexaborane(6) would be close to a spherical rotor, and that there might be considerable trouble in locating the inertial axes and the orientation of the dipole moment. Thus, predicted spectra were computed for the molecular dipole moment oriented along each of the inertial axes. For each case, rotational transitions were predicted to occur in the 8–40-Gc microwave frequency band. Furthermore, the predicted spectral patterns were not uniquely different although they favored *A* and *C* selection rules so that a cursory study would not allow an immediate choice of the correct type of selection rules. In addition, there would be at least six isotopic species of the molecule, with overlapping spectral patterns.

A search of the 18–26-Gc microwave frequency band revealed several densely populated groups of absorption lines. Most of these lines were characteristic of high *J* transitions, but a few low *J* lines with resolvable Stark effects were isolated. The Stark effects of these lines were then analyzed to determine the most probable *J* values. Attempts were then made to correlate these transitions with the different sets of predicted values. The uncertainties in the original parameters were such that the molecule could be either an oblate or a prolate rotor. Assignment attempts were made for both types of rotors. These early assignment attempts were singularly unsuccessful. Therefore, the spectral scanning was extended to both higher and lower frequencies. A set of lines was finally isolated which could be postulated as belonging to the $J = 1 \leftarrow 0$, $J = 2 \leftarrow 1$, and $J = 3 \leftarrow 2$ transitions. Trial

choices, which were made using lines in the $J = 2 \leftarrow 1$ set and C-type selection rules, were not productive. It was only possible to assign the normal species using B type selection rules. Computations of the other isotopic species rotational constants were then made with approximate moment corrections determined by using Kraitchman's equations (Ref. 70). As might be expected, the initial predictions of the moments of the various isotopic species were considerably in error because of the lack of knowledge of the actual structural configuration. With each assigned isotopic species, the prediction of the next species rotational moments became easier because of the greater certainty in the molecular configuration.

As in all boron-containing compounds, two boron isotopes normally are present: ^{11}B, with a natural abundance of 81%, and ^{10}B, with an abundance of 19%. There are four boron atoms in this molecule, and there are nine distinct isotopic forms of the molecules which occur in the natural state. Assuming that the most abundant species (containing all ^{11}B atoms) has a relative intensity of unity, each of the two singly substituted ^{10}B species has a relative intensity of 0.5, and each of the three doubly substituted species has a relative intensity of 0.125. The triple substituted species, each of which has a relative intensity of 0.025, were too weak to observe and have been neglected in this study. The weaker transitions belonging to the all ^{11}B species are comparable in intensity to the stronger transitions belonging to the two ^{10}B singly substituted species, a fact which caused some difficulties in the assignment procedure. Because the all ^{11}B species had lines with fairly large intensities, it was possible to study and assign all of the singly and doubly ^{10}B-substituted molecules. This provides additional information on the bond distances.

Each of the four boron atoms possesses a quadrupole moment and can produce a splitting of the rotational transitions into a larger group of lines. In the present study, the quadrupolar splittings were too small to be observable, and gave no trouble in the analysis of the spectrum. However, these splittings did produce a slight broadening of the lower J transitions. This made it necessary to use the $J = 3 \leftarrow 2$ and $J = 4 \leftarrow 3$ transitions for obtaining accurate rotational constants.

The rotational constants and the corresponding moments of inertia are given in Tables 7 and 8.

The final molecular structural analysis results are not available at present. However, preliminary results may be summarized in Fig. 21, for the normal all ^{11}B molecule.

Table 7. Rotational constants for six isotopic molecular species of 2,3-dicarbohexaborane(6)

Species	Rotational constants, Mc/sec		
	A	B	C
Normal, all ^{11}B	6162.320	5930.000	5929.410
Apex ^{10}B	6162.125	6035.758	6035.515
Ring ^{10}B	6277.005	6035.646	5929.415
Apex ^{10}B, Apex ^{10}B	6162.018	6142.819	6142.325
Ring ^{10}B, Apex ^{10}B	6276.710	6145.600	6035.420
Ring ^{10}B, Ring ^{10}B	6395.846	6038.393	6032.739

Table 8. Moments of inertia for six isotopic molecular species of 2,3-dicarbahexaborane(6)

Species	Moments of inertia, amu-Å^2		
	I_A	I_B	I_C
Normal, all ^{11}B	82.0358	85.2498	85.2582
Apex ^{10}B	82.0384	83.7560	83.7594
Ring ^{10}B	80.5370	83.7576	85.2582
Apex ^{10}B, Apex ^{10}B	82.0399	82.2963	82.3029
Ring ^{10}B, Apex ^{10}B	80.5408	82.2590	83.7607
Ring ^{10}B, Ring ^{10}B	79.0405	83.7195	83.7979

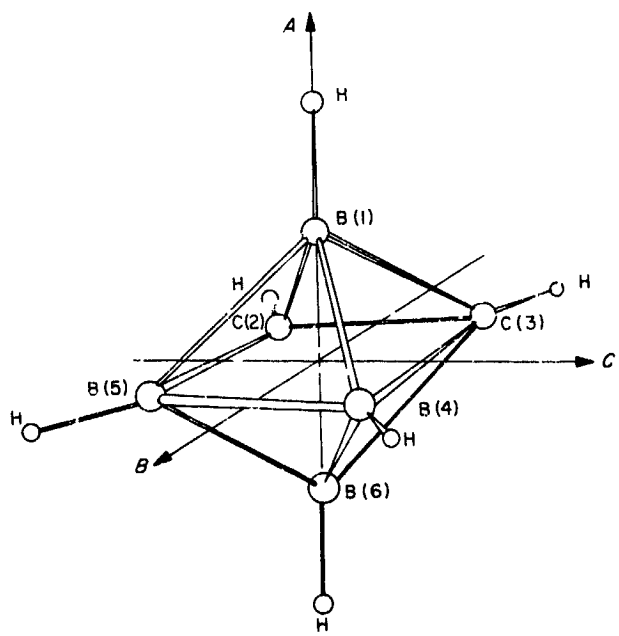

Fig. 21. Atomic configuration of 2,3-dicarbahexaborane(6) (principal axes are shown by arrows for the all ^{11}B isotopic species)

Bond distances and angles which are omitted in Fig. 21 will be given at a later date. The shift in molecular principal axes upon isotopic substitution is illustrated in Fig. 22.

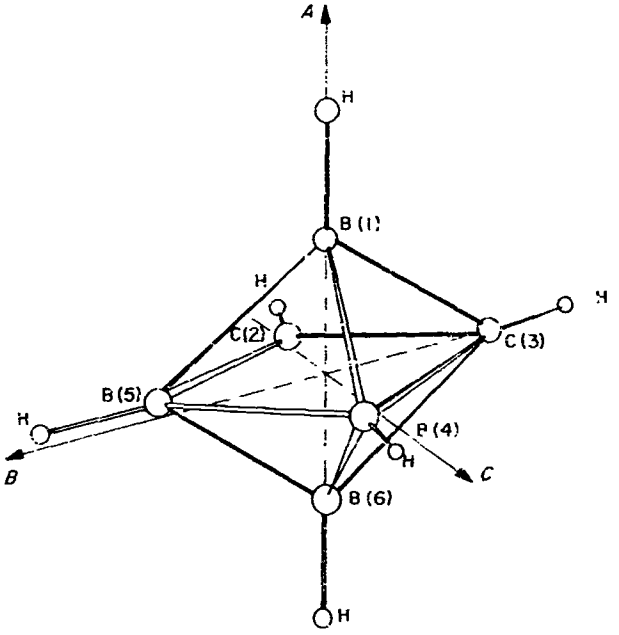

Fig. 22. Orientation of principal axes after ^{10}B isotopic substitution at Atom B(4) for 2,3-dicarbahexaborane(6)

4. Dipole Moment

The molecular dipole moment was determined by analyzing the Stark effect splittings for the $M = 0$ Stark lobes of the $J = 2_{02} \leftarrow 1_{11}$ and the $J = 2_{12} \leftarrow 1_{01}$ transitions. Linearity of the plot of frequency shift as a function of the square of the applied electric field confirms the negligible effects from the boron nuclear quadrupole moments. The Stark effect absorption cell was calibrated with OCS immediately before and after the measurements were made upon 2,3-dicarbahexaborane(6) in order to minimize temperature effects. The results are given in Table 9. The mean dipole moment is 1.501 ± 0.03 Debye units and is oriented along the B principal axis, as shown in Fig. 21.

Table 9. Dipole moment of 2,3-dicarbahexaborane(6)

Transition	$\Delta\nu/E^2$	μ
$2_{12} \leftarrow 1_{01}, M = 0$	$0.602_4 \times 10^{-3}$	1.52
$2_{02} \leftarrow 1_{11}, M = 0$	1.019×10^{-3}	1.48
		1.50 ± 0.03 (average)

N65-32458

I. Detection of a Signal on a Paper Chromatograph

G. F. Steffensen

The use of conductivity changes to detect separations on a thin-layer or paper chromatograph would be a practical solution to the problem of colorless mixtures and possible quantitative analysis without destroying the sample. A simple test was set up (Fig. 23) to see if this method of detection was possible. Preliminary tests without the preamplifier indicated the method would work with a sensitivity equal to or better than existing chemical methods.

To detect the conductivity change a pair of gold wires was placed on opposite sides of the chromatograph paper. This was treated as a resistor and placed in a bridge circuit. A Princeton Applied Research lock-in amplifier tuned to 1 kc was used to generate a signal across the bridge and also to detect the signal from the bridge. This detected signal was applied to a strip chart recorder.

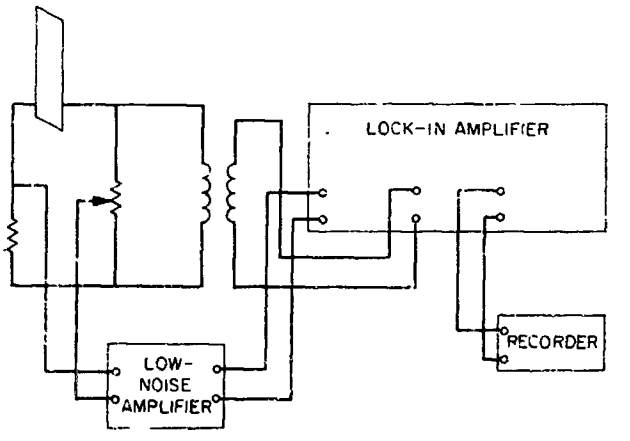

Fig. 23. Experimental setup for paper chromatography detector

Operation of the system consisted of establishing a water flow down the paper and balancing the bridge. After suitable warm-up for stabilization, a 1-μl sample was placed on the paper and its passage recorded. The sample concentration was varied and the results noted. A 10^{-4} M test sample of $CuSO_4$ is detectable and was used to determine the limiting sensitivity of the method (Fig. 24). To detect a nonconducting compound, such as methyl alcohol, the carrier water conductivity was adjusted with NaCl to a suitable steady-state level. It was then possible to detect non-conducting compounds which are injected into the carrier solution. The polarity of the output signal was opposite to that observed for $CuSO_4$, showing that phase detection techniques allow a clear distinction of the unknown compounds conductivity relative to the carrier conductivity. Various methods of enhancing the signal, such as different detector designs, paper widths, and paper notching, could be used. Any or all of these methods would probably improve the system performance.

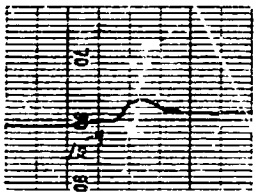

Fig. 24. Passage of a 1-μl sample of 10^{-4} M $CuSO_4$

Although this basic idea appears new, its simplicity implies that it may amount to a rediscovery. A brief literature search has not disclosed any prior discussion, however. The application of phase detection methods in this work appears to increase sensitivity by about 100. Work is being continued.

References

1. Whitehouse, M. W., "Lipid Pharmacology," Chapter 4, Editor: Paoletti, R., Academic Press, Inc., New York, N. Y., 1964.
2. Neher, R., "Steroid Chromatography," p. 218 *et seq*, Elsevier Publishing Co., New York, N. Y., 1964.
3. Kushinsky, S., and Otterness, I., *Steroids*, Vol. 3, pp. 331–325. 1964.
4. Stames, W. R., et al, *Analytical Biochemistry* Vol. 6, pp. 82–99, 1963.
5. Vandenheuvel, F. A., et al, *Journal of American Oil Chemists' Society*, Vol. 42, (4), pp. 283–290, 1965.
6. Dorner, G., and Stahl, F., *Acta Biologica et Medica Germanica*, Vol. 12, pp. 606–611, 1964.
7. Bennett, R. D., and Heftman, E. J., *Chromatography*, Vol. 9, pp. 348–352, 1962.
8. Ross, E. J., *Journal of Clinical Endocrinology and Metabolism*, Vol. 20, pp. 1360–65. 1960.
9. Nikiforoff, C. C., "General Trends of the Desert Type of Soil Formation," *Soil Science*, Vol. 43, pp. 105–131, 1937.
10. Russell, E. W., "Soil Conditions and Plant Growth, Ninth Edition," John Wiley & Sons, Inc., New York, N. Y., p. 216, 1951.
11. Cameron, R. E., and Blank, G. B., *Soil Organic Matter*, Technical Report No. 32-443, Jet Propulsion Laboratory, Pasadena, California, May 23, 1963.

References (Cont'd)

12. Jackson, M. L., "Chemical Composition of Soils," In: "Chemistry of the Soil, Second Edition," Editor: Bear, F. E., Reinhold Publishing Corporation, New York, N. Y., pp. 71–141, 1964.

13. Vinogradov, A. P., "The Geochemistry of Rare and Dispersed Chemical Elements in Soils, Second Edition," Translation by Consultants Bureau, Inc., New York, N. Y., 1959.

14. Cameron, R. E., Morelli, F. A., and Blank, G. B., "Soil Studies—Desert Microflora. VI. Abundance of Microflora in an Area of Soil at White Mountain Range, California," *SPS No. 37-32*, Vol. IV, pp. 212–214, Jet Propulsion Laboratory, Pasadena, California.

15. Jackson, M. L., "Soil Chemical Analysis," Prentice-Hall, Inc., Englewood Cliffs, N. J., pp. 452–485, 1958.

16. Chapman, H. D., and Pratt, P. F., "Methods of Analysis for Soils, Plants, and Waters," University of California, Berkeley, California, 1961.

17. Moore, W. R., and Ward, H. R., *Journal of the American Chemical Society*, Vol. 80, p. 2909, 1958.

18. King, J., *Journal of Physical Chemistry*, Vol. 67, p. 1397, 1963.

19. Gant, P. L., and Yang, K., *Science*, Vol. 129, p. 1548, 1959.

20. Mohnke, M. and Saffert, W., *Proceedings of the 4th International Gas Chromatography Symposium*, Editor: Van Swaay, M., Butterworth, Inc., Washington, D. C., 1962.

21. Farkas, E., "Orthohydrogen, Parahydrogen and Heavy Hydrogen," Cambridge University Press, Cambridge, England, 1935.

22. Hirschfelder, Curtis, and Bird, "Molecular Theory of Gases and Liquids," p. 947, John Wiley & Sons, Inc., New York, N. Y., 1954.

23. Hill, T. L., *The Journal of Chemical Physics*, Vol. 16, p. 181, 1948.

24. White, D., and Lassettre, E. N., *The Journal of Chemical Physics*, Vol. 32, p. 72, 1960.

25. Stratton, Morse, Chu, Shittle and Corbato, "Spheroidal Wave Function," The Technology Press of Massachusetts Institute of Technology; John Wiley & Sons, Inc., New York, N. Y., 1956.

26. Landolt-Bornstein, "Zahlenwerte und Funktionen aus Physik, Chemie, Astronomie, Geophysik, und Technik," 6th Edition, Vol. 1, Part 3, Springer-Verlag, Berlin, 1951, p. 5 (9-512).

27. Ford, H., and Endow, N., *The Journal of Chemical Physics*, Vol. 27, p. 1156, 1957.

28. Ford, H., and Jaffe, S., *The Journal of Chemical Physics*, Vol. 38, p. 2935, 1963.

29. Holmes, H., and Daniels, F., *Journal of the American Chemical Society*, Vol. 56, p. 360, 1934.

30. Norrish, R. G. W., *Journal of the Chemical Society (London)*, Vol. 51, p. 1158, 1929.

References (Cont'd)

31 Blacet, F., Hall, T., and Leighton, P., *Journal of the American Chemical Society*, Vol. 84, p. 4011, 1962.

32. Harris, L., King, G., Benedict, W., and Pearce, R., *The Journal of Chemical Physics*, Vol. 8, p. 765, 1940.

33. Von Bahr, E., *Annalen der Physik*, Vol. 33, p. 585, 1910.

34. Harris, L., and King, G., *The Journal of Chemical Physics*, Vol. 2, p. 51, 1934.

35. Guttman, A., "Absolute Infra-red Intensity Measurements of NO_2 and N_2O_4," Thesis, California Institute of Technology, Pasadena, California, 1961.

36. Karplus, M., and Anderson, D. H., *The Journal of Chemical Physics*, Vol. 30, p. 6, 1959; Gutowsky, H. S., Karplus, M., and Grant, D. M., *ibid*, Vol. 31, p. 1278, 1959.

37. Barfield, M., and Grant, D. M., *Journal of the American Chemical Society*, Vol. 85, p. 1899, 1963.

38. Fraser, R. R., Lemieux, R. V., and Stevens, J. D., *Journal of the American Chemical Society*, Vol. 83, p. 3901, 1961; Kaplan, F., and Roberts, J. D., *ibid*, Vol. 83, p. 4474, 1961; Reilly, C. A., and Swalen, J. D., *The Journal of Chemical Physics*, Vol. 35, p. 1522, 1961; Finegold, H., *Proceedings of the Chemical Society (London)*, p. 213, 1962.

39. Freeman, R., McLaughlan, K. A., Musher, J. I., and Pachler, K. G. R., *Molecular Physics*, Vol. 5, p. 321, 1962; Freeman, R., and Anderson, W. A., *The Journal of Chemical Physics*, Vol. 37, p. 2053, 1963; Freeman, R., and Bhacca, N. S., *ibid*, Vol. 38, p. 1088, 1963.

40. McLaughlan, K. A., and Whiffen, D. H., *Proceedings of the Chemical Society (London)*, p. 144, 1962.

41. Goldish, E., *Journal of Chemical Education*, Vol. 36, p. 408, 1959 (for structural data on ethylene oxide, ethylene imine, and ethylene sulfide).

42. Lynden-Bell, R. M., *Molecular Physics*, Vol. 6, p. 537, 1963 (for the case of vinyl bromide-^{13}C).

43. Glick, R. E., and Bothner-By, A. A., *Journal of the American Chemical Society*, Vol. 25, p. 362, 1956.

44. Sheppard, N., and Farner, J. J., *Proceedings of the Royal Society (London)*, Vol. A 252, p. 506, 1959.

45. Schaefer, T., *Canadian Journal of Chemistry*, Vol. 40, p. 1, 1962.

46. Williamson, K. L., *Journal of the American Chemical Society*, Vol. 85, p. 516, 1963.

47. Williamson, K. L., Lanford, C. A., and Nicholsen, G. R., *ibid*, Vol. 86, p. 762, 1964.

48. Abraham, R. J., and Pachler, K. G. R., *Molecular Physics*, Vol. 7, p. 165, 1963.

49. Lehn, J., and Riehl, J., *ibid*, Vol. 8, p. 33, 1964.

50. Muller, N., and Pritchard, D. E., *The Journal of Chemical Physics*, Vol. 31, p. 1471, 1959.

References (Cont'd)

51. Huggins, M. L., *Journal of the American Chemical Society*, Vol. 75, p. 4123, 1953.

52. Mulier, N., and Rose, P. I., *ibid*, Vol. 84, p. 3973, 1962.

53. Juan, C., and Gutowsky, H. S., *The Journal of Chemical Physics*, Vol. 37, p. 2198, 1962.

54. Mortimer, F. S., *Molecular Spectroscopy*, Vol. 5, p. 199, 1960.

55. Potel, D. J., Howden, M. E. H., and Roberts, J. D., *Journal of the American Chemical Society*, Vol. 85, p. 3218, 1963.

56. Wiberg, K. B., and Nist, B. J., *ibid*, Vol. 85, p. 2788, 1963.

57. Bernstein, H. J., and Shepperd, N., *The Journal of Chemical Physics*, Vol. 37, p. 3012, 1962 (suggested such a correlation for the geminal coupling).

58. Karabatsos, G. J., and Orzech, C. E., *Journal of the American Chemical Society*, Vol. 86, p. 3575, 1964.

59. Pople, J. A., and Santry, D. P., *Molecular Physics*, Vol. 8, p. 1, 1964.

60. Levine, P. A., and Walti, A., *Journal of Biological Chemistry*, Vol. 68, p. 415, 1926.

61. Price, C. C., and Osgan, M., *Journal of the American Chemical Society*, Vol. 78, p. 4787, 1956.

62. Steiner, E., Pelletier, R. R., and Trucks, R. O., *Journal of the American Chemical Society*, Vol. 86, p. 4678, 1964.

63. Elleman, D. D., Manatt, S. L., and Pierce, C. D., *The Journal of Chemical Physics*, Vol. 42, pp. 650–667, 1965.

64. Stanley, E., and Litt, M., *Journal of Polymer Science*, Vol. 43, p. 453, 1960.

65. Onak, T. P., Williams, R. E., and Weiss, H. G., *Journal of the American Chemical Society*, Vol. 84, p. 2830, 1962.

66. Shapiro, I., Good, C. D., and Williams, R. E., *Journal of the American Chemical Society*, Vol. 84, p. 3837, 1962.

67. Beaudet, R. A., and Poynter, R. L., *Journal of the American Chemical Society*, Vol. 86, p. 1258, 1964.

68. Boer, F. P., Streib, W. E., and Lipscomb, W. N., *Inorganic Chemistry*, Vol. 3, p. 1666, 1964.

69. Poynter, R. L., *The Journal of Chemical Physics*, Vol. 39, p. 1962, 1963.

70. Kraitchman, J., *American Journal of Physics*, Vol. 21, p. 17, 1953.

Errata

The following corrections should be noted for *SPS 37-30*, Vol. IV: on Fig. 6, p. 135, resistors R9 and R10 should read 100 Ω instead of 100K.

XXII. Applied Science

A. A Combined Focusing X-Ray Diffractometer and Non-dispersive X-Ray Spectrometer for Remote Analysis: A Preliminary Report

H. W. Schnopper,[1] A. E. Metzger, R. A Shields, and K. Das Gupta[2]

1. Introduction

When illuminated by a suitable source of X-rays, a crystalline sample will scatter this radiation in a way which is characteristic of the space lattice of the crystal. The scatterer can be in the form of either a single crystal or a polycrystalline sample. A variety of instrumentation has been developed to handle each case. For purposes of sample identification, the powder method is used most commonly. The scattering process is essentially elastic and if a roughly monochromatic beam of wavelength λ is used, then the scattering angle θ can be related to the lattice spacing d by Bragg's Law $n\lambda = 2d \sin \theta$, where n is the reflection order. Various standard analysis procedures can be used to give a complete structural analysis of the sample.

If the incident X-ray has an energy above the K ionization potential of the elements in the sample then a chemical analysis is also possible. The sample will emit characteristic X-rays which may be measured with either dispersive or nondispersive instruments. The secondary emission process is not very efficient because it depends upon a combination of absorption coefficient and fluorescence yield. Lunar applications involving the detection of light elements by the use of fluorescent excitation rather than electron excitation, dictate a low energy incident beam, and nondispersive analysis.

The instrument to be described is intended to perform a dual-purpose (elemental as well as mineralogical) analysis consistent with these boundary conditions: reasonably high sensitivity, atomic number resolution, lattice spacing resolution, low power requirements, rapid data accumulation, and simplicity of mechanical construction and operation. The primary objective has been the remote analysis of lunar material; however, the instrument also may have application in the laboratory.

[1]Physics Department, Cornell University, Ithaca, New York.
[2]Department of Material Science, California Institute of Technology, Pasadena, California.

2. Choice of Instrumentation

The use of a scaled-down version of a standard diffractometer for space flight was proposed by Dr. W. Parrish of Philips Laboratories (Ref. 1). This design was developed to the preprototype stage by Philips Electronic Instruments (PEI) of Mount Vernon, New York, and has since undergone further modification at JPL (Ref. 2). At one time this instrument was to be used in conjunction with a fixed channel X-ray spectrograph designed by PEI, to give a complete chemical and structural analysis (Ref. 3). The diffractometer, illustrated in Fig. 1, is a nonfocusing device and operates as follows: A stationary line source of X-rays (with suitable divergence collimation) illuminates a powdered briquet sample located on a rotating axis. A photon detector (proportional counter tube) with a narrow entrance slit is mounted to rotate about the same axis, and the angular motions of sample and detector are correlated in a 1:2 ratio. The angular region of interest is scanned, and diffraction peaks are recorded as changes in intensity versus angle.

Based on the method of focusing, diffractometers are classified into two categories:

(1) Bragg focusing: The distance from the sample to the source slit is equal to its distance from the detector slit.

(2) Seeman–Bohlin focusing: The source slit, the powdered sample, and the detector slit all lie on the circumference of the focusing circle.

In Bragg focusing the detector moves in a circle with the sample at the center, while in the Seeman–Bohlin method the detector moves in a circle with the sample on the circumference of the circle.

The PEI instrument uses Bragg focusing. Although this approach has been successful in retaining a high level of intensity and resolution with only a fraction of the power and weight required by a laboratory diffractometer, the Seeman–Bohlin focusing principle lends itself to more efficient power use, a simpler mechanical design, and a more rapid analysis. In order to take advantage of these potentialities, a new instrument based on the Seeman–Bohlin focusing principle was designed and breadboarded at JPL.

The JPL instrument (Fig. 2) is based on a fixed source-sample relationship which allows a simple focusing design. The conventional Seeman–Bohlin optics have been modified, however, by placing a line source directly on the focusing circle in a manner suggested in 1957 by K. Das Gupta (Ref. 4). This arrangement provides the most efficient utilization of the source. The line source of

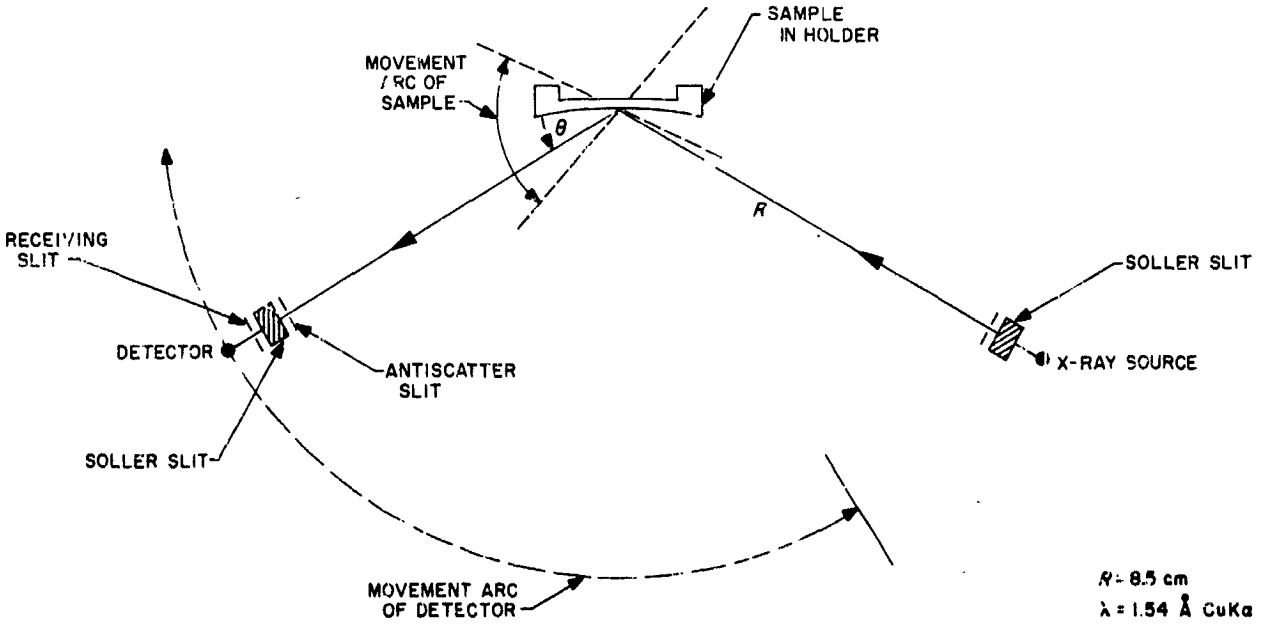

Fig. 1. Schematic of PEI diffractometer

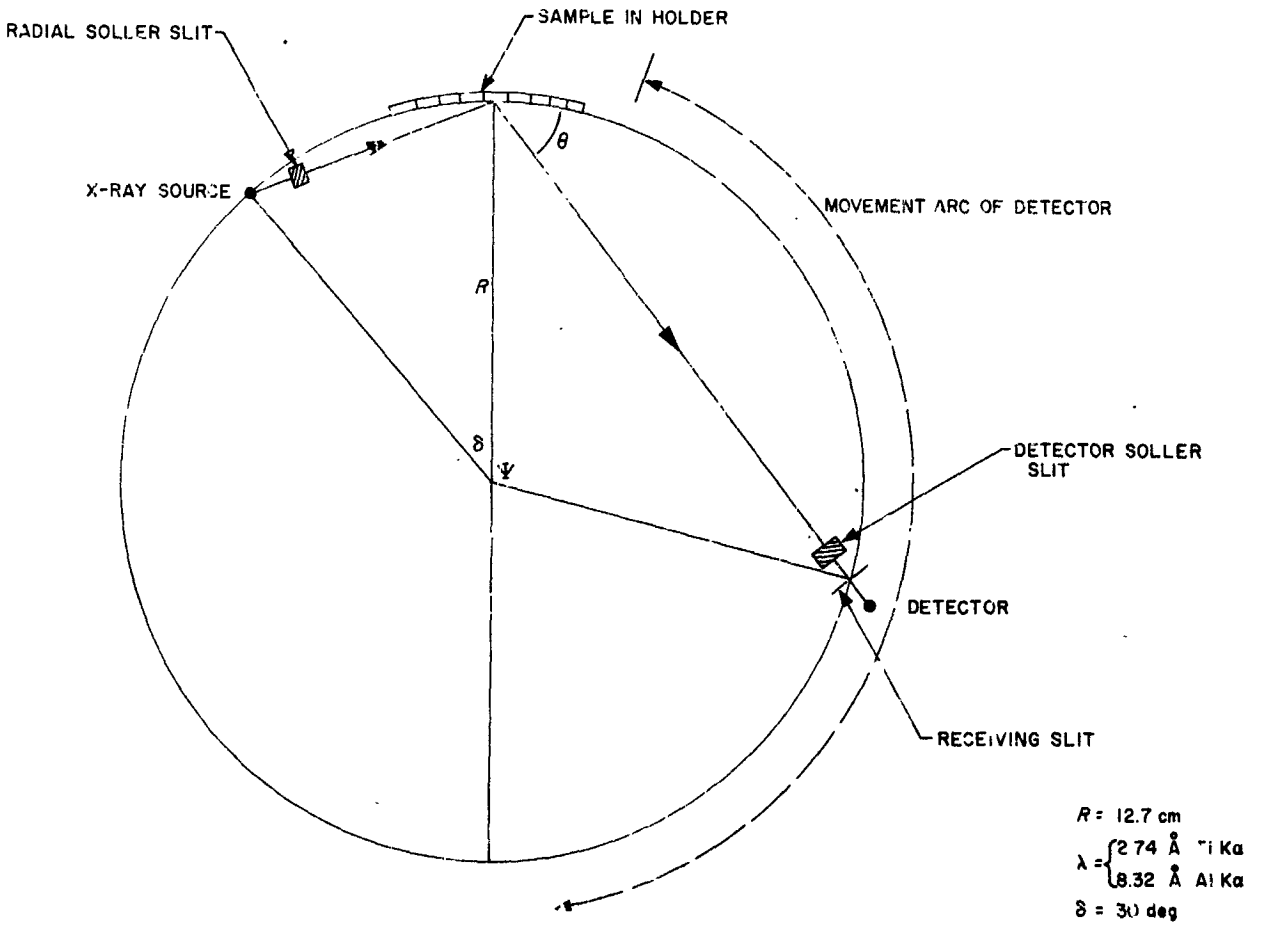

Fig. 2. Schematic of focusing diffractometer

the focusing circle is imaged at points appropriate to the various lattice spacings by diffraction from a curved sample. By means of a simple linkage, the detector is made to rotate about the center of the focal circle and point a narrow receiving slit at the center of the sample. One or more fixed counters observe the source directly and are used for a nondispersive chemical analysis.

The advantages offered by the JPL instrument are: (1) high diffracted beam intensity per power input; (2) mechanical simplicity by decreasing the number of moving assemblies from two to one; (3) light weight; (4) adaptability to multiple detectors for a rapid diffractometer scan; (5) simultaneous chemical and diffraction analysis, and (6) adaptability to several nondispersive counters "tuned" through an appropriate choice of window mass and gas fill for optimum spectral response. Items 4, 5, and 6 are important innovations for lunar application.

3. Design Considerations for the JPL Instrument (Diffractometer Portion)

The requirements of line resolution and intensity follow a quasi-exclusion principle; i.e., their product is roughly a constant. Given a particular design type, the choices of instrumental parameters which tend to increase one will decrease the other. In practice, a compromise is reached and this philosophy is applied here.

The angular extension of the image of the source and the angular projection of the detector entrance window determine the resolution (defined here as $D/\Delta D$, where D is the lattice spacing). These contributions are augmented somewhat by vertical divergence (divergence normal to the plane of dispersion), various alignment errors, sample penetration, etc. To begin with, these latter effects will be considered negligible on the assumption that the over-all resolution required will not be too

high. They will be treated empirically from an experimental viewpoint when necessary.

The parameters to be treated are (see Fig. 2):

R = the radius of the focal circle

ds = the linear extension of the source along the focal circle

dl = the width of the receiving slit

δ = the angular position of the source with respect to the sample

λ = the wavelength of the incident X-ray beam

These parameters are discussed in terms of the dispersion and the resolution of the instrument. The instrumental variable is Ψ, the angle from the center of the sample to a diffraction peak. It can be shown from Fig. 2 that

$$\Psi = 2(\theta + \theta - \delta/2) = 4\theta - \delta, \tag{1}$$

where θ is the Bragg angle of interest corresponding to a diffraction peak. Thus θ is given by

$$\theta = \frac{\Psi + \delta}{4}. \tag{2}$$

From Bragg's Law, the lattice spacing D is

$$D = \frac{n\lambda}{2\sin\theta} = \frac{n\lambda}{2\sin[1/4(\Psi + \delta)]}. \tag{3}$$

The dispersion of the instrument is then

$$\frac{\partial D}{\partial \Psi} = \frac{\partial D}{\partial \delta} = -\frac{n\lambda}{8}\frac{\cos[1/4(\Psi + \delta)]}{\sin^2[1/4(\Psi + \delta)]} = -\frac{n\lambda}{8}\frac{\cos\theta}{\sin^2\theta}. \tag{4}$$

Since $\Psi = a/R$, where a is the circumferential distance from the center of the sample to the diffraction peak, then

$$\partial\Psi = \frac{1}{R}\partial a \tag{5}$$

and

$$\frac{\partial D}{\partial a} = \frac{1}{R}\frac{\partial D}{\partial \Psi} = -\frac{n\lambda}{8R}\frac{\cos[1/4(\Psi + \delta)]}{\sin^2[1/4(\Psi + \delta)]} = -\frac{D}{4R}\cot\theta. \tag{6}$$

The value of $\partial D/\partial a$ for the PEI instrument is

$$\left[\frac{\partial D}{\partial a}\right]_{\text{PEI}} = -\frac{D}{2R}\cot\theta = 2\left[\frac{\partial D}{\partial a}\right]_{\text{JPL}} \tag{7}$$

This factor of two is significant as it means that, with the same radius for both types of focusing, the diffraction peaks are more widely spaced out along the circle in the JPL machine. Alternatively, in order to give the same spacing, the PEI instrument must have twice the radius of the JPL instrument with a subsequent loss of intensity because of the increased source to detector distance. This argument is important since the resolution of either instrument is determined by extensions along the focal circle which cannot be made arbitrarily small. Note also, that for a given D, as λ increases, θ increases and $\cot\theta$ decreases. This is important because the finite extension of the sample along the focal circle imposes a lower limit on the θ, hence an upper limit on the D which can be observed. These limits are eased by going to a longer wavelength of irradiation.

The resolution of the instrument imposes a limit on the precision of the D value measurement. For present purposes the resolution is defined as D/dD. In the simplest approximation, D is a function of only Ψ and δ given by

$$D = D(\Psi, \delta). \tag{8}$$

Thus,

$$dD = \frac{\partial D}{\partial \Psi}d\Psi + \frac{\partial D}{\partial \delta}d\delta. \tag{9}$$

Substituting from Eq. (2) and Eq. (6)

$$dD = -D/4[\cot\theta(d\Psi + d\delta)]. \tag{10}$$

The angular extension of the receiving slit along the focal circle is given by

$$d\Psi = \frac{dl}{R\sin\Psi/2}, \tag{11}$$

and the angular extension of the source along the focal circle is given by

$$d\delta = ds/R. \tag{12}$$

By differentiating Eq. (2) and using the last three equations, the resolution can be expressed as

$$\frac{D}{dD} = -\left(\frac{4}{d\Psi + d\delta}\right)\tan\theta = -\frac{\tan\theta}{d\theta}$$

$$= -\frac{4R}{dl/\sin(\Psi/2) + ds}\tan\theta. \tag{13}$$

From Eq. (13), it is evident that high resolution is achieved with large R, large θ (or λ), and small dl and ds as expected.

As a first approximation, the following parameters were chosen for the instrument:

$$dl = ds = 1 \text{ mm};\ R = 12.7 \text{ cm (5 in.)};\ \delta = 30 \text{ deg}$$

with three possible wavelengths of diffraction.

$$\lambda = 1.54 \text{ Å CuK}\alpha;\ \lambda = 2.74 \text{ Å TiK}\alpha;\ \lambda = 8.32 \text{ Å AlK}\alpha.$$

Table 1 lists some of the properties of the instrument with these parameters.

Table 1. Angular position, D spacings, and resolutions

Ψ, deg	θ, deg	CuK		TiK		AlK		All λ
		D, Å	dF, Å	D, Å	dD, Å	D, Å	dD, Å	D/dD
22.9	13.2	3.37	0.174	5.98	0.307	18.1	0.933	19.4
45.8	19.0	2.37	0.0489	4.22	0.0872	12.8	0.265	48.5
68.8	24.7	1.85	0.0226	3.28	0.0397	9.95	0.121	82.0
91.7	30.4	1.53	0.0137	2.71	0.0221	8.20	0.0670	112
114.6	36.2	1.31	0.0080	2.32	0.0141	7.05	0.0427	165
137.5	41.9	1.16	0.0060	2.05	0.0095	6.13	0.0268	210
160.4	47.6	—	—	1.86	0.0068	5.63	0.0202	272
183.4	53.3	—	—	1.71	0.0051	5.18	0.0155	333
206.3	59.1	—	—	1.60	0.0039	4.84	0.0117	413
229.2	64.8	—	—	1.51	0.0030	4.60	0.0091	505
252.1	70....	—	—	1.45	0.0023	4.41	0.0069	641
275.0	76.3	—	—	1.41	0.0017	4.27	0.0052	826

The three wavelengths show some overlap in D value ranges. The choice of TiKα seems to be a reasonable compromise between the range of D value to be covered and the cutoff at low θ.

4. Results

The breadboard instrument shown in Fig. 3 was constructed using the results outlined in the previous sections as a guide. The aluminum plate on which it is mounted also provides shielding protection. It was decided to make all preliminary alignments and measurements using quartz as a standard. This material has a wealth of diffraction structure. Although the instrument was planned for a Ti target tube, the long time required for procurement made it necessary to use a Cu target tube in the preliminary work. A Cu tube, identical in construction to the one used on the PEI instrument, was used even

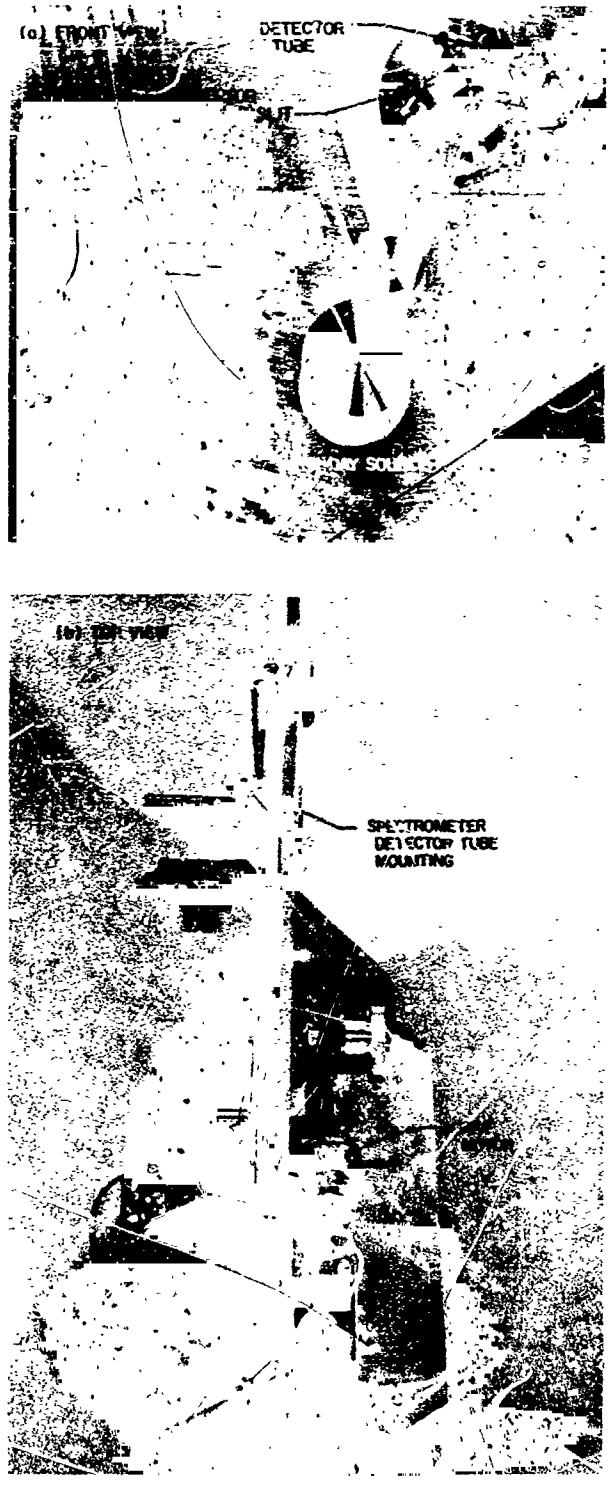

Fig. 3. Breadboard of combined diffractometer–spectrometer

though this meant a loss of the low angle region. However, this made it possible to make a more direct comparison with the performance of the PEI instrument.

The initial results indicated a rather asymmetric line shape, poor resolution, unsatisfactory intensity, and a low signal-to-noise ratio. Fortunately, the instrument was provided with sufficient flexibility, and these faults were quickly corrected. A large part of the trouble was cured by controlling the beam divergence in the plane perpendicular to the plane of dispersion with Soller slits. A radial Soller slit was installed to give a better definition to the line focus, and scatter slits were used to eliminate extraneous signals. A variable width receiving slit could be used to vary resolution, intensity, and signal-to-noise ratio.

A systematic approach to alignment was developed as testing proceeded. The cause of various undesirable features in a diffractogram could be established and corrected.

After a period of initial testing, a comprehensive study was made to compare the JPL instrument with the PEI and standard laboratory diffractometers. Tables 2, 3, 4, and 5 summarize these results. The focusing diffractometer has been operated at three values of receiving slit width (dl). A 400-mesh quartz sample was used in all cases.

The increased intensity with a receiving slit of 0.014 in. sacrifices too much resolution to be acceptable. A slit width of 0.008 in. may be a good compromise. Fig. 4 is the focusing diffractometer scan for dl = 0.008 in., Fig. 5 is the diffraction scan by the laboratory instrument.

Table 2. Operating conditions

	Tube target	Voltage, kv	Current, ma	Counter	Scan speed, deg/min	Receiving slit, in.
Lab diffractometer (Norelco)	Cu	40	10	Scintillation	1	0.003
PEI diffractometer (P-3D)	Cu	25	1	Proportional	0.5	0.006
Focusing diffractometer	Cu	25	1	Proportional	2	0.004 0.008 0.014

Table 3. Intensity, counts/sec

Quartz peak, deg		Laboratory diffractometer	PEI diffractometer	Focusing diffractometer		
				dl = 0.004 in.	dl = 0.008 in.	dl = 0.014 in.
101	(26.6)	2,020	4,550	8,200	10,400	12,200
110	(36.4)	147	345	830	1,390	2,020
112	(50.1)	252	520	1,000	1,640	2,600
203	(68.2)	106	255	430	720	1,280

Table 4. Signal-to-noise

Quartz peak, deg		Laboratory diffractometer	PEI diffractometer	Focusing diffractometer		
				dl = 0.004 in.	dl = 0.008 in.	dl = 0.014 in.
101	(26.6)	100	60	41.0	26	16
110	(36.4)	17.3	8.5	10.4	9.9	8.2
112	(50.1)	38.0	14	30.8	27.4	26
203	(68.2)	19.4	11.3	23.0	24.0	21.2

Table 5. Resolution (half-width)

Quartz peak, deg		Laboratory diffractometer	PEI diffractometer	Focusing diffractometer		
				dl = 0.004 in.	dl = 0.008 in.	dl = 0.014 in.
101	(26.6)	0.18	0.18	0.29	0.42	0.61
110	(36.4)	0.18	0.20	0.21	0.24	0.32
112	(50.1)	0.17	0.25	0.19	0.27	0.30
211	(60.0)	0.15	0.28	0.18	0.20	0.28

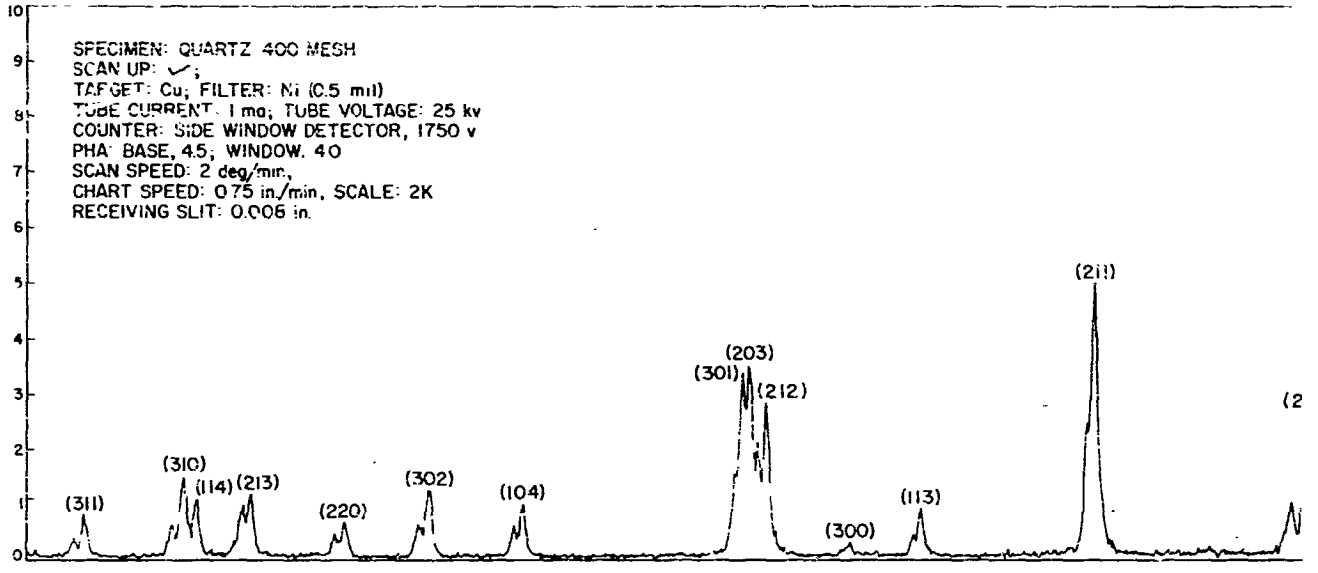

SPECIMEN: QUARTZ 400 MESH
SCAN UP: ✓;
TARGET: Cu, FILTER: Ni
TUBE CURRENT: 0.01 amp; TUBE VOLTAGE: 40 kv
COUNTER: SCINTILLATION, 800 v
PHA: BASE, 3.0, WINDOW, 16.0
SCAN SPEED: 1 deg/min
CHART SPEED: 1/2 in./min; SCALE: 200
DIVERGENCE SLIT: 1 deg; RECEIVING SLIT: 0.003 in.

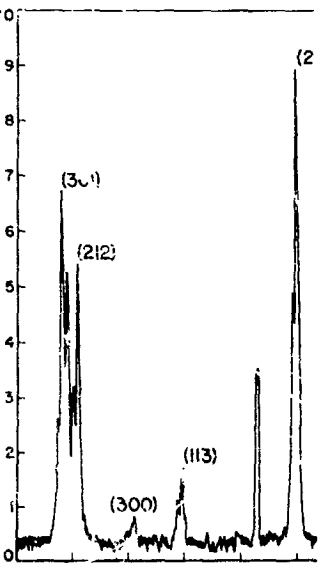

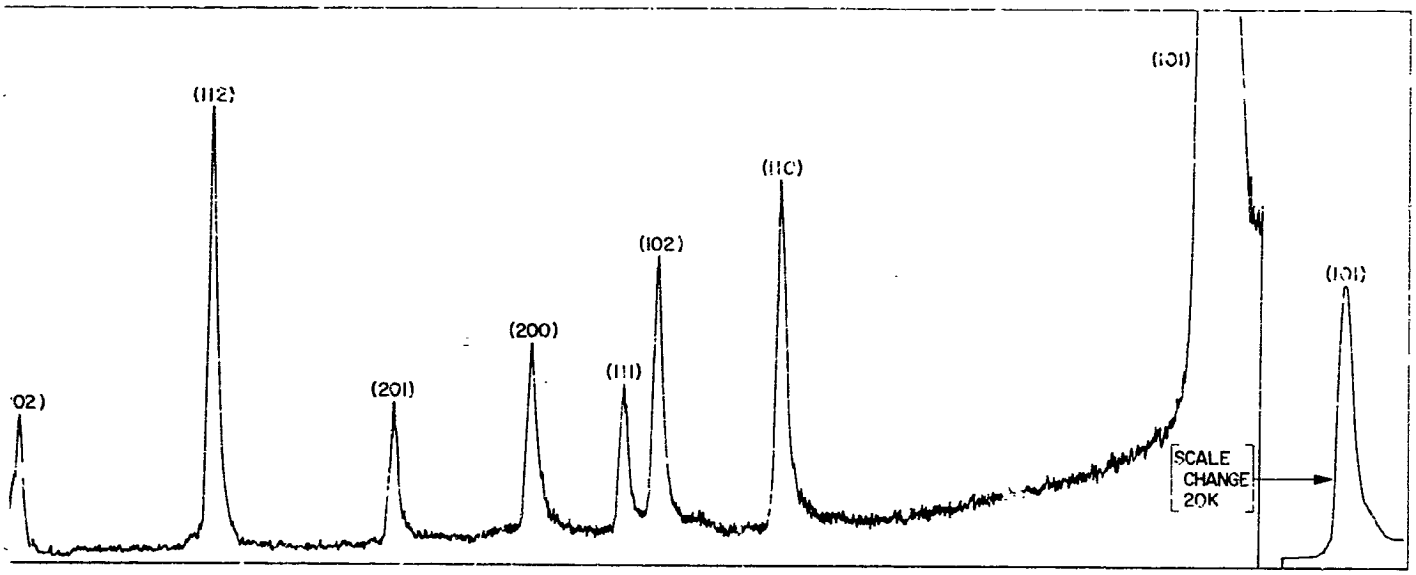

Fig. 4. Quartz scan with focusing diffractometer breadboard

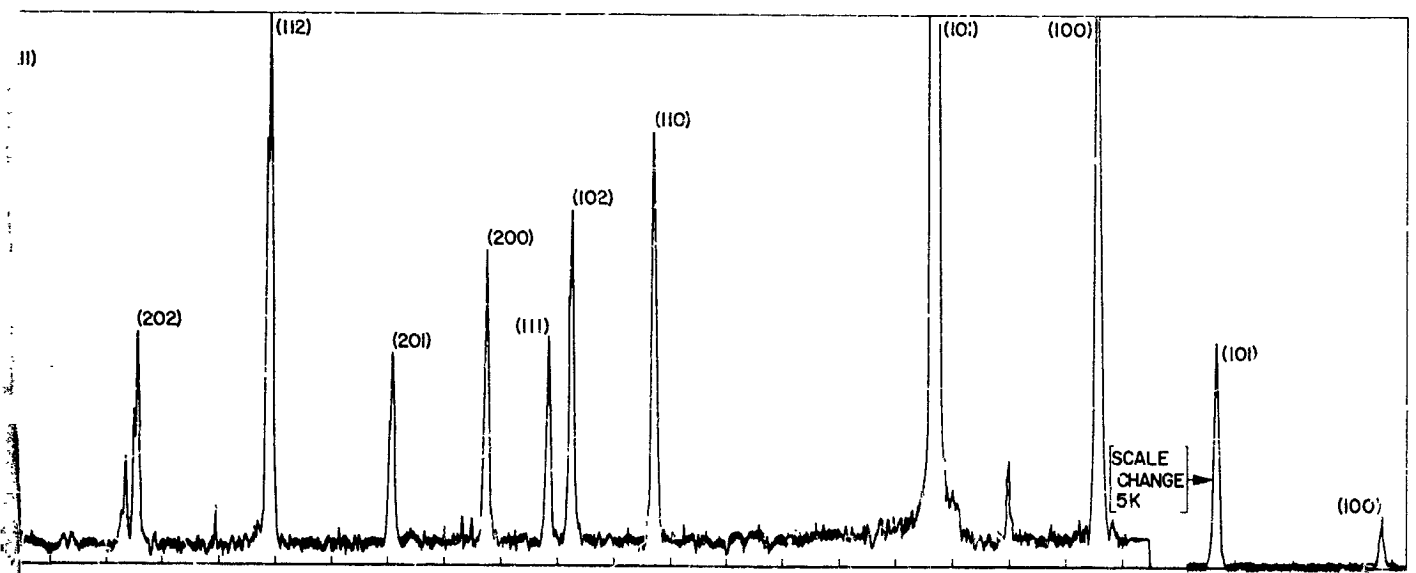

Fig. 5. Quartz scan with laboratory diffractometer

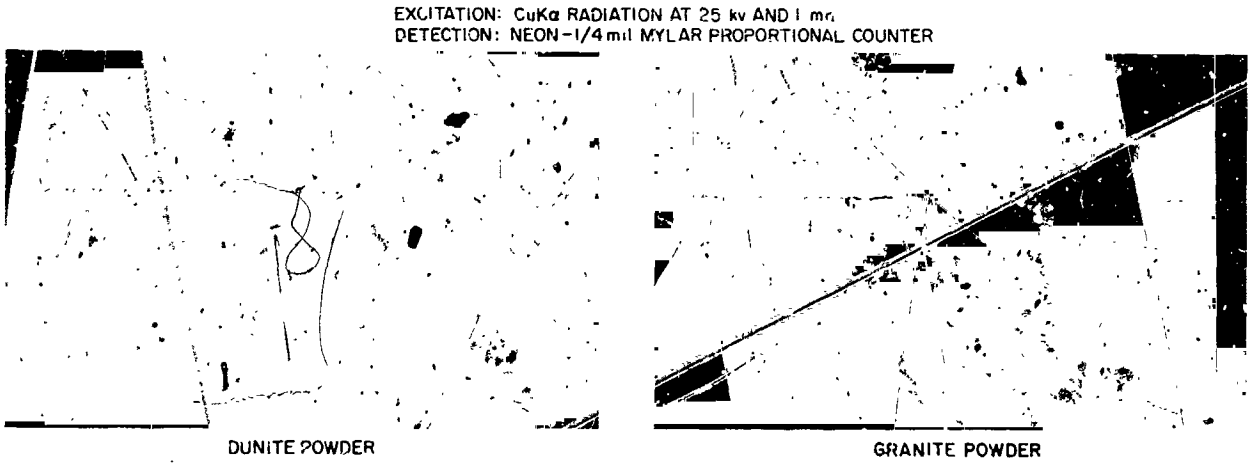

Fig. 6. Nondispersive spectra with combined diffractometer–spectrometer breadboard

The results have confirmed the design expectations. Poor performance at the quartz 101 peak is due to use of Cu radiation instead of Ti, as previously discussed.

The feasibility of nondispersive elemental analysis has been discussed in *SPS 37-31*, Vol. IV, pp. 273–277. In this design, the nondispersive spectrometer shares a common X-ray tube and high voltage supply with the diffractometer. It requires, in addition, a system of pulse height analysis for energy discrimination. The spectrometer is capable of detecting all elements present as major constituents from atomic number 11 (Na), and higher. Resolution of adjacent elements is difficult but can be assisted by the use of selective absorption filters. Fig. 6 shows two contrasting nondispersive spectra for elemental analysis obtained with the combined instrument.

5. Future Plans

The installation of a Ti target will be accomplished soon. It is expected that this will improve the resolution of the quartz lines by putting them in a more favorable angular region (Table 1). The upper region of the D spacing range will be extended and the low angle region, where sample scattering is excessive (Fig. 4), will be avoided. Preliminary tests indicate that the line intensity will remain high. It also is expected that the quantity of scattered radiation passing through the detector can be reduced by improvements in shielding.

The low angle limit of scan of the JPL diffractometer breadboard is 24 deg (2θ), which for titanium radiation corresponds to a D spacing of 6.5 Å. This compares with a scanning limit of 7 deg and a D spacing of approximately 10 Å for the PEI diffractometer. If the region above 6.5 Å is considered sufficiently important geologically, it may be possible to scan up to 15 Å with the softer radiation from an aluminum target (Table 1).

A further significant feature must be noted. The focusing diffractometer is scanned by moving only the detector. It is possible to mount a number of detectors, say eight, on the focusing circle, each one covering a portion of the scanning range with some overlap with its neighbor. The detectors would scan simultaneously. The normal scanning time for the JPL instrument is less than half that of the PEI instrument (Table 2). The combination of multiple detectors and faster scanning is expected to allow the focusing diffractometer to obtain a pattern in approximately one-tenth the time required by the PEI diffractometer. These same features, plus the intensity ratio of three in favor of the JPL design, would provide an energy (watt-hour) saving in spacecraft power of a factor of thirty.

The authors wish to thank N. L. Nickle for providing the standard diffractometer scan.

References

1. Parrish, W., "Lunar Diffractometer Geometry," (in press), 1965.

2. Speed, R. C., Nash, D. B., and Nickle, N. L., "A Lunar X-Ray Diffraction Experiment," *Advances in X-Ray Analysis*, Vol. 8, Plenum Press, 1964.

3. Miller, D. C., and Hendee, C. F., "X-Ray Analysis of the Lunar Surface," Paper presented at the National IAS-ARS joint meeting, Los Angeles, California, June 13–16, 1961.

4. Das Gupta, K., and Pan, N., "A New Experimental Technique for X-Ray Diffraction Study," *Journal of Scientific and Industrial Research*, No. 17B, pp. 131–133, India, 1958.

XXIII. Communications Elements Research

A. Low-Noise Amplifiers

C. T. Stelzried, W. V. T. Rusch and M. S. Reid[1]

1. 90-Gc Millimeter Wave Work,

C. T. Stelzried and W. V. T. Rusch

The objective of the millimeter wave work is to investigate millimeter wave components and techniques to ascertain the future applicability of this frequency range to space communications and tracking. This involves the development of instrumentation for accurate determination of insertion loss, VSWR, power and equivalent noise temperature of passive elements, and gain and bandwidth of active elements at millimeter wavelength. Observations of the Moon taken during the total lunar eclipse on the night of December 18–19, 1964 have been reduced and the data presented. The equivalent noise temperature of the calibrating noise source has been measured.

In order to bring together state-of-the-art millimeter wave circuit elements and evaluate their use in a system, a radio telescope consisting of a 60-in. antenna and a superheterodyne radiometer have been built (*SPS* 37-28, Vol. IV, p. 147 and 37-29, Vol. IV, p. 191). The radio telescope was used to observe the 90-Gc temperature of the Moon during the December 30, 1963 eclipse (*SPS 37-26*, Vol. IV, p. 181) and the most recent eclipse, December 18, 1964. These experiments were joint efforts by personnel from JPL and the Electrical Engineering Department of the University of Southern California.

a. Radiometer-waveguide calibrations. Data from the 71 observations of the Moon during the total lunar eclipse on the night of December 18–19, 1964 have been reduced (*SPS* 37-32, Vol. IV, p. 243). The data reductions were made relative to the gas tube. Fig. 1 is a block diagram of the millimeter radiometer. The "hot" loads are temperature-controlled with mercury thermostats.

A breakdown of the waveguide losses is shown in Fig. 2. The terminations have measured thermal temperatures T_1 and T_2. The ambient temperature is T_0. The waveguide losses (power ratio) are:

L_{11} = Loss from T_1 with temperature distribution from T_1 to T_0.

L_{21} = Loss from T_2 with temperature distribution from T_2 to T_0.

[1]On leave of absence from National Institute for Telecommunications Research, Johannesburg, South Africa.

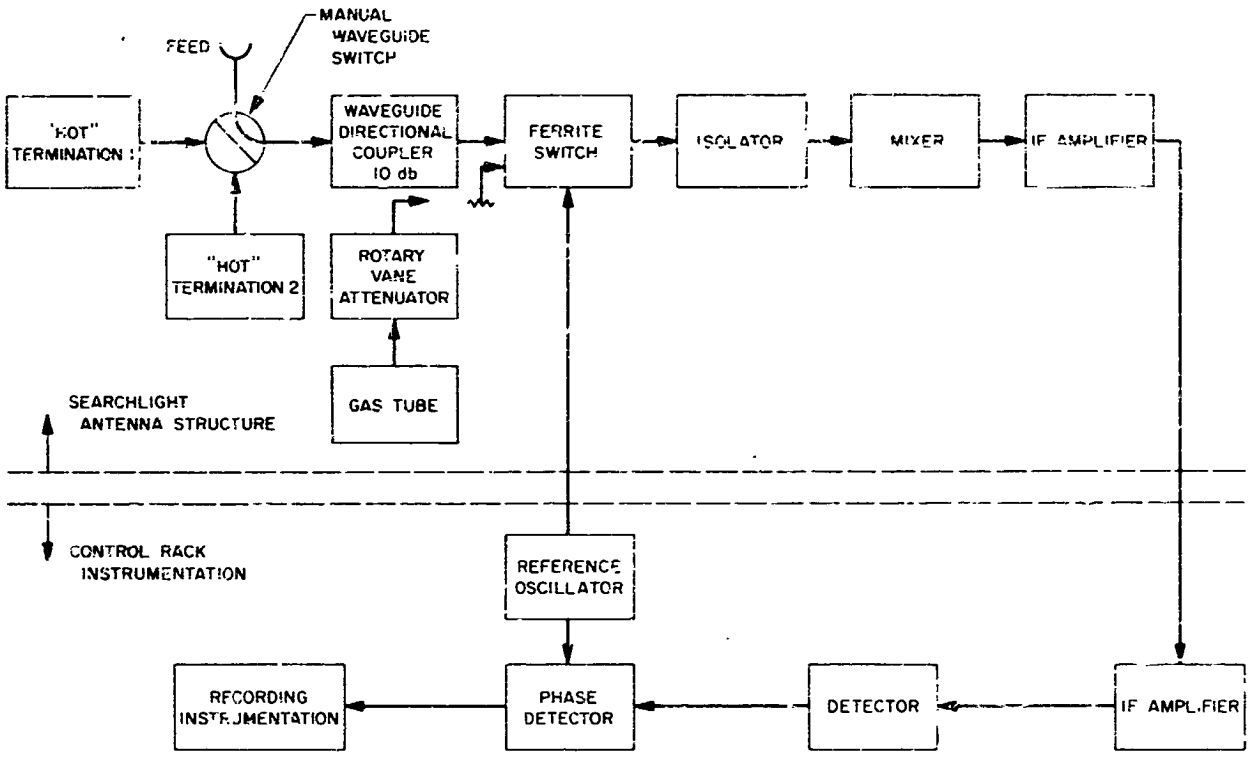

Fig. 1. Millimeter radiometer

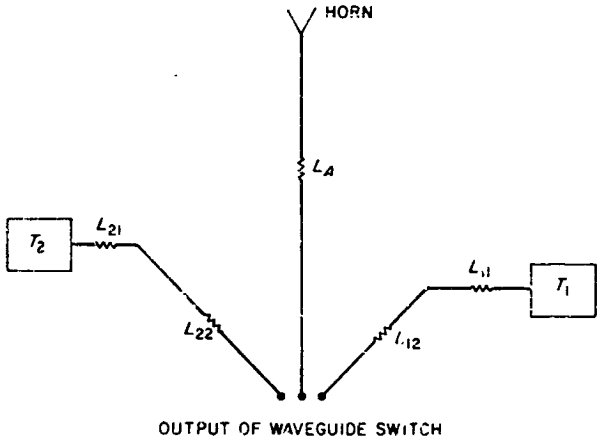

Fig. 2. 90-Gc radiometer waveguide losses

L_{12} = Loss from T_1 with constant temperature T_0 to the output of the waveguide switch.

L_{22} = Loss from T_2 with constant temperature T_0 to the output of the waveguide switch.

L_A = Loss from the horn with constant temperature T_0 to the output of the waveguide switch.

The equivalent noise temperature difference $(T_2' - T_1')$ at the output of the waveguide switch due to T_2 and T_1, accounting for the waveguide losses and assuming a linear temperature distribution in L_{11} and L_{21} is (Ref. 1)

$$(T_2' - T_1') = \frac{\log_{10} e}{10}\left[(T_2 - T_0)\frac{L_{21} - 1}{L_{21}L_{22}L_{21}\,(\text{db})} - (T_1 - T_0)\frac{L_{11} - 1}{L_{11}L_{12}\,(\text{db})}\right]. \quad (1)$$

The losses were measured with the 90-Gc insertion loss test set (Ref. 2) to be

$$L_{11} = 0.169\,\text{db}$$

$$L_{12} = 0.327\,\text{db}$$

$$L_{21} = 0.156\,\text{db}$$

$$L_{22} = 0.376\,\text{db}$$

Substituting into Eq. (1):

$$(T_2' - T_1') = 0.9009T_2 - 0.9053T_1 + 0.00863T_0. \quad (2)$$

The "hot" waveguide terminations were used to determine the equivalent noise temperature of the noise source defined at the output of the waveguide switch. The rotary vane precision attenuator, shown in Fig. 1 between the side arm of the 10-db directional coupler and the noise source, was set to 10 db for both the eclipse measurements and the subsequent calibrations. The "hot" loads each have two separate mercury thermostats. The calibrations were made with the nominal "hot" load temperatures given in Table 1. The temperatures were checked with thermocouples during the calibrations. The radiometer output for the calibrations was displayed on a digital paper recorder. The digital recorder output difference $(T_2' - T_1')$ (digital, average) due to switching the radiometer between T_2 and T_1 was determined by averaging the sequence of 10 measurements, each of which consisted of approximately 10 counts with 10 sec between counts. The output due to the gas tube T_E (digital, average) was determined in the same way, by turning the gas tube on and off sequentially. The equivalent noise temperature of the noise source defined at the waveguide switch output is:

$$T_E(^\circ\mathrm{K}) = T_E(\text{digital, average}) \times \frac{(T_2' - T_1')(^\circ\mathrm{K})}{(T_2' - T_1')(\text{digital, average})} \quad (3)$$

Table 1. Identification of "hot" load temperatures

Test identification No.	Nominal temperature, °K	
	T_1	T_2
1	40	95
2	40	145
3	50	145
4	50	95

The results of three separate evaluation sequences are given in Table 2. The averages and standard deviations, σ are indicated by date and test number. The standard deviations are not affected by the test number but drop significantly with the later dates. This could be because of increased care being taken with the manual waveguide switch, radiometer, and test sequence. Significantly lower standard deviations listed by test number, would indicate an error in the thermal temperatures. The over-all average determined from the daily average weighted by the square of the probable error is 126°K. This calibration is defined at the output of the waveguide switch. The measured Moon temperatures also will be defined at this point. To obtain the Moon brightness temperature, account must be taken of L_a, atmospheric loss, Moon diameter, and antenna gain and beamwidth. These effects are under investigation.

2. *Equivalent Noise Temperature of a Precision Waveguide Microwave Termination,*

C. T. Stelzried and M. S. Reid

a. Summary. The equivalent input noise temperature derivation for a cryogenic cooled waveguide termination is reviewed in this article. The effects of barometric pressure, ambient temperature and frequency are taken into account with the calibration formula

$$T' = T'' + a_- P + b\Delta T_0 + c_- f$$

The terms are defined and derived in the text. Account is taken of both dielectric and waveguide wall conduction losses in the frequency term.

A description is given of a compact, precision WR-430 waveguide liquid nitrogen cooled termination to be used primarily in the laboratory for calibration and evaluation of traveling wave maser amplifiers. Details are given of the

Table 2. 90-Gc radiometer noise source evaluations

Test No.	T_N, °K				
	Date			Average	σ
	January 27, 1965	January 28, 1965	February 1, 1965		
1	136.8	119.9	126.2	128.3	7.84
2		119.1	130.4	124.8	5.60
3	117.6	111.3	127.3	118.7	6.62
4	120.9	135.7	123.1	126.6	6.49
Average	125.1	121.5	127.3	124.5 / 124.6	
σ	10.15	8.86	2.63		

calibration techniques. The insertion loss measurements of the waveguide components are made to a probable error on the order of 0.0001 db.

b. Introduction. Cryogenic cooled microwave terminations are used to calibrate the low-noise receiving systems in use at Goldstone. These calibrations are used in the radar–radio astronomy observation and spacecraft tracking missions to determine system sensitivity, and also in data interpretation. Calibration precision and long-term stability are prime requirements for the termination.

c. Calibration theory. The equivalent input noise temperature T' for a transmission line of length l with an arbitrary temperature distribution $T_L(x)$ and loss L independent of temperature with a termination at a temperature T is (Ref. 1)

$$T' = Te^{-2\alpha l} + 2\alpha \int_0^l e^{2\alpha(x-l)} T_L(x)\, dx \tag{1}$$

where

x = distance from termination

α = attenuation constant

$$2\alpha l = \frac{L(\text{db})}{10 \log_{10} e} \simeq 0.23026 L(\text{db})$$

With a linear temperature distribution from T to T_0 and loss L_1 on the first section of the transmission line and a constant temperature distribution T_0 and loss L_2 in the second section of the transmission line

$$T' = T + (T_0 - T)\left[1 - \frac{(L_1 - 1)\, 10 \log_{10} e}{L_1 L_2 L_1(\text{db})}\right]. \tag{2}$$

With small losses, this can be approximated to good accuracy by

$$T' = T + 0.23026 (T_0 - T) \times \left[\frac{L_1}{2}(\text{db}) + L_2(\text{db}) - \left(\frac{L_1}{6}\right)^2 (\text{db}) - \left(\frac{L_1}{2}\right)^2 (\text{db}) - \frac{L_1}{2}(\text{db})\, L_2(\text{db})\right]. \tag{3}$$

Eq. (3) can be written

$$T' = T + (T_0 - T) L_0. \tag{4}$$

A rectangular waveguide operated in the TE_{10} mode has dielectric losses given by (Ref. 3)

$$\alpha_d = \frac{k\varepsilon''/\varepsilon'}{2[1 - (fc/f)^2]^{1/2}} \tag{5}$$

where

$$k = 2\pi f (\mu\varepsilon)^{1/2}$$

$\varepsilon''/\varepsilon'$ = loss tangent

fc = cutoff frequency $= \dfrac{c}{2a}$

c = propagation velocity $\simeq 3 \times 10^{10}$ cm sec

f = operating frequency

Differentiating with respect to f (assuming ε'' ε' constant over a small frequency range and dividing by α_d)

$$\frac{d\alpha_d}{\alpha_d} = \left[\frac{\left(\frac{f}{fc}\right)^2 - 2}{\left(\frac{f}{fc}\right)^2 - 1}\right]\frac{df}{f}. \tag{6}$$

Similarly for the wall losses for a rectangular waveguide operated in the TE_{10} mode (*SPS 37-32*, Vol. IV, p. 247)

$$\frac{d\alpha_c}{\alpha_c} = \left\{\frac{\left(\frac{f}{fc}\right)^4 - 6\left(\frac{f}{fc}\right)^2 + 1}{2\left[\left(\frac{f}{fc}\right)^4 - 1\right]}\right\}\frac{df}{f}. \tag{7}$$

The calibrated termination equivalent noise temperature can be presented to a good approximation assuming small transmission line losses in the form

$$T' \simeq T'' + a\Delta P + b\Delta T_0 + c\Delta f \tag{8}$$

where

$$P = 760 + \Delta P$$

$$T_0 = 273 + \Delta T_0$$

$$f = f_0 + \Delta f$$

and

$T'' + T(760) + [273 - T(760)]\, L_0$

a = pressure coefficient of cryogenic liquid (°K/mm Hg)

$b = L_0$

$$c = (0.23026)\frac{[273 - T(760)]}{f_0}\left[\left(\frac{L_1}{2}\right)_d (\text{db}) + (L_2)_d(\text{db})\right] \times \left[\frac{\left(\frac{f_0}{f_c}\right)^2 - 2}{\left(\frac{f_0}{f_c}\right)^2 - 1}\right] + \left[\left(\frac{L_1}{2}\right)_c (\text{db}) + (L_2)_c(\text{db})\right] \times \left\{\frac{\left(\frac{f_0}{f_c}\right)^4 - 6\left(\frac{f_0}{f_c}\right)^2 + 1}{2\left[\left(\frac{f_0}{f_c}\right)^4 - 1\right]}\right\}$$

with

$T(760)$ = cryogenic liquid temperature at 760 mm Hg (°K)

$(L_1)_d$ db) = component of loss L_1 due to dielectric

$(L_2)_d$ (db) = component of loss L_2 due to dielectric

$(L_1)_c$ (db) = component of loss L_1 due to wall conduction losses

$(L_2)_c$ (db) = component of loss L_2 due to wall conduction losses

$$L = \frac{L_1}{2}(\text{db}) + L_2(\text{db}) - \left(\frac{L_1}{6}\right)^2(\text{db})\,L_2(\text{db})$$

f_0 = nominal evaluation frequency

d. WR-430 waveguide liquid nitrogen cooled termination. A compact precision WR-430 waveguide liquid nitrogen cooled termination is under construction for use in calibrating low-noise receiving systems. The principal components are shown in Fig. 3 and described here. This termination should be especially useful for maser amplifier evaluations in the laboratory. The 5-liter Dewar has an operating life of 5 hr without the termination. The corresponding operating life with the termination installed should approach several hours. A coaxial termination is used to insure that the load element is at the temperature of the cryogenic liquid. It is possible to have some heating of a waveguide termination due to infrared radiation and conductive heating. The aluminum mounting plate will be heated to maintain a constant temperature on this portion of the waveguide and to prevent cooling and possible dew formation.

Since the insertion loss measurements are particularly important in the equivalent noise temperature evaluation, considerable effort has been expended to achieve maximum accuracy. The insertion loss is determined (Ref. 2) by measuring the difference in signal level due to the unknown. The calibration heads (Fig. 4) are mated to produce the reference signal level and the unknown is inserted between the heads to produce the difference signal level. The heads are matched with a reflectometer tuned with a precision WR-430 waveguide sliding termination. This process is repeated a number of times and an average taken. Statistical methods may be applied to the data to estimate measurement errors. The VSWR looking into each head is better than 1.005. In a series of measurements, the first and last measurements are not equally weighted when an average is taken of the differences. A better way to average the sequence of measurements can be derived using the least-squares method (Ref. 4). If a constant $L_1/2$ is added to each power level measurement with the unknown disconnected and the

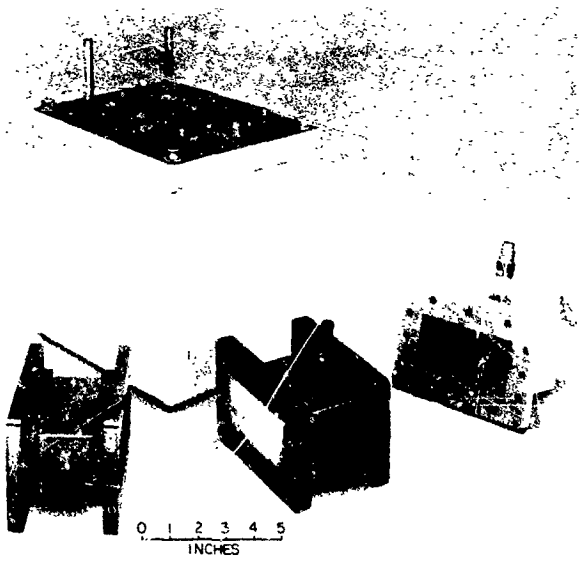

Fig. 3. WR-430 waveguide liquid nitrogen cooled termination assembly and Dewar

Fig. 4. Calibration heads of insertion loss test set

same constants subtracted from each power level measurement with the unknown connected, the standard deviation σ of the measurements from the best-fit straight line, $a + bx$ is

$$(\sigma)^2 = \frac{\sum_o \left(y + \frac{\overline{L}}{2} - a - bx\right)^2 + \sum_e \left(y - \frac{\overline{L}}{2} - a - bx\right)^2}{m} \tag{9}$$

where

o = the odd measurements (unknown disconnected)

e = the even measurements (unknown connected)

m = total number of measurements

Differentiating with respect to a, b, and $\overline{L}$ equating to zero,

$$\left.\begin{aligned} \sum_o \left(y + \frac{\overline{L}}{2} - a - bx\right) &= 0 = \sum_e \left(y - \frac{\overline{L}}{2} - a - bx\right) \\ \sum_o x\left(y + \frac{\overline{L}}{2} - a - bx\right) &= 0 = \sum_e x\left(y - \frac{\overline{L}}{2} - a - bx\right) \\ \sum_o \left(y + \frac{\overline{L}}{2} - a - bx\right) &= 0 = \sum_e \left(y - \frac{\overline{L}}{2} - a - bx\right) \end{aligned}\right\} \tag{10}$$

$$\left.\begin{aligned} -\frac{\overline{L}}{2} - am + b\sum x &= \sum y \\ \frac{\overline{L}}{2}\left(\sum_o x - \sum_e x\right) + a\sum x + b\sum x^2 &= \sum xy \\ \frac{\overline{L}}{2} + a + b\left(\sum_o x - \sum_e x\right) &= \left(\sum_o y - \sum_e y\right) \end{aligned}\right\} \tag{11}$$

Solving for $\overline{L}$,

$$\overline{L} = 2\,\frac{\begin{vmatrix} \sum y & m & \sum x \\ \sum xy & \sum x & \sum x^2 \\ \left(\sum_o y - \sum_e y\right) & 1 & \left(\sum_o x - \sum_e x\right) \end{vmatrix}}{\begin{vmatrix} -1 & m & \sum x \\ -\left(\sum_o x - \sum_e x\right) & \sum x & \sum x^2 \\ -m & 1 & \left(\sum_o x - \sum_e x\right) \end{vmatrix}} \tag{12}$$

In this solution the values of x are the measurement numbers which are equally spaced. A simplification can be made for this situation if the middle measurement number is chosen as the origin so that the summation of all odd powers of x is zero. Then

$$\left.\begin{aligned} \overline{L} &= \frac{\sum_e y}{(m-1)/2} - \frac{\sum_o y}{(m+1)/2} \\ a &= \frac{\sum_e y}{m-1} - \frac{\sum_o y}{m-1} \\ b &= \frac{\sum xy}{\sum x^2} \end{aligned}\right\} \tag{13}$$

The probable errors of the data points are

$$\left.\begin{aligned} PE_{vo} &= 0.6745\sqrt{\frac{\sum_o \left(y + \frac{\overline{L}}{2} - a - bx\right)^2}{(m+1)/2 - 1}} \\ PE_{ve} &= 0.6745\sqrt{\frac{\sum_e \left(y - \frac{\overline{L}}{2} - a - bx\right)^2}{(m-1)/2 - 1}} \end{aligned}\right\} \tag{14}$$

The probable error of $\overline{L}$, the mean insertion loss, is found by expanding $\overline{L}$ in terms of the coefficients of the data points and summing (Ref. 4, p. 229) to be

$$PE_{\overline{L}} = \sqrt{\frac{(PE_{vo})^2}{(m+1)/2} + \frac{(PE_{ve})^2}{(m-1)/2}} \tag{15}$$

Eqs. (13), (14), and (15) have been programmed for the 1620 computer[2] and are used with the insertion loss measurements data reduction. If the probable errors in Eq. (14) are significantly different, a fault is indicated in one of the transmission line connections. The probable errors given by Eqs. (14) and (15) are due only to the random measurement errors and do not indicate bias or nonlinearity errors.

Several sets of measurements were made on various waveguide sections for the calibration of the cooled termination. Each transmission line section (Part Nos. 226 and 239) shown in Fig. 3 was measured, as well as a section of copper waveguide (Part No. 240), and various combinations of Nos. 239 and 240. The insertion loss of Nos. 226 and 239 is fundamental to the calibration of the cooled termination. No. 240 was examined so that a silicone grease film and a Mylar window could be evaluated in conjunction with No. 239.

[2]Lois Busch of JPL programmed the 1620 computer for the insertion loss measurement data reduction.

No. 226 is a stainless steel WR-430 waveguide section 4.0 in. long. It has a wall thickness of 0.025 in. and copper plating and gold flash on the inside of 0.000120 and 0.000010 in., respectively. It is filled with a half-wavelength piece of polystyrene foam. The VSWR of this section is less than 1.005. The polystyrene window is required to prevent moisture condensation which will form on thin membrane windows. No. 239 is a 4.0-in.-long brass waveguide section with an irridite plate. No. 240 is a 4.0-in.-long copper waveguide section.

The following insertion loss measurements were made:

Part Nos. 226, 239, and 240 alone.

Part Nos. 239 and 240 in combination.

Part Nos. 239 and 240 with a 0.001-in.-thick Mylar window between them.

Part Nos. 239 and 240 with a thin silicone grease film on their mating flanges.

Table 3. Insertion loss measurements: Set No. 1 at 2295 Mc; WR-430 waveguide section; Part No. 239

Ratio, R	y, db	Difference from straight-line fit, db × 10^{-3}	Insertion loss L, db
0.99558	0.038476	−0.6689	0.00279
0.99526	0.041268	0.2622	0.00271
0.99557	0.038563	0.3430	0.00183
0.99536	0.040395	0.3142	0.00270
0.99567	0.037691	0.3953	0.00105
0.99555	0.038738	−0.4190	0.00253
0.99584	0.036208	−0.1685	0.00192
0.99559	0.038127	−0.1049	0.00262
0.99592	0.035510	−0.0641	0.00174
0.99572	0.037254	−0.0526	0.00270
0.99603	0.034551	0.0295	

Straight-line constants: $a = 0.0380$ db, $b = -0.00462$ db/No.
Mean insertion loss: $\bar{L} = 0.00232$ db
Probable errors: $PEy_a = 0.00026$ db
$PEy_b = 0.00020$ db
$PE_{\bar{L}} = 0.00014$ db

On each unknown, 5 sets of 11 measurements were made. After every set, the match of each calibration head was checked and corrected if the VSWR became 1.005 or worse. The flanges of the calibration heads and of the unknown were lapped after every set as well. All of the waveguide flanges were pinned, except the stainless steel section, No. 226.

Table 3 shows a typical insertion loss measurement set taken on Part No. 239. This table is also the format of the computer output. The first column lists the readings taken. The y values are these ratios converted to decibels by

$$y = -20 \log_{10} R. \tag{16}$$

The third column shows the difference of each y value from the straight line fit, and the last column is the insertion loss in decibels for each pair of readings. The probable errors from Eqs. (14) and (15) also are shown.

The averages for the five sets of independent measurements for Part No. 239 are shown in Table 4. The mean insertion loss for each set $\bar{L}_1$ through $\bar{L}_5$, is shown as well as the best-fit straight line constants and the probable errors of the odd and even y values, and, finally, the probable error of the mean insertion loss of each set. The weighted mean of the insertion loss is then found with the probable error of each set used as a weighting factor, and the grand mean $\bar{\bar{L}}_1$ is shown in Table 5. A nonweighted mean, $\bar{\bar{L}}_2$, of $\bar{L}_1$ through $\bar{L}_5$ also is shown in Table 5, with the associated probable error. The average measured insertion loss of each set is shown graphically, with a horizontal bar, in Fig. 5. The associated probable errors are shown as vertical lines. The grand weighted mean $\bar{\bar{L}}_1$ and its probable error are shown.

Measurement time is approximately 3 hr for the five sets of readings required for a grand mean.

Table 5 summarizes the various insertion loss measurements. It may be seen that the weighted insertion loss

Table 4. Mean insertion loss of waveguide Part No. 239 at 2295 Mc

Set No.	Mean insertion loss $\bar{L}$, db	Straight-line constants		Probable errors		
		a	b	PEy_a, db	PEy_b, db	$PE_{\bar{L}}$, db
1	0.00232	0.0380	−0.000462	0.000267	0.000020	0.00014
2	0.00259	0.0327	−0.000044	0.000240	0.000109	0.00011
3	0.00227	0.0321	−0.000021	0.000157	0.000175	0.00010
4	0.00229	0.0319	−0.000080	0.000167	0.000066	0.00007
5	0.00249	0.0294	−0.000266	0.000169	0.000094	0.00008

Table 5. Summary of insertion loss measurements at 2295 Mc

Description	Insertion loss $\bar{\bar{L}}_1$, db	Probable error of $\bar{\bar{L}}_1$, db $\times 10^{-4}$	Insertion loss $\bar{\bar{L}}_2$, db	Probable error of $\bar{\bar{L}}_2$, db $\times 10^{-4}$
Part No. 226, WR-430 stainless steel waveguide section	0.00689	0.40	0.00689	0.26
Part No. 239, WR-430 brass waveguide section	0.00239	0.42	0.00239	0.42
Part No. 240, WR-430 copper waveguide section	0.00123	0.40	0.00126	0.34
Sum of Part Nos. 239 and 240	0.00362	0.58	0.00365	0.54
Part Nos. 239 and 240 in combination	0.00361	0.47	0.00360	0.34
Part Nos. 239 and 240 with Mylar window	0.00422	0.45	0.00423	0.34
Part Nos. 239 and 240 with silicone grease	0.00355	0.35	0.00349	0.35

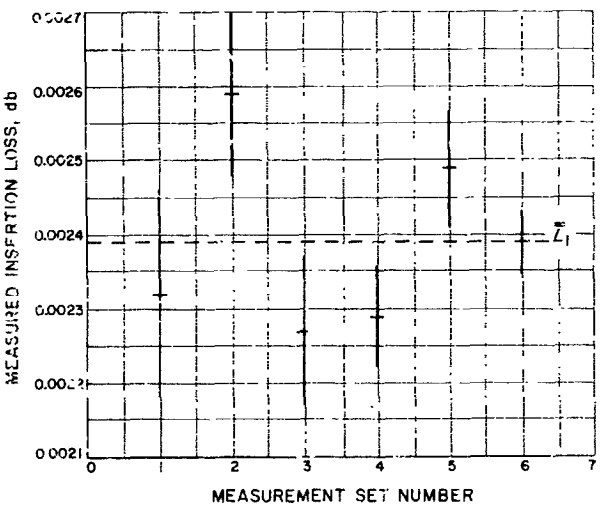

Fig. 5. Insertion loss measurements of Part No. 239 at 2295 Mc

$\bar{\bar{L}}_1$ is very close to the nonweighted insertion loss $\bar{\bar{L}}_2$, and differs at the most by only a few parts in 10^6. The probable errors of $\bar{\bar{L}}_1$ and $\bar{\bar{L}}_2$ are essentially the same which is expected assuming only random measurement errors. If the probable error of $\bar{\bar{L}}_2$ was appreciably greater than $\bar{\bar{L}}_1$, bias errors would be indicated for some of the individual sets

The insertion loss of the brass waveguide section No. 239 is shown to be 0.00239 db with a probable error of 0.42×10^{-4} db and the insertion loss of the copper section No. 240 is 0.00123 db with a probable error of 0.40×10^{-4} db The sum of these two insertion losses is 0.00362 db with their probable errors combined as 0.58×10^{-4} db. This figure of 0.00362 db must be compared with the measured value of the insertion loss of Nos. 239 and 240 in combination, which is 0.00361 db—a difference of 10^{-5} db. It must be noted that the difference in $\bar{\bar{L}}_2$ values is 5×10^{-5} db. The probable errors of the sums are somewhat higher than the probable errors of the combinations, as expected.

The theoretical insertion loss for No. 240 (copper waveguide 4 in. long) is (Ref. 5) 0.00091 db. This theoretical value does not account for surface roughness and metal impurities and nonhomogenity. A correction estimate for surface roughness increases the insertion loss by 15% (Ref. 6) to 0.00105 db. This agrees with our measurement within 0.00018 db.

Part No. 240 was then used in conjunction with No. 239 to evaluate a 0.001-in.-thick Mylar window. This material is presently under consideration as an additional window. Table 5 shows that the excess insertion loss due to the Mylar window is 0.00061 db with a probable error of 0.65×10^{-4} db.

A thin silicone grease film is required between the flanges of the waveguide sections of dissimilar metals in the cooled termination. This film helps prevent corrosion which, with time, changes the insertion loss hence the calibration of the termination. The effect of a silicone grease film between the flanges of Nos. 239 and 240 was investigated. The results, presented Table 5, show that: (1) the effect of the film on the insertion loss is negligible, and (2) the insertion loss appears to drop when the grease is added. The lower insertion loss in (2) may be apparent, and explained by the spread of the probable errors. On the other hand, the effect may

be real and the insertion loss lower owing to the high dielectric content of the grease filling the low spots in the flange faces and thus decreasing the reactance. The average of the probable errors of the measured values of $\bar{L}_1$ from Table 5 is 0.42×10^{-4}.

It may be concluded, therefore, that if statistical methods are used with a sufficient number of observations, and if the measurement procedure is carried out as described in this report with the indicated precautions, then insertion loss can be measured with a probable error of 0.4×10^{-4} db. This does not include the bias and nonrandom errors. It is anticipated that the WR-430 waveguide liquid nitrogen cooled termination can be calibrated to an over-all accuracy of better than 0.1°K.

B. Solid-State Circuits

R. Brantner

1. Summary

Some insulated-gate field effect transistors (IGFET) have been tested to determine their potential use as voltage-controlled resistors. A voltage-tunable filter using these devices has been constructed and tested.

2. Test Results

Four IGFET, Type 2N3609 (GME),[1] have been obtained for experimental purposes. The 2N3609 consists of two isolated IGFET in a TO-5 package; they are *P*-channel devices that operate in the enhancement mode. Each unit was checked to determine the variation of dynamic channel resistance versus control voltage for each 2N3609 and the degree of tracking between the two halves of each unit. A typical curve of dynamic channel resistance versus gate-to-channel (control) voltage is shown in Fig. 6. Threshold voltage fell between −3.0 and −3.5 v for all units, and the dynamic resistance could be varied from well over 10 MΩ to approximately 300 Ω. The tracking error of each unit was calculated from the dynamic resistance (r_{ch}) of each half using the relationship:

$$\text{tracking error} = \frac{r_{ch1} - r_{ch2}}{r_{ch2}} \times 100\%$$

[1]General-Micro Electronics, Inc., Santa Clara, Calif.

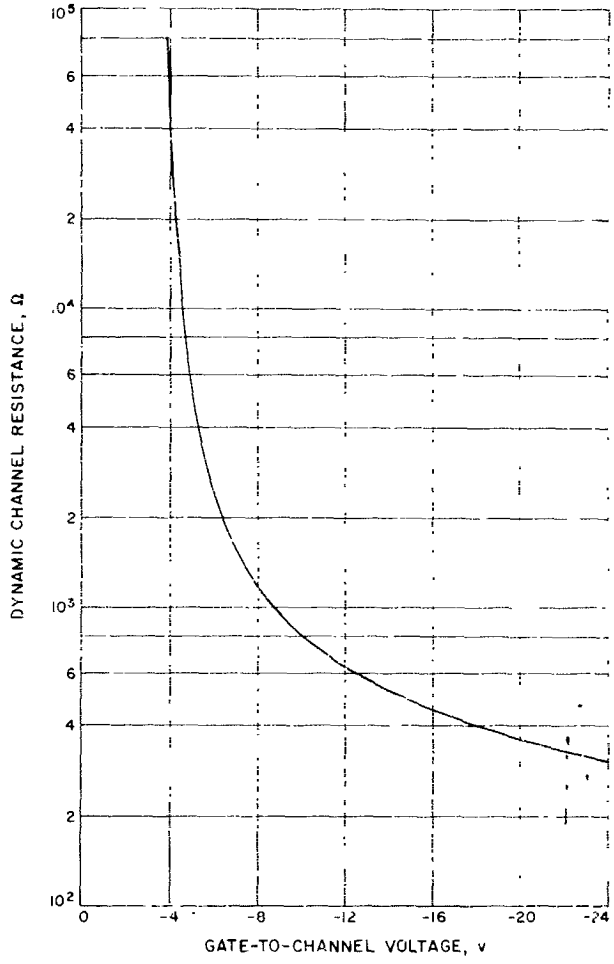

Fig. 6. Dynamic channel resistance versus gate voltage

where r_{ch1} was taken to be the higher of the two resistance values. A plot of tracking error versus gate-to-channel voltage is shown in Fig. 7. As can be seen, tracking is fairly good above −5 to −6 v of control voltage. This corresponds to a typical resistance range of about 300 Ω minimum to a maximum of 2.5 to 7 kΩ, depending on the individual unit.

Using the results of these tests, two units having approximately the same resistance versus voltage characteristics were used to construct a parallel-T filter, the schematic of which is shown in Fig. 8. The four samples on hand comprised two fairly well matched pairs. The 1-MΩ resistors in the gate circuits were introduced to minimize the effects of channel-to-gate capacity. Since the construction of an IGFET is essentially that of a capacitor, care must be taken to prevent static charges

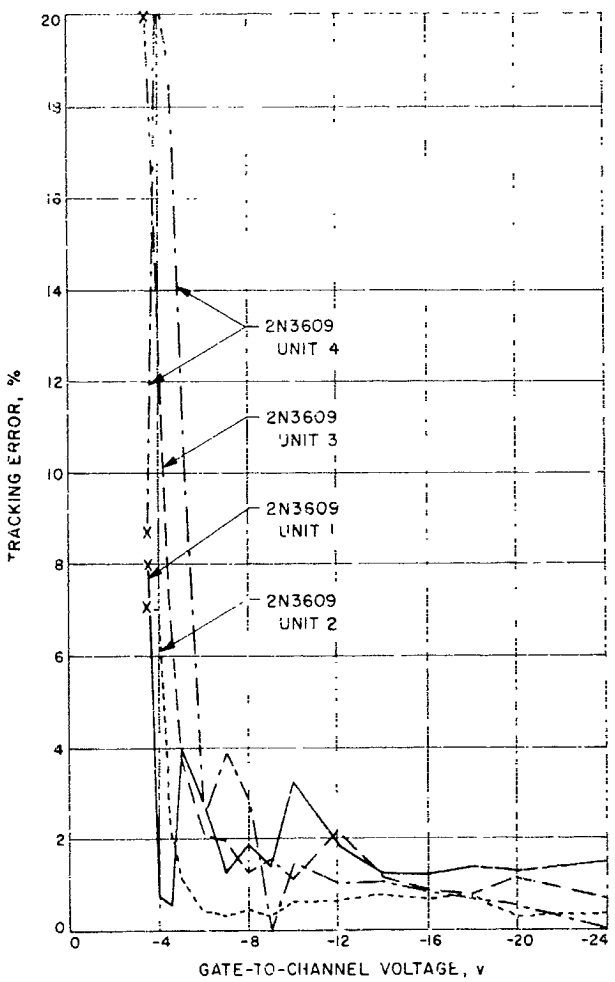

Fig. 7. Tracking error versus gate voltage

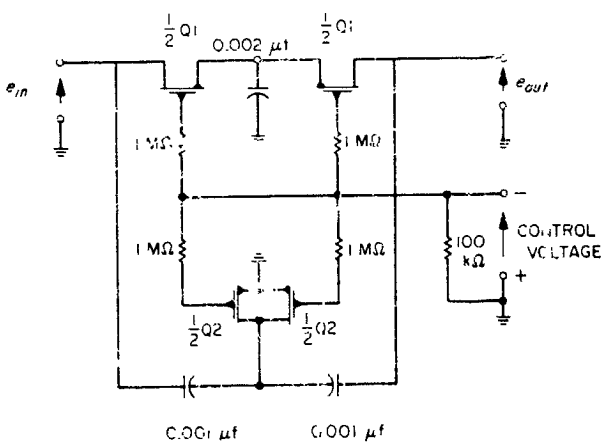

Fig. 8. Voltage-tunable parallel-T filter

from building up on its gate; failure to take proper precautions can easily result in the destruction of the transistor. The 100-kΩ resistor across the control voltage terminals prevents such a static charge accumulation.

Using various values of capacitors in the filter, tuning ranges of more than 200:1 were observed, and usable characteristics were obtained at frequencies as high as 5 Mc. It proved desirable to use a load impedance of a level much higher than the highest dynamic channel resistance that was expected over the tuning range of the filter. With an appropriate set of capacitors, as shown in Fig. 8, the response of the filter was measured with the filter tuned to 500 and 50 kc. The response curves, normalized to the center frequencies are shown in Fig. 9.

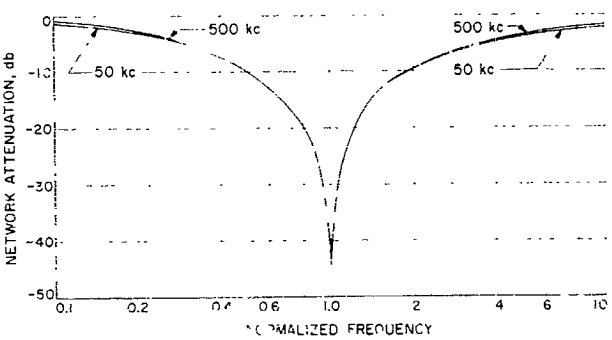

Fig. 9 Filter response at 50 and 500 kc

N65 32462

C. Optical Communications Components

W. H. Wells

1. Variable Q Optical Resonators Having Tilted Mirrors for Far Infrared Laser

The study of optical resonator modes, reported previously in *SPS 37-29* and *37-30*, Vol. IV, has been completed. The purpose was to find the shape, frequency, and output coupling of the normal modes of an optical resonator consisting of two tilted plane mirrors. The pertinent modes are thin fringes, close to the pair of opposing mirror edges, that are spread farther apart by the tilt. This resonator is especially suited for intercepting a molecular beam with optical gain in the far infrared

and for providing an oscillation with output coupling, in the form of radiation, which spills over the edge of the shorter mirror.

Previous studies found the lowest order modes, i.e., TEM_{00}, for tilt angles requiring from 3 to 28% net gain per pass to reach oscillation threshold. This gain requirement is the same as the percentage of power that leaves the resonator per pass between mirrors. Now, with the aid of an improved computer program, there have been found all of the first three modes for eight values of $\beta = \alpha(b/\lambda)^{1/2}$ (b = mirror separation, α = tilt angle, λ = wavelength) ranging from 10^{-2} to 10^{-1}. The TEM_{01} and TEM_{02} modes have gains only very slightly higher than the TEM_{00}. The more interesting results are mode shapes and frequency shifts. As could be expected, the TEM_{01} mode has two bright fringes that straddle the position of the single TEM_{00} fringe. Similarly, the TEM_{02} mode has three fringes that straddle those of the TEM_{01}. In all cases there are many small intensity maxima farther from the edge of the mirror which represent large angle diffraction from the edge (side lobes).

To describe the frequency shifts, it is convenient to consider an imaginary transverse mode that corresponds to the limiting rays of geometric optics which touch the output edge of the shorter mirror, bounce off the larger mirror at normal incidence, and then return to the output edge. The various longitudinal modes that follow this ray would have frequencies that are multiples of $c/2b$, the reciprocal of the time a light pulse requires for a round trip. The frequencies of real modes will be referred to this value. They are all slightly higher since real fringes occupy a finite width back from the edge where the spacing between mirrors is slightly less. The frequency shift for each mode is given by

$$\Delta f = \frac{c}{2b}\,\frac{\delta + \pi/4}{2\pi},$$

where $(\delta - \pi/4)$ is the phase shift that occurs when the transverse mode is propagated through one round trip between mirrors by means of the standard integral of Huygens-Fresnel scalar diffraction theory. The frequency shift of a TEM_{0n} mode is approximately described by the empirical formula

$$\frac{\pi}{4} - \delta_n \approx \frac{(0.2 \text{ to } 0.3)(n+1)}{(1.5\beta)(0.8 + n \cdot 20)}$$

for small n (say 0 to 3) and for the range $10^{-2} \leq \beta \leq 10^{-1}$. The threshold gains fit the empirical form

$$(G - 1)(100\%) \approx 300\beta + 700\beta^2$$

to an accuracy of $\pm 2\%$ for $n = 0$, 1, and 2. To this accuracy, G is independent of n.

Typical amplitude distributions for TEM_{0n} modes were shown in the earlier reports. As examples of higher order modes, Figs. 10 and 11 show the amplitude distributions $|\Psi(y)|$ for the third mode (TEM_{02}) with $\beta = 10^{-2}$ and 10^{-1}.

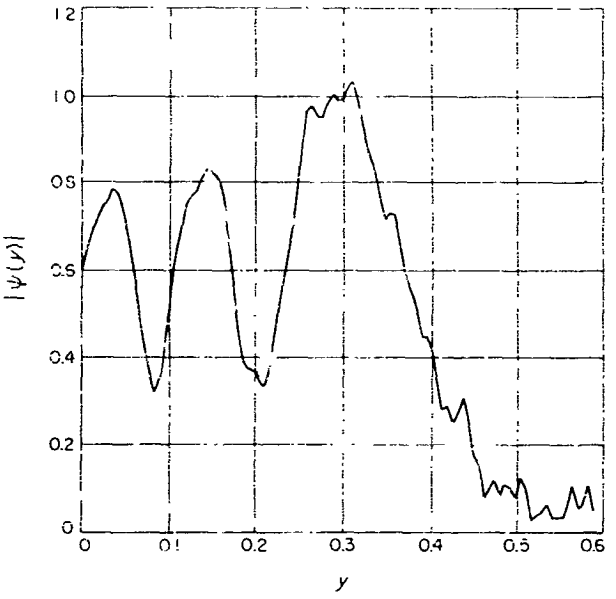

Fig. 10. Amplitude distribution of TEM_{02} mode with $\beta = 1.00 \times 10^{-2}$, $G - 1 = 3.1\%$, $\delta = -0.064$ rad

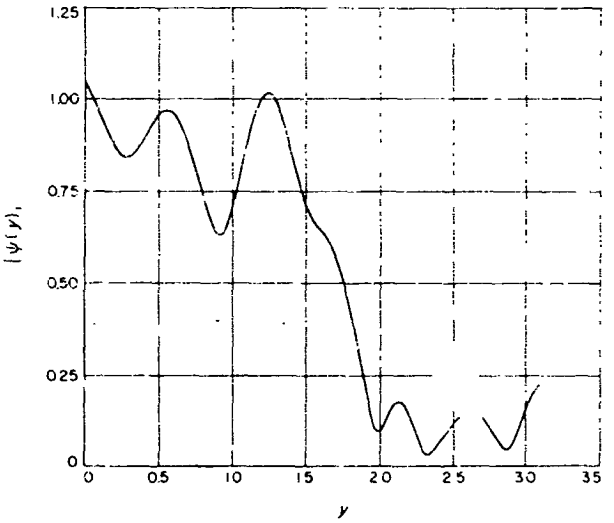

Fig. 11. Amplitude distribution of TEM_{02} mode with $\beta = 1.00 \times 10^{-1}$, $G - 1 = 39.9\%$, $\delta = 2.44$ rad

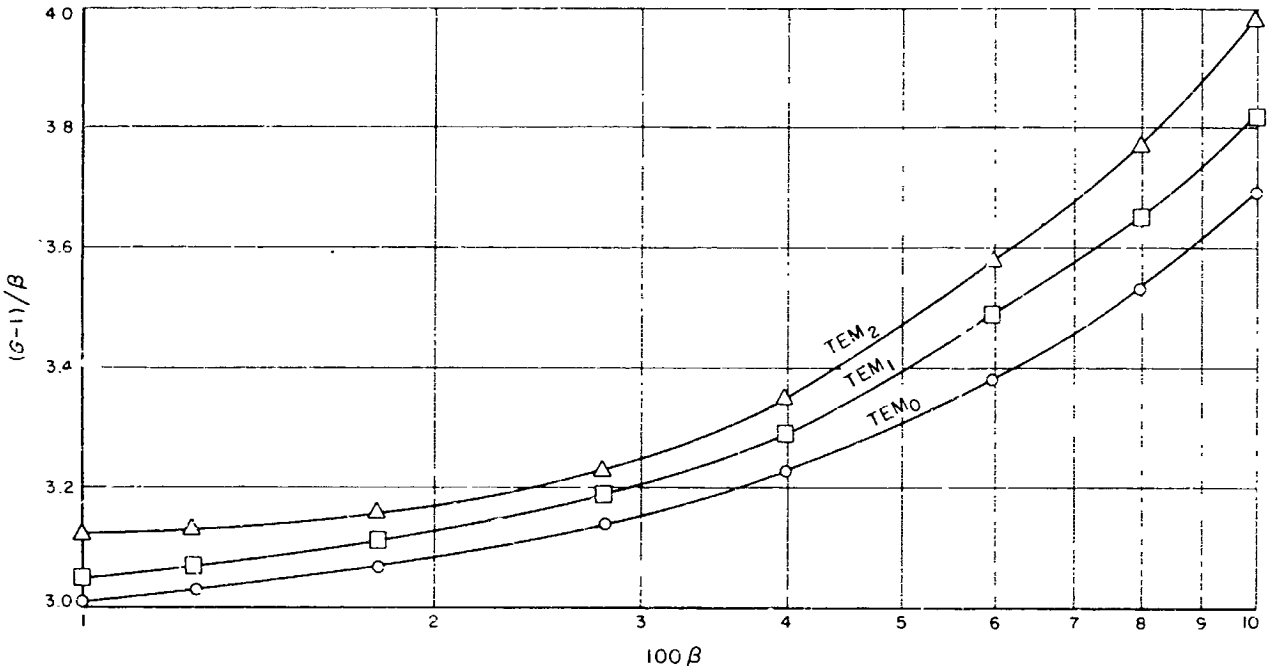

Fig. 12. (G − 1) β^{-1} as a function of β for calculating required gain

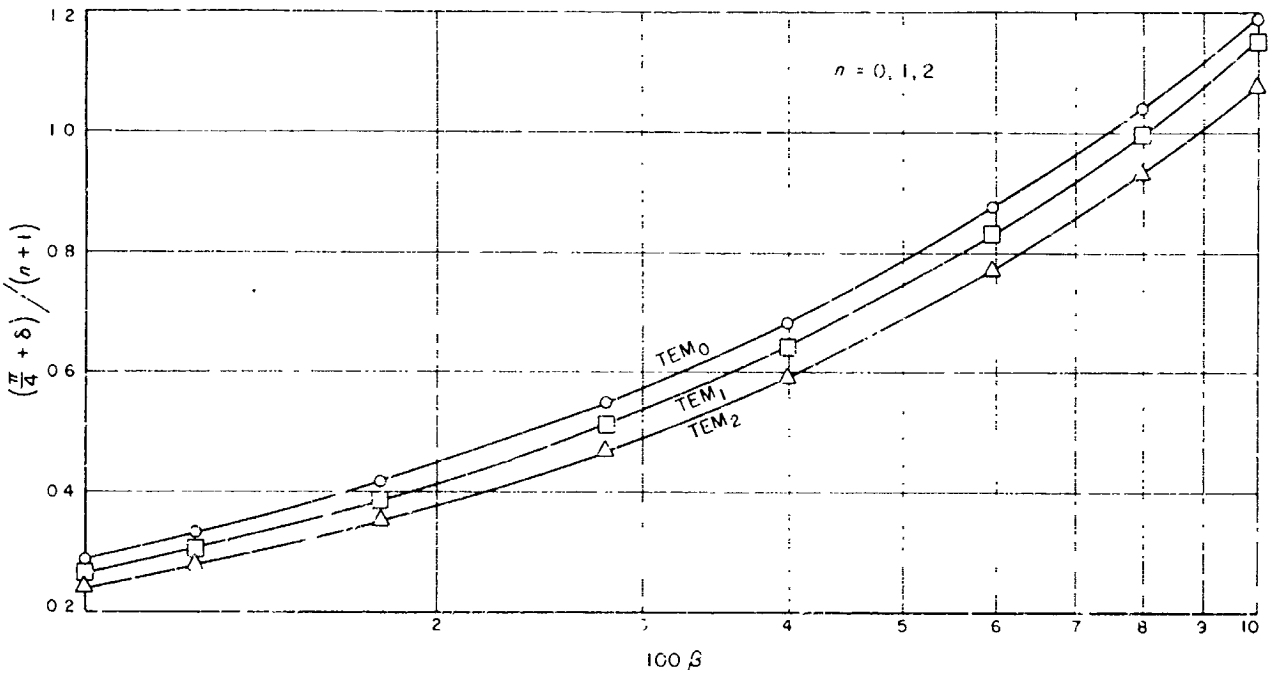

Fig. 13. $(\pi/4 + \delta)/(n + 1)$ for TEM_n modes $n = 0, 1, 2$ to be used in calculating frequency shifts

As before, $y = 2\pi\alpha x / \lambda$, a dimensionless measure of distance from the mirror's edge. These two modes have threshold gain requirements of 3 and 40%, respectively. All gains and frequency shifts as functions of β are summarized in Figs. 12 and 13 which are plots of $(G - 1)\ \beta$ and $(\pi + \delta)\ (n + 1)$, respectively. The shapes of modes are summarized in Fig. 14 which gives positions of the centers of the main fringes of the three modes as a function of β. Scatter of points represents lack of precision in defining the quantities plotted, not the accuracy of solution of the eigenvalue problem. The positions are given in units of $y\beta^{-1/2} = 2\pi\alpha^{1/2}\lambda^{-3/2}b^{-1/2}x$, because the positions are approximately stationary when expressed in this modified dimensionless form. The positions plotted are not the maxima of $|\Psi(y)|$, since this function is complicated by fine structure. Instead, we sketched smooth curves over the graphs of $|\Psi(y)|$, and estimated their maxima. Fig. 14 also gives the extent of appreciable power in the modes in the form of a quantity called the "intercept." In all cases, it happens that the trailing edge of the innermost fringe is almost linear (with fine structure) on an amplitude plot of $|\Psi(y)|$ (quadratic intensity drop-off). The intercept is the point where a straight-edge fit to this slope intercepts the y axis.

The successful computer program[1] is a slight modification of the interference method discussed in *SPS 37-30*, Vol. IV. The mathematical procedure corresponds to a

[1]Wiley Bunton of JPL programmed this problem for the IBM 7090, and modified the program for the various convergence techniques.

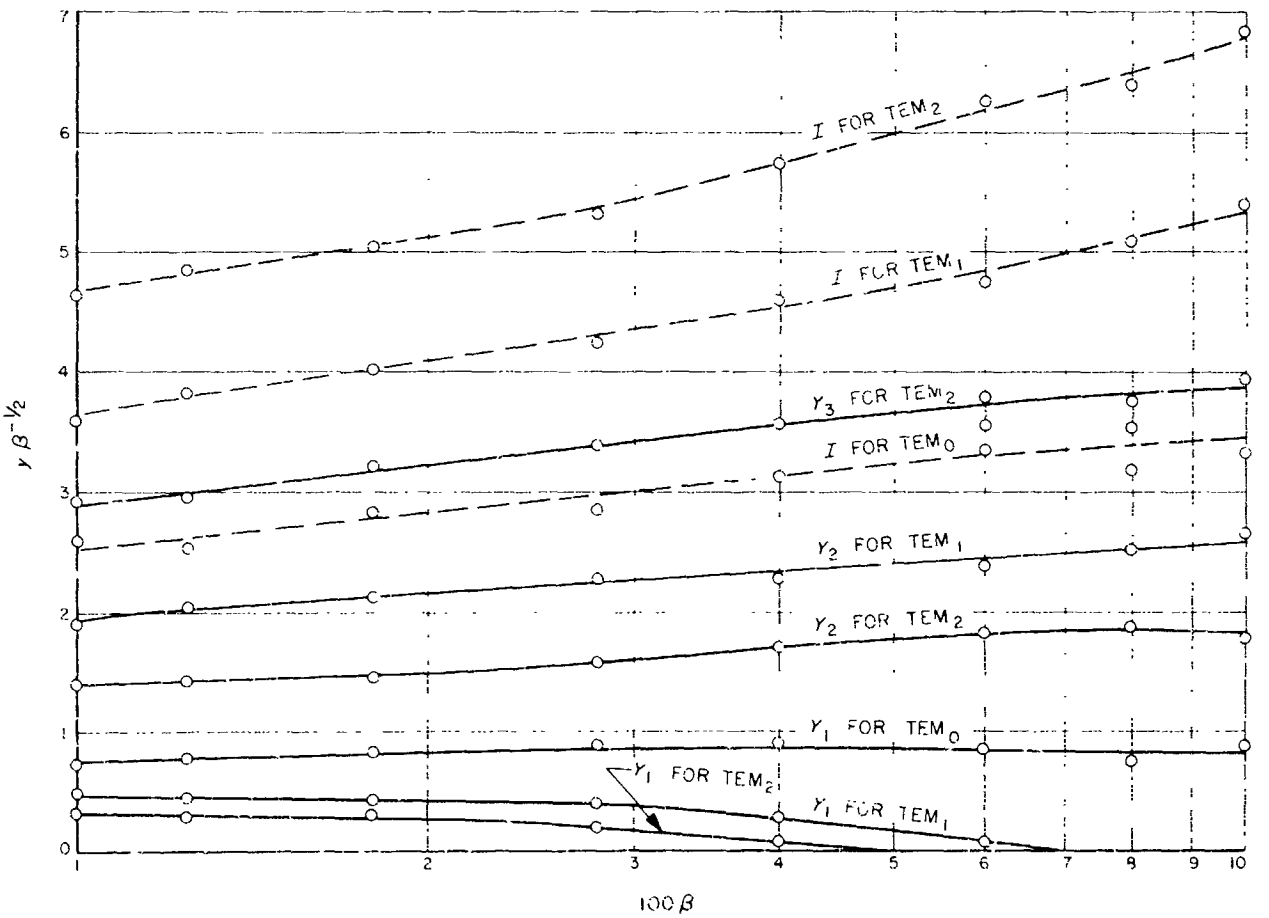

Fig. 14. Principal fringe positions (solid lines) and intercepts (dashed lines) for $TEM_{0,0}$, $TEM_{1,1}$, and $TEM_{2,1}$ modes as a function of β; I = intercept; $Y_{1,2,3}$ = position of successive intensity maxima

simple physical idea. Light extracted from one mirror is superimposed upon light extracted one round trip later (time $2b/c$), but with a phase shift introduced so that a troublesome mode is eliminated by destructive interference, leaving only the desired mode.

Formally, a round trip of the light corresponds to one iteration of the basic integral equation for light diffraction from the mirror:

$$\int_0^\infty K(y,s)\,\Psi_i(s)\,ds = \Lambda\Psi_{i-1}, \qquad (1)$$

$$\text{where } K = \exp j\left[-(y+s) + \frac{(y-s)^2}{8\pi\beta^2}\right].$$

When a normal mode is found, $\Psi_i = \Psi_{i-1}$, and Λ is the complex eigenvalue which gives G and δ the required gain and frequency shifts (in units of $c/2b$) of the mode:

$$\Lambda = \frac{(8)^{1/2}\pi\beta}{Ge^{j\delta}}. \qquad (2)$$

Now consider the (open-ended) integral operator

$$\left[-\Lambda' + \int_0^\infty ds K(y,s)\right].$$

When $\Lambda' = \Lambda_n$, the eigenvalue of the nth mode, this operator gives zero when it operates on the nth eigenfunction Ψ_n. Therefore, we used it as an annihilation operator with various values of Λ' to eliminate troublesome modes from an arbitrary function. The resulting function then became the starting function for the normal iterative process Eq. (1). For example, in finding a TEM_2 mode the annihilation operator was applied with three values of Λ', namely the eigenvalues of the TEM_0, TEM_1, and TEM_3 modes. Higher modes decayed rapidly upon iterating Eq. (1) because there was not room for all their fringes to fit on the range of integration (corresponds to a strip mirror of restricted width). Of course, the eigenvalues were not known exactly, especially the TEM_3 values that were beyond the scope of the program. Nevertheless, reasonable guesses could be made from the semisuccessful programs discussed previously, and by extrapolation. Where there was considerable doubt, the annihilation operator became a "suppression" operator and was applied repeatedly until the undesired modes were reduced by factors of 10^{-3} to 10^{-4}.

D. Antennas for Space Communications

A. Ludwig

1. Gain Loss Calculations

a. Summary. The change rate of gain loss due to phase errors with respect to frequency is investigated as a function of total gain loss. Upper limits on this slope are predicted and related to physical deformations in the system.

b. Analysis. The gain efficiency of a radiating aperture-type antenna is, in general, a function of frequency. This dependence can arise due to the amplitude distribution over the system varying with frequency, or because of physical deformations which generally have a more severe effect as frequency increases. An interesting question concerns the rate at which loss may vary with frequency. Usually phase effects will predominate, and we will consider this component of loss only.

Consider a radiating system which has a resultant phase at the point of maximum gain of α deg. Assume that there is some effect which causes a certain percentage of energy to change phase with respect to the remainder of the energy, by an angle β (Fig. 15). The resultant amplitude r is given by

$$r^2 = a^2 + 2ab\cos\beta + b^2. \qquad (1)$$

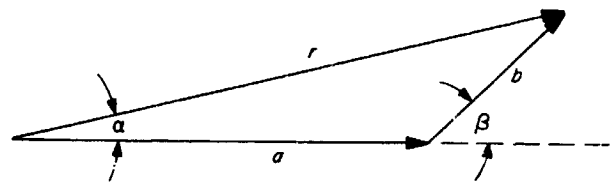

Fig. 15. Effect of phase error

The loss in decibels with respect to the in-phase condition $\beta = 0$ is given by

$$L = 10\log_{10}\frac{a^2 + 2ab\cos\beta + b^2}{a^2 + 2ab + b^2} \text{ db} \qquad (2)$$

and

$$\frac{\partial L}{\partial\beta} = -4.3429\frac{2ab\sin\beta}{a^2 + 2ab\cos\beta + b^2} \text{ db/rad.} \qquad (3)$$

Values of $\partial L/\partial\beta$ versus L are shown in Fig. 16 for various values of b and β where the restriction $a^2 + b^2 = 1$ has

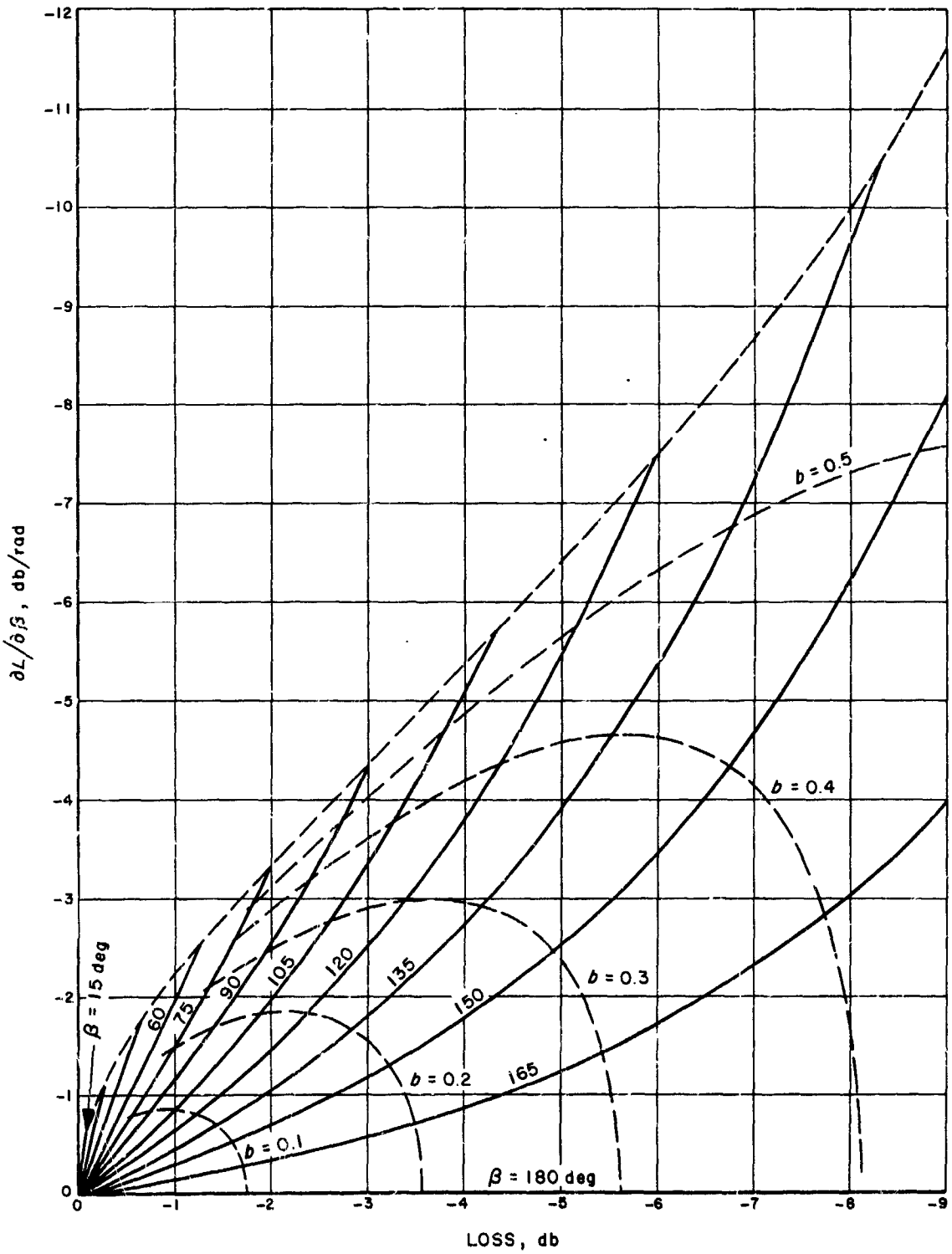

Fig. 16. $\partial L/\partial\beta$ versus β for various β and b

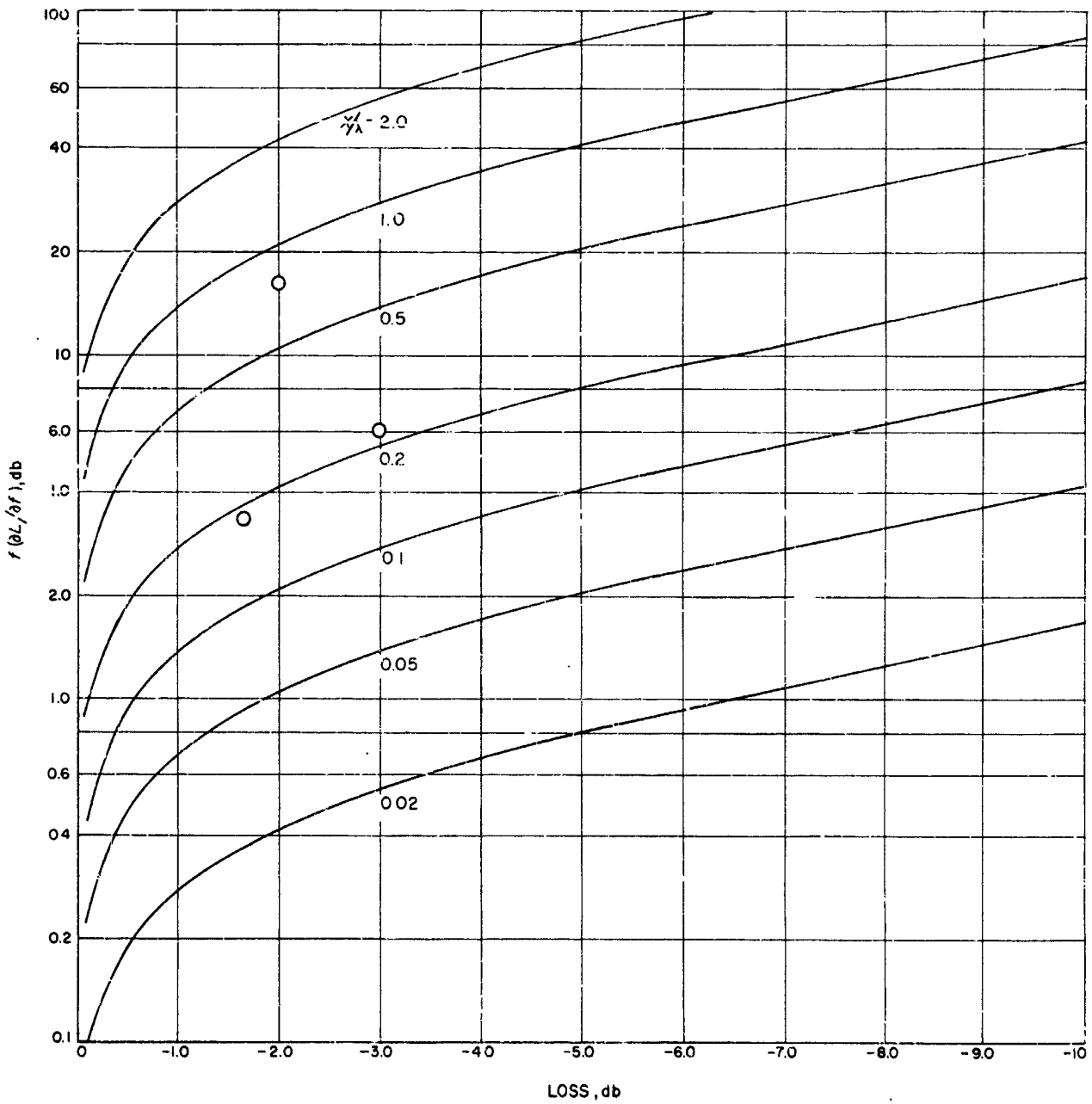

Fig. 17. Change in loss with respect to frequency versus loss for a given physical error

been imposed. It is seen that there is a limit on $\partial L/\partial\beta$ for a given loss, corresponding to the worst-case combination of b and β. Thus, for example, a system with a 1-db loss relative to zero phase loss cannot vary more than 2½ db rad change in β.

Suppose that physically the phase error is caused by a path-length error of X in. between one portion of the energy and the remainder of the energy. Then

$$\beta = 2\pi \frac{X}{\lambda} = \frac{2\pi X}{c} \cdot f \tag{4}$$

$$\frac{\partial L}{\partial f} = \frac{\partial \beta}{\partial f} \cdot \frac{\partial L}{\partial \beta} = \frac{2\pi X}{c} \frac{\partial L}{\partial \beta} \tag{5}$$

$$f \frac{\partial L}{\partial f} = 2\pi \frac{X}{\lambda} \frac{\partial L}{\partial \beta}. \tag{6}$$

Fig. 17 shows $f(\partial L/\partial f)$ versus L for various values of X/λ. The value of Fig. 17 is the ability to determine minimum physical errors which must be present to produce a given slope $f(\partial L/\partial f)$ at a given loss L. For example, three points have been plotted from a 22-Gc gain calculation (*SPS 37-33*, Vol. III, p. 69). The two points at 1.5- and 3-db loss are theoretical, based on a surface with a full path length error of 0.052 and 0.080 in. RMS deviation from a perfect paraboloid, respectively. The minimum physical error predicted from Fig. 17 is 0.10 and 0.12 in., respectively. This relates well to the assumed RMS since there must be peak-to-peak errors on the order of 0.104 in. to produce a RMS of 0.052 in. The third point is based on experimental data, and indicates a minimum error of 0.41 in. in the system.

2. Antenna Feed Research

a. Summary. The theoretical limits on the performance of multimode feed horns are investigated, and the current state-of-the-art in experimentally realized multimode horn patterns is presented.

b. Introduction. The performance of a paraboloidal antenna is quite sensitive to the illumination provided by the antenna feed system. Feed efficiency is conventionally defined as the ratio of gain provided by the given system to the gain if the aperture were uniformly illuminated. A major purpose of antenna feed research is to increase feed efficiency, thereby increasing the gain of a given antenna. One approach to this end is the multimode horn, a feedhorn utilizing the radiation patterns of higher order waveguide modes (*SPS 37-19*, Vol. IV, pp. 190–196).

c. Multimode horn study. Multimode horn research is concerned primarily with: (1) the determination of maximum performance potentially available from multimode feedhorns, and (2) the realization of this performance.

The question of optimum performance may also be approached using spherical wave theory. It can be shown that the maximum order, N, of spherical wave which may eminate from a given object which can be enclosed in a sphere of radius R, is given by $N < kR$ where k is the free-space propagation constant (*SPS 37-24*, Vol. IV, pp. 150–154). Fig. 18 is a plot of the maximum efficiency available from this limited number of spherical waves versus D/λ, the diameter of the object in free-space wavelengths. It is seen that it is theoretically impossible to reach 100% efficiency with a feed system of any type, of finite size (with the assumption of $N < kR$). The combinations of spherical modes yielding maximum efficiency for an illumination edge half angle of 15 deg are shown in Fig. 19 for $N = 15$ and $N = 25$, corresponding to D/λ of 4.7 and 8.0, respectively.

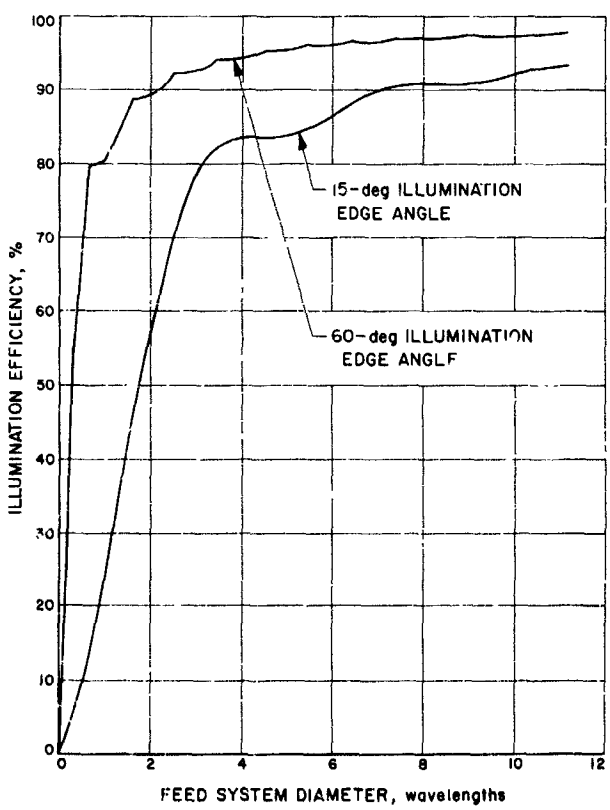

Fig. 18. Theoretical limitation on efficiency versus feed system diameter

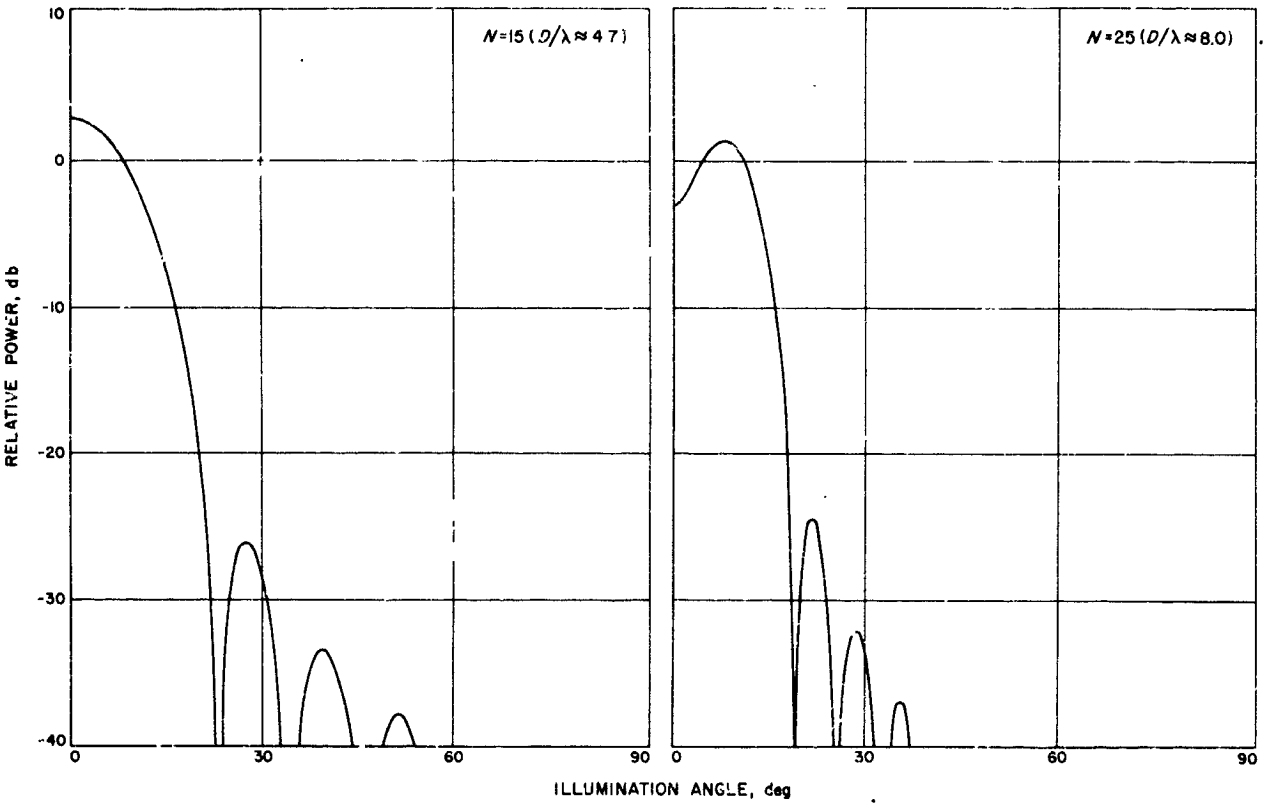

Fig. 19. Spherical wave functions; best N-term fit to uniform illumination

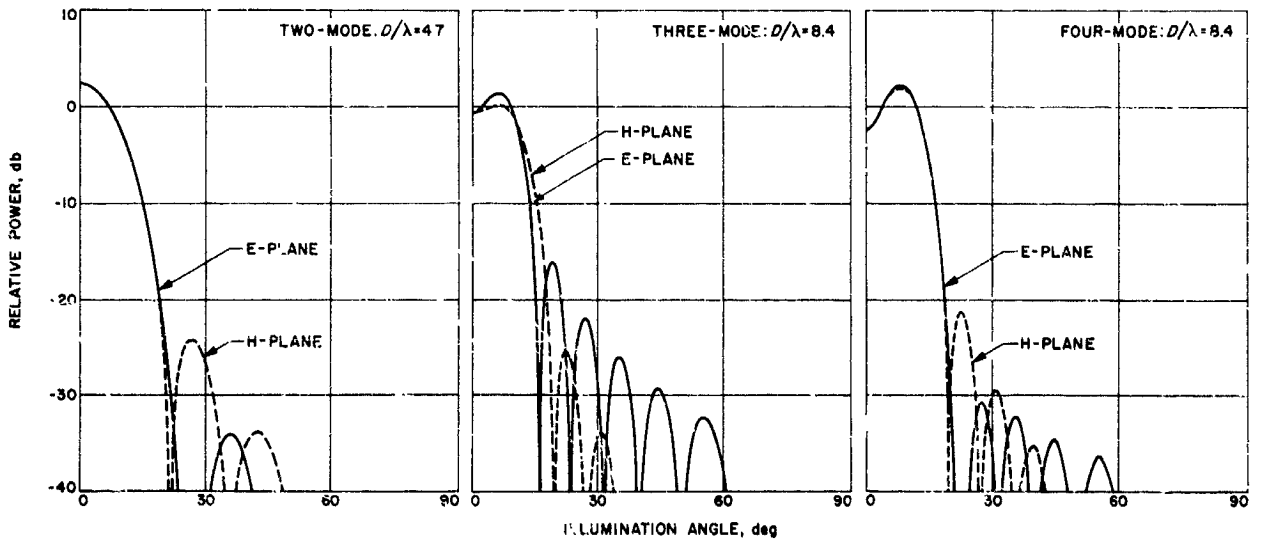

Fig. 20. Optimum theoretical patterns, multimode conical horn

To determine maximum performance available from multimode horns, linear combinations of radiation patterns of cylindrical waveguide modes, for $D \cdot \lambda$ apertures of 4.7 and 8.4, were input to a computer program which determines efficiency (*SPS 37-26*, Vol. IV, pp. 200–208). The combinations were then empirically optimized. Optimum two-, three-, and four-mode patterns are shown in Fig. 20. The resemblance between the spherical mode and multimode horn dual- and four-mode optimum patterns is quite striking, and illustrates the fact that a multimode horn is an excellent means of realizing the theoretical maximums predicted by spherical wave theory.

The optimum two-mode pattern closely resembles the pattern of the dual-mode horn currently in use as a JPL feed (Ref. 7).

Realization of good three- and four mode horn patterns has been the subject of research effort for some time. A tri-mode horn with good efficiency has been previously realized, (*SPS 37-26*, Vol. IV, pp. 207–208) but its efficiency maximizing at an illumination angle of 24 deg is much too wide for JPL Cassegrainian systems. Recently a four-mode horn with good patterns has been obtained. Fig. 21 shows the four-mode horn amplitude and phase

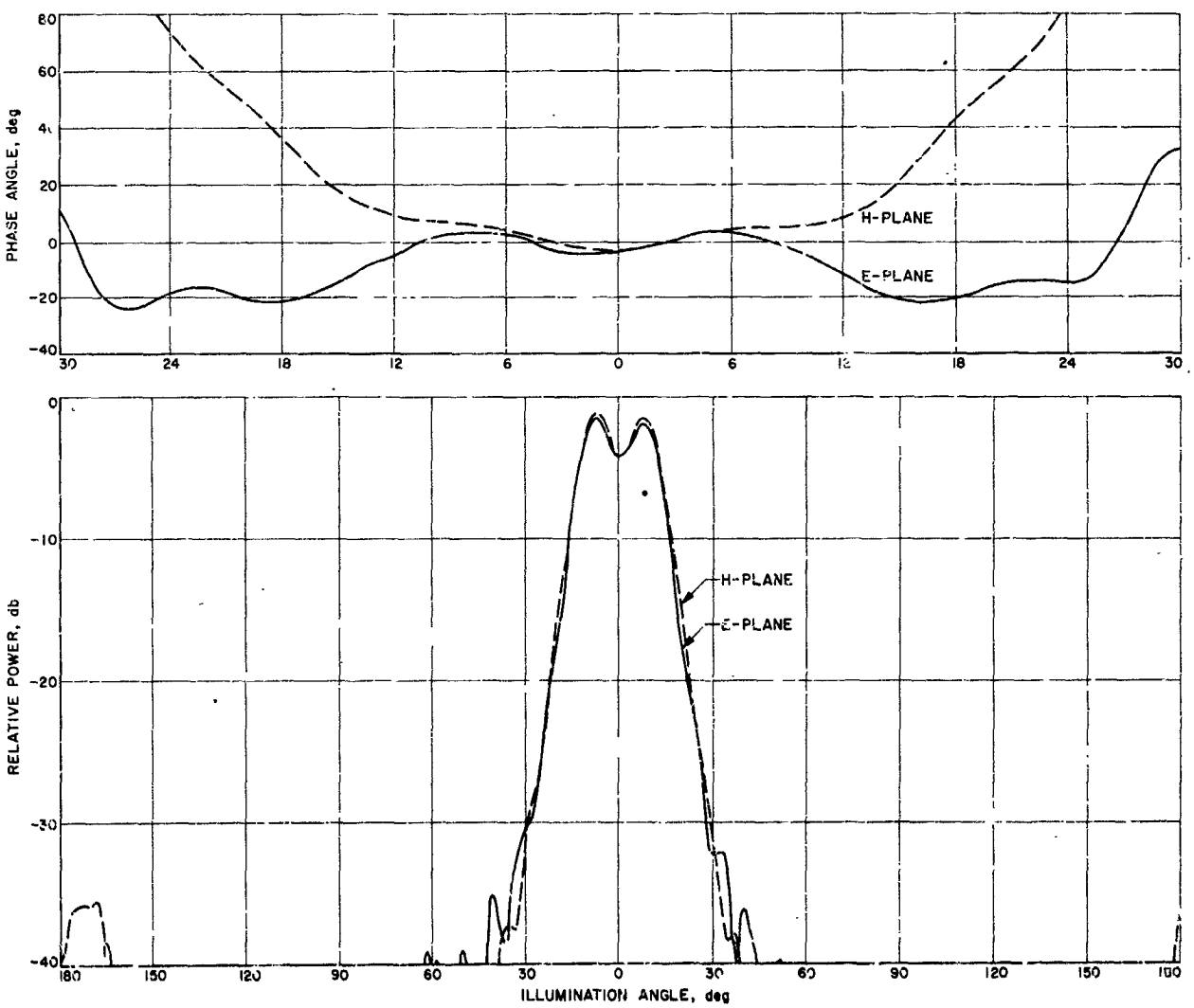

Fig. 21. Four-mode horn, experimental amplitude and phase patterns

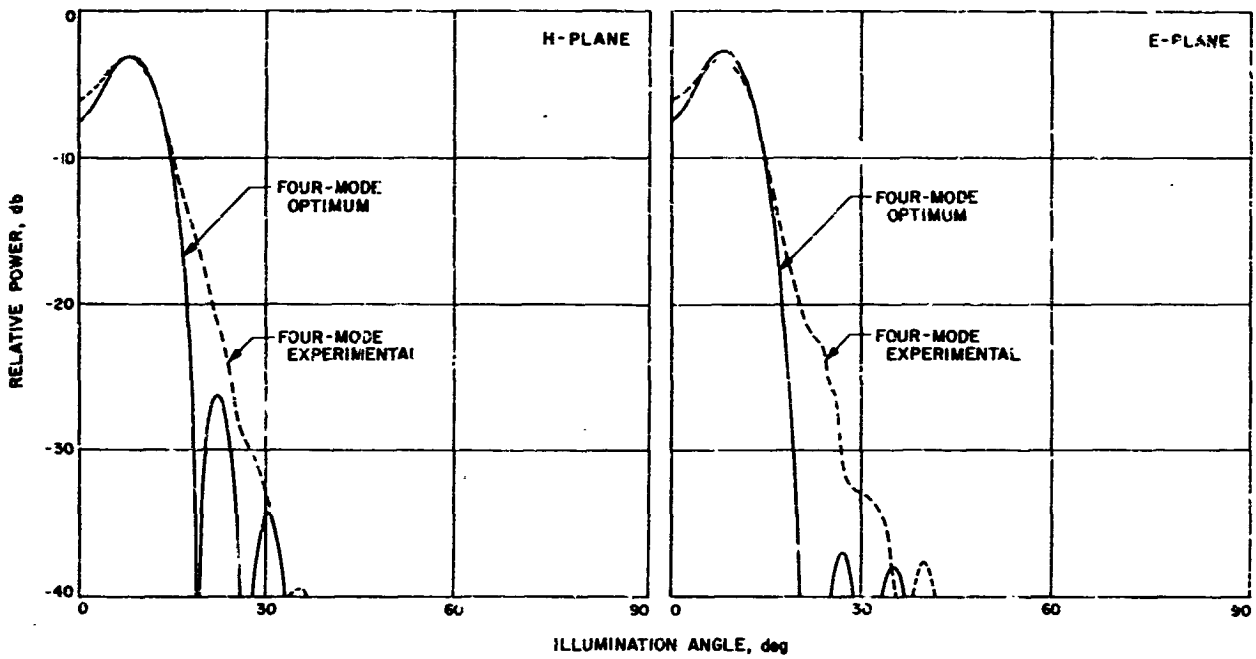

Fig. 22. Four-mode theoretical optimum pattern compared to experimental pattern

patterns, and Fig. 22 shows a superposition of the realized four-mode pattern and the optimum (calculated) four-mode pattern. The only appreciable difference between the realized and the optimum pattern lies in the spillover region. Unfortunately this difference is enough to cut the efficiency to the point where the usefulness of the horn is debatable; the broadened pattern would require a subreflector subtending a 17-deg half-illumination angle, whereas the current JPL systems utilize a 14½-deg subreflector. Efforts to narrow the pattern by the usual means of increasing the horn aperture size have been unsuccessful. Apparently the phase error across the aperture is so severe at this size that increasing the aperture causes more broadening due to phase error than narrowing due to the larger size. The same aperture phase error is almost certainly also the cause of the increased spillover.

Fig. 23 summarizes the efficiencies of the patterns discussed so far. Patterns are evaluated on the basis of optical reflection from a hyperboloidal subreflector with approximately a 15-deg edge angle. The tri-mode horn was scaled from a 24-deg angle to a 15-deg edge angle. It is now clear that this scaling is not easy to achieve in practice, and pattern degradation does occur due to increased aperture phase error. Therefore the values given for the tri-mode are artificially high. The dashed areas above the tri- and four-mode horns represent efficiency if the phase patterns of the horns were uniform. Fig. 24 shows the efficiency after scattered patterns from the hyperboloid have been calculated using a JPL-developed computer program (Ref. 8). Vertex blockage loss has been included in the values given in Fig. 24 based on the JPL Advanced Antenna System design. It is seen from this figure that the four-mode horn provides an increase in efficiency of approximately 4% over the dual-mode horn. Because of the high cost of large paraboloidal antennas, a 4% increase in efficiency may not be economically insignificant. The physical configuration used to produce the patterns shown in Fig. 21 is shown in Fig. 25. The existing model works at 9550 Mc. It is empirically known that this design is narrow band (about 50 Mc) and very sensitive to the physical configuration.

It is felt that the four-mode patterns might be improved by extending the horn with a length of cylindrical section of the end of the horn, thus presumably reducing the phase error across the aperture. However, this will also affect relative mode amplitudes and phasing, probably requiring readjustment of the mode generating sections.

In any case, an absolute upper limit on the performance which could be obtained in this manner is that of the optimum four-mode horn, about 10% better than the existing dual-mode horn. A realistic limit, taking into

account phase loss and the fact that there will always be some aperture phase error, would be about 3% lower.

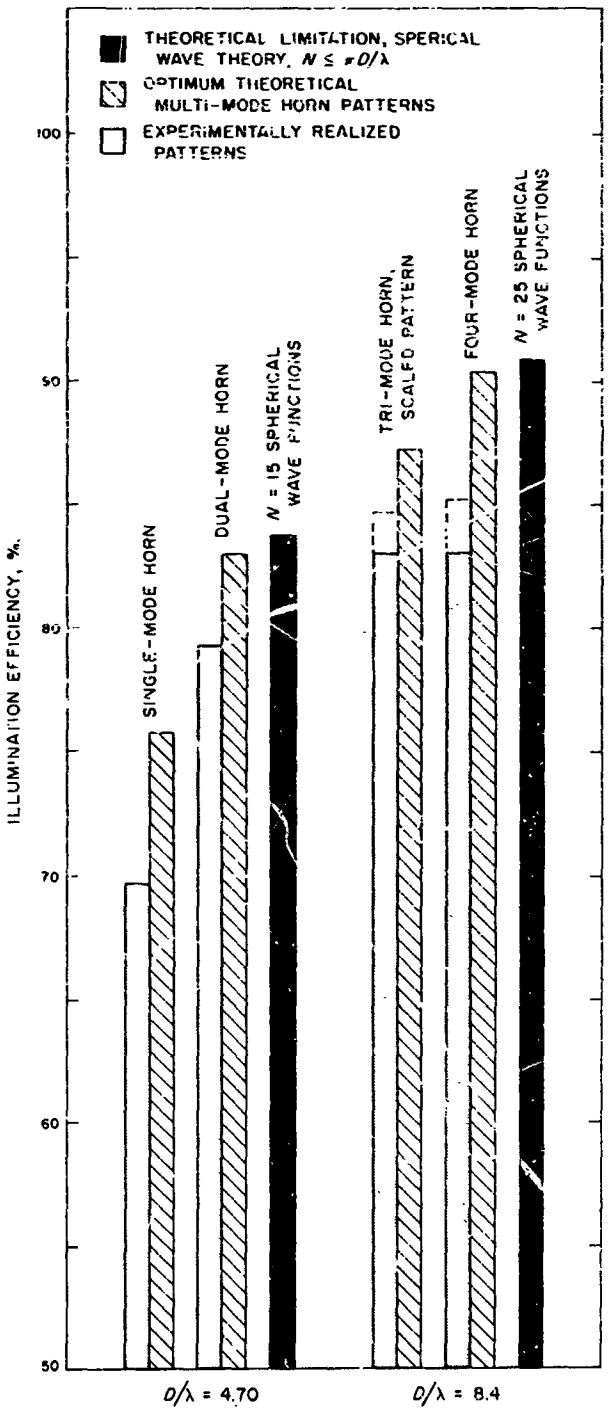

Fig. 23. Efficiency of various primary feed patterns, 15-deg illumination edge angle

The possibility of a five- or six-mode horn is very unlikely. One obstacle is that even larger aperture sizes would be required, compounding the aperture phase error problem. Also, generating and controlling three and four cylindrical waveguide modes has proved extremely difficult; the excitation and control of five or six modes is felt to be impracticable.

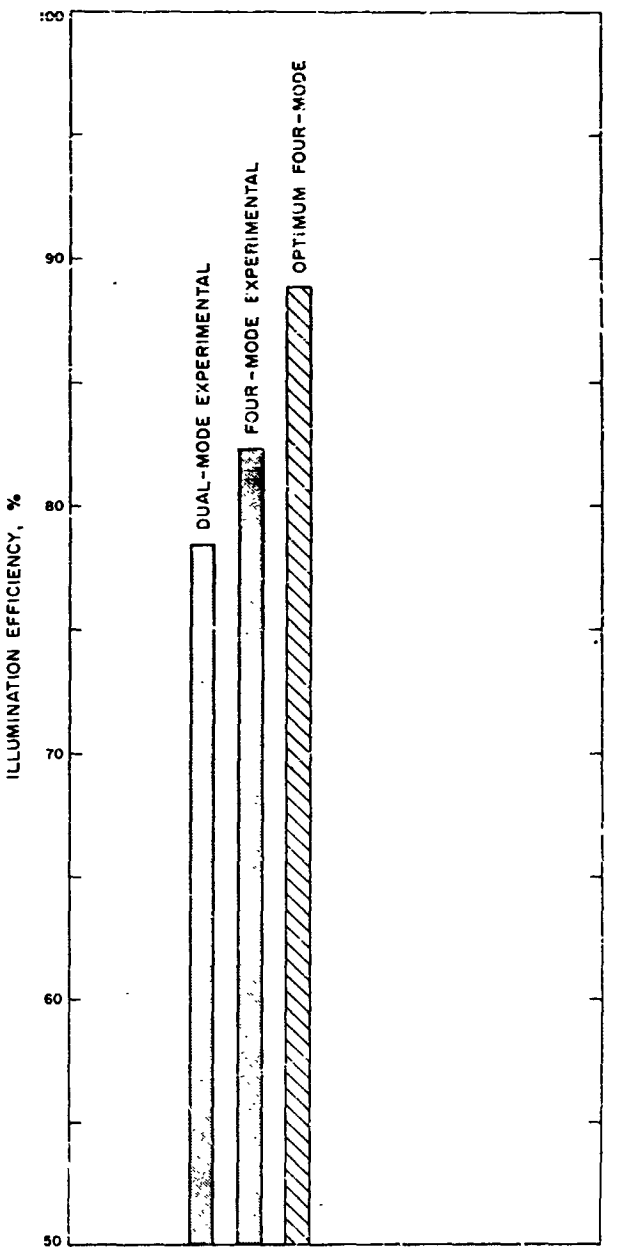

Fig. 24. Efficiency of fields scattered from hyperboloid, 60-deg illumination edge angle

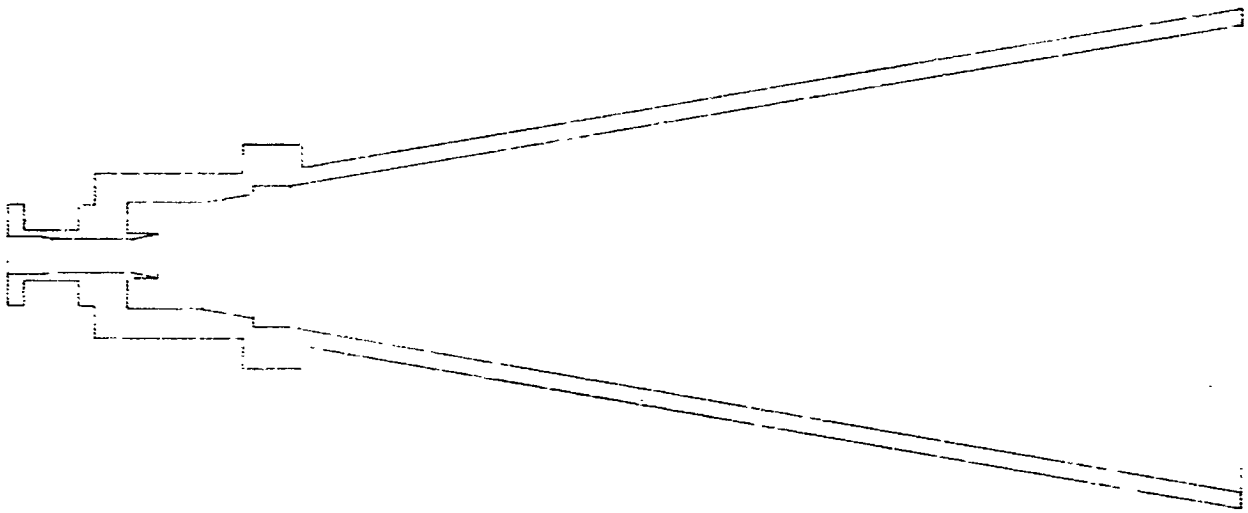

Fig. 25. Four-mode horn physical configuration

d. Conclusion. Upper limits on performance potentially available from multimode horns have been defined. It has been shown that these performance maxima approach very closely theoretical limits for any type of feed device of the same size, showing that conical feedhorns are potentially ideal. A four-mode horn pattern has been experimentally realized yielding an efficiency 4% above the best existing JPL feed and 7% below the theoretically optimum pattern. It is felt that an additional 4% might be obtained with further research effort.

References

1. Stelzried, C. T., "Temperature Calibration of Microwave Thermal Noise Sources," *IEEE Transactions on Microwave Theory and Techniques*, Vol. MTT-13, No. 1, p. 128, January 1965.
2. Stelzried, C. T., Petty, S. M., "Microwave Insertion Loss Test Set," *IEEE Transactions on Microwave Theory and Techniques*, Vol. MTT-12, No. 4, p. 475, July 1964.
3. Ramo, S., and Whinnery, J., "Fields and Waves in Modern Radio," Second Edition, p. 371, John Wiley & Sons, Inc., New York, 1962.
4. Worthing, A. G., and Geffner, J., "Treatment of Experimental Data," 9th Printing, John Wiley and Sons, Inc., New York. 1960.
5. Terman, F. E., "Radio Engineering," p. 128, McGraw-Hill Book Co., Inc., New York, 1947.
6. Harvey, A. F., "Microwave Engineering," p. 46, Academic Press, 1963.
7. Potter, P. D., "A New Horn Antenna with Suppressed Sidelobes and Equal Beamwidths," *Microwave Journal*, Vol. VI, No. 6, pp. 71–79, June 1963.
8. Rusch, W. V. T. "Scattering of a Spherical Wave by an Arbitrary Truncated Surface of Revolution," Technical Report No. 32-434, Jet Propulsion Laboratory, Pasadena, California, May 1963.

TELECOMMUNICATIONS DIVISION

XXIV. Communications Systems Research: Mathematical Research

A. Hadamard Matrices of Order 20

M. Hall, Jr.[1]

1. Introduction

In a recent summary, Baumert reviewed the connection between Hadamard matrices and orthogonal codes for space telemetry (*SPS 37-29*, Vol. IV, pp. 213–214). It is useful to know how many different classes of these matrices of given order there are; *class* refers to permutation of rows and columns, and changing the sign of entire rows and columns. These transformations leave the code unchanged for the purposes of error probability, but they can change the self-synchronizing properties. Thus, the best self-synchronizing orthogonal code of given order can be more easily found if the equivalence classes are known. This discussion describes the work done to show that there are exactly 3 classes of Hadamard matrices of size 20. The classes are found explicitly.

[1]At the California Institute of Technology, performing work supported by the Jet Propulsion Laboratory.

2. Description of the Three Classes

There are exactly three distinct classes of Hadamard matrices of order 20, if matrices equivalent under permutation of rows or columns or change of sign of rows or columns are considered in the same class. These three classes are labeled class Q, class P, and class N (Figs. 1, 2, and 3).

Class Q contains the matrix derivable from the quadratic residues modulo 19. Class P contains the matrix which can be constructed from GF(9) as a special case of Paley's general construction (Ref. 1) for orders $2(1 + p^r)$, where p^r is a prime power and $p^r \equiv 1 \pmod 4$. The matrix of order 20 constructed by Williamson in Ref. 2 is also in this class. Class N is a new class not previously known. Each of the three classes possesses a symmetric representative, and so each is its own transpose class.

3. Search Procedures

The search for all Hadamard matrices of order 20 is greatly facilitated by the fact that it can be shown that

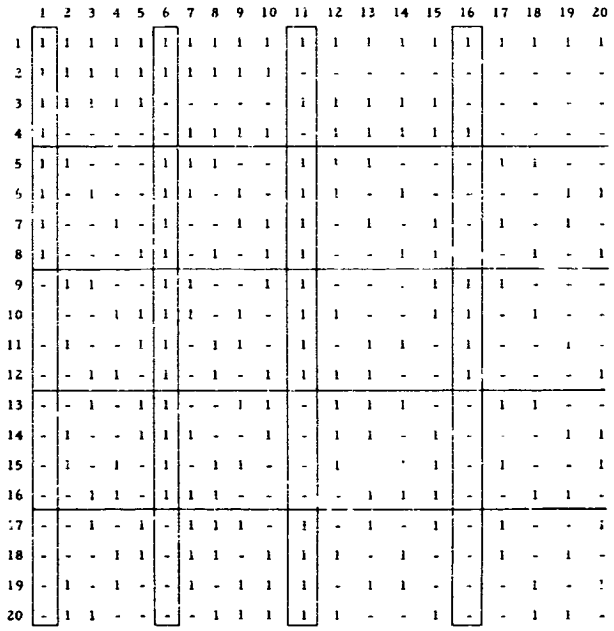

Fig. 1. Class Q

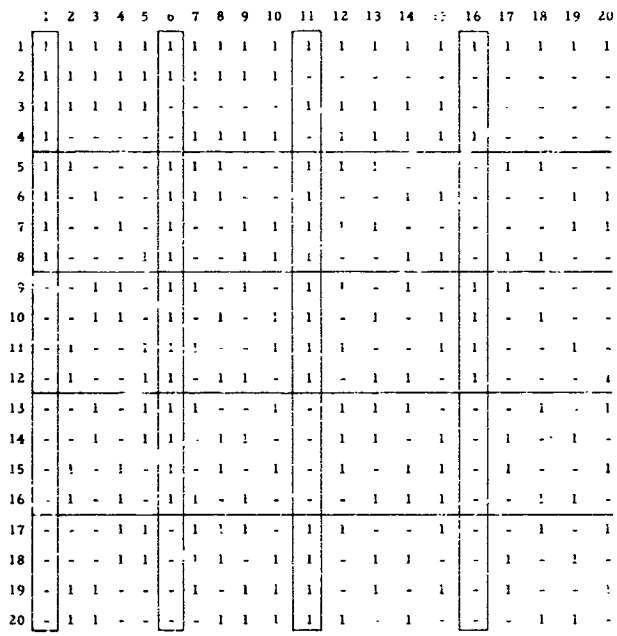

Fig. 2. Class P

if any three rows are put into the standard form: (writing – for –1 as a convenience)

$$\begin{array}{c|c|c|c} 1\,1\,1\,1\,1 & 1\,1\,1\,1\,1 & 1\,1\,1\,1\,1 & 1\,1\,1\,1\,1 \\ 1\,1\,1\,1\,1 & 1\,1\,1\,1\,1 & - - - - - & - - - - - \\ 1\,1\,1\,1\,1 & - - - - - & 1\,1\,1\,1\,1 & - - - - - \end{array} \qquad (1)$$

then there is exactly one more row which can be put in the form,

$$1 - - - -\,|\,- 1\,1\,1\,1\,|\,- 1\,1\,1\,1\,|\,1 - - - - \qquad (2)$$

along with the three rows of (1). Also, any three of these four rows determines the fourth in this manner. These row quadruples are very useful. The twenty rows of H_{20} break up naturally into five disjoint quadruples as may be seen in the representatives of classes Q, P, N.

This finding contrasts somewhat with Ref. 3, where it was shown that there are five classes of Hadamard matrices of order 16. Theoretical considerations make it plausible to expect more classes of Hadamard matrices of order n when $n \equiv 0 \pmod 8$ than when $n \equiv 4 \pmod 8$.

With the four rows of (1) and (2) to begin with, it is not difficult to show that a second disjoint quadruple may be taken to form rows 5, 6, 7, 8, and that, to within equivalence, there are only three possible eight row starts.

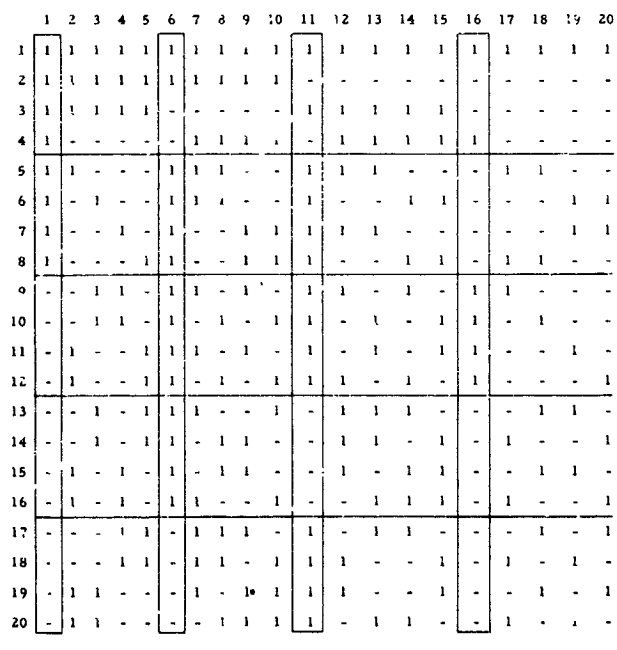

Fig. 3. Class N

A total of twenty-two completions of these eight row starts were found, which included all possible matrices to within equivalence. This was not difficult, but it was time consuming. Showing that these were equivalent to

one of Q, P, N and that Q, P, N are inequivalent was more difficult. This last was accomplished by a study of the patterns of row quadruples, under the action of known automorphisms of these matrices.

More details will be published in a JPL report.

B. Further Investigation of Random Numbers

R. C. Tausworthe

1. Introduction

In Ref. 4, the author derived a method for the generation of random numbers which results, on the average, in a pseudostochastic series as good as the best known today. There were several conditions placed upon the parameters of generation that were necessary to the analysis of the numbers produced. It is natural to ask if the limitations placed upon parameters are necessary to the production of good sequences of random numbers or are they merely needed to effect an algebraic analysis. This article analyzes this question, and reaches the conclusion that if the parameters are not limited as specified, the degree of randomness in the generated sequence is degraded, sometimes to a very high degree.

2. Random Numbers Generated by Linear Recurrence Modulo 2

Let $a = \{a_k\}$ be the (0, 1) sequence generated by an nth-degree maximal length linear recurrence relation modulo (mod) 2, as described in Ref. 4, and define a set of numbers of the form

$$y_k = 0.\, a_{qk+r-1}\, a_{qk+r-2} \cdots a_{qk+r-L} \quad \text{(base 2)}$$

where r is a randomly chosen integer, $0 \leq r \leq 2^n - 1$.

Physically, the sequence $\{a_k\}$ can be viewed as an infinite stream of 0's and 1's, and the y_k are generated by taking L tuples every q digits, as

$$\underbrace{\cdots 0\ 1\ 1\ 1\ 0}_{y_1}\ \underbrace{0\ 1\ 1\ 0\ 1\ 0}_{y_2}\ \underbrace{0\ 0\ 1\ 0\ 0\ 1\ 1}_{y_3}\ \cdots$$

($L = 4$, $q = 6$)

we can also express y_k algebraically as

$$y_k = \sum_{t=1}^{L} 2^{-t}\, a_{qk+r-t}$$

Such numbers always lie in the interval $0 \leq y_k < 1$. By making r a random choice, the initial value y_0 is completely random. But once y_0 is specified the remainder of the sequence $\{y_k\}$ is deterministic. We often find it convenient to work with a transformed set of numbers w_k rather than y_k. Specifically, let $\alpha = \{\alpha_k\}$ be the ± 1-sequence corresponding to a by $\alpha_k = (-1)^{a_k}$ and define

$$w_k = \sum_{t=1}^{L} 2^{-t}\, \alpha_{qk+r-t}$$

It is easy to verify that w_k and y_k are related by

$$w_k = 1 - 2^{-L} - 2y_k$$

The result contained in the work cited is repeated here for reference:

Theorem: If $\{a_k\}$ is a (0, 1) binary sequence generated by an nth degree maximal-length linear recursion relation modulo 2, if for $(q, 2^n - 1) = 1$ and $q \geq L$, $y_k = 0.\, a_{kq-1}\, a_{kq-2} \cdots a_{kq-L}$ is the binary expansion of a real positive number in the interval [0, 1), and if w_k is a real number in the interval $(-1, +1)$ related to y_k by $w_k = 1 - 2y_k - 2^{-L}$, then averaged over all possible (assumed equally likely) initial values y_0 (or w_0),

(1) The mean value μ of the sequence $\{w_k\}$

$$\mu = -2^{-n}\left(\frac{1 - 2^{-L}}{1 - 2^{-n}}\right) \approx 0$$

and variance σ^2

$$\sigma^2 = \frac{1}{3} + 2^{-n}\left[\frac{1}{3}\left(\frac{1 - 2^{-2L}}{1 - 2^{-n}}\right) - \frac{(1 - 2^{-L})^2}{1 - 2^{-n}} - 2^{-n}\left(\frac{1 - 2^{-L}}{1 - 2^{-n}}\right)^2\right] \approx \frac{1}{3}$$

(2) The sample autocorrelation function, defined by

$$\hat{R}(m) = \frac{1}{N}\sum_{k=1}^{N} w_k\, w_{k+m}$$

has as its mean value R(m), given by

$$R(m) = -2^{-n}\left(\frac{1 - 2^{-L}}{1 - 2^{-n}}\right) \approx 0$$

for nonzero integral values of $|m|$ less than $(p - L)/q$. The variance of $\hat{R}(m)$ about $R(m)$ is bounded by

$$\text{var}\left[\hat{R}(m)\right] < \frac{1}{N}\left[1 + \frac{1}{(2^n - 1)}\right] \approx \frac{1}{N}$$

(3) The relative number of times $\hat{T}$ that y_k falls in the interval for which the first d positions of the binary expansion are fixed, i.e., a neighborhood of length 2^{-d} in the interval [0. 1), has mean value

$$T = E\left[\hat{T}\right] = 2^{-d}\left[1 + \frac{1}{(2^n - 1)}\right] + \frac{1}{2}\left[g(\mathbf{0}) - 1\right]\left(\frac{1}{2^n - 1}\right) \approx 2^{-d}$$

for any number N of points y_k. The variance of $\hat{T}$ is bounded by

$$\text{var}\left[\hat{T}\right] < \frac{1}{4}\left[1 + \frac{1}{(2^n - 1)}\right]\left[\frac{1}{N} + \frac{2}{(2^n - 1)}\right] \approx \frac{1}{4N}$$

(4) The relative number of times $\hat{T}$ that $(y_k, y_{k-l_2}, \cdots, y_{k-l_M})$ falls in the interval of the unit M-cube for which the first d_i positions of the binary expansion of y_{k+l_1} is fixed, i.e., in a $2^{-d_1} \times 2^{-d_2} \times \cdots \times 2^{-d_M}$ interval in the unit M-cube, has as a mean value

$$T = E(\hat{T}) = 2^{-(d_1 + \cdots + d_M)}\left(1 + \frac{1}{2^n - 1}\right) + 2^{-n-1}\left(\frac{g(\mathbf{0}) - 1}{1 - 2^{-n}}\right) \approx 2^{-(d_1 + d_2 + \cdots + d_M)}$$

for any number N of points $(y_k, y_{k-l_2}, \cdots, y_{k-l_M})$, provided $0 < l_2 < \cdots < l_M < n/q - 1$. The variance of $\hat{T}$ is then bounded by

$$\text{var}\left[\hat{T}\right] < \frac{1}{4}\left[\frac{1}{N} + \frac{2}{2^n + 1}\right]\left[1 + \frac{1}{2^n + 1}\right] \approx \frac{1}{4N}$$

3. Correlation Properties

It is quite easy to verify that part 1 of the theorem above follows even if q is not relatively prime to $2^n - 1$, regardless of the value of q and L. However, the other three results of the theorem do depend on the relations between q, L, and n.

Consider first $\hat{R}(m)$, the sample autocorrelation function. Its mean value $R(m)$ is obtained by averaging $\hat{R}(m)$ over all initial starting values y_0 (or w_0) of the sequence. For convenience, set $p = 2^n - 1$.

$$R(m) = E\left[\hat{R}(m)\right] = \frac{1}{pN}\sum_{k=1}^{N}\sum_{t=1}^{L}\sum_{u=1}^{L} 2^{-(t+u)} \times \sum_{r=0}^{p-1} \alpha_{qk+r-t}\ \alpha_{q(k+m)+r-u}$$
$$= \sum_{t=1}^{L}\sum_{u=1}^{L} 2^{-(t+u)} \times \left[\frac{1}{p}\sum_{r=0}^{p-1} \alpha_r\, \alpha_{r+qm+t-u}\right]$$

and so far, no restriction has been placed on q, L, and n. One of the fundamental properties of a maximal-length linear sequence α is

$$\frac{1}{p}\sum_{r=0}^{p-1} \alpha_r\, \alpha_{r+v} = \begin{cases} +1 & \text{if } v \equiv 0 \pmod{p} \\ -\dfrac{1}{p} & v \not\equiv 0 \pmod{p} \end{cases}$$

Thus, in the equation for $R(m)$, the last sum can be replaced by unity whenever $qm + t - u \equiv 0 \pmod{p}$ and by $-1/p$ otherwise. For a particular fixed m, there is at most one pair (t, u) such that $qm + t - u \equiv 0 \pmod{p}$, and because $u, t \leq L < p$, it is possible that no t or u satisfies the condition. We are interested primarily in the first "few" values of m, so let us restrict our attention to $m \leq (p - L)/q$ (which is ordinarily quite a large number anyway). In this case the bracketed sum in $R(m)$ is 1 only when $m \geq 1$ and $u - t = qm \leq L - 1$, so $1 \leq m \leq (L - 1)/q$. As a consequence, when $q \geq L$ the bracketed sum is never 1, and the first part of 2 in the theorem results. However, in the case $L > q$ there may be values of u and t such that the bracketed sum is 1, and this results in the general formulation

$$R(m) = \begin{cases} \dfrac{1}{3}\left[2^{-qm} - 2^{-(2L-qm)}\right] + \epsilon & \text{if } 1 \leq m < \dfrac{L}{q} \\ \epsilon & \text{if } m > \dfrac{L}{q} \end{cases}$$

where $|\epsilon| < 2/p$. This result is general, and does not depend on any relation between q, L, and n. [But $m \leq (p - L)/p$].

The sample autocorrelation function is a function of r and is itself a random process; its mean-squared value for $m \neq 0$ is

$$E\left[\hat{R}^2(m)\right] = \sum_{t=1}^{L}\sum_{u=1}^{L}\sum_{i=1}^{L}\sum_{j=1}^{L} 2^{-(t+u+i+j)}\ \mu_{tuij}$$

where μ_{tuij} is defined by

$$\mu_{tuij} = \frac{1}{pN^2}\sum_{k=1}^{N}\sum_{l=1}^{N}\sum_{r=0}^{p-1}\alpha_{r+kq-t}\ \alpha_{r+(k+m)q-u}\ \alpha_{l+lq-i}\ \alpha_{r+(l+m)q-j}$$

$$= \frac{1}{N^2}\sum_{k=1}^{N}\sum_{l=1}^{N} \times \frac{1}{p}\left[\sum_{r=0}^{p-1}\alpha_r\,\alpha_{r+qm+t-u}\ \alpha_{r+q(l-k)+t-i}\ \alpha_{r+(l+m-k)q+t-j}\right]$$

The latter two terms in the product are, by the *cycle and add property* of maximum-length linear sequences,

$$\alpha_{r+q(l-k)+t-i}\ \alpha_{r+q(l-k)+mq+t-j} = \begin{cases} 1 & \text{if } j \equiv i + mq \pmod{p} \\ \alpha_{r+q(l-k)+v_2} & \text{otherwise} \end{cases}$$

in which v_2 depends only upon t, i, j, and m. The entire product takes the value unity in only two cases: (1) both $u \equiv t + mq \pmod{p}$ and $j \equiv i + mq \pmod{p}$, or (2) $v_1 \equiv v_2 + q(l-k) \pmod{p}$. In the first case, $\mu_{tuij} = 1$; in the second, assuming that (1) is not also in effect, there are at most (q, p) values of k for each l which satisfy the conditions. So μ_{tuij} is bounded by

$$\mu_{tuij} < \frac{(q, p)}{N}$$

We can separate the summing process for $E[\hat{R}^2(m)]$ into two parts: over those (t, u, i, j) giving (1) above and the remainder. This produces the bound

$$E[\hat{R}^2(m)] < [R(m) - \epsilon]^2 + \frac{(q, p)}{N}$$

By this, it is easy to see that the variance of our sample autocorrelation function is

$$\mathrm{var}[\hat{R}(m)] < \frac{(q, p)}{N} + \epsilon^2$$

The value of $|\epsilon|$ is less than $2/p$ and, for practical purposes, can be neglected.

4. Distribution Properties

Carefully following the proof in Ref. 4, part 3 of the theorem follows for every $d \leq L \leq n$ without restriction on q. Thus, the numbers w_k (or y_k) are "white" and uniformly distributed.

Now we consider the distribution of $(y_k, y_{k-l_2}, \cdots, y_{k-l_M})$ where we order $0 < l_1 < l_2 < l_M$ for convenience. Part 4 of the theorem states that these numbers lie uniformly distributed on the M-cube when $q(l_M + 1) \leq n$ and $q \geq L$. Let us relax these constraints for the treatment which is to follow. We shall count the relative number of times the M-tuple $y = (y_k, y_{k-l_2}, \cdots, y_{k-l_M})$ lies in an arbitrary given $2^{-d_1} \times \cdots \times 2^{-d_M}$ interval. Let the initial positions in the binary expansion of y_{k-l_i} be $0.e_1^i e_2^i \cdots e_{d_i}^i$ for $i = 1, 2, \cdots, M$, where each $d_i \leq L$. Whenever $q(l_j - l_{j-1}) < d_j$, the numbers y_{k-l_j} and $y_{k-l_{j+1}}$ have an overlap; that is, the first $d_j - (l_j - l_{j-1}) = b_{ji}$ binary digits of y_{k-l_j} appear in the first d_j digits of $y_{k-l_{j-1}}$. There cannot be equidistribution in this case, and in fact, the distribution is nonzero only in those intervals such that $(e_1^1, e_2^1, \cdots, e_{b_{j1}}^1)$ is the same as $(e_{d_1-b_{j1}}^1, \cdots, e_{d_j}^j)$.

By the same token, if $q(l_j - l_{j-1}) \geq d_j$ for all i and j, and if, in addition, $ql_M + d_M \leq n$, equidistribution does result. (See Ref. 4).

The remaining case that we must consider is that for which $q(l_j - l_{j-1}) \geq d_j$ for all i and j, but $ql_M + d_M > n$ In the remainder of this section we shall assume that this is the case.

Define a Boolean function $g(\mathbf{x}) = g(x_1, \cdots, x_{l_M q+d_M})$ as follows:

$$g(\mathbf{x}) = \begin{cases} -1 & \text{if } x_{l_i q+j} = e_j^i \\ & \text{for } i = 1, 2, \cdots, M \text{ and } j = 1, 2, \cdots, d_i \\ +1 & \text{otherwise} \end{cases}$$

If we let the Boolean function variables be

$$x_t = a_{qk+r-t}$$

then $\gamma_k = g(\mathbf{x}) = -1$ whenever $\mathbf{y}$ lies in the proper interval; otherwise $\gamma_k = g(\mathbf{x}) = 1$.

The relative number of times $\hat{T}$ that an M-tuple $\mathbf{y}$ falls in the specified interval is thus

$$\hat{T} = \frac{1}{2N}\left[N - \sum_{k=1}^{N}\gamma_k\right]$$

We can use the transformed equation (Ref. 4) to express γ_k

$$\gamma_k = \sum_{\mathbf{s}} G(\mathbf{s})\,\alpha_{qk+r-1}^{s_1} \cdots \alpha_{qk+r-ql_M-d_M}^{sql_M+d_M}$$

By the cycle-and-add property, products in the summand are

$$\alpha_{r-1}^{s_1} \cdots \alpha_{r-ql_M-d_M}^{sql_M+d_M} = \begin{cases} 1 \text{ if } f(\mathbf{x}) \text{ divides } \sum_{i=1}^{ql_M+d_M} s_i x^i \\ \alpha_{r+v(\mathbf{s})} \qquad \text{otherwise.} \end{cases}$$

Now if we denote $S = \left\{ s \,;\, f(x) \text{ divides } \sum_{i=1}^{ql_M+d_M} s_i x^i \right\}$,

we have the result

$$\gamma_k = \sum_{s \in S} G(s) + \sum_{s \notin S} G(s)\, \alpha_{qk-r+r(s)}$$

The expected value of $\hat{T}$ is now

$$T = E\left[\hat{T}\right] = \frac{1}{p} \sum_{r=0}^{p-1} \hat{T}$$

$$= \frac{1}{2} - \frac{1}{2}\left(1 + \frac{1}{p}\right) \sum_{s \in S} G(s) + \frac{1}{2p}\, g(0)$$

$$\approx \frac{1}{2}\left[1 - \sum_{s \in S} G(s)\right]$$

of course, $\mathbf{0}$ is always in S. Excluding this element, $S' = S - \{\mathbf{0}\}$; and using $G(\mathbf{0}) = 1 - 2^{1-(d_1+d_2+\cdots+d_M)}$,

$$T \approx 2^{d_1+d_2+\cdots+d_M} - \frac{1}{2} \sum_{s \in S'} G(s)$$

Thus, the relative frequency T depends on the interval being tested [i.e., the choice of $g(\mathbf{x})$], so the distribution is not necessarily uniform.

5. Conclusions

In order that all the results of the theorem be true it is necessary that all the stated hypotheses be true. However, as some of these are relaxed, one can conclude the following:

(1) If $(q, p) \neq 1$, only part 4 of the theorem is affected, and this only to the extent

$$\text{var}\left[\hat{R}(m)\right] < \frac{(q,p)}{N} + \delta\,, \text{ where } [\delta] < \frac{4}{p^2}$$

(2) Generally, for $1 \leq |m| \leq \dfrac{p-L}{q}$

$$R(m) = \begin{cases} -\dfrac{1}{3}\left(2^{-qm} - 2^{2m-2L}\right) + \epsilon & \text{if } 1 \leq m < \dfrac{L}{q} \\ \epsilon & m \geq \dfrac{L}{q} \end{cases}$$

with $|\epsilon| < \dfrac{2}{p}$. In addition, (1) above holds.

(3) The distribution is not uniformly distributed unless $ql_M + d_M \leq n$ and $q(l_i - l_{i-1}) \geq d$, for all i, j. In fact, the distribution lies concentrated in intervals such that $(e^i, e^i_2, \cdots, e^i_{b_{j,i}}) = (e^j_{d_{i-1}+1}, \cdots, e^j_{d_i})$ whenever the latter condition fails. If only the former condition fails, distribution depends upon which interval we scrutinize and which polynomial $f(x)$ generates $\{a_k\}$.

References

1. Paley, R. E. A. C., *On Orthogonal Matrices*, Journal of Mathematics and Physics, 12 (1933), pp. 311–320.
2. Williamson, J., *Hadamard's Determinant Theorem and the Sum of Four Squares*, Duke Mathematical Journal, 11 (1944), pp. 65–81.
3. Hall, Marshall, Jr., *Hadamard Matrices of Order 16*, Research Summary, No. 36–10, Jet Propulsion Laboratory, Pasadena, pp. 21–26.
4. Tausworthe, R. C., "Random Numbers generated by Linear Recurrence, Modulo 2," *Mathematics of Computation*, 19 No. 90 (1965), pp. 201 and SPS 37–27 and 37–29, Vol. IV, pp. 185–189 and 211–213, respectively.

XXV. Communications Systems Research: Information Processing

A. Onto Finite State Machines

E. C. Posner

This article continues the discussion on finite state machines previously reported in *SPS 37-32*, Vol. IV, pp. 256–259. Here onto machines are considered, that is, machines that have every output sequence arise from some input sequence. It is shown that if every output sequence arises from at most a bounded number of input sequences, then the machine is onto; the converse is due to D. Blackwell.

1. Introduction

A *finite state machine* is defined as an abstraction of the behavior of a digital machine such as might be found in the Deep Space Network (DSN) for signal generation and processing. The key part of the definition of a finite state machine is that the machine can read the input tape in one direction only, and it produces an output which is no longer available to the machine. Thus a finite state machine is more specialized than a "general purpose computer," and yet the concept includes many types of "stored program controllers" used throughout the DSIF.

The rigorous abstract definition of a finite state machine is found on p. 257 of *SPS 37-32*, Vol. IV. Informally, there is a finite collection S of *states*, a finite *input alphabet* A and *output alphabet* B. Also defined are two functions, ϕ and ψ, which yield respectively the output symbol and next state for the given input symbol and present state. The functions ϕ and ψ can also be thought of as being defined on all input sequences of given length n, in the sense that ϕ and ψ give respectively the output sequence and the final state for a given input sequence and initial state.

In this article, A will be taken equal to B; that is, the input and output alphabets are the same. Usually in applications A and B are the set $\{0, 1\}$, although this assumption is not needed here. Another case of interest in the DSN is when $A = B$ and has 32 elements, the 32 teletype characters. Cases in which A and B do not have the same number of elements can arise in coding theory, where B is a set of codewords which may be smaller than a set of received words.

2. Irreducibility

The concept of an irreducible machine is needed. A finite state machine is called *irreducible* if and only if given two states there is an input of some length which sends the first state as initial state onto the second as final state; this language is borrowed from the theory of Markov chains.

D. Blackwell (Ref. 1) proved the following: let M be an onto finite state machine in which $A = B$. Then the number of inverse images of any output sequence of any length whatever is bounded by s^2, where s is the number of states.

It is easy to prove that if there is any bound, then the bound is s^2. For if some output β had more than s^2 inverse images, then there would be two states S_1 and S_2 and two distinct input sequences α_1 and α_2 whose lengths are the length of β, such that the output sequence is β and the final state is S_2 if the initial state is S_1 and the input is either α_1 or α_2. For there are s^2 pairs (S_1, S_2), so that one of them must occur twice as initial and final states giving β as an output. By irreducibility, α_1 and α_2 can be extended so as to produce the same output β' and final state S_1 starting from initial state S_1 with different inputs α_1' and and α_2'. For there is an input γ such that γ brings S_2 to S_1. Let δ be the output; then $\beta' = \beta\delta$, $\alpha_1'\gamma = \alpha_1\gamma$, $\alpha_2'\gamma = \alpha_2\gamma$.

Now there are 2^l inputs of the form $\alpha_{i_1}'\alpha_{i_2}'\cdots\alpha_{i_l}'$, $i_j = 1, 2$, $(1 \leq j \leq l)$. Furthermore, all these are distinct and each gives an output $(\beta')^l$ when the initial state is S_1. This contradicts the assumption that the size of the number of input sequences with a given output sequence is bounded. Hence, if there is a bound for an irreducible machine, then a bound is the square of the number of states.

3. Boundedness Implies Ontoness

In this section, the converse of Blackwell's result will be proved.

Theorem: Let M be a finite state machine in which the input and output alphabets are identical. Let M be irreducible. Then if the size of the set of input sequences producing a given output sequence is bounded, the machine is onto.

Proof: Let the size of the alphabet be q, which clearly may be assumed greater than 1. Let β be an m-tuple not the output starting from any initial state. We shall show that the number of sequences of length n composed of elements of A which do not contain β is an arbitrarily small fraction of the total number of sequences n of length n.

This fact will be proved probabilistically. We may suppose n is a multiple km of m, the length of β. Consider the random process consisting of choosing with equal probability $1/q^m$ one of the q^m sequences of length m. Repeat this experiment k times. Given $\epsilon > 0$, there is a k so large that the probability of not getting β in k trials is less than $(1 - 1/q^m)^k < \epsilon$.

But the probability of not getting β at least once in k trials is less than the probability of there being no β anywhere in the sequence of n symbols, where each symbol is chosen independently with probability $1/q$. Hence, there is an n so large that the probability of not having a β in n symbols is also less than ϵ. Since every sequence of length n in this model has the same probability, we can make a nonprobabilistic statement: if n is sufficiently large, fewer than ϵq^n of the q^n sequences of length n fail to contain the m-length sequence β, for ϵ an arbitrary positive number, and given m.

Now suppose the class of output sequences is contained in the set of sequences not containing β; that is, let β not be an output. Then fewer than ϵq^n sequences of length n are outputs. Furthermore, a given input sequence yields at most s outputs, since there is an output for each initial state. Since there are q^n input sequences, some output sequence occurs for more than $1/s\epsilon$ input sequences. Since ϵ is arbitrarily small, $1/s\epsilon$ is unbounded. Therefore, if the sizes of inverse images are bounded, M is onto. This proves the theorem.

The upshot of this result is that for irreducible machines in which A and B have the same number of elements, ontoness is equivalent to the property that the number of inverse images of any output sequence is bounded by s^2, the square of the number of states. If an irreducible machine with the same input and output alphabet is desired which produces a certain output for t different inputs and yet can produce any output, then $s \geq (t)^{1/2}$. This result may be of use in machine design.

B. Generalized Barker Sequences

S. W. Golomb and R. A. Scholtz[1]

A generalized Barker sequence is a finite sequence $\{a_\tau\}$ of complex numbers having an absolute value 1 and possessing a correlation function $C(\tau)$ satisfying the constraint $|C(\tau)| \leq 1$, $\tau \neq 0$. Classes of transformations leaving

[1]Prepared under purchase order 951076 with the Electrical Engineering Department, University of Southern California.

$|C(\tau)|$ invariant are exhibited. Constructions for generalized Barker sequences of various lengths and alphabet sizes are given. Sextic Barker sequences are investigated and examples given for all lengths through thirteen. No theoretical limit to the length of sextic sequences has been found. These sequences generalize to polyphase modulated radars the binary Barker sequences used in certain biphase modulated radars for range gating.

author

1. Introduction

A Barker sequence (Ref. 2) is a sequence $\{a_r\}$ of $+1$'s and -1's of some finite length k such that the correlation function $C(\tau)$ defined by $C(\tau) = \sum_{r=1}^{k-\tau} a_r a_{r+\tau}$ satisfies $|C(\tau)| \leq 1$ for $\tau \neq 0$. In this discussion consider "generalized Barker sequences" $\{a_r\}$ of finite length k, where the terms a_r are allowed to be complex numbers of absolute value 1, where correlation is now the Hermitian dot product $C(\tau) = \sum_{r=1}^{k-\tau} a_r a_{r+\tau}^*$ (z^* denotes the complex conjugate of z), and the same restriction $|C(\tau)| \leq 1$ for $\tau \neq 0$ is imposed. We will exhibit a class of transformations which leave the absolute value of the correlation function unaltered, so that, in particular, generalized Barker sequences are changed into other generalized Barker sequences. We examine the effect of these transformations on the original (± 1) Barker sequences and on four-valued (± 1, $\pm i$) Barker sequences; and then exhibit constructions for generalized Barker sequences of a variety of lengths and all possible alphabet sizes. Finally, we observe some very interesting facts about sextic Barker sequences, including that they have occurred for all lengths tested (i.e. for $k \leq 13$) and could conceivably occur for all possible sequence lengths.

2. Barker-Preserving Transformations

Let $\{u_r\}$ be a complex-valued sequence of length k, and let its autocorrelation function $C_u(\tau) = \sum_{r=1}^{k-\tau} u_r u_{r+\tau}^*$. We define a new complex-valued sequence $\{v_r\}$ of length k as follows:

$$v_r = u_r e^{\frac{2\pi i r}{m}} \tag{1}$$

where m is any nonzero integer. Then we observe that the autocorrelation function $C_v(\tau)$ of $\{v_r\}$ satisfies

$$C_v(\tau) = \sum_{r=1}^{k-\tau} v_r v_{r+\tau}^* = \sum_{r=1}^{k-\tau} u_r e^{\frac{2\pi i r}{m}} u_{r+\tau}^* e^{\frac{-2\pi i (r+\tau)}{m}}$$

$$= \sum_{r=1}^{k-\tau} u_r^* u_{r+\tau} e^{\frac{-2\pi i \tau}{m}} = e^{\frac{-2\pi i \tau}{m}} C_u(\tau) \tag{2}$$

for all τ. In particular, since $|e^{(-2\pi i \tau)/m}| = 1$, we have $|C_v(\tau)| = |C_u(\tau)|$ for all τ, as well as $|v_r| = |u_r|$ by virtue of Eq. (1). As a special case, if $|u_r| = 1$ for all r, transformation (1) takes a generalized Barker sequence of length k into another generalized Barker sequence of length k.

Further we observe that the somewhat more general transformation

$$v_r = u_r e^{\frac{2\pi i (r-\alpha)}{x}} \tag{3}$$

where α and x are any real numbers, $x \neq 0$, also preserves $|v_r| = |u_r|$ and $|C_v(\tau)| = |C_u(\tau)|$. Finally, the transformation $v_r = u_{k-r+1}$, which merely runs the sequence backwards, clearly preserves the Barker property, as does the transformation $u_r = u_r^*$ (where the asterisk again denotes complex conjugation).

In summary, there is a group of $4m^2$ transformations, each of which takes m-phase Barker sequences into m-phase Barker sequences. As generators of this group, we may take the two order-2 transformations of time reversal and complex conjugation and the two order-m transformations of constant multiplication by ζ and progressive multiplication by successive powers of ζ, where $\zeta = e^{2\pi i/m}$.

3. Specific Examples

If we take $m = 2$ in Eq. (1) then the sequence $(u_1, u_2, u_3, u_4, \cdots, u_k)$ is changed into $(u_1, -u_2, u_3, -u_4, \cdots, (-1)^{k-1}u_k)$. In particular, this transformation changes ordinary binary Barker sequences into other such sequences, though nothing very startling is obtained in this way. Taking $m = 4$, the sequence $(u_1, u_2, u_3, u_4, \cdots, u_k)$ is changed into $(u_1, iu_2, -u_3, -iu_4, \cdots, i^{k-1}u_k)$. In particular, this transformation sets up a one-to-one correspondence between ordinary (binary) Barker sequences and four-symbol Barker sequences (the symbols being ± 1, $\pm i$) in which real and imaginary terms alternate. This correspondence is illustrated in Table 1 for binary Barker sequences of all known lengths. [From the results of Storer and Turyn (Ref. 3) there are no other binary Barker sequences of odd length, and the possibility of other such sequences of even length seems quite remote.] Another description of the correspondence is that between successive terms in the binary sequence there is a transition of either 0 or 180 deg, while between successive terms in the alternating quaternary sequence, there is a transition of either 90 or 270 deg. We let 0-deg transitions correspond to 90-deg transitions, while 180-deg transitions correspond to 270-deg transitions, respectively.

Table 1. Correspondence between binary and alternating quaternary Barker sequences

Length	k binary sequence
1	+1
2	+1, +1
3	+1, +1, −1
4	+1, +1, +1, −1
5	+1, +1, +1, −1, +1
7	+1, +1, +1, −1, −1, +1, −1
11	+1, +1, +1, −1, −1, −1, +1, −1, −1, +1, −1
13	+1, +1, +1, +1, +1, −1, −1, +1, +1, −1, +1, −1, +1
	Quaternary Barker sequence
1	+1
2	+1, +i
3	+1, +i, +1
4	+1, +i, −1, +i
5	+1, +i, −1, +i, +1
7	+1, +i, −1, +i, −1, +i, +1
11	+1, +i, −1, +i, −1, −i, −1, +i, −1, +i, +1
13	+1, +i, −1, −i, +1, −i, +1, −i, +1, −i, −1, +i, +1

It is interesting to note that the quaternary alternating Barker sequences of odd length are all *palindromic* (i.e., read the same forward and backward), thus evidencing a symmetry which is obscured in the binary representation.

Next, we consider a quaternary Barker sequence of length 15 (Ref. 4) which is not equivalent to a binary Barker sequence. In Table 2, we see such a sequence, together with its transforms corresponding to $m = 2$ and $m = 4$.

We observe that the effect of the $m = 2$ transformation is to replace the original terms by their complex conjugates in reverse order. Since reversal of order and conjugation of elements are both elementary symmetries which preserve Barker correlation, nothing essentially new has been obtained. However, the transformation with $m = 4$ yields a very different sequence from the original. For example, whereas the original sequence had one run of length 3 and two runs of length 2 each, the transformed sequence has one run of length 3 but only one run of length 2. Also the original sequence has its run of length 3 at the end, whereas the transformed sequence has its longest run near the middle.

Table 2. Transformations on a quaternary Barker sequence

Original sequence
+1, −1, +i, +i, −i, −1, +i, −i, −i, +1, +i, +i, +1, +1, +1
Transform with $m = 2$
+1, +1, +1, −i, −i, +1, +i, +i, −i, −1, +i, −i, +1, −1, +1
Transform with $m = 4$
+1, −i, −1, +1, −i, −i, −i, −1, −i, +i, −i, +1, +1, +i, −1

It may be mentioned in passing that, despite its title, Ref. 5 contains no examples of quaternary Barker codes.

4. General Alphabets

Let $\rho = e^{2\pi i/n}$, and define the alphabet A_n to be the set $\{1, \rho, \rho^2, \rho^3, \cdots, \rho^{n-1}\}$. For subsequent convenience, we also define $\eta = \rho^{[(n-1)/2]}$, the lowest power of ρ whose phase angle is at least 180 deg.

We ask the general question on the existence of Barker sequences as follows: "For a given sequence of length k, what are all the values of n such that a Barker sequence of length k can be constructed from the alphabet A_n?"

In Table 3, we answer this question completely for $k = 1,2,3,4,5$ by exhibiting constructions which work for all $n \geq 2$. A couple of simple observations will assist the reader in verifying that the out-of-phase correlations are indeed ≤ 1.

(1) The sum of 2 unit vectors lies within the unit circle if and only if the angle between these vectors is between 120 and 240 deg. (In particular, $1 + \eta$ lies within or on the unit circle for $\eta \geq 2$, with the tightest squeeze when $\eta = 3$. $\rho + \eta$ lies within or on the unit circle except, when $\eta = 1,2,4$, with the tightest squeezes when $\eta = 3$ and 6.

(2) The sum of 3 unit vectors lies within the unit circle if and only if there is no semicircle properly containing all three vectors. (In particular, since the sets $1, \eta, \eta^*$ and $1, \rho, \eta$ each defy containment within a semicircle, the vectors $1 + \eta + \eta^*$ and $1 + \rho + \eta$ do not extend beyond the unit circle.) Finally, we may observe that $1 + \rho + \eta + \eta^*$ lies outside the unit circle for $n = 1,2,4$; on the unit circle for $n = 3,5,6$; and within the unit circle for $n \geq 7$. (In fact, this vector sum decreases in magnitude to zero as n increases to infinity.)

Table 3. Construction for generalized Barker sequences for all lengths up to 5 and all alphabet sizes greater than 1

k	Sequence	Correlation function	Which n?
1	1	1	all $n \geq 1$
2	1, 1	2, 1	all $n \geq 1$
3	1, 1, η	3, 1 + η, η	all $n \geq 2$
4	1, 1, η, 1	4, 1 + η + η^*, 1 + η, 1	all $n \geq 2$
5	1, 1, 1, −1, 1 1, 1, ρ, η, ρ	5, 0, 1, 0, 1 5, 1 + ρ + η + η^*, 1 + ρ + η, ρ + η, ρ	all even n all n except 1, 2, 4 — all $n \geq 2$

A simple necessary and sufficient condition for the sum of four unit vectors to lie within the unit circle has not been found. However, the following two necessary conditions are sharp.

(1) The four vectors must not be contained within an arc of less than $2\cos^{-1}(1/4) \approx 151$ deg.

(2) No three of the four vectors may be contained within an arc of less than 180 deg − $\cos^{-1}(1/4) \approx$ 104.5 deg.

For the case $k = 6$, it has long been known that there is no binary Barker sequence. An exhaustive search has shown that there is also no generalized Barker sequence of length 6 for alphabet sizes of 3, 4, or 5. However, the following example using the alphabet A_6 has been found

$$1, 1, \epsilon, -1, 1, -\epsilon$$

where $\epsilon = e^{2\pi i/6}$. The correlation values for this sequence are 6, ϵ^2, ϵ^1, ϵ^3, ϵ^5, ϵ^4.

Except for the Barker-preserving transformations discussed earlier, this example is unique. However, in one of its transformed avatars, it takes the form

$$1, \epsilon, -1, 1, -\epsilon, -1$$

for which the correlation values are 6, −1, −1, 1, −1, −1.

A Barker sequence is called *palindromic* if the sequence reads the same forward and backward, except for at most a real constant factor. Clearly the correlation function of a palindromic sequence is real. We have observed that there are sextic palindromic sequences of every length through 9, none of length 10 and one of length 11.

5. The Sextic Alphabet

There is strong evidence to indicate that a Barker sequence of length 6 can only be achieved over an alphabet A_n for which n is a multiple of 6. Moreover, the sixth roots of unity (with zero adjoined) have remarkable arithmetic which is partially closed under addition, as well as closed under multiplication.

In Table 4, we see the present state of knowledge concerning binary, ternary, quaternary, and sextic Barker sequences. The appropriate earlier references for these cases are: binary (Ref. 3), ternary (Ref. 6), and quaternary (Ref. 4). However, these cases have all been rechecked. In Table 4 a blank indicates that no such

Table 4. Comparison of the sequences available from the alphabet A_2, A_3, A_4, and A_6

k \ n	2	3	4	6
1	✓	✓	✓	✓
2	✓	✓	✓	✓
3	✓	✓	✓	✓
4	✓	✓	✓	✓
5	✓		✓	✓
6				✓
7	✓	✓	✓	✓
8				✓
9		✓		✓
10				✓
11	✓		✓	✓
12				✓
13	✓		✓	✓
14				?
15			✓	?

sequence exists, while a question mark means that the question has not yet been exhaustively searched. We see that for lengths $k = 6$, 8, 10, and 12, there are no examples of binary, ternary, or quaternary sequences, but that sextic examples exist, as follows:

$$S_6 = 1, 1, \epsilon, -1, 1, -\epsilon$$

$$S_8 = 1, 1, \epsilon, 1, -\epsilon, \epsilon, -1, \epsilon^*$$

$$S_{10} = 1, 1, -\epsilon, -1, -\epsilon^*, -\epsilon, -1, \epsilon^*, -\epsilon^*, -\epsilon$$

$$S_{12} = 1, 1, \epsilon, 1, \epsilon^*, -\epsilon^*, -\epsilon^*, -\epsilon, 1, -\epsilon, \epsilon, -1$$

Examples of lengths 6, 8, and 10 were first discovered by the authors. Examples of length 12 were found in a computer search conducted by Harold Fredricksen. Of these, only S_6 is unique up to Barker-preserving transformations. This is one of several facts supporting the highly tentative conjecture that sextic Barker sequences exist for all sequence lengths, in sharp contrast to the binary case (Ref. 3). That is, the search routines indicate that sextic examples may become more numerous as the sequence length increases.

6. Sequences of Length 7

The case of sequence length 7 has been settled definitively, as shown in Table 5, which augments Table 3.

Table 5. Sequences of length 7

k	Sequence	Correlation function	Remarks
7	1, 1, 1, −1, −1, 1, −1	7, 0, −1, 0, −1, 0, −1	All even n
	1, 1, β, β, 1, β, 1	7, 2 (1 + υ), 2 + υ + β, 2 + υ, 1 + υ, 1 + β, 1 Where $\upsilon = \beta + \beta^*$	All odd $n > 1$ except 5 & 7 as well as large even n

Here β is an element of A_n with a phase angle between 120 deg and $\pi - \cos^{-1}(3/4) \approx 138\frac{1}{2}$ deg. Not only are there no 5th or 7th roots of unity with phase angles in this range but an exhaustive search has shown that there are no Barker sequences of length 7 over A_5 or A_7.

N65-32468

C. Weights of Cyclic Codes

G. Solomon

A new formula is presented for the weight or number of ones in a binary cyclic code. The formula allows quick computation of the error-correcting properties of a large class of codes.

1. Introduction

In the past few years, coding theory has witnessed the discovery of new classes of practical codes of a highly algebraic nature. These codes are easily encodable and their error-correcting procedure is a sequence of easily mechanizable algebraic operations. These codes (Ref. 7) (Bose-Chaudhuri, cyclic, polynomial, shift register...) use the shift register device both as part of the systematic encoding as well as for the multiplication operations in the associated finite fields. While certain group codes can be characterized by specifying the encoding and decoding procedures in terms of certain polynomials and field parameters, there are many cases for which the precise error-correcting properties of these codes (i.e., the minimum weight of all nonzero vectors of a code) are not known. Indeed, the distribution of weights of a code is not known in general.

To be specific, for n odd, let A be any (n,k) group code, i.e., a k-dimensional subspace of $V_n(F)$, the vector space of dimension n over the field F of two elements. The weight of a vector $a = (a_i) \in A$, $w(a)$, is defined to be the number of a_i equal to 1. A classical coding theory problem is to determine the error-correcting properties of the code A, i.e., the minimum weight of all nonzero vectors in A. We also want to know the values of the weights actually occurring for all words in the code, and, in fact, sometimes we even need the number of vectors having a given weight. This counting problem — this looked-for formula or analytic expression for the weight of a vector in terms of the parameters which characterize the code — is made interesting by the fact that our code operations are all modulo (mod) 2, whereas the weight function is integer-valued.

We present in this discussion an explicit expression for the weight of a vector $w(a) = \sum_{i=0}^{N} \Gamma_{2^i}(a) 2^i$. The Γ_i are expressed as a function of several variables. These variables are the parameters in the general representation of cyclic codes in Mattson–Solomon (Ref. 8). The coefficients of the formula are obtained by using elementary field

operations in the cyclic group of the n^{th} roots of unity. Γ_1 has been known for some time. We obtain here an expression for Γ_2. Using this expression, we obtain general results for weights occurring in certain cyclic codes. The method is extendable to Γ_4 and the higher Γ's; Γ_4 gives information about the number of code words of given weight. The higher order Γ's are left for a subsequent issue of this summary.

2. The Binary Representation of the Weight Vector

Let $a = (a_0, a_1, \cdots, a_{n-1})$ be a binary n-tuple. If w is the number of ones in a, then the following equations are true

$$\Gamma_1 = \sum_{i=0}^{n-1} a_i \equiv \binom{w}{1} \pmod 2$$

$$\Gamma_2 = \sum_{i<j} a_i a_j \equiv \binom{w}{2}$$

$$\Gamma_w = \sum_{i_1<i_2<i_3<\cdots<i_w} a_{i_1} a_{i_2}, \cdots, a_{i_w} \equiv \binom{w}{w}$$
$$\equiv 1 \pmod 2$$

$$\Gamma_l = 0 \qquad l > w.$$

The weight of a, $w(a)$, is given in dyadic form uniquely by $\sum_{i=1}^{N} w_i 2^i$ where $N = [\log_2 n]$; and, as usual, $w_i = 0$ or 1. The following lemma is crucial.

Lemma: If $\sum w_i 2^i$ is the dyadic expansion of w, then $w_i \equiv \binom{w}{2^i} \bmod 2$. That is, $w_i = \Gamma_{2^i}$.

Proof: We expand the polynomial $(1 + x)^w$ in two different ways

$$(1+x)^w = (1+x)^{\sum w_i 2^i};$$

$$\sum \binom{w}{i} x^i = \prod_{i=0}^{N} (1+x)^{w_i 2^i}$$

$$= \prod_{i=0}^{r} (1 + w_i x)^{2^i}$$

$$= \prod_{i=0}^{w} (1 + w_i^{2^i} x^{2^i}); \text{ but } w_i^i = w_i \text{ so}$$

$$\sum_{i=0}^{w} \binom{w}{i} x^i = \prod_{i=0}^{w} (1 + w_i x^{2^i}).$$

The coefficient of x^{2^i} on the left side of the equation is equal to $\binom{w}{2^i}$. If we examine the right-hand side of the equation, we see that the coefficient of x^{2^i} can only arise from multiplying the $w_i x^{2^i}$ term by $(N - 1)$ ones. Since this is a formal identity, we have $\binom{w}{2^i} = w_i$. This proves Lemma 1. We thus have our weight formula for a vector a,

$$w(a) = \sum_{i=0}^{w} \Gamma_{2^i}(a) 2^i.$$

We shall express the $\Gamma_{2^i}(a)$ as functions of the coefficients of the Mattson-Solomon polynomials for cyclic codes.

3. Representation of Cyclic Codes

Let A be an (n,k) cyclic code generated by the recursion rule $\sum_{i=0}^{k} u_i a_{n-i} = 0$, whose associated polynomial is $f(x) = \sum_{i=0}^{k} u_i x^i$, $u_i \epsilon F$. To every code word $a \epsilon A$ is associated a polynomial $g_a(x) = \sum_{i=0}^{n-1} c_i x^i$, with the following properties. Let β be a fixed primitive n^{th} root of unity. Then

(1) If $a = (a_0, a_1, \cdots, a_{n-1})$ then $g_a(\beta^j) = a_j$;

(2) The c_j are given by the Reed formula

$$c_j = \sum_{i=0}^{n-1} a_i \beta^{-ij} \cdot j = 0, 1, \cdots, n-1.$$

Thus, the c_j are contained in the field containing the n^{th} roots of unity. Note $c_0 = \sum_{i=0}^{n-1} a_i = w(a) \bmod 2$; also,

$$c_{2j} = c_j^2 \qquad \text{all } j.$$

(3) $c_j = 0$ if $f(\beta^j) \neq 0$; i.e., the only c_j that can enter in $g_a(x)$ are those j such that $f(\beta^j) = 0$;

(4) If $a = (a_0, a_1, \cdots, a_{n-1})$ is given by $(g_a(x)^j)$, $g_a(x) = \sum c_j x^j$, then the cyclic shift of a, $Ta = (a_1, a_2, \cdots, a_{n-1}, a_0)$ is given by $g_{Ta}(\beta^j)$ when $g_{Ta}(x) = \sum c_j \beta^j x^j$. Thus, shifting a vector is equivalent to multiplying each c_j by β^j.

(5) If $f(x) = f_1(x) f_2(x), \cdots, f_r(x)$ where $f_i(x)$ is irreducible over F, then there are r independent variables c_{i_r} in $g(x)$, $f_j(\beta^{ij}) = 0$, $f_j(\beta^{ik}) \neq 0$, $j \neq k$, and $g_a(x)$ can be written

$$g_a(x) = Tr\, c_{i_1} x^{i_1} + Tr\, c_{i_2} x^{i_2} + , \cdots, Tr\, c_{i_r} x^{i_r}.$$

Here $Tr(a)$ denotes the trace of a, given by $Tr\ a = \sum_{j=0}^{m} a^{2^j}$ where m is the degree of the irreducible polynomial over F with a as a root.

We note that the c_n term corresponds to the $(x+1)$ factor in $f(x)$, or the all-ones vector. Note $c_n = 1$ implies the weight if a is odd. Thus every odd weight vector a is the sum of the all-one vector and an even-weight vector. Thus we have

(6) The odd weight vectors can be computed from the even-weight vectors, w_{2i} by taking $n - w_{2i}$. Thus, we need only devise our formula for even-weight factors.

4. $\Gamma_i(a)$ as Functions of c_j

We have $w(a) = \sum_{i=1}^{N} \Gamma_{2i}(a) 2^i$, $N = [\log_2 n]$, $w(a) \equiv 0 \bmod 2$. Now

$$\begin{aligned}\Gamma_{2i}(a) &= \sum_{i_1 < i_2 < \cdots < i_{2i}} a_{i_1}, \cdots, a_{i_{2i}}, \\ &= \sum g_a(\beta^{i_1}) g_a(\beta^{i_2}), \cdots, g_a(\beta^{i_{2i}}) \\ &= P(c_{j_1 - j_2}, \cdots, c_{j_{2i}}), \text{ which is a polynomial in } c\text{'s.}\end{aligned}$$

Since $w(Ta) = w(a)$, and since Property (4) of Section 3 above holds, we have

$$P(c_{j_1}, c_{j_2}, \cdots, c_{j_{2i}}) = P(\beta^{j_1} c_{j_1}, \beta^{j_2} c_{j_2}, \cdots, \beta^{j_{2i}} c_{j_{2i}}).$$

So $\sum_{i=1}^{2i} j_i \equiv 0 \bmod n$. This sum-of indices property is essential in the formula for Γ_2.

5. Computation of $\Gamma_2(a)$

We evaluate $\Gamma_2(a)$ in our formula, and using this value, we obtain some new results about cyclic codes.

Theorem:

$$\Gamma_2(a) = \sum_{i=1}^{(n-1)/2} c_i c_{-i}.$$

Proof:

$$\Gamma_2(a) = \sum_{i<j} a_i a_j = \sum_{i \neq j} g_a(\beta^i) g_a(\beta^j) :$$

Let $x = \beta^i$, $y = \beta^j$ say, where $x < y$ if $i < j$. Then we have

$$\begin{aligned}\Gamma_2(a) &= \left(\sum_{i=1}^{n-1} c_i x^i\right)\left(\sum_{i=1}^{n-1} c_j x^j\right) \\ &= \sum_{x<y} \sum_{i,j} c_i c_j x^i y^j.\end{aligned}$$

The coefficient of $c_i c_j$ is given by $\sum_{x<y} (x^i y^j + x^j y^i)$. Now $\sum_{x<y} x^i y^j + x^j y^i = \sum_{x \neq y} x^i y^j$. Thus the conditions $x < y$ is replaced by the more general condition $x \neq y$. To evaluate the sum $\sum_{x \neq y} x^i y^j$, we need to know the following:

$$\sum_{j=0}^{n-1} y^j = 0 \quad \text{unless } j = 0 \text{ (a well-known result).}$$

Thus,

$$\sum_{y \neq x} y^j = \sum_{y^n = 1} (y^j) + x^j = x^j, \text{ whenever } j \neq 0.$$

Therefore

$$\begin{aligned}\sum_{x \neq y} x^i y^j &= \sum_{x^n = 1} x^i \sum_{y \neq x} y^j = \sum_{x^n = 1} x^i x^{-j} - \sum_{x^n = 1} x^{i-j} \\ &\begin{cases} = 0 \text{ if } i + j \equiv 0 \bmod n \\ = n = 1 \text{ (in } F) \text{ if } i + j \equiv 0 \bmod n. \end{cases}\end{aligned}$$

Therefore we have the theorem

$$\Gamma_2 = \sum_{i=1}^{\frac{n-1}{2}} c_i c_{n-i} = \sum_{i=1}^{\frac{n-1}{2}} c_i c_{-i}$$

6. Corollaries of the Γ_2 Formula

Corollary 1. Let A be a cyclic code generated by $f(x)$. If, for every γ such that $f(\gamma) = 0$, we have $f(\gamma^{-1}) \neq 0$, then Γ_2 for the code A is 0.

Proof: Note that c_j corresponds to $f(\beta^j) = 0$. Thus, c_i and c_{-i} are never simultaneously nonzero by hypothesis.

Corollary 2. If $w(a) \equiv 2 \pmod 4$, then $\Gamma_2(a) = 1$.

Proof: $\Gamma_2 = \binom{w}{2} = \dfrac{(4m+2)(4m+1)}{1 \cdot 2}$

$$= (2m+1)(4m+1 \equiv 1 \bmod 2.$$

Corollary 3. All cyclic codes A with $\Gamma_2(A) = 0$ have even weights w which are multiples of 4.

Corollary 3′. All cyclic codes A with $\Gamma_2(A) = 0$ of length $n \equiv 3 \pmod 4$ have only weights $\equiv 0$ or $3 \pmod 4$ occurring. Similarly, if $n \equiv 1$ (4) and $\Gamma_2(A) = 0$, only weights $\equiv 0$ or $1 \pmod 4$ can occur.

7. A General Theorem on Weights

Theorem: Every vector in the class of $[p, (p+1)/2]$ cyclic codes, where $p \equiv -1 \pmod 8$ and $x^n + 1 =$

$(x - 1)\, f_0(x)\, f_1(x)$ where $f_0(x)$, and $f_1(x)$ are irreducible of degree $(p - 1)/2$, has weight $\equiv 0 \pmod 4$.

Proof. It can be shown that $\Gamma_2(a)$ is for even-weight words in these codes. The details are omitted.

The last theorem, when applied to the famous Golay (23,12) code (Ref. 7, p. 70), proves that the code is triple-error-correcting. For the Bose–Chaudhuri bound says that the minimum weight of code words is at least 5. Now $5 \not\equiv 2 \pmod 4$, so 7 is the minimum possible odd weight. And no words of weight 6 occur, since $6 \not\equiv 0 \pmod 4$. This weight of 7 is attained, since the sphere packing bound says that the minimum weight is at most 7. Other proofs of this result have been given by computer search, as well as by projective geometry methods (A. Gleason, unpublished), but the present proof is the shortest known.

D. The Index of Comma Freedom in Kronecker Product Code Dictionaries

J. J. Stiffler

This article relates the comma-free properties of the Kronecker product of two linear codes to the comma-free properties of the constituent codes. These relations are useful in quickly producing codes with special comma-free properties.

1. Introduction

Let A be a dictionary having M m-symbol words $a_j = \alpha_1^j, \alpha_2^j, \cdots, \alpha_m^j$, the symbols α_i^j being elements of an r-ary field. The dictionary is said to have an index of comma freedom $d_m(A)$ if $m - d_m(A)$ equals the maximum number of zeros in the *m-tuple*

$$\{\alpha_1^{j_1} - \alpha_l^{j_2}, \alpha_2^{j_1} - \alpha_{l+1}^{j_2}, \cdots, \alpha_{m-l+1}^{j_1} - \alpha_m^{j_2}, \alpha_{m-l+2}^{j_1} - \alpha_1^{j_3}, \alpha_{m-l+3}^{j_1} - \alpha_2^{j_3}, \cdots, \alpha_m^{j_1} - \alpha_{l-1}^{j_3}\} \tag{1}$$

where the maximization is to be taken over all values of j_1, j_2, j_3 and of $l \not\equiv 0$ modulo m. Thus, $d_m(A)$ is a measure of the difference between any code word overlap and any true dictionary code word.

Let A be as defined in the previous paragraph, and let B represent a dictionary having N n-symbol r-ary words, $b_i = (\beta_1^i, \beta_2^i, \cdots, \beta^i)$. The Knonecker production dictionary $A \times B$ is defined as

$$A \times B = \begin{matrix} \alpha_1^1 B\ \alpha_2^1 B, \cdots, \alpha_m^1 B \\ \alpha_1^2 B\ \alpha_2^2 B, \cdots, \alpha_m^2 B \\ \vdots \\ \alpha_1^M B\ \alpha_2^M B, \cdots, \alpha_m^M B \end{matrix} \tag{2}$$

The dictionary $A \times B$, then has MN words of length mn, a typical word having the form

$$\alpha_1^i b_i, \alpha_2^j b_i, \cdots, \alpha_m^j b_i \tag{3}$$

where

$$\alpha_\nu^j b_i = \alpha_\nu^j + \beta_1^i, \alpha_\nu^j + \beta_2^i, \cdots, \alpha_\nu^j + \beta_n^i \tag{4}$$

the addition being taken modulo r. The distance properties of Kronecker product codes are well known. In this article we are concerned with the index of comma freedom of such codes which is considered later in Section 2.

The index of comma freedom is a meaningful measure when the code in question is to be used over the r-ary symmetric channel.

Another application of the codes defined above, however, might be in the generation of phase-codes. Here if the ν^{th} symbol of the j^{th} word of the code is a α_ν^j, it is represented by the waveform $(2)^{1/2} \cos\left[\omega_c t + (2\pi\alpha_\nu^j)/r\right]$.

In this case the number of components which two code words have in agreement ceases to be of prime concern. Rather, it is the correlation between these code words that is the measure. Thus, in Section 3 we consider the maximum correlation that can occur between any true code word of a Kronecker product dictionary and any overlap word. This is the analogue of the index of comma freedom for phase codes.

2. The Index of Comma Freedom

Theorem 1: Let A denote a dictionary with m-symbol r-ary words $a_j = (\alpha_1^j, \alpha^j, \cdots, \alpha_m^j)$ and B a dictionary of

n-symbol r-ary words $b_i = (\beta_1^i, \beta_2^i, \cdots, \beta_n^i)$. Let $M_A(j,l)$ be the maximum number of times any one of the r symbols of the alphabet occurs in any l-tuple obtained by subtracting the l symbol suffix of the j^{th} word in A from the l symbol prefix of any word in A, where the two words need not be different unless $l \equiv 0$, modulo m, and let $N_A(j,l)$ be identically defined except for the interchange of the words "prefix" and "suffix."

Let $M_B(i,k)$, $N_B(i,k)$, $M_{AxB}(i,j,t)$, and $N_{AxB}(i,j,t)$ be similarly defined in terms, respectively, of the dictionary B and the Kronecker product dictionary A x B.

Then

$$\max_{i,j,t} \left[M_{AxB}(i,j,t) + N_{AxB}(i,j,mn-t)\right] \leqslant \max \left\{ m \max_{i,k} \right. \tag{5}$$

$$\left. \times [M_B(i,k) + N_B(i,n-k)], n \max_{j,l} \left[M_A(j,l) + N_A(j,m-l)\right] \right\}.$$

Proof: Consider the maximum number $M_{AxB}(i,j,t)$ of times any symbol of the alphabet can occur in the t-tuple formed by subtracting the last $t = ln + k$ symbols of the mn-symbol word of AxB

$$\alpha_1^j + \beta_1^i, \alpha_1^j + \beta_2^i, \cdots, \alpha_1^j + \beta_n^i, \alpha_2^j + \beta_1^i, \cdots,$$

$$\alpha_2^j + \beta_n^i, \alpha_3^j + \beta_1^i, \cdots, \alpha_m^j + \beta_n^i$$

from the corresponding symbols of any overlap word (i_1 and i_2 can be any integer from 1 to n, j_1 and j_2 any integer from 1 to m)

$$\alpha_{l+1}^{j_1} + \beta_{k+1}^{i_1}, \cdots, \alpha_{l+2}^{j_1} + \beta_n^{i_1}, \alpha_{l+2}^{j_1} + \beta_1^{i_2}, \cdots, \alpha_m^{j_1} + \beta_n^{i_1}, \alpha_1^{j_2}$$

$$+ \beta_1^{i_2}, \cdots, \alpha_l^{j_2} + \beta_n^{i_2}, \alpha_{l+1}^{j_2} + \beta_1^{i_2}, \cdots, \alpha_{l+1}^{j_2} + \beta_k^{i_2}$$

By definition

$$M_{AxB}(i,j,t) = \max_{i_2,j_2\rho} \left\{ \sum_{\nu=m-l}^{m} \sum_{\mu=n-k+1}^{n} d_\rho \left[(\alpha_\nu^j + \beta_\mu^i) - (\alpha_{\nu-(m-l)+1}^{j_2} \right.\right.$$

$$\left. + \beta_{\mu-(n-k)}^{i_2})\right] + \sum_{\nu=m-l+1}^{m} \sum_{\mu=1}^{n} d_\rho \left[(\alpha_\nu^j + \beta_\mu^i)\right.$$

$$\left.\left. - (\alpha_{\nu-(m-l)}^{j_2} + \beta_{\mu+k}^{i_2})\right]\right\}$$

where $d_\rho(x) = \begin{cases} 0 & \text{if } x \neq \rho \\ 1 & \text{if } x = \rho \end{cases}$ Rearranging terms, we have

$$M_{AxB}(i,j,t) = \max_{i_2,j_2\rho} \left\{ \sum_{\nu=m-l}^{m} \sum_{\mu=n-k+1}^{n} d_\rho \left[(\alpha_\nu^j - \alpha_{\nu-(m-l)+1}^{j_2}) \right.\right.$$

$$+ (\beta_\mu^i - \beta_{\mu-(n-k)}^{i_2})\left] + \sum_{\nu=m-l+1}^{m} \sum_{\mu=1}^{n-k} d_\rho \left[(\alpha_\nu^j \right.\right.$$

$$\left.\left. - \alpha_{\nu-(m-l)}^{j_2}) + (\beta_\mu^i - \beta_{\mu+k}^{i_2})\right]\right\}. \tag{6}$$

But, unless $k \equiv 0 \bmod n$,

$$\max_{i_2,j_2,\rho} \sum_{\mu=n-k+1}^{n} d_\rho \left[(\alpha_\nu^j - \alpha_{\nu-(m-l)+1}^{j_2}) + (\beta_\mu^i - \beta_{\mu-(n-k)}^{i_2})\right] \tag{7}$$

$$\leq M_B(i,k)$$

and

$$\max_{i_2,j_2,\rho} \sum_{\mu=1}^{n-k} d_\rho \left[(\alpha_\nu^j - \alpha_{\nu-(m-l)}^{j_2}) + (\beta_\mu^i - \beta_{\mu+k}^{i_2})\right] \leq N_B(i,n-k). \tag{8}$$

Consequently, if $k \not\equiv 0 \bmod n$,

$$M_{AxB}(i,j,t=ln+k) \leqslant (l+1) M_B(i,k) + l N_B(i,n-k) \tag{9}$$

A similar argument establishes that, if $k \not\equiv 0 \bmod n$,

$$N_{AxB}(i,j,mn-t) \leqslant (m-l) N_B(i,n-k) + (m-l-1) M_B(i,k). \tag{10}$$

Consequently, if $k \not\equiv 0 \bmod n$,

$$M_{AxB}(i,j,t) + N_{AxB}(i,j,mn-t) \leqslant (l+1) M_B(i,k)$$

$$+ l N_B(i,n-k) + (m-l) N_B(i,n-k)$$

$$+ (m-1-1) M_B(i,k) = m\left[M_B(i,k) + N_B(i,n-k)\right] \tag{11}$$

If both $l \equiv 0 \bmod m$ and $k \equiv 0 \bmod n$, then $t \equiv 0 \bmod mn$; and the "overlap" word is actually a true word. If $k \equiv 0 \bmod n$ and $l \not\equiv 0 \bmod m$, it follows from Eq. (6) that

$$M_{AxB}(i,j,t) = \max_{i_2,j_2,\rho} \sum_{\mu=1}^{n} \sum_{\nu=m-l+1}^{m} d_\rho \left[(\alpha_\nu^j - \alpha_{\nu-(m-l)}^{j_2}) + (\beta_\mu^i \right.$$

$$\left. - \beta_\mu^{i_2})\right] \leqslant n M_A(j,l). \tag{12}$$

Similarly,

$$N_{AxB}(i,j,mn-t) = \max_{i_1,j_1,\rho} \sum_{\mu=1}^{n} \sum_{\nu=1}^{m-l} d_\rho \left[(\alpha_\nu^{j_1} - \alpha_{\nu+l}^{j_1}) + (\beta_\mu^i - \beta_\mu^{j_1}) \right] \leqslant n N_A(j,m-l) \tag{13}$$

Thus, if $t \neq 0 \bmod mn$,

$$\max_t \left[M_{AxB}(i,j,t) + N_{AxB}(i,j,mn-t) \right] \leqslant \max \left\{ \max_{k \neq 0} m \left[M_B(i,k) + N_B(i,n-k) \right], \max_{l \neq 0} n \left[M_A(j,l) + N_A(j,m-l) \right] \right\}, \tag{14}$$

which was to be proved.

Corollary 1: Let A be a dictionary of r-ary m-symbol words and B be a dictionary of r-ary n-symbol words; and let $M_A(j,l)$, $N_A(j,l)$, $M_B(i,k)$ and $N_B(ik)$ be defined as in Theorem 1. Then the index of comma freedom d_{mn} of the Kronecker product dictionary $A x B$ is bounded by

$$d_{mn} \geq \min \left\{ m \min_{\substack{i,k \\ k \neq 0}} \left[n - M_B(i,k) - N_B(i,n-k) \right], \; n \min_{\substack{j,l \\ l \neq 0}} \left[m - M_A(j,l) - N_A(j,m-l) \right] \right\} \tag{15}$$

Proof: This follows immediately from Theorem 1 upon observing that the index of comma freedom d_s of a dictionary D of s-symbol words is bounded by

$$d_s \geqslant \min_{\substack{\nu,t \\ t \neq 0}} \left[s - M_D(\nu,t) - N_D(\nu,s-t) \right] \tag{16}$$

Note that, from Theorem 1, the index of comma freedom of dictionaries, which are Kronecker products of Kronecker products, can also be bounded. Suppose, in particular, that D is a dictionary of s-symbol words and that

$$\max_{\substack{\nu,t \\ t \neq 0}} \left[M_D(\nu,t) + M_D(\nu,s-t) \right] \leqslant s-1.$$

Then $d_s \geqslant 1$, d_{s^2}, the index of comma freedom of the dictionary $D x D$, is bounded by

$$d_{s^2} \geqslant s$$

Similarly, the dictionaries $(D x D) x D$, $(D x D) x (D x D)$, etc., have indicies of comma freedom bounded by

$$d_{s^3} \geqslant s$$
$$d_{s^4} \geqslant s^2,$$

respectively; and in general, it is possible to generate a dictionary having s^{2^ν}-symbol words such that

$$d_{s^{2^\nu}} \geqslant s^{2^\nu} - 1.$$

Corollary 2: If the code dictionaries A and B form groups of m — and n — tuples, respectively, over some finite field and if A contains the m-tuple $11\ldots.1$ and B the m-tuple $11\ldots.1$ (e.g., if each group is generated by a polynomial which is divisible by the polynomial $x - 1$), then

$$d_{mn} \geqslant \min \left[m d_n, n d_m \right] \tag{17}$$

where d_m and d_n are, respectively, the indicies of comma freedom of the dictionaries A and B, and d_{mn} is the index of comma freedom of their Kronecker product $A x B$.

Proof: If A contains the m-tuple $11\ldots.1$, then

$$d_m(A) = \min_{i,j_1,j_2,l \neq 0} \left\{ m - \sum_{\nu=1}^{m-l} d_0(\alpha_\nu^{j_1} - \alpha_{\nu+l}^{j_1}) - \sum_{\nu=m-l+1}^{m} d_0(\alpha_\nu^{j_2} - \alpha_{\nu-(m-l)}^{j_2}) \right\} \tag{18}$$

where

$$d_0(x) = \begin{cases} 1 & x = 0 \\ 0 & x \neq 0 \end{cases}$$

Changing the second index of summation

$$d_m(A) = \min_{i,j_1,j_2,l \neq 0} \left\{ m - \sum_{\nu=1}^{m-l} d_0(\alpha_\nu^{j_1} - \alpha_{\nu+l}^{j_1}) - \sum_{\nu=1}^{l} d_0(\alpha_\nu^{j_2} - \alpha_{\nu+(m-l)}^{i}) \right\} \tag{19}$$

$$= \min_{i,j_1,j_2,l \neq 0,\beta_1,\beta_2} \left\{ m - \sum_{\nu=1}^{m-l} d_0(\alpha_\nu^{j_1} - \alpha_{\nu+l}^{j_1} - \beta_1) - \sum_{\nu=1}^{l} d_0(\alpha_\nu^{j_2} - \alpha_{\nu+(m-l)}^{i} + \beta_2) \right\}$$

The last step follows from the observation that if $a_i = (\alpha_1^i, \alpha_2^i, \cdots, \alpha_m^i)$ is in A, then so is $a_i + b = (\alpha_1^i + \beta,$

$\alpha_2^i + \beta, \cdots, \alpha_m^i + \beta j$ for any element β in the field over which the group is defined. Therefore,

$$d_m(A) = \min_{\substack{i,l \\ l \neq 0}} \left\{ m - \max_{j_1,\beta_1} \sum_{\nu=1}^{m-l} d_{\beta_1}(\alpha_\nu^{j_1} - \alpha_{\nu-l}^{j_1}) - \max_{j_2,\beta_2} \sum_{\nu=1}^{l} d_{\beta_2}(\alpha_\nu^{j_2} - \alpha_{\nu-(m-l)}^{j_2}) \right\} = \min_{\substack{i,k \\ l \neq 0}} \left\{ m - M_A(i,l) - M_A(i,m-l) \right\}$$

This, combined with Eq. (15) of Corollary 1 proves the result.

Again, notice that the Kronecker product of two dictionaries contains the constant all-ones vector if the original dictionaries both contain the all-ones vector. The property of Corollary 2, therefore, also propagates; the relationship holds for Kronecker products of dictionaries which are themselves Kronecker products.

3. Maximum Word-Overlap Correlation

When correlation rather than distance is the measure, it is possible to obtain results similar to those of Section 2.

Theorem 2: Let A be a dictionary of m-symbol r-ary words $a_j = \{\gamma_1^j \gamma_2^j, \cdots, \gamma_m^j\}$ and B be a dictionary containing n-symbol r-ary words $b_i = \{\delta_1^i \delta_2^i, \cdots, \delta_n^i\}$ where $m \mid \gamma_\nu^i \mid = n \mid \delta_\mu^i \mid = 1$ for all μ, ν, i and i. If $\rho_A(j_1,j_2,l)$ is defined as the correlation between the first l symbols of a_{j_1} and the last l symbols of

$$a_{j_2}\left[\rho_A(j_1,j_2,l) = \sum_{\mu=1}^{l} \gamma_\mu^{j_1} (\gamma_{\mu+(m-l)}^{j_2})^*\right]$$

and $\rho_B(i_1,i_2,k)$ is similarly defined, then the correlation between the word

$$\gamma_1^{j_1}\delta_1^{i_1}, \gamma_1^{j_1}\delta_2^{i_1}, \cdots, \gamma_1^{j_1}\delta_n^{i_1}, \gamma_2^{j_1}\delta_1^{i_1}, \cdots, \gamma_2^{j_1}\delta_n^{i_1}, \gamma_1^{j_1}\delta_1^{i_2}, \cdots\cdots, \gamma_m^{j_1}\delta_n^{i_1}$$

of the Kronecker product dictionary $A \times B$ and the overlap word

$$\gamma_{l+1}^{j_1}\delta_{k+1}^{i_1}, \gamma_{l+1}^{j_1}\delta_{k+2}^{i_1}, \cdots, \gamma_{l+1}^{j_1}\delta_n^{i_1}, \gamma_{l+2}^{j_1}\delta_1^{i_2}, \cdots$$

$$\cdots, \gamma_m^{j_1}\delta_n^{i_1}, \gamma_1^{j_2}\delta_1^{i_2}, \cdots, \gamma_1^{j_2}\delta_n^{i_2}, \gamma_2^{j_2}\delta_1^{i_2}, \cdots, \gamma_{l+1}^{j_2}\delta_k^{i_2}$$

is given by $\rho_{A\times B}(i,i_1,j,j_1,t) + \rho^*_{A\times B}(i_2,i,j_2,j,mn-t) =$

$$\rho_A(j,j_1,m-l)\,\rho_B(i,i_1,n-k) + \rho_A(j,j_1,m-l-1)\,\rho_B^*(i_1,i,k)$$

$$+ \rho_A^*(j_2,j,l+1)\,\rho_B^*(i_2,i,k) + \rho_A^*(j_2,j,l)\,\rho_B(i,i_2,n-k)$$

where $t = nl+k$.

Proof: The result follows immediately from the definitions:

$$\rho_{A\times B}(i,i_1,j,j_1,t) + \rho^*_{A\times B}(i_2,i,j_2,j,mn-t)$$

$$= \sum_{\nu=1}^{m-l}\sum_{\mu=1}^{n-k} \gamma_\nu^j\,\delta_\mu^i\,(\gamma_{l+\nu}^{j_1}\,\delta_{k+\mu}^{i_1})^* + \sum_{\nu=1}^{m-l-1}\sum_{\mu=n-k+1}^{n} \gamma_\nu^j\,\delta_\mu^i\,(\gamma_{l+1+\nu}^{j_1}\,\delta_{\mu-(n-k)}^{i_1})^*$$

$$+ \sum_{\nu=m-l}^{m}\sum_{\mu=n-k+1}^{n} \gamma_\nu^j\,\delta_\mu^i\,(\gamma_{\nu-(m-l)+1}^{j_2}\,\delta_{\mu-(n-k)}^{i_2})^* + \sum_{\nu=m-l+1}^{m}\sum_{\mu=1}^{n-k} \gamma_\nu^j\,\delta_\mu^i\,(\gamma_{\nu-(m-l)}^{j_2}\,\beta_{\mu+k}^{i_2})^*$$

$$= \sum_{\nu=1}^{m-l} \gamma_\nu^j\,(\gamma_{\nu+l}^{j_1})^* \sum_{\mu=1}^{n-k} \delta_\mu^i\,(\delta_{\mu+k}^{i_1})^* + \sum_{\nu=1}^{m-l-1} \gamma_\nu^j\,(\gamma_{\nu+l+1}^{j_1})^* \sum_{\mu=n-k+1}^{n} \delta_\mu^i\,(\delta_{\mu-(n-k)}^{i_1})^*$$

$$+ \sum_{\nu=m-l}^{m} \gamma_\nu^j\,(\gamma_{\nu-(m-k)+1}^{j_2})^* \sum_{\mu=n-k+1}^{n} \delta_\mu^i\,(\delta_{\mu-(n-k)}^{i_2})^* + \sum_{\nu=m-l+1}^{m} \gamma_\nu^j\,(\gamma_{\nu-(m-l)}^{j_2})^* \sum_{\mu=1}^{n-k} \delta_\mu^i\,(\delta_{\mu-k}^{i_2})^* \qquad (20)$$

$$= \rho_A(j,j_1,m-l)\,\rho_B(i,i_1,n-k) + \rho_A(j,j_1,m-l-1)\,\rho_B^*(i_1,i,k)$$

$$+ \rho_A^*(j_2,j,l+1)\,\rho_B^*(i_2,i,k) + \rho_A^*(j_2,j,l)\,\rho_B(i,i_2,n-k).$$

The result is proved.

Theorem 3: If $\max_{j,j_1} |\rho_A(j,j_1,l)| = |\rho_A(l)|$,

$\max_{i,i_1} |\rho_B(i,i_1,k)| = |\rho_B(k)|$, and $\max_{i,i_1,j,j_1} |\rho_{A\times B}(i,i_1,j,j_1,t)|$

$= |\rho_{A\times B}(t)|$, then

$$|\rho_{A\times B}(t)| + |\rho_{A\times B}(mn-t)| \leq |\rho_A(m-l)||\rho_B(n-k)|$$

$$+ |\rho_A(m-l-1)||\rho_B(k)| + |\rho_A(l+1)||\rho_B(k)|$$

$$+ |\rho_A(l)||\rho_B(n-k)|.$$

Further,

$$\max_{\substack{t\\ t\neq 0}} \left\{ |\rho_{A\times B}(t)| + |\rho_{A\times B}(mn-t)| \right\} \leqslant \max$$

$$\left\{ \max_{\substack{k\\ k\neq 0}} \left(|\rho_B(k)| + |\rho_B(n-k)| \right), \max_{\substack{l\\ l\neq 0}} \left(|\rho_A(l)| + |\rho_A(m-l)| \right) \right\} \quad (22)$$

Proof: $|\rho_{A\times B}(t)| + |\rho_{A\times B}(mn-t)|$

$$= \max_{i,i_1,j,j_1} |\rho_A(j,j_1,m-l)\,\rho_B(i,i_1,n-k) + \rho_A(j,j_1,m-l-1)\,\rho_B^*(i_1,i,k)|$$

$$+ \max_{i,i_2,j,j_2} |\rho_A^*(j_2,j,l+1)\,\rho_B^*(i_2,i,k) + \rho_A^*(j_2,j,l)\,\rho_B(i,i_2,n-k)|$$

$$\leqslant \max_{i,i_1,j,j_1} |\rho_A(j,j_1,m-l)|\,|\rho_B(i,i_1,n-k)| + \max_{i,i_1,j,j_1} |\rho_A(j,j_1,m-l-1)|\,|\rho_B(i,i_1,k)|$$

$$+ \max_{i,i_2,j,j_2} |\rho_A(j,j_2,l+1)|\,|\rho_B(i,i_2,k)| + \max_{i,i_2,j,j_2} |\rho_A(j,j_2,l)|\,|\rho_B(i,i_2,n-k)|$$

$$= |\rho_A(m-l)|\,|\rho_B(n-k)| + |\rho_A(m-l-1)|\,|\rho_B(k)| + |\rho_A(l+1)|\,|\rho_B(k)| + |\rho_A(l)|\,|\rho_B(n-k)|;$$

$$\times \max_{\substack{t\\ t\neq 0}} \left\{ |\rho_{A\times B}(t)| + |\rho_{A\times B}(mn-t)| \right\}$$

$$\leqslant \max_{\substack{k\\ ln+k\neq 0}} \left\{ |\rho_A(m-l)|\,|\rho_B(n-k)| + |\rho_A(m-l-1)|\,|\rho_B(k)| + |\rho_A(l+1)|\,|\rho_l(k)| + |\rho_A(l)|\,|\rho_B(n-k)| \right\} \quad (23)$$

$$\leqslant \max \left\{ \max_{\substack{k\\ k\neq 0}} \left[\frac{m-l}{m} \left| \rho_B(n-k) \right| + \frac{m-l-1}{m} \left| \rho_B(k) \right| + \frac{l+1}{m} \left| \rho_B(k) \right| + \frac{l}{m} \left| \rho_B(n-k) \right| \right], \max_{\substack{l\\ l\neq 0}} \left[|\rho_A(m-l)| + |\rho_A(l)| \right] \right\}$$

$$= \max \left\{ \max_{\substack{k\\ k\neq 0}} \left(|\rho_B(n-k)| + |\rho_B(k)| \right) \max_{\substack{l\\ l\neq 0}} \left(|\rho_A(m-l)| + |\rho_A(l)| \right) \right\}$$

Theorem 3 is proved.

Thus, again, we have a situation in which the desired property in dictionaries is conserved in their Kronecker product.

$$\begin{aligned} \text{Since Re } \{\rho_{A\times B}(t) + \rho_{A\times B}(mn-t)\} & \\ \leqslant |\rho_{A\times B}(t) + \rho_{A\times B}(mn-t)| & \quad (24) \\ \leqslant |\rho_{A\times B}(t)| + |\rho_{A\times B}(mn-t)| & \end{aligned}$$

both the real part and the absolute value of maximum correlation between any code word and any overlap word of the Kronecker product dictionary are also bounded.

References

1. Welch, Lloyd R., "Blackwell's Theorem Concerning Entropy of Automata" (private communication), 1965.
2. Barker, R. H., "Group Synchronizing of Binary Digital Systems," *Communication Theory*, London, 1953, pp. 273–287.
3. Turyn, R. and Storer, J., "On Binary Sequences," *Proceedings of the American Mathematical Society*, Vol. 12, No. 3, June 1961, pp. 394–399.
4. Carley, G., Massachusetts Institute of Technology, unpublished report, 1964.
5. Welti, G. R., "*Quaternary Codes for Pulsed Radar*," *IRE Transaction on Information Theory*, IT-6, No. 3, June 1960.
6. de Long, D. F., Jr., *Three-Phase Codes*, Group Report No. 47-28, Massachusetts Institute of Technology, Lincoln Laboratory, Lexington, Massachusetts, July 24, 1959.
7. Peterson, W. W., *Error-Correcting Codes*, John Wiley and Sons, New York, 1961.
8. Mattson, H. F., and Solomon, G., "A New Treatment of Bose-Chaudhuri Codes," *Society of Industrial and Applied Mathematics Journal*, Vol. 9, No. 4, December 1961, pp. 654–669.

XXVI. Communications Systems Research: Communication and Tracking

A. Minimizing VCO Noise Effects in Phase-Locked Loops

R. C. Tausworthe

1. Introduction

One of the limiting factors governing the design of narrow-band phase-locked devices is the phase-noise inherent in the output of the voltage controlled oscillator (VCO). This noise, which appears as random fluctuations, drift, etc., is sometimes referred to as "oscillator instability." However, the term "instability" in oscillator context usually refers to frequency deviations. Whereas the quantity of concern in phase-locked-loop theory is (naturally) phase deviations.

One well known characteristic of loop bandwidth is that the output noise due to noise in the VCO goes up as bandwidth goes down; whereas for output noise due to input noise, the opposite is true. Thus, there is an optimum bandwidth for the loop. But there are also other effects: at a given loop bandwidth, the loop damping behavior can be optimized; and one may also expect these answers to change according to which type of spectral law the VCO noise follows.

This article presents a model for VCO noise which agrees well with the observed behavior of some actual VCO's. It also shows that an overdamped loop is preferable to an underdamped loop. Depending on measured parameters, the optimum bandwidth can then be computed.

2. Fundamental Loop Behavior

Using a linear theory of the phase-locked loop (Ref. 1), the output phase is (Fig. 1)

$$\hat{\theta}(t) = L(p)\left[\theta(t) + \frac{n(t)}{A}\right] + \left[\frac{1-L(p)}{p}\right] n_v(t)$$

in which the quantities above are defined as follows:

$\hat{\theta}(t)$ = output phase function

$\theta(t)$ = input phase function

$L(s)$ = overall closed loop phase response function

$p = \frac{d}{dt}$, the "Heaviside operator"

$n(t)$ = input noise translated to baseband

A = rms input signal power

$n_v(t)$ = the equivalent VCO phase noise referred to a unit-gain VCO input.

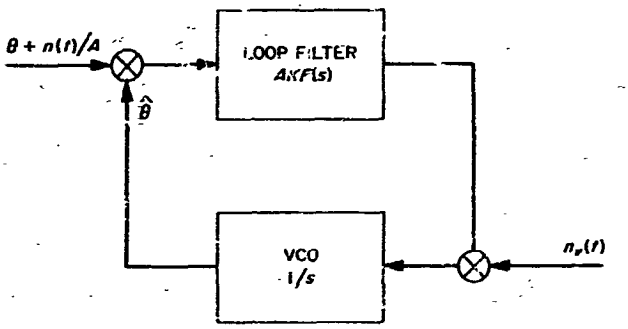

Fig. 1. Linear model of phase-locked loop showing VCO noise present

More specifically, the loop response $L(s)$ is given by

$$L(s) = \frac{AKF(s)}{s+AKF(s)}$$

where K is the total open loop gain, and $F(s)$ is the loop filter. For the purposes of this analysis, we shall assume that $AK \gg 1$ and that $F(s)$ takes the much-used form

$$F(s) = \frac{1+\tau_2 s}{1+\tau_1 s}$$

then $L(s)$ takes the form

$$L(s) = \frac{1+\tau_2 s}{1+\tau_2 s+\frac{\tau_1}{AK}s^2}$$

It is also convenient to define a ratio r

$$r = \frac{AK\tau_2^2}{\tau_1}$$

It is quite straightforward to show that the loop bandwidth B_L, defined as

$$B_L = \frac{1}{2\pi}\int_0^\infty \left|L(j\omega)\right|^2 d\omega$$

is approximately

$$B_L = \frac{r+1}{4\tau_2},$$

that critical damping occurs for $r = 4$, and that for $r < 4$ the damping factor ζ is approximately

$$\zeta = \frac{1}{2}\sqrt{r}$$

[1]This bandwidth is not the same as the "equivalent noise bandwidth" as defined by Davenport and Root, (Ref. 2), who define it as doubly infinite integral divided by $|L(j\omega)|^2_{maximum}$.

In these terms, the loop response is

$$L(s) = \frac{1+\left(\frac{r+1}{4B_L}\right)s}{1+\left(\frac{r+1}{4B_L}\right)s+\left(\frac{r+1}{4rB_L}\right)s^2}$$

That part of the output phase due to "noise" thus has variance

$$\sigma^2 = \frac{kTB_L}{A^2} + \frac{1}{2\pi}\int_{-\infty}^{+\infty}\frac{|1-L(j\omega)|^2}{\omega^2}S_{n_v n_v}(j\omega)d\omega$$

where $S_{n_v n_v}(j\omega)$ is the spectral density (Ref. 2) of the VCO noise (referred to its input), k is Boltzmann's constant, and T is the effective input noise temperature.

3. The Effects of VCO Noise

There are several factors which contribute to the spectral makeup of $n_v(t)$. The two most important terms which logically, as well as in practice, make up $S_{n_v n_v}(j\omega)$ are (1) white noise (such as thermal noise) generated in resistance and vacuum tubes in the oscillator input circuit, and (2) noise with a $1/f$ spectrum (as discussed in Ref. 3) associated with the transistors, varactor diodes, carbon resistors, etc. This suggests that the equivalent VCO input noise has a spectrum of the form

$$S_{n_v n_v}(j\omega) = N_{0v} + \frac{2\pi N_{1v}}{|\omega|}$$

Of course, the $1/f$ law cannot extend completely down to zero frequency (otherwise there would be infinite noise power generated); rather, it only extends down to some small frequency ϵ. However $[1-L(s)]/s$ has a zero at the origin which nullifies the necessity of having to evaluate ϵ. Insertion of the above expression into that for σ^2 yields the following:

$$\sigma^2 = \frac{kTB_L}{A^2} + \left(\frac{r+1}{8r}\right)\frac{N_{0v}}{B_L} + g(r)\frac{N_{1v}}{B_L^2}$$

The function $g(r)$, shown in Fig. 2, is given by

$$g(r) = \begin{cases} \dfrac{(r+1)^2}{16\left[r^3(r-4)\right]^{1/2}}\ln\left[\dfrac{r-2+\sqrt{r(r-4)}}{r-2-\sqrt{r(r+4)}}\right] & r \geq 4 \\ \dfrac{25}{64} & r = 4 \\ \dfrac{(r+1)^2}{8\left[r^3(4-r)\right]^{1/2}}\left[\dfrac{\pi}{2}-\tan^{-1}\dfrac{r-2}{\sqrt{r(4-r)}}\right] & r < 4 \end{cases}$$

Note that the expression for σ^2 exhibits the behavior we referred to earlier; namely, that there is some optimum way to pick B_L and r, depending on the VCO noise spectral density. The constants N_{0r} and N_{1r} can be evaluated by measurements on the VCO such as those appearing, for example, in Ref. 4.

4. Optimization of B_L and r

As shown in Fig. 2, there is quite a broad range of r for which $g(r)$ is fairly constant and nearly equal to its minimal value of 0.3872 at $r = 5.22$. A quite useful range to use this approximation for $g(r)$ is from about $r = 3$ to $r = 10$. Outside this region $g(r)$ is increasing, drastically when $r < 3$ and more slowly for $r > 10$.

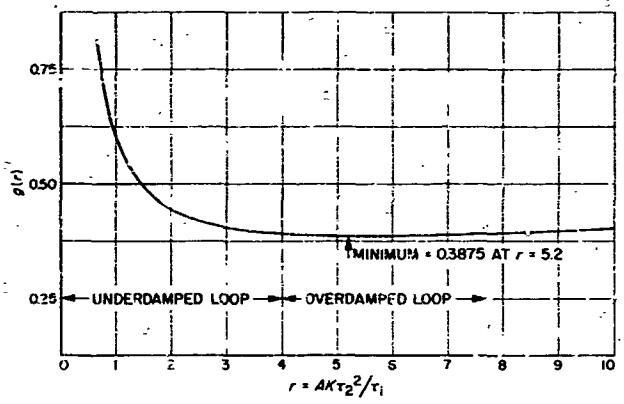

Fig. 2. Relative contribution of 1/f VCO noise to closed-loop output jitter, as a function of r

On the other hand, the coefficient of N_{0r}, i.e., $(r+1)/8r$, is monotone decreasing for all r, asymptotically approaching the value 0.125 as r becomes infinite. However, for r larger than 5 or 6, for most practical purposes, we can easily use the value 0.125 with little consequence.

As a conclusion, then, we see that the optimum value of r lies to the right of 5.22 and probably is less than 10, if any N_{1r} component is present at all. In fact, the difference between $\sigma_{minimum}^2$ and σ^2 for any r between 5 and 10 is inconsequential insofar as σ is concerned. The same statement cannot, however, be made for $r<4$ (an underdamped loop). Thus we may take a value of $r = 7$ as being practically as good as $r_{optimum}$, regardless of the other parameters. (This reasoning removes the necessity for differentiating σ^2 to find the exact value of r_{opt}.)

We can now use this value of r, differentiate σ^2 with respect to B_L, equate the zero, and solve for B_L to find its best value. Straightforwardly, B_L is the solution to the equation

$$B_L^3 - 0.143\left(\frac{A^2N_{0r}}{kT}\right)B_L - 0.774\left(\frac{A^2N_{1r}}{kT}\right) = 0$$

5. An Example

Just to see how a typical design should be made, let us assume that we have parameters

$$\frac{A^2}{kT} = 3 \times 10^4$$

$$N_{0r} = 0$$

$$N_{1r} = 0.08$$

The first of these is typical for an Earth-spacecraft link at the distance of Mars, while the values of N_{0r} and N_{1r} have been approximated from VCO records in Ref. 4. The best value of B_L is, therefore,

$$B_L = \sqrt[3]{0.774\left(\frac{A^2N_{1r}}{kT}\right)}$$

$$= 13 \text{ cps}$$

and the optimum loop transfer function is

$$L_{optimum}(s) = \frac{1 + 0.154s}{1 + 0.154s + 3.38 \times 10^{-3}s^2}$$

These parameters also produce a phase deviation of

$$\sigma = 2.5 \times 10^{-2} \text{ rad} = 1.43 \text{ deg rms}$$

6. Conclusion

Perhaps it should be mentioned that designs of this type are most valid for oscillator "clean-up" loops, spacecraft tracking loops, and situations where the tone to be tracked is very pure. Design of the ground receiver tracking loop would probably not use this analysis since its loop must track phase deviations imposed on the carrier by the noise in the spacecraft system. There are other considerations, also, which must be made, such as frequency acquisition interval, lock-in time, and doppler tracking rate. This discussion should be treated merely as a guide to determining what the ideal bandwidth is from a minimal noise point of view.

B. Optimal Design of One-Way and Two-Way Coherent Communication Links

W. C. Lindsey

In the design of one- or two-way communication links (or n-step links for that matter), the design engineer usually has at his disposal a set of basic communication parameters and constraints which determine and affect the performance of the overall system. In *SPS 37-32*, Vol. IV, and Ref. 5, a theory was presented which specified the unoptimized performance of an "n-step" communication network (Ref. 6); these basic communication parameters were introduced for several system configurations. It was shown, among other things, that the performance characteristic for a coherent two-way communication link (of the *Mariner* type) possesses an irreducible error probability which depends on the additive noise on the up-link. No attempt, however, was made at optimizing system performance with respect to variations in the design parameters, e.g., minimizing the error probability by selecting optimum values for the modulation indices.

In this article we consider the communication link depicted in Fig. 3 (Ref. 5) and specify design trends which will enable the design engineer to arrive at the "best" choice of up-link parameters.

(1) Total power radiated on up-link P_1

(2) Single-sided noise special density N_{01} at vehicle

(3) Up-link data rate $\mathcal{R}_1 = T_{b1}^{-1}$

(4) Vehicle carrier tracking loop bandwidth B_{L1}

(5) Up-link modulation index $m_1 = P_{c1}/P_1$

and also the corresponding down link parameters P_2, N_{02}, $\mathcal{R}_2 = T_{b2}^{-1}$, B_{L2}, and $m_2 = P_{c2}/P_2$. We shall then determine that value of $m_n (n = 1, 2)$ which minimizes the probability of error $P_E(n)$ $(n = 1, 2)$ say $P_{E_0}(n)$, for a fixed total power $P_n (n = 1, 2)$ and for a fixed data-rate-to-carrier tracking loop bandwidth ratio, say $\mathcal{R}_n/B_{Ln}$ $(n = 1, 2)$. This design technique will be given in the form of a universal set of system design curves.

1. Review of the Basic Model

We assume that we have available a set of signals, say $x_k(t)$ $(k = 1, 2)$, which are used to phase modulate an RF carrier. The relative cross-correlation between this signal set is given by

$$\lambda = \frac{1}{E}\int_0^{T_b} x_1(t)\, x_2(t)\, dt$$

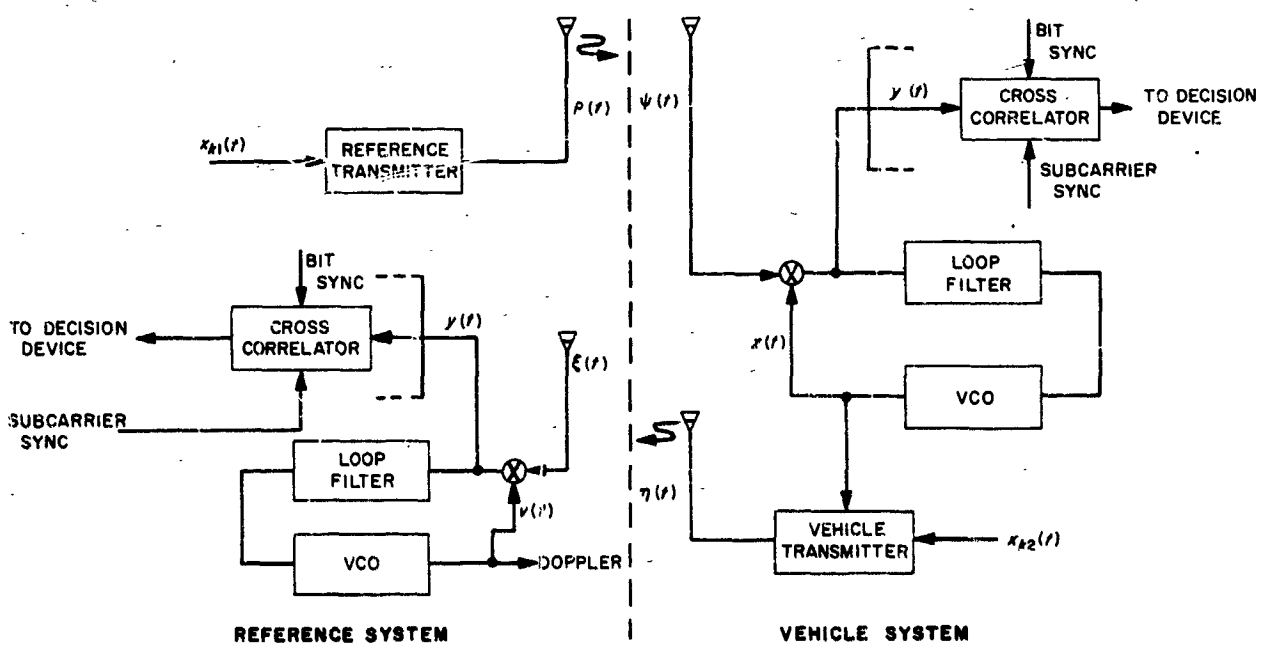

Fig. 3. Two-way communication link

where E is the common signal energy

$$E = \int_0^{T_b} | x_k(t) |^2 \, dt$$

and T_b is the duration of each signal. For transmission of negatively correlated signals (*PSK/PM*) $\lambda = -1$, and $x_k(t) = \pm 1$. For the transmission of orthogonal signals $\lambda = 0$, $x_1(t) = 0$ and $x_2(t) = 1$; however, in this case the transmitted waveform must be of the form

$$\zeta(t) = \sqrt{2mP} \sin \omega t + \sqrt{2(1 - m^2)P} x_k(t) \cos \omega t; \lambda = 0$$

which is a bit more difficult to generate than is

$$\zeta(t) = \sqrt{2P} \sin \{\omega t + [\cos^{-1} m] x_k(t)\}; \lambda = -1$$

for the *PSK/PM* waveform.

Without belaboring the mathematical details, which are not of great interest here, we specify the probability that our detector will err. This probability, as a function of link position, is given by

$$P_E(n) = \frac{1}{\pi} \int_0^{\pi} \frac{I_0 \left[|\alpha_1 + m_2^2 \delta_2 R_2 \exp(j\phi_2)| \right]}{I_0(\alpha_1) I_0(m_2^2 \delta_2 R_2)} \, d\phi_2$$

$$\int_{\sqrt{(1-m_2^2)R_2} \cos \phi_2}^{\infty} \frac{1}{\sqrt{2\pi}} \exp\left(-\frac{x^2}{2}\right) dx \qquad (1)$$

where

$$R_2 = \frac{P_2 T_{b2}(1-\lambda)}{N_{02}} \; ; \; \alpha_1 = \frac{2P_{c1}}{N_{01} B_{L1}} \; ; \; \delta_2 = \frac{2\mathcal{R}_2}{B_{L2}(1-\lambda)}$$

$$= \frac{\alpha_2}{m_2^2 R_2}$$

If we let α_1 approach infinity ($n = 1$) and drop all subscripts on the remaining variable in Eq. (1), we have the performance of the detector in the vehicle. Further, it may be shown that Eq. (1) integrates to

$$P_E(n) = \frac{1}{2}\left\{1 - \sqrt{\frac{4R_n(1-m_n^2)}{\pi}} \sum_{k=0}^{\infty} \exp\left[-\frac{R_n}{2}(1-m_n^2)\right] \right.$$

$$\left. (-1)^k \epsilon_k b_{2k+1}(n) (1 - 4k^2)^{-1} I_k\left[\frac{R_n}{2}(1-m_n^2)\right]\right\}$$

where

$$b_k(n) = \prod_{i=1}^{n} \frac{I_k(\alpha_i)}{I_0(\alpha_i)} \qquad (2)$$

$$\epsilon_k = \begin{cases} 1 & \text{if } k = 0 \\ 2 & \text{if } k > 0 \end{cases}$$

and $I_k(x)$ is the modified Bessel function of order k and argument x. It is quite apparent that any attempt to find the value of m, which minimizes $P_E(n)$, by differentiation immediately presents formidable difficulties. However, the surface generated by this equation can be easily studied on the IBM 7090 computer. In the next section we shall present the results obtained by this method.

2. Design Characteristics

A careful study of the parameters involved in Eqs. (1) and (2) leads one to the conclusion that by fixing α_1 and the data-rate-to-loop-bandwidth ratio, the error rate $P_E(n)$ versus "modulation index" $m = P_c/P$ (using R_n as a running parameter) characteristic serves to illustrate contours on the surface of $P_E(n)$. Since $P_E(n)$ will reach a minimum value for some $0 \leqslant m \leqslant 1$, the optimum m and error rate will be clearly depicted.

To illustrate the results graphically, we consider the one-way link performance characteristic, i.e., $\alpha_1 = \infty$. Fig. 4 represents the $P_E(n)$ versus m characteristic. Notice that this characteristic assumes its minimum value at $m = m_{optimum}$ and increases to one-half on either side of $m_{optimum}$. This interesting behavior may be explained as follows: For $m < m_{optimum}$ the tradeoff between power in the carrier and power in the data is overexpended in the data, and the performance of the carrier tracking loop suffers. For $m > m_{optimum}$ the tradeoff between power in the carrier and power in the data is overexpended in the carrier so that the performance of the demodulator suffers at the expense of a smaller phase error in the carrier tracking loop.

Fig. 5 represents the performance of the ground receiver. In this case we have set the signal-to-noise ratio in the vehicle carrier tracking loop at 9 db. This corresponds to a typical *Mariner* design near threshold, i.e., communication at the greatest range expected. The behavior of $P_E(n)$ versus m is similar to that obtained for the one-way link. The major difference is that for large values of R the $P_E(n)$ versus m characteristic exhibits a "bottoming" behavior which is due to the presence of additive noise on the up-link. These results serve to illustrate the deleterious effects which are introduced by demanding that a two-way link be established for transmission of

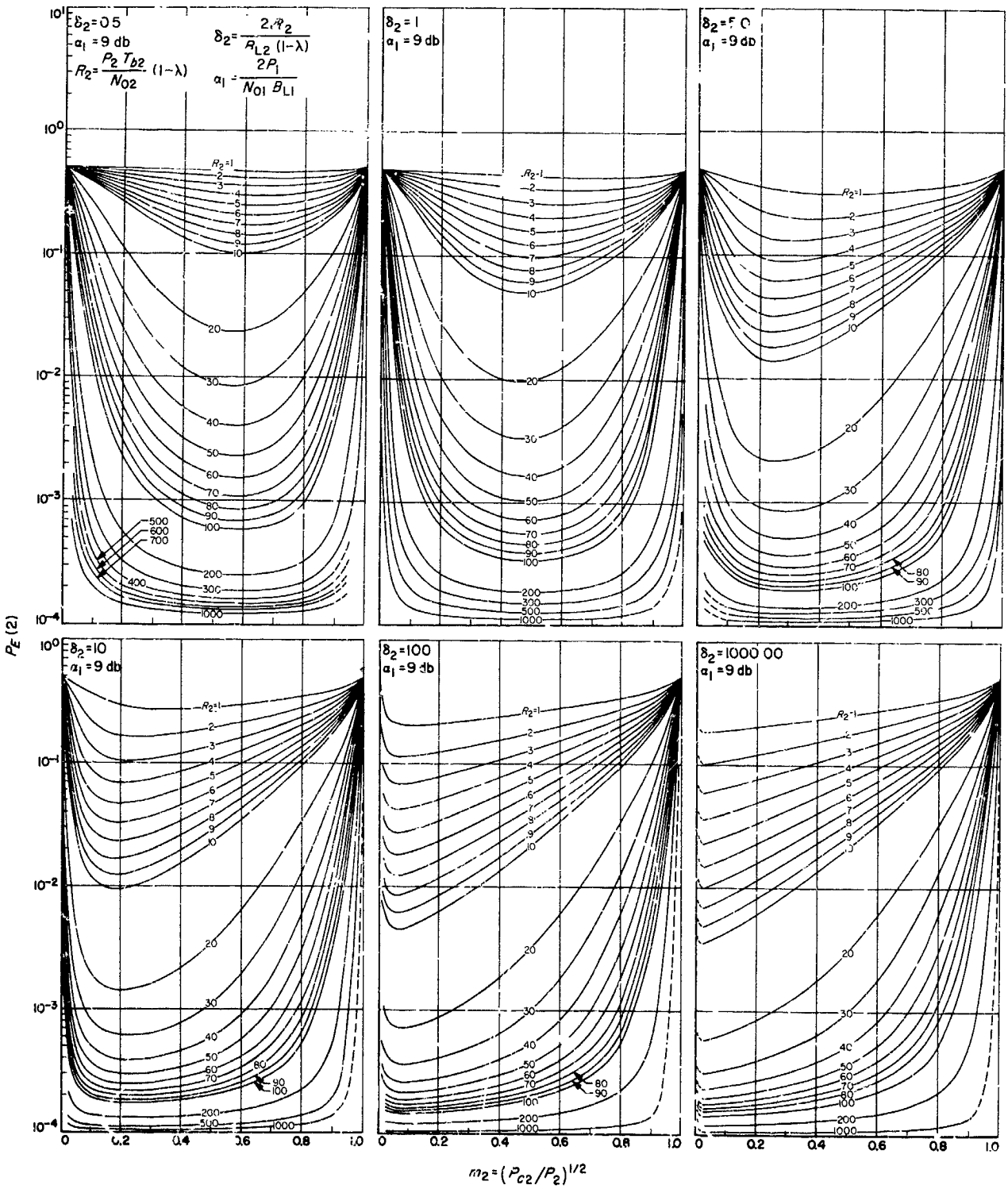

Fig. 4. Error probability vs modulation index for two-way links

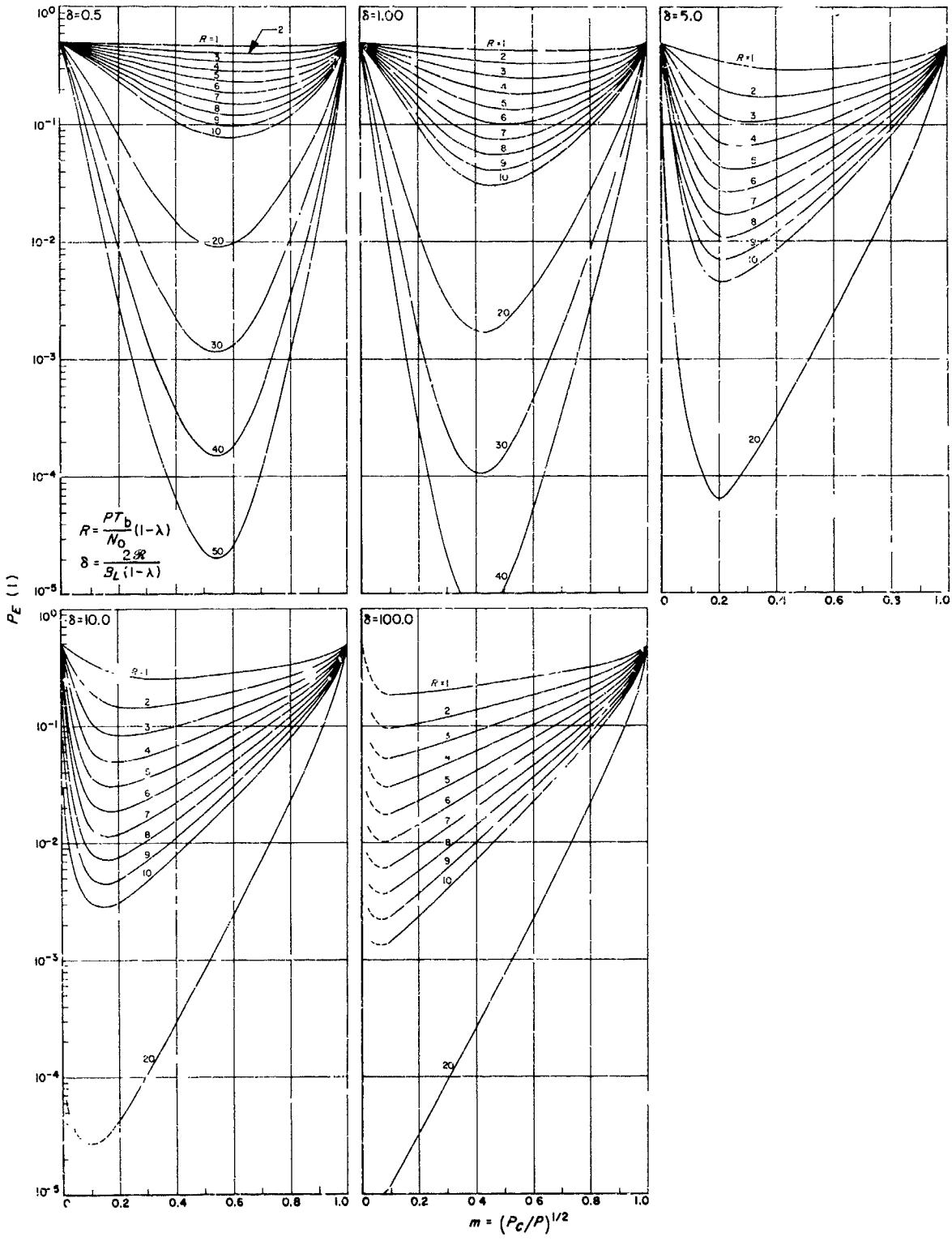

Fig. 5. Error probability vs modulation index for one-way links

telemetry data. A better route to take is to use a clean carrier reference in the vehicle when telemetry data are desired. It seems, therefore, that in the engineering an effort to develop such a system would be of interest.

Finally, Figs. 6 and 7 represent the optimized performance of the link. These curves were extracted from Figs. 3 through 5 by taking that value of $P_E(n)$ for which $m = m_{optimum}$ and plotting the result versus $R = PT_b/N_o$ for a fixed δ and α. Using these results the design engineer can predict the performance of a one-way or two-way link given the link parameters; alternatively, he may carry out a particular design given the required performance constraints.

Similar design characteristics for coded one-way and coded two-way links would be of interest. Preliminary results indicate a very interesting phenomena at the end points $m = 0$ and $m = 1$, which is not noticeable in the performance of binary links.

3. Suboptimum Design

In the preceding sections we elected to base the system design on attaining the minimum error probability by selecting that value of m which yielded the minimum error rate given a fixed total power, system noise temperature, and data rate. Another design criterion (which is not as difficult to carry out) is to select that value of m

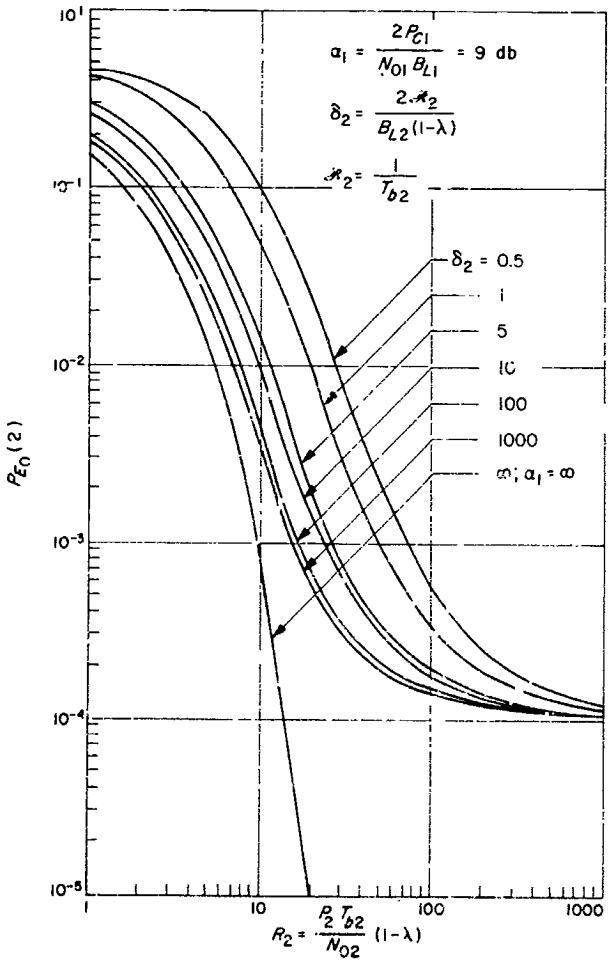

Fig. 6. Optimized performance characteristics for one-way links

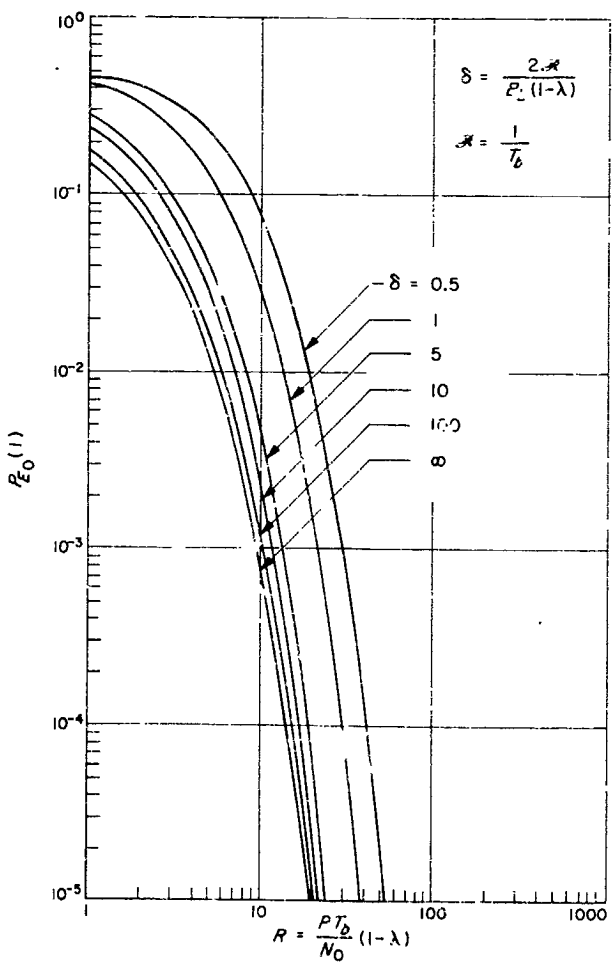

Fig. 7. Optimized performance characteristics for two-way links

which yields the maximum signal-to-noise ratio from the demodulator. If, in fact, this criterion is selected, then it is possible to show that the signal-to-noise ratio at the output of the demodulator is given by

$$(SNR)_2 = 2(1-m^2)\frac{P_r T_{bu}}{N_{u2}}\left[\frac{I_1(m^2\delta_2 R_2)}{I_0(m^2\delta_2 R_2)}\right]^2\left[\frac{I_1(\alpha_1)}{I_0(\alpha_1)}\right]^2$$

for the two-way link, and the signal-to-noise ratio at the output of the vehicle demodulator is given by

$$(SNR)_1 = \left[\frac{I_0(\alpha_{12})}{I_1(\alpha_1)}\right]^2 (SNR)_2$$

Design curves using this criterion are given in Fig. 8

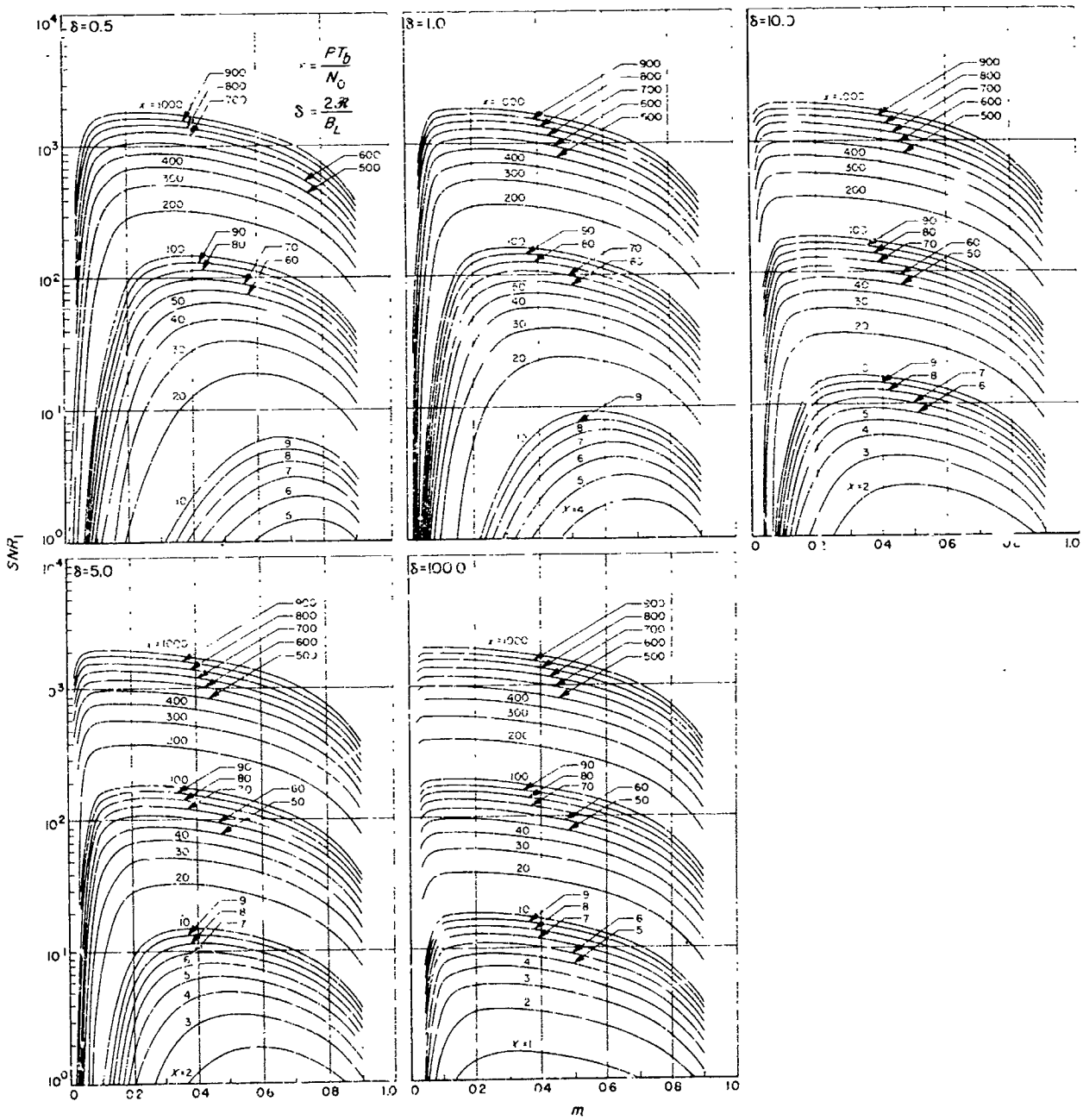

Fig. 8. Output signal to noise ratio for one-way links

Comparing the two different methods of design, given a particular set of design constraints, indicates that the value of m which maximizes the signal-to-noise ratio yields a value of m which is slightly larger than the value of m which minimizes the error probability. These curves should prove quite useful in checking a particular design using experimental methods.

4. Performance of One-Way Coded Links

In this section we present preliminary results relative to the problem of designing a coded telemetry system which communicates information to the receiver in blocks of n bits per message stored at the transmitter. Briefly, depending on the information to be sent, one of 2^n words (orthogonal) is used to phase modulate the RF carrier during a time period of nT_b seconds. The demodulator is the cross-correlator type and computes the conditional probability that a particular message was sent, given the output $y(t)$ of the carrier tracking loop. The decision device then examines all the correlator outputs and selects that message which corresponds to the maximum correlator output.

Specifically, the design trends are determined as before; i.e., the average error probability is computed as a function of the modulation index for various values of the parameter δ. From these characteristics the minimum error probability is plotted as a function of the total transmitted energy-per-bit-to-noise ratio.

Fig. 9 shows these results for $n = 5$; i.e., the signaling alphabet consists of 32 orthogonal code words for various values of δ. For values of $\delta < n = 5$ the assumption that the cosine of the phase error remains constant might be suspect. If, however, it is assumed to be constant the results are shown in Fig. 9 for $\delta = 1$. On the other hand, given the fact that the phase error varies over the word length then it is the author's conjecture that the result provides a lower bound on the performance of the system (Fig. 3). Variations of the phase error during time intervals on the order of nT_b seconds is analogous to the problem encountered in fast-fading communication channels. This is a particularly difficult problem to model and treat analytically. At the other extreme, i.e., where the phase error is constant over nT_b seconds, the problem is analogous to that encountered in determining the performance of communication links which are disturbed by the slow-fading phenomena and additive noise. Consequently, in carrying out any particular design where orthogonal codes are to be used as a means of conveying information, it seems necessary to constrain the data-

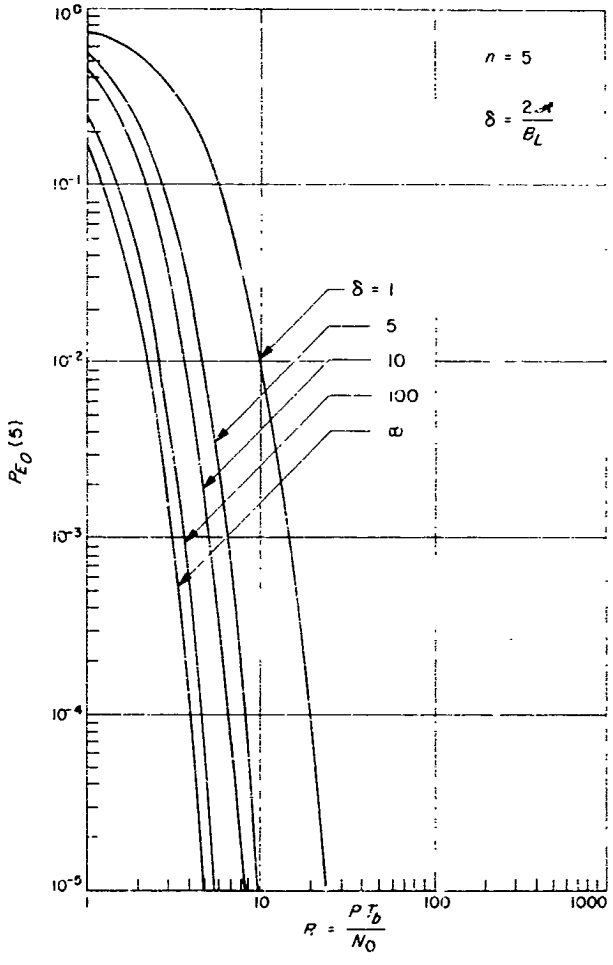

Fig. 9. Optimized performance characteristics for one-way coded links ($n = 5$)

rate-to-loop bandwidth ratio $\mathcal{R}/B_L$ to be equal to or greater than the number of bits per code word. This constraint and its implications will be explored in the next SPS.

N65-32472

C. Probabilities of Overflow and Error in Coded Phase-Shift-Keyed Systems with Sequential Decoding

I. Jacobs

32472

A coded binary phase-shift-keyed (PSK) system, in which sequential decoding is normally performed in real

time but occasionally off-line, is considered for use over an additive Gaussian noise channel. Both the probability of an undecodable block and the probability of undetected error in a decoded block are determined to be less than 10^{-5} when the energy utilized per bit is 3.8 db above the minimum set by the infinite-bandwidth channel capacity. After accounting for a 0.5 db degradation to permit word and decoder synchronization, an advantage remains over a system using biorthogonal signaling (but no further coding) of 4.3 db for 32 biorthogonal signals and 2.3 db for 1024 biorthogonal signals. (In both biorthogonal cases, optimum receivers are assumed with a word error probability of 10^{-5}.) Thus, this system has signal-to-noise advantages over biorthogonal telemetry.

Author

1. Introduction

In the analysis of sequentially-decoded systems, two parameters are of central importance, the probability distribution of computation time F_c and the probability of error per bit P_E (*SPS 37-32*, Vol. IV, pp. 303-306). It now appears that both can be expressed in terms of Gallager's function $E_0(\rho)$ (Ref. 7), specialized to channels with input symmetry, A input letters, Q output letters, and probability q_{ij} of channel transition from input i to output j

$$E_0(\rho) = -\ln \sum_{j=1}^{Q}\left[\sum_{i=1}^{A}\frac{1}{A}\,q_{ij}^{\frac{1}{1+\rho}}\right]^{1+\rho} \qquad (1)$$

In particular, sufficient (but not conclusive) analysis has now been completed on upper and lower bounds (Refs. 8, 9) to indicate that the probability $F_c(L)$ that the mean computation-per-bit is greater than L is of Pareto form

$$F_c(L) = L^{-\alpha}, \qquad L >> 1, \qquad (2)$$

where the Pareto exponent α is related to the rate R_c (in natural units) by

$$R_c = E_0(\alpha)/\alpha \qquad \text{nats/channel use.} \qquad (3)$$

For the range of rates of interest, it also appears that for most codes P_E is conservatively bounded by

$$P_E < \min_{\rho} e^{-\frac{K}{R_c}[E_0(\rho) - \rho R_c]}, \qquad (4)$$

where K is the convolutional coder constraint length.

2. System Efficiency

The Pareto exponent α of Eq. (2) affects the rate [through Eq. (3)] and thereby the achievable value of $E_b/E_{b,min}$. Large exponents α are achieved only at a cost of increased energy-per-bit E_b. Plots of $E_b/E_{b,min}$ versus the storage parameter β for several values of α are presented in Fig. 10. The curve $\alpha = 1$ corresponds to the curve for operation at R_0 presented in *SPS 37-32*, Vol. IV, p. 305. For $\alpha \leq 1$ the expected number of computations calculated from Eq. (2) is infinite.

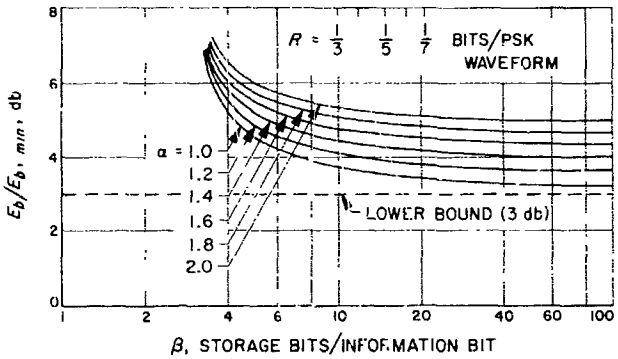

Fig. 10. Efficiency of coded PSK system with 3-bit quantized detection and sequential decoding for several values of the Pareto exponent α

3. Probability of Overflow

Assume, as in *SPS 37-32*, Vol IV, pp. 303–306, a buffer capable of storing 4000 words, each of β bits, and a decoder capable of performing 25 computations during the time interval between successive information bits. Then the probability of buffer overflow, assuming an initially empty buffer, is just the probability that the number of computations exceeds $25 \times 4000 = 10^5$, which is equal to

$$F_c(10^5) = 10^{-5\alpha} \qquad (5)$$

The probability P_o that a block of 1000 bits cannot be decoded without an overflow is approximately

$$P_o \approx 1000\, F_c(10^5) = 10^{3-5\alpha}$$

or

$$P_o \approx \begin{cases} 10^{-3}, & \alpha = 1.2 \\ 10^{-5}, & \alpha = 1.6. \end{cases} \qquad (6)$$

Thus maintaining a satisfactorily small probability of overflow sets a lower limit to α and hence to $E_b/E_{b,\,min}$.

It appears, however, that a P_o of 10^{-3} or even larger might be acceptable in a system that permitted storage, rather than discard, of undecoded blocks. Additional factors of 1000 in time-to-decode might then be tolerable, and the probability that a block would not be completely decoded might then be reduced to 10^{-6} or smaller. In such a case, $\alpha = 1.2$ would be an acceptable exponent. From Fig. 10, we observe that $\alpha = 1.2$ can be achieved with $E_b/E_{b,\,min} = 3.8$ db and $\beta = 21$ storage bits/information bit ($\beta = 21$ implies a rate R equal to 1/7; —i.e., 7 channel symbols per information bit—and 3-bit quantization). An improvement of ½ db could be achieved if $\alpha = 1.0$ were acceptable (operation at computational cutoff rate R_o), while only a 0.1 db degradation occurs with $\alpha = 1.2$ if β is decreased to 15 (rate equal to 1/5).

4. The $E_o(\rho)$ Curve

The set of parameters $\alpha = 1.2$, $\beta = 21$, $E_b/E_{b,\,min} = 3.8$ db is achieved with a signal-energy-to-noise-power-density ratio E/N_o for each PSK waveform equal to

$$\frac{E}{N_o} = \frac{RE_b}{N_o} = R \cdot \frac{E_b/N_o}{E_{b,\,min}/N_o} \cdot \frac{E_{b,\,min}}{N_o}$$

or

$$\left.\frac{E}{N_o}\right|_{db} = 10 \log_{10} \frac{1}{7} + 3.8 \text{ db} + 10 \log_{10} (\ln 2)$$

$$= -8.45 \text{ db} + 3.8 \text{ db} - 1.59 \text{ db} \approx -6 \text{ db}. \quad (7)$$

When $E/N_o = -6$ db, the cascade of modulator, channel, and quantized detector (see Fig. 15 of *SPS 37-32*, Vol. IV, p. 304 for details) can be represented by the transition probability diagram of Table 1. The resulting $E_o(\rho)$ curve is presented in Fig. 11.

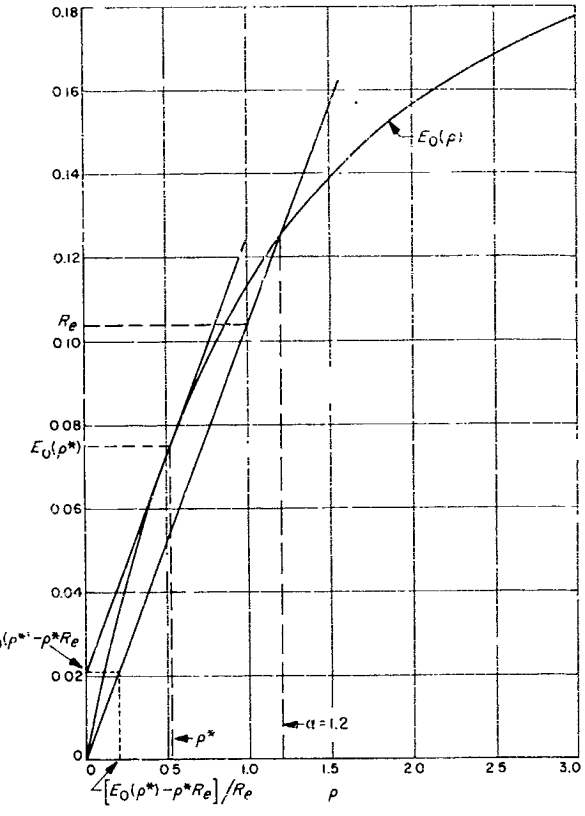

Fig. 11. Exponent curve for the discrete memoryless channel defined by transition probabilities of Table 1

5. Error Probability Exponent

The exponent in the error probability bound of Eq. (4) can be obtained from Fig. 11 by a geometrical construction, as shown. The line from the origin to $E_o(\alpha)$ has slope $E_o(\alpha)/\alpha = R_o$, by Eq. (3). The intersection of the straight line with the abscissa $\rho = 1$ is the rate R_e, in this case equal to 0.104 nats or (0.104/0.697) = 1/6.7 bits, which is close to the rate $R = 1/7$-bits/channel symbol expected. The discrepancy is due to the roundoff to −6 db in Eq. (7) in the value of E/N_o at which $R = 1/7$ is achieved. The maximum value of $[E_o(\rho) - \rho R_e]$ is achieved by the

Table 1. Transition probability diagram, $E/N_o = -6$ db

Input	Output							
	0	0′	0″	0‴	1‴	1″	1′	1
0	0.01695	0.22280	0.26025	0.26025	0.16110	0.06170	0.01675	0.00020
1	0.00020	0.01675	0.06170	0.16110	0.26025	0.26025	0.22280	0.01695

value of ρ, say ρ^*, at which a line of slope R_c is tangent to $E_r(\rho)$, as shown. This maximum, $[E_o(\rho^*) - \rho^* R_c]$, can also be read directly as the $\alpha = 0$ intercept of the tangent line.

Finally, $[E_o(\rho^*) - \rho^* R_c] / R_c$ is obtained by the construction shown in the figure and has value 0.20. Thus, the bound of Eq. (4) becomes

$$P_E < 2^{-0.2K} = \begin{cases} 0.7 \times 10^{-4}, & K = 48 \\ 0.6 \times 10^{-5}, & K = 60 \\ 0.55 \times 10^{-6}, & K = 72 \end{cases} \quad (8)$$

Experimental evidence (Ref. 10) as well as certain analytical work (Ref. 11) indicates that most blocks in which errors occur require so much computation that they are essentially undecodable anyway. Thus, the probability of an undetected error is smaller than the bound of Eq. (8), perhaps much smaller.

6. Conclusion

Both the probability of an undecoded block and the probability of an undetected error in a block appear to be less than 10^{-5} when a convolutional coder with constraint length of 60 or larger is used together with a PSK modulator, 3-bit quantized detector, and a sequential decoder with provision for occasional nonreal-time decoding. The required energy-per-bit is only 3.8 db above the absolute minimum. However, assuming that the data are divided into blocks of 1000 information bits and that decoder resetting and word synchronization require 100 bits to be "wasted," an additional ½ db must be added to the energy used per information bit, producing the final value of $E_b/E_{b,min} = 4.3$ db. Biorthogonal signaling with optimum reception and a word error probability of 10^{-5} requires $E_b/E_{b,min} = 8.6$ db, if $M = 32$ biorthogonal signals are used; and $E_b/E_{b,min} = 6.6$ db, if $M = 1024$ signals are used. This latter number appears to be an upper bound to the values of M for which optimum reception can be implemented for biorthogonal coding.

The analysis reported here is not numerically tight, but it is intended as a guide for experimentation. The value of α, K, β, and E_b, together with the choice of a code, can be tested by computer simulation. The programming of a general purpose computer as a decoder appears quite feasible for data rates under 100 bits/sec.

D. Sequential Decoding with Biorthogonal Alphabet and List Decoding

I. Jacobs

M-ary biorthogonal modulation and list decoding is considered for use with convolutional encoding and sequential decoding on a coherent additive Gaussian noise channel. Performance is found to be degraded from that achieved with binary phase-shift-keyed (PSK) modulation and 3-bit quantized detection (*SPS 37-32*, Vol. IV, pp. 303–306). The preceding article entitled, "Probabilities of Overflow and Error in Coded Phase-Shift Keyed System with Sequential Coding" extends the analysis of the binary PSK system.

1. The System

In *SPS 37-32*, Vol. IV, p. 303, a communication system is evaluated. It consists of a concatenation of convolutional coder, binary PSK modulator, coherent additive white Gaussian noise channel, correlation detector with amplitude-quantized output, and sequential decoder. Assuming operation at the computational cutoff rate R_o of the sequential decoder, the ratio $E_b/E_{b,min}$ and the storage-per-bit β were determined as parameters of system bandwidth (i.e., of energy per PSK waveform), where E_o is the energy used per information bit transmitted; $E_{b,min} = N_o \ln 2$ is the minimum value of E_b determined by the channel capacity of an infinite bandwidth additive white Gaussian noise channel; and β is the number of bits of storage required in the sequential decoder per information bit. In particular,

$$\beta = \frac{1}{R_o} \log_2 Q \quad (1)$$

where Q is the number of quantizer levels at the detector output.

We here consider the use of an M-ary biorthogonal signal modulator in place of the PSK modulator. A coherent correlation detector is again used; but now, following reception of each biorthogonal signal, an ordered list of the L most likely signals (signals with largest correlation) is provided the decoder. Since $\log_2 M$ bits is sufficient to store each member of the list and since $1/R_o$ biorthogonal signals are transmitted per bit of information (assuming operation at rate R_o bits/channel use), we now have

$$\beta = \frac{L}{R_o} \log_2 M \text{ storage bits/information bit.} \quad (2)$$

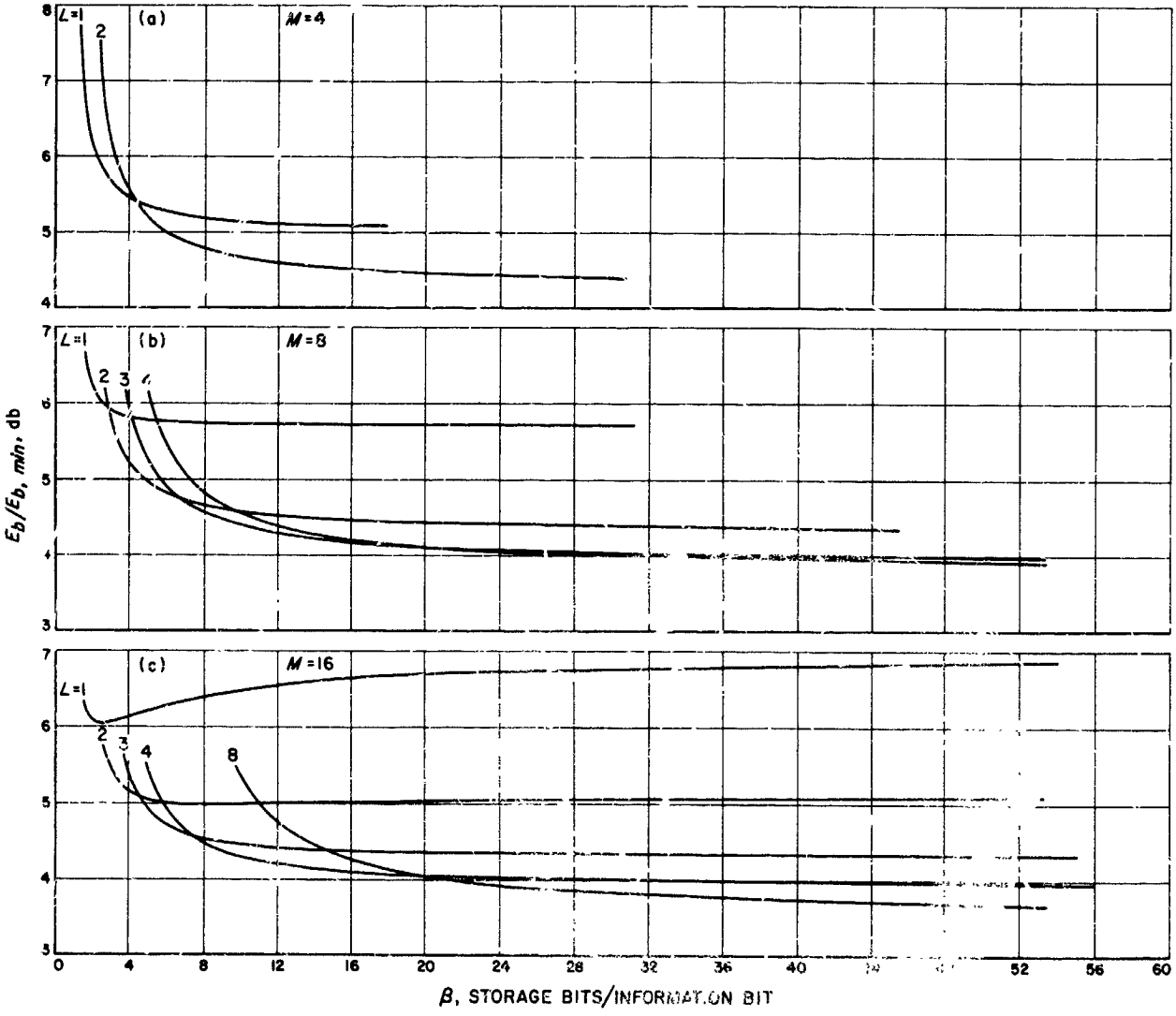

Fig. 12. Efficiency of M-signal biorthogonal modulation operating with sequential decoding and list-of-L detection; (a) $M = 4$, (b) $M = 8$, (c) $M = 16$

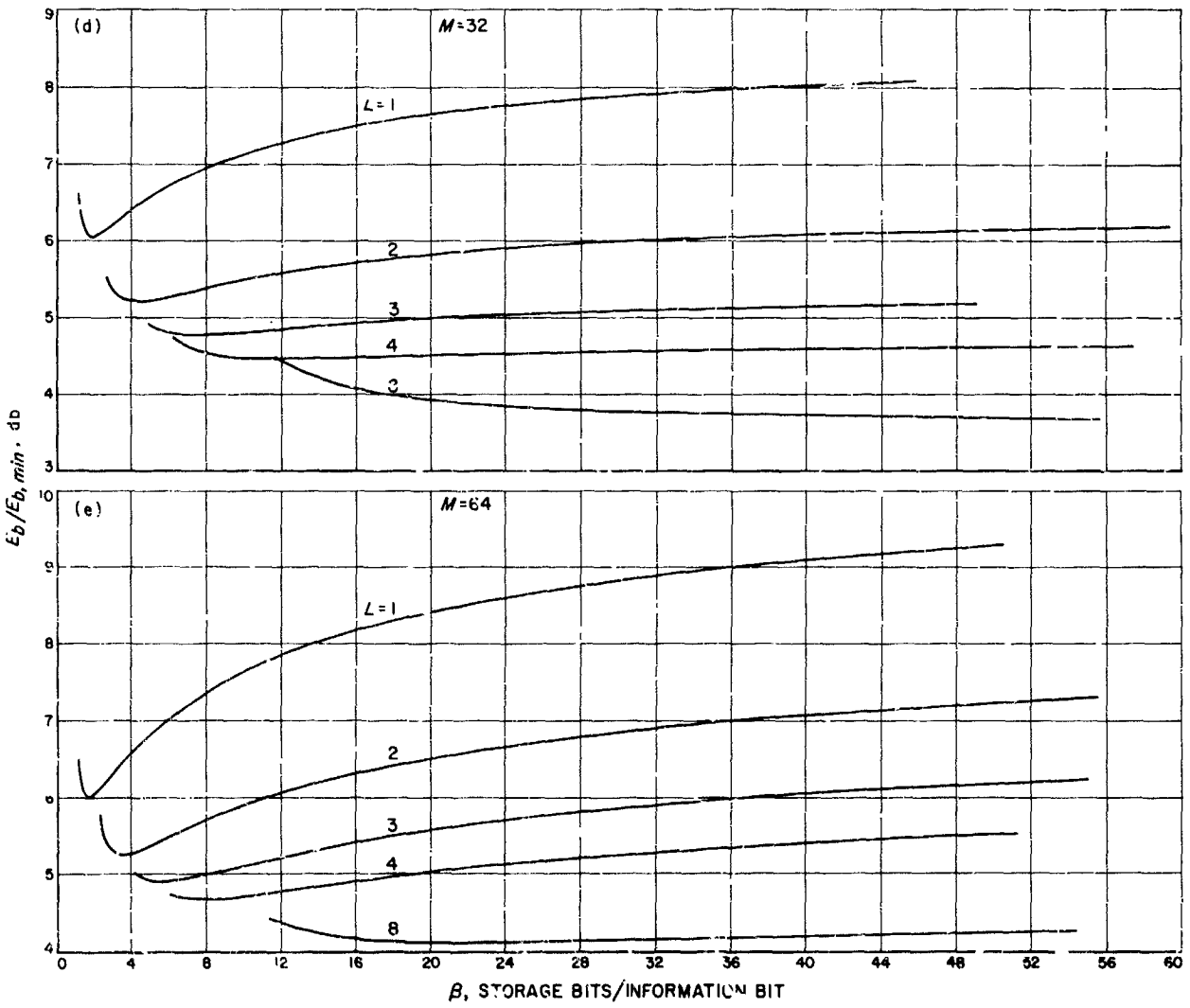

Fig. 12. Efficiency of M-signal biorthogonal modulation operating with sequential decoding and list-of-L detection; (d) $M = 32$, (e) $M = 64$

Furthermore, if the energy in each biorthogonal signal is E, then the energy-per-bit E_b at rate R_o is

$$E_b = E/R_o . \tag{3}$$

In *SPS 37-23*, Vol. IV, p. 303 we found that the PSK modulator and 3-bit quantized correlation detector provided values of $E_b/E_{b,min}$ within ½ db of the minimum possible for operation at R_o while using moderate bandwidth and a value of β in the order of 15. The substitution of biorthogonal signals is intended to achieve a decrease in β for a given $E_b/E_{b\ min}$. The hope was that by using larger signal alphabets, part of the reception burden could be transferred from decoder to detector, permitting decoder simplification. In every case considered, however, binary modulation proved preferable.

It should be noted that biorthogonal modulation is superior to orthogonal modulation for the system considered. Not only is the signal structure more efficient but also a detector output list of size $M/2$ suffices to provide complete information about the ordering of M biorthogonal signal correlations, whereas a list of size $M-1$ is required for orthogonal signals.

2. Analysis

Let Q_i, $1 \leq i \leq L$, be the probability that the transmitted biorthogonal signal appears in the i^{th} position in the list of detector outputs. That is, Q_i is the probability that exactly $(i-1)$ nontransmitted signals have a larger correlation with the received signal than does the transmitted signal. Let Q_{-i} be the probability that the negative of the transmitted signal appears i^{th} on the list. It is easily shown that, for M biorthogonal signals of energy E and for white noise with double-sided spectral density $N_o/2$,

$$Q_i = \binom{\frac{M}{2}-1}{i-1} \int_0^\infty \frac{1}{\sqrt{\pi}} exp\left\{-\left(y-\sqrt{\frac{E}{N_o}}\right)^2\right\} \left[erfc\,(y)\right]^{i-1} \left[erf(y)\right]^{\frac{M}{2}-i} dy ,$$

$$Q_{-i} = \binom{\frac{M}{2}-1}{i-1} \int_0^\infty \frac{1}{\sqrt{\pi}} exp\left\{-\left(y+\sqrt{\frac{E}{N_o}}\right)^2\right\} \left[erfc\,(y)\right]^{i-1} \left[erf\,(y)\right]^{\frac{M}{2}-i} dy , \tag{4}$$

where

$$erf\,(y) = \frac{2}{\sqrt{\pi}} \int_0^y e^{-t^2} dt$$

and

$$erfc\,(y) = 1 - erf\,(y). \tag{5}$$

In terms of these probabilities, R_o for list-of-L decoding can be written

$$R_o(L) = \log_2 M - 2\log_2 \left[\sum_{i=1}^{L} (\sqrt{Q_i} + \sqrt{Q_{-i}}) + \sqrt{(M-2L)\left\{1 - \sum_{i=1}^{L}(Q_i + Q_{-i})\right\}}\right],$$

$$1 \leq L \leq \frac{M}{2} . \tag{6}$$

3. Evaluation

Eq. (2)–(6) were programmed on a digital computer for $M = 4, 8, 16, 32$ and 64 and $L = 1, 2, \ldots,$ min, $\left\{\frac{M}{2}, 8\right\}$ for a range of values of $\frac{E}{N_o}$. The results are presented in Fig. 12 as plots of $E_b/E_{b,min}$ vs β. We observe that in no case does the performance match that of PSK modulation with 3-bit detector quantization; namely $E_b/E_{b,min} = 3.5$ db with $\beta = 15$. We conclude that with sequential decoding, use of biorthogonal modulation and list decoding is inferior to PSK modulation and 3-bit quantization on a coherent additive Gaussian noise channel.

References

1. Jaffee, R., and Rechtin, E., "Design and Performance of Phase-lock Circuits Capable of Near Optimum Performance Over a Wide Range of Input Signals and Noise Levels," *IRE Transactions on Information Theory*, IT-1:66-72, March 1955.

2. Davenport, W., and Root, W., *Random Signals and Noise*, McGraw-Hill Book Co., New York 1957.

3. Pierce, J. R., "Physical Sources of Noise," *Proceedings of the IRE*, Vol. 44, May 1956, pp. 601–608.

4. Malling, L., "Phase-Stable Oscillators for Deep-Space Communication," *Space Communications*. McGraw-Hill Book Co., New York, 1963.

5. Lindsey, W. C. "The Detection of PSK Signals With a Noisy Phase Reference," *Proceedings of the National Telemetering Conference*, April, 1965, pp. 50–54.

6. Lindsey, W. C., "Two-Way Doppler and Phase Measurements in Communication Networks" (to be published).

7. Gallager, R. G., "A Simple Derivation of the Coding Theorem and Some Applications," *IEEE Transactions on Information Theory*, Vol. IT-11, 1965, pp. 3–18.

8. Savage, J. E., *The Computation Problem with Sequential Decoding*, PhD Thesis, Department of Electrical Engineering, Massachusetts Institute of Technology, Cambridge, Massachusetts, February 1965.

9. Shannon, C. E., Gallager, R. G., and Berlekamp, E. R., paper on coding lower bounds (private communication), 1965.

10. Blustein, G., and Jordan, K. L., Jr., *An Investigation of the Fano Sequential Decoding Algorithm by Computer Simulation*, Massachusetts Institute of Technology, Lincoln Laboratory Report No. 62 G-5, July 12, 1963.

11. Stiglitz, I. G., *Sequential Decoding with Feedback*, PhD Thesis, Department of Electrical Engineering, Massachusetts Institute of Technology, Cambridge, Massachusetts, August 1963.

12. Wozencraft, J. M., and Kennedy, R. S., "Modulation and Demodulation for Probabilistic Coding," (to appear in *IEEE Transactions on Information Theory*).

QUALITY ASSURANCE AND RELIABILITY OFFICE

XXVII. Parts Reliability

A. Capacitor Sterilization Test Program

K. Stern

In compliance with the NASA policy of sterilizing all spacecraft having a possibility of planetary impact an extensive electronic component sterilization test program is under way at JPL. The primary objective of this program is to establish a sterilization parts list (JPL Specification ZPP-2010-SPL) that tabulates the electronic component parts capable of withstanding several 36-hr periods of non-operational storage at 145 C without significant degradation. Secondary objectives are to study derating effects, compare vendor quality, and perform analyses on long-term failure modes. A general discussion of the component parts sterilization program was previously presented in *SPS 37-30*, Vol. IV, pp. 279, 280. A summation of the capacitor sterilization test program is presented here.

Each of the selected manufacturers' part types is divided into four groups. Group A, consisting of 45 specimens, is not temperature-cycled and is the control group; Group B, consisting of 45 specimens, is temperature-cycled three times, each cycle consisting of 36 hr at 145°C followed by 24 hr at 25°C; Group C, consisting of 45 specimens, is temperature-cycled six times under the same conditions as those for Group B; Group D, consisting of 15 specimens, is temperature-cycled six times under the same conditions as those for Group B.

After temperature cycling, parametric measurements for capacitance, dissipation factor, and insulation resistance are compared with the initial test results and analyzed for significant changes. All test groups are then subjected to a 10,000-hr life test to simulate the long flight periods of planetary missions. During this life test, Groups A, B, and C are operated at maximum rated DC voltage and temperature. Group D parts are stored at maximum rated temperature, non-operational. Group B (3 cycles) and Group C (6 cycles) are compared with Group A (control group) at specific periods during the life test to detect significant parametric changes. Also, the "catastrophic" failures are monitored daily during the test.

Upon completion of the 10,000-hr life test, Group D is removed from temperature storage and, in conjunction

with Group C, is subjected to maximum rated DC voltage and temperature for an additional 250-hr life-test period. The purpose of testing Group D is to simulate conditions where flight equipment is involved in extended non-operational-type missions, being turned on remotely at or near its destination. Group C is included as a control group operated at maximum rated DC voltage and temperature to simulate an extended operational mission.

1. Description of Test Items

A total of 4200 capacitors representing 28 distinct types of the following dielectrics was selected for the test program: ceramic (medium K style), porcelain, glass, mica (dipped style), solid tantalum, foil tantalum, paper/plastic, and Mylar. Prior to ordering the units, the purpose of the sterilization test program was explained to each capacitor manufacturer whose parts were selected for evaluation. Therefore, each manufacturer had the same opportunity to submit "premium" capacitors with the best capabilities of meeting the objectives of this test program. In addition, the manufacturers were required to burn-in each capacitor for 250 hr at maximum rated DC voltage and temperature prior to shipment.

2. Status of Test Program

The capacitor phase of the program is nearing completion; the test was initiated on July 15, 1963, and is expected to be completed by June 15, 1965.

3. Test Conclusions

a. Effect of sterilization. The dielectrics most significantly affected by sterilization temperature cycling were the ceramic and solid tantalum types.

Ceramic dielectric. The capacitance and dissipation factor of the ceramic dielectric increased as a result of sterilization. However, during the 8000-hr life test at rated DC voltage and temperature, the capacitance and dissipation factor decreased gradually and approximated the values observed before sterilization. The temporary increase in capacitance and dissipation factor resulting from sterilization is probably acceptable, providing the circuit applications permit a maximum capacitance increase of 20% and a maximum dissipation factor value of 2.5% at 1 kc.

Solid tantalum dielectric. As a result of sterilization, the insulation resistance of certain test codes decreased by a factor of 10. After 100 hr of life testing at rated DC voltage and temperature, the insulation resistance of these test codes increased to the values observed prior to sterilization. However, at the same time several catastrophic failures occurred in one of the test codes whose insulation resistance was affected by sterilization, whereas the first catastrophic failures of the test codes unaffected by sterilization occurred after 4000 hr. After 8000 hr of life testing, the test codes affected by sterilization had only a slightly greater number of catastrophic failures.

Although this evidence is inconclusive, it would appear that solid tantalum capacitors whose insulation resistance is significantly decreased as a result of sterilization are more likely to become catastrophic failures in a shorter time when stressed at rated DC voltage and temperature. However, test codes whose insulation resistance was unaffected by sterilization produced catastrophic failures after 4000 hr of life and became progressively worse through 8000 hr, probably due to wear-out caused by stressing at maximum rated DC voltage and temperature. In an attempt to reduce the number of catastrophic failures and to isolate the effect of sterilization from normal wear-out, a retest of solid tantalum using a voltage/temperature type of matrix will soon be initiated.

4. Future Tests

a. Continuation of life testing. In order to acquire useful information regarding the wear-out behavior of specific dielectrics under longer-term operating life conditions, the following dielectric types will be tested for an additional 5000 hr: ceramic (medium K style), porcelain, glass, solid tantalum, foil tantalum, and Mylar.

b. Retest of new specimens. It is planned to retest new specimens of certain dielectrics using JPL specifications for procurement in order to test the effectiveness of this method of procurement in providing product improvement. The new specimens to be tested are: ceramic (medium K style), porcelain, glass, solid tantalum, foil tantalum, paper/plastic, and Mylar. In addition, a voltage/temperature matrix will be used for this retest to determine the possibilty of extending the time to wear-out by means of derating.